FUNDAMENTAL PARAMETERS IN COSMOLOGY

Paramètres fondamentaux en cosmologie

XXXIIIrd Rencontres de Moriond
Les Arcs, Savoie, France - January 17-24, 1998

Fundamental Parameters in Cosmology
Series: Moriond Workshop

ISBN 2-86332-233-8
© Copyright 1998 by Editions Frontières

All rights reserved.
This book, or parts thereof, may not be reproduced in any form or by any means, electronic or mechanical, including photocopying, recording or any information storage retrivial system now known or to be invented, without written permission from the Publisher.

EDITIONS FRONTIERES
22, rue Malher
75004 Paris - France

Printed in France

Proceedings of the XXXIIIrd RENCONTRES DE MORIOND
Series : Moriond workshops
Les Arcs, France *January 17-24, 1998*
Euroconference

FUNDAMENTAL PARAMETERS IN COSMOLOGY

edited by

J. Trân Thanh Vân
Y. Giraud-Héraud
F. Bouchet
T. Damour
Y. Mellier

EDITIONS
FRONTIÈRES

The XXXIIIrd Rencontres de Morlond

FUNDAMENTAL PARAMETERS IN COSMOLOGY

were organized by :

J. Trân Thanh Vân (Orsay)

with the active collaboration of :

R. Ansari (Orsay)
F. Bernardeau (Saclay)
M. Boratav (Paris)
F. Bouchet (Paris)
S. Colafrancesco (Roma)
T. Damour (Bures/Yvette)
J. Dumarchez (Paris)
O. Fackler (Livermore)
G. Fontaine (Palaiseau)
Y. Giraud-Héraud (Paris)
R. Gispert (Orsay)
B. Gulderdoni (Paris)
M. Kamionkowski (New York)
E. Kolb (FNAL)
C. Magneville (Saclay)
Y. Mellier (Paris)
J. Silk (Berkeley)

'98 RENCONTRES DE MORIOND

The XXXIIIrd Rencontres de Moriond were held in Les Arcs 1800, Savoie, France.

The first meeting took place at Moriond in the French Alps in 1966. There, experimental as well as theoretical physicists not only shared their scientific preoccupations but also the household chores. The participants in the first meeting were mainly French physicists interested in electromagnetic interactions. In subsequent years, a session on high energy strong interactions was also added.

The main purpose of these meetings is to discuss recent developments in contemporary physics and also to promote effective collaboration between experimentalists and theorists in the field of elementary particle physics.

By bringing together a relatively small number of participants, the meeting helps to develop better human relations as well as a more thorough and detailed discussion of the contributions.

This concern of research and experimentation of new channels of communication and dialogue which from the start has animated the Moriond meetings, inspired us to organize a simultaneous meeting of biologists on Cell Differenciation (1980) and to create the Moriond Astrophysics Meeting (1981). In the same spirit, we have started a new series on Condensed Matter Physics in January 1994. Common meetings between biologists, astrophysicists, condensed matter physicists and high energy physicists are organized to study the implications of the advances of one field into the others. I hope that these conferences and lively discussions may give birth to new analytical methods or new mathematical languages.

At the XXXIIIrd Rencontres de Moriond in 1998, three physics sessions, one astrophysics session and one biology session were held :

* January 17-24 "Fundamental Parameters in Cosmology"
* March 14-21 "Electroweak Interactions and Unified Theories"
  "Dwarf Galaxies and Cosmology"
* March 21-28 "QCD and High Energy Hadronic Interactions"
  "Rencontre de Biologie - Méribel "

I thank the organizers of the XXXIIIrd Rencontres de Moriond :

- R. Ansari, F. Bernardeau, M. Boratav, F. Bouchet, S. Colafrancesco, T. Damour, J. Dumarchez, O. Fackler, G. Fontaine, Y. Giraud-Héraud, R. Gispert, B. Guiderdoni, M. Kamionkowski, E. Kolb, C. Magneville, Y. Mellier and J. Silk

- P. Binetruy, J. Bagger , A. Blondel, G. Coignet, L. Fayard, P. Fayet, J.-M. Frère, H. Frisch, L. Krauss, S. Loucatos, L. Okun, L. Randall, C. Savoy, G. Unal and D. Wood for the Electroweak Interaction session,

- C. Balkowski, V. Cayatte and Trinh Xuân Thuân for the Extragalactic Astronomy in the Infrared session,

- E. Augé, P. Aurenche, E. Berger, A. Capella, D. Denegri, B. Klima, L. Kluberg, L. McLerran, L. Montanet, B. Pietrzyck, D. Schiff, Tan Chung I and C. Voltolini for the QCD and Hadronic Interaction session,

- M. Fellous, C. Le Guern, P. Sonigo and K. Tran Thanh Van for the Biology meeting,

and the conference secretariat : C. Barthélémy, R. Bilhaut, I. Cossin, F. Delmas, S. Kimmel, C. Le Marec, H. Mauger, C. Morel, Pham Duy Tu, A. M. Renault-Perrin, M. Ruffler and C. Windrif.

I am also grateful to Mr. and Ms. E. Rocca-Serra, Ms. C. Dufourny, Ms. S. Kovalevsky who contributed through their hospitality and cooperation to the well-being of the participants enabling them to work in a relaxed atmosphere.

These Rencontres were sponsored by the European Union Training and Mobility of Researchers Program, the Centre National de la Recherche Scientifique (INSU, SPM and FP), the Institut National de Physique Nucléaire et de Physique des Particules (IN2P3-CNRS), the Commissariat à l'Energie Atomique (DAPNIA), the Ministère de l'Enseignement Supérieur et de la Recherche (programme ACCES) and the National Science Foundation. I would like to express my thanks for their encouraging support.

I sincerely wish that a fruitful exchange and an efficient collaboration between the physicists, the astrophysicists and the biologists will arise from these Rencontres as from the previous ones.

J. Trân Thanh Vân

CONTENTS

Foreword

I - THE VERY EARLY UNIVERSE

Cosmic microwave background observations as a way to discriminate among inflation models.	*W. Kinney*	3
Could the CMBR dipole be cosmological ?	*D. Langlois*	9
Topological defects in multi-connected universes.	*J.Ph. Uzan*	15
Cosmological and astrophysical implications of superconducting cosmic strings and vortons.	*A. Gangui*	19
Structure formation and light gravitinos warm dark matter.	*E. Pierpaoli*	25
Preheating the universe in hybrid inflation.	*J. Garcia-Bellido*	29
Non-equilibrium aspects of inflationary cosmology.	*R. Holman*	35
Recent developments in electroweak baryogenesis.	*A. Riotto*	41
Pre-big bang cosmology: an introduction.	*G. Veneziano*	47
Primeval magnetic seeds from pre-big bang string cosmology.	*A. Buonanno*	55
Cosmic gravitational wave background in string cosmology.	*R. Brustein*	59
Seeds of large-scale CMB anisotropy in string cosmology.	*M. Sakellariadou*	65
U-duality and M-theory cosmology.	*B.A. Ovrut*	71
CDM models with a broken-scale-invariant spectrum.	*J. Lesgourgues*	77
Inflation and the microwave background.	*A. R. Liddle*	81
Primordial magnetic fields that last ?	*S.M. Carroll*	87
Nonzero Ω_Λ and a new type of a dissipative structure.	*Y. Fujii*	93
Amplitude of superhorizon cosmological perturbations.	*J. Martin*	97

II - THE COSMIC MICROWAVE BACKGROUND

Constraints on cosmological parameters from existing CMB data.	*J.G. Bartlett*	103
Polarization of microwave background: statistical and physical properties.	*U. Seljak*	107
Cosmological-parameter determination with cosmic microwave background temperature anisotropies and polarization.	*M. Kamionkowski*	117
Probing cosmic topology using CMB anisotropy.	*T. Souradeep*	131
Topological defects with broken scale invariance.	*U.L. Pen*	135
Cosmic strings in a universe with non-critical matter density.	*R. Battye*	139
Extragalactic point sources and the Planck Surveyor mission.	*G. De Zotti*	143
Rising spectrum foreground sources.	*K. Grainge*	151
Lensed submillimetre-wave foregrounds and the CMBR.	*A.W. Blain*	157
Why H_o from S-Z + X-ray works in practice.	*R. Saunders*	161
Fast determination of the power spectrum from cosmic microwave background sky maps .	*A. Refregier*	165
Moving gravitational lens effect.	*N. Aghanim*	169
Main beam and sidelobe effects on Planck observations.	*C. Burigana*	171
Synchrotron emission from the galaxy.	*A. Wilkinson*	175
Galactic free-free emission and Hα.	*P. Amram/J. Bartlett*	183
Galactic dust polarized emission at high latitudes and CMB polarization.	*S. Sethi*	191
Multi-frequency Wiener filtering of CMB data with polarization and estimation of cosmological parameters.	*S. Prunet*	195
Measuring the cosmic microwave background at 3 cm.	*S.T. Staggs*	199
Multifractal analysis of the 4-yr COBE DMR experiment.	*J.M. Diego*	201
Theoretical predictions of CMB anisotropies generated by scaling seeds versus current observational data.	*M. Sakellariadou*	205
CMB anisotropy measurements using stratospheric balloons.	*P. De Bernardis*	209

Review of ground-based CMB experiments.	*A. Lasenby*	221
Detection of CMB anisotropies in a second field with CAT.	*J. Baker*	229
The very small array : status report.	*M.E. Jones*	233
Topological analysis of high-resolution CMB MAPS.	*B.D. Wandelt*	237
The effect of point sources on satellite observations of the CMB.	*M.P. Hobson*	241
Electronic intracluster gas temperature determination with SZ measurements.	*E. Pointecouteau*	245
MAP. The microwave anisotropy probe.	*N. Jarosik*	249
The current status of Planck.	*J.A. Tauber*	255
Studies on the optical characteristics of the Planck telescope.	*F. Villa*	261
CMB anisotropies on circular scans.	*J. Delabrouille*	263
Large scale properties of the far-infrared background.	*L. Popa*	267

III - New approaches to measure fundamental parameters

Testing Ω_o from clusters: low and high redshift.	*A. Blanchard*	273
The Ω_M - Ω_Λ constraint from CNOC clusters.	*R.G. Carlberg*	279
Testing Ω_0 with X-ray clusters : a physical approach.	*P. Tozzi*	283
Evolution of the cluster abundance from the RDCS.	*S. Borgani*	289
The effects of large scale structure on cluster substructure and cluster temperature distributions.	*W. Forman*	293
Clusters, cosmology and AXAF.	*C. Jones*	297
Cosmology and clusters of galaxies with XMM, the X-ray multi-mirror mission.	*M. Arnaud*	301
The XMM medium deep survey.	*M. Pierre*	307
Probing the hot IGM with AXAF.	*C.R. Canizares*	309
High-redshift quasars as probes of primordial large-scale structure and galaxy formation.	*S.G. Djorgovski*	313
Global cosmological parameters measured using classical double radio sources.	*R.A. Daly*	323
Short review on non-baryonic dark matter searches (mostly cryogenic experiments).	*M. Chapellier*	327
Microlensing: thème et variations. A review.	*M. Moniez*	331
Comparison of the SFI peculiar velocities with the IRAS 1.2 Jy gravity field.	*A. Nusser*	343
Large-scale density-velocity relations.	*M.J. Chodorowski*	347
What should be the geometry of a galaxy catalog ?	*S. Colombi*	351
Cosmic complementarity: combining CMB and supernova observations.	*M. Tegmark*	355
Weak lensing effects to probe the cosmological parameters.	*F. Bernardeau*	359
Numerical investigations of weak lensing by large-scale structure.	*B. Jain/U. Seljak*	367
Weak gravitational lensing and foreground-background correlations.	*J.L. Sanz*	375
Cluster mass profile from combined strong and weak lensing.	*H.M. Abdelsalam*	381
Weak lensing around clusters to constrain Ω and Λ.	*L. Gautret*	385
Arcs statistics as a probe of galaxy evolution.	*J. Bezecourt*	389
Gravitational lens magnification : analysis of A1689.	*S. Dye*	393
Hipparcos and distance and age primary indicators.	*C. Turon*	397
Period-luminosity relation for short periods Cepheids towards the SMC.	*F. Bauer*	403
Intermediate redshift supernova search with EROS.	*D. Hardin*	407
A review of the high-redshift supernova searches.	*A. Kim*	411
Cosmic deceleration measured with type Ia supernovae.	*B. Leibundgut*	417

IV - Summary and conclusions

Today's cosmological constants.	*R.G. Carlberg*	423
The golden age of cosmology	*E.W. Kolb*	429
Abstracts in French		433
List of participants		447

THE VERY EARLY UNIVERSE

COSMIC MICROWAVE BACKGROUND OBSERVATIONS AS A WAY TO DISCRIMINATE AMONG INFLATION MODELS

WILLIAM H. KINNEY[a], SCOTT DODELSON[a], EDWARD W. KOLB[a,b]
[a] *Fermi National Accelerator Laboratory*
Batavia, IL 60510-0500
[b] *Department of Astronomy and Astrophysics, Enrico Fermi Institute, The University of Chicago, Chicago. IL 60637*

The upcoming satellite missions MAP and Planck will measure the spectrum of fluctuations in the Cosmic Microwave Background with unprecedented accuracy. We discuss the prospect of using these observations to distinguish among proposed models of inflationary cosmology. (Fermilab CONF-98/102-A)

1 Introduction

There has been great interest recently in the topic of parameter reconstruction from the Cosmic Microwave Background (CMB). Most of the emphasis in the literature is on the question of determining cosmological parameters such as the density Ω_0, the Hubble constant H_0, or the value of the cosmological constant Λ. The purpose of this talk is to take a different approach and apply the machinery of CMB parameter estimation to the subject of inflationary model building.[1] We assume generic features of the universe consistent with inflation (a flat universe, vanishing Λ), but allow parameters sensitive to inflation to vary. The goal is to determine how well we will be able to distinguish between popular inflation models using upcoming CMB experiments, in particular the all-sky satellite missions MAP and Planck.

The parameters that are of interest for inflation are the ratio of tensor to scalar fluctuation amplitudes measured at the quadrupole $r \equiv C_2^{\rm tensor}/C_2^{\rm scalar}$, and the spectral index of scalar fluctuations n. Fixed parameters are the density of the universe $\Omega_0 = 1$, and the present vacuum energy $\Lambda = 0$. Other parameters are allowed to vary, and we plot the expected sensitivity of NASA's MAP satellite[2] and the ESA's Planck Surveyor[3] as ellipses projected onto the $r - n$ plane.

2 Parameterizing Inflation

Inflation in its most general sense can be defined to be a period of accelerated expansion of the universe, during which the universe evolves toward homogeneity and flatness. This acceleration is typically due to the energy density of the universe being dominated by vacuum energy, with equation of state $p \simeq -\rho$. Within this broad framework, many specific models for inflation have been proposed. We limit ourselves here to models with "normal" gravity (i.e., general relativity) and a single order parameter for the vacuum, described by a slowly rolling scalar field ϕ (the *inflaton*). These assumptions are not overly restrictive – most widely studied inflation models

fall within this category, including Linde's "chaotic" inflation scenario, inflation from pseudo Nambu-Goldstone bosons ("natural" inflation), dilaton-like models involving exponential potentials (power-law inflation), hybrid inflation, and so forth. Other models, such as Starobinsky's R^2 model and verions of extended inflation, can, through a suitable transformation, be viewed in terms of equivalent single-field models.

The slow-roll approximation, in which the field evolution is dominated by drag from the cosmological expansion, is consistent if both the slope and curvature of the potential are small, V', $V'' \ll V$. This condition is conventionally expressed in terms of the "slow-roll parameters" ϵ and η

$$\epsilon \equiv \frac{M_{Pl}^2}{4\pi}\left(\frac{H'(\phi)}{H(\phi)}\right) \simeq \frac{M_{Pl}^2}{16\pi}\left(\frac{V'(\phi)}{V(\phi)}\right)^2, \tag{1}$$

and

$$\eta(\phi) \equiv \frac{M_{Pl}^2}{4\pi}\left(\frac{H''(\phi)}{H(\phi)}\right) \simeq \frac{M_{Pl}^2}{8\pi}\left[\frac{V''(\phi)}{V(\phi)} - \frac{1}{2}\left(\frac{V'(\phi)}{V(\phi)}\right)^2\right]. \tag{2}$$

Slow-roll is then a consistent approximation for ϵ, $\eta \ll 1$. The parameter ϵ can in fact be shown to directly parameterize the equation of state of the scalar field, $p = -\rho(1 - 2/3\epsilon)$, so that the condition for inflation of accelerating expansion is exactly equivalent to $\epsilon < 1$. To match the observed degree of flatness and homogeneity is the universe, we require many e-folds of inflation, typically $N \simeq 50$.

Inflation not only explains the high degree of large-scale homogeneity in the universe, but also provides a mechanism for explaining the observed *inhomogeneity* as well. The metric perturbations created during inflation are of two types: scalar, or *curvature* perturbations, which couple to the stress-energy of matter in the universe and form the "seeds" for structure formation, and tensor, or gravitational wave perturbations, which do not couple to matter. Both scalar and tensor perturbations contribute to CMB anisotropy. Scalar fluctuations can be quantitatively described by perturbations $P_{\mathcal{R}}$ in the intrinsic curvature scalar

$$P_{\mathcal{R}}^{1/2}(k) = \left.\frac{1}{\sqrt{\pi}}\frac{H}{M_{Pl}\sqrt{\epsilon}}\right|_{k^{-1}=d_H}. \tag{3}$$

The fluctuation power is in general a function of wavenumber k, and is evaluated when a given mode crosses outside the horizon during inflation $k^{-1} = d_H$. Outside the horizon, modes do not evolve, so the amplitude of the mode when it crosses back *inside* the horizon during a later radiation or matter dominated epoch is just its value when it left the horizon during inflation. The *spectral index* n is defined by assuming an approximately power-law form for $P_{\mathcal{R}}$ with

$$n - 1 \equiv \frac{d\ln(P_{\mathcal{R}})}{d\ln(k)} \simeq 1 - 4\epsilon + 2\eta, \tag{4}$$

so that a scale-invariant spectrum, in which modes have constant amplitude at horizon crossing, is characterized by $n = 1$. Instead of specifying the fluctuation amplitude directly as a function of k, it is often convenient to specify it as a function of the number of e-folds N before the end of inflation at which a mode crossed outside the horizon. Scales of interest for current measurements of CMB anisotropy crossed outside the horizon at $N \simeq 50$, so that $P_{\mathcal{R}}$ is conventionally evaluated at $P_{\mathcal{R}}(N = 50)$. Similarly, the power spectrum of tensor fluctuation modes is given by

$$P_T^{1/2}(k_N) = \left.\frac{1}{\sqrt{\pi}}\frac{H}{M_{Pl}}\right|_{N=50} \tag{5}$$

The tensor spectral index is

$$n_T = -2\epsilon = -2\frac{P_T}{P_{\mathcal{R}}}. \tag{6}$$

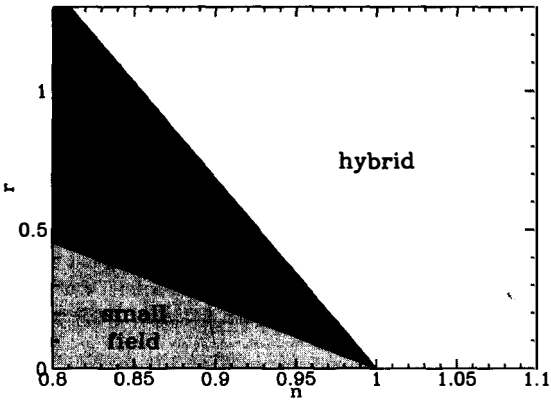

Figure 1: The parameter space divided into regions for small-field, large-field and hybrid models. The linear case is the dividing line between large- and small-field.

Note that n_T is *not* independent of the other parameters $P_{\mathcal{R}}$, P_T, and n. Equation (6) is known as the *consistency condition*, and is true only for single-field models. (In models with multiple degrees of freedom, Eq. (6) weakens to an inequality.) We then have three independent parameters for describing inflation models: $P_{\mathcal{R}}$, P_T, and n. Equivalently, we can use normalization $P_{\mathcal{R}}$ and the two slow-roll parameters ϵ and η. This will prove to be the more convenient choice for categorizing models. For comparing to observation, it proves convenient to use a different set of three parameters: normalization at the quadrupole $Q_{\rm rms-PS}$ (equivalent to $P_{\mathcal{R}}$), spectral index n, and tensor-to-scalar ratio r. The ratio r of tensor to scalar modes *measured at the quadrupole* is[4]

$$r \equiv \frac{C_2^{\rm Tensor}}{C_2^{\rm Scalar}} = 13.7\epsilon, \tag{7}$$

so that tensor modes are negligible for $\epsilon \ll 1$. It is a simple matter to transform between slow-roll parameters ϵ, η and the parameters n and r.

3 Inflationary Zoology

Even with the restriction to single-field, slow-roll inflation, the number of models in the literature is large. It is convenient to define a general classification scheme, or "zoology" for models of inflation. we divide models into three general types: *large-field*, *small-field*, and *hybrid*, with a fourth classification, *linear* models, serving as a boundary between large- and small-field. A generic single-field potential can be characterized by two independent mass scales: a "height" Λ^4, corresponding to the characteristic vacuum energy density during inflation, and a "width" μ, corresponding to the characteristic change in the field value $\Delta\phi$ during inflation. The height Λ is fixed by normalization, so the only remaining free parameter is the width μ. Different classes of model are distinguished by the value of the second derivative of the potential, or, equivalently, by the relationship between the values of the slow-roll parameters ϵ and η. These different classes of models have readily distinguishable consequences for the CMB. Figure 1 shows the $r - n$ plane divided up into regions representing the large-field, small-field and hybrid cases, describe in detail below.

3.1 *Large-field models:* $0 < \eta \leq \epsilon$

Large-field models are potentials typical of "chaotic" inflation scenarios, in which the scalar field is displaced from the minimum of the potential by an amount usually of order the Planck mass. Such models are characterized by $V''(\phi) > 0$, and $0 < \eta \leq \epsilon$. The generic large-field potentials we consider are polynomial potentials $V(\phi) = \Lambda^4 (\phi/\mu)^p$, and exponential potentials, $V(\phi) = \Lambda^4 \exp(\phi/\mu)$. For the case of power-law inflation, $V(\phi) \propto \exp(\phi/\mu)$, the slow-roll parameters are

$$\epsilon = \eta \propto (M_{Pl}/\mu)^2 , \tag{8}$$

and $r = 7(1-n)$. This result is often incorrectly generalized to all slow-roll models, but is in fact characteristic *only* of power-law inflation. Note that we have a one-parameter family of models, parameterized by the width μ. For chaotic inflation with a polynomial potential $V(\phi) \propto \phi^p$, the slow-roll parameters are

$$\epsilon = \frac{p}{p+200} = \left(\frac{p}{p-2}\right)\eta. \tag{9}$$

Again we have $r \propto 1-n$, so that tensor modes are large for significantly tilted spectra. Unlike the case of the exponential potential, the scale μ drops out of the expressions for the observables, and the models are parameterized by the *discrete* exponent p.

3.2 *Small-field models:* $\eta < 0 < \epsilon$

Small-field models are the type of potentials that arise naturally from spontaneous symmetry breaking. The field starts from near an unstable equilibrium and rolls down the potential to a stable minimum. Small field models are characterized by $V''(\phi) < 0$ and $\eta < 0 < \epsilon$. The generic small-field potentials we consider are of the form $V(\phi) = \Lambda^4 [1 - (\phi/\mu)^p]$. In all cases, the slow-roll parameter ϵ is very small, so that tensor modes are negligible. The cases $p = 2$ and $p > 2$ have very different behavior. For $p = 2$, the slow-roll parameter η is

$$\eta \propto -(M_{Pl}/\mu)^2, \tag{10}$$

so that the width of the potential $\Delta\phi \sim \mu$ must be of order M_{Pl} for the spectral index $n \simeq 1+2\eta$ to satisfy observational constraints. As in the case of the exponential potential, the $p = 2$ small-field case is a one-parameter family of models. For $p > 2$,

$$\eta \propto -\left(\frac{p-1}{p-2}\right) \tag{11}$$

is *independent* of M_{Pl}/μ, so that $\Delta\phi \sim \mu \ll M_{Pl}$ is consistent with a nearly scale-invariant scalar fluctuation spectrum.

3.3 *Hybrid models:* $0 < \epsilon < \eta$

The hybrid scenario frequently appears in models which incorporate inflation into supersymmetry. In a hybrid inflation scenario, the scalar field responsible for inflation evolves toward a minimum with nonzero vacuum energy. The end of inflation arises as a result of instability in a second field. Hybrid models are characterized by $V''(\phi) > 0$ and $0 < \epsilon < \eta$. We consider generic potentials for hybrid inflation of the form $V(\phi) = \Lambda^4 [1 + (\phi/\mu)^p]$. The field value at the end of inflation (and hence $\phi_{N=50}$) is determined by some other physics, and we treat $\phi_{N=50}$ in this case as a freely adjustable parameter. The slow-roll parameters are then related as

$$\frac{\eta}{\epsilon} = \frac{2(p-1)}{p}\left(\frac{\mu}{\phi_{N=50}}\right)^p \tag{12}$$

The distinguishing feature of many hybrid models is a *blue* scalar spectral index, $n > 1$. This corresponds to the case $\eta >> \epsilon$, or $\phi_{N=50} \ll \mu$. Because of the extra freedom to choose the field value at the end of inflation, hybrid models form a *two*-parameter family. There is, however, no overlap in the $r - n$ plane between hybrid inflation and other models.

3.4 Linear models: $\eta = -\epsilon$

Linear models, $V(\phi) \propto \phi$, live on the boundary between large-field and small-field models, with $V''(\phi) = 0$ and $\eta = -\epsilon$.

4 Parameter Estimation from the CMB

Observations of the CMB don't directly measure r and n. What is actually measured is anisotropy in the temperature of the CMB as a function of angular scale. It is convenient to expand the temperature anisotropy on the sky in spherical harmonics:

$$\frac{\delta T(\theta,\phi)}{T_0} = \sum_{l=0}^{\infty} \sum_{m=-l}^{l} a_{lm} Y_{lm}(\theta,\phi) \tag{13}$$

where $T_0 = 2.726°K$ is the average temperature of the CMB today. Inflation predicts that each a_{lm} will be Gaussian distributed with mean zero and variance $C_l \equiv \langle |a_{lm}|^2 \rangle$. For Gaussian fluctuations, the set of C_l's completely characterizes the fluctuations. The spectrum of the C_l's is in turn dependent on cosmological parameters - Ω_0, H_0, Ω_B, and so forth. The dependence on parameters is complicated, and a spectrum of C_l's for a given set of cosmological parameters is calculated by numerically evaluating a Boltzmann equation[6]. Given a set of observational uncertainties ΔC_l in the CMB spectrum, the goal is to determine observational uncertainties in n and r. Given a set of parameters $\{\lambda_i\}$, assume a true set of values λ^{true}. The *Fisher information matrix*, given by

$$\alpha_{ij} = \sum_l \left(\frac{\partial C_l}{\partial \lambda_i}\right)_{\lambda=\lambda^{\text{true}}} \frac{1}{(\Delta C_l)^2} \left(\frac{\partial C_l}{\partial \lambda_j}\right)_{\lambda=\lambda^{\text{true}}}, \tag{14}$$

characterizes the accuracy with which the parameters λ_i can be measured, with the typical error in the i^{th} parameter being of order $\sqrt{(\alpha^{-1})_{ii}}$. The parameters we marginalize over are the spectral index n, the tensor to scalar ratio r, the normalization $Q_{\text{rms-PS}}$, baryon fraction Ω_B, and the Hubble constant H_0. Fixed parameters are the matter fraction $\Omega_0 = 1$ and the cosmological constant $\Omega_\Lambda = 0$. We consider central values for the parameters

$$\{\lambda^{\text{true}}\} = \{n, r, Q_{\text{rms-PS}}, \Omega_B, H_0\} = \{0.9, 0.7, 18\mu\text{K}, 0.08, 50\}. \tag{15}$$

The expected uncertainty in the C_l's for a given experiment can be estimated as[7]

$$\Delta C_l = \sqrt{\frac{2}{2l+1}} \left[C_l + \sigma^2_{\text{pixel}} \Omega_{\text{pixel}} \exp\left(l^2 \sigma^2_{\text{beam}}\right)\right], \tag{16}$$

where σ^2_{pixel} is the rms pixel nose, Ω_{pixel} is the area of a pixel in steradians, and σ^2_{beam} is the width of the beam, which is assumed to be gaussian. For MAP, we take $\sigma_{\text{beam}} = 0.425 \times 0.3°$ and $\sigma^2_{\text{pixel}} \Omega_{\text{pixel}} = (35\mu\text{K})^2 (0.3°)^2$. For Planck, we take $\sigma_{\text{beam}} = 0.425 \times 0.167°$ and $\sigma^2_{\text{pixel}} \Omega_{\text{pixel}} = (3\mu\text{K})^2 (0.167°)^2$. Figure 2 shows the generic inflation models plotted in the $r - n$ plane with typical 2σ error ellipses from MAP and Planck.

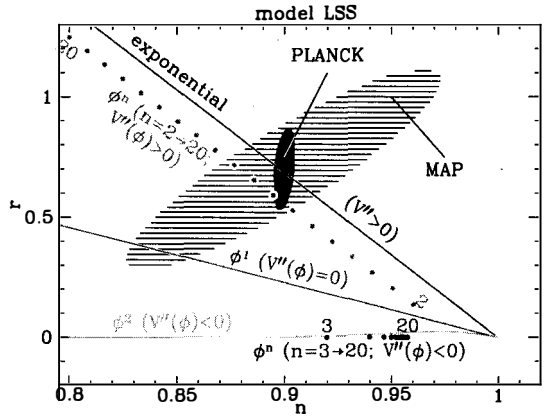

Figure 2: Inflation models plotted in the $r - n$ plane, with 2σ error ellipses from MAP and Planck.

5 Conclusions

It is evident from Figure 2 that MAP will allow at least rough distinction between large-field, small-field, and hybrid models. Planck, on the other hand, will allow for the beginnings of real precision work in constraining inflation models. Planck will be capable, for instance, of distinguishing the exponent p in a chaotic inflation model $V(\phi) \propto \phi^p$. David Lyth has presented arguments that an appreciably large r is theoretically disfavored.[5] We finish by noting that these arguments will be put to observational test within the next few years!

Acknowledgments

We thank Uros Seljak and Matias Zaldarriaga for use of their CMBFAST code. This work was supported in part by DOE and NASA grant NAG5-7092 at Fermilab.

References

1. For details and additional references, see S. Dodelson, W. H. Kinney, and E. W. Kolb, *Phys. Rev. D* **56**, 3207 (1997).
2. http://map.gsfc.nasa.gov/
3. http://astro.estec.esa.nl/SA-general/Projects/Planck/
4. M. S. Turner, M. White and J. E. Lidsey, *Phys. Rev. D* **48**, 4613 (1993).
5. D. H. Lyth, *Phys. Rev. Lett.* **78**, 1861 (1997).
6. U. Seljak and M. Zaldarriaga, astro-ph/9603033.
7. L. Knox, *Phys. Rev. D* **52**, 4307 (1995).

COULD THE CMBR DIPOLE BE COSMOLOGICAL ?

DAVID LANGLOIS
Département d'Astrophysique Relativiste et de Cosmologie,
C.N.R.S., Observatoire de Paris-Meudon, 92195 Meudon, France

The observed dipole is generally interpreted as a Doppler effect due to the motion of the Earth with respect to the CMBR frame. An alternative, or complementary, interpretation, which has been proposed in the past years, is that the CMBR dipole, or at least a significant part of it, could be produced by an entropy gradient. We examine this idea in the framework of cosmological perturbation theory in both flat and open FLRW models. It is shown that a significant CMBR dipole, compatible with small quadrupole and higher multipoles, can be obtained from *ultra-large scale* (larger than one hundred times the current Hubble radius) *isocurvature* perturbations, but only in a *flat or quasi-flat* universe. Finally, it is shown that a simple model of double inflation can produce the spectrum of perturbations required to get a significant cosmological contribution to the dipole.

1 Introduction

In the standard Big Bang scenario, the oldest relic from the early universe is the Cosmic Microwave Background Radiation (CMBR). This radiation is remarkably close to isotropy. When it is decomposed into multipoles,

$$\frac{\Delta T}{T}(\theta,\phi) = \sum_{l=1}^{\infty} \sum_{m=-l}^{l} a_{lm} Y_{lm}(\theta,\phi), \tag{1}$$

one finds that the dipole contribution is of the order $(\Delta T/T)_{l=1} \sim 10^{-3}$, while the contribution from higher multipoles is only $(\Delta T/T)_{l>1} \sim 10^{-5}$. Usually, the dipole term is interpreted as a Doppler effect, i.e. as the consequence of our local motion with respect to the "CMBR rest frame". However, cosmological perturbations also give a contribution to the dipole. In most scenarios, the cosmological contribution to the dipole is negligible with respect to the expected

Doppler contribution. But, in some cases, investigated here, the contribution can turn out to be significant.

The main difficulty to obtain an important cosmological contribution to the dipole is that, generally, one will expect a similar contribution to the next multipoles, whereas observations show that they are two orders of magnitude smaller than the dipole. The only way to satisfy these strong observational constraints is to consider ultra large scale perturbations, i.e. perturbations whose wavelength is much bigger than the current Hubble radius. We are thus faced with an old question: can we "see" perturbations of sizes beyond our Hubble radius ? This question was answered positively by Grishchuk and Zel'dovich[1] in 1978, provided perturbations are assumed to be statistically independent. Recently, the same question was addressed in the case of an open universe[2].

The question we are concerned with here is more specific: can such long wavelength perturbations give a significant contribution to the dipole ? But our investigations are broader in the sense that we allow for both flat and open universes and for both adiabatic and isocurvature perturbations. First hints were given originally[3] by a toy-model based on a Tolman-Bondi spacetime. This was generalized to the more general context (for cosmology) of the standard theory of cosmological linear perturbations about a Friedmann-Lemaître-Robertson-Walker universe, first in the flat case[4], then in the open case[5].

2 From long wavelength primordial perturbations to the CMBR multipoles

We consider a scalarly perturbed FLRW universe, endowed with the metric (in the longitudinal gauge)

$$ds^2 = a^2(\eta)\left[-(1+2\Phi)d\eta^2 + (1-2\Psi)\gamma_{ij}dx^i dx^j\right]. \tag{2}$$

where γ_{ij} is the metric of a flat or curved maximally symmetric space. The anisotropic stress of matter will be assumed to vanish so that $\Phi = \Psi$. The CMBR fluctuations can be written in the form[5]

$$\left(\frac{\delta T}{T}\right)_R = \left(\frac{\delta T}{T}\right)_{int} + \left(\frac{\delta T}{T}\right)_{pSW} + \left(\frac{\delta T}{T}\right)_{Dop} + \left(\frac{\delta T}{T}\right)_{ISW}, \tag{3}$$

with

$$\left(\frac{\delta T}{T}\right)_{int} = \frac{1}{4}\delta_{\gamma|ls}, \quad \left(\frac{\delta T}{T}\right)_{pSW} = (\Phi + hV)_{ls}, \quad \left(\frac{\delta T}{T}\right)_{Dop} = e^i\partial_i(V_0 - V_{ls}), \tag{4}$$

and

$$\left(\frac{\delta T}{T}\right)_{ISW} = \int_{ls}^{0} d\lambda\,(\Phi' + \Psi'), \tag{5}$$

where $\delta_{\gamma|ls}$ is the radiation density contrast on the last scattering surface, $h \equiv a'/a$ and V is the matter velocity potential. The four terms on the right hand side of (3) are called respectively the intrinsic term (int), the pure Sachs-Wolfe term (pSW), the Doppler term (Dop) and the integrated Sachs-Wolfe term (ISW). Note that this decomposition is made only for convenience, only the sum is physically relevant.

Any gaussian random field can be expanded in the form

$$f(r,\theta,\phi,\eta) = \int_0^\infty dk \sum_{l=0}^{\infty}\sum_{m=-l}^{l} f_{klm}(\eta)Q_{klm}(r,\theta,\phi), \tag{6}$$

where the Q_{klm} are eigenfunctions of the spatial Laplacian with eigenvalues $-k^2$. They can be chosen of the form

$$Q_{klm} = \Pi_{kl}(r)Y_{lm}(\theta,\phi), \tag{7}$$

where $Y_{lm}(\theta,\phi)$ are the usual spherical harmonics on the two-sphere. In the case of a flat universe, the $\Pi_{kl}(r)$ are related to the spherical Bessel functions by

$$\Pi_{kl}(r) = \sqrt{\frac{2}{\pi}} k j_l(kr) \qquad \text{(flat)}. \tag{8}$$

In the case of an open universe, the radial functions are more complicated[6]. They can be divided into supercurvature modes ($q^2 \equiv k^2 - 1 < 0$) and subcurvature modes ($q^2 > 0$).

Once a power spectrum is given, defined by

$$\langle \Phi_{klm} \Phi^*_{k'l'm'} \rangle = \frac{2\pi^2}{k|q|^2} \mathcal{P}_\Phi(k) \delta(k-k') \delta_{ll'} \delta_{mm'}, \tag{9}$$

(the definition in the flat case is obtained simply by substituting k^2 to $|q|^2$) the expectation values for the harmonic coefficients can then be written in the form

$$\langle |a_{lm}|^2 \rangle = \frac{4\pi}{9} \int \frac{dk}{k} \mathcal{P}_\Phi(k) \mathcal{W}_l^2(k), \tag{10}$$

where $\mathcal{W}_l(k)$ is the sum of all the relevant window functions, whose explicit form[5] follows from Eq. (3) and the perturbed Einstein equations.

3 Adiabatic versus isocurvature pertubations in flat or open universes

After having set the general formalism in the previous section, let us now examine in turn the observational consequences of adiabatic or isocurvature perturbations, both on scales larger than the present Hubble radius. The essential difference lies in the intrinsic contribution. For *adiabatic* initial conditions, the intrinsic term can be neglected, both in the open and flat cases. But, for *isocurvature* initial conditions,

$$\delta_{\gamma|ls} \simeq -\frac{4}{3} S \simeq \frac{20}{3} \Phi \qquad \text{(isocurvature)}, \tag{11}$$

where $S \equiv \delta_\gamma - (3/4)\delta_r$ is the entropy perturbation ($\delta_m \equiv \delta\rho_m/\rho_m$ is the density contrast of pressureless matter).

Let us now turn to the differences that arise from the curvature of space. They are of two types. The first difference comes from the different behaviour of the radial mode functions on large scales. Typically, in the flat case, going from one multipole to the next one will decrease the corresponding amplitude by a factor $k/(aH)$. But this is no longer true in an open universe where the radial mode functions also depend on the curvature scale. The second distinction between a flat universe and an open universe comes from the evolution of the gravitational potential. In the flat case, the superhorizon modes for Φ are constant in time and $hV = -(2/3)\Phi$, whereas

	Adiabatic	Isocurvature
$\Omega = 1$	0 $[pSW]$	Int $[Int + pSW]$
$\Omega < 1$	ISW $[pSW + ISW]$	$Int + ISW$ $[Int + pSW + ISW]$

Table 1: Main cosmological contribution to the CMBR dipole [and to the quadrupole] from long wavelength *adiabatic* or *isocurvature* perturbations in *flat* or *open* universes

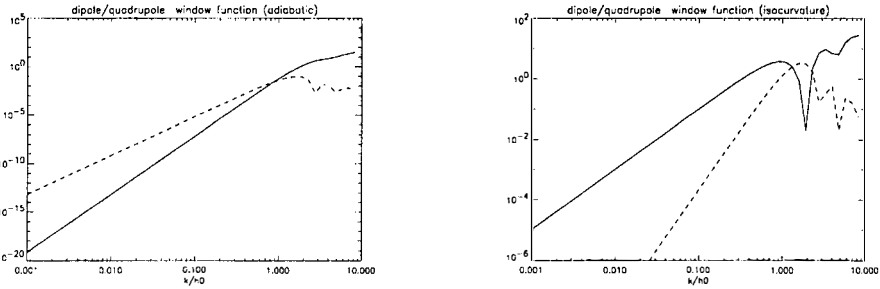

Figure 1: squared amplitude of the window functions for the dipole (solid curve) and the quadrupole (dashed curve) in the *adiabatic* case (left figure) and in the *isocurvature* case (right figure).

one finds explicit time dependence in the open case. The consequence will be that the ISW contribution will vanish for $\Omega = 1$.

Finally there is a remarkable feature that appears only in the case of adiabatic perturbations in a flat universe. It turns out that the corresponding dipole is suppressed with respect to the quadrupole. This is due to a cancellation between the terms $\Phi/3$ and **e.v.** It can be shown that the dipole is then of the same order of magnitude as the octupole.

Table 1 summarizes these various results.

All the mentioned cases can be illustrated quantitatively by plotting the dipole and quadrupole window functions in the flat case (Fig. 1) and, in the open case, the first multipole window function (ultra large scale limit) relative amplitudes as a function of Ω. The key result of this analysis is that a significant cosmological dipole is possible only with isocurvature perturbations in a flat (or quasi-flat) universe. The resulting "cosmological" dipole will then be [4]

$$a_1^2 = \frac{1}{3}\int \frac{dk}{k}\mathcal{P}_S(k) j_1^2(2k/a_0 H_0). \tag{12}$$

4 The double inflation model

The previous section has restricted the geometry of the universe and the type of perturbations in order to obtain an important cosmological dipole. The question now arises whether one can find early cosmology models that could explain the physical origin of such perturbations. It turns out that a very simple model of double inflation can provide the required spectrum of perturbations [7].

The simplest model of double inflation (see e.g. [8]), consisting of two minimally coupled massive scalar fields, is described by the Lagrangian

$$\mathcal{L} = \frac{^{(4)}R}{16\pi G} - \frac{1}{2}\partial_\mu\phi_l\partial^\mu\phi_l - \frac{1}{2}m_l^2\phi_l^2 - \frac{1}{2}\partial_\mu\phi_h\partial^\mu\phi_h - \frac{1}{2}m_h^2\phi_h^2, \tag{13}$$

where ϕ_l and ϕ_h are respectively the light and heavy scalar fields; $^{(4)}R$ is the scalar spacetime curvature and G is Newton's constant. In addition to m_l and m_h, which from now on are assumed to satisfy $m_h/m_l \gg 1$, there is a third parameter s_0 corresponding to the initial conditions for the two scalar fields ($s_0 = 4\pi G\phi_h^2$ when $\phi_h = \phi_l$). It is convenient to label any moment during inflation by the corresponding number of e-folds before the end of inflation, s. There is a natural scale associated with it, which is the comoving Hubble radius at this moment.

The first phase of inflation, driven by the heavy scalar field, lasts until equality of the energies of the two scalar fields ($m_h\phi_h = m_l\phi_l$), which occurs for $s_b \simeq s_0$. If $s_0 > (m_h/m_l)^2$, which will be

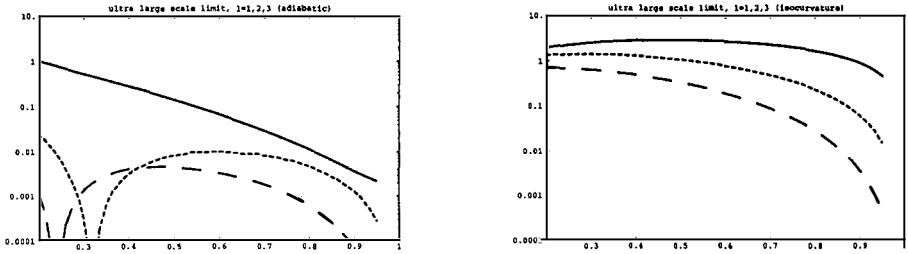

Figure 2: squared amplitude of the total window functions (intrinsic and Sachs-Wolfe) for ultra large scale (limit $k \to 0$) perturbations as a function of Ω, for the three multipoles $l = 1, 2, 3$ (from top to bottom) in the *adiabatic* case (left figure) and in the *isocurvature* case (right figure).

assumed here, inflation goes on, now driven by the light scalar field. Meanwhile the heavy scalar field continues its slow-rolling until $H \sim m_h$, corresponding to $s = s_c$, after which it oscillates. Finally the Hubble parameter reaches the value m_l and inflation stops. In the "standard" model of double inflation[8], the scales λ_b and λ_c (one always has $\lambda_b > \lambda_c$) are within the Hubble radius today, denoted λ_H, whereas, here, the parameters of the model are chosen such that these two scales are *outside* the present Hubble radius λ_H.

The spectrum of adiabatic perturbations today, which it is convenient to express in terms of Φ, is computed from the vacuum quantum fluctuations of the two scalar fields in the inflationary period. This spectrum has two plateaus[8]. Since, here, the transition scale is larger than the Hubble radius today, only the lower plateau, corresponding to the second phase of inflation (driven by the light scalar field), and given by

$$\mathcal{P}_\Phi = \frac{12}{25\pi} s^2 \frac{m_l^2}{m_P^2}, \tag{14}$$

will be accessible to observations ($s(k) \simeq \ln(k_e/k)$). Assuming the quadrupole to be essentially due to adiabatic perturbations, the COBE measurement of $Q_{rms-PS}(n = 1) \simeq 18\mu K$ implies $m_l \simeq 7.8 \times 10^{-5} m_P s_{\dot{H}}$ (for $s_H = 60$, $m_l \simeq 1.3 \times 10^{-6} m_P$).

In addition to adiabatic pertubations, this model can also produce isocurvature perturbations[9]. This is the case for example if one assumes that the light scalar field, after inflation, will decay into ordinary matter, while the heavy scalar field remains decoupled from ordinary matter. The subsequent spectrum of isocurvature perturbations is given by[7]

$$\mathcal{P}_S = \frac{4G}{3\pi} m_l^2 \left(\frac{s_0}{s}\right)^{m_h^2/m_l^2} \tag{15}$$

until $s = s_c$, after which the production of isocurvature perturbations falls abruptly. Substituting this spectrum in (12) and introducing the variable $X = \ln(k_c/k)$, the expected dipole reads

$$a_1^2 = \frac{16}{81\pi} \left(\frac{m_l}{m_P}\right)^2 e^{2(s_H - s_c)} \left(\frac{s_0}{s_c}\right)^{m_h^2/m_l^2} \int_0^\infty dX \frac{e^{-2X}}{(1 + X/s_c)^{m_h^2/m_l^2}}, \tag{16}$$

where has been used the fact that $j_1(x) \sim x/3$ for small x. The integral in (16) is well approximated as $(2 + (m_h/m_l)^2/s_c)^{-1}$. For consistency, one must also check that the quadrupole generated by isocurvature perturbations is smaller than the adiabatic quadrupole. This requires the condition[7]

$$s_c > s_H + 4.6, \tag{17}$$

i.e. that the cut-off scale λ_c is one hundred times larger than the Hubble radius today. The value s_H is of the order of 60, its exact value depending on the history of the universe. Because of the power law dependence in (16), *the dipole can be much bigger than the quadrupole.* Because of the condition (17), implying that m_h^2/m_l^2 must be large, the main constraint, surprisingly, comes from requiring that the dipole is not too high with respect to the quadrupole: this requires that s_0/s_c must be very close to 1. In this range of parameters, double inflation thus provides adequate spectra of perturbations, giving a dipole and higher multipoles with amplitude comparable to the observed ones.

5 Conclusion

The main conclusion of the work summarized here is that, remarkably, whereas a significant dipole can be obtained in a *flat* universe with ultra-large scale isocurvature perturbations [4], it is not possible in an *open* universe, unless the geometry is quasi-flat. Moreover, after having obtained the necessary conditions on the perturbations, it has been shown that a simple double inflation model can indeed produce the required isocurvature and adiabatic perturbation spectra to explain cosmologically both the dipole and the subsequent low multipoles [7]. Any future discrepancy between the observed CMBR dipole and the peculiar velocicy dipole (extremely difficult to measure) could therefore be interpreted as the manifestation of ultra large scale isocurvature perturbations in a flat universe. In addition, the present analysis also constrains all scenarios of multiple field inflation with isocurvature perturbations surviving till the last scattering epoch.

References

1. L.P. Grishchuk and Ya.B. Zel'dovich, *Astron. Zh* **55**, 209 (1978) [*Sov. Astron.* **22**, 125 (1978)].
2. J. Garcia-Bellido, A.R. Liddle, D.H. Lyth, D. Wands, *Phys. Rev.* D **52**, 6750 (1995).
3. B. Paczynski and T. Piran, *Astrophys. J.* **364**, 341 (1990)
4. D. Langlois and T. Piran, *Phys. Rev.* D **53**, 2908 (1996).
5. D. Langlois, *Phys. Rev.* D **55**, 7389 (1997).
6. D.H. Lyth, A. Woszczyna,*Phys. Rev.* D **52**, 3338 (1995).
7. D. Langlois, *Phys. Rev.* D **54**, 2447 (1996).
8. D. Polarski, A.A. Starobinsky, Nuclear Physics B 385, 623 (1992)
9. D. Polarski, A.A. Starobinsky, Phys. Rev. D50, 6123 (1994)

TOPOLOGICAL DEFECTS IN MULTI-CONNECTED UNIVERSES

Jean-Philippe UZAN
Departement d'Astrophysique Relativiste et de Cosmologie,
UPR 176 du CNRS, Observatoire de Paris,
92195 Meudon cedex, France.

When the topology of the universe is non trivial, there is a constraint on the network of topological defects that may appear during a symetry breaking phase transition in the early universe. I first review this constraint and then its cosmological implications. I explain how the topology can be reduced to a set of parameters and give the bounds on these parameters that the observation of a single extended defect.

1 Introduction

Einstein equations, being local differential equations, enable us to determine the local geometry of the universe but remain mute about its global structure, i.e. its topology. If the spacetime describing the universe is globally hyperbolic (which is the case of the Friedmann-Lemaître solution) then the study of the topology of the universe reduces to the study of the topology of its spatial sections Σ. Indeed, the geometry constrains the topology since all topological structures are not compatible with all local geometries (e.g. the topology of the torus is only compatible with flat spatial sections, Σ). Many arguments have been proposed to consider such universes [1,2].

At the time being, there exist observational constraints on the characteristic size of multi-connected universes from the non detection of multiple images in clusters catalogs [3]. The best tool to study topology is however the cosmic microwave background (CMB) since it is extended and since all the CMB photons were emitted approximately at the same time. The non detection of a cut-off in the CMB temperature anisotropy spectrum allows to exclude multi-connected flat universes whith a size smaller than the horizon [4]. However, this method does not apply to universes with hyperbolic spatial sections.

Recently two methods have been proposed to detect and/or constrain the topology of the

universe : the *method of circles*[5] is based on the fact that the last scattering surface is a 2-sphere that must intersect itself on circles if the topology is observable. One should, in principle, be able to detect these circles on which the CMB temperature anisotropies are correlated. The *method of images* uses the CMB power spectrum computed in the universal covering and "projects" it on the multi-connected space (see the contribution by T. Souradeep). Both methods assume that the initial inhomogeneities responsible for the temperature anisotropy of the CMB were produced during an inflationary phase. It is thus of interest to examine whether they still apply in the presence of topological defects since they will go on seeding perturbations between the last scattering surface and today.

If we restrict our analysis to universes with compact, locally hyperbolic spatial sections, the *rigidity theorem*[10] ensures that the volume V, the in- and out-radii (respectively r_- and r_+) of Σ (i.e the radius of the smallest (biggest) geodesic ball contained in (containing) the fundamental polyhedron) are topological invariants. One can thus consider (V, r_+, r_-) as a cosmological parameter, the standard framework being recovered when they go to infinity. Mathematically, it has been shown [12] that

$$V \geq 0.166 \Longleftrightarrow r_+ \geq 0.3383 \tag{1}$$

in unity of the curvature radius.

Indeed the fact that topology be detectable in the cosmic microwave background requires that the fundamental cell dropped into the horizon before decoupling (otherwise the diameter of the last scattering surface will be smaller than the compactification scale of the universe), i.e. that[5]

$$r_- \leq \operatorname{arg\,cosh}\left(\frac{2-\Omega_0}{\Omega_0}\right). \tag{2}$$

I will now focuss on topological defects and show that there exists a constraint on their network that can lead to new bounds on (V, r_+, r_-) and draw its cosmological implications.

2 The No-defect conjecture and its cosmological implications

The appearance and the nature of defects during a phase transition depend only on the topology of the vacuum manifold G/H when a larger group G is broken down to a smaller group H[6].

We have shown[7] that if we assume that the field theory is not twisted and if the characteristic lengths of the fundamental polyhedron were smaller than the horizon size today, the constraints imposed by the global topology on the topological defects network imply that extended defects (namely strings and walls) and textures[8] cannot exist today. Here, I refer to the horizon size as the size of the *particle horizon*[9], i.e. of causally connected regions.

I now present the main implications of this constraints, the derivation of which can be found in [7,8]

Let us evaluate the redshift z_{disp} at which all the defects have disappeared. We restrict our attention to locally hyperbolic Friedmann-Lemaître universes. The spatial sections Σ are thus homogeneous and isotropic and the line element reads

$$ds^2 = a^2(\eta)\left\{-d\eta^2 + d\chi^2 + \sinh\chi^2(d\theta^2 + \sin^2\theta d\varphi^2)\right\}, \quad \text{with} \tag{3}$$

$$\frac{a}{a_0} = \frac{\Omega_0}{2(1-\Omega_0)}(\cosh\eta - 1), \tag{4}$$

where Ω_0 is the density parameter and all present time quantities have a subscript 0. We introduce the redshift z by $1 + z \equiv a_0/a$. Once the fundamental polyhedron has entered the

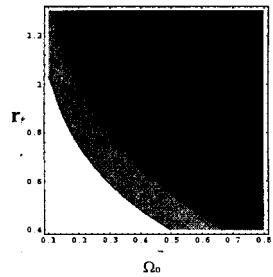

Figure 1: An estimation of the redshift at which all defects have disappeared from the universe in function of the topological invariant r_+ and the density parameter Ω_0.

horizon, it takes a time of order r_+ for all the defect to completely disappear so that

$$\eta_{disp} \simeq 2r_+; \quad z_{disp} \simeq \frac{2(\Omega_0^{-1}-1)}{\cosh 2r_+ - 1} - 1. \tag{5}$$

On the one hand, if we were able to detect the topology of the universe then we could conclude that it is unlikely that any topological defect exists for $z < z_{disp}$ (see figure 1). That would severely constrain structure formation models. On the other hand, the observation of an extended defect at a redshift z_{obs} will give a constraint on the value of the invariant r_+,

$$r_+ \geq \frac{1}{2} \operatorname{arg\,cosh}\left(1 + \frac{2(\Omega_0^{-1}-1)}{1+z_{obs}}\right). \tag{6}$$

Let us now turn to the consequences on the cosmic microwave background. The multipole moments C_ℓ of the angular power spectrum of the CMB anisotropies are related to the temperature two point correlation function according to

$$\left\langle \frac{\delta T}{T}(\vec{n}_1)\frac{\delta T}{T}(\vec{n}_2)\right\rangle_{\vec{n}_1.\vec{n}_2=\cos\theta} = \sum_l \frac{(2\ell+1)}{4\pi} C_\ell P_\ell(\cos\theta), \tag{7}$$

where the P_ℓ are the Legendre polynomials. The brackets denote an average on the sky, i.e. on all pairs $(\vec{n}_1, \vec{n}_2)$ such that $\vec{n}_1.\vec{n}_2 = \cos\theta$. Since the ℓ^{th} Legendre polynomial has 2ℓ zeros in $[-\pi, \pi]$ with approximatively equal spacing, we can estimate that a parameter ℓ corresponds to an angular scale of $\theta \simeq \pi/\ell$. Observationally, for small ℓ the C_ℓ behave as

$$C_\ell \sim \frac{A}{\ell(\ell+1)}, \tag{8}$$

A being a constant. This called the "Sachs-Wolfe plateau".

In a simply-connected universe the process of decay and motion of the defects on the line of sight account for the Sachs-Wolfe plateau. In a multi-connected universe this process is stopped after z_{disp} and no perturbation can be seeded on angular scales larger than the one corresponding to the angle under which we see the fundamental polyhedron at a redshift z_{disp}. This induces a cut-off in the C_ℓ at a multipole $\ell_{min}(\Omega_0, r_+)$ (see [8] for the details concerning this computation and for the exact expression of ℓ_{min}). Now, according to the value of (Ω_0, r_+), we can say from fig. 2 whether or not in a multi-connected universe topological defects can explain the Sachs-Wolfe plateau or not.

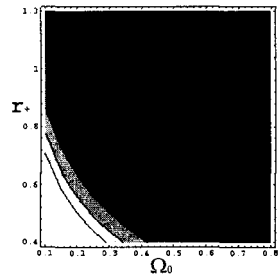

Figure 2: An estimation of the cut-off in the CMB angular power spectrum in function of the topological invariant r_+ and the density parameter Ω_0.

3 Conclusions

After arguing for considering the topology, we have

- introduced a new set of cosmological parameters related to the topology and given bounds on these parameters,
- shown that there exists constraints on the network of topological defects,
- deduced new bounds on r_+ in the case we observe an extended defect
- studied the signature of these defects on the CMB in a multi-connected universe and showed that they cannot explain the Sachs-Wolfe plateau, this result being independent of the kind of defect (string, wall, texture). This ensures that if the topology is observable, topological defects cannot explain the observed Sachs-Wolfe plateau.

References

1. M. Lachièze-Rey & J.-P. Luminet, *Phy. Rep.* **254,** 135 (1995)
2. J-P. Uzan, *Int. Journal of Theor. Physics* **36**, 2167 (1997)
3. R. Lehoucq, M. Lachièze-Rey & J-P. Luminet, *Astron. Astrophys.* **313**, 339 (1996)
4. D. Stevens, D. Scott & J. Silk,*Phys. Rev. Lett.* **71**, 20 (1993); A. de Oliveira Costa, G.F. Smoot & A.A. Starobinsky *Ap. J.* **468**, 457 (1996)
5. N.J. Cornish, D.N. Spergel & G.D. Starkman, gr-qc/9708225; *Phys. Rev. Lett.* **77**, 215 (1996); gr-qc/9602039; gr-qc/9708083.
6. T.W.B. Kibble, *J. Math. Phys.* **A9**, 1387 (1976); E.P.S. Shellard & A. Vilenkin, *Cosmic strings and other topological defects*, Cambridge University Press (1994).
7. J-P. Uzan & P. Peter,*Phys. Lett.* **B406**, 20 (1997)
8. J-P. Uzan, *Phys. Rev. D* , submitted (1998)
9. W. Rindler, *Mon. Not. R.A.S.* **116**, 663 (1956)
10. G.D. Mostow, *Ann. Math. Studies* **78**, Princeton University Press (1973); G. Prasad, *Invent. Math.* **21**, 255 (1973)
11. G.F. Smoot *et al.*, *Ap. J.* **396**, L1 (1992)
12. D. Gabai, G.R. Meyerhoff & N. Thurston, *MSRI preprint* , 1996-058 (1996)

COSMOLOGICAL AND ASTROPHYSICAL IMPLICATIONS OF SUPERCONDUCTING COSMIC STRINGS AND VORTONS

Alejandro Gangui and Patrick Peter
Département d'Astrophysique Relativiste et de Cosmologie,
Observatoire de Paris-Meudon, 92195 Meudon, France.

We present here an extensive review of various issues relevant for superconducting cosmic strings and vortons. We first address the microscopic aspects of various possible currents confined to the defect core and their ability to sustain loop equilibrium configurations. We then survey recent developments in the macroscopic description of vortons, especially regarding the stability under general perturbations and inclusion of electromagnetic effects. Standard cosmology imposes important constraints on both past and present distributions of these defects, and on their evolution, and we here briefly summarize them. We then describe those noteworthy astrophysical signatures that could be unambiguous tracers of their existence, like peculiar features in the lensing of distant sources and in the spectra of ultra high energy cosmic rays. Overall, we highlight the remaining open questions and future prospects.

1 Introduction

Cosmic strings [1], with or without current carrying capabilities, are predicted by many theories of high energy physics, and they have been postulated *ad hoc* as a possible explanation of various phenomena, such as galaxy formation. However, there is still no firm evidence that this actually occurs. In what follows we will show various reasons why we think their existence is likely, and may even help towards the reconciliation between theory and observations in some cases, as well as leads to interesting and testable predictions in others. We shall structure our discussion in the sometimes overlapping following different domains: the study of their microphysics, which means the field theoretical reasons for their existence and structure, the dynamics of equilibrium configurations of superconducting cosmic string loops, and finally the cosmological and astrophysical consequences they may be responsible for.

This work is thus presented as a review of the existing results (and related references) concerning cosmic strings in general, and of the superconducting kind in particular, with special emphasis on the methodology (or lack thereof) on which cosmological deduction relies upon. It should be clear from this review that more precise analysis of the implications of currents should be carried on and we will present the results based on work done in this research direction.

2 Current microphysics

In the past few years it has become clear that topological defects of the vacuum, and in particular strings, may have a considerably richer structure than previously envisaged. Many natural couplings among fundamental fields in grand unified models having string-like vortex solutions lead to the existence of massless modes flowing along those vortices. Recent works have focused

on these zero modes [2] produced at very high energies and on their ability to survive subsequent phase transitions [3] (like the electroweak, for instance). Also, studies of non–Abelian string loops have indicated that, in the absence of external fields, persistent vector boson [4] currents could not be supported [5]. Regarding massive modes, the diffusion of massive fermion bound states to free ones could make fermions escape the core, therefore diminishing the strength of the current [6]. *Vortons* [7] are equilibrium configurations of superconducting cosmic string loops, where the string tension, tending to make the loop collapse, is balanced by the centrifugal repulsion due to rotation. The relevance of the above mentioned studies to the vorton survival as a form of dark matter has also been emphasized. Currents may arise due to the existence of, for example, right handed neutrinos [8,9] (neutral fermionic currents) confined to the core of the string within grand unified models, or even due to the flow of squarks or other sleptons (bosonic case) in supersymmetric [10] extensions of the standard model. For the simplest supersymmetric string models explicit solutions for fermionic zero modes were found and related through supersymmetry transformations to bosonic currents [11]. It seems that currents in such theories happen even more generally than in non supersymmetric theories, but it is yet unclear whether they are stable.

3 Dynamical stability

Circular rotating loops are believed to be the possible end result of the dynamical evolution of current-carrying loops. Those actually reaching these states could have survived until now in such numbers as to have given rise to a *vorton excess problem*, provided they are stable enough, both classically [12] and quantum mechanically [13]. This last issue is however still a very much open one, and its approach is furthermore presumably very model dependent. Nevertheless, realistic quantum models are currently being investigated.

Classical stability of rings has been clarified using the string's equation of state, namely the relation between the values of the energy per unit length U and tension T, and a classification was achieved through the transversal and longitudinal perturbation velocities $c_T^2 = T/U$ and $c_L^2 = -dT/dU$ respectively. It was found [14] that rings were absolutely stable with respect to perpendicular to the string loop's plane perturbations, whatever the equation of state, whereas in the loop's plane, those strings for which the relation $c_L > c_T$ (the so-called subsonic equations of state) held were stable with respect to any such perturbation. The opposite case of supersonic equations of state exhibits unstable modes. Unfortunately however (having in mind the vorton excess problem) this is not always the case (see below): It was found that for macroscopic models such as the one suggested by Witten [15] (supposed to describe faithfully the characteristic features of a realistic underlying theory), the equation of state turns out to be of the supersonic kind [16,17], and moreover derivable analytically [18]; a region exists however in the Witten model where classically stable rings can be found, and corresponds to the presumably statistically favored region where the current tends to be chiral [19]. These equilibrium configurations could make up a large excess of non–baryonic dark matter and thus pose problems to standard cosmology. The fate of exponentially growing unstable modes that would develop in such models is yet unknown and currently under investigation [20].

Finally, the conditions for avoidance of collapse and the motion of a circular loop on its way to equilibrium was investigated in detail [21]. From this the region of parameter space for which vortons could indeed form was derived. It was then shown how the electromagnetic self-correction on the dynamics of the loop, at first order in the coupling between the current and the self-generated electromagnetic field, modified the picture. This correction, which neglects energy non conservation, e.g. in the form of radiation, is accounted for by a simple modification of the loop's equation of state [22]. The evaluation of the necessary modifications in presence of radiation are largely unexplored yet. Taking it into account it has been shown that there

is a tendency to reduce the available parameter space region for stability, thereby effectively diminishing the severity of the vorton excess problem [23].

4 Cosmology

Let us focus now on some implications that these conducting defects may have in cosmology. On the side of conducting strings, the build up of growing current–coherent regions was shown to occur for some models [24]. This follows from the realization that, after intercommutation of strings, there is formation of regions where charges pile up. These charges however have a strength decreasing with time[25], which shows that an equilibration process between neighboring regions is in place. These recent toy models however do not yet include charge losses by radiation or other mechanisms relevant during the relativistic evolution regime after the friction dominated era. Still, the hope is that the derived orders of magnitude will be correct.

Regarding vortons, their presence and evolution was recently the subject of much study, and grand unified models producing them were confronted with standard cosmological tests, as the primordial nucleosynthesis bounds and the dark matter content in the universe today[26]. Without entering into too much detail, in order for the density of grand unified vortons at temperatures roughly around 10 MeV not to affect nucleosynthesis results for the light elements, the maximum energy scale for current condensation cannot exceed 10^{12} GeV (see the summary panels below for other schemes). Dark matter bounds are even stronger and a maximum $T_{\rm condensation} \sim 10^9$ GeV is imposed on these models This latter energy scale however matches perfectly well the requirements for vortons to explain current cosmic ray data – see below.

Fermionic zero modes may sustain vorton configurations. In grand unified models, like SO(10), where the symmetric phase is restored in the interior of the string, there will be gauge bosons in the core. If vortons diffuse after a subsequent phase transition these bosons will be released and their out-of-equilibrium decay may lead to a baryon asymmetry compatible with nucleosynthesis limits[3]. Another recent mechanism for the generation of baryon asymmetry, this time at temperatures much lower than the weak scale, takes advantage of the fact that superconducting strings may act like baryon charge 'bags', protecting it against sphaleron effects [27].

The cosmic microwave background radiation might also be used as a charged string loop detector. In fact vortons are like point masses with quantized electric charge and angular momentum. They are peculiar for, if they are formed at the electroweak scale, their characteristic size cannot be larger than a hundredth the classical electron radius, while their mass would be some five orders of magnitude heavier than the electron. They can however contain up to $\alpha^{-1} \sim 137$ times the electron charge, and hence Thomson scattering between vortons and the background radiation at recombination would be just nearly at the same level as the standard one (with important consequences for, e.g., the polarization of the relic radiation). The signature would depend on the actual distribution of relic vortons at $z \sim 1000$, something that is presently largely unknown. According to current estimates however electroweak vortons would contribute a mere $\Omega_V \sim 10^{-9}$ and thus their trace would be hidden in the 'noise' of the vastly too numerous electrons.

5 Astrophysical signatures

Interestingly enough, hypothetical as they may be, models producing superconducting strings may be confronted with real data. Ultra relativistic swinging strings would produce high energy regions known as *cusps* from which trapped particles can quantum tunnel free to the outside [28]. With rather modest efficiencies, between $\sim 10^{-10}$ and 10^{-6}, the energy conversion of string cusps (moving with Lorentz factors between $\gamma \sim 100$ and 10^5) at large redshifts $1 \ll z < 1000$

may give rise to particles whose subsequent decay would lead to gamma ray bursts [29] reaching the Earth with integrated energy fluxes (fluences) of $\sim$ MeV cm^{-2}.

Moreover, as it can be guessed, huge concentrations of mass–energy localized in the core of cosmic strings may lead to interesting gravitational effects. One such signature is the lensing of distant sources. The expected double images of quasars or far away galaxies (separations of a few arcminutes) due to, say, a vertically oriented string would behave in a well studied manner if a pulse of lightlike current flows along the conducting string that acts as the gravitational deflector[30]. These images would describe approximate mirror-symmetric ellipses on the sky and at the same time (due to the temporary modification of the space time around the string caused by the pulse) change their color (frequency) on the order of $\Delta\nu/\nu \sim 10^{-4}$, all this taking place in a few years time for grand unified strings a few Mpc away from us. This yields a characteristic moving pattern that would be easily recognizable, thus leading to a potentially unambiguous observational detection signature.

Regarding the generation of primordial galactic magnetic fields, recent models of superconducting cosmic strings [31] may explain the production of interesting seed mean values of order 10^{-20} Gauss with a protogalactic coherence length ($\sim$ 100Kpc); the field would have been generated by the vorticity induced in the primordial plasma because of the string's motion. This yields a bigger magnetic field than in the ordinary string case because the motion is on average slower and more tangled [32].

Turning now to the highest energy phenomena around us, disintegration of superconducting strings has been proposed as the origin of ultra high energy cosmic rays [33] (see however [34]), with the advantage of getting round the difficulties of the conventional shock acceleration of cosmic rays. This mechanism will also produce neutrinos of up to 10^{18} eV energies. Horizontal air shower measurements, like the Akeno Giant Air Shower Array (AGASA) experiment [35], however, constrain $\nu_e + \bar{\nu}_e$ fluxes, and current estimates from superconducting strings seem to exceed these bounds [36].

Finally, stable loop configurations formed at $\sim 10^9$GeV could be easily accelerated in active galactic nuclei and propagate through the intergalactic medium with negligible losses of energy. These features were recently recognized [37] and it was proposed that vortons *themselves* could be a candidate for the so far puzzling ultra high energy cosmic rays with energies well above the exaelectronvolt ($= 10^{18}$eV), like the Fly's Eye event[38] for example. Moreover the interaction of (bound state) current carriers (in the vorton) and the quarks (bounded in atmospheric protons) will proceed via inelastic scattering and yield a characteristic line spectrum followed by a continuum. Interaction probabilities range between 10^{-5} and 10^{-4} and hence important horizontal showers are expected, well suited for the future *Auger* observatory for example[39].

As a recap of the many topics discussed above and with the idea of highlighting those areas of current development we include an *executive summary* in two panels below.

Acknowledgments

We have benefited from discussions with too many people to quote, but we shall make an exception for Brandon Carter and Edgard Gunzig for their feedback. This work was partially supported by the Société de Secours des Amis des Sciences, EEC grants N° PSS*0992 and CI1*CT94-0004, and by the programme Antorchas/British Council (project N° 13422/1–0004).

References

1. E. P. S. Shellard, A. Vilenkin, *Cosmic strings and other topological defects*, Cambridge University Press (1994);
   M. B. Hindmarsh, T. W. B. Kibble, *Cosmic strings*, Rept. Prog. Phys. **58**, 477 (1995). [hep-ph/9411342];
   T. Vachaspati, *Topological defects in the cosmos and lab.* [hep-ph/9802311]
2. R. Jackiw, P. Rossi, *Zero modes of the vortex-fermion system*, Nucl. Phys. **B 190**, 681 (1981);
   E. Weinberg, *Index calculations for the fermion-vortex system*, Phys. Rev. **D 24**, 2669 (1981);
   M. Hindmarsh, *Superconducting cosmic strings with coupled zero modes*, Phys. Lett. **B 200**, 429 (1988).
3. A. C. Davis, W. B. Perkins, *Dissipating cosmic vortons and baryogenesis*, Phys. Lett. **B 393**, 46 (1997);
   S. C. Davis, A. C. Davis, W. B. Perkins, *Cosmic string zero modes and multiple phase transitions*, Phys. Lett. **B 408**, 81 (1997).
4. A. E. Everett, *New mechanism for superconductivity in cosmic strings*, Phys. Rev. **D 61**, 1807 (1988);
   M. Alford, K. Benson, S. Coleman, J. March-Russell, *Zero modes of non-Abelian vortices*, Nucl. Phys. **B 349**, 414 (1991).
5. T. W. B. Kibble, G. Lozano, A. J. Yates, *Non-Abelian string conductivity*, Phys. Rev. **D 56**, 1204 (1997). [hep-ph/9701240]
6. A. Gangui, P. Peter, E. Gunzig, *Fermionic currents in cosmic strings*, Int. Journal of Theor. Physics, in press (1998).
7. R. L. Davis, E. P. S. Shellard, *Cosmic vortons*, Nucl. Phys. **B 323**, 209 (1989);
   B. Carter, *Cosmological relic distribution of conducting string loops*, Ann. N.Y. Acad. Sci. **647**, 758 (1991);
   B. Carter, *Recent developments in vorton theory*, Int. Journal of Theor. Physics **36**, 2451 (1997). [astro-ph/9712116]
8. A. C. Davis, S. C. Davis, *Microphysics of SO(10) cosmic strings*, Phys. Rev. **D 55**, 1879 (1997). [hep-ph/9608206]
9. R. Jeannerot, *A supersymmetric SO(10) model with inflation and cosmic strings*, Phys. Rev. **D 53**, 5426 (1996). [hep-ph/9509365]
10. A. Riotto, *Cosmological implications of low energy supersymmetry breaking models*, Phys. Lett. **B 413**, 22 (1997). [hep-ph/9708304].
11. S. C. Davis, A. C. Davis, M. Trodden, *Cosmic strings, zero modes and SUSY breaking in non-Abelian N=1 gauge theories*, to appear in Phys. Rev. **D** (1998) [hep-ph/9711313];
    S. Davis, A. C. Davis, M. Trodden, *N=1 supersymmetric cosmic strings*, Phys. Lett. **B 405**, 257 (1997). [hep-ph/9702360]
12. B. Carter, X. Martin, *Dynamical instability criterion for circular string loops*, Ann. Phys. (N. Y.) **227**, 151 (1993).
13. R. Davis, *Semi-topological solitons*, Phys. Rev. **D 38**, 3722 (1988).
14. X. Martin, *Zones of dynamical instability for rotating string loops*, Phys. Rev. **D 50**, 7479 (1994).
15. E. Witten, *Superconducting strings*, Nucl. Phys. **B 249**, 557 (1985).
16. P. Peter, *Superconducting cosmic strings: Equation of state for spacelike and timelike current in the neutral limit*, Phys. Rev. **D 45**, 1091 (1992).
17. P. Peter, *Influence of the electric coupling strength in current-carrying cosmic strings*, Phys. Rev. **D 46**, 3335 (1992).

18. B. Carter, P. Peter, *Supersonic string model for Witten vortices*, Phys. Rev. **D 52**, R1744 (1995). [hep-ph/9411425]
19. X. Martin, P. Peter, *Dynamical stability of Witten vortons*, Phys. Rev. **D 51**, 4092 (1995).
20. X. Martin, P. Peter, in preparation.
21. B. Carter, P. Peter, A. Gangui, *Avoidance of collapse by circular current–carrying cosmic string loops*, Phys. Rev. **D 55**, 4647 (1997). [hep-ph/9609401]
22. B. Carter, *Electromagnetic self interaction in strings*, Phys. Lett. **B 404**, 246 (1997). [hep-th/9704210]
23. A. Gangui, P. Peter, C. Boehm, *Could electromagnetic corrections solve the vorton excess problem ?*, Phys. Rev. **D 57**, 2580 (1998). [hep-ph/9705204]
24. C. J. A. P. Martins, E. P. S. Shellard, *Evolution of superconducting string currents.* [hep-ph/9706533]
25. P. Laguna, R. A. Matzner, *Numerical simulation of bosonic superconducting string interactions*, Phys. Rev. **D 41**, 1751 (1990).
26. R. Brandenberger, B. Carter, A. C. Davis, M. Trodden, *Cosmic vortons and particle physics constraints*, Phys. Rev. **D 54**, 6059 (1996). [hep-ph/9605382]
27. R. Brandenberger, A. Riotto, *A mechanism for baryogenesis in low energy supersymmetry breaking models*, [hep-ph/9801448]
28. R. L. Davis, *Fermion masses on the vortex world sheet*, Phys. Rev. **D 36**, 2267 (1987).
29. B. Paczyński, *Gamma ray bursts from cusps on superconducting cosmic strings at large redshifts*, Ap. J **335**, 525 (1988).
30. J. Garriga, P. Peter, *Lensing properties of lightlike current-carrying cosmic strings*, Class. Quantum Grav. **11**, 1743 (1994).
31. C. J. A. P. Martins, E. P. S. Shellard, *Galactic magnetic fields from superconducting strings*, [astro-ph/9706287]
32. K. Dimopoulos, *Primordial magnetic fields from superconducting cosmic strings*, to appear in Phys. Rev. **D** (1998). [hep-ph/9706513]
33. C. T. Hill, D. N. Schramm, T. P. Walker, *Ultra-high energy cosmic rays from superconducting cosmic strings*, Phys. Rev. **D 36**, 1007 (1987).
34. A. J. Gill, T. W. B. Kibble, *Cosmic rays from cosmic strings*, Phys. Rev. **D 50**, 3660 (1994). [hep-ph/9403395]
35. S. Yoshida et al., *The cosmic ray energy spectrum above* 3×10^{18} *eV measured by the Akeno Giant Air Shower Array*, Astropart. Phys. **3**, 105 (1995).
36. J. J. Blanco-Pillado, R. A. Vazquez, E. Zas, *Limits on topological defect neutrino fluxes from horizontal air shower measurements*, Phys. Rev. Lett. **78**, 3614 (1997). [astro-ph/9612010]
37. S. Bonazzola, P. Peter, *Can high energy cosmic rays be vortons ?* Astropart. Phys. **7**, 161 (1997). [hep-ph/9701246]
38. D. J. Bird et al., *Evidence for correlated changes in the spectrum and composition of cosmic rays at extremely high energies*, Phys. Rev. Lett. **71**, 3401 (1993); *The cosmic ray spectrum observed by the Fly's Eye*, Ap. J., **424**, 491 (1994).
39. The Pierre Auger Project Design Report, Fermilab (1995).

STRUCTURE FORMATION AND LIGHT GRAVITINOS WARM DARK MATTER

ELENA PIERPAOLI
Department of Physics, Theoretical Physics, 1 Keble Road, Oxford OX1 3NP, England

Light gravitinos (m $\simeq$ 0.1 – 1 KeV) are predicted to be the lightest supersimmetric particles in the gauge-mediated supersimmetric models. We investigate the possibility that they constitute the dominant fraction of dark matter in the Universe. After showing that they typically behave like warm dark matter (WDM) with a free–streaming scale of the order of the galaxy mass scale, we study the formation of cosmic structures within this frame. Different variants of the WDM scenario are considered : open models with and without cosmological constant and flat Hot + Warm dark matter models. Predictions of these models on the local cluster number density and abundance of neutral hydrogen in high redshift objects are evaluated and compared with current data. None of these models satisfies the two constraints at the same time: the requirement of ensuring the adequate clusters abundance prevents from having enough power on small scale to form objects at high redshifts.

1 Introduction

Given supersimmetry (SUSY) as starting framework, the two best candidates we have to play the role of lightest SUSY particle (LSP) are the lightest neutralino and the gravitino. If gauge interactions are responsable for SUSY breaking, then the LSP is the gravitino, with an expected mass in a range from a fraction of eV up to O(GeV).

From a cosmological point of view, the neutralino LSP scenario leads to a cold dark

matter (CDM) scenario, which, in its standard version, fails in reproducing several observational tests (Peacock and Dodds [1] 1994, White et al. [2] 1993). These failure may be overcome in these SUSY models by finding a way to suppress fluctuations on $10\,h^{-1}$Mpc scales, without decreasing too much power on the $\sim 1\,h^{-1}$Mpc scale. A first possibility consists in adding to the LSP CDM candidate some massive light neutrino, a further possibility in assuming a density parameter substantially smaller than unity (either with or without a cosmological constant).

If the gravitino is the LSP, it behaves more like warm dark matter (WDM), provided that its mass lies in the range [0.1–1] keV (a heavier gravitino would overclose the universe; see below). Our aim is to verify whether either WHDM models or low-density WDM models provide a good agreement with observational constraints on scales $10 - 1h^{-1}$Mpc, and also we would like to make use of the cosmological constraints to infer constraints on the "Gauge Mediated SUSY Breaking" class of theories.

2 Light gravitinos and Cosmology

Light gravitinos were in thermal equilibrium at an early epoch. At their decoupling from radiation, the number of gravitinos per comoving volume was frozen out. This freeze-out took place while the gravitinos were relativistic. The relic density of gravitinos is: $\Omega_{\tilde{G}}h^2 = 1.17\,(100/g_*)\,(m_{\tilde{G}}/(10^3\mathrm{eV}))$, where $\Omega_{\tilde{G}}$ is the contribution of the gravitinos to the density parameter, h is the Hubble parameter in units of 100 km/s/Mpc, and g_* stands for the effective degrees of freedom of relativistic particles when the freeze-out of the gravitinos takes place. In the models studied here, g_* is typically $\simeq 100$ (see Pierpaoli et al. [3] 1998 for a detailed computation of g_*); we may consider also $g_* \simeq 200$ as an extreme case.

Adopting these values for g_*, we computed numerically the transfer functions for WDM and WHDM in the case $\Omega_0 = 1$. In order to provide an analytical fitting to the transfer functions for the class of purely WDM models, we resorted to the expression provided by Bardeen et al. [4] (1986)

$$T_{WDM}(k) = T_{CDM}(k)\,\exp\left(-\frac{kR_{fs}}{2} - \frac{(kR_{fs})^2}{2}\right), \qquad (1)$$

where

$$T_{CDM} = \frac{\ln(1+2.34q)}{2.34q}\left[1+3.89q+(16.1q)^2+(5.46q)^3+(6.71q)^4\right]^{-1/4} \qquad (2)$$

is the transfer function for CDM models. Here, $q = k/\Gamma h$ and $\Gamma = \Omega_0 h \exp(-\Omega_B - \sqrt{2h}\Omega_B/\Omega_0)$.

By fitting the transfer function, as computed by the Boltzmann code, with eqs.(1) and (2) one obtains the value for the free-streaming scale, R_{fs}.

As a result, we find that

$$R_{fs} = 0.51\,(\Omega_{\tilde{G}}h^2)^{-1}\left(\frac{g_*}{100}\right)^{-4/3}\mathrm{Mpc} \qquad (3)$$

$$M_{fs} = (2\pi R_{fs}^2)^{3/2}\bar{\rho} \simeq 0.55 \left(\frac{g_*}{100}\right)^{-4} (\Omega_{\tilde{G}}h^2)^{-3}\Omega_0 h^2 M_{12}\,, \qquad (4)$$

Therefore, eq.(4) provides the limiting mass for the development of hierarchical clustering: structures of smaller masses form after structure of mass larger than M_{fs}, as a product of their fragmentation.

For what concerns WHDM, a similar procedure was adopted. Substituting T_{CDM} with T_{CHDM} in eq.(1), one obtains the same expression for R_{fs}, provided that $\Omega_{\tilde{G}} = \Omega_0 - \Omega_\nu$ is taken.

3 Observational tests

In the following we will use the abundance of local galaxy clusters and of high-redshift protogalaxies, through data about damped Ly-α systems (DLAS), to constrain the whole class of WDM-dominated models. Power spectra are COBE normalized, considering a primordial spectral index $n_{pr} = 1$.

As a constraint on DLAS, we will consider the value of Ω_{HI} reported by Storrie-Lombardi et al.[5] (1995) at redshift $z \simeq 4.25$ and will assume that all the HI gas at that redshift is involved in the absorbers: $\Omega_{HI} = \Omega_B\Omega_{coll}$, where $\Omega_{coll} = \mathrm{erfc}\left[\delta_c(z)/\sqrt{2}\sigma_M(z)\right]$ ($\sigma_M(z)$ is the r.m.s. fluctuation at the scale M at redshift z within a top-hat sphere). In our approach, we will give up the dependence on mass scale M, which amounts to assume that DLASs are hosted within protostructures of mass of about M_{fs}; protostructures of smaller mass, instead, are produced later by fragmentation of larger lumps. We prefer to maintain a conservative approach here and to consider a model as ruled out if it predicts Ω_{HI} to be less than the observational 1σ lower limit.

As for the cluster abundance, the number density of clusters with mass exceeding a given value is exponentially sensitive to the r.m.s. fluctuation on the cluster mass scale. Fitting the local X-ray cluster temperature function with the Press-Schechter approach led several authors to obtain rather stringent relationships between σ_8, the r.m.s. fluctuation value within a top-hat sphere of $8\,h^{-1}$Mpc radius, and Ω_0 . In the following we will resort to the constraint by Viana & Liddle[6] (1996).

4 Conclusions

Results are summerized in figs. 1 and 2 for open WDM and WHDM models respectively. The finely shaded area corresponds to the 95% c.l. region allowed by the cluster abundance, solid curve delimiting the coarsely shaded area represents the limit of the region allowed by the data about the Ω_{HI} in DLAS, horizontal dashed curves connect models having the same age of the Universe: $t_0 = 9, 11, 13, 15, 17$ Gyrs from upper to lower curves. In fig.1 we note that in ΛWDM there is almost no overlapping between the regions allowed by the two observational constraints: for fixed values of the Hubble parameter, cluster

abundance tends to select relatively smaller Ω_0 while DLAS constraint favour higher density parameters, which has the effect of both decreasing the free-streaming scale and to increase the small-scale power even in the absence of any free-streaming. A residual possibility seems to exist to reach a concordance for $\Omega_0 \lesssim 0.5$ and a high Hubble parameter, $h \gtrsim 0.9$ for OWDM models. However, all the current determinations of the Hubble constant indicate $0.5 < h < 0.8$; and furthermore the resulting age of the Universe would be definitely too small. We also verified that changing the primordial spectral index does not improve the general results.

The situation becomes even worse when considering $\Omega_0 = 1$ WHDM models (fig. 2). The regions allowed by DLAS and cluster abundance are largely disjoined, especially as higher Ω_ν are considered. Indeed, increasing the neutrino fraction has the effect of further reducing the power on small scales, thus further suppressing the high-redshift galaxy formation.

Based on such results we should conclude that none of the variants of the WDM gravitino-dominated scenario is able to account at the same time for the relatively small abundance of clusters at low redshift and for the relatively high Ω_{HI} in collapsed structures at high redshift.

Fig. 1: constraints on WDM models.

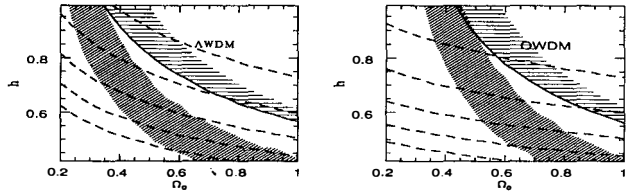

Fig.2 constraints on WHDM models.

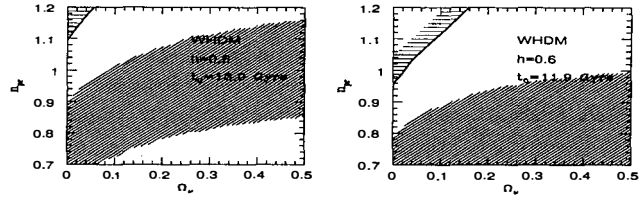

References

1. J.A. Peacock and S.J. Dodds, *Mon. Not. R.A.S.* **267**, 1020 (1994).
2. White S., Efstathiou and Frenk *Mon. Not. R.A.S.* **262**, 1023 (1993).
3. Pierpaoli E., Borgani S., Masiero A. Yamaguchi M. *Phys. Rev.* D **57**, 2089 (1998).
4. J.M. Bardeen, J.R. Bond, N. Kaiser and A.S. Szalay, *Astrophys. J.* **304**, 15 (1986).
5. Storrie-Lombardi, R.G. McMahon, M.J. Irwin and C. Hazard, in *Proceeding of the ESO Workshop on QSO Absorbtion Lines* (preprint astro-ph/9503089 (1995)).
6. P.T.P. Viana and A.R. Liddle, *Mon. Not. R.A.S.* **281**, 323 (1996).

PREHEATING THE UNIVERSE IN HYBRID INFLATION

JUAN GARCÍA-BELLIDO
Theory Division, C.E.R.N., CH-1211 Genève 23, Switzerland

One of the fundamental problems of modern cosmology is to explain the origin of all the matter and radiation in the Universe today. The inflationary model predicts that the oscillations of the scalar field at the end of inflation will convert the coherent energy density of the inflaton into a large number of particles, responsible for the present entropy of the Universe. The transition from the inflationary era to the radiation era was originally called reheating, and we now understand that it may consist of three different stages: preheating, in which the homogeneous inflaton field decays coherently into bosonic waves (scalars and/or vectors) with large occupation numbers; backreaction and rescattering, in which different energy bands get mixed; and finally decoherence and thermalization, in which those waves break up into particles that thermalize and acquire a black body spectrum at a certain temperature. These three stages are non-perturbative, non-linear and out of equilibrium, and we are just beginning to understand them. In this talk I will concentrate on the preheating part, putting emphasis on the differences between preheating in chaotic and in hybrid inflation.

1 Introduction

At the end of inflation all the energy density is in the homogeneous zero mode of the inflaton field. The Universe is in a vacuum-like state with zero temperature and vanishing particle and entropy densities. The problem of reheating is how to convert all this coherent energy into a state of thermalized relativistic particles. The original analysis [1] assumed the perturbative decay of the inflaton into bosons and fermions, as if the inflaton were already an ensemble of decoherent *particles*. Reheating ended when the total decay rate of the inflaton was of the order of the expansion rate of the Universe, $\Gamma \sim H$, while the total energy of the inflaton field decayed exponentially fast into other particles. As a consequence, the final reheating temperature only depended upon Γ. We understand today that, for certain parameter ranges, there is a new decay channel that is non-perturbative,[2] due to the coherent oscillations of the inflaton field,

which induces stimulated emission of bosonic[a] particles into energy bands with large occupation numbers. The modes in these bands can be understood as Bose condensates, and they behave like classical waves. The backreaction of these modes on the homogeneous inflaton field and the rescattering among themselves produce a state that is far from thermal equilibrium and may induce very interesting phenomena, such as non-thermal phase transitions [3] with production of topological defects, a stochastic background of gravitational waves,[4] production of heavy particles in a state far from equilibrium, which may help GUT baryogenesis[5] or constitute today the dark matter in our Universe.[6] These classical waves eventually reach a state of turbulence where, hopefully, decoherence will occur and thermalization will follow, although these stages are not yet fully understood, either analytically or numerically.

The period in which particles are produced via parametric resonance is called *preheating*.[2] The idea is relatively simple, the oscillations of the inflaton field induce mixing of positive and negative frequencies in the quantum state of the field it couples to. In the language of quantum fields in curved space, creation and annihilation operators mix via Bogoliubov transformations,[b] $a_k = \alpha_k \bar{a}_k + \beta^* \bar{a}^\dagger_{-k}$, and with every oscillation of the inflaton field, new particles are produced, $n_k \equiv \langle \bar{0}|a^\dagger_k a_k|\bar{0}\rangle = |\beta_k|^2$. In the case of chaotic inflation, with a massive inflaton ϕ coupled to a massless scalar field χ, the evolution equation for the Fourier modes, $\ddot{X}_k + \omega_k^2 X_k = 0$, with $X_k = a^{3/2}(t)\chi_k$ and $\omega_k^2 = k^2/a^2(t) + g^2\phi^2(t)$, can be cast in the form of a Mathieu equation, with coefficients $A = k^2/4a^2m^2 + 2q$ and $q = g^2\Phi^2/4m^2$, where Φ is the amplitude and m is the frequency of inflaton oscillations, $\phi(t) = \Phi(t)\sin mt$. For certain values of the parameters (A, q) there are exact solutions that grow exponentially with time, and each mode k belongs to an instability band of the Mathieu equation.[c] These instabilities can be interpreted as coherent "particle" production with large occupation numbers. One way of understanding this phenomenon is to consider the energy of these modes as that of a harmonic oscillator, $E_k = |\dot{X}_k|^2/2 + \omega_k^2|X_k|^2/2 = \hbar\omega_k(n_k + 1/2)$. The occupation number of level k can grow exponentially fast, $n_k \sim \exp(2\mu_k mt) \gg 1$, and these modes soon behave like classical waves. It is analogous to the well-known mechanism of generation of density perturbations during inflation.[1] The parameter q during preheating determines the strength of the resonance. It is possible that the model parameters are such that parametric resonance does *not* occur, and then the usual perturbative approach would follow, with decay rate Γ. In fact, as the Universe expands, the growth of the scale factor and the decrease of the amplitude of inflaton oscillations shifts the values of (A, q) along the stability/instability chart of the Mathieu equation, going from broad resonance, for $q \gg 1$, to narrow resonance, $q \ll 1$, and finally to the perturbative decay of the inflaton. Parametric resonance will stop whenever the inflaton decay is dominated by the perturbative decay, $qm < \Gamma$, or when the instability modes are redshifted away from the (last) narrow resonance band, $q^2 m < H$.

2 Preheating in hybrid inflation

Until recently, preheating had been studied in chaotic and new inflation only,[9] where the end of inflation occurs when the rate of expansion is of order the mass of the field, $m \sim H$, and the inflaton starts to oscillate around the minimum of its potential, inducing particle production.[d] In a recent paper,[10] we have studied the case of hybrid inflation, where the end of inflation is triggered by the symmetry breaking of another scalar field coupled to the inflaton, and not

[a] Fermions can also be parametrically amplified, but their occupation numbers are constrained, $n_k \leq 1$, by Pauli's exclusion principle.

[b] For an introduction to particle production in strong external fields, see Grib et al.[7]

[c] For a recent comprehensive review on preheating after chaotic inflation see Kofman [8] and references therein.

[d] Although production of classical "waves" is more appropriate, we will nevertheless use the terminology of "particle" production with large occupation numbers.

by slow-roll.[11] This fact alone gives hybrid inflation several advantages with respect to chaotic inflation. First, we can consider models of inflation at low-energy scales, say the electroweak scale, which nevertheless give the correct amplitude of temperature fluctuations in the CMB. Second, we may have an effective frequency of oscillation of one or both of the scalar fields being much larger than the rate of expansion. As we will see, this induces a very efficient and long-lived narrow resonance, where many oscillations occur in one Hubble time, and a large number of particles are produced before their momenta are redshifted by the expansion of the Universe. Preheating can be very efficient in this case. Third, at the stage of rescattering, gravitational waves are produced with wavelengths at most of order the size of the horizon at that time, large enough today to be detected at gravitational wave interferometers such as LIGO.

There are two fields in hybrid models, ϕ drives slow-roll inflation and σ triggers its end through a symmetry-breaking potential,

$$V(\phi,\sigma) = \frac{1}{4\lambda}(M^2 - \lambda\sigma^2)^2 + \frac{1}{2}m^2\phi^2 + \frac{1}{2}g^2\phi^2\sigma^2 . \tag{1}$$

These fields may couple to yet another one, χ, with couplings $(h_1^2\phi^2 + h_2^2\sigma^2)\chi^2/2$. Preheating depends very strongly on the model parameters. During inflation, the symmetry-breaking field σ has a large mass, due to its coupling to ϕ, and is fixed at $\sigma = 0$. The inflaton ϕ slow-rolls down its effective potential $V(\phi) = V_0 + m^2\phi^2/2$, driving inflation and producing the metric fluctuations that later will give rise to temperature anisotropies in the CMB and density perturbations for large-scale structure. The amplitude of temperature anisotropies on the scale of the horizon, as seen by COBE,[12] constrains the parameters of the model to satisfy

$$\frac{g}{\lambda\sqrt{\lambda}}\frac{M^5}{m^2M_P^3} \simeq 3.5\times10^{-5} , \tag{2}$$

$$n - 1 \simeq \frac{\lambda}{\pi}\frac{m^2M_P^2}{M^4} < 0.2 . \tag{3}$$

Contrary to the case of chaotic inflation, these constraints leave plenty of freedom to chose the model parameters. One of the advantages of hybrid inflation is that the rate of expansion at the end of inflation, $H \sim M^2/\sqrt{\lambda}M_P$, could be in a wide range of scales, from just below Planck scale, as in models of supergravity hybrid inflation,[15] all the way to the electroweak scale. In terms of the rate of expansion, COBE constraints can be written as $g = 2\times10^{-4}(n-1)\,M/H$ and $n - 1 = 2m^2/3H^2 < 0.2$.

When the inflaton ϕ falls below $\phi_c = M/g$, the field σ triggers the end of inflation via a sudden or "waterfall" spontaneous symmetry breaking. This process occurs because of the exponential growth of quantum fluctuations. In most models of hybrid inflation, the mass-squared of the σ field changes from large and positive to large and negative in much less than one e-fold.[c] It can then be shown that all tachyonic modes grow at approximately the same speed and thus the σ field can be described as a homogeneous field.[10] The behaviour of ϕ and σ after the end of inflation therefore follows the homogeneous field equations, and depends crucially on the ratio of couplings,

$$\frac{g}{\sqrt{\lambda}} \simeq (n-1)\frac{M_P}{M}10^{-4} . \tag{4}$$

Depending on whether $g^2 \ll \lambda$, $g^2 \gg \lambda$ or $g^2 \sim \lambda$, the oscillations around the minimum will occur mainly along the ϕ field, the σ field, or both, respectively. Due to their mutual couplings, the resonant production of particles could be very efficient or completely suppressed, depending on this ratio.[10] Another important factor is the relation of the frequency of oscillations to the rate of expansion. In chaotic inflation this was fixed by the end of slow-roll condition, $m \sim H$.

[c] There are hybrid models with two stages of inflation where this condition is not satisfied.[13,14]

However, in hybrid inflation we have the freedom to lower the rate of expansion with respect to the mass M and thus we can consider models where the field oscillates many times, as much as 10^8 times, in one Hubble time.[10] Thus, the resonant modes remain for a long time in their instability bands and may produce large occupation numbers before they are redshifted away by the expansion.[9] In particular, in hybrid preheating, the narrow resonance may be long-lived, $q^2\bar{m} > H$, even for very small parameters $q \ll 1$, thanks to $\bar{m} \gg H$. This is a fundamental difference with respect to chaotic inflation. Let us now consider in some detail the three different cases mentioned above.

In the first case, $g^2 \ll \lambda$, the frequency of oscillations of the ϕ field is $\bar{m} \simeq gM/\sqrt{\lambda} \gg m$ and, depending on the model parameters, can be much greater than the rate of expansion. For $\bar{m} \sim H$, the symmetry-breaking field soon settles at its minimum σ_0, giving large masses to any field it couples to, while the amplitude of inflaton oscillations quickly decays with the expansion of the Universe. As a consequence, there is essentially no production of either ϕ or σ particles.[10] However, if a massless scalar (or vector) field χ couples to ϕ, and not to σ (for whatever symmetry reason), it is possible to produce χ-particles in the broad resonance regime, for a wide range of couplings. This is the situation that most resembles that of chaotic inflation; the growth parameter is $\mu \sim 0.13$ and backreaction sets in after about 20 oscillations of the ϕ field. In the other case, $\bar{m} \gg H$, the amplitude of oscillations of ϕ after the end of inflation remains large, of order ϕ_c, during many oscillations, driving explosive particle production even in the narrow resonance, for $\mu_k \ll 1$. Since the rate of expansion is so small, the modes remain in the narrow resonance for a long time, and backreaction on the inflaton oscillations occurs before the modes are redshifted away from the resonance.[10] This is very different from the behaviour in chaotic inflation. However, even if χ particles are quickly produced, we still do not have a significant production of ϕ or σ particles before χ-production backreacts on ϕ.

In the case $g^2 \gg \lambda$, the situation described above is reversed: it is now the symmetry-breaking field that oscillates around its minimum, while the inflaton field becomes negligible. The frequency of σ oscillations is $\bar{m} = \sqrt{2}M$ and, as before, it can be much larger than the rate of expansion. For $\bar{m} \sim H$, the inflaton settles at $\phi = 0$ while σ oscillates with ever-decreasing amplitude. In this case, there is an insignificant production of either ϕ or σ particles, due to their large effective masses.[10] Furthermore, if a field χ couples to either ϕ or σ its production via parametric resonance is suppressed, because of the small amplitude of ϕ oscillations or of the effective mass induced by σ_0, respectively. It follows that preheating in this case is very inefficient. On the other hand, for $\bar{m} \gg H$, explosive particle production occurs for all fields, but mainly for σ particles. Even though the resonance is not particularly broad, $q \sim 6$, the growth parameter is very large, $\mu \sim 0.3$, and there is very efficient preheating in just a few oscillations, before backreaction sets in. At the same time, production of ϕ and χ particles is possible, although not as efficiently as for σ.[10] Note that preheating in this model could occur even in the absence of extra fields χ, simply due to the self-coupling of the symmetry-breaking field.

Finally, in the case $g^2 \sim \lambda$, typical of certain models of hybrid inflation in supergravity,[15] the two homogeneous fields oscillate with similar amplitudes and frequencies around the global minimum ($\phi = 0, \sigma = \sigma_0$). Since they are coupled, their frequencies and amplitudes vary rather chaotically and it takes many oscillations for their behaviour to stabilize around a periodic oscillation. During the chaotic motion, there can be no parametric resonance since this effect requires a periodic behaviour. By the time the oscillations become periodic, the amplitude has decreased so much that not even the narrow resonance can be excited. Thus, for $\bar{m} \sim H$, there is no particle production in either of the three fields.[10] However, for $\bar{m} \gg H$, there are many oscillations in one Hubble time and eventually the motion becomes periodic while the amplitude of oscillations is still large. This results in a mild production of ϕ and σ particles and an explosive production of χ particles, if coupled only to the ϕ field.[10]

It should be noted that, in hybrid preheating, the equation that describes the instability growth of modes χ_k is not exactly of the Mathieu type. Even if the χ field couples only to one of the fields, ϕ or σ, the fact that the two homogeneous fields follow coupled equations implies that the frequencies of oscillations of each field will vary strongly with time, unless the other field is fixed at its minimum. This does no preclude parametric resonance, it simply modifies the stability/instability chart. In some of the cases we studied,[10] the analysis with the Mathieu equation is a reasonably good approximation; in others, one has to compute the corresponding spectrum of instability bands. This is particularly important for the case $g^2 \sim \lambda$, where both fields oscillate simultaneously in a rather chaotic way and their frequencies of oscillation depend explicitly on the value of the other field, which changes within one oscillation.

3 Phenomenological consequences

The processes by which the classical waves with large occupation numbers produced at preheating decohere and become an ensemble of relativistic particles in thermal equilibrium is still uncertain. Numerical lattice simulations have been performed to try to understand the process of backreaction and rescattering of those waves among themselves and with the inflaton background;[16] however, no one has yet been able to compute the final reheating temperature of a model in which preheating was important. It could be that, in the end, the reheating temperature is precisely the one computed from the usual perturbative analysis, $T_{rh} \sim 0.1\sqrt{\Gamma M_P}$. However, the reheating temperature is not the only observable one can consider; in fact, preheating has opened the door to very exotic phenomena that might have novel experimental signatures with which to test our models of inflation. The interesting period is that after backreaction and before thermalization, where large numbers of particles (or waves) rescatter off themselves in a state far from equilibrium. Among these new phenomena, there are non-thermal phase transitions [3] with production of topological defects; generation of gravitational waves;[4] or production of heavy particles in a state far from equilibrium, which may help GUT baryogenesis [5] or constitute the dark matter in our Universe.[6]

I will concentrate here on the production of a stochastic background of gravitational waves, which has specific signatures in the case of hybrid preheating. The idea is the following: the collisions among coherent waves of particles during rescattering radiates a reasonable fraction of energy, typicaly $\sim 10^{-5}$, in the form of gravitational waves. Their spectrum today depends on the details of rescattering and can be computed only numerically in lattice simulations.[4] However, the low-frequency end of the spectrum, for wavelengths of order the size of the horizon at rescattering, can be computed analytically since in that case it is dominated by the gravitational bremsstrahlung associated with the scattering of χ particles off the inflaton condensate, with the corresponding "evaporation" of inflaton particles. Taking into account that the occupation numbers of χ particles are typically of order $n_k(\chi) \sim 10^2 h_1^{-2}$ at the end of rescattering,[9] and assuming that decoherence and thermalization occurred immediately after this stage, one can estimate the fraction of energy density in gravitational waves today [4]

$$\Omega_{gw}(\omega)h^2 \sim \Omega_{rad}h^2 \frac{\bar{m}^2}{h_1^2 M_P^2} \frac{\omega}{H_{rs}} \left(\frac{g_0}{g_*}\right)^{1/3}, \qquad (5)$$

where $\Omega_{rad}h^2 \simeq 4 \times 10^{-5}$ and $\Omega_{gw}(\omega) \equiv (\rho_c^{-1} d\rho_{gw}/d\ln\omega)_0$. On the other hand, the wavelengths $2\pi/k_{rs}$ of the gravitational wave spectrum are redshifted to $\lambda \simeq 0.5(M_P H_{rs})^{1/2} k_{rs}^{-1}$ today.[4] In particular, the largest wavelength today corresponds to the size of the horizon at rescattering, or $k_{rs} \sim H_{rs}$, and therefore the minimum frequency in the spectrum is $f_{min} \simeq 2\times 10^2\, (H_{rs}/TeV)^{1/2}$ Hz, which is right in the centre, for $H_{rs} \sim 1$ TeV, of the range of frequencies detectable by LIGO, $10\,Hz \leq f \leq 10^4$ Hz. In chaotic inflation, the fraction in gravitational waves today is typically [4] of order $\Omega_{gw}h^2 \sim 10^{-12}$ at the minimum frequency $f_{min} \sim 10^6$ Hz, which lies outside the range of

frequencies and expected sensitivity of LIGO. The large rate of expansion at rescattering turns out to be a disadvantage for detecting gravitational waves from preheating in chaotic inflation. One would require a much lower rate, of order a few TeV, to be within the range of LIGO.

Let us consider now a concrete hybrid inflation model with a low rate of expansion at the end of inflation, $H \sim 10^2$ TeV. Such a model could be consistent with COBE observations with very natural parameter values, $g^2 \sim 0.01, \lambda \sim 1, M \sim 10^{12}$ GeV and $m \sim 1$ TeV. This model is of the first type, $g^2 \ll \lambda$, and has a large frequency of oscillations of the inflaton field, $\bar{m} \sim 10^6 H$. There will be explosive production of χ particles even in the narrow resonance, $q \sim 10^4 h_1^2 \sim 10^{-3}$, with a very small growth parameter $\mu \simeq q/2$. Backreaction in this model occurs at $\bar{m}t_1 \simeq (1/4\mu)\ln(10^6 \bar{m}(\bar{m}t_1)^3/h_1^5 M_P)^{1/2} \sim 33/q$, which is still below one Hubble time, $t_1 \sim H^{-1}/30$, after the end of inflation. The occupation numbers of χ particles at this stage can be estimated[9] as $n_k(\chi) \simeq 3 \times 10^2 h_1^{-2} q^{-1/4} \sim 30\, h_1^{-5/2}$. Therefore, the estimate of Eq.(5) should be modified with an extra factor $10h_1$ in the denominator. Taking $H_{rs} \sim 10$ TeV at the end of rescattering, the fraction of energy density in gravitational waves today is $\Omega_{gw} h^2 \sim 4 \times 10^{-10}$ at the minimum frequency $f_{min} \sim 600$ Hz, just in the appropriate range for detection by LIGO.

We conclude that preheating in hybrid inflation has many features that differs from the usual chaotic or new inflation type of preheating, and makes it phenomenologically attractive: inflation may occur at a much lower scale, and still give the desired amplitude of temperature anisotropies in the CMB; there could be many oscillations of the inflaton field per Hubble time after inflation, which allows for a long-lived narrow resonance and very efficient preheating; and it is possible, in certain models, to generate a stochastic background of gravitational waves in a range accesible to observations.

Acknowledgements

I thank Andrei Linde for generous discussions and insights into the problems of reheating.

References

1. A.D. Linde, *Particle Physics and Inflationary Cosmology* (Harwood, Chur, 1990).
2. L. Kofman, A.D. Linde and A.A. Starobinsky, *Phys. Rev. Lett.* **73**, 3159 (1994).
3. L. Kofman, A.D. Linde and A.A. Starobinsky, *Phys. Rev. Lett.* **76**, 1011 (1996); I.I. Tkachev, *Phys. Lett.* B **376**, 35 (1996).
4. S.Yu. Khlebnikov and I.I. Tkachev, *Phys. Rev.* D **56**, 653 (1997).
5. E.W. Kolb, A.D. Linde and A. Riotto, *Phys. Rev. Lett.* **77**, 4290 (1996).
6. D.J.H. Chung, E.W. Kolb and A. Riotto, `hep-ph/9802238` (1998).
7. A.A. Grib, S.G. Mamayev and V.M. Mostepanenko, *Vacuum Quantum Effects in Strong Fields* (Friedmann Laboratory Publishing, St. Petersburg, 1994).
8. L. Kofman, `astro-ph/9605155`, `astro-ph/9802221`, `astro-ph/9802285` (1998).
9. L. Kofman, A.D. Linde and A.A. Starobinsky, *Phys. Rev.* D **56**, 3258 (1997); P.B. Green, L. Kofman, A.D. Linde and A.A. Starobinsky, *Phys. Rev.* D **56**, 6175 (1997).
10. J. Garcí a-Bellido and A.D. Linde, `hep-ph/9711360`, to appear in *Phys. Rev.* D (1998).
11. A.D. Linde, *Phys. Lett.* B **259**, 38 (1991); *Phys. Rev.* D **49**, 748 (1994).
12. C.L. Bennett *et al.*, *Astrophys. J.* **464**, L1 (1996).
13. L. Randall, M. Soljačić and A.H. Guth, *Nucl. Phys.* B **472**, 377 (1996).
14. J. Garcí a-Bellido, A.D. Linde and D. Wands, *Phys. Rev.* D **54**, 6040 (1996).
15. A.D. Linde and A. Riotto, *Phys. Rev.* D **56**, 1841 (1997).
16. S.Yu. Khlebnikov and I.I. Tkachev, *Phys. Rev. Lett.* **77**, 219 (1996); **79**, 1607 (1997); T. Prokopec and T.G. Roos, *Phys. Rev.* D **55**, 3768 (1997); B.R. Greene, T. Prokopec and T.G. Roos, *Phys. Rev.* D **56**, 6484 (1997).

NON-EQUILIBRIUM ASPECTS OF INFLATIONARY COSMOLOGY

D. BOYANOVSKY[a], D. CORMIER[b], H. J. DE VEGA[c], R. HOLMAN[b], S.PREM KUMAR[b]
(a)Department of Physics and Astronomy, University of Pittsburgh, Pittsburgh PA 15260, U.S.A.
(b) Department of Physics, Carnegie Mellon University, Pittsburgh PA 15213, U.S.A
(c) LPTHE, Universite Pierre et Marie Curie (Paris VI) et Denis Diderot (Paris VII), Tour 16 1er. etage, 4, Place Jussieu. 75252, cedex 05, France

Non-equilibrium quantum field theory is applied to the dynamics of the inflaton. We show how, in new inflation models, non-perturbatively large quantum fluctuations are generated. We then discuss how perturbatively small metric perturbations can be made compatible with this, at least within the large N approximation.

1 Introduction

It has become ever clearer that knowledge of the equilibrium behavior of quantum field theories is not enough to provide an understanding of the quantum *dynamics* of the system. This has inspired the development and application of new techniques based on the so-called Schwinger-Keldysh[1] or Closed Time Path (CTP) approach to non-equilibrium dynamics.

For the past few years our group, as well as others, has applied these techniques to questions involving various aspects of inflation[2].

The basic question we deal with is: how do the quantum fluctuations of a field influence its dynamics? Put another way, we can ask to what extent can an analysis of inflaton dynamics beased solely on the classical potential or the quantum effective potential be trusted? We have examined this problem in some detail[3] and have arrived at some very interesting conclusions.

For models using initial conditions of the chaotic inflation[4] type, where the initial value of the inflaton zero momentum mode is far from the potential minimum, we can show explicitly that quantum fluctuations always remain small and the dynamics is essentially classical.

However, for initial conditions of the new inflation[5] type, where the inflaton zero mode starts off at or near an unstable extremum, the quantum fluctuations grow due to spinodal instabilities and eventually grow larger than the value of the zero mode, thus rendering perturbation theory useless! Dealing with such a situation requires some way to go beyond perturbation theory in a systematic way.

We have develop the relevant techniques and are able to give a reasonable interpretation to these large field fluctuations. The key point to observe is that it is the very long wavelength modes that experience the spinodal instabilities the longest and thus grow largest. From the vantage point of observers today, these are modes that are still superhorizon today, which leads to the speculation that maybe they should be lumped in with the original zero mode in some way as to create an *effective* zero mode. We have shown[3] that this is exactly what happens, at least

in models where the non-perturbative growth can be dealt with in the large N approximation. The effective zero mode satisfies the classical field

equations, and drives the FRW expansion, if the coupling of the quantum field to gravity is done within the context of the semiclassical gravity approximation[6].

In the rest of the paper we review the large N approximation for scalar fields and its use in describing inflationary cosmology. The relevant non-equilibrium quantum field theory background can be found in [7], and will not be discussed here.

2 The Model

As mentioned in the introduction, the more interesting case, in terms of seeing significant departures from classical behavior, is found when new inflation initial conditions are used. This means that the field has a potential admitting spontaneous symmetry breaking and the zero mode of the field is taken to start with nearly zero velocity and near or at the unstable extremum. Due to the existence of a spinodal line, above which the potential has negative curvature, some modes will experience instabilities and grow non-perturbatively large. This growth will then back react on the zero mode, influencing its dynamics.

In order to deal with field theory beyond perturbation theory, we introduce the large N approximation[8], which is essentially a consistent resummation of perturbation theory. Let $\vec{\Phi}$ be an N column vector transforming as the fundamental representation of a global $O(N)$ symmetry. This field will represent the inflaton. The Lagrangian for this field is given by

$$\mathcal{L} = a^3(t) \left[\begin{array}{c} \frac{1}{2}\partial\vec{\Phi}\cdot\partial\vec{\Phi} - \frac{1}{2}\left(m^2 + \xi\,\mathcal{R}\right)\vec{\Phi}\cdot\vec{\Phi} - \\ \frac{\lambda}{8\,N}\left(\vec{\Phi}\cdot\vec{\Phi}\right)^2 \end{array} \right], \tag{1}$$

where we allow for a coupling to the curvature scalar $\mathcal{R}$. We can make use of the $O(N)$ symmetry to choose the homogeneous mode to lie in the direction of the first component of $\vec{\Phi}$ so that:

$$\begin{aligned} \left(\vec{\Phi}\right)_1 &= \sqrt{N}\,\sigma(t) + \psi(\vec{x},t), \\ \left(\vec{\Phi}\right)_i &= \pi_i(\vec{x},t) \qquad i \geq 2. \end{aligned} \tag{2}$$

The factors of N are placed in such a way so that a non-trivial large N limit can be attained. The field σ will be the actual inflaton field.

The large N approximation consists of factoring the potential term $\left(\vec{\Phi}\cdot\vec{\Phi}\right)^2$ in such a way so as to render the theory quadratic, without losing all the effects of the interactions and making sure that in the ground state, the fields $\pi_i(\vec{x},t)$ are the Goldstone bosons of the spontaneously broken $O(N)$ symmetry. Doing this, yields the following set of equations:

$$\ddot{\sigma} + 3\,H\,\dot{\sigma} + \left(m^2 + \xi\,\mathcal{R}\right)\sigma + \frac{\lambda}{2}\sigma^3 + \frac{\lambda}{2}\sigma\left\langle\vec{\pi}^2\right\rangle = 0 \tag{3}$$

$$\left[\frac{d^2}{dt^2} + 3\,H\,\frac{d}{dt} + \frac{k^2}{a^2(t)} + m^2 + \xi\,\mathcal{R} + \frac{\lambda}{2}\sigma^2 + \frac{\lambda}{2}\sigma\left\langle\vec{\pi}^2\right\rangle\right] f_k(t) = 0, \tag{4}$$

$$\left\langle\vec{\pi}^2\right\rangle = \int \frac{d^3k}{2\,(2\pi)^3}\,|f_k(t)|^2\,. \tag{5}$$

The $f_k(t)$ comoving momentum modes corrresponding to the fluctuations in the pion directions.

Note that if $m^2 < 0$ than for low enough $k/a(t)$, some fluctuations will feel the effects of a negative *effective* mass squared; this is the root cause of the instabilities driving the growth

of $\langle \vec{\pi}^2 \rangle$. Also note that the equation for $f_{k=0}(t)$ is the same as that for $\sigma(t)$. This is a very important point and does *not* happen in other approximation schemes such as the Hartree approximation.

We need to couple this theory to Einstein gravity and this brings up some issues in itself. No complete theory of quantum gravity exists today. Thus we have to make a (hopefully!) reasonable guess as to how gravity will know about the field $\vec{\Phi}$. Following historical precedent of the early days of QED, we use the semiclassical approximation[8], where the quantum mechanics of the field is incorporated into gravity by taking $\langle T_{\mu\nu} \rangle$ as the source in the Einstein equations. Here $T_{\mu\nu}$ is the stress energy operator, and the brackets denote an expectation value taken in the density matrix of the system. The problem becomes highly non-linear since the density matrix evolves according to the Liouville equation, which in turn depends on the scale factor $a(t)$ which in *its* turn depends on the semiclassical Einstein equation. Doing this yields the following equations for the gravity sector

$$-\frac{1}{8\,\pi\,G_N} G_{\mu\nu} + \left(-\frac{\Lambda}{8\,\pi\,G_N} g_{\mu\nu} \right) + \alpha\, H_{\mu\nu} = \langle T_{\mu\nu} \rangle\,, \tag{6}$$

where $G_{\mu\nu}$ is the Einstein tensor, Λ is the (bare) cosmological constant and $H_{\mu\nu}$ contains terms of higher order in the curvature tensor. Both this term and the cosmological constant term are necessary in order to absorb divergences in $\langle T_{\mu\nu} \rangle$ via the renormalization procedure.

The renormalization issues in this approach are tricky and must be approached with care. These, as well as related issues involving the initial conditions have been studied carefully and are under control[9]; using these techniques we can numerically evolve the above system of equations.

3 Results

Let's look at the case where $\sigma(0) = 0,\ \dot{\sigma}(0) = 0$; generic new inflation initial conditions can be represented by small deviations from this and are described by essentially the same physics.

Initially, we can omit the backreaction due to the growth of fluctuations, since they start off small (actually zero). The energy density of the Universe is dominated by the false vacuum energy and thus enters a DeSitter phase with Hubble parameter H. The modes are then described by:

$$\begin{aligned} f_k(t) &= e^{-\frac{3}{2}Ht} \left[A_k\, J_\nu \left(\frac{k}{H} e^{-Ht} \right) + B_k\, J_{-\nu} \left(\frac{k}{H} e^{-Ht} \right) \right], \\ \nu &= \sqrt{\frac{9}{4} + \frac{m^2}{H^2}}. \end{aligned} \tag{7}$$

The important thing to note is that as the modes cross the horizon, i.e. when $\frac{k}{H} e^{-Ht} << 1$ the mode functions factorize[10]:

$$f_k(t) \simeq \frac{B_k}{\Gamma(1-\nu)} \left(\frac{2\,H}{k} \right)^\nu e^{(\nu - \frac{3}{2})Ht} = C_k\, f_{k=0}(t) \tag{8}$$

¿From this result, we can compute the fluctuations integral to determine when it becomes (in the appropriate dimensionless units) of order unity; this is when perturbation theory breaks down and the backreaction has to be treated in some other way:

$$\tau_{spin} \simeq \frac{1}{2\nu - 3}\, \frac{m}{H}\, \ln \left(\frac{8\pi^2 m^2}{\lambda\, H^2} \right).$$

After this spinodal time $\langle \vec{\pi}^2 \rangle$ becomes large enough to sample the minima of the potential and inflation ends.

We can track the equation of state of the system from the onset of inflation through its end. At the beginning, we find $p = -\rho$ as expected for DeSitter inflation. When inflation ends, however, we might have expected an equation of state corresponding to a radiation dominated universe, since pion quanta are produced and they are massless in the asymptotic state. However, what we find is $p \simeq 0$, i.e. a matter dominated equation of state!

What this should bring to mind is a zero mode oscillating around its potential minimum; however, the original zero mode is fixed at the origin, and by symmetry, it will remain there throughout the time evolution of the system. Another hint as to what is going on can be obtained by looking at which modes are driving the growth of the fluctuations integral $\langle \vec{\pi}^2 \rangle$; it is the very long wavelength modes that dominate this integral.

The natural inference to make is that these long wavelength modes are dynamically assembling themselves into an *effective* zero mode. This is in fact what is happening, although showing this and actually constructing the relevant effective operator is highly non-trivial[8]. In the more general situation where the original zero mode starts from near the origin, we show that the effective zero mode is given by

$$\sigma_{eff}(t) = \sqrt{\sigma(t)^2 + \langle \vec{\pi}^2 \rangle}. \tag{9}$$

The factorization of the mode functions after a sufficient number of e-folds have passed is crucial in order to prove that $\sigma_{eff}(t)$ satisfies the classical equation and that its energy density and pressure drive the FRW expansion.

The perturbatively small fluctuations left over after this zero mode "reassembly" procedure give rise to the metric perturbations and the standard gauge invariant treatement[11] can then be used to compute the power spectrum. We can also show, by computing the density matrix that the inflationary proceedure induces decoherence in the sense that the off-diagonal elements of the density matrix oscillate wildly at late times, thus washing out any contribution in expectation values. This is a generalization of the the work of Polarski and Starobinski[12] on "decoherence without decoherence" to the case of an interacting field theory.

While it may appear obvious that the large superhorizon modes should be interpreted as part of an effective zero mode, it is really a very non-trivial statement. First, this is only true once the fluctuations operator is made finite, a complex task. Furthermore, there are models that cannot be treated within the large N approximation, such as Natural Inflation[13] for which this zero mode reassembly does *not* occur! In this case we would be left with the situation of having acutal large fluctuations which would naturally drive the generation of large metric perturbations. Whether this is a real effect or an artifact of having to make a non-perturbative approximation to the full theory is under study[14]

4 Conclusions

Inflation is an inherently out of equilibrium phenomenon, and must be treated as such. The Schwinger-Keldysh or Closed Time Path formalism is ideally suited to doing this and we have applied it here to better understand that quantum dynamics of the inflaton.

New Inflation models exhibit very interesting behavior in that they admit spinodal decomposition and thus large growth of field fluctuations. These become non-perturbative by the end of inflation and have to be dealt with in some approximation scheme such as the large N approximation or the Hartree approximation.

In tha large N case, we find that we have to redefine what we mean by the zero momentum mode of the inflaton; it becomes a reassembled combination of the original zero mode and the fluctuations integral, taken in quadrature.

Is this a generic feature? We have been able to show that in some interesting cases, it does not occur. These and other questions are currently under investigation.

Acknowledgments

R.H. would like to thank the Organizers of the Moriond conference for a very enjoyable and fruitful meeting. R.H., D.C. and S.P.K were supported in part by DOE grant DE-FG02-91-ER40682. D.B. was supported in part by NSF grant PHY-9605186.

References

1. J. Schwinger, J. Math. Phys, **2**, 407 (1961); L.V. Keldysh, Sov. Phys. JETP **20**, 1018 (1965).
2. A.H. Guth, *Phys. Rev.* D **23**, 347 (1981).
3. D. Boyanovsky, D. Cormier, H. J. de Vega, R. Holman, S. P. Kumar, *Phys. Rev.* D **57**, 2166 (1998).
4. A.D. Linde, *Phys. Lett.* **175** B, 395 (1986)
5. .A.Albrecht and P. J. Steinhardt, *Phys. Rev.Lett.* **48**, 1220 (1982); A.D. Linde, *Phys. Lett.* **108** B, 389 (1982).
6. N.D. Birrell and P.C.W. Davies, *Quantum Fields in Curved Space*, Cambridge University Press (1986).
7. D.Boyanovsky, H.J. de Vega and R. Holman in *Proceedings of the International School of Astrophysics, D. Chalonge: 5th Course: Current Topics in Astrofundamental Physics*, edited by Norma Sanchez and A. Zichichi (World Scientific, Singapore, 1997).
8. F.Cooper, S. Habib, Y. Kluger and E. Mottola, *Phys. Rev.* D **55**, 6471 (1997).
9. D. Boyanovsky, D. Cormier, H. J. de Vega, R. Holman, A. Singh, M. Srednicki, *Phys. Rev.* D **56**, 1939 (1997).
10. A.H. Guth and S.Y. Pi, *Phys. Rev.* D **32**, 1899 (1985).
11. R.H. Brandenberger, H..A. Feldman, V.F. Mukhanov, *Phys. Rep.* **215** 293 (1992).
12. D.Polarski and A.A. Starobinski, *Class. Quant. Grav.* **13**, 377 (1996); J. Lesgourgues, D.Polarski and A.A. Starobinski, *Nucl.Phys.* **B497** 479 (1997).
13. Fred Adams, J. R. Bond, Katherine Freese, Joshua Frieman, Angela Olinto, *Phys. Rev.* D **47**, 426 (1993).
14. D. Boyanovsky, D. Cormier, H. J. de Vega, R. Holman, S. P. Kumar, in preparation (1998).

RECENT DEVELOPMENTS IN ELECTROWEAK BARYOGENESIS

A. RIOTTO
CERN Theory Division,
CH-1211 Geneva 23, Switzerland

We discuss some recent developments made in the computation of the baryon asymmetry generated at the electroweak scale. We emphasize that the local number density asymmetries of the particles involved in supersymmetric electroweak baryogenesis must be described by a set of Quantum Boltzmann Equations. These diffusion equations automatically and self-consistently incorporate the CP-violating sources which fuel baryogenesis and manifest "memory" effects which are typical of the quantum transport theory and are not present in the classical approach.

1 Prologo

Because of the presence of unsuppressed baryon number violating processes at high temperatures, the Standard Model (SM) of weak interactions fulfills all the requirements for a successful generation of the baryon number at the electroweak scale. The baryon number violating processes also impose severe constraints on models where the baryon asymmetry is created at energy scales much higher than the electroweak scale. Unfortunately, the electroweak phase transition is too weak in the SM. This means that the baryon asymmetry generated during the transition would subsequently be erased by unsuppressed sphaleron transitions in the broken phase.

The most promising and well-motivated framework for electroweak baryogenesis beyond the SM seems to be supersymmetry (SUSY). Electroweak baryogenesis in the framework of the Minimal Supersymmetric Standard Model (MSSM) has attracted much attention in the past years, with particular emphasis on the strength of the phase transition [1,2,3] and the mechanism of baryon number generation [4,5,6,7].

Recent analytical [8,9] and lattice computations [10] have also revealed that the phase transition can be sufficiently strongly first order if the ratio of the vacuum expectation values of the two neutral Higgses $\tan\beta$ is smaller than ~ 4. Moreover, taking into account all the experimental bounds as well as those coming from the requirement of avoiding dangerous color breaking

minima, the lightest Higgs boson should be lighter than about 105 GeV, while the right-handed stop mass might be close to the present experimental bound and should be smaller than, or of the order of, the top quark mass[9].

Moreover, the MSSM contains additional sources of CP-violation besides the CKM matrix phase. These new phases are essential for the generation of the baryon number since large CP-violating sources may be locally induced by the passage of the bubble wall separating the broken from the unbroken phase during the electroweak phase transition. Baryogenesis is fuelled when transport properties allow the CP-violating charges to efficiently diffuse in front of the advancing bubble wall where anomalous electroweak baryon violating processes are not suppressed. The new phases appear in the soft supersymmetry breaking parameters associated to the stop mixing angle and to the gaugino and neutralino mass matrices; large values of the stop mixing angle are, however, strongly restricted in order to preserve a sufficiently strong first order electroweak phase transition. Therefore, an acceptable baryon asymmetry from the stop sector may only be generated through a delicate balance between the values of the different soft supersymmetry breaking parameters contributing to the stop mixing parameter, and their associated CP-violating phases[5]. As a result, the contribution to the final baryon asymmetry from the stop sector turns out to be negligible. On the other hand, charginos and neutralinos may be responsible for the observed baryon asymmetry if the phase of the parameter μ is large enough[5,7]. Yet, this is true within the MSSM. If the strength of the electroweak phase transition is enhanced by the presence of some new degrees of freedom beyond the ones contained in the MSSM, *e.g.* some extra standard model gauge singlets, light stops (predominantly the right-handed ones) and charginos/neutralinos are expected to give quantitatively the same contribution to the final baryon asymmetry.

2 The old wisdom

In this talk we will mainly concern ourselves with the recent developments done in the computation of the baryon asymmetry. Since it not our intention to get into technical details, we will only try to give the feeling of what is going on.

Let us first mention what was done in the old days.

The baryon asymmetry has been usually computed using the following separate steps[4,5]:

1) Look for those charges which are approximately conserved in the symmetric phase, so that they can efficiently diffuse in front of the bubble where baryon number violation is fast, and non-orthogonal to baryon number, so that the generation of a non-zero baryon charge is energetically favoured. Charges with these characteristics in the MSSM are the axial stop charge and the Higgsino charge, which may be produced from the interactions of squarks and charginos and/or neutralinos with the bubble wall, provided a source of CP-violation is present in these sectors;

2) Compute the CP-violating currents of the plasma locally induced by the passage of the bubble wall. The methods present in the literature properly incorporate the decoherence effects which may have a crucial impact on the generation of the CP-violating observable;

3) Write and solve a set of coupled differential diffusion equations for the local particle densities, including the CP-violating source terms derived from the computation of the current at step *2)* and the particle number changing reactions. The solution to these equations gives a net baryon number which is produced in the symmetric phase and then transmitted into the interior of the bubbles of the broken phase, where it is not wiped out if the first transition is strong enough. It is important to notice that the CP-violating sources have been usually inserted into the diffusion equations by hand only after the CP-violating currents have been defined and computed. This procedure is certainly appropriate to describe the damping effects on the CP-violating observables originated by the plasma interactions, but it does not incorporate any

relaxation time scale arising when diffusion and particle changing interactions are included (even though this approximation might be good if the diffusion time scales are larger than the damping time scales) and is theoretically *not* consistent. More important, since a certain degree of arbitrariness is present in the way the CP-violating sources may be defined, different CP-violating sources have been adopted for the stop and the Higgsino sectors in the literature [4,5]. This is certainly not an academic question since different sources may lead to different numerical results for the final baryon asymmetry (especially if the sources are expressed in terms of a different number of derivatives of the Higgs bubble wall profile and, therefore, in terms of different powers of the bubble wall velocity v_ω and bubble wall width L_ω).

3 The new wisdom

It is indisputable that a set of transport (diffusion) equations *already* incorporating the CP-violating sources in a self-consistent way may be obtained only by means of a more complete treatment of the problem. Non-equilibrium Quantum Field Theory provides us with the necessary tools to write down a set of quantum Boltzmann equations (QBE's) describing the local particle densities and automatically incorporating the CP-violating sources. The most appropriate extension of the field theory to deal with these issues it to generalize the time contour of integration to a closed time-path (CTP). The CTP formalism is a powerful Green's function formulation for describing non-equilibrium phenomena in field theory and it leads to a complete non-equilibrium quantum kinetic theory approach.

3.1 Out-of-equilibrium field theory with a broad rush

The CTP formalism (often dubbed as in-in formalism) is a powerful Green's function formulation for describing non-equilibrium phenomena in field theory. It allows to describe phase-transition phenomena and to obtain a self-consistent set of quantum Boltzmann equations. The formalism yields various quantum averages of operators evaluated in the in-state without specifying the out-state. On the contrary, the ordinary quantum field theory (often dubbed as in-out formalism) yields quantum averages of the operators evaluated with an in-state at one end and an out-state at the other.

The partition function in the in-in formalism for a *complex* scalar field is defined to be

$$\begin{aligned} Z\left[J, J^\dagger\right] &= \mathrm{Tr}\left[T\left(\exp\left[i\int_C \left(J\phi + J^\dagger\phi^\dagger\right)\right]\right)\rho\right] \\ &= \mathrm{Tr}\left[T_+\left(\exp\left[i\int \left(J_+\phi_+ + J_+^\dagger\phi_+^\dagger\right)\right]\right)\right. \\ &\times \left. T_-\left(\exp\left[-i\int \left(J_-\phi_- + J_-^\dagger\phi_-^\dagger\right)\right]\right)\rho\right], \end{aligned} \tag{1}$$

where the suffic C in the integral denotes that the time integration contour runs from minus infinity to plus infinity and then back to minus infinity again. The symbol ρ represents the initial density matrix and the fields are in the Heisenberg picture and defined on this closed time contour.

As with the Euclidean time formulation, scalar (fermionic) fields ϕ are still periodic (anti-periodic) in time, but with $\phi(t, \vec{x}) = \phi(t - i\beta, \vec{x})$, $\beta = 1/T$. The temperature appears due to boundary condition, but time is now explicitly present in the integration contour.

For non-equilibrium phenomena and as a consequence of the time contour, we must now identify field variables with arguments on the positive or negative directional branches of the time path. This doubling of field variables leads to six different real-time propagators on the contour [11]. It is possible to employ fewer than six propagators since they are not independent,

but using six simplifies the notation. For a generic bosonic charged scalar field ϕ they are defined as

$$\begin{aligned} G^{>}_{\phi}(x,y) &= -i\langle\phi(x)\phi^{\dagger}(y)\rangle, \\ G^{<}_{\phi}(x,y) &= -i\langle\phi^{\dagger}(y)\phi(x)\rangle, \\ G^{t}_{\phi}(x,y) &= \theta(x,y)G^{>}_{\phi}(x,y)+\theta(y,x)G^{<}_{\phi}(x,y), \\ G^{\bar{t}}_{\phi}(x,y) &= \theta(y,x)G^{>}_{\phi}(x,y)+\theta(x,y)G^{<}_{\phi}(x,y), \\ G^{r}_{\phi}(x,y) &= G^{t}_{\phi}-G^{<}_{\phi}=G^{>}_{\phi}-G^{\bar{t}}_{\phi}, \quad G^{a}_{\phi}(x,y)=G^{t}_{\phi}-G^{>}_{\phi}=G^{<}_{\phi}-G^{\bar{t}}_{\phi}, \end{aligned} \tag{2}$$

where the last two Green functions are the retarded and advanced Green functions respectively and $\theta(x,y)=\theta(t_x-t_y)$ is the step function. Analogous formulae hold for fermion fields. The reader is referred to [12] for more technical details.

For interacting systems whether in equilibrium or not, one must define and calculate self-energy functions. There are six of them: Σ^t, $\Sigma^{\bar{t}}$, $\Sigma^{<}$, $\Sigma^{>}$, Σ^r and Σ^a. There are some relationships among them, such as

$$\Sigma^r=\Sigma^t-\Sigma^{<}=\Sigma^{>}-\Sigma^{\bar{t}}, \quad \Sigma^a=\Sigma^t-\Sigma^{>}=\Sigma^{<}-\Sigma^{\bar{t}}. \tag{3}$$

The self-energies are incorporated into the Green functions through the use of Dyson's equations which are the starting point to get the Quantum Boltzmann equations. The latter look as follow [12]

$$\begin{aligned} \frac{\partial n_{\phi}(X)}{\partial T} &+ \vec{\nabla}_R\cdot\vec{j}_{\phi}(X) = -\int d^3r_3\int_{-\infty}^{T}dt_3\Big[\Sigma^{>}_{\phi}(X,x_3)G^{<}_{\phi}(x_3,X) \\ &- G^{>}_{\phi}(X,x_3)\Sigma^{<}_{\phi}(x_3,X)+G^{<}_{\phi}(X,x_3)\Sigma^{>}_{\phi}(x_3,X) \\ &- \Sigma^{<}_{\phi}(X,x_3)G^{>}_{\phi}(x_3,X)\Big]. \end{aligned} \tag{4}$$

Here n_{ϕ} and $\vec{j}_{\phi}$ are the particle density and current asymmetry, respectively, and the right-hand side represents the "scattering" term. It contains all the information necessary to describe the temporal evolution of the particle density asymmetries: particle number changing reactions and CP-violating source terms, which will pop out from the corresponding self-energy Σ_{CP}. In supersymmetric baryogenesis one has to consider the Quantum Boltzmann equations for right-handed stops and higgsinos [12].

3.2 It is worth doing out-of-equilibrium field theory

One of the merits of the CTP formalism is to guide us towards a rigorous and self-consistent definition of the CP-violating sources *within* the quantum Boltzmann equations [12]. On the contrary, previous treatments [4,5] are characterized by the following common feature: CP-violating currents were first derived and then converted into sources for the diffusion equations. More specifically, CP-violating sources $\mathcal{S}$ associated to a generic charge density j^0 were constructed from the current j^{μ} by the definition $\mathcal{S}=\partial_0 j^0$ [4,5]. A rigorous computation of the CP-violating currents for the right-handed stop $\tilde{t}_R$ and higgsino $\tilde{H}$ local densities was performed in [5] by means of the CTP formalism. Since currents were proportional to the first time derivative of the the Higgs profile, sources turned out to be proportional to the second time derivative of the Higgs profile [5]. The results obtained in [12], however, indicate that the sources in the quantum diffusion equations are proportional to the first time derivative of the Higgs configuration. A comparison between the sources $\mathcal{S}$ obtained in [12] and the currents j^0 given in ref. [5] indicate that they may be related as

$$\mathcal{S}(T)\sim\frac{j^0(T)}{\tau} \tag{5}$$

and it may be interpreted as the time derivative of the current density accumulated at the time T after the wall has deposited at a given specific point the current density j^0 each interval τ

$$\mathcal{S}(T) \sim \partial_0 \int^T dt \, \frac{j^0(t)}{\tau}. \tag{6}$$

Here $\tau = \Gamma^{-1}$ is the thermalization time of the right-handed stops and higgsinos, respectively. The integral over time is peculiar of the quantum approach and it induces memory effects. This tells us that the source obtained self-consistently in the present work differs from the one adopted in[5] by a factor $\sim L_\omega \Gamma / v_\omega$ (in the rest frame of the advancing bubble wall). Since $L_\omega \Gamma / v_\omega \gtrsim 1$ for the Higgs derivative expansion to hold, this result is important as far as the numerical estimate of the final baryon number is concerned.

3.3 Memory effects

Baryogenesis is fuelled when transport properties allow the CP-violating charges to efficiently diffuse in front of the advancing bubble wall where anomalous electroweak baryon violating processes are not suppressed. However, the CP-violating processes of quantum interference, which build up CP-violating sources, must act in opposition to the incoherent nature of plasma physics responsible for the loss of quantistic interference. If the particles involved in the process of baryon number generation thermalize rapidly, CP-violating sources loose their coherence and are diminished. The CTP formalism properly describes the quantum nature of CP-violation and tells us that CP-violating sources evaluated at some time T are always proportional to an integral over the past history of the system. Therefore, it is fair to argue that these memory effects lead to "relaxation" times for the CP-violating sources which are typically longer than the ones dictated by the thermalization rates of the particles in the thermal bath. In fact, this observation is valid for all the processes described by the "scattering" term in the right-handed side of the quantum diffusion equations. The slowdown of the relaxation processes may help to keep the system out of equilibrium for longer times and therefore enhance the final baryon asymmetry. There are two more reasons why one should expect quantum relaxation times to be longer than the ones predicted by the classical approach. First, the decay of the Green's functions as functions of the difference of the time arguments; secondly, the rather different oscillatory behaviour of the functions $G^>$ and $G^<$ present in the CTP formalism [12] for a given momentum, as functions of the time argument difference.

3.4 Resonance effects

In the limit of thick bubble walls, the CP-violating sources are characterized by resonance effects[5] when the particles involved in the construction of the source are degenerate in mass. The interpretation of the resonance is rather straightforward if we think in terms of scatterings of the quasiparticles off the advancing low momentum bubble wall configuration. A similar effect has been found in ref. [7] where the system was studied in the classical limit. The classical treatments should provide reasonable approximations to our formulae to those particles whose wavelength is short compared to v_ω/Γ. On the other hand, formulae should not agree for small Γ because our source is dominated by particles with long wavelength. In this regime, the classical approximation breaks down since it requires that the mean free path should be larger than the Compton wavelength of the underlying particle. This is relevant because quasiparticles with long wavelengths give a significant contribution to CP-violating sources.

Acknowledgments

I would like to thank M. Carena, J. Cline, M. Quiros and C.E.M. Wagner for useful discussions and Rocky Kolb for saying during his summary talk that I should have talked about something else. I would also like to thank all the organizers of this conference for the nice atmosphere they have been able to create. Last, but not least, many thanks to my ski-teacher. AR is on leave of absence from Theoretical Physics Dept., University of Oxford, Oxford, U.K.

References

1 G.F. Giudice, *Phys. Rev.* D45, 3177 (1992).
2 S. Myint, *Phys. Lett.* B287, 325 (1992).
3 J.R. Espinosa, M. Quirós and F. Zwirner, *Phys. Lett.* B307, 106 (1993); A. Brignole, J.R. Espinosa, M. Quirós and F. Zwirner, *Phys. Lett.* B324, 181 (1994).
4 P. Huet and A.E. Nelson, *Phys. Rev.* D53, 4578 (1996).
5 M. Carena, M. Quiros, A. Riotto, I. Vilja and C.E.M. Wagner, *Nucl. Phys.* B503, 387 (1997), [hep-ph/9702409].
6 A. Riotto, OUTP-97-43-P preprint, [hep-ph/9709286].
7 J.M. Cline, M. Joyce and K. Kainulainen, McGill 97-26 preprint [hep-ph/9708393].
8 M. Carena, M. Quiros and C.E.M. Wagner, *Phys. Lett.* B380, 81 (1996); D. Delepine, J.M. Gerard, R. Gonzalez Felipe and J. Weyers, *Phys. Lett.* B386, 183 (1996); J.R. Espinosa, *Nucl. Phys.* B475, 273 (1996); B. de Carlos and J.R. Espinosa, UPR-0737-T preprint, [hep-ph/9703317].
9 M. Carena, M. Quiros and C.E.M. Wagner, CERN-TH/97-190, [hep-ph/9710401].
10 M. Laine, *Nucl. Phys.* B481, 43 (1996); J.M. Cline and K. Kainulainen, *Nucl. Phys.* B482, 73 (1996).
11 K. Chou, Z. Su, B. Hao and L. Yu, *Phys. Rep.* 118, 1 (1985).
12 A. Riotto, CERN-TH-97-348 [hep-ph/9712221].

PRE-BIG BANG COSMOLOGY: AN INTRODUCTION

G. VENEZIANO
Theoretical Physics Division, CERN, CH - 1211 Geneva 23
Switzerland

The aim of this talk is twofold: i) presenting the general picture/idea of pre-big bang cosmology; ii) providing a template/framework for the following four talks on the subject.

1 Preamble

Almost exactly 100 years ago, in 1897, J.J. Thompson discovered the electron. Even today the origin of the small electron mass is clouded in mystery. In the same year, French impressionist Paul Gauguin signed one of his most famous paintings, whose title consists of three questions:

D'où venons-nous? Que sommes-nous? Où allons-nous?

100 years later, Gauguin's questions are still very much with us. Modern versions of the second and third questions (What is the value of Ω? Will the Universe expand forever?) have been discussed at length at this Conference. What about Gauguin's first question? In a recent article, E. Witten [1], defending US participation in the LHC project, argued that discovering supersymmetry would "give a huge boost to ... string theory." He then goes on to explain why non-specialists should care about this: it is because strings may hold "the key to answering some of the questions that people who are not scientists most often ask". These modern versions of Gauguin's first question, prompted by experimental evidence that a Big Bang did occur in the early Universe, are (quoting again [1]):

"What happened *before* the Big Bang? What was the beginning of time?"

i.e. precisely the subject of this talk.

2 Two attitudes towards two puzzles

It is commonly believed (see e.g. [2]) that the Universe –and time itself– started some 15 billion years ago from some kind of primordial explosion, the famous Big Bang. Indeed, the experi-

mental observations of the red-shift and of the Cosmic Microwave Background (CMB) lead us quite unequivocally to the conclusion that, as we trace back our history, we encounter epochs of increasingly high temperature, energy density, and curvature. However, as we arrive close to the singularity, our classical equations are known to break down. The earliest time we can think about classically is certainly larger than the so-called Planck time, $t_P = \sqrt{G_N \hbar} \sim 10^{-43} s$ ($c = 1$ throughout). Hence, the honest answer to the question: Did the Universe –and time– have a beginning? is: We do not know, since the answer lies in the unexplored domain of quantum gravity.

Besides the initial singularity problem –and in spite of its successes– the hot big bang model also has considerable phenomenological problems. Amusingly, these too can be traced back to the nature of the very early state of the Universe. Let us briefly recall why.

The observable part of our Universe, our present horizon, is about 10^{28} cm large. At earlier times, the horizon was much smaller: a few Planck times after the Big Bang, the horizon was not much larger that a few Planck lengths, say about 10^{-32} cm. Instead, the portion of space that corresponds to our present horizon was about 1 mm large, i.e. some 30 orders of magnitude larger than the horizon. In other words, at that time, the Universe consisted of $(10^{30})^3 = 10^{90}$ Planckian-size, causally disconnected regions.

The *homogeneity* problem of standard cosmology is the observation that there is no reason to expect that conditions in all those 10^{90} regions were initially the same, since there had never been any causal contact among them. Yet, today, all those regions make up our observable Universe and are homogeneous to one part in 10^5. A related puzzle is the so-called *flatness* problem: How come the primordial Universe had a (spatial) curvature radius 30 orders of magnitude larger that H^{-1}?

In my opinion there are three possible attitudes towards solving the above puzzles, but only two of them are scientifically sound. These are:

- The Universe *was not* particularly homogeneous and flat at the big bang, but a period of accelerated expansion (inflation) *after* the big bang made it that way. This is the standard *post-big bang* inflation idea (see e.g. [3]).
- The Universe *was* already homogeneous and flat at the big bang, since a long period of inflation *before* the big bang cooked it up that way. This is basically the *pre-big bang* (PBB) idea.
- There is always, of course, a third answer: some unknown Planckian physics produced an incredibly homogeneous/flat Universe, which is essentially like saying that God decided things that way (see, in this connection, a nice picture in Penrose's book [4]).

How come string theory prefers the second answer in the above list?

3 String Theory hints

The following properties of superstrings strongly speak in favour of the PBB scenario over the one of conventional inflation:

- String theory does *not* automatically give Einstein's General Relativity at low energy/curvature. Rather, it leads to a scalar-tensor theory of the Jordan–Brans–Dicke (JBD) variety, moreover with a dangerously small ω_{JBD} parameter. The extra scalar particle/field, called the dilaton, is unavoidable in string theory.
- The dilaton, which we denote by ϕ, provides the overall strength of all interactions via relations like (here $\lambda_s = \sqrt{\alpha' \hbar}$ is the fundamental string-length parameter):

$$l_P^2 / \lambda_s^2 \sim \alpha_{gauge} \sim e^{\phi} \,, \tag{1}$$

from which we deduce that the weak coupling region is $\phi \ll -1$. At present, $e^{\phi} \sim 1/25$, implying $\lambda_s \sim 10 l_P \sim 10^{-32}$ *cm*.

- Dilaton exchange produces a "fifth force", which threatens precision tests of the equivalence principle [5], hence string theory itself. The simplest way out of this problem (see [6] for an amusing alternative) is to assume that the dilaton has a mass of at least 10^{-4} eV, coming from supersymmetry-breaking non-perturbative effects. These are negligible at small coupling and therefore the dilaton, when large and negative, behaves like a massless particle.

- Interesting new symmetries (generically called "dualities") thrive on the existence of ϕ. For cosmology, their most relevant representative is the so-called **Scale-Factor duality** (SFD), whose action is as follows.

An FRW cosmology at $t > 0$, i.e. a *decelerating expansion* of the Universe (apparently) originating *from* a singularity as $t \to 0^+$

gets mapped, via SFD, into

an inflationary cosmology at $t < 0$, i.e. an *accelerated expansion* of the Universe (apparently) going *towards* a singularity as $t \to 0^-$.

This second cosmology looks impossible at first since, in order to have inflation, one needs a peculiar equation of state $(3p + \rho < 0)$, and a scalar field with no potential energy cannot satisfy that condition. The puzzle is solved, within string (or JBD) gravity, by observing that $G_N^{eff} \sim l_P^2$ is controlled by ϕ through (1). It is indeed perfectly possible for H to grow, even though the energy density decreases, provided ϕ is also growing. We thus come to an important conclusion:

Pre-Big Bang inflation needs a growing dilaton.

4 Pre-big bang's postulate/conjecture

If we wish to use a dual cosmology for the prehistory of the Universe, given the positive signs of $\dot{H}$ and $\dot{\phi}$, we have to start from (very?) small initial values for H and e^{ϕ}. Although not strictly necessary, we will also impose, for the sake of simplicity, an almost empty initial Universe. This leads us to the following basic postulate of PBB cosmology:

The Universe started its evolution from the simplest conceivable initial state in string theory, its perturbative vacuum. This corresponds to an (almost)

EMPTY, COLD, FLAT, FREE

Universe as opposed to the standard

DENSE, HOT, HIGHLY-CURVED

initial state of conventional cosmology.

For this assumption to make sense, the new initial conditions should be able to provide, at later times, a hot big bang with the desired characteristics. This looks like a very hard task, but, as the following speakers will explain, it is all but impossible.

The above postulate is good news for the theorist. Indeed, if both coupling and curvature are small, physics is adequately described by the tree-level low-energy effective action of string theory, which is something we know all about. Its form reads:

$$\Gamma_{eff} = \frac{1}{2}\int d^4x\sqrt{-g}\; e^{-\phi}\left[\lambda_s^{-2}(\mathcal{R} + \partial_\mu\phi\partial^\mu\phi + H^2_{\mu\nu\rho}) + F^2_{\mu\nu} + \ldots\right], \qquad (2)$$

where we have included the contributions of the Kalb–Ramond antisymmetric tensor field $B_{\mu\nu}$ through its field strength $H_{\mu\nu\rho}$, as well as some typical gauge fields.

The suggestion from string theory now becomes almost a compelling one[7]: Can one combine a standard cosmology at $t > 0$ with a dual PBB cosmology at $t < 0$ to construct a smooth cosmology containing both? Since, in such a scenario, the Hubble parameter grows for $t < 0$ and decreases for $t > 0$, it should reach its maximum at $t = 0$, instant to be identified with the Big Bang of standard cosmology. The problem is that this maximum is actually infinite, if one works in the context of the low-energy effective theory (2). The pre- (post-) big bang phases have singularities in the future (past). However, the low-energy approximation breaks down as soon as the Hubble parameter reaches values $O(\lambda_s^{-1})$, leading us to expect that the maximal value of H, reached at $t = 0$, should actually be finite and of that order. All this leads to the main conjecture of PBB cosmology, the so-called *graceful-exit* assumption:

Pre-big bang and FRW phases smoothly join
through a high-curvature/large-coupling (string) phase

Before discussing some recent work (and controversy) on the first (pre-big bang) phase, I wish to mention how the following talks on string cosmology can be situated within the general picture I have outlined. Alessandra Buonanno and Ramy Brustein will discuss cosmological particle production (mainly photons and gravitons, respectively) during the transition between the PBB and the FRW phase. Mairi Sakellariadou will discuss whether large-scale inhomogeneities in the energy density of those particles (around recombination) could explain CMB anisotropies. Finally, Burt Ovrut's talk may well contain the key to answering the graceful-exit problem through the latest developments of string theory.

5 Pre-big bang as classical gravitational collapse

The PBB postulate can be rephrased in more precise terms as a postulate of **Asymptotic Triviality** (AT), where *asymptotic* means at (timelike and null) past infinity, and *triviality* refers both to space-time and to the dilaton. In analogy with QCD's asymptotic freedom AT is very different from just triviality. Actually, while the trivial vacuum of string theory is a very special point in the space of classical solutions, AT vacua are generic, in the technical sense that they depend on as many arbitrary functions as the general solution.

Determining the properties of a generic solution to the field equations implied by (2) is a formidable task, even if one neglects the Kalb–Ramond field. Fortunately, however, we can map our problem into one that has been much investigated, both analytically and numerically, in the literature: the problem of gravitational collapse of a scalar field. This is simply done by "going to the Einstein frame", i.e. by the field redefinition

$$g_{\mu\nu} = g^{(E)}_{\mu\nu} e^{\phi - \phi_0} \ , \tag{3}$$

in terms of which (2) becomes:

$$\Gamma_{eff} = \frac{1}{2l_P^2} \int d^4x \sqrt{-g^{(E)}} (\mathcal{R}^{(E)} - \frac{1}{2} g^{\mu\nu}_{(E)} \partial_\mu \phi \partial_\nu \phi) \ , \tag{4}$$

where ϕ_0 ($l_P = e^{\frac{1}{2}\phi_0}\ \lambda_s$) is the present value of the dilaton (of Planck's length).

This problem has been considered precisely in the regime of interest to us, i.e. starting from very "weak" initial data with the aim of finding under which conditions gravitational collapse must occur later. Gravitational collapse basically means that the (Einstein) metric shrinks to zero at a spacelike singularity. However, typically, the dilaton blows up at that same singularity. Given the relation (3) between the Einstein and the (physical) string metric, we can easily imagine that the latter blows up near the singularity, thus giving inflation and a big bang. What can we say at the moment about details on all this? Not much, since this part of the game is just starting, but here it is.

Assume that, deeply into the PBB phase, the Universe was not particularly homogeneous, spatial gradients and time derivatives being comparable and, in accordance with the PBB postulate, both tiny in string units. It can be argued [8] that such initial conditions can lead to a chaotic version of PBB inflation since, if a certain patch develops where time derivatives slightly dominate over spatial gradients, then inflation turns on in that patch. Thereafter, the evolution of the system can be studied by analytic methods [9], since the approximation of neglecting spatial gradients becomes increasingly accurate within the inflating patch.

In the general case, no analytic methods are known for analysing the system at even earlier times (i.e. before the inflationary patch forms), while numerical codes are still largely inadequate. Both analytic and numerical methods are instead available for solutions exhibiting some symmetry, e.g. spherical symmetry. In that case, recent numerical work [10] has fully confirmed the occurrence of inflation and the validity of the gradient expansion [9]. However, in the spherically symmetric case, the most promising avenue [11] appears to consist in making use of the powerful analytic results by Christodoulou [12], which provide sufficient criteria for collapse (or for its absence). Those criteria are "scale-free": in no way does the collapse theorem of [12] fix the absolute curvature scale at the onset of collapse (i.e. when a closed trapped surface first forms). This curvature scale becomes [11] the scale of inflation (the Hubble parameter) at the onset of inflation in the original PBB problem. But why is this scale so important?

The point is that, in order to solve the homogeneity/flatness problems, dilaton-driven inflation has to last sufficiently long. Its duration is not infinite, since it is limited in the past by the conditions of collapse and, in the future, by the time at which curvatures become so large that we can no longer trust the low-energy approximation. Thus, as was actually noticed from the very beginning [7], a successful PBB scenario does require very perturbative initial conditions, so that it takes a long time to reach the BB singularity. Fortunately, both the initial coupling and the initial curvature are free classical parameters, possibly with a random distribution throughout space.

A particular case of this "fine-tuning" was discussed recently by Turner and Weinberg and by Kaloper et al. [13]. These authors consider a homogeneous -but not spatially flat- Universe and notice that the duration of PBB inflation is limited in the past by the initial value of the spatial curvature. This has to be taken very small in string units if sufficient inflation is to be achieved. The issue is whether or not this is fine-tuning. String theory has a single length parameter, λ_s, but, fortunately for us, it also has massless states and low-energy vacua (such as Minkowski space-time), whose characteristic scale is arbitrarily larger than λ_s. Thus I see no fine-tuning in starting the evolution of the Universe in a state of low-energy, small curvatures, and small coupling. On the contrary, I find it very amusing/exciting to realize that a well-known classical instability pushes the Universe from low energy (curvature) and small coupling towards high energy (curvature) and large coupling.

But this is certainly not the last word on the subject ...

6 Conclusions

Pre-big bang cosmology appears to have survived its first 6 or 7 years of life. Interest in (and criticism of) it is growing. It is perhaps time to make a balance sheet.

Conceptual (technical?) and phenomenological problems include:

- Graceful exit from dilaton-driven inflation to FRW cosmology is not fully understood, in spite of recent progress [14]. Possibly, new ideas borrowed from M-theory and D-branes could help in this respect (see B. Ovrut's talk).

- A scale-invariant spectrum of large-scale perturbations is not automatic, although, thanks to possibly flat axion spectra, it does not look inconceivable either (see M. Sakellariadou's

talk).

Attractive features include:

- No need to "invent" an inflaton, or to fine-tune potentials.
- Inflation is "natural", thanks to the duality symmetries of string cosmology.
- The initial conditions problem is decoupled from the singularity problem: a solution to the former is already shaping up and looks exciting.
- A classical gravitational instability (similar to the one giving gravitational collapse and singularities in General Relativity) finds a welcome use in providing inflation.
- A quantum instability (pair creation) is able to heat up an initially cold Universe and generate a hot big bang (see A. Buonanno's and R. Brustein's talks) with the additional virtues of homogeneity and flatness.
- Last but not least: we are dealing with a highly constrained, predictive scheme, which can be tested/falsified by low-energy experiments, as will be explained in the following talks.

What is my own forecast? It is simple: probably, PBB cosmology will not reach age 10. However, it will not be killed by Hawking, Linde, or Turner, but, more likely, by Planck ... and I do *not* mean Max!

References

1. E. Witten, *The New Republic*, Dec. 29, 1997.
2. S. Hawking, Proceedings of the Texas/ESO-CERN Symposium on Relativistic Astrophysics, Cosmology, and Fundamental Physics, Brighton, 1990, eds. J.D. Barrow, L. Mestel and P.A. Thomas, Ann. NY Acad. Sci. **647** (1991) 315.
3. E. W. Kolb and M. S. Turner, *The Early Universe* (Addison-Wesley, 1990).
4. R. Penrose, *The Emperor's New Mind* (Oxford University Press, 1989), Fig. (7.19).
5. T.R. Taylor and G. Veneziano, Phys. Lett. **B213** (1988) 459.
6. T. Damour and A.M. Polyakov, Nucl. Phys. **B423** (1994) 532.
7. G. Veneziano, Phys. Lett. **B265** (1991) 287; M. Gasperini and G. Veneziano, Astropart. Phys. 1 (1993) 317; Mod. Phys. Lett. **A8** (1993) 3701; Phys. Rev. **D50** (1994) 2519; an updated collection of papers on the PBB scenario is available at *http*://www.to.infn.it/teorici/gasperin/.
8. G. Veneziano, Phys. Lett. **B406** (1997) 297;
   A. Buonanno, K. A. Meissner, C. Ungarelli and G. Veneziano, Phys. Rev. **D57** (1998) 2543;
   A. Feinstein, R. Lazkoz and M.A. Vazquez-Mozo, *Closed inhomogeneous string cosmologies*, hep-th/9704173;
   J. D. Barrow and M. P. Dabrowski, *Is there chaos in low-energy string cosmology?*, hep-th/9711049;
   J. D. Barrow and K. E. Kunze, *Spherical curvature inhomogeneities in string cosmology*, hep-th/9710018;
   K. Saygily, *Hamilton-Jacobi approach to pre-big bang cosmology at long wavelengths*, hep-th/9710070.
9. V. A. Belinskii and I.M. Khalatnikov, Sov. Phys. (JETP) **36** (1973) 591; N. Deruelle and D. Langlois, Phys. Rev. **D52** (1995) 2007; J. Parry, D. S. Salopek and J. M. Stewart, Phys. Rev. **D49** (1994) 2872.

10. J. Maharana, E. Onofri and G. Veneziano, *A numerical approach to pre-big bang cosmology*, gr-qc/9802001, to appear in JHEP.
11. A. Buonanno, T. Damour and G. Veneziano, to appear.
12. D. Christodoulou, Comm. P. A. Math., **44** (1991) 339, and references therein.
13. M. Turner and E. Weinberg, Phys. Rev. **D56** (1997) 4604;
N. Kaloper, A.D. Linde and R. Bousso, *Pre-big bang requires the Universe to be exponentially large from the very beginning*, hep-th/9801073.
14. M. Gasperini, M. Maggiore and G. Veneziano, Nucl. Phys. **B494** (1997) 315; R. Brustein and R. Madden, Phys. Lett. **B410** (1997) 110; Phys. Rev. **D57** (1998) 712.

PRIMEVAL MAGNETIC SEEDS FROM PRE-BIG BANG STRING COSMOLOGY

A. BUONANNO
Institut des Hautes Etudes Scientifiques, 91440 Bures-sur-Yvette, France

We investigate the generation of galactic magnetic fields in a specific pre-big bang scenario of string cosmology, including dynamical moduli and Kaluza-Klein abelian gauge bosons. We assume that the onset of the radiation era is determined by the energy stored in the amplified quantum-vacuum fluctuations. We find values of the effective temperature and the gauge coupling (at the beginning of the standard radiation phase) which are compatible with the production of magnetic fields strong enough to seed the galactic dynamo.

1 Introduction

Current observations show that magnetic fields are present throughout the Universe: in galaxy disks and halos and in clusters of galaxies [1]. They should play an important role in many astrophysical processes, such as the propagation of cosmic rays and the formation of stars. The Milky way and many spiral galaxies are endowed with a coherent magnetic field B of the order of 10^{-6} Gauss (G) on scales $l \gtrsim 10\,\mathrm{kpc}$. It is common to relate the energy density stored in magnetic fields, ρ_B, to the energy density in the cosmic microwave background, ρ_γ, introducing the quantity $r = \rho_B/\rho_\gamma$.

Until now the astrophysical mechanism responsible for the origin of the galactic magnetic fields has not been completely understood. Essentially there are two schools of thought. Some astrophysicists believe that strong primordial magnetic fields ($B \sim 10^{-6}\,\mathrm{G}$) could have been produced in the pregalactic era and remained trapped in the gas that subsequently collapsed forming the galaxy [2], while other astrophysicists support the scenario in which galactic magnetic fields are generated through a galactic dynamo mechanism [3], i.e. a weak seed field is exponentially amplified by the turbulent motion of the ionized gas which follows the differential rotation of the galaxy. In this case $B \simeq e^{\gamma t} B_{seed}$. Supposing that the e-folding time is at most on the order of the rotation period of the galaxy and that the dynamo has operated for the entire age of

the galaxy, we get $B_{\rm seed} \gtrsim 10^{-19}$ G on the scale of several kiloparsec ($r \gtrsim 10^{-34}$ on megaparsec scale).

An interesting possibility arises if the magnetic seeds were truly primordial. In fact in this case cosmic magnetic fields could provide direct information about the very early universe. In the literature there have been different attempts to explain the origin of the seeds, including early time cosmological phase transitions, superconducting cosmic strings and inflationary models [4]. However, in standard inflation it is not possible to amplify quantum-vacuum electromagnetic fluctuations because the Robertson-Walker spacetime is conformally flat and the coupling between the photons and the gravitational field is conformally invariant. Hence, it is necessary to appeal to non-minimal couplings or to break the conformal invariance at the quantum level[4].

2 Non-minimal couplings in string theory

String theory predicts naturally a non-minimal coupling between the electromagnetic field ($F_{\mu\nu}$) and the gravitational background ($g_{\mu\nu}$). The low-energy effective action of (heterotic) superstring theory is

$$\Gamma^1_{\rm eff} = \frac{1}{2\lambda_s^2} \int d^4x \sqrt{-\det g_{\mu\nu}}\, e^{-\varphi} \left[\mathcal{R}(g) + g^{\mu\nu}\, \partial_\mu\varphi\, \partial_\nu\varphi - \frac{1}{4} F_{\mu\nu}\, F^{\mu\nu} \right], \qquad (1)$$

where $\mu, \nu = 0, \ldots 3$, λ_s is the string-length parameter and φ is the effective four dimensional dilaton field which determines the gauge coupling g, i.e. $g^2 = e^{\varphi}$. In the cosmological scenario of pre-big bang the dilaton is time-dependent at very early time. It undergoes an accelerated evolution from the perturbative vacuum of string theory to the strong coupling regime [5] and it is then responsible for the amplification of the electromagnetic fluctuations [6, 7] (as well as perturbations of different kind, see e.g. [8, 9] and references therein).

For the particular pre-big bang scenario in which the dilaton-inflationary phase is followed by a "string" phase (Hubble parameter $H = {\rm const}_1$, $\varphi = {\rm const}_2 \times t$ and internal moduli frozen) Gasperini et al. [7] investigated under which conditions it is possible to produce primordial magnetic fields coherent on scales on the order of the megaparsec and strong enough to seed the galactic dynamo. The success of the mechanism requires that a long "string" phase is present and the coupling g at the time of exit of the galactic scale is very small.

In Ref. [9] we considered a different string cosmology scenario, we allowed the internal dimensions to be time-dependent (at least in the pre-big bang inflationary phase) and we derived the electromagnetic spectrum for both the heterotic gauge fields ($F_{\mu\nu}$) and the Kaluza-Klein abelian gauge fields $V_{\mu\nu}{}^a$ and $W_{\mu\nu a}$, originated in a generic compactification. The effective action is, in this case, $\Gamma_{\rm eff} = \Gamma^1_{\rm eff} + \Gamma^2_{\rm eff}$, with [9]

$$\Gamma^2_{\rm eff} = -\frac{1}{2\lambda_s^2} \int d^4x \sqrt{-\det g_{\mu\nu}}\, e^{-\varphi} \left[\partial_\mu\sigma_a\, \partial_\nu\sigma_a + \frac{1}{4} e^{2\sigma_a}\, V_{\mu\nu}{}^a\, V^{\mu\nu a} + \frac{1}{4} e^{-2\sigma_a}\, W_{\mu\nu a}\, W^{\mu\nu}_{\ \ a} \right], \qquad (2)$$

where we have chosen an internal diagonal metric $g_{ab} = e^{2\sigma_a}\, \delta_{ab}$ with $a, b = 4, \ldots, 9$.

We restrict ourselves to the following pre-big bang scenario. The Universe starts its evolution from a very weakly-coupled and cold state and evolves through an inflationary phase driven by the kinetic energy of the dilaton [5] ($\dot\varphi > 0$, $\dot H > 0$). We then suppose [9] that at conformal time η_d the higher order α' corrections of the effective action $\Gamma_{\rm eff}$, provide by themselves (without appealing to loop corrections) the transition from the perturbative inflationary phase to another duality-related vacuum phase (in particular, the Hubble parameter H has a bounce around its maximal value $H_s \simeq \lambda_s^{-1}$). The standard radiation-dominated era starts at time η_1 when the energy stored in the quantum fluctuations becomes critical.

3 Amplification of quantum-vacuum electromagnetic fluctuations

We investigate electromagnetic fluctuations around a homogeneous background and we expand all the gauge fields around zero values. In the radiation gauge, we get

$$\partial_\mu(\sqrt{g}\, e^{-\varphi}\, F^{\mu\nu}) = 0\,, \qquad \partial_\mu(\sqrt{g}\, e^{-\varphi+2\sigma_a}\, V^{\mu\nu a}) = 0\,, \qquad \partial_\mu(\sqrt{g}\, e^{-\varphi-2\sigma_a}\, W_a^{\mu\nu}) = 0\,. \quad (3)$$

Introducing the canonical variables $\mathcal{C}_A^j = A^j\, e^{-\varphi/2}$, $\mathcal{C}_V^{ja} = V^{ja}\, e^{-\varphi/2+\sigma_a}$, $\mathcal{C}_{Wa}^j = W_a^j\, e^{-\varphi/2-\sigma_a}$ (which are of the general form $C_\chi = (\text{field}) \times \tilde{a}_\chi$, where $\tilde{a}_\chi$ is generally called the "pump" field) we obtain the following simple equation in Fourier space

$$\frac{d^2\mathcal{C}_\chi}{d\eta^2} + \left[k^2 - U(\eta)\right] \mathcal{C}_\chi = 0\,, \qquad U(\eta) = \frac{1}{\tilde{a}_\chi}\frac{d^2\tilde{a}_\chi}{d\eta^2}\,. \quad (4)$$

Solving Eq. (4) in the three phases: inflationary pre-big bang, dual-dilaton and radiation ones, imposing the continuity of the perturbed fields and their first derivative at the transitions and considering normalized modes with positive frequency at very early time, we get the mean number of amplified gauge fields $\langle n_\chi \rangle$. The fluctuations that exit in the inflationary phase and reenter in the radiation-dominated era, i.e. $f \ll f_1$, f_d, with $f_d \sim 1/(|\eta_d| a_0)$, $f_1 \sim 1/(|\eta_1| a_0)$, are the relevant ones for the production of magnetic fields on scales of megaparsec [9]. The electromagnetic spectrum for these perturbations is found to be

$$r_\chi(f) = \frac{1}{\rho_\gamma}\frac{d\rho_\chi}{d\log f} = \frac{16\pi^2}{\rho_\gamma} f^4 \langle n_\chi \rangle \simeq g_1^2\, z_d^{2(2\gamma_\chi(\delta)-3)/(\sqrt{3}+1)} \left(\frac{f}{f_1}\right)^{n_s(\delta)}\,. \quad (5)$$

We use n_s to denote the spectral slope (it varies in the range $1-4$), while γ_χ is defined by the relation $\tilde{a}_\chi = (\eta/\eta_d)^{\gamma_\chi}$ in the inflationary epoch [9]. The spectrum depends on the two free parameters of the model: the duration of the intermediate dual-dilaton phase $z_d \equiv a(\eta_1)/a(\eta_d)$ and the power, in the cosmological time t, of the scale factor during the inflationary era $a(t) \sim (-t)^\delta$. Note that, due to the dynamics of the internal dimensions, $-1/\sqrt{3} < \delta < 0$ [9].

4 Allowed parameter space of the model

We study the range of the free parameters (δ and $\zeta \equiv \mathrm{Log}_{10} z_d$) for which galactic magnetic seeds are produced and the bounds they impose at the beginning of the radiation era. As stated previously, we suppose that the transition from the dual dilaton phase to the standard-radiation-dominated one occurs at time η_1 when the energy density in the quantum fluctuations becomes critical. [Actually, in our model [9] this is caused by the axionic perturbations, whose spectral slope is negative in the high frequencies range.] The critical density is given by

$$H^2 = \frac{8\pi}{3} G_N\, \rho_{cr}\,, \qquad l_{Pl}^2(\eta) \equiv (8\pi\, G_N) = e^\varphi\, \lambda_s^2 \qquad \Rightarrow \qquad \rho_{cr} = \frac{3}{g^2}\frac{H^2}{\lambda_s^2}\,. \quad (6)$$

Note that from the classical equations of motion we have $\dot{\varphi} = 3H - \sqrt{3H^2 + 2\lambda_s^2\, e^\varphi\, \rho_{qf}}$, hence when the energy density ρ_{qf} becomes critical $\dot{\varphi}(\eta_1) = 0$. That is the dilaton field will stop. We further assume that the effective temperature of the Universe at the onset of the radiation era is given by the energy density of the quantum fluctuations, notably $T_{eff} \propto (\rho_{qf}(\eta_1))^{1/4}$. In conclusion, the condition $\rho_{qf}(\eta_1) = \rho_{cr}(\eta_1)$ fixes the physical parameters g_1 and T_{eff} in terms of ζ and δ.

Our results are summarized in Fig. 1. The plot on the l.h.s describes the region of allowed parameter ζ and δ in which the amplified magnetic fields, associated with the Kaluza-Klein photons V_μ, are strong enough to seed the galactic dynamo. The plot on the r.h.s shows the

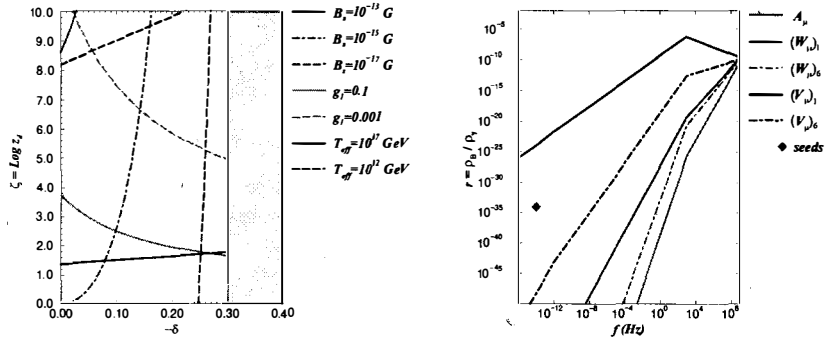

Figure 1: On the l.h.s the parameter-space plot for the Kaluza-Klein photons V_μ when only a single internal dimension is considered. The magnetic seeds refer to a scale of several kiloparsec. The region in gray is excluded by the axionic fluctuations [8]. On the r.h.s the spectra for all the fields when $z_d = 10^8$, $\delta = -0.1$, $T_{\rm eff} = 4 \cdot 10^{12}$ GeV and $g_1 = 2 \cdot 10^{-3}$.

spectrum $r(f)$ for all the "photons" present in the model and for a particular choice of the free parameters. The indices 1 and 6 correspond to two extreme cases for the internal dimensions, the most anisotropic (only a single internal dimension) and the most isotropic one, respectively.

5 Conclusions

We have shown that string cosmology provides in a natural way the amplification of electromagnetic fluctuations through non-minimal couplings involving the dilaton and/or moduli fields. There is a region of parameter space that allows the productions of galactic magnetic seeds in the range $B_{\rm seed} \simeq 10^{-13} - 10^{-17}$ G on kiloparsec scales. Within the particular model analyzed, it is not possible to get simultaneously, at the beginning of the standard radiation-dominated era, a value of the gauge coupling very near the present one together with an effective temperature much below the string scale.

Acknowledgments

I am grateful to T. Damour, M. Lemoine, K. Meissner, C. Ungarelli and G. Veneziano for comments and many instructive discussions.

References

1. P.P. Kronberg, Rep. Progr. Phys. 57 (1994) 325.
2. R.M. Kulsrud and S.W. Anderson, Astrophys. J 396 (1992) 606.
3. E.N. Parker, *Cosmical Magnetic Fields* (Clarendon, 1979); Ya.B. Zel'dovich, A.A. Ruzmaikin and D.D. Sokoloff, *Magnetic fields in astrophysics*, (Gordon and Breach, 1983).
4. M.S. Turner and L.M. Widrow, *Phys. Rev.* D37 (1988) 2743; B. Ratra, Astrophys. J. Lett. 391 (1992) L1; W.D. Garretson, G.B. Field and S.M. Carroll, *Phys. Rev.* D46 (1992) 5346; A.D. Dolgov, *Phys. Rev.* D48 (1993) 2499; B. Cheng and A.V. Olinto, *Phys. Rev.* D50 (1994) 2421; T.W.B. Kibble and A. Vilenkin, *Phys. Rev.* D52 (1995) 679.
5. M. Gasperini and G. Veneziano, Astrop. 1 (1993) 317.
6. D. Lemoine and M. Lemoine, *Phys. Rev.* D52 (1995) 1955.
7. M. Gasperini, M. Giovannini and G. Veneziano, *Phys. Rev. Lett.* 75 (1995) 3796; M. Gasperini, *Status of string cosmology: phenomenological aspects*, [hep-th/9509127].
8. R. Brustein and M. Hadad, *Phys. Rev.* D57 (1998) 725.
9. A. Buonanno, K. Meissner, C. Ungarelli and G. Veneziano, JHEP 1 (1998) 004.

COSMIC GRAVITATIONAL WAVE BACKGROUND IN STRING COSMOLOGY

RAM BRUSTEIN
Department of Physics, Ben-Gurion University, Beer-Sheva 84105, Israel

String cosmology models predict a stochastic cosmic background of gravitational waves with a characteristic spectrum. I describe the background, present astrophysical and cosmological bounds on it, and outline how it may be possible to detect it with gravitational wave detectors.

1 Introduction

A robust prediction of models of string cosmology which realize the pre-big-bang scenario [1,2] is that our present-day universe contains a cosmic gravitational wave background [3,4,5], with a spectrum which is quite different than that predicted by many other early-universe cosmological models [6,7,8,9]. In the pre-big-bang scenario the evolution of the universe starts from a state of very small curvature and coupling and then undergoes a long phase of dilaton-driven kinetic inflation reaching roughly Planckian energy densities [10], and at some later time joins smoothly standard radiation dominated cosmological evolution, thus giving rise to a singularity free inflationary cosmology.

It is the purpose of this talk to explain the properties of the cosmic gravitational wave background predicted by string cosmology, to explain astrophysical and cosmological bounds on its shape and strength and to show that currently operating and planned gravitational wave detectors could further constrain the spectrum and perhaps even detect it. The emphasis is on the general properties of the spectrum and the basic experimental setup needed for its detection, rather than on precise numerical estimates and technical details.

Because the gravitational interaction is so weak, a background of gravitational radiation decouples from the matter in the universe at very early times and carries with it a picture of the state of the universe when energy densities and temperatures were extreme. The weakness of the gravitational interaction makes a detection of such a background very hard, and necessitates a strong signal. String cosmology provides perhaps the strongest source possible: the whole

universe, accelerated to roughly Planckian energy densities. A discovery of any primordial gravitational wave background, and in particular, the one predicted by string cosmology, could therefore provide unrivaled exciting information on the very early universe.

2 Cosmic gravitational wave background in string cosmology

In models of string cosmology [3], the universe passes through two early inflationary stages. The first of these is called the "dilaton-driven" period and the second is the "string" phase. Each of these stages produces stochastic gravitational radiation by the standard mechanism of amplification of quantum fluctuations [11]. Deviations from homogeneity and isotropy of the metric field are generated by quantum fluctuations around the homogeneous and isotropic background, and then amplified by the accelerated expansion of the universe. The transverse and traceless part of these fluctuations are the gravitons. In practice, we compute graviton production by solving linearized perturbation equations with vacuum fluctuations boundary conditions. The production strength of gravitons depends on the curvature and coupling. Since at the end of the accelerated expansion phase curvatures reach the string curvature, and the coupling reaches approximately today's coupling, graviton production is expected to be at the strongest possible level.

In order to describe the background of gravitational radiation, it is conventional to use a spectral function $\Omega_{GW}(f) = \frac{1}{\rho_{critical}} \frac{d\rho_{GW}}{d \ln f}$. Here $d\rho_{GW}$ is the (present-day) energy density in stochastic gravitational waves in the frequency range $d \ln f$, and $\rho_{critical}$ is the critical energy-density required to just close the universe, $\rho_{critical} = \frac{3c^2 H_0^2}{8\pi G} \approx 1.6 \times 10^{-8} h_{100}^2 \, ergs/cm^3$, where the Hubble expansion rate H_0 is the rate at which our universe is currently expanding, $H_0 = h_{100}\, 100 \, \frac{Km}{sec-Mpc} = 3.2 \times 10^{-18} h_{100} \frac{1}{sec}$. h_{100} is believed to lie in the range $0.5 < h_{100} < 0.8$. The spectral function is related to the dimensionless strain h, $\Omega_{GW}(f) \simeq 10^{36} h_{100}^{-2} (f/Hz)^2 h(f)^2$ and to the strain in units $1/\sqrt{Hz}$, $\sqrt{S_h(f)}$, $\Omega_{GW}(f) \simeq 10^{36} h_{100}^{-2} (f/Hz)^3 S_h(f)$.

The spectrum of gravitational radiation produced in the dilaton-driven (and string) phase was estimated in [3], $\Omega_{GW}(f) \simeq z_{eq}^{-1} g_s^2 \left(\frac{f}{f_S}\right)^3 \left[1 + z_S^{-3} \left(\frac{g_1}{g_S}\right)^2\right], f < f_S$, where some logarithmic correction factors were dropped. The coupling g_1 is today's coupling, assumed to be constant from the end of the string phase until today, g_S is the coupling at the end of the dilaton-driven phase, and f_S is the frequency marking the end of the dilaton-driven phase. The frequency $f_1 = f_S z_S$ is the frequency at the end of the string phase, where z_S is the total redshift during the string phase and $z_{eq} \sim 10^4$ is the redshift from matter-radiation equality until today. The spectrum can be expressed in a more symmetric form [12], $\Omega_{GW}(f) \simeq z_{eq}^{-1} g_1^2 \left(\frac{f}{f_1}\right)^3 \left[z_S^3 (g_S/g_1)^2 + z_S^{-3} (g_S/g_1)^{-2}\right]$. Note that the spectrum is invariant under the exchange $z_s^3 (g_s/g_1)^2 \leftrightarrow z_s^{-3} (g_s/g_1)^{-2}$ and that this implies a lower bound on the spectrum, $\Omega_{GW}(f) \gtrsim 2 z_{eq}^{-1} g_1^2 \left(\frac{f}{f_1}\right)^3$. The lower bound is obtained for the "minimal spectrum" with $z_S = 1$ and $g_S/g_1 = 1$ describing a cosmology with almost no intermediate string phase.

In the simplest model, which we will use to estimate the spectrum and prospects for its detection, the spectrum depends upon four parameters. The first pair of parameters are the maximal frequency f_1 above which gravitational radiation is not produced and g_1, the coupling at the end of the string phase. The second pair of these are z_S and g_S. The second pair of parameters can be traded for the frequency $f_S = f_1/z_S$ and the fractional energy density $\Omega_{GW}^S = \Omega_{GW}(f_S)$ produced at the end of the dilaton-driven phase. At the moment, we cannot compute g_S and z_S from first principles, because they involve knowledge of the evolution during the high curvature string phase. We do, however, expect z_S to be quite large. Recall that z_S is the total redshift during the string phase, and that during this phase the curvature and expansion rate are approximately string scale, therefore, z_S grows roughly exponentially with

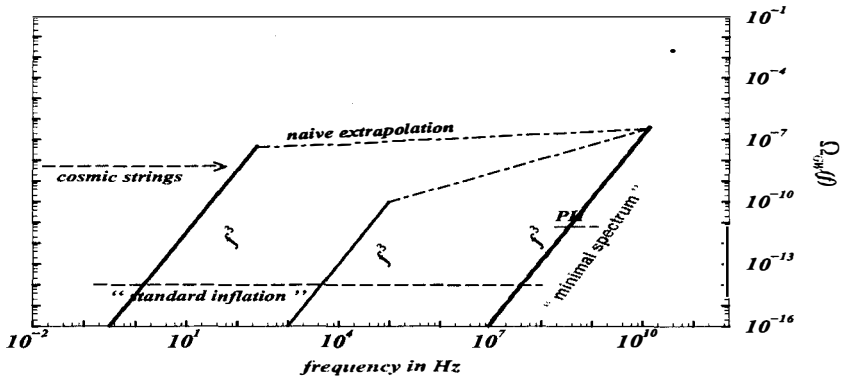

Figure 1: Spectrum of GW background. The minimal spectrum discussed in the text and two other possible spectra are shown. Also shown are estimated spectra in other cosmological models.

the duration (in string times) of this phase. Some particular exit models [13] suggest that z_S could indeed be quite large. I cannot estimate, at the moment, a likely range for the ratio g_1/g_S except for the reasonable assumption $g_1/g_S > 1$.

A useful approximate form for the spectrum in the range $z_S > 1$ and $g_1/g_S \gtrsim 1$ is the following [14]

$$\Omega_{GW}(f) = \begin{cases} \Omega^S_{GW}(f/f_S)^3 & f < f_S \\ \Omega^S_{GW}(f/f_S)^\beta & f_S < f < f_1 \\ 0 & f_1 < f \end{cases} \qquad (1)$$

where $\beta = \frac{\log[\Omega_{GW}(f_1)/\Omega^S_{GW}]}{\log[f_1/f_S]}$ is the logarithmic slope of the spectrum produced in the string phase (see also other models [15]). If we assume that there is no late entropy production and make reasonable choices for the number of effective degrees of freedom, then two of the four parameters may be determined in terms of the Hubble parameter H_r at the onset of radiation domination immediately following the string phase of expansion [16], $f_1 = 1.3 \times 10^{10}\, Hz \left(\frac{H_r}{5\times 10^{17}\, GeV}\right)^{1/2}$ and $\Omega_{GW}(f_1) = 1\times 10^{-7} h_{100}^{-2} \left(\frac{H_r}{5\times 10^{17}\, GeV}\right)^2$. Spectra for some arbitrarily chosen parameters and possible backgrounds from other cosmological models are shown in Fig. 1. The label PH denotes preheating after inflation [17].

3 Astrophysical and cosmological bounds

At the moment, the most restrictive observational constraint on the spectral parameters comes from the standard model of big-bang nucleosynthesis (NS) [18]. This restricts the total energy density in gravitons to less than that of approximately one massless degree of freedom in thermal equilibrium. This bound implies that [19]

$$\int \Omega_{GW}(f) d\ln f = \Omega^S_{GW}\left[\frac{1}{3} + \frac{1}{\beta}\left((f_1/f_S)^\beta - 1\right)\right] < 0.7\times 10^{-5} h_{100}^{-2}. \qquad (2)$$

where we have assumed an allowed $N_\nu = 4$ at NS, and have substituted in the spectrum (1). The NS bound and additional cosmological and astrophysical bounds are shown in Fig. 2, where h_{100} was set to unity.

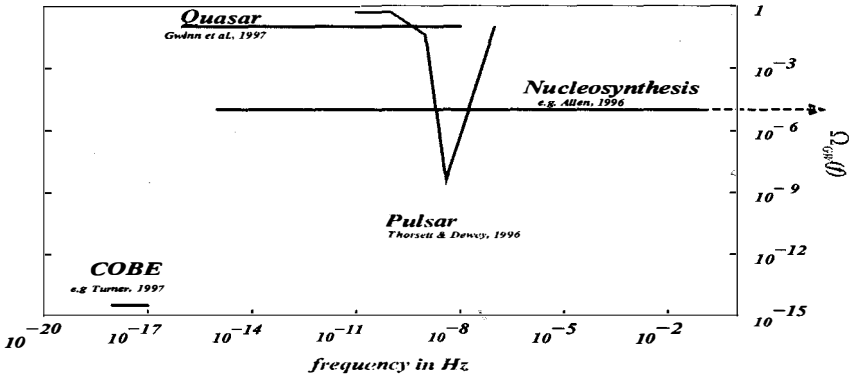

Figure 2: Cosmological and astrophysical upper bounds on the cosmic gravitational wave background.

The line marked "Quasar" in Fig. 2 corresponds to a bound coming from quasar proper motions. A stochastic background of gravity waves (GW) makes the signal from distant quasars scatter randomly on its way to earth. This may cause quasar proper motions. An upper bound on quasar proper motions can be translated into an upper bound on a stochastic background [20]. A typical strain h may induce proper motion μ, $h/f \sim \mu$. The sensitivity reached was approximately microarcsecond per year [20], corresponding to a dimensionless strain of about $h \sim 5 \times 10^{-9}$ at frequencies below the observation time: approximately (20 years)$^{-1} \sim 5 \times 10^{-9} Hz$, leading to $\Omega_{GW} \lesssim 0.1 h_{100}^{-2}$.

The line marked "COBE" in Fig. 2 corresponds to the bound coming from energy density fluctuations in the cosmic microwave background, which can be expressed in terms of the measured temperature fluctuations $\Delta T/T$, $\Omega(perturbations) \simeq (\frac{\Delta T}{T})^2 \Omega_\gamma \sim 10^{-10} \times 10^{-4} = 10^{-14} h_{100}^{-2}$. Since it is known [7] that $\Omega_{GW} \lesssim 0.1 \Omega(perturbations)$, it follows that $\Omega_{GW} h_{100}^2 \lesssim 10^{-15}$ at frequencies $10^{-18} h_{100} Hz - 10^{-16} h_{100} Hz$.

The curve marked "Pulsar" represents the bound coming from millisecond pulsar timing [21]. Assuming known distance and signal emission times, the pulsar functions as a giant one-arm interferometer. The statistics of pulse arrival time residuals ΔT, puts an upper bound on any kind of noise in the system, including a stochastic background of GW. The typical strain sensitivity is $h \sim \frac{\Delta T}{T}$, where T is the total observation time, reaching by now 20 years $\sim 6 \times 10^8 sec$ and $\Delta T \sim 10 \mu s$ is the accuracy in measuring time residuals. Translated into $\Omega_{GW}(f)$, this yields the bound shown in the figure, which is most restrictive at frequencies $f \sim 1/T \sim 5 \times 10^{-9} Hz$.

Notice that all the existing bounds are in the very low frequency range, while the expected signal from string cosmology is in a higher frequency range. The bounds are therefore not very restrictive.

4 Detecting a string cosmology stochastic gravitational wave background

A number of authors [22,23,24] have shown how one can use a network of two or more gravitational wave antennae to detect a stochastic background of gravitational radiation. The basic idea is to correlate the signals from separated detectors, and to search for a correlated strain produced by the gravitational wave background, which is buried in the instrumental noise. It has been shown by these authors that after correlating signals for time T the ratio of "Signal" to "Noise"

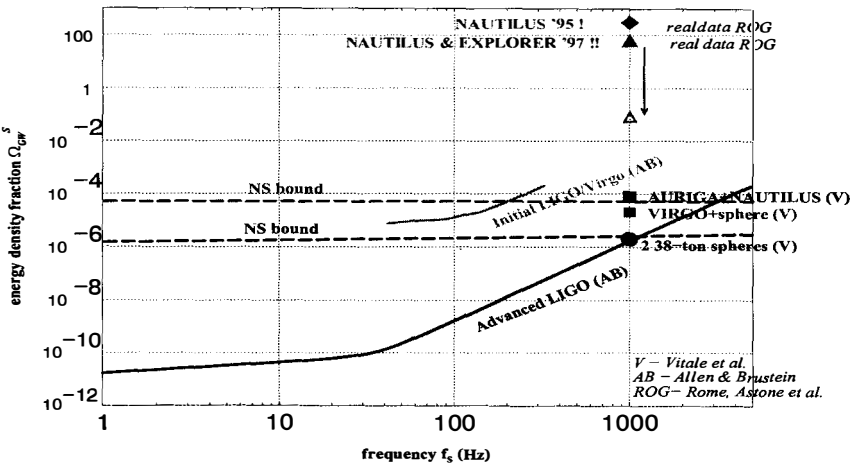

Figure 3: Detection sensitivity of relic GW by operating and planned GW detectors. The interesting region of parameter space is below the "NS bound" lines.

(squared) is given by an integral over frequency f:

$$\left(\frac{S}{N}\right)^2 = \frac{9H_0^4}{50\pi^4} T \int_0^\infty df \, \frac{\gamma^2(f)\Omega_{GW}^2(f)}{f^6 P_1(f) P_2(f)}. \tag{3}$$

The instrument noise in the detectors is described by the one-sided noise power spectral densities $P_i(f)$. The LIGO project is building two identical detectors, which we will refer to as the "initial" detectors. These detectors will be upgraded to so-called "advanced" detectors. Since the two detectors are identical in design, $P_1(f) = P_2(f)$. The design goals for the detectors specify these functions[25]. The design noise power spectrum for the Virgo detector[26] and noise power spectral densities of operating and planned resonant mass GW detectors ("bars")[27,28] are also known. The overlap reduction function $\gamma(f)$ is determined by the relative locations and orientations of the two detectors. It is identical for both the initial and advanced LIGO detectors, and has been determined for many pairs of GW detectors[23,24].

Making use of the prediction from string cosmology (1), we may use equation (3) to assess the detectability of this stochastic background. For any given set of parameters we may numerically evaluate the signal to noise ratio S/N; if this value is greater than 1.65 then with at least 90% confidence, the background can be detected by a given pair of detectors. The regions of detectability in parameter space are shown in Fig. 3. The region below the NS bound lines and above the advanced LIGO curve is the region of interest. Two NS bounds are shown, the upper, more relaxed bound, assumes no GW production during the string phase[19]. The points at 1 KHz come from operating and planned resonant mass detectors. Some are taken from real experiments, an upper bound from a single detector run [29], and the first modern 12.5 hours correlation experiment between Nautilus and Explorer[30]. The arrow points to a hollow triangle showing by how much the correlation experiment can be improved if Nautilus works properly and the experiment could be done for one year. Other points are from theoretical calculations[23]. For Fig. 3 we have assumed $h_{100} = 0.65$ and $H_r = 5 \times 10^{17}\, GeV$.

Acknowledgments

I would like to thank my collaborators Bruce Allen, Maurizio Gasperini and Gabriele Veneziano. Thanks to many GW experimentalists for their help and special thanks to the ROG collaboration and Pia Astone for access to their data. This work is supported in part by the Israel Science Foundation administered by the Israel Academy of Sciences and Humanities.

References

1. G. Veneziano, *Phys. Lett.* B265 (1991) 287.
2. M. Gasperini and G. Veneziano, *Astropart. Phys.* 1 (1993) 317.
3. R. Brustein, M. Gasperini, M. Giovannini and G. Veneziano *Phys. Lett.* B361 (1995) 45.
4. M. Gasperini and M. Giovannini, *Phys. Rev.* D47 (1993) 1519.
5. M. Gasperini, in proceedings of the 2nd Edoardo Amaldi Conference on Gravitational Waves, Geneva, Switzerland, 1-4 Jul 1997, gr-qc/9707034.
6. L.P. Grishchuk, *Sov. Phys. JETP* 40 (1975) 409.
7. M. S. Turner, *Phys. Rev.* D55 (1997) 435.
8. B. Allen, in Proceedings of the Les Houches School on Astrophysical Sources of Gravitational Radiation, Springer-Verlag, 1996.
9. M. Maggiore, gr-qc/9803028.
10. R. Brustein and G. Veneziano, *Phys. Lett.* B329 (1994) 429; N. Kaloper, R. Madden and K.A. Olive, *Nucl. Phys.* B452 (1995) 677.
11. N.D. Birrell and P.C.W. Davies, Quantum fields in curved space, Cambridge University Press 1984; V. F. Mukhanov, A. H. Feldman and R. H. Brandenberger, *Phys. Rep.* 215 (1992) 203.
12. R. Brustein, M. Gasperini and G. Veneziano, hep-th/9803018.
13. M. Gasperini, M. Maggiore and G. Veneziano, *Nucl. Phys.* B494 (1997) 315; R. Brustein and R. Madden, *Phys. Lett.* B410 (1997) 110; R. Brustein and R. Madden *Phys. Rev.* D57 (1998) 712.
14. R. Brustein, in Cascina 1996, Gravitational waves pp. 149-152, hep-th/9604159.
15. A. Buonanno, M. Maggiore and C. Ungarelli , *Phys. Rev.* D55 (1997) 3330; M. Galluccio, M. Litterio and F. Occhionero, *Phys. Rev. Lett.* 79 (1997) 970; M. Maggiore, *Phys. Rev.* D56 (1997) 1320; M. Gasperini, *Phys. Rev.* D56 (1997) 4815.
16. R. Brustein, M. Gasperini and G. Veneziano, *Phys. Rev.* D55 (1997) 3882.
17. S. Y. Khlebnikov and I. I. Tkachev, *Phys. Rev.* D56 (1997) 653.
18. V. F. Schwartzmann, *JETP Lett.* 9 (1969) 184; T. Walker et al., *Ap. J.* 376 (1991) 51.
19. B. Allen and R. Brustein, *Phys. Rev.* D55 (1997) 3260;
20. Carl R. Gwinn et al., *Ap. J.* 485 (1997) 87.
21. S. E. Thorsett and R. J. Dewey, *Phys. Rev.* D53 (1996) 3468.
22. P. Michelson, MNRAS 227 (1987) 933; N. Christensen, *Phys. Rev.* D46 (1992) 5250; E. Flanagan, *Phys. Rev.* D48 (1993) 2389.
23. S. Vitale, M. Cerdonio, E. Coccia and A. Ortolan, *Phys. Rev.* D55 (1997) 1741.
24. B. Allen and J. D. Romano, gr-qc/9710117.
25. A. Abramovici, et. al., *Science* 256 (1992) 325.
26. B. Caron et al., *Class. Quant. Grav.* 14 (1997) 1461.
27. P. Astone et al., ROG collaboration, *Astropart. Phys.* 7 (1997) 231.
28. M. Cerdonio et al., *Class. Quant. Grav.* 14 (1997) 1491.
29. P. Astone et al., ROG collaboration, *Phys. Lett.* B385 (1997) 421.
30. P. Astone, et al., ROG collaboration, to appear in Proceedings of the Eighth Marcel Grossmann Meeting, (World Scientific, 1998).

SEEDS OF LARGE-SCALE CMB ANISOTROPY IN STRING COSMOLOGY

M. SAKELLARIADOU [a]
Département de Physique Théorique, Université de Genève,
24 quai Ernest Ansermet, CH-1211 Genève 4, Switzerland.
Institut für Theoretische Physik, Universität Bern,
Sidlerstrasse 5, CH-3012 Bern, Switzerland.

Within the framework of string cosmology, we investigate whether electromagnetic or axionic seed generated perturbations could be at the origin of the density fluctuations, needed for the observed structure formation, and the measured anisotropy of the CMB radiation.

An alternative scenario to the standard cosmological picture has been recently proposed, motivated by string theory. According to this proposal [1], the universe starts very near to the string perturbative vacuum, it then evolves through an inflationary pre-big ban era, and then finally enters the standard radiation-dominated period. Within this model, we address the issue of the origin of the observed structure formation and the tiny anisotropies measured by the COBE satellite. In particular, we will study whether electromagnetic or axionic seed generated perturbations could give consistent predictions with the measured Sachs-Wolfe plateau.

We first briefly discuss the cosmological gauge-invariant perturbation theory in the presence of seeds. By *seeds*, we mean an inhomogeneously distributed form of energy, which contributes only a small fraction to the total energy density of the universe and it only interacts gravitationally with the cosmic fluid. We restrict to scalar adiabatic perturbations. We parametrize the scalar component of an inhomogeneous energy-momentum distribution, $T^{(s)}_{\mu\nu}$, generated by seed fields, in terms of four scalar *seed-functions* f_ρ, f_p, f_v and f_π, defined by

$$T^{(s)}_{00}(\mathbf{k},\eta) \;=\; M^2 f_\rho(\mathbf{k},\eta) \quad , \qquad T^{(s)}_{j0}(\mathbf{k},\eta) = -iM^2 k_j f_v(\mathbf{k},\eta) \; ,$$

[a] Work done in collaboration with R. Durrer, M. Gasperini and G. Veneziano

$$T_{ij}^{(s)}(\mathbf{k},\eta) \;=\; M^2\left[\left(f_p(\mathbf{k},\eta)+\frac{k^2}{3}f_\pi(\mathbf{k},\eta)\right)\gamma_{ij}-k_ik_jf_\pi(\mathbf{k},\eta)\right]\,. \tag{1}$$

By M we denote a convenient mass scale, introduced for dimensional reasons; η stands for the coformal time, and k for the comoving wave number.

The large-scale anisotropies measured by the COBE-DMR experiment, are determined by the combination $\Psi-\Phi$, where Ψ,Φ (called Bardeen potentials) express the perturbations of the spacetime geometry. This combination is found to be[2]

$$\Psi-\Phi\sim\max\left\{\epsilon f_\pi,\epsilon\eta^2\left(f_\rho+3\frac{\dot a}{a}f_v\right)\right\}\;; \tag{2}$$

$\epsilon\equiv 4\pi GM^2$ and a denotes the cosmic scale factor. Depending on whether $\eta^2\left(f_\rho+3\frac{\dot a}{a}f_v\right)$ or f_π dominates in Eq. (2), we distinguish seeds with small from those with large anisotropic stresses.

Let us now study CMB anisotropies for models where perturbations are generated by seeds, and more particularly, calculate their contribution to $\Delta T/T$ via the Sachs-Wolfe effect. The temperature difference of photons coming from different directions $\mathbf{n}$ and $\mathbf{n}'$ is defined as

$$\frac{\Delta T}{T}\equiv\frac{\delta T(\mathbf{n})}{T}-\frac{\delta T(\mathbf{n}')}{T},$$

$$\text{with}\qquad \frac{\delta T(\mathbf{n})}{T}=\left[\frac{1}{4}D_g^{(\gamma)}+V_j^{(m)}n^j+\Psi-\Phi\right](\eta_{dec},\mathbf{x}_{dec})+\int_{\eta_{dec}}^{\eta_0}(\dot\Psi-\dot\Phi)(\eta,\mathbf{x}(\eta))d\eta\,, \tag{3}$$

where $\mathbf{x}(\eta)=\mathbf{x}_0-(\eta_0-\eta)\mathbf{n}$ is the photon position at time η for an observer at $\mathbf{x}_0$.

The first term in Eq. (3) describes the intrinsic inhomogeneities on the surface of last scattering, due to acoustic oscillations prior to decoupling. [In general it also contains contributions to the geometrical perturbations.] The second term describes the relative motions of emitter and observer; the Doppler contribution to CMB anisotropies. It appears on the same angular scales as the acoustic term, so we denote their sum by *acoustic peaks*. The last two terms are due to the inhomogeneities in the spacetime geometry; the first contribution determines the change in the photon energy, the *ordinary* Sachs-Wolfe effect. The other term accounts for red-shifting or blue-shifting, denoted as the Integrated Sachs-Wolfe (ISW) effect. The sum of these last two terms is the full Sachs-Wolfe contribution (SW). On angular scales $0.1^\circ\lesssim\theta\lesssim 2^\circ$, the main contribution to CMB anisotropies is due to the acoustic peaks, while the SW effect becomes dominant on large angular scales. On scales smaller than about 0.1°, the anisotropies are damped due to the finite thickness of the recombination shell, as well as by photon diffusion during recombination (Silk damping).

The angular power spectrum of CMB anisotropies is expressed in terms of the coefficients C_ℓ's in the expansion of the angular correlation function in terms of Legendre polynomials P_ℓ:

$$\left\langle\frac{\delta T}{T}(\mathbf{n})\frac{\delta T}{T}(\mathbf{n}')\right\rangle\Big|_{(\mathbf{n}\cdot\mathbf{n}'=\cos\vartheta)}=\frac{1}{4\pi}\sum_\ell(2\ell+1)C_\ell P_\ell(\cos\vartheta)\,. \tag{4}$$

To determine the C_ℓ's of Eq. (4), we Fourier transform Eq. (3), according to the definition

$$\varphi(\mathbf{k})\equiv\frac{1}{\sqrt V}\int_V\varphi(\mathbf{x})\exp(i\mathbf{k}\mathbf{x})d^3x\,, \tag{5}$$

and making use of the identity

$$e^{iz\cos\vartheta}=\sum_\ell(2\ell+1)i^\ell j_\ell(z)P_\ell(\cos\vartheta)\,, \tag{6}$$

where j_ℓ is the spherical Bessel function of order ℓ. We thus obtain [2]

$$C_\ell = \frac{2}{\pi}\int \frac{<|\Delta_\ell(\mathbf{k})|^2)}{(2\ell+1)^2}k^2dk \quad , \quad \text{with} \tag{7}$$

$$\frac{\Delta_\ell}{2\ell+1} = \frac{1}{4}D_g^{(r)}(\mathbf{k},\eta_{dec})j_\ell(k\eta_0) - j'_\ell(k\eta_0)\mathbf{V}_r(\mathbf{k},\eta_{dec}) + k\int_{\eta_{dec}}^{\eta_0}(\Psi-\Phi)(\mathbf{k},\eta')j'_\ell(k(\eta_0-\eta'))d\eta' \ ,$$

where j'_ℓ stands for the derivative of j_ℓ with respect to its argument; η_{dec} denotes the conformal time at decoupling. On large angular scales, $k\eta_{dec} \ll 1$, corresponding to $\ell \ll 100$, the dominant contribution to the power spectrum comes from the Sachs-Wolfe effect,

$$C_\ell^{SW} = \frac{2}{\pi}\int k^4dk\left\langle\left[\int_{\eta_{dec}}^{\eta_0}(\Psi-\Phi)(\mathbf{k},\eta)j'_\ell(k(\eta_0-\eta))d\eta\right]^2\right\rangle \ . \tag{8}$$

On super-horizon scales, we approximate [2] the Bardeen potentials by a power-law spectrum, and we only consider [2] models where the seed contribution does not grow on sub-horizon scales. This physical requirement, implies that on sub-horizon scales, the Bardeen potentials are constant in time. We therefore approximate the Bardeen potentials by [2]

$$\Psi - \Phi \approx \begin{cases} C(k)(k\eta)^\gamma & , \ k\eta \ll 1 \\ C(k) & , \ k\eta \gg 1 \ . \end{cases} \tag{9}$$

We further assume [2] that $C(k)$ is given by a simple power-law, which by dimensionality is [2]

$$C(k) = \begin{cases} \mathcal{N}^2k^{-3/2}(k/k_1)^\alpha & , \ k \leq k_1 \\ 0 & , \ k > k_1 \ . \end{cases} \tag{10}$$

$\mathcal{N}$ is a dimensionless constant, and k_1 denotes a comoving cut-off scale. Inserting this in Eq. (8) and denoting $x \equiv k\eta$, we obtain [2]

$$C_\ell^{SW} \approx \mathcal{N}^2\frac{2}{\pi}\int_0^{k_1}\frac{dk}{k}\left(\frac{k}{k_1}\right)^{2\alpha}|I(k)|^2 \ , \ \text{where} \quad I(k) = j_\ell(x_0-1) + \int_{x_{dec}}^1 dx x^\gamma j'_\ell(x_0-x) \ . \tag{11}$$

To impose limits on α, we compare C_ℓ^{SW} with the standard inflationary scenario result [4],

$$C_\ell^{SW} \propto \frac{\Gamma(\ell-1/2+n/2)}{\Gamma(\ell+5/2-n/2)} \ , \tag{12}$$

where n denotes the spectral index. Since the scale invariant spectrum measured by the COBE-DMR experiment [5] requires $0.8 \leq n \leq 1.4$, we obtain [2] the following limits on α:

$$-0.1 \leq \alpha \leq 0.2 \ , \quad -1 < \gamma \leq 0 \ , \tag{13}$$

$$\text{and} \qquad -1.1 < \gamma+\alpha < -0.8 \ , \ \gamma+1 < 0 \ , \ \alpha+\gamma < 0 \ . \tag{14}$$

The $\alpha+\gamma > 0$ is excluded observationally (C_ℓ's are dominated by the large k-contribution).

We proceed with two examples of seed perturbations within the framework of string cosmology, electromagnetic and axionic perturbations. We first consider the electromagnetic fluctuations, in the transition from a pre-big bang phase, with growing dilaton ($\phi = -2\beta\log|\eta|$), to the radiation-dominated era, with $\phi = $ const. The electromagnetic perturbations are directly coupled to the dilaton background and the electromagnetic energy-density distribution is [6,7]

$$\frac{d\rho(k)}{d\log k} \cong \left(\frac{k_1}{a}\right)^4\left(\frac{k}{k_1}\right)^{3-2\mu} \ , \quad k < k_1 \ ; \tag{15}$$

$\mu \equiv |\beta - (1/2)| \leq 3/2$ to avoid photon overproduction, and $k_1 = 1/|\eta_1|$ denotes the maximal amplified frequency. At large times $\eta \gg |\eta_1|$ there is a stochastic electromagnetic background of fluctuations [6]. For a long enough pre-big bang phase with $\beta \leq 2$, the spectrum of fluctuations is rather flat, and could provide the origin of the galactic magnetic fields [6].

Let us determine the spectrum of the inhomogeneous stress tensor associated with the stochastic electromagnetic background. Since the electric component of the stochastic background is rapidly dissipated, due to the conductivity of the cosmic plasma, the seed stress tensor can be expressed in terms of the magnetic field only, $B_m(k) = i\epsilon_{mjl}k_j A_l(k)$, where the vector potential, in momentum space and in the radiation gauge, is

$$A_i(\mathbf{k},\eta) = \frac{c_i(\mathbf{k})}{\sqrt{k}}\sin k\eta, \qquad k_i A_i = 0, \qquad A_0 = 0\,. \tag{16}$$

The fluctuations, having quantum origin, satisfy the stochastic average condition,

$$\langle B_i(\mathbf{k}) B_j^*(\mathbf{k}')\rangle = \frac{(2\pi)^3}{2}\delta^3(k-k')\left(\delta_{ij} - \frac{k_i k_j}{k^2}\right)|\mathbf{B}(\mathbf{k},\eta)|^2\,, \tag{17}$$

$$\text{where} \qquad |\mathbf{B}(\mathbf{k},\eta)|^2 = k^2\,|\mathbf{A}(\mathbf{k},\eta)|^2 = k\,|\mathbf{c}(\mathbf{k})|^2 \sin^2 k\eta. \tag{18}$$

Using for $|\mathbf{c}(\mathbf{k})|^2$ a power-law spectrum, characterized by a cut-off frequency k_1,

$$|\mathbf{c}(\mathbf{k})|^2 = \begin{cases} (k/k_1)^{-2\mu-1} & , \; k \leq k_1 \\ 0 & , \; k > k_1\,, \end{cases} \tag{19}$$

where μ is a model-dependent parameter, we reproduce the spectral distribution (15).

The next step is the computation of the two-point correlation function for the components of the inhomogeneous stress tensor T_μ^ν, associated to the electromagnetic background:

$$\xi_\mu^\nu(x,x') = \langle T_\mu^\nu(x) T_\mu^\nu(x')\rangle - \langle T_\mu^\nu(x)\rangle\langle T_\mu^\nu(x')\rangle\,, \tag{20}$$

where there is no sum over μ,ν; the brackets denote stochastic average.

The two-point correlation function ξ_μ^μ, being the Fourier transform of the power spectrum, it detremines the spectra $|f_\bullet|^2$ of the seed functions $f_\bullet$. The spectral components $f_\bullet(k)$ will give us the spectrum of electromagnetic inhomogeneities, which we will use [2] as seeds for the scalar part of the metric perturbations. For purely magnetic seeds, $f_v = 0$ and $f_\pi \gg f_\rho$ on super-horizon scales, leading to [2]

$$k^3|\Phi - \Psi|^2(k,\eta) \sim \mathcal{N}^2 (k\eta)^{2\gamma}\left(\frac{k}{k_1}\right)^{2\alpha}\,, \tag{21}$$

$$\text{with} \qquad \gamma = \begin{cases} -4 & \text{for } \mu \leq 3/4 \\ 2\mu - 11/2 & \text{for } 3/4 \leq \mu \leq 3/2 \end{cases} \tag{22}$$

$$\alpha = \begin{cases} 7/2 & \text{for } \mu \leq 3/4 \\ 5 - 2\mu & \text{for } 3/4 \leq \mu \leq 3/2 \end{cases} \tag{23}$$

$$\mathcal{N} = \frac{\epsilon c_\pi}{(4\pi)^2}(k_1\eta_{eq})^2 \text{ in both cases;} \tag{24}$$

η_{eq} denotes the time of matter-radiation equilibrium.

Since in both cases, $\gamma + 1 < 0$, the seeds decay fast enough, as assumed earlier on. However, in both cases $\gamma + \alpha = -0.5$, which leads to the spectral index $n = 2$, incompatible with the limits from the COBE-DMR experiment, Eq. (14).

The quadrupole amplitude $Q_{rms-PS} = \sqrt{(5/4\pi)C_2}T_0$, which has been measured [8] to be $Q_{rms-PS} = 18 \pm 2\mu K$, leads to $C_2 = (1.09 \pm 0.23)10^{-10}$. In our model for electromagnetic seed perturbations, we obtain [2] the quadrupole amplitude

$$C_2 \approx \frac{\epsilon^2 c_\pi^2}{10(4\pi)^4(\gamma+1)^2}(k_1\eta_{eq})^{4-2\alpha}\left(\frac{\eta_{dec}}{\eta_0}\right)^{2(\gamma+1)}\left(\frac{\eta_{eq}}{\eta_0}\right)^{2\alpha} . \tag{25}$$

For all values of μ, the exponent $4 - 2\alpha \leq 0$. Thus the factor $(k_1\eta_{eq})^{4-2\alpha}$ is an enormous suppression, unless $\mu \cong 3/2$ (the exponent $4 - 2\alpha$ vanishes); but even then C_2 is suppressed by the factor $(\eta_{dec}/\eta_0)^{2(\gamma+1)}(\eta_{eq}/\eta_0)^{2\alpha}$. The finding that electromagnetic seeds lead to the wrong spectrum, does not rule them out as origin of the magnetic fields, since their contribution to the CMB power spectrum is in all cases negligible [2].

Let us consider the second example of seed perturbations within string cosmology, the case of a pseudoscalar stochastic background

$$\sigma(\mathbf{k},\eta) = \frac{c(\mathbf{k})}{a\sqrt{k}}\sin k\eta \quad , \qquad \langle\sigma(\mathbf{k})\sigma^*(\mathbf{k}')\rangle = (2\pi)^3\delta^3(k-k')\,|\sigma(\mathbf{k},\eta)|^2 , \tag{26}$$

characterized by a number-density spectrum

$$|c(\mathbf{k})|^2 = \begin{cases} (k/k_1)^{-2\mu-1} & , \; k \leq k_1, \; \mu \leq 3/2 \\ 0 & , \; k > k_1 . \end{cases} \tag{27}$$

We refer to it as the case of axionic perturbations (not to be confused with the axions produced at the Peccei-Quinn symmetry breaking). The energy density of axion background is [2]

$$\frac{d\rho(k)}{d\log k} \cong \left(\frac{k_1}{a}\right)^4\left(\frac{k}{k_1}\right)^{3-2|r|} , \quad k < k_1 ; \tag{28}$$

by r we parametrize the kinematics of the axion scale factor, $a_A(\eta) \sim \eta^{r+1/2}$. As it was shown [9], the energy density of a massless axion background has a flat spectral distribution.

We study separately the case of massless than that of massive axions. For a massless axion background,

$$T^\nu_\mu = \partial_\mu\sigma\partial^\nu\sigma - \frac{1}{2}\delta^\nu_\mu(\sigma_{,\lambda}\sigma^{,\lambda}) . \tag{29}$$

The dominant contribution to the Bardeen potentials is [2] always f_π, leading to

$$k^{3/2}\,|\Psi - \Phi| \sim \begin{cases} 4\pi G(a\eta)^2(k_1/a)^4(k/k_1)^{-1/2}(k_1\eta)^{-2} & , \; \mu \leq 3/4 \\ 4\pi G(a\eta)^2(k_1/a)^4(k/k_1)^{-1/2}(k_1\eta)^{2\mu-7/2}(\eta/\eta_{eq})^2 & , \; 3/4 \leq \mu \leq 3/2 . \end{cases} \tag{30}$$

For $\mu \leq 3/4$, we obtain [2] the same spectrum for the Bardeen potentials as in the electromagnetic case, and the same axionic contribution to the angular power spectrum and to C_2^{SW}. On the other hand, for $3/4 \leq \mu \leq 3/2$, we have $\gamma = 2\mu - 7/2 < 0$ and $\alpha = 3 - 2\mu > 0$. In particular, for $\mu = 3/2$, we get $\gamma = -1/2$ and $\alpha = 0$, implying a flat Harrison-Zel'dovich spectrum. In this limiting case,

$$\mathcal{N} \sim \frac{\rho_\sigma}{\rho_c}(\frac{\eta}{\eta_{eq}})^2 \sim \frac{\rho_\sigma}{\rho_\gamma} \sim 10^{-4} ; \tag{31}$$

ρ_σ denotes the energy density in masless axions, ρ_c stands for the critical energy density, and ρ_γ is the energy density in photons. Thus, massless axionic seeds, with $\mu = 3/2$, lead [2] to a flat Harrison-Zel'dovich spectrum, with an amplitude which is compatible with the observed large-scale anisotropy.

On the other hand, for massive axions,

$$T^{\nu}_{\mu} = \partial_{\mu}\sigma\partial^{\nu}\sigma - \frac{1}{2}\delta^{\nu}_{\mu}\left[(\nabla\sigma)^2 - m^2\sigma^2\right] \ , \tag{32}$$

where m denotes the axion mass. Assuming the mass term becomes dominant still during the relativistic era, we obtain [2]

$$\sigma = A\left(\frac{\eta_{eq}}{\eta}\right)^3 C(k)k^{1/2} \qquad \text{with} \qquad A = -\frac{\Gamma(1/4)\sqrt{2\pi}}{2^{1/4}\Gamma(3/4)}\eta_{eq}^{1/4}m^{-3/4} \tag{33}$$

and a primordial distribution again characterized by the index μ.

In what follows we only consider the case $\mu > 3/4$, since the other one ($\mu < 3/4$) leads to growing Bardeen potentials Φ, Ψ, and therefore it is not allowed [2]. To obtain a Harrison-Zel'dovich spectrum, we then need $\mu \sim 3/2$. The COBE normalization, the bounds on the spectral index, and the constraint $\mu < 3/2$ to avoid over-critical axion production, imply that the allowed range on the parameter μ is [2]

$$1.4 \leq \mu \leq 1.5 \ . \tag{34}$$

In addition, the present axion energy density is constrained by the critical density bound, $\Omega_{\sigma}(\eta_0) \leq 1$, where $\Omega_{\sigma}(\eta)$ denotes the fraction of critical energy density in axions at a given time η. Thus, for a typical string cosmology scale $H_1 \sim M_s \sim (10^{-1} - 10^{-2})M_{Pl}$ (where H_1 denotes the transition cut-off scale as the universe goes from radiation- to matter-dominated era, and M_s, M_{Pl} stand for string and Planck scales respectively), the maximal allowed window for the mass m of axions is [2]

$$10^{-27}eV \sim m \sim 10^{-17}eV \ . \tag{35}$$

Thus, in the case of massive axions — provided their mass is large enough so that all modes outside the horizon at the time of decoulping are already non-relativistic — there is an appropriate window for the axion mass, for which the amplitude and slope of the angular power spectrum are compatible with the COBE measurements.

Acknowledgments

I would like to thank the organizers of the *XXXIIIrd Rencontres de Moriond* on *Fundamental Parameters in Cosmology*, for inviting me to present this work.

References

1. G. Veneziano, *Phys. Lett.* **B265**, 287 (1991);
   M. Gasperini and G. Veneziano, *Astropart. Phys.* **1**, 317 (1993); *Mod. Phys. Lett.* **A8** 3701 (1993) (1993); *Phys. Rev.* **D50**, 2519 (1994).
2. R. Durrer, M. Gasperini, M. Sakellariadou and G. Veneziano, "Seeds of large-scale anisotropy in string cosmology", CERN-TH/97-13.
3. R. Durrer, *Fund. of Cosmic Physics* **15**, 209 (1994).
4. R. Bond and G. Efstathiou, *MNRAS* **226**, 655 (1987).
5. G.F. Smoot and D. Scott, in L. Montanet *et al.*, *Phys. Rev.* **D50**, 1173 (1994) (update 1996).
6. M. Gasperini, M. Giovannini and G. Veneziano, *Phys. Rev. Lett.* **75**, 3796 (1995).
7. D. Lemoine and M. Lemoine, *Phys. Rev.* **D52**, 1955 (1995).
8. A.J. Banday *et al.*, *Ap. J. Lett.* (1996).
9. E. J. Copeland, R. Easther and D. Wands, "Vacuum fluctuations in axion-dilaton cosmologies", SUSSEX-TH-97001 (hep-th/9701082).

U-DUALITY AND M-THEORY COSMOLOGY

B.A. OVRUT
Department of Physics, University of Pennsylvania,
Philadelphia, PA 19104-6396, USA

A manifestly U-duality covariant approach to M-theory cosmology is discussed and applied to cosmologies in dimension $D = 5$.

1 Introduction

In this talk, we will discuss a manifestly U-duality covariant formulation of M-theory cosmology first presented in [1]. We are going to reduce 11-dimensional supergravity on a Ricci-flat manifold to D dimensions, thereby keeping the breathing mode of the internal space as the only modulus [2] and focusing on the D-dimensional "external" part of U-duality. As an explicit example, we will study the case $D = 5$, corresponding to the U-duality group $G = SL(5)$. This example is motivated by the Horava-Witten construction of M-theory on S^1/Z_2 [3,4] which represents the effective theory of strongly coupled heterotic string theory .

2 Compactification of 11-dimensional Supergravity

The relevant bosonic part of the 11-dimensional supergravity Lagrangian reads

$$\mathcal{L} = \sqrt{-\hat{g}} \left[\hat{R} - \frac{1}{2 \cdot 4!} \hat{F}_{MNPQ} \hat{F}^{MNPQ} \right] . \tag{1}$$

We are using the conventions of ref. [5]. The 4-form field strength $\hat{F}_{MNPQ}$ is expressed in terms of the 3-form gauge field $\hat{A}_{NPQ}$ as $\hat{F}_{MNPQ} = 4 \partial_{[M} \hat{A}_{NPQ]}$. We have omitted the Chern-Simons term in eq. 1 since this vanishes for the class of compactifications we will be interested in. Our main purpose is to investigate the relation of cosmological solutions and U-duality symmetries

for the action 1. In our reduction to D dimensions we will keep a minimal moduli content only, that is, the breathing mode of the Ricci–flat manifold.

We are using indices $\mu, \nu ... = 0, ..., d \equiv D-1$ for the external space–time, indices $m, n, ... = 1, ..., d$ for the external spatial directions and indices $a, b, ... = d+1, ..., 10$ for the δ–dimensional internal space, where $\delta = 11 - D$. Our Ansatz for the 11–dimensional fields is as follows

$$\begin{aligned} \hat{g}_{\mu\nu} &= g_{\mu\nu}(x^\rho) \\ \hat{g}_{\mu b} &= 0 \\ \hat{g}_{ab} &= \bar{b}^2(x^\rho)\emptyset_{ab}(x^c) \\ \hat{A}_{\mu\nu\rho} &= B_{\mu\nu\rho}(x^\sigma)\,. \end{aligned} \tag{2}$$

All other components of $\hat{A}_{NPQ}$ are set to zero. Here $\emptyset_{ab}$ is the metric of a δ–dimensional Ricci–flat manifold and $\bar{b}$ is its breathing mode. Depending on the dimension, this manifold can be a Calabi–Yau space, a torus or even a product of both.

Using the truncation 2 the action 1 turns into

$$\mathcal{L} = \sqrt{-\bar{g}}\left[\bar{R} - k^2\,\bar{b}^{-2}(\partial_\mu \bar{b})^2 - \bar{b}^{\frac{6(11-D)}{D-2}}\frac{1}{2\cdot 4!}F_{\mu\nu\rho\sigma}F^{\mu\nu\rho\sigma}\right] \tag{3}$$

where $F_{\mu\nu\rho\sigma} = 4\,\partial_{[\mu}B_{\nu\rho\sigma]}$, $k^2 = \frac{D-1}{D-2}\delta^2 - \delta(\delta-1)$ and to get a canonical curvature term we have performed a Weyl rotation to the Einstein frame metric $\bar{g}_{\mu\nu}$. For a study of cosmological solutions of this Lagrangian we consider the Ansatz

$$\begin{aligned} \bar{g}_{\mu\nu} &= \begin{pmatrix} -\bar{N}^2(\tau) & 0 \\ 0 & \bar{G}_{mn}(\tau) \end{pmatrix} \\ B_{mnr} &= B_{mnr}(\tau) \\ \bar{b} &= \bar{b}(\tau)\,. \end{aligned} \tag{4}$$

Here, time has been denoted by τ. The equations of motion with these specialized fields inserted can be derived from the 1–dimensional Lagrangian

$$\begin{aligned} \mathcal{L} &= \bar{N}^{-1}\sqrt{\bar{\Phi}}\left[k^2\,\bar{b}^{-2}\dot{\bar{b}}^2 - \frac{1}{4}\bar{\Phi}^2\dot{\bar{\Phi}}^2 - \frac{1}{4}\dot{\bar{G}}_{mn}\dot{\bar{G}}^{mn}\right. \\ &\qquad \left. + \bar{b}^{\frac{6(11-d)}{D-2}}\bar{G}^{mm'}\bar{G}^{nn'}\bar{G}^{rr'}\dot{B}_{mnr}\dot{B}_{m'n'r'}\right] \end{aligned} \tag{5}$$

where $\bar{\Phi} = \det(\bar{G})$. The dot denotes the derivative with respect to the time τ.

One should expect the U–duality group of $(11-d)$–dimensional maximal supergravity as a symmetry group of the Lagrangian 5. For example, for $D = 5$ $(d = 4)$ one expects $G = SL(5)$, the U–duality group of 7–dimensional supergravity. It is, however, hard to see directly from the Lagrangian in the form 5. One can perform nonlinear field redefinitions which express the physical Einstein frame fields in terms of the new fields G_{mn}, N, b and $\Phi = \det(G)$. Written in terms of these new variables the Lagrangian 5 finally reads

$$\begin{aligned} \mathcal{L} &= N^{-1}\,b^\delta\left[-\delta(\delta-1)\,b^{-2}\dot{b}^2 + \frac{1}{4(10-D)}\Phi^{-2}\dot{\Phi}^2 - \frac{1}{4}\dot{G}_{mn}\dot{G}^{mn}\right. \\ &\qquad \left. + \frac{1}{2\cdot 3!}G^{mm'}G^{nn'}G^{rr'}\dot{B}_{mnr}\dot{B}_{m'n'r'}\right]\,. \end{aligned} \tag{6}$$

3 U–Duality Covariant Formulation

For arbitrary D, all cases can be treated uniformly by considering an $SL(n)/SO(n)$ sigma model (where $n = 5$ for $D = 5$, for example) written in terms of the coset parameterization $M \in SL(n)/SO(n)$. The coset M can be characterized by the conditions $\det(M) = 1$ and $M = M^T$. We are therefore considering the Lagrangian

$$\mathcal{L}_1 = N^{-1} b^\delta \left[-\delta(\delta-1) b^{-2} \dot{b}^2 + \frac{1}{4} \mathrm{tr}\left(M^{-1}\dot{M} M^{-1}\dot{M} \right) \right] + l\,(\det(M) - 1) + \mathrm{tr}\left(\gamma (M - M^T) \right) \quad (7)$$

with the Lagrange multipliers l, γ. The $SL(n)$ symmetry transformations are given by

$$\begin{aligned} b &\to b \quad , \quad l \to l \\ M &\to P M P^T \quad , \quad \gamma \to P^{T^{-1}} \gamma P^{-1} \, , \end{aligned} \quad (8)$$

where $P \in SL(n)$. After eliminating the Lagrange multipliers, we find as the $SL(n)$ covariant equations of motion for M, b and N (in the gauge $N = 1$)

$$\begin{aligned} \frac{d}{d\tau}\left(M^{-1}\dot{M} \right) + \delta H M^{-1}\dot{M} &= 0 \\ (\delta - 1)\dot{H} + \frac{1}{2}\delta(\delta-1)H^2 &= -\rho \\ \frac{1}{2}\delta(\delta-1)H^2 &= \rho \, , \end{aligned} \quad (9)$$

respectively. The Hubble constant H and the energy density ρ are defined by

$$H = \frac{\dot{b}}{b} \, , \qquad \rho = \frac{1}{8}\mathrm{tr}\left(M^{-1}\dot{M} M^{-1}\dot{M} \right) \, . \quad (10)$$

The second and third equation in 9 can be combined give

$$H = \frac{1}{\delta\tau} \, , \qquad b = b_0 |\tau|^{1/\delta} \, , \quad (11)$$

where b_0 is an arbitrary constant. Inserting this into the first equation 9 we find for the coset M

$$M = M_0 \, e^{I \ln|\tau|} \, , \quad (12)$$

where

$$\begin{aligned} \det(M_0) = 1 \quad &, \quad \mathrm{tr}(I) = 0 \\ M_0 = M_0^T \quad &, \quad M_0 I = I^T M_0 \, . \end{aligned} \quad (13)$$

Furthermore, from the last cquation 9 one obtains the zero energy constraint

$$\mathrm{tr}(I^2) = 4\frac{\delta - 1}{\delta} \, . \quad (14)$$

Eqs. 11–14 represent the complete solution of the Lagrangian 7 written in a manifestly $SL(n)$ covariant form. The $SL(n)$ transformation 8 on the coset M acts as

$$\begin{aligned} M_0 &\to P M_0 P^T \\ I &\to P^{T^{-1}} I P^T \, . \end{aligned} \quad (15)$$

The matrices M_0, I satisfying the constraints 13 contain n^2+n-2 independent parameters. The zero energy condition 14 eliminates one of them so that n^2+n-3 remain. On the other hand,

the group $SL(n)$ consists of n^2-1 parameters which implies that for $n>2$ not all solutions can be connected to each other by $SL(n)$ transformations. More precisely, the total n^2+n-3–dimensional solution space splits into n^2-1–dimensional equivalence classes, each consisting of solutions related to each other by $SL(n)$ transformations via eq. 15. The remaining $n-2$ integration constants label different equivalence classes. It is useful in the following to make this structure more explicit. Diagonalizing M_0 and I using eq. 15 with appropriate matrices P, eqs. 12, 13, 14 can be written in the form

$$M = P\,\mathrm{diag}(|\tau|^{p_1},...,|\tau|^{p_n})\,P^T \tag{16}$$

with

$$\sum_{i=1}^{n} p_i = 0\,, \qquad \sum_{i=1}^{n} p_i^2 = 4\frac{\delta-1}{\delta} \tag{17}$$

and $P\in SL(n)$. The equivalence classes of $SL(n)$ unrelated solutions are parameterized by the $n-2$ constants $\{p_i\}$ subject to the constraints 17. On the other hand, a specific class, characterized by a fixed set $\{p_i\}$, is generated by the matrices $P\in SL(n)$ in eq. 16.

4 The Example $D=5$

The U–duality group in the $D=5$ case is $G=SL(5)$. Let us define the vector $\mathbf{B}=(B^s)$ by $B_{mnr}=\frac{1}{\Phi}\epsilon_{mnrs}B^s$. Then the $SL(5)/SO(5)$ coset $\mathcal{M}$ can be parameterized by[6]

$$\mathcal{M}=\Phi^{-2/5}\begin{pmatrix} G & -G\mathbf{B} \\ -\mathbf{B}^TG & \Phi+\mathbf{B}^TG\mathbf{B}\end{pmatrix}\,, \tag{18}$$

where we have used a matrix notation $G=(G_{mn})$ for the metric. With the internal dimension $\delta=6$, Lagrangian 6 can then be put into the form

$$\mathcal{L}=N^{-1}b^6\left[-30\,b^{-2}\dot{b}^2-\frac{1}{4}\mathrm{tr}\left(\dot{\mathcal{M}}\dot{\mathcal{M}}^{-1}\right)\right]\,, \tag{19}$$

which has manifest $SL(5)$ invariance. The explicit transformations are given by

$$\begin{aligned} b &\rightarrow b \\ \mathcal{M} &\rightarrow P\mathcal{M}P^T \end{aligned} \tag{20}$$

with $P\in SL(5)$.

The equations of motion for the Lagrangian 19 are given by the general expressions 9, 10 with $\delta=6$ and $M=\mathcal{M}$ inserted. Here $\mathcal{M}$ is the $SL(5)/SO(5)$ coset explicitly given in terms of the metric and the 3–form in eq. 18. The solution for the breathing mode can be read off from eq. 11

$$H=\frac{1}{6\tau}\,, \quad b=b_0\,|\tau|^{1/6}\,. \tag{21}$$

For the coset $\mathcal{M}$ we have from eq. 16 and 17

$$\mathcal{M}=P\,\mathrm{diag}(|\tau|^{p_1},...,|\tau|^{p_5})P^T\,, \tag{22}$$

with

$$\sum_{i=1}^{5} p_i = 0\,, \quad \sum_{i=1}^{5} p_i^2 = \frac{10}{3} \tag{23}$$

and $P\in SL(5)$. We require $p_i\geq p_j$ for $i<j$. The solution 22 contains 27 integration constants. Three of them are given by the parameters $\{p_i\}$ subject to the constraints 23, labeling the $SL(5)$

equivalence classes. The remaining 24 integration constants parameterize the $SL(5)$ matrix P in eq. 22.

What is the general physical picture emerging from the solution 22? One expects that in the asymptotic regions, the evolution rates are controlled by the $\{p_i\}$ and are therefore $SL(5)$ invariant. The $SL(5)$ parameters, however, determine the precise time range for the asymptotic regions and the time of transition.

We will concentrate on the physically interesting case of FRW universes in the following. For the metric and the form field this implies

$$G = \begin{pmatrix} c\mathbf{1}_3 & 0 \\ 0 & \phi \end{pmatrix}, \quad \mathbf{B} = \begin{pmatrix} \mathbf{0}_3 \\ B \end{pmatrix}, \tag{24}$$

where c, ϕ, B are time dependent scalars. Inserting 24 into the coset parameterization 18 for $\mathcal{M}$ results in

$$\mathcal{M} = \begin{pmatrix} \mathcal{M}_3 & 0 \\ 0 & \mathcal{M}_2 \end{pmatrix}, \quad \mathcal{M}_3 = c\Phi^{-2/5}\mathbf{1}_3, \quad \mathcal{M}_2 = \Phi^{-2/5}\begin{pmatrix} \phi & -\phi B \\ -\phi B & \Phi + B^2\phi \end{pmatrix}, \tag{25}$$

with $\Phi = c^3\phi$. Eq. 25 shows that FRW universes can be mapped into anisotropic solutions and vice versa using appropriate $SL(5)$ transformations. Since we wish to stay within the class of FRW solutions, we should restrict ourselves to the subgroup $H \equiv SL(3) \times SL(2) \times U(1) \subset SL(5)$ which leaves the structure of $\mathcal{M}$ in eq. 25 invariant. The FRW universes are specified by

$$p \equiv p_1 = p_2 = p_3 \tag{26}$$

in eq. 22. From eq. 23 we derive

$$p_{4,5} = -\frac{3p}{2} \pm \sqrt{\frac{5}{3} - \frac{15}{4}p^2}, \quad |p| \leq \frac{2}{3}. \tag{27}$$

We have therefore found a one parameter set (with parameter p) of H–inequivalent classes of FRW universes, each equivalence class for a fixed p spanned by the action of the group H. How does H act explicitly? First of all, $GL(3) \subset H$ is again part of the global coordinate transformations and therefore trivial. We concentrate on the $SL(2)$ part and write

$$P_2 = \begin{pmatrix} \alpha & \beta \\ \gamma & \delta \end{pmatrix}, \quad \alpha\delta - \beta\gamma = 1. \tag{28}$$

Then, $\mathcal{M}_2$, $\mathcal{M}_3$ take the form

$$\mathcal{M}_2 = \begin{pmatrix} \alpha^2|\tau|^{p_4} + \beta^2|\tau|^{p_5} & \alpha\gamma|\tau|^{p_4} + \beta\delta|\tau|^{p_5} \\ \alpha\gamma|\tau|^{p_4} + \beta\delta|\tau|^{p_5} & \gamma^2|\tau|^{p_4} + \delta^2|\tau|^{p_5} \end{pmatrix}, \quad \mathcal{M}_3 = |\tau|^p\mathbf{1}_3, \tag{29}$$

where $p_{4,5}$ are given by 27 in terms of the free parameter p. By comparison with eq. 25 we can read off the expressions for c, Φ, B, ϕ and convert them to the physical fields. We can then solve for the comoving time t in two asymptotic regions, leading to

$$\begin{aligned} t &= \frac{2b_0^2\,|\alpha|}{3p + p_4 + 8/3}|\tau|^{3p/2+p_4/2+4/3}\,\mathrm{sgn}(\tau), \quad \text{for} \quad |\tau| \gg \tau_{\text{form}} \\ t &= b_0^2\,|\beta|\frac{2}{3p + p_5 + 8/3}|\tau|^{3p/2+p_5/2+4/3}\,\mathrm{sgn}(\tau), \quad \text{for} \quad |\tau| \ll \tau_{\text{form}}, \end{aligned} \tag{30}$$

where

$$\tau_{\text{form}} = \left(\frac{\beta}{\alpha}\right)^{\frac{2}{p_4 - p_5}}. \tag{31}$$

In these regions, we find for the Hubble parameter H_a

$$H_a = \frac{P(p)}{t}\,, \quad P(p) = \begin{cases} \frac{2}{3}\frac{3p+p_4+1}{3p+p_4+8/3} & \text{for} \quad |\tau| \gg \tau_{\text{form}} \\ \frac{2}{3}\frac{3p+p_5+1}{3p+p_5+8/3} & \text{for} \quad |\tau| \ll \tau_{\text{form}} \end{cases} . \tag{32}$$

The expansion coefficient $P(p)$ depends on the free parameter p and is generically different in the two asymptotic regions. We can show that it is always positive for large $|\tau| \gg \tau_{\text{form}}$ and can have both signs for $|\tau| \ll \tau_{\text{form}}$. For the positive branch $t > 0$ this implies a universe which is expanding or contracting at early time and is turned into an expanding universe at late time. The situation for the negative branch is reversed; the universe is always contracting at early time ($|t|$ large and $t < 0$) and can be contracting or expanding later. The Hubble parameter 32 and hence the aforementioned properties are $SL(2)$ invariant. The transition time given by

$$|\tau| \sim \tau_{\text{form}} = \left(\frac{\beta}{\alpha}\right)^{\frac{2}{p_4-p_5}}\,, \tag{33}$$

on the other hand, depends on $SL(2)$ parameters along with the details of the transition.

Suppose now, we choose a solution in the positive branch which is contracting for a short period of time and then turns into expansion. By applying appropriate $SL(2)$ transformations to this solution the contraction period can be made arbitrarily long. An additional time reversal $t \to -t$ leads to a negative branch solution with an expansion period that can be arbitrarily long. The extreme limits are possible. By choosing $P_2 = \mathbf{1}$ ($\beta = 0$ in particular) we have a positive branch solution which is always expanding. As the other extreme we may set

$$P_2 = \begin{pmatrix} 0 & 1 \\ -1 & 0 \end{pmatrix}$$

($\alpha = 0$ in particular) which generates an expanding negative time branch solution. We have therefore shown that a combination of U–duality and time reversal can map expanding negative and positive time branch solutions into each other.

Acknowledgments

Supported in part by DOE under contract No. DE-AC02-76-ER-03071.

References

1. A. Lukas, B. A. Ovrut, hep-th/9709030, to appear in Phys. Lett. B.
2. K. Maeda, *Phys. Lett.* B **166**, 59 (1986).
3. P. Horava and E. Witten, NPB **475**, 94 (1996); NPB **460**, 506 (1996).
4. E. Witten, NPB **471**, 135 (1996).
5. E. Cremmer, B. Julia and J. Scherk, *Phys. Lett.* B **76**, 409 (1978); E. Cremmer and B. Julia, *Phys. Lett.* B **80**, 48 (1978); NPB **159**, 141 (1979); E. Cremmer, LPTENS 81/18, Lectures given at ICTP Spring School Supergravity, Trieste 1981, published in Trieste Supergrav.School 1981:313.
6. M. J. Duff and J. X. Lu, NPB **347**, 394 (1990).

CDM models with a broken-scale-invariant spectrum

J. LESGOURGUES
Laboratoire de Mathématiques et de Physique Théorique, UPRESA 6083 CNRS, Université de Tours, Parc de Grandmont, F-37200 Tours, France

We compare two inflationary models leading to a broken-scale-invariant spectrum with observational data from large-scale structures and CMB anisotropies. It appears that these models can hardly save the standard CDM scenario with $\Omega = 1$. On the other hand, in presence of a cosmological constant, one of the models is in good agreement with the data, and could explain the observation of a peak in the present power spectrum.

1 Introduction

It is well-known that the Cold Dark Matter model, in a flat universe, and with standard cosmological parameters, does not fully agree with observations of large scale structures and CMB anisotropies, at least whith a flat Harrison-Zel'dovitch primordial spectrum (indeed, once the fluctuations have been normalized to COBE, too much power is predicted at small scales in the density present power spectrum). This is why a second free parameter in the primordial spectrum is often considered, namely, a tilt $n < 1$. However, tilted models don't solve all the problems, since, for instance, after COBE normalization, different values of the tilt are required to fit either the constraint on σ_8, or those from redshift surveys. So a natural idea in order to save sCDM is to turn to the next level of complexity, *i.e.*, a primordial spectrum with 3 free parameters. Some specific inflationary models predict such spectra. In a recent work [1,2], we first compared a double inflationary model with observations, and then focused on a single inflationary model with a rapid change in the derivative of the inflaton potential (for similar studies, see also [3]). As said before, our first motivation is to check wether sCDM can be saved by a breaking-scale-invariant (BSI) spectrum or not. In addition, last year, some evidence was found for a feature in the density power spectrum, studying Abell galaxy clusters [4,5], or APM galaxies [6]. Our second motivation is then to find out wether the BSI spectra considered here can explain this feature.

2 Presentation of the two studied BSI spectra

We first assume that inflation is driven by two uncoupled fields, with different masses. The asymptotic behaviour of the primordial density power spectrum at small and large scales can be derived analytically [7], but a numerical calculation is necessary to obtain the whole spectrum of adiabatic perturbations [8,9] and gravitational waves [10]. Both spectra are flat at small scales and have a logarithmic dependance at large scales. In this model, the ratio between scalar and tensor perturbations is given by the theory, and we are left with only 3 free parameters, that can be chosen as : the overall normalization, the scale of the break k_0, and the ratio between the masses, p, that acts as a shape parameter, giving the amplitude of the break ($p = 1$ corresponds to a flat spectrum).

In a second model, we assume that inflation is driven by a single field ϕ, and that around some value ϕ_0, the derivative of the potential goes from V'_+ to V'_- inside a region of negligible width. In this model, the exact power spectrum can be derived analytically [11], and consists in a step with superimposed oscillations. It is flat at both large and small scales. Again, there are 3 free parameters : the overall normalization, the scale of the break k_0, and $p = V'_-/V'_+$, that gives the ratio between the plateaux. When $p > 1$ (resp. $p < 1$), the increase is towards large scales (resp. small scales). In fact, in this model, the amount of primordial gravitational waves is still a free parameter; we considered the case with no gravitational waves at all. Including tensors would be the next level of complexity.

3 Can we save sCDM with these models ?

We consider flat CDM with $h = 0.5$, $\Omega_b h^2 = 0.015$, and the double inflationary spectrum. For each set of inflationary parameters (p, k_0), we test the model with five observational constraints: COBE normalization, σ_8 estimate [12], peculiar velocities [13], redshift surveys (through a χ^2 test), and small scales anisotropies measurements (computing the C_l's with CMBFAST [14]). We find that 3 of these 5 constaints can be satisfied simultaneously. For instance, when $10 < p < 20$, and $2 < k_0 < 2.5\, h\,\mathrm{Mpc}^{-1}$, the model is in agreement with COBE, σ_8 and redshift surveys, in contrast with tilted models. Peculiar velocities are low, but still correct if one invokes cosmic variance. However, small scales anisotropies are obviously too small. It is easy to understand why. Taking (p, k_0) in the previous region, the logarithmic decrease between large and intermediate scales causes a lack of power between 0.01 and 0.05 $h\,\mathrm{Mpc}^{-1}$, i.e., at scales relevant for both peculiar velocities and the first CMB peak. We tried small variations of h up to 0.7, and of the amount of baryons up to $\Omega_b h^2 = 0.025$. Since no significant improvement can be seen, we conlude that unless the CMB peaks turn out to be smaller than expected, the double inflationary spectrum is excluded in the sCDM context, especially because of its logarithmic decrease at intermediate scales.

A better behaviour is expected from the steplike spectrum. Indeed, after normalization at COBE and galaxy scales, the power at intermediate scales can be preserved (see figure 1). For $p \simeq 2.1$, and $k_0 \simeq 0.03\, h\,\mathrm{Mpc}^{-1}$, a very good agreement is found with COBE, σ_8, redshift surveys, and bulk velocities. Moreover, the first peak is given by the upper plateau, so it is as high as in the Harrison-Zel'dovitch case. The only problem comes from small scales anisotropies, especially the second CAT point. So the crucial test for this model will be the future CMB measurements at small scales. If the second CAT point turns out to be too high, then the steplike spectrum will become a very attractive possiblility. But if CAT is confirmed, it is likely that we can exclude not only this type of BSI primordial spectrum, which we expect to be the best, but also probably all attempts to cure sCDM with a BSI spectrum. So one couldn't escape to introducing other parameters like a cosmological constant, neutrino mass or curvature of the universe.

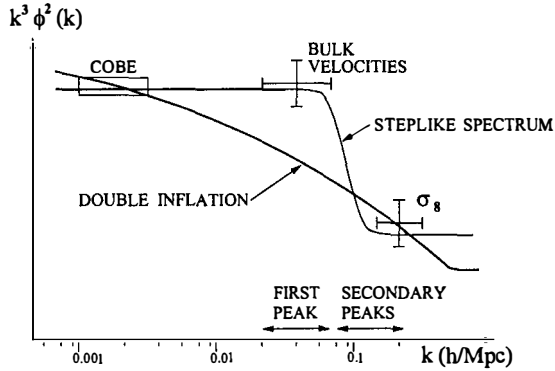

Figure 1: A sketchy outline of two primordial power spectra, compared with a few constraints (COBE, bulk velocities, σ_8) and also indicating CMB peaks scales.

4 Can the steplike spectrum exlain the observed peak in the present spectrum ?

Of course, we can do both, *i.e.*, study a BSI spectrum in the context, fot instance, of ΛCDM. Until last year, there was no strong motivation for such complication, since ΛCDM models already explain most observations with a simple flat spectrum, but the situation changed when some evidence for a peak in the present power spectrum was found in Abell galaxy clusters[4,5], and in APM galaxies[6]. If this peak really exists, it must be generated either in the primordial power spectrum, or in the matter transfer function. It was shown that the Sakharov oscillations in the transfer function caused by baryons do not fit the Einasto *et al.* results[15,16]. Our idea was then to consider a cosmological model that already works well, namely, ΛCDM, and introduce the steplike spectrum studied before.

So we perform exactly the same study, with just one more parameter: Λ. We vary $0.5 < h < 0.7$, $0 < \Omega_\Lambda < 1$, p and k_0. When $p = 1$, an allowed window is found around $\Omega_\Lambda = 0.5$, in agreement with[17], and fairly high Doppler peaks are predicted in the CMB anisotropies. We can play now the following game:

- take $p > 1$. Then whe have less primordial perturbations at small scales. So, in order to obtain as much power in the present power spectrum, one must increase the transfer function by lowering Ω_Λ or by increasing h. However, these changes all contribute to lower CMB anisotropies, and set a bound to high p's.

- take $p < 1$ ("inverted step"). This is exaclty the opposite: we must consider higher Ω_Λ's or lower h's, and are limited by exceedingly high CMB anisotropies.

The introduction of the two parameters p and k_0 enlarges significantly the (h, Ω_Λ) allowed window. This is an interesting result in itself. But now let us compare with the peak measured by Einasto *at al.* . The best model turns out to be an "inverted step": $p \simeq 0.8$, $k_0 \simeq 0.015\, h\,\mathrm{Mpc}^{-1}$ (see figure 2). Since for these values, we are in good agreement with all cosmological tests, we can say that this model is quite attractive. We now have to wait for a confirmation of the feature in the power spectrum. In addition, BSI steplike models predict C_l curves that are not degenerated with other current cosmological scenarios, and so the forthcoming CMB anisotropies measurements will easily exclude or bring evidence for steplike primordial spectra.

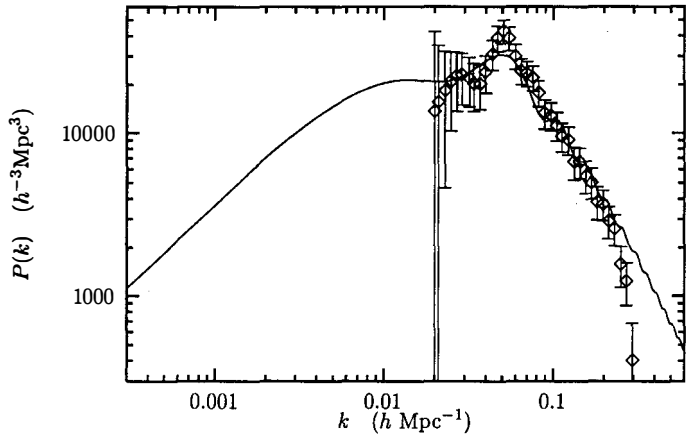

Figure 2: Theoretical power spectrum for $h = 0.7$, $\Omega_\Lambda = 0.72$, $p = 0.75$ and $k_0 = 0.016\,h\,\mathrm{Mpc}^{-1}$ compared with the power spectrum of rich Abell galaxy clusters, taken from Einasto *et al.* [4] and divided by $b^2 = 5$.

Acknowledgments

I would like to thank the organizers for their decision to cover my expenses with a EC TMR grant.

References

1. J. Lesgourgues, D. Polarski, *Phys. Rev.* D **36**, 6425 (1997)
2. J. Lesgourgues, D. Polarski and A. A. Starobinsky, accepted in *MNRAS* , E-print Archive astro-ph/9711139
3. S. Gottlöber, J. P. Mücket and A. A. Starobinsky, *Ap. J.* **434**, 417 (1994);
   S. Gottlöber and J. P. Mücket, *Astron. Astrophys.* **272**, 1 (1993);
   S. Gottlöber, V. Müller and A. A. Starobinsky, *Phys. Rev.* D **43**, 2510 (1991)
4. J. Einasto, M. Einasto, S. Gottlöber, V. Muller *et al.*, *Nature* **385**, 139 (1997)
   J. Einasto, M. Einasto, P. Frisch, S. Gottlöber *et al.*, *MNRAS* **289**, 801 (1997)
   J. Einasto, M. Einasto, P. Frisch, S. Gottlöber *et al.*, *MNRAS* **289**, 813 (1997)
5. J. Retzlaff, S. Borgani, S. Gottlöber and V. Müller, E-print Archive astro-ph/9709044
6. E. Gaztañaga and C. M. Baugh, accepted in *MNRAS* , E-print Archive astro-ph/9704246
7. D. Polarski and A.A. Starobinsky, *Nucl. Phys.* B **385**, 623 (1992)
8. D. Polarski, *Phys. Rev.* D **49**, 6319 (1994)
9. P. Peter, D. Polarski and A. A. Starobinsky, *Phys. Rev.* D **50**, 4827 (1994)
10. D. Polarski and A. A. Starobinsky, *Phys. Lett.* B **356**, 196 (1995)
11. A. A. Starobinsky, *JETP Lett.* **55**, 489 (1992)
12. M. Davis, G. Efstathiou, C. S. Frenk and S. D. M. White, *Ap. J.* **292**, 371 (1985)
13. T. Kolatt and A. Dekel, *Ap. J.* **479**, 592 (1997)
14. U. Seljak and M. Zaldarriaga, *Ap. J.* **469**, 7 (1996)
15. F. Atrio-Barandela *et al.*, *JETP Lett.* **66**, 397 (1997)
16. D. J. Eisenstein, W. Hu, J. Silk and A. S. Szalay, E-print Archive astro-ph/9710303
17. L. A. Kofman, N. Y. Gnedin and N. A. Bahcall, *Ap. J.* **413**, 1 (1993)

INFLATION AND THE MICROWAVE BACKGROUND

Andrew R. Liddle
Astronomy Centre, University of Sussex,
Brighton BN1 9QJ, Great Britain

I discuss the interplay between inflation and microwave background anisotropies, stressing in particular the accuracy with which inflation predictions need to be made, and the importance of inflation as an underlying paradigm for cosmological parameter estimation.

1 Introduction

Because of calculational simplicity, and because it provides a good fit to the observational data, an initial spectrum of adiabatic density perturbations is normally assumed responsible for all the observed structures in the Universe, such as galaxy clusters and microwave background anisotropies. The inflationary cosmology provides a natural explanation for such an initial spectrum, and indeed the causal generation of large-scale adiabatic perturbations requires a period of inflation.[1]

In studying the microwave background anisotropies, we believe we have a tool through which all of the cosmological parameters, such as the Hubble constant h and the density parameter Ω_0, can be probed. This is because the evolution of perturbations in the matter and radiation fields depends on all the cosmological parameters. On the other hand, the microwave background anisotropies are entirely due to linear perturbation theory, and hence entirely dependent on the initial perturbations you have in the first place. The only reason that one can indeed hope to extract cosmological parameters is because one believes that the initial spectrum takes on a simple form, perhaps a power-law, which can be parametrized simply and then those initial parameters thrown into the melting pot along with the cosmological ones and fitted by the data. One of the delights of inflation is that the initial spectrum is indeed typically predicted to take on a simple form, and furthermore one which can readily be calculated to high precision for a given inflationary model.

2 Models of inflation

In common with normal practice, I'll focus my discussion on the simplest sub-class of inflationary models, where there is a single scalar field ϕ rolling slowly down some potential $V(\phi)$. The full range of inflationary models currently under discussion mostly consists of models which fit into this simple class, though I'm keen to stress that there are more complicated models on the market, in particular so-called open inflation models which, needless to say, give an open Universe. I'll come back to some of these complexities later.

The simplest models give rise to a flat spatial geometry, so first let's think about how they compare to the observational data. In recent years the flood of data supporting a low matter density has become an avalanche, leaving even the most hard-bitten theorist feeling guilty to suggest otherwise. However, interestingly, the two probes which actually constrain the geometry, rather than just the matter density, appear to favour a flat geometry. One is the location of the first peak in the microwave background spectrum, which is not particularly strongly constrained but certainly looks closer to the $\ell = 220$ or so of a flat model than the $\ell = 500$ or so of a low-density open model. The second, more secure, evidence comes from the recent type Ia supernovae results (Perlmutter et al.[2] and Kim in these proceedings), which, for a matter density of around 0.3 (the favoured value), support the existence of a cosmological constant at just the right density to make the Universe flat.

The type of person who likes inflation is rather prone to disliking the cosmological constant, on the grounds that it represents exactly the kind of fine-tuning which inflation was supposed to liberate us from. On the other hand, inflation says nothing about the present matter content of the Universe; it just provides a flat spatial geometry and the way in which the matter is divided into different classes is, most likely, a property of present-day physics. So the presence or otherwise of a cosmological constant says nothing about whether inflation really occurred. In fact, one can rescue something from this sorry state of affairs, by noting that the favoured region corresponds to a Universe which is accelerating today. Once people become convinced that the Universe is presently accelerating, it will presumably become rather easier to suggest that the Universe might also have accelerated at some point in its distant past, and as it happens the definition of inflation is precisely any epoch during which the Universe experiences accelerated expansion.

3 Perturbations from inflation

During an inflationary epoch, comoving length scales are continually being stretched to scales larger than the Hubble length. As this happens, quantum fluctuations in the fields, which have to exist in accordance with the uncertainty principle, become 'frozen in' — unable to evolve on the Hubble timescale as their wavelength is so long — and begin to act like classical perturbations. The amplitude of these perturbations is readily calculable, and has been studied in many papers. See Liddle and Lyth[3] for a review.

Because the Heisenberg uncertainty principle democratically affects everything, there are perturbations not only in the scalar field, which become adiabatic density perturbations, but also in the gravitational field which become gravitational waves. The precise form of both types of perturbation, their amplitude and scale-dependence, will depend on the potential energy $V(\phi)$, it being the only input into the problem.

If the inflationary expansion is sufficiently rapid, those scales on which observable perturbations are generated all cross outside the Hubble radius during a very narrow interval of time. In that event, physical conditions were clearly pretty much the same when the smallest interesting scales (corresponding to galaxies) and when the largest interesting scales (corresponding to COBE) acquired their perturbations. Hence a first guess is that the density perturbations on

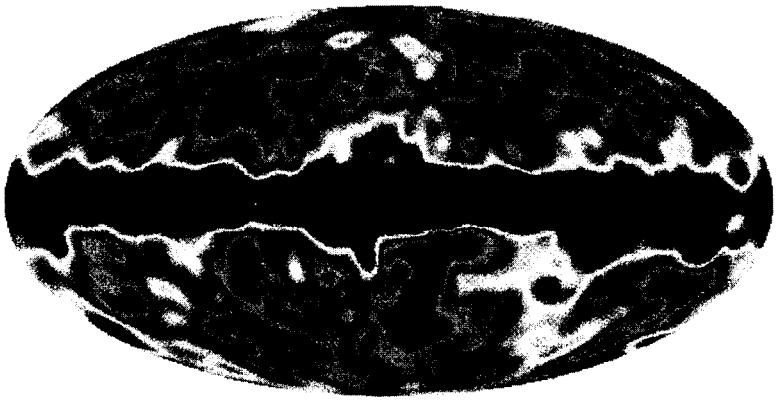

Figure 1: One of the maps from the COBE four-year data set.

all scales will be the same, the scale-invariant or Harrison–Zel'dovich spectrum. Within this approximation all inflation models predict exactly the same outcome, so in particular observations could not distinguish between different models.

Whether this approximation is adequate depends on the data set under consideration. Throughout the nineteen eighties, it was advertised as the prediction of inflation because existing data, basically the galaxy correlation function out to around $10h^{-1}$ Mpc, covered only a narrow range of scales and hence said little about the scale-dependence. Interestingly, the COBE data set [4] (seen in Figure 1) taken in isolation can also be discussed in this approximation. It is consistent with the scale-invariant spectrum and only weakly constrains scale-dependence of the spectrum, insufficiently to rulc out any inflation model on its own.

Fortunately, current data sets, where COBE is combined with short-scale information such as the galaxy power spectrum and the galaxy cluster abundance, are already of high enough quality that the scale-invariant assumption is inadequate, and one must be more precise in assessing the inflationary predictions. The next level of sophistication approximates the density perturbations and gravitational waves as power-laws[5,3]; each needs an amplitude and a spectral index making four numbers in all, and these can readily be computed in any given inflation model. In fact there is a degeneracy between density perturbations and gravitational waves, the so-called consistency equation, which reduces this to three, but in practice it seems optimistic to believe that more than one piece of information about the gravitational waves can be observationally extracted, and one normally just considers a quantity r which measures the fractional contribution of gravitational waves to the COBE signal.[5,3]

Within the power-law approximation different inflation models give different predictions for the spectra. This represents a reduction in the predictability of inflation as a paradigm, but on the other hand means that more information is potentially available to observation, yielding extra information on the inflation mechanism and hence, perhaps, on very high energy physics.

Although it is often suggested otherwise, the realization that inflation doesn't give a perfect scale-invariant spectrum is a huge success for the inflationary cosmology. It means that the lowest-order approximation fits the data well enough that one has to worry about corrections to it, and that the data has reached a quality whereby one can attempt to measure the size of these corrections. This is progress of the same sort as occurs in particle physics when one realizes that a tree-level calculation is no longer good enough and one has to worry about the one-loop corrections.

Table 1: Estimated uncertainties on parameters expected from the Planck satellite, assuming the Standard Cold Dark Matter model is correct. Successive columns introduce more freedom into the description of the initial parameters. The upper block contains the cosmological parameters and the lower one the inflationary parameters. Here Ω_b is the baryon density, h the Hubble parameter, Ω_Λ a possible cosmological constant and τ the optical depth to the last-scattering surface. Ω_{cdm} is fixed by the assumption of spatial flatness so the second row estimates the uncertainty in h.

Parameter	Planck with polarization		
$\delta\Omega_b h^2/\Omega_b h^2$	0.007	0.009	0.01
$\delta\Omega_{cdm} h^2/h^2$	0.02	0.02	0.02
$\delta\Omega_\Lambda h^2/h^2$	0.04	0.05	0.05
τ	0.0006	0.0006	0.0006
δn	0.004	0.04	0.14
δr	0.04	0.05	0.05
$dn/d\ln k$	–	0.006	0.04
$d^2n/d(\ln k)^2$	–	–	0.005

4 Scale-dependence of the spectral index

We're always being told how vastly superior the upcoming microwave background observations will be in comparison to the data we presently have, so given that present observations already require corrections to the Harrison–Zel'dovich spectrum, might we have to worry about correcting the corrections? This requires one to consider scale dependence of the spectral indices. The optimal strategy appears to be to expand the log of the spectra as Taylor series in $\ln k$, i.e.

$$\ln\delta_H(k) = \ln\delta_H(k_*) + (n_* - 1)\ln\frac{k}{k_*} + \frac{1}{2}\left.\frac{dn}{d\ln k}\right|_* \ln^2\frac{k}{k_*}\cdots . \quad (1)$$

Further details can be found in Lidsey et al.[6] The expansion scale k_* is arbitrary but presumably best chosen in the centre of the data. This expansion is to be truncated as soon as an adequate fit to the data is obtained. The first term corresponds to the Harrison–Zel'dovich spectrum, and the first two taken together to the power-law approximation. To these, a general inflationary model adds a sequence of derivatives of the spectral index, evaluated at the scale k_*. In a given model, these are readily calculable, in the same way n itself is [7,8]. Typically one finds that only the first two terms are significant, but there are models where higher terms are important too [9,10].

In general, then, one might want to fit the microwave anisotropy data not just for the amplitudes and n, but also one or possibly more derivatives of n. From an inflationary point of view, this looks like a good thing, because we are saying that there is an extra piece of information available in the microwave anisotropies which we can extract from the data. However, there is a downside, which is that the extra piece of information has been stolen at the expense of all the other parameters; if we say we need to make a fit including one or more extra parameters, then the expected uncertainties on *all* cosmological parameters will be increased.

We have examined [9] the extent to which the uncertainties are likely to increase, using the Fisher information matrix technique [11]. We consider the standard Cold Dark Matter model for illustration; the actual numbers aren't very important, what is interesting is the trend as extra parameters describing the initial conditions are added. The results are shown in Table 1.

We assume an experimental configuration of the Planck satellite with polarized detectors. The first column shows the results when the power-law approximation is assumed, and the successive columns each introduce an additional derivative of n. First the good news — the cos-

mological parameters take only a very minor hit as extra initial condition freedom is introduced. This leads to the encouraging conclusion that the modelling of the initial perturbation spectra may not have much of an influence on the satellites' abilities to constrain our cosmology.

The bad news is largely concentrated into the determination of the inflationary parameters, and in particular the measurement of n itself, whose uncertainty is greatly increased. Note that unless a power-law is *assumed*, this increase in uncertainty applies even if the values of the derivatives are zero to within the observational uncertainties. Nevertheless, the loss in accuracy on n may well be overcompensated by the gain in information on higher derivatives [10]; indeed, one might expect that, as sneaking in an extra inflationary parameter is a way of transferring a small part of the information content in the microwave background away from the cosmological parameters and into the inflationary ones.

5 Inflationary expectations

As to whether this scale-dependence is likely to show up in practice, we have no better guide than the current theoretical prejudice, which says

- Most slow-roll inflation models do not give a significant scale-dependence, even by the standards of Planck.
- "Designer" models of inflation, for example the broken scale-invariance models, do give a large effect, but not one which is adequately treated within the perturbative framework I've outlined. Such models must be confronted with observation on a model-by-model basis.
- Hybrid inflation models can give an observable effect. Partly this is due to the so-called η-problem; inflation requires that two slow-roll parameters ϵ and η be less than one [5,3], but on the other hand supergravity models generically predict $\eta = 1+$'something'. Since the 'something' is unlikely to be extremely good at cancelling the 1, such models may well not respect slow-roll very well and this enhances the chance of getting detectable scale-dependence. The best-motivated models at the moment are those of Stewart.[12]

6 Conclusions

Inflation as a paradigm is both eminently and imminently testable by upcoming microwave background observations. For example, the prediction of a peak structure is extremely generic and quite specific to the situation where perturbations begin their evolution on scales much larger than the Hubble radius, and details such as the peak spacing promises a very strong test [13]. Something as simple as an observed spectrum without multiple peaks appears sufficient to rule out inflation (see e.g. Barrow and Liddle [14]). If inflation passes these tests, then detailed fitting to the observations promises startlingly high quality information about the inflationary mechanism.

However, the main purpose of my presentation is to provide a reminder of the important role inflation has in underpinning the microwave background endeavour. I stressed at the start that we can only get highly quality constraints from the present radiation power spectrum if we have a simple form, preferably motivated by theory, for the initial perturbations. Since the observations aim to be accurate at the percent level, the input information needs this accuracy too, and inflationary theory is now in a position where predictions at this level of accuracy can be made for all known models.

This can be contrasted with the situation for topological defect models, where it has proven much harder to make accurate theoretical predictions. Less accurate theoretical predictions will

naturally lead to much more poorly determined cosmological parameters. [In fact, Pen (these proceedings) has also argued that in a defect model the observed spectrum is less sensitive to the cosmological parameters, implying poorer parameter estimation even if the theoretical calculations can after all be made more accurate.]

If all goes well with the observations, and inflation proves to be right, we can indeed look forward to the tiny error bars one hears about so often. If inflation is not correct, the results will still be spectacular but yet after the hype the constraints may seem disappointing.

Acknowledgments

The author was supported by the Royal Society.

References

1. A.R. Liddle, *Phys. Rev. D* **51**, R5347 (1995).
2. S. Perlmutter et al., *Nature* **391**, 51 (1998).
3. A.R. Liddle and D.H. Lyth, *Phys. Rep.* **231**, 1 (1993).
4. C.L. Bennett et al., *Astrophys. J.* **464**, L1 (1996).
5. A.R. Liddle and D.H. Lyth, *Phys. Lett.* B **291**, 391 (1992).
6. J.E. Lidsey, A.R. Liddle, E.W. Kolb, E.J. Copeland, T. Barreiro and M. Abney, *Rev. Mod. Phys.* **69**, 373 (1997).
7. E.J. Copeland, E.W. Kolb, A.R. Liddle and J.E. Lidsey, *Phys. Rev. D* **48**, 2529 (1993), **49**, 1840 (1994).
8. A. Kosowsky and M.S. Turner, *Phys. Rev. D* **52**, 1739 (1995).
9. E.J. Copeland, I.J. Grivell and A.R. Liddle, to appear, *Mon. Not. Roy. Astr. Soc.*, `astro-ph/9712028`.
10. E.J. Copeland, I.J.Grivell, E.W. Kolb and A.R. Liddle, `astro-ph/9802209`.
11. G. Jungman, M. Kamionkowski, A. Kosowsky and D.N. Spergel, *Phys. Rev. D* **54**, 1332 (1996); J.R. Bond, G. Efstathiou and M. Tegmark, *Mon. Not. Roy. Astr. Soc.* **291**, L33 (1997); M. Zaldarriaga, D.N. Spergel and U. Seljak, *Astrophys. J.* **488**, 1 (1997).
12. E.D. Stewart, *Phys. Lett. B* **391**, 34 (1997), *Phys. Rev. D* **56**, 2019 (1997).
13. W. Hu and M. White, *Phys. Rev. Lett.* **77**, 1687 (1996).
14. J.D. Barrow and A.R.Liddle, *Gen. Rel. Grav.* **29**, 1501 (1997).

PRIMORDIAL MAGNETIC FIELDS THAT LAST?

SEAN M. CARROLL* and GEORGE B. FIELD†
* *Institute for Theoretical Physics, University of California, Santa Barbara, CA 93106, USA*
† *Harvard-Smithsonian Center for Astrophysics, 60 Garden St., Cambridge, MA 02138, USA*

The magnetic fields we observe in galaxies today may have their origins in the very early universe. While a number of mechanisms have been proposed which lead to an appreciable field amplitude at early times, the subsequent evolution of the field is of crucial importance, especially whether the correlation length of the field can grow as large as the size of a protogalaxy. This talk is a report on work in progress, in which we consider the fate of one specific primordial field scenario, driven by pseudoscalar effects near the electroweak phase transition. We argue that such a scenario has a number of attractive features, although it is still uncertain whether a field of appropriate size can survive until late times.

1 Introduction

Observations clearly indicate that galaxies typically possess magnetic fields of strength $B \sim 10^{-6}$ Gauss which are coherent over length scales comparable to the size of the galaxies.[1] At this point it is unclear whether these fields originate in astrophysical processes operating during the epoch of galaxy formation and afterward, or can be traced back to a primordial mechanism in the early universe. If a primordial mechanism is responsible, it is necessary to generate a field of amplitude $B \sim 10^{-9}$ G over a comoving scale $\lambda \sim 10^6$ pc (the comoving size of a region which condenses to form a galaxy); such a field can be amplified during the process of condensation to the amplitudes observed today.

There are a number of requirements such a scenario must satisfy. First, it is necessary to generate a field of significant size in the early universe, as the field will tend to decay as $B \propto R^{-2}$ as the universe expands. (This simple scaling will be modified when we take into account plasma effects, but the need for a large initial field will only become more acute.) Second, the fields must not be significantly damped in between their formation and the condensation of protogalaxies. Damping can take different forms, including ordinary Ohmic dissipation (the exponential decay of electromagnetic fields in plasmas of finite conductivity) and "Silk" damping of MHD modes by

photon and neutrino viscosity. Third, it is necessary to boost the coherence length of the fields, which are typically formed with much smaller length scales than those of galaxies. For example, the comoving horizon size at the electroweak scale (which sets an upper limit to the correlation length of any field generated by a causal mechanism at the electroweak phase transition) is smaller by a factor of 10^{-10} than the comoving length scale associated with a protogalaxy.

With these requirements in mind, we will examine the prospects of a particular scenario for primordial field generation. Similar arguments will apply to other possibilities, although we will see that this scenario has a number of attractive features.

2 Magnetic Fields from Pseudoscalars

Consider a pseudoscalar field ϕ which couples to electromagnetism via an interaction Lagrange density

$$\mathcal{L} = \phi F_{\mu\nu}\tilde{F}^{\mu\nu} \ , \tag{1}$$

where the dual field strength tensor is defined by $\tilde{F}^{\mu\nu} = \frac{1}{2}\epsilon^{\mu\nu\rho\sigma}F_{\mu\nu}$. Such an interaction leads to a modified form of Maxwell's equations, given by

$$\begin{aligned} -\partial_t E + \nabla \times B &= 4\pi J - \dot{\phi}B + \nabla\phi \times E & (2)\\ \nabla \cdot E &= 4\pi\rho - \nabla\phi \cdot B & (3)\\ \partial_t B + \nabla \times E &= 0 & (4)\\ \nabla \cdot B &= 0 \, . & (5) \end{aligned}$$

(For simplicity we are working in flat spacetime, but the generalization to Robertson-Walker universes is straightforward.) In a conducting plasma we will also have Ohm's Law, $J = \sigma E$, where σ is the conductivity.

We assume that the pseudoscalar is spatially homogeneous, so $\nabla\phi$ can be neglected. We also drop ρ, assuming there is no net charge density, and $\partial_t E$, as time variations in the electric field will be small. Under these assumptions we derive an equation for the magnetic field in Fourier space,

$$\partial_t B = -\frac{1}{4\pi\sigma}(k^2 B + i\dot{\phi}k \times B) \, . \tag{6}$$

This equation can be analyzed by decomposing B into orthonormal modes perpendicular to the wavevector k, $B(k) = b_1 u_1 + b_2 u_2$. In fact, it is most convenient to work with circularly polarized modes, $b_\pm = b_1 \pm i b_2$. We can then solve explicitly for the time evolution:

$$b_\pm(t,k) = b_\pm(0,k)\exp\left[-\frac{k}{4\pi\sigma}\left(kt \pm \int \dot{\phi}\, dt\right)\right] \, . \tag{7}$$

We see that the b_- modes can grow exponentially if $\dot{\phi} > k$, with maximum growth for $k = \frac{1}{2}\dot{\phi}$.

The existence of such an exponentially growing mode suggests that such a pseudoscalar could generate large field strengths in the early universe. It remains to specify an identity and dynamics for the ϕ field itself. A scenario along these lines was proposed by Turner and Widrow,[2] who noted that the axion was a particle with appropriate couplings, but did not analyze the possibility in detail. Garretson, Field and Carroll[3] considered a generic pseudo-Goldstone boson evolving during inflation, and found that it was not possible to generate fields which were both of sufficient strength and interestingly large length scales. More recently, Joyce and Shaposhnikov[4] note that a chemical potential for right-handed electron number, generated by processes at the grand unification scale, interacts with electromagnetism in an equivalent fashion, if we simply identify the chemical potential with $\dot{\phi}$. (See also the work of Cornwall.[5])

The Joyce and Shaposhnikov scenario, which involves only standard electroweak physics once the chemical potential is generated, is less flexible than a generic pseudoscalar boson and

accordingly more predictive. For definiteness we will consider the fate of the magnetic fields generated by such a mechanism, although other pseudoscalars would have very similar effects. Joyce and Shaposhnikov estimate that their scenario can lead to magnetic fields of order $B \sim 10^{22}$ G on a length scale $\lambda \sim 10^{-8} H_{EW}^{-1}$, where H_{EW} is the Hubble parameter at the electroweak scale. As this is 18 orders of magnitude smaller than the desired comoving length scale, we must seek a mechanism for increasing the coherence length of the field.

3 The Inverse Cascade

A well-known property of ordinary hydrodynamical turbulence is the cascade of energy, injected at a certain length scale, down to smaller scales. In MHD, however, magnetic energy can both cascade to small scales and inverse cascade to large scales. This phenomenon was investigated numerically and analytically in the 1970's and 1980's by Pouquet and collaborators,[6] and has been advocated as an important factor in the evolution of primordial magnetic fields by Brandenburg, Enqvist and Olesen.[7]

In order for an inverse cascade to be operative, two requirements must be met: an injection of turbulence into the medium, and a nonvanishing expectation value for some pseudoscalar quantity. Turbulence, which is needed to transfer energy between disparate length scales, can arise from (for example) bubble collisions during a first-order electroweak phase transitions. We will assume that this is the case, although little is known about the order of the electroweak transition in the real world. The necessity of a nonvanishing pseudoscalar can be seen by considering the time variation of the magnetic field, which satisfies $\partial_t B(k) \sim k \times E$. To obtain exponential growth in B at a wavenumber k, we require $E(k) = \alpha(k) B(k)$, where α is a manifestly pseudoscalar coefficient. Numerical simulations by Pouquet et al.[6] have verified the existence of an inverse cascade if and only if the configuration possesses significant magnetic helicity, $H^M = \int A \cdot B d^3x$.

The pseudoscalar mechanism discussed in the previous section creates a field with maximal magnetic helicity. The circularly polarized modes $b_\pm$ are of opposite helicity, and one will be suppressed while the other is amplified as ϕ evolves; the resulting field is maximally helical. Hence, such a field should have magnetic energy transferred to larger scales, while we would not expect such behavior in a generic situation.

The transfer of energy to large scales is typically very efficient; numerical simulations indicate[6] that the scale increases linearly by a factor $\Delta t / t_{turb}$, where the turbulence timescale t_{turb} can be taken (somewhat optimistically) to be $T_{EW}^{-1} \sim 10^{-15} H_{EW}^{-1}$. Since the naive picture of linear growth would increase the coherence length beyond the Hubble distance, we can assume that the growth would saturate at that point. In the (once again optimistic, but not implausible) assumption that the field strength is undiminished by this process, we are therefore left with a field of amplitude $B \sim 10^{22}$ G and a length scale $\lambda \sim H_{EW}^{-1}$ (a comoving scale of 10^{-4} pc).

4 Subsequent Evolution

A potentially important role in the evolution of the field from the electroweak scale to today can be played by the damping of MHD modes by photon and neutrino viscosity.[8] This damping can dramatically decrease the amplitude of primordial magnetic fields before they have a chance to form galactic fields. However, these modes do not necessarily represent oscillations around a zero-field configuration, but around a force-free field, for which $J \times B = 0$. For the situation under consideration, such damping will not be important, as numerical simulations [6] (as well as experiments in tokamaks[9]) indicate that the result of an inverse cascade is a force-free field configuration.

This leaves us with the question of whether the length scale of the magnetic field can be expanded to the dimensions of a protogalaxy. Presumably an inverse cascade mechanism cannot be very helpful, as there is likely to be no source of turbulence subsequent to the electroweak phase transition. A pessimistic scenario would imagine that the field is frozen in and expands with the universe, redshifting as R^{-2}. We would then be left with a field amplitude $B \sim 10^{-8}$ G on a scale of 10^{-4} pc today. To estimate the amplitude on galactic scales, we can consider the incoherent superposition of fields in uncorrelated domains. Since the resulting field goes like one over the square root of the number of domains, which in turn goes as the volume of the region under consideration, the field on megaparsec scales is

$$B(\mathrm{M}pc) \sim \left(\frac{1\ \mathrm{M}pc}{10^{-4}\ pc}\right)^{-3/2} B(10^{-4}\ \mathrm{pc}) \sim 10^{-23}\ \mathrm{G}\ . \tag{8}$$

This is much less than the sought-after amplitude 10^{-9} G, so it is necessary to imagine a more active mechanism for increasing the coherence length.

In fact, the coherence length will certainly grow faster, as uncorrelated domains come into causal contact and magnetic field lines smooth themselves out.[10] At this point we do not have a reliable estimate of the rate at which this happens, nor of the potential dilution of the field strength during this process. Instead, we can proceed under optimistic assumptions to see whether there is any prospect of generating the required field.

The optimistic expectation we consider is that the field rearranges itself at the Alfvén speed,

$$v_A = \left(\frac{\rho_B}{\rho_{tot}}\right)^{1/2}\ , \tag{9}$$

which has the value $v_A \sim 10^{-2}$ during the radiation dominated era (for the parameters used above) and $10^{-2}T(\mathrm{eV})$ during matter domination. The correlation length will then obey

$$\frac{d\lambda}{dt} = H\lambda + v_A\ , \tag{10}$$

representing the separate effects of Hubble expansion and Alfvén rearrangement. Plugging in the appropriate numbers, we find that the Alfvén speed dominates until the time of matter-radiation equality, after which the Hubble expansion is most important (so that the comoving length remains constant). It so happens that the Hubble size at matter-radiation equality, which will characterize the correlation length of the magnetic field under these assumptions, corresponds to a comoving scale of 1 Mpc, nicely consistent with the size of a protogalaxy.

Under our optimistic scenario, then, we are able to generate fields of the appropriate length scale, but no larger. Under the additional optimistic assumption that the amplitude of the field remains undiminished as it smoothes out, we obtain $B(1\ \mathrm{M}pc) \sim 10^{-8}$ G, just as required for the primordial scenario.

The fact that we are only able to achieve this result under such optimistic conditions is somewhat discouraging. A more realistic calculation would include both the fact that viscosity will act to retard the Alfvén rearrangement, and that dissipation will act to diminish the amplitude of the field. At this point we are not confident in our understanding of the magnitude of these effects; work in this direction is in progress. While the prospects for primordial mechanisms for magnetic field generation do not seem hopeful in light of this analysis, there is still a chance that a more careful examination will reveal that our optimistic assumptions are actually warranted. The importance of this topic justifies a concerted effort to understand whether this possibility can be realized.

Acknowledgments

This work was supported in part by the National Science Foundation under grant PHY/94-07195 and NASA under grant NAGW-931.

References

1. E.G. Zweibel and C. Heiles, *Nature* **385**, 131 (1997).
2. M.S. Turner and L.M. Widrow, *Phys. Rev. D* **37**, 2743 (1988).
3. W.D. Garretson, G.B. Field, and S.M. Carroll, *Phys. Rev. D* **46**, 5346 (1992); hep-ph/9209238.
4. M. Joyce and M. Shaposhnikov, *Phys. Rev. Lett.* **79**, 1193 (1997); astro-ph/9703005.
5. J.M. Cornwall, *Phys. Rev. D* **56**, 6146 (1997); hep-th/9704022.
6. U. Frisch, A. Pouquet, J. Léorat, and A. Mazure, *J. Fluid Mech.* **68**, 769 (1975); A. Pouquet, U. Frisch, and J. Léorat, *J. Fluid Mech.* **77**, 321 (1976); A. Pouquet and G.S. Patterson, *J. Fluid Mech.* **85**, 305 (1978); M. Meneguzzi, U. Frisch and A. Pouquet, *Phys. Rev. Lett.* **47**, 1060 (1981).
7. A. Brandenburg, K. Enqvist and P. Olesen, *Phys. Rev. D* **54**, 1291 (1996), hep-ph/9608422; P. Olesen, astro-ph/9610154; K. Enqvist, astro-ph/9707300.
8. K. Jedamzik, V. Katalinić, and A.V. Olinto, *Phys. Rev. D* **57**, 3264 (1998); astro-ph/9606080.
9. S. Ortolani and D.D. Schnack, *Magnetohydrodynamics of Plasma Relaxation*, World Scientific (1993).
10. C. Hogan, *Phys. Rev. Lett.* **51**, 1488 (1983); K. Dimopoulos and A.-C. Davis, *Phys. Lett.* **B390**, 87 (1997), astro-ph/9610013.

NONZERO Ω_Λ AND A NEW TYPE OF A DISSIPATIVE STRUCTURE

Yasunori FUJII
Nihon Fukushi University, Handa, 475 Japan
and
ICRR, University of Tokyo, Tanashi, Tokyo, 188 Japan

To understand recent cosmological results indicating nonzero Ω_Λ, we discuss a theoretical model, which seems to suggest, rather unexpectedly, an interesting new type of dissipative structure.

The cosmological constant problem has two faces; an upper bound and a lower bound. The former is given by the critical density $\rho_{\rm cr}$, or $\Omega_\Lambda \equiv \Lambda/\rho_{\rm cr} \lesssim 1$. In the Planckian unit system with $8\pi G = c = \hbar = 1$, we know $\rho_{\rm cr} \equiv 3H_0^2 \sim t_0^{-2}$, and the present age of the universe $t_0 \sim 10$Gy is of the order of 10^{60}; hence the upper bound $\Lambda_{\rm ob} \lesssim 10^{-120}$. On the other hand, almost any theoretical models of unification gives $\Lambda_{\rm th} \sim 1$. The discrepancy is the well-known disaster. Recent observations seem to indicate a lower bound as well; $\Omega_\Lambda \sim 0.7$. Let us try to understand this "small but nonzero cosmological constant."

A solution for the upper bound may come from a scalar field ϕ of the Brnas-Dicke type:

$$\mathcal{L} = \sqrt{-g}\left(\frac{1}{2}\xi\phi^2 R - \frac{1}{2}\epsilon g^{\mu\nu}\partial_\mu\phi\partial_\nu\phi + \Lambda + L_{\rm matter}\right), \tag{1}$$

where ξ is a dimensionless constant related to BD's parameter ω by $\omega\xi = 1/4$, and $\epsilon = \pm 1$. The scalar field contribution is shown to cancel the effect of Λ asymptotically. To see this, it is most convenient to apply a conformal transformation moving to the Einstein frame (as denoted by $*$) with nonminimal coupling removed. The same Lagrangian as Eq. 1 is now put into

$$\mathcal{L} = \sqrt{-g_*}\left(\frac{1}{2}R_* - \frac{1}{2}g_*^{\mu\nu}\partial_\mu\sigma\partial_\nu\sigma - V(\sigma) + L_{*\rm matter}\right), \tag{2}$$

where the new canonical scalar field σ is related to the original ϕ; $\phi = \xi^{-1/2}e^{\zeta\sigma}$, with $\zeta = (6+\epsilon\xi^{-1})^{-1/2}$. We also find that Λ now acts as a potential $V(\sigma)$:

$$V(\sigma) = \Lambda e^{-4\zeta\sigma}, \tag{3}$$

which pushes σ toward infinity; the effect of Λ continues to decrease.

In spatially flat RW cosmology, the cosmological equations are

$$3H^2 = \rho_\sigma + \rho_{\rm m} \equiv \rho, \quad \text{and} \quad \ddot{\sigma} + 3H\dot{\sigma} + V'(\sigma) = 0, \tag{4}$$

where we omit the symbol $*$ to simplify the notation. We should also supply the equation for the matter density $\rho_{\rm m}$ as usual. Notice that $\rho_\sigma = \frac{1}{2}\dot{\sigma}^2 + V(\sigma)$ is the energy density of the scalar field to be interpreted as an "effective cosmological constant" $\Lambda_{\rm eff}$.

As an asymptotic solution, we obtain (for assumed radiation dominance)

$$a(t) = t^{1/2}, \quad \text{and} \quad \sigma(t) = \bar{\sigma} + \frac{1}{2}\zeta^{-1}\ln t, \tag{5}$$

$$\rho(t) = \frac{3}{4}\left(1 - \frac{1}{4}\zeta^{-2}\right)t^{-2}, \quad \text{with} \quad \rho_\sigma(t) = \frac{3}{16}\zeta^{-2}t^{-2}. \tag{6}$$

The last equation shows that $\Lambda_{\rm eff} = \rho_\sigma$ does decay like t^{-2}, hence implementing the scenario of a "decaying cosmological constant." *Today's Λ is small only because our universe is old.* [1]

We notice, however, that $\Lambda_{\rm eff}(t)$ falls off in the same way as the ordinary matter density $\rho_{\rm matter}(t)$ does. Not qualified to be called a "constant," it is simply another form of dark matter. It does not help understanding the lower bound. We must include something that behaves more or less like a constant or at least falls off more slowly than t^{-2}. On the other hand, the behavior $\sim t^{-2}$ was the key to have a "small" Λ. As a compromise we expect that $\Lambda_{\rm eff}(t)$ would decay like $\sim t^{-2}$ as an overall behavior, but with some "landings," in one of which we today happen to be, and which mimics a cosmological "constant" for some duration of time.

Trying to implement the idea, we came across a model on a try-and-error-basis, by introducing another scalar field Φ which couples to σ. [2,3] The Lagrangian is the same as Eq. 2 with the added kinetic term of Φ and $V(\sigma)$ replaced by (see Fig. 2 of Ref. 2)

$$V(\sigma, \Phi) = e^{-4\zeta\sigma}\left(\Lambda + \frac{1}{2}m^2\Phi^2\left[1 + \beta\sin(\kappa\sigma)\right]\right), \tag{7}$$

where m, β, κ are the constants naturally of the order unity. It has a "central valley" given by Eq. 3, but shows an oscillatory behavior $\sim \sin(\kappa\sigma)$ if we climb the wall in the direction of Φ.

A typical solution is shown in Fig. 1. We started the integration at some time in the post-inflation era. We also *mildly* fine-tuned initial conditions such that Ω_Λ somewhat smaller than 1, say, at $t_0 \approx 10^{60}$. Notice a sequence of alternate occurrence of a rapid change and a nearly standstill of the scalar fields. Also toward the end of each "landing" of $\rho_s (= \Lambda_{\rm eff}(t))$, which is now the energy density of the coupled σ-Φ system, the scale factor $a(t)$ shows a mini-inflation, an expected behavior. Magnifying a portion of Fig. 1(b) around the present time ($\log t_0 \sim 60$) extending to a tiny interval ($\Delta \log t \sim 1$) yields a "practical" plot going back to $z \sim 5$, showing $\Lambda_{\rm eff}$ which looks nearly constant.

These landings, as indicated also by other examples, tend to occur *nearly periodically* with respect to $\ln t$. This seems to suggest that some cosmological anomalies might have taken place nearly periodically with respect to $\ln t$.

As we find, the results depend on the choice of the parameters quite sensitively, particularly on the initial conditions. In this connection, we first point out that the most important ingredients are present in the dynamics of the system of the two scalar fields. We find the alternate occurrence of the "wake-up phase" and the "dormant phase" of the scalar fields even without the cosmological environments, provided the frictional coefficients $3H$ vary as $\sim t^{-1}$.

Fig. 2 is one of the examples of the solutions of the isolated 2-scalar system with the same potential with the frictional constants $\Gamma = \gamma/t$. Suppose we start from an initial position off the central valley on the potential Eq. 7. σ will be pushed in the positive direction. The potential

will decrease quickly because it falls off like $e^{-4\zeta\sigma}$. Soon both fields will be virtually free. Due to the frictional forces they will be decelerated almost to a complete stop. However, as the time goes on, the frictional forces will also decrease according to $\sim t^{-1}$. They will become even weaker than the forces derived from the potential which had much dwindled. Then the fields are suddenly pushed again. But the potential will be weakened soon again leading to the next dormant period.

However, in order for the fields to be pushed strongly after the dormant phase, their positions and velocities must "match" the previous values to some extent. Otherwise, the fields will not be waken up, beginning simply to fall the potential slope slowly toward and along the central valley. This is the asymptotic behavior, as we find in this example, reached commonly for any initial conditions. Obviously this corresponds to a "fixed-point attractor," like in standard damped oscillators.

The "matching condition" is rather subtle. This is the reason why a slight change of initial values may sometimes result in a considerable change in the behaviors afterward. This sensitivity to the initial values reminds us of a well-known *chaotic behavior in nonlinear systems.* Sudden change of the number of repetitions before reaching the smooth asymptotic behavior, for example, might be compared to sudden occurrence of "bifurcation" in typical chaotic solutions.

However, there is an important difference from purely chaotic systems. Usually a chaotic behavior is characterized by "strange attractors," while our solutions tend to a simple fixed-point attractor. Complicated hard-to-predict states occur only during a finite transient period. In accordance with this no fractal structure is produced in the orbits in phase space; fractal structure might be present only to a limited "depth."

We thus find what might be called an "incomplete chaos" or an "incomplete fractals." They can be still interesting because genuine chaos might be a mathematical idealization for natural phenomena. Also chaotic behaviors are seen almost every aspect of life. But obviously life lasts only during a limited lifetime; the ultimate destination is a non-chaotic death, corresponding to a fixed-point attractor. In this sense, our model might provide a primitive example of a living system. On the other hand, it seems to give a model of pattern formation (with variable period).

In our model, near periodicity in $\ln t$ is a consequence of $\Gamma \sim t^{-1}$. There are many examples of pattern formation with some periodicity. Patterns on sea shells, for example, can be reproduced by certain nonlinear equations of rather simple structure.[4] Periods of these patterns are not determined by the restoring force but, unlike in simple systems, primarily by friction or dissipation. This feature is shared in our model. In this sense also, our nonlinear equations might provide another example of "dissipative structure." It is interesting to notice that a model of game dynamics with more than three species also generates periodicity with respect to $\ln t$.[5]

Did we introduce as many degrees of freedom and parameters as we need? The answer: the cosmological constant problem is so challenging that we may not have reached even close to any promising result no matter how many ingredients we introduced if we have come in a wrong direction. It seems we are on a right track.

References

1. Y. Fujii and T. Nishioka, *Phys. Rev.* D **42**, 361 (1990).
2. Y. Fujii and T. Nishioka, *Phys. Lett.* B **254**, 347 (1991).
3. Y. Fujii, Astrop. Phys. **5**, 133 (1996).
4. H. Meinhardt, *The algorithmic beauty of sea shells*, Springer-Verlag, 1995.
5. T. Chawanya, Prog. Theor. Phys. **94**, 163 (1995).

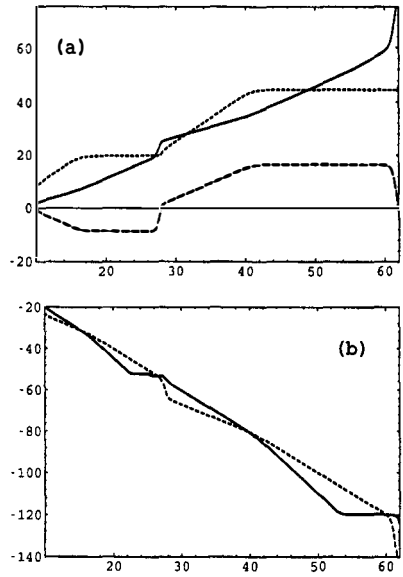

Figure 1: (a) $\ln a$ (solid; a for the scale factor), σ (dotted), 2Φ (broken) against $\log t$. (b) $\log \rho_s$ (solid), $\log \rho_m$ (dotted). The parameters are $\Lambda = 1, \zeta = 1.582, m = 4.75, \beta = 0.8, \kappa = 10$. The initial values at $t_1 = 10^{10}$ are $\sigma_1 = 6.75442, \dot{\sigma}_1 = 0, \Phi_1 = 0.212, \dot{\Phi}_1 = 0$. At $\log t_0 = 60.15$ corresponding to the present age chosen to be 1.21×10^{10}y, we obtain $H_0 = 81$km/s/Mpc and $\Omega_\Lambda = 0.67$. See also Captions to Figs. 1 and 2 in Ref. 3.

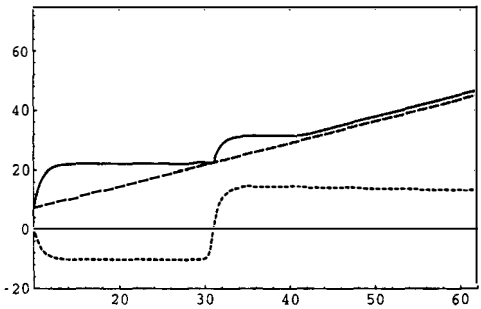

Figure 2: An example of the two-scalar system, in which the solution enters the asymptotic behavior after two repeated patterns. σ (solid) and 2Φ (dotted) and the broken line for the asymptotic behavior of σ. Φ will tend to zero slowly. The parameters and the initial values are the same as those in Fig. 1 except for the frictional coefficient chosen to be $(3/2)t^{-1}$. See also Caption to Fig. 3 in Ref. 3. A slight change of the initial values may result in a sudden change of the repetition number to three, for example, also changing the time of the end of the repetition period.

AMPLITUDE OF SUPERHORIZON COSMOLOGICAL PERTURBATIONS

JÉRÔME MARTIN
DARC, Observatoire de Paris,
UPR 176 CNRS, 92195 Meudon Cedex, France.
e-mail: martin@edelweiss.obspm.fr

DOMINIK J. SCHWARZ
Institut für Theoretische Physik,
Robert-Mayer-Straße 8 - 10, Postfach 11 19 32,
D-60054 Frankfurt am Main, Germany.
e-mail: dschwarz@th.physik.uni-frankfurt.de

We study the influence of reheating on super-horizon density perturbations and gravitational waves. We correct wrong claims [1] about the joining of perturbations at cosmological transitions and about the quantization of cosmological perturbations.

1 Introduction

The aim of these proceedings, based on Ref. 2, is to clear up the recent controversy on the relative contribution of density perturbations and gravitational waves to the CMBR today.

The background model is taken to be a spatially flat FLRW model. We restrict our considerations to density perturbations and gravitational waves. The most general line element reads:

$$\mathrm{d}s^2 = a^2(\eta)\{-(1+2\phi)\mathrm{d}\eta^2 + 2B_{|i}\mathrm{d}x^i\mathrm{d}\eta + [(1-2\psi)\gamma_{ij} + 2E_{|i|j} + h_{ij}^{TT}\mathrm{d}x^i\mathrm{d}x^j\} \ . \qquad (1)$$

In the synchronous gauge, without loss of generality, the same line element can be written as:

$$\mathrm{d}s^2 = a^2(\eta)\{-\mathrm{d}\eta^2 + [(1+hQ)\delta_{ij} + \frac{h_l}{k^2}Q_{,i,j} + h_{\mathrm{g}w}Q_{ij}]\mathrm{d}x^i\mathrm{d}x^j\}. \qquad (2)$$

The scalar function Q satisfies the Helmholtz equation and Q_{ij} is a symmetric, transverse and traceless spherical harmonic. k is the comoving wave number. In the following we use this form of the line element to make contact with previous works [1]. It is convenient to define $\mathcal{H} \equiv a'/a$, which is related with the Hubble constant H by the relation $H = \mathcal{H}/a$. A prime denotes a derivative with respect to conformal time. The quantity γ is defined by the expression: $\gamma(\eta) \equiv 1 - \mathcal{H}'/\mathcal{H}^2$. For the de Sitter space-time γ vanishes.

Let us now consider the equations of motion for the perturbed metric. For density perturbations (in the case of a vanishing anisotropic pressure), all relevant quantities can be expressed in terms of the variable μ defined by: $\mu \equiv a(h' + \mathcal{H}\gamma h)/(\mathcal{H}\sqrt{\gamma})$, except in the de Sitter case, which must be treated separately. For gravitational waves, the relevant quantity is $\mu_{\mathrm{g}w} \equiv ah_{\mathrm{g}w}$.

Using the perturbed Einstein equations, one can show that both types of perturbations obey the same class of equation, i.e. the equation of a parametric oscillator:

$$\mu'' + [k^2 - U(\eta)]\mu = 0 \,, \tag{3}$$

with $U_{\rm dp} = (a\sqrt{\gamma})''/(a\sqrt{\gamma})$ and $U_{\rm gw} = a''/a$. But there is a fundamental difference: the presence of the factor $\sqrt{\gamma}$ in the effective potential of density perturbations.

Equation (3) is valid for any model. However, it is important to consider cases where exact analytical solutions can be found. This happens for power law inflation where the scale factor is given by $a(\eta) = l_0|\eta|^{1+\beta}, \beta \leq -2$. We will consider a model with three epochs in succession: inflation, radiation-dominated era, and matter-dominated era. For this simple model, the function $\gamma(\eta)$ is a constant during each epoch and is given by: $\gamma_{\rm i} = (2+\beta)/(1+\beta), \gamma_{\rm r} = 2, \gamma_{\rm m} = 3/2$. Therefore the constant factor $\sqrt{\gamma}$ drops out of $U_{\rm dp}(\eta)$, and the solutions for density perturbations and gravitational waves are given by the same Bessel functions:

$$\mu(\eta) = (k\eta)^{1/2}[A_1 J_{\beta+1/2}(k\eta) + A_2 J_{-(\beta+1/2)}(k\eta)]. \tag{4}$$

The aim is now to compute the amplitude of both types of perturbations during the matter-dominated era. In order to perform this calculation, two questions must be addressed:

1) The initial conditions must be fixed. This amounts to choose the coefficients A_1 and A_2. This will be done with the help of quantum mechanical considerations.

2) The way the solutions are matched between different epochs must be specified. This is no problem for gravitational waves since the effective potential is well-defined (although discontinuous). This is more tricky for density perturbations. γ is a Heaviside function. This means that the effective potential of the density perturbations is not defined in the sense of distributions at the different transitions. Recently, there was a controversy on this point [1,3]. One purpose of Ref. 2 and this paper is to clear up this question. This question arises because we consider simple models which allow analytical solutions. In reality, the transition is smooth and the effective potential is never ill-defined.

2 Determination of the initial conditions

Let us start with the first question. The normalization of the perturbed scalar field is fixed by the uncertainty principle of Quantum Mechanics. In the high frequency regime, this leads to:

$$\delta\hat{\varphi}(\eta, \mathbf{x}) = \frac{1}{(2\pi)^{2/3}} \int {\rm d}\mathbf{k} \hat{\varphi}_1(\eta, \mathbf{k}) e^{i\mathbf{k}\cdot\mathbf{x}} = \frac{\sqrt{\hbar c}}{a(\eta)} \frac{1}{(2\pi)^{3/2}} \int \frac{{\rm d}\mathbf{k}}{\sqrt{2k}} [c_{\mathbf{k}}(\eta) e^{i\mathbf{k}\cdot\mathbf{x}} + c^{\dagger}_{\mathbf{k}}(\eta) e^{-i\mathbf{k}\cdot\mathbf{x}}], \tag{5}$$

where the annihilation and creation operators satisfy the usual commutation relation. A hat indicates that we are now dealing with operators. The normalization of the scalar perturbations is fixed by the normalization of the perturbed scalar field since they are linked through Einstein's equations. In the high frequency limit, this link is expressed as:

$$\lim_{k \to +\infty} \hat{\mu}(\eta, \mathbf{k}) = -\sqrt{2\kappa} a \hat{\varphi}_1(\eta, \mathbf{k}), \tag{6}$$

where $\kappa \equiv 8\pi G$. For the model under considerations, it is easy to find the time dependence of the creation and annihilation operators. As a consequence all quantities are fixed uniquely, if at some initial time η_0 the scalar field is placed in the vacuum state $c_{\mathbf{k}}(\eta = \eta_0)|0\rangle = 0$. For gravitational waves the line of reasoning is similar. The result[2] is that the A's satisfy $|A_1^{(gw)}| = |A_1^{(dp)}| = |A_2^{(gw)}| = |A_2^{(dp)}| = (2\pi l_{\rm Pl})/(|\cos(\pi\beta)|\sqrt{k})$. We will show below that $|A_1^{(gw)}/A_1^{(dp)}| = 1$ turns out to be crucial to predict the relative contribution of both types of perturbations.

3 The junction conditions

Let us now turn to the second question, i.e. the junction conditions. We analyze the approach taken by Grishchuk[1] and compare it with the claims of Deruelle and Mukhanov[3]. Suppose that the spatial transition hypersurface Σ is defined by its normal n^μ. To join two space-time manifolds along Σ without a surface layer the induced spatial metric $h_{ij} \equiv g_{ij} + n_i n_j$ and the extrinsic curvature $K_{ij} \equiv (-1/2)\mathcal{L}_n h_{ij}$ should be continuous on Σ. In order to compute K_{ij} the system of coordinates (i.e. the gauge) and the vector n^μ (i.e. the surface of transition) have to be specified. Different choices for n^μ lead to inequivalent junction conditions. If the surface of transition is defined by $q(\eta, x^i) = cte$, it was shown by Deruelle and Mukhanov [3] that the matching conditions read:

$$[\psi + \mathcal{H}\frac{\delta q}{q_0'}]_\pm = 0, \qquad [E]_\pm = 0, \tag{7}$$

$$[\psi' + \mathcal{H}\phi + (\mathcal{H}' - \mathcal{H}^2)\frac{\delta q}{q_0'}]_\pm = 0, \qquad [B - E' + \frac{\delta q}{q_0'}]_\pm = 0. \tag{8}$$

This result was generalized for spatially curved backgrounds and for the other types of perturbations in Ref. 2. If the surface of transition is a surface of constant time, the matching conditions in the synchronous gauge are:

$$[h]_\pm = [h']_\pm = [h_l]_\pm = [h_l']_\pm = 0. \tag{9}$$

For a sharp transition (i.e. if γ is discontinuous) the two sets are not equivalent. Since it is believed that the transition occurs on a surface of constant energy which is not a surface of constant time, using the second set of joining conditions in this situation leads to an error. However, if the transition is smooth, i.e. $[p]_\pm = 0$, then the two sets are equivalent, see Ref. 2.

We use this result to study the regularisation scheme of Grishchuk[1]: Instead of matching inflation to the radiation epoch directly, Grishchuk introduced a smooth transition in between. Physically, this smooth transition represents the reheating of the Universe. It starts at $\eta = \eta_1 - \epsilon$ (end of inflation) and ends at $\eta = \eta_1 + \epsilon$ (beginning of radiation). Here, ϵ is small compared to η_1 because we assume that reheating is a fast process. In the limit ϵ goes to zero, we recover the sharp transition considered before and $\gamma(\eta)$ becomes a Heaviside function jumping from $(2+\beta)/(1+\beta)$ to 2. For a smooth transition, without taking all the details of the reheating process into account, we do not know how the scale factor (and therefore γ) evolves between $\eta_1 - \epsilon$ and $\eta_1 + \epsilon$. The idea of Ref. 1 was to assume that the function $\gamma(\eta)$ is given by:

$$\gamma(\eta) = \frac{4+3\beta}{2(1+\beta)} + \frac{\beta}{2(1+\beta)} \tanh\left(\frac{\eta - \eta_1}{s}\right) , \tag{10}$$

where s is a parameter controlling the sharpness of the transition. This equation holds for inflation and reheating, i.e. for η between $-\infty$ and $\eta_1 + \epsilon$. Formula (10) leads to a reasonable equation of state $p/\rho = -1 + 2/3\gamma(\eta)$ and therefore gives a reasonable approximation to the real (exact) complicated function $\gamma(\eta)$ even if details of the reheating process cannot be taken into account in such a simple approach.

From the previous discussion, it is clear that $\gamma(\eta)$ is always continuous, even at $\eta = \eta_1 + \epsilon$ where the explicit joining was performed in Ref. 1 [a]. This means that $[p]_\pm$ vanishes. In Ref. 3, Deruelle and Mukhanov criticized the calculations done in Ref. 1 by means of the smooth transition described before, arguing that the junction conditions were not taken into account properly. We have shown that for continuous pressure the two sets of matching conditions are

[a] In this paper η_1 was used instead of $\eta_1 + \epsilon$ to denote the end of reheating. It is very important to distinguish these two events.

equivalent. Therefore the claim of Deruelle and Mukhanov is not appropriate. For a smooth transition, the matching conditions used by Grishchuk are perfectly justified since they coincide with the ones derived in Ref. 3. The argument of Deruelle and Mukhanov would be relevant if the transition was sharp and $\gamma(\eta)$ discontinuous at $\eta = \eta_1 + \epsilon$.

Even the simple form (10) is too complicated to allow a direct integration of the equation of motion for μ. Nevertheless, we can follow the evolution of μ through inflation and reheating. For $\eta < \eta_1 - \epsilon$, $\gamma(\eta)$ is a constant and the solution for μ is given by Eq. (4). The value of $\mu(\eta)$ just before reheating can be easily computed:

$$\mu(\eta_1 - \epsilon) \simeq \frac{A_1^{(dp)}}{2^{\beta+\frac{1}{2}}\Gamma(\beta+\frac{3}{2})}[k(\eta_1-\epsilon)]^{\beta+1} \simeq \frac{A_1^{(dp)}}{2^{\beta+\frac{1}{2}}\Gamma(\beta+\frac{3}{2})}(k\eta_1)^{\beta+1}\,, \tag{11}$$

because $k\eta_1 \ll 1$ and $\epsilon \ll \eta_1$. Between $\eta_1 - \epsilon$ and $\eta_1 + \epsilon$ the function $\gamma(\eta)$ is no longer a constant and the solution (4) can no longer be used. In order to evolve μ through the reheating transition we use the superhorizon solution of Eq. (3), $\mu \sim a\sqrt{\gamma}$, to obtain

$$\mu(\eta_1+\epsilon) \simeq \frac{\mu(\eta_1-\epsilon)}{a(\eta_1-\epsilon)\sqrt{\gamma(\eta_1-\epsilon)}}a(\eta_1+\epsilon)\sqrt{\gamma(\eta_1+\epsilon)} \simeq \mu(\eta_1-\epsilon)\sqrt{\frac{2}{\gamma_{\rm i}}}\,, \tag{12}$$

because $a(\eta_1+\epsilon) \approx a(\eta_1-\epsilon)$. This relation should be compared to Eq. (81) and to the relation $\mu|_{\eta_1-0} = \mu|_{\eta_1+0}$ below Eq. (48) of Ref. 1. From Eq. (12), it is clear that the ratio $\mu(\eta_1+\epsilon)/\mu(\eta_1-\epsilon)$ is not 1 but proportional to $1/\sqrt{\gamma_{\rm i}}$. This factor is huge when $\gamma_{\rm i}$ is close to 0 (de Sitter). Therefore the mistake in Ref. 1 was not the use of wrong junction conditions but the fact that $\mu(\eta)$ was not evolved correctly through the reheating transition: $\gamma(\eta_1-\epsilon) \neq \gamma(\eta_1+\epsilon)$ implies $\mu(\eta_1-\epsilon) \neq \mu(\eta_1+\epsilon)$.

Let us turn to the radiation-matter transition taking place at equality. In Ref. 1 the equality transition was treated as a sharp transition. The joining conditions (9) are not correct in general (i.e., for any residual gauge fixing). However, if one specifies the synchronous gauge in the matter dominated epoch to be the comoving one, then the joining conditions (9) are fine at the equality transition[3]. That is because the density contrast vanishes at the leading order [i.e., it is proportional to $(k\eta)^2$].

Using the previous results, it is interesting to calculate the ratio of the Bardeen potential $\Phi \equiv \phi + [a(B-E')]'/a$ and h_{gw} at superhorizon scales today. We obtain (see Ref. 2):

$$\left.\frac{h_{gw}}{\Phi}\right|_{today} = \frac{10\sqrt{2}}{3}\frac{A_1^{(gw)}}{A_1^{(dp)}}\frac{\mu(\eta_1-\epsilon)}{\mu(\eta_1+\epsilon)} = \frac{10}{3}\sqrt{\gamma_{\rm i}}\,. \tag{13}$$

This equation illustrates the importance of the initial conditions and the importance of the evolution of density perturbations during reheating. For small values of $\gamma_{\rm i}$ the amplitude of scalar metric perturbations is larger than the amplitude of gravitational waves, which implies that the main contribution to the large scale fluctuations in the cosmic microwave background is due to density fluctuations.

Acknowledgments

D.J.S. thanks the Alexander von Humboldt foundation for a fellowship.

References

1. L. P. Grishchuk, Phys. Rev. D **50**, 7154 (1994); preprint gr-qc/9801011 (1998).
2. J. Martin and D. J. Schwarz, Phys. Rev. D **57**, 15 March 1998 (gr-qc/9704049).
3. N. Deruelle and V. F. Mukhanov, Phys. Rev. D **52**, 5549 (1995).

THE COSMIC MICROWAVE BACKGROUND

Constraints on Cosmological Parameters from Existing CMB Data

J.G. Bartlett, A. Blanchard, M. Le Dour, M. Douspis & D. Barbosa[t]
Observatoire de Strasbourg, 11, rue de l'Université, 67000 Strasbourg, France
[t] *present address: Astronomy Centre, University of Sussex, Falmer, Brighton BN2 1TN, UK*

We use current cosmic microwave background data to constrain cosmological parameters. The results are presented as confidence regions in the (Ω–H_o) – plane for both open and flat geometries, and are based on a χ^2 minimization to the power spectrum. Although such an approach does not strictly apply to power spectrum estimates, the results should nonetheless be indicative. We find that purely open, low-Ω models are strongly disfavored, due to the position of the "Doppler Peak" at high l; flat models are less strongly constrained. The parameter space explored is the largest to date, covering Ω, H_o, n, Q and $\Omega_B h^2$.

1 Introduction

It is already possible, with existing data on the fluctuations of the cosmic microwave background (CMB), to constrain some cosmological parameters (Rocha & Hancock 1996; Bond & Jaffe 1996; Lineweaver et al. 1997). Of course, the actual data is far from providing the kind of constraints eagerly awaited from the next generation of experiments (Jungman et al. 1996; Bond et al. 1997), but there are nevertheless more than 10 different experiments detecting fluctuations over a large range of angular scales. To place our present work in context, consider the general problem of analyzing the results (say, a map) of a CMB experiment. If the true sky fluctuations and, as is fortunately often the case, the instrumental noise are gaussian, then the probability of obtaining any particular set of N pixel values is a multivariate gaussian in the pixel vector $\vec{d}$ (a one–dimensional listing of the possible pixel values):

$$\mathcal{L}(\vec{p}) = \mathcal{P}(\vec{d}/\vec{p}) = \frac{1}{(2\pi)^{N/2}|C|^{1/2}} e^{-(\vec{d})^t \cdot C^{-1} \cdot (\vec{d})/2}$$

The cosmological model is completely embodied (as well as the noise) in the covariance matrix of the pixels, $C \equiv C^T(\vec{p}) + C(noise)$, where we denote the underlying model parameters by

the vector $\vec{p}$. Thus, we have a likelihood function for $\vec{p}$, given a particular $\vec{d}$, i.e., a map of the sky. It is important to note that even if the pixels are gaussian, the likelihood function $\mathcal{L}(\vec{p})$ is NOT so, in general, because the parameters enter into the *covariance* matrix and not as linear combinations of the pixel values themselves. Maximization of this likelihood function is one way to estimate cosmological parameters.

Another approach is to work in Fourier space with estimates of the power spectrum, i.e., the C_l. These are nothing more than the variances of the individual spherical harmonic coefficients of the temperature fluctuations. We are really doing the same thing as before, just working with the covariances of Fourier coefficients instead of the measured pixel values. A practical reason for using this method is that band–power estimates and their uncertainties are readily available in the literature, this being the most common way of concisely reporting the results of an experiment.

In the present contribution, we assemble various band–power estimates (e.g., C_l intergrated over experimental window functions) and constrain certain cosmological parameters by fitting to these power spectrum data points. We must mention several caveats applying to the results given here: Firstly, the data set is certainly not homogeneous, if for no other reason than for the different ways that the so–called cosmic variance has been estimated and included in the quoted error bars. Secondly, we have not yet fully accounted for the experimental window functions. A third important point is that the C_l are NOT gaussian random variables, unlike the individual pixel values (or Fourier coefficients). This is clear – the C_l represent the variance of gaussian random variables, and thus are themselves distributed according to a χ^2 distribution. We have, for the work presented in this contribution, effectively assumed gaussianity in the sense that we apply a χ^2 minimization for the fitting. In principle, this could lead to biased best–estimates and incorrect confidence intervals. We are currently working on improving these aspects of our calculations. The results presented here should therefore be taken as indicative, but perhaps relatively good indications, all the same, given the current status of affairs (Jaffe & Bond 1997).

	Open Models		Flat Models	
parameter	range	step	range	step
Ω	0 – 0.95	0.05	0 – 1	0.05
H_o	15 – 100 km/s/Mpc	5 km/s/Mpc	15 – 100 km/s/Mpc	5 km/s/Mpc
n	0.5 – 1.5	0.03	0.55 – 1.45	0.09
Q	14 – 20 μK	1 μK	14 – 20 μK	1 μK
$\Omega_B h^2$	0.015	—	0.006 – 0.030	0.002

2 The models

We consider two broad class of inflation–based models (e.g., gaussian fluctuations): Open and flat with a non–zero cosmological constant. For the **open** models, we explored the four–dimensional parameter space of Ω, H_o, n, Q, where n is the spectral index of an assumed power–law power spectrum and Q is the normalization expressed as the CMB quadrupole; the baryon density was fixed at its nucleosythesis predicted value of $\Omega_b h^2 = 0.015$. For the **flat** models, we varied the baryon density in addition to these four parameters, thereby exploring a five–dimensional space. This is all summarized in the Table, where we also provide the individual step sizes on each parameter and the range covered. The calculations were performed with CMBFAST (Seljak & Zaldarriaga 1996). To cover the parameter space indicated, the slower open model calculations required a couple of months of uninterrupted computing time.

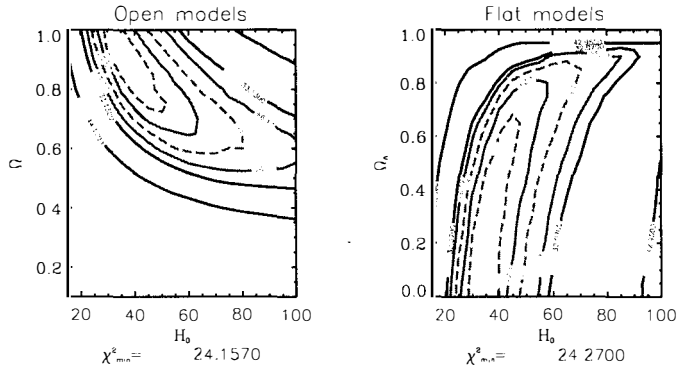

Figure 1: LEFT: Contours in the (Ω, H_o) – plane for the **Open** models. The light colored solid lines define confidence contours corresponding, if everything were gaussian, to 68% ($\chi^2_{min} + 2.3$) and 95% ($\chi^2_{min} + 6.17$). The dashed lines are confidence ellipses whose projection onto the axes provides the estimated range on each individual parameter. The darker solid lines are contours of constant goodness–of–fit at 68% and 95% probability, respectively, if the statistics were gaussian. RIGHT: Contours in the (Ω_v, H_o) – plane for the **Flat** models, where $\Omega_v = 1 - \Omega$ is the vacuum density. The contours are defined as in the left–hand panel.

3 Results

Our results in the (Ω, H_o)–plane for both types of model are shown in Figure 1. The light solid contours are defined by $\chi^2_{\rm min}+2.3$ and $+6.17$, which would correspond to 1σ and 2σ limits in this plane for a gaussian likelihood function (of the *parameters*), which, as we have mentioned, is not really the case. Nevertheless, this gives some idea of the region favored by the data: in general, we find that it corresponds to high Ω and low values of H_o. The dashed lines show the contours whose projection onto the axes give the confidence range on each parameter individually. Finally, for comparison, the dark solid lines (outer contours) are contours of constant *goodness–of–fit* for, if all were normal, 68% and 95% probability.

The most interesting aspect of these results concerns the open models. We see from Figure 1 that the contours place a lower limit on Ω; values as low as $\Omega = 0.2$ are strongly disfavored for any H_o. The reason for this is clear from the left–hand–side of Figure 2. The "Doppler Peak" is displaced too far to the right, due to the focusing of light rays in an open geometry (Hu & White 1996). Thus we find that a "comfortable" model with $\Omega = 0.2$ and $H_o = 60$ km/s/Mpc has *very serious difficulty* with the CMB data.

How about the cosmological constant? Here, the constraints on Ω are much less stringent, as can be seen from the contours shown in the right–hand panel of Figure 1. In contrast to the purely open model with $\Omega = 0.2$, the corresponding flat model, with $\Lambda = 0.8$, is acceptable and provides a good–looking fit to the power spectrum (right–hand–side of Figure 2).

4 Conclusions

It is a little early to draw detailed conclusions from the CMB concerning the cosmological parameters, but it is worth noting that some conclusions are already possible with existing data; and the next round of data releases will not be long in coming. Despite the various caveats of the method used here, it seems that one result should remain rather robust - that low–Ω, purely open models are strongly disfavored, for the clear and simple reason that the "Doppler Peak" is just not in the correct place due to the large angular distance to the surface of last scattering in such models.

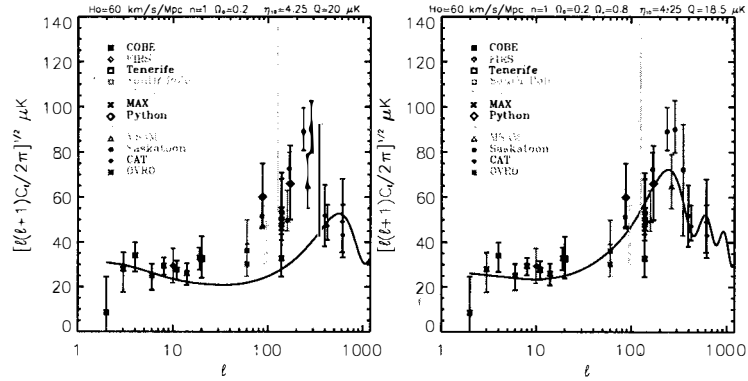

Figure 2: LEFT: Power spectrum of an **Open** model, with the parameters given at the top of the figure, compared to the data. The relation between η_{10} and the baryon density is: $\Omega_B h^2 = 0.0036\eta_{10}$, for a present-day CMB temperature of $T = 2.726$ K. RIGHT: Power spectrum of the corresponding **Flat** model.

5 Acknowledgements

D.B.acknowledges support by a PhD Praxix XXI grant atributed by JNICT/FDC, Portugal.

References

1. Bond J.R., Efstathiou G. & Tegmark M. 1997, MNRAS 291, L33
2. Bond J.R. & Jaffe A.H. 1996, in "Microwave Background Anisotropies" (proceedings of the XVIth Moriond Astrophysics meeting), F.R. Bouchet, R. Gispert et al. (Eds), Editions Frontières (Gif-sur-Yvette) p. 197
3. Hu W. & White M. 1996, ApJ 471, 30
4. Jaffe A.H. & Bond J.R. 1997, proceedings of the 18th Texas Symposium, astro-ph/9702109.
5. Jungman G., Kamionkowski M., Kosowsky A. & Spergel D. 1996, PhyRev D54, 1332
6. Lineweaver C.H., Barbosa D., Blanchard A. & Bartlett J.G. 1997, A&A 322, 365
7. Rocha G. & Hancock S. 1996, in "Microwave Background Anisotropies" (proceedings of the XVIth Moriond Astrophysics meeting), F.R. Bouchet, R. Gispert et al. (Eds), Editions Frontières (Gif-sur-Yvette) p. 189
8. Seljak U. & Zaldarriaga M. 1996, ApJ 469, 437

Polarization of Microwave Background: Statistical and Physical Properties

Uroš Seljak [1], Matias Zaldarriaga [2]
[1] *Harvard Smithsonian Center For Astrophysics, Cambridge, MA 02138, USA*
[2] *MIT, Cambridge, MA 02139, USA*

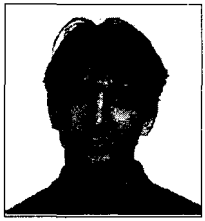

We discuss statistical and physical properties of cosmic microwave background polarization, both in Fourier and in real space. The latter allows for a more intuitive understanding of some of the geometric signatures. We present expressions that relate electric and magnetic type of polarization to the measured Stokes parameters in real space and discuss how can be constructed locally. We discuss necessary conditions to create polarization and present maps and correlation functions for some typical models.

1 Introduction

Cosmic microwave background (CMB) anisotropies offer one of the best probes of early universe, which could potentially lead to a precise determination of a large number of cosmological parameters [1,2,3]. The main advantage of CMB versus more local probes of large-scale structure is that the fluctuations were created at an epoch when the universe was still in a linear regime. While this fact has long been emphasized for temperature anisotropies (T), the same holds also for polarization in CMB and as such it offers the same advantages as the temperature anisotropies in the determination of cosmological parameters. The main limitation of polarization is that it is predicted to be small: theoretical calculations show that CMB will be polarized at 5-10% level on small angular scales and much less than that on large angular scales. Future CMB missions (MAP, Planck) will have sufficient sensitivity that even such low signals will be measurable. This will allow one to exploit the wealth of information present in the polarization.

Recent work has emphasized the rich geometrical structure present in polarization [4,5,6]. In particular, linear polarization has been decomposed into electric (E) and magnetic (B) types, which transform as scalars and pseudoscalars, respectively. With polarization there are three additional power spectra that can be measured, in addition to E and B autocorrelation there is also E and T cross-correlation. Each of these can provide unique information about our universe.

Most of this work has developed the formalism by using multipole expansion on a sphere or on a plane. Here we will develop some of the properties of polarization fields E and B directly in real space, which allows for a more intuitive understanding of their geometrical properties.

2 Statistical description of polarization

The CMB radiation field is characterized by a 2×2 intensity tensor I_{ij}. The intensity tensor is a function of direction on the sky $\boldsymbol{n}$ and two directions perpendicular to $\boldsymbol{n}$ that are used to define its components $(\hat{e}_1, \hat{e}_2)$. The Stokes parameters Q and U are defined as $Q = (I_{11} - I_{22})/4$ and $U = I_{12}/2$, while the temperature anisotropy is given by $T = (I_{11} + I_{22})/4$ (the factor of 4 relates fluctuations in the intensity to those in the temperature). In figures 5 we represent the polarization using "vectors" with magnitude $P = \sqrt{Q^2 + U^2}$ that form an angle $\alpha = \frac{1}{2} \arctan(\frac{U}{Q})$ with $\hat{e}_1$. These are not real vectors since they map into themselves after 180° rotation, which is why we do not assign them a direction. In principle the fourth Stokes parameter V that describes circular polarization would also be needed, but in cosmology it can be ignored because it cannot be generated through Thomson scattering. While the temperature is invariant under a right handed rotation in the plane perpendicular to direction $\boldsymbol{n}$, Q and U transform under rotation by an angle ψ as

$$\begin{aligned} Q' &= Q \cos 2\psi + U \sin 2\psi \\ U' &= -Q \sin 2\psi + U \cos 2\psi \end{aligned} \tag{1}$$

where $\hat{e}'_1 = \cos\psi\ \hat{e}_1 + \sin\psi\ \hat{e}_2$ and $\hat{e}'_2 = -\sin\psi\ \hat{e}_1 + \cos\psi\ \hat{e}_2$. The Stokes parameters are not invariant under rotations in the plane perpendicular to $\boldsymbol{n}$. For this reason it is more convenient to work with scalar and pseudoscalar polarization fields $E(\boldsymbol{n})$ and $B(\boldsymbol{n})$, respectively, which are invariant under rotations. In the small scale limit $\boldsymbol{n}$ is close to $\hat{\boldsymbol{z}}$ and we can parametrize the direction in the sky with two-dimensional angle $\boldsymbol{\theta}$ relative to a fixed coordinate system perpendicular to $\hat{\boldsymbol{z}}$. The two rotationally invariant fields can be written in terms of the Stokes parameters as

$$\begin{aligned} E(\boldsymbol{l}) &= \int d^2\boldsymbol{\theta}\ [Q(\boldsymbol{\theta}) \cos(2\phi_l) + U(\boldsymbol{\theta}) \sin(2\phi_l)]\ e^{-i\boldsymbol{l}\cdot\boldsymbol{\theta}} \\ B(\boldsymbol{l}) &= \int d^2\boldsymbol{\theta}\ [U(\boldsymbol{\theta}) \cos(2\phi_l) - Q(\boldsymbol{\theta}) \sin(2\phi_l)]\ e^{-i\boldsymbol{l}\cdot\boldsymbol{\theta}}, \end{aligned} \tag{2}$$

Here $E(\boldsymbol{l})$ and $B(\boldsymbol{l})$ are components of the two scalar fields in Fourier space. To obtain them in real space we can perform a Fourier transform

$$\begin{aligned} E(\boldsymbol{\theta}) &= (2\pi)^{-2} \int d^2\boldsymbol{l}\ e^{i\boldsymbol{l}\boldsymbol{\theta}}\ E(\boldsymbol{l}) \\ B(\boldsymbol{\theta}) &= (2\pi)^{-2} \int d^2\boldsymbol{l}\ e^{i\boldsymbol{l}\boldsymbol{\theta}}\ B(\boldsymbol{l}). \end{aligned} \tag{3}$$

These two quantities describe completely the polarization field. They can be expressed directly in terms of real space quantities $Q(\boldsymbol{\theta})$ and $U(\boldsymbol{\theta})$ as

$$\begin{aligned} E(\boldsymbol{\theta}) &= -\int d^2\boldsymbol{\theta}'\ \omega(\tilde{\theta})\ [Q(\boldsymbol{\theta}') \cos(2\tilde{\phi}) - U(\boldsymbol{\theta}') \sin(2\tilde{\phi})] \\ &= -\int d^2\boldsymbol{\theta}'\ \omega(\tilde{\theta})\ Q_r(\boldsymbol{\theta}') \\ B(\boldsymbol{\theta}) &= -\int d^2\boldsymbol{\theta}'\ \omega(\tilde{\theta})\ [U(\boldsymbol{\theta}') \cos(2\tilde{\phi}) + Q(\boldsymbol{\theta}') \sin(2\tilde{\phi})] \\ &= -\int d^2\boldsymbol{\theta}'\ \omega(\tilde{\theta})\ U_r(\boldsymbol{\theta}'). \end{aligned} \tag{4}$$

The variables $(\tilde{\theta}, \tilde{\phi})$ are the polar coordinates of the vector $\boldsymbol{\theta} - \boldsymbol{\theta}'$. In equation (4) Q_r and U_r are the Stokes parameters in the polar coordinate system centered at $\boldsymbol{\theta}$. For example, if $\boldsymbol{\theta}$ is zero, $Q_r = \cos 2\phi' \, Q(\boldsymbol{\theta}') - \sin 2\phi' \, U(\boldsymbol{\theta}')$ and $U_r = \cos 2\phi' \, U(\boldsymbol{\theta}') + \sin 2\phi' \, Q(\boldsymbol{\theta}')$. The window can be shown to be $\omega(\theta) = 1/\pi\theta^2$ $(\theta \neq 0)$, $\omega(\theta) = 0$ $(\theta = 0)$.

From equation 4 we can understand how to obtain two rotationally invariant quantities out of Q and U directly in real space: to obtain $E(\boldsymbol{\theta})$ and $B(\boldsymbol{\theta})$ we radially integrate over circles centered at $\boldsymbol{\theta}$ the values of Q_r and U_r, respectively. Each circle is weighted by $\omega(\tilde{\theta})$. By construction these two quantities are rotationally invariant: the Stokes parameters Q_r and U_r do not depend on the coordinate system, as they are defined relative to the $\boldsymbol{\theta} - \boldsymbol{\theta}'$ vector. The weight function ω is also rotationally invariant. We are giving the same weight to all the points in each circle and we are using the Stokes parameters defined in their *natural* coordinate system, defined parallel and perpendicular to the line joining the two points (denoted with r in equation 4). The variable B is clearly a pseudoscalar because it is the average of U_r and U_r changes sign under parity. Note that the window extends out to infinity and so the quantities E and B are nonlocal. This is not the only possible choice: one can construct finite extent versions of E and B from Q and U using a compensated window such that $\int \theta d\theta \; g(\theta) = 0$, e.g. $\tilde{E} = \int E g(\theta) d^2\theta$ and similarly for B. The relation between these averaged $\tilde{E}$ and $\tilde{B}$ and Q, U is still given by equation 4 using

$$\omega(\theta) = -g(\theta) + \frac{2}{\theta^2} \int_0^\theta d\theta' \theta' g(\theta'). \tag{5}$$

We can therefore construct pure E or B quantities which are obtained from an integral over a finite region and test the geometrical structure of polarization without measuring the whole sky, as long as the measured field is contiguous. Note that for these real space quantities there is no need to worry about mode coupling because of incomplete sky coverage, which would for example mix some E into B in Fourier space.

Let us further explore properties of E and B type polarizations in real space. For simplicity we will continue to use small scale limit. Figure 5a shows the E polarization field and the polarization vectors for a typical (standard CDM) model. There is only E type polarization associated with this model, because this is the only pattern that is produced by density perturbations and we did not include a stochastic background of gravity waves. We discuss this point further below. In figures 5a and 1 we can see that hot spots of the E map correspond to points with tangential polarization pattern (negative Q_r). Radial polarization pattern is found around the cold spots of E. From equation 4 we can read directly the relations between the pattern of polarization and the sign of E and B. Note that there is a formal similarity between weak lensing and polarization: E plays a role of convergence κ, while Q and U can be viewed as the two shear components γ_1 and γ_2. Since weak lensing is only important for scalar perturbations B mode is not excited, which provides a consistency check. The sign convention for E agrees with weak lensing [7]: positive mass density (positive κ) generates a tangential pattern of shear, so likewise positive E gives rise to a tangential polarization pattern.

To obtain B type polarization we can rotate all polarization "vectors" by 45°. *Hot* and *cold* spots of the B field correspond to places where the polarization vectors circulate around in opposite directions (figure 1). It is clear from this figure that such polarization pattern is not invariant under reflections (parity transformation). This is the main distinction between E and B type of polarization: under parity operation E transforms as a scalar and B as a pseudoscalar.

We can now address the polarization pattern induced by different types of perturbations. In particular, we want to show why scalar perturbations cannot induce B type of polarization. Without loss of generality we may consider only one Fourier mode of scalar perturbations at a time, since an arbitrary field can always be expanded in a linear superposition of Fourier modes. Let us assume we are observing in direction $\boldsymbol{n}$, while the mode is oriented in direction $\hat{\boldsymbol{k}}$. In the plane perpendicular to $\boldsymbol{n}$ we can define a local coordinate system with axis aligned parallel and

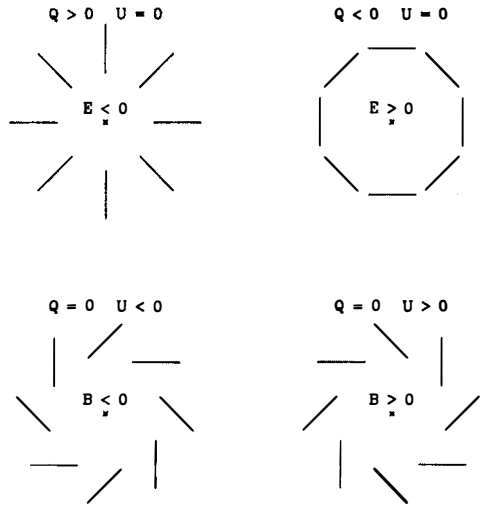

Figure 1: Polarization patterns that lead to positive and negative values of the E and B fields. The Stokes parameters are measured in the polar coordinate system centered at the cross. All four patterns are invariant under rotation but the two patterns that generate B are not invariant under reflections.

perpendicular to the plane that contains both $\hat{k}$ and $\boldsymbol{n}$. Scalar modes have a rotation symmetry around $\hat{k}$, which implies that $U = 0$ in this frame (figure 2). Let us now look at the polarization pattern in the circle around direction $\boldsymbol{n}$ in the plane perpendicular to it. Polarization is directed either in the direction towards $\hat{k}$ or perpendicular to this direction, since only Q is generated in the frame determined by that direction (for simplicity only radial case is depicted in figure 2). Polarization is invariant under the reflection across the axis determined by the $\hat{k}$ and $\boldsymbol{n}$ line, because polarization amplitude only depends on the angle between $\hat{k}$ and $\boldsymbol{n}$. Therefore any integration around this circle will produce only E and not B. Since both E and B are obtained by radial averaging of contributions from individual circles and B vanishes for each for each of them it follows that $B = 0$ in general. By construction this is coordinate independent, hence one cannot produce B polarization with scalar perturbations in general.

For tensor perturbations this argument no longer applies, as shown in figure 2. Here the amplitude of perturbation depends also on the orientation of the stretching and squeezing of space in the direction perpendicular to the direction of plane propagation (figure 2). There is no parity symmetry and both E and B will be generated in general. This is also true for vector modes. For these modes velocity is perpendicular to the direction of wave propagation. Its direction in the plane perpendicular to $\hat{k}$ breaks the symmetry and generates B modes.

3 Generation of Polarization

The standard picture of big bang model is that the universe was hot in the beginning and was expanding and cooling thereafter. At high temperatures electrons and protons were free in the universe, because photons were sufficiently energetic to prevent any recombination to survive. Once the energy of most of the photons dropped below 13.6eV ionization was no longer possible

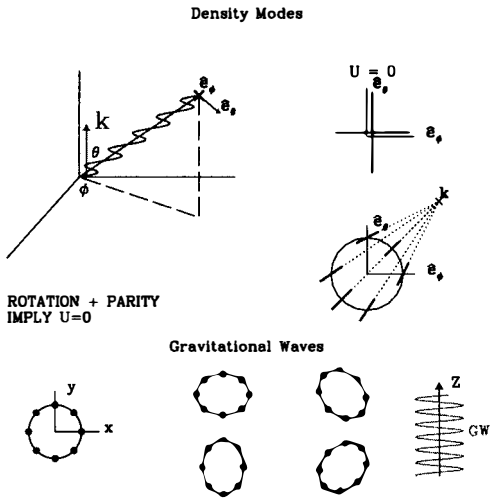

Figure 2: A single mode of density perturbations has symmetries under rotation around the $\hat{k}$ axis and reflection around any plane containing it. Only Q Stokes parameter can be present in this reference frame, implying no B polarization is created (see the text). Gravitational waves do not have these symmetries as illustrated by the deformation suffered by a ring of test particles as wave propagating in direction $\hat{k}$ passes by. There is a particular direction associated with the direction of the stretching and there is no rotational or parity symmetry. The same is true for vector modes, which induce velocities perpendicular to the wave direction.

and at that time (at energies around 0.3eV) the universe recombined and became transparent for photons. The recombination was very rapid. Before recombination the density of free electrons was very high, so that the photon mean free path was very short. Together with electrons they formed a single fluid, with pressure provided by the photons and inertia by the baryons. This fluid supported the analog of acoustic oscillations where both the density and velocity were oscillating functions of time[8,9]. The density was proportional to $\cos(c_s k\tau + \delta)$, while the velocity to $\sin(c_s k\tau + \delta)$, where c_s is the sound speed and the phase δ depends on initial conditions and is in general time dependent.

To generate polarization we need Thomson scattering between photons and electrons. Electric field incident on the electron causes this electron to oscillate in the direction of the field and electron radiates according to the dipole emission formula. Looking for example perpendicular to the incoming light direction only one polarization of incident light will be seen to cause electron to oscillate, the one perpendicular to the plane containing the incoming and outgoing directions. Dipole radiation emits preferentially perpendicular to the direction of oscillation, so the light we observe will be polarized. To get the total effect we need to integrate over the light intensity in all the directions. If the radiation incident on the electron is isotropic there will be no net polarization generated after the scattering, simply by symmetry. Dipole distribution also does not generate polarization. For example, consider the case where the intensity of the incident radiation is higher from the top and lower from th e bottom, with the average intensity incident from the sides. Observing from above the plane scattered light from photons incident from either the bottom or top of the plane will be polarized in the horizontal direction, while

that coming from the sides will be polarized in the vertical direction. Adding up all the components we find that horizontal and vertical components are equal, implying no polarization. We therefore need a quadrupolar pattern of intensity, in which case there is an excess of horizontal polarization from both top and bottom, which does not cancel the smaller vertical polarization from the sides.

Since we need Thomson scattering it is clear that polarization cannot be generated after recombination of electrons and protons into hydrogen, when the universe becomes transparent for the photons. We still need to show however that there is sufficient quadrupole moment prior to last scattering, because only then will polarization be generated. In the electron rest frame one sees photons coming from distances of the order of a mean free path λ_p. The photons that are scattered off a given electron come from places where the fluid has velocity v and because of the tight coupling between photons and electrons the photon distribution function has a dipole term $T_1 = \hat{n} \cdot v$. To generate quadrupole moment one requires a gradient in the velocity field across the mean free path, $T_2 = \lambda_p n^i n^j \partial_i v_j$ in the rest frame of the electron. But since the mean free path was so short prior to recombination the induced quadrupole was very small, until the last moment during recombination when mean free path started to grow. This implies that the mean free path is of the order of the duration of recombination and a detailed analysis gives [10]

$$(Q + iU)(\hat{n}) \approx 0.17 \Delta\tau_* m^i m^j \partial_i v_j|_{\tau_*}, \tag{6}$$

where $\Delta\tau_*$ is the width of the last scattering surface, happening at τ_*. The appearance of $m = \hat{e}_1 + i\hat{e}_2$ in equation 6 assures that $(Q+iU)$ transforms correctly under rotations of $(\hat{e}_1, \hat{e}_2)$ (equation 1).

Figure 3 shows the temperature, E polarization and $T - E$ cross-correlation power spectra. The oscillations in the spectra can be understood with the tight coupling approximation described above. At the time of recombination waves of different wavevectors k are at different phases in their oscillations. The phase only depends on the amplitude of the wavevector, so all the modes with the same amplitude of wavevector have the same phase. For particular values of this amplitude all the corresponding modes vanish. A given physical scale is related to the corresponding angular scale via the angular diameter distance, but the correspondence is not perfect because of 3-d to 2-d projection. If it were perfect the power spectrum of polarization would vanish at some values, but in reality it does not (figure 3). Nevertheless, the oscillations in polarization are much more pronounced than in temperature, because the latter receives contributions both from density and velocity and the two are out of phase with each other, so that even if one vanishes for some value of k the other does not.

On large scales polarization is strongly suppressed. Correlations over large angles can only be created by the long wavelength perturbations, but these cannot produce a large polarization because of the tight coupling between photons and electrons prior to recombination: only wavelengths that are small enough to produce anisotropies over the mean free path of the photons will give rise to a significant quadrupole in the temperature distribution, and thus to polarization. On small scales ($l \geq 1000$) both polarization and temperature anisotropies are suppressed by photon diffusion. Here the wavelength of the perturbation becomes comparable to the mean free path of the photons prior to recombination. Photons can diffuse out of density peaks smaller than a diffusion length, thereby erasing the anisotropies. Note also that there is an extra gradient in polarization relative to temperature (equation 6), which explains why polarization amplitude peaks at a smaller angular scale. The fact that the polarization field has relatively more small scale power is particularly evident when we compare the the T and E fields in figures 5a and 5c. Finally, temperature polarization cross-correlation oscillates just like the other two spectra, but can be either positive or negative (figure 3).

Figure 4 shows the correlation functions in real space. The spectrum has been smoothed with a $\theta_{fwhm} = 0.2^\circ$ gaussian, similar to the MAP beam. The correlation functions are defined

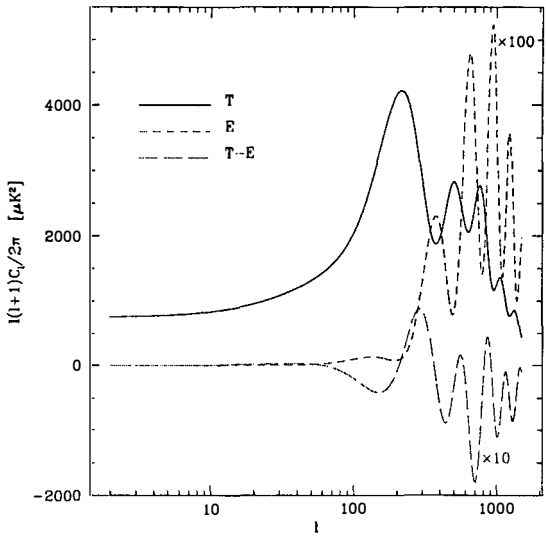

Figure 3: Power spectra for COBE normalized SCDM. The E and the $T - E$ spectra have been rescaled for convenience.

in their natural coordinate system. In this frame there is no cross-correlation between U_r and T. An interesting point is that both polarization auto-correlation functions are negative for some angular range, which does not happen for the temperature. To interpret the cross correlation we can consider the polarization pattern around a hot spot ($T > 0$). The cross correlation starts positive, implying a radial pattern of polarization. Not all the polarization is correlated with the temperature so it is difficult to see this trend in figure 5c. In figure 5d we only plot the correlated part of the polarization and here one can see more clearly that polarization "vectors" are preferentially radial around hot spots.

Moving to larger angular scales the cross correlation changes sign. When it is negative the pattern becomes tangential. For large separations the polarization around a hot (cold) spot is tangential (radial). A point worth noting is that the cross correlation vanishes at $\theta = 0$, in contrast to what happens for the other correlation functions. This follows simply from symmetry, since there is no preferred direction that polarization should take. Only when we consider two points separated by some distance is the symmetry broken. The vector joining the two points becomes the privileged direction and the polarization can be preferentially parallel or perpendicular to this direction.

4 Conclusions

Polarization has a rich geometrical structure, which can be simply understood using a real space construction of scalar and pseudoscalar fields. These can be constructed as integrals over Stokes Q and U parameters. Finite extent versions exist which allow one to search for B polarization without measuring the whole sky.

Generation of polarization requires both Thomson scattering and significant quadrupole

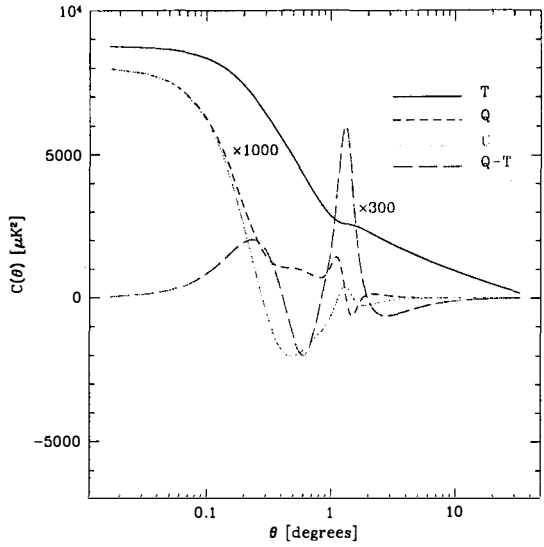

Figure 4: Correlation functions in real space for COBE normalized standard CDM model. The spectra have been smoothed with a $\theta_{fwhm} = 0.2^{\circ}$ corresponding to the beam size of MAP.

moment of photon distribution in electron rest frame. We give simple arguments why this is so and discuss predictions for some realistic models. Realistic attempts to extract polarization information have to include complications such as instrument noise and foregrounds and are given elsewhere in these proceedings [11].

References

1. G. Jungman, M. Kamionkowski, A. Kosowsky, & D. N. Spergel, Phys. Rev. Lett. **76**, 1007 (1996); Phys. Rev. D **54** 1332 (1996).
2. J. R. Bond, G. Efstathiou & M. Tegmark, Mon. Not. R. Astron. Soc. **291**, 33 (1997).
3. M. Zaldarriaga, D. N. Spergel & U. Seljak, Astrophys. J. **488**, 1, (1997).
4. U. Seljak, Astrophys. J., **482** 6 (1996)
5. M. Kamionkowski, A. Kosowsky & A. Stebbins, Phys. Rev. D **55** 7368 (1997).
6. M. Zaldarriaga & U. Seljak, Phys. Rev. D **55**, 1830 (1997).
7. N. Kaiser, Astrophys. J. **388**, 272 (1992).
8. U. Seljak, Astrophys. J. **435**, L87 (1994).
9. W. Hu & N. Sugiyama, Phys. Rev D **51**, 2599 (1995).
10. M. Zaldarriaga & D. Harari, Phys. Rev D **52**, 3276 (1995).
11. S. Prunet, S. K. Sethi & F. R. Bouchet, these proceedings; S. K. Sethi, S. Prunet & F. R. Bouchet, these proceedings.

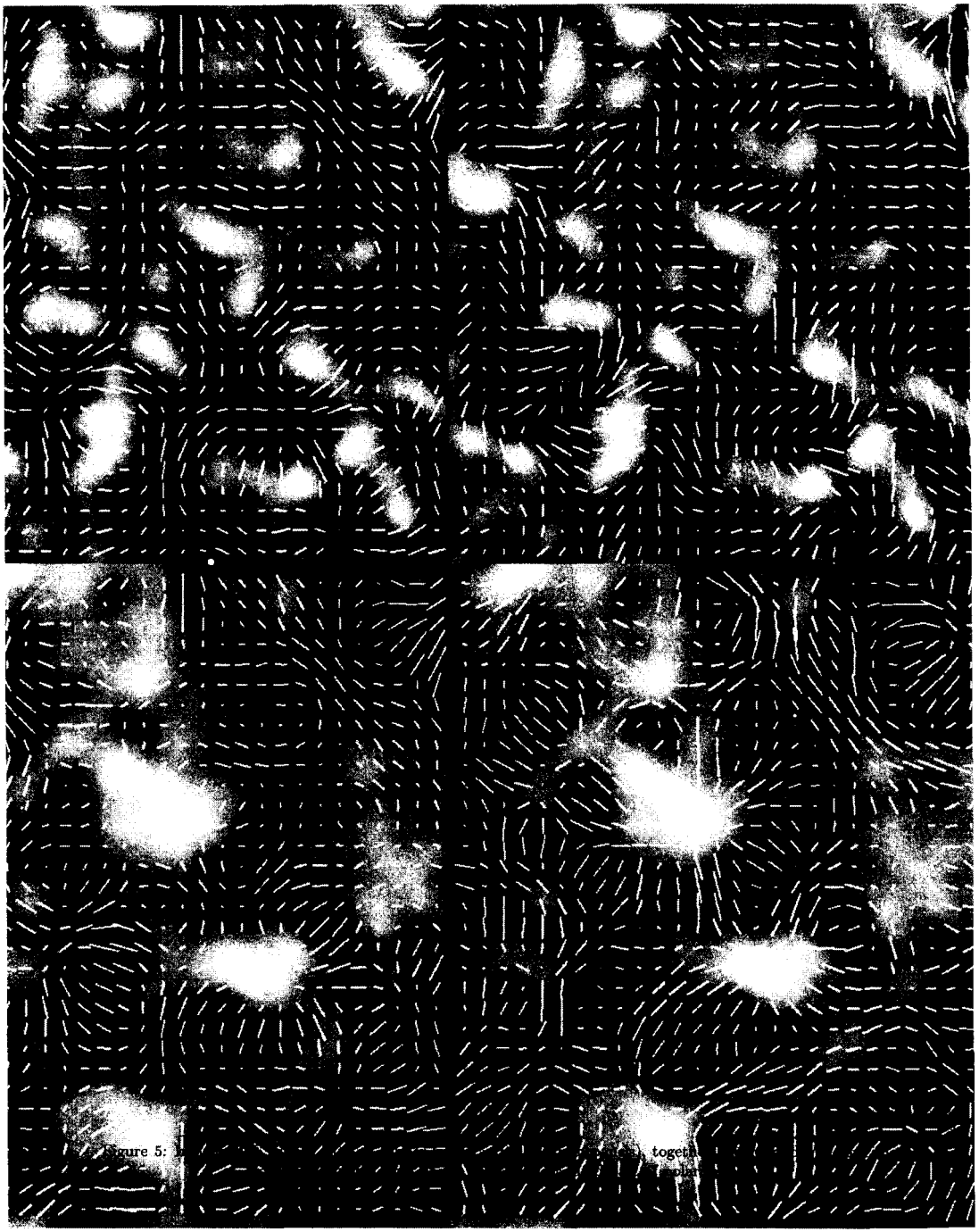

Fig 5. Images of E (upper left), B (upper right) and T (bottom panels), together with Q and U polarization pattern. Bottom right shows only the correlated part of polarization.

COSMOLOGICAL-PARAMETER DETERMINATION WITH COSMIC MICROWAVE BACKGROUND TEMPERATURE ANISOTROPIES AND POLARIZATION

M. KAMIONKOWSKI
Department of Physics, Columbia University, 538 West 120th St., New York, NY 10027 U.S.A

Forthcoming cosmic microwave background experiments (CMB) will provide precise new tests of structure-formation theories. The geometry of the Universe may be determined robustly, and the classical cosmological parameters, such as the cosmological constant, baryon density, and Hubble constant, may be determined as well. In addition, the "inflationary observables," which parameterize the shapes and amplitudes of the primordial spectra of density perturbations and long-wavelength gravitational waves produced by inflation, may also be measured and thus provide several new tests of inflation. Although most attention has focussed on the more easily observed temperature anisotropies, recent work has shown that the CMB polarization provides a wealth of unique information that may be especially important for determination of the inflationary observables. Secondary anisotropies at small angular scales produced by re-scattering of photons from partial reionization may be used to constrain the ionization history of the Universe.

1 Introduction

Despite its major triumphs (the expansion, nucleosynthesis, and the cosmic microwave background), the big-bang theory for the origin of the Universe leaves several questions unanswered. Chief amongst these is the horizon problem: When cosmic microwave background (CMB) photons last scattered, the age of the Universe was roughly 100,000 years, much smaller than its current age of roughly 10 billion years. After taking into account the expansion of the Universe, one finds that the angle subtended by a causally connected region at the surface of last scatter is roughly 1°. However, there are 40,000 square degrees on the surface of the sky. Therefore, when we look at the CMB over the entire sky, we are looking at 40,000 causally disconnected regions of the Universe. But quite remarkably, each has the same temperature to roughly one part in 10^5!

The most satisfying (only?) explanation for this is slow-roll inflation,[1] a period of accelerated expansion in the early Universe driven by the vacuum energy most likely associated with a symmetric phase of a GUT Higgs field (or perhaps Planck-scale physics or Peccei-Quinn symmetry breaking). Although the physics responsible for inflation is still not well understood, inflation generically predicts (1) a flat Universe; (2) that primordial adiabatic (i.e., curvature) perturbations are responsible for the large-scale structure (LSS) in the Universe today;[2] and (3) a stochastic gravity-wave background.[3] More precisely, inflation predicts a spectrum $P_s = A_s k^{n_s}$ (with n_s near unity) of primordial density (scalar metric) perturbations, and a stochastic gravity-wave background (tensor metric perturbations) with spectrum $P_t = A_t \propto k^{n_t}$ (with n_t small compared with unity). (4) Inflation further uniquely predicts specific relations between the "inflationary observables," the amplitudes A_s and A_t and spectral indices n_s and n_t of the scalar and tensor perturbations.[4] The amplitude of the gravity-wave background is proportional to the height of the inflaton potential, and the spectral indices depend on the shape of the inflaton potential. Therefore, determination of these parameters would illuminate the physics responsible for inflation.

Until recently, none of these predictions could really be tested. Measured values for the density of the Universe span almost an order of magnitude. Furthermore, most do not probe the possible contribution of a cosmological constant (or some other diffuse matter component), so they do not address the geometry of the Universe. The only observable effects of a stochastic gravity-wave background are in the CMB. COBE observations do in fact provide an upper limit to the tensor amplitude, and therefore an inflaton-potential height near the GUT scale. However, there is no way to disentangle the scalar and tensor contributions to the COBE anisotropy.

In recent years, it has become increasingly likely that adiabatic perturbations are responsible for the origin of structure. Before COBE, there were numerous plausible models for structure formation: e.g., isocurvature perturbations both with and without cold dark matter, late-time or slow phase transitions, topological defects (cosmic strings or textures), superconducting cosmic strings, explosive or seed models, a "loitering" Universe, etc. However, after COBE, only primordial adiabatic perturbations and topological defects were still considered seriously. And in the past few months, some leading proponents of topological defects have conceded that these models have difficulty reproducing the observed large-scale structure.[5]

We are now entering an exciting new era, driven by new theoretical ideas and developments in detector technology, in which the predictions of inflation will be tested with unprecedented precision. It is even conceivable that early in the next century, we will move from verification to direct investigation of the high-energy physics responsible for inflation.

The purpose of this talk is to review how forthcoming CMB experiments will test several of these predictions. I will first review the predictions of inflation for density perturbations and gravity waves. I will then discuss how CMB temperature anisotropies will test the inflationary predictions of a flat Universe and a primordial spectrum of density perturbations. I review how a CMB polarization map may be used to isolate the gravity waves and briefly review how detection of these tensor modes may be used to learn about the physics responsible for inflation. I then discuss some recent work on secondary anisotropies at smaller angular scales, and how these may be used to probe the epoch at which objects first underwent gravitational collapse in the Universe. I close with some brief remarks about further testable consequences of inflation.

2 Inflationary Observables

Inflation occurs when the energy density of the Universe is dominated by the vacuum energy $V(\phi)$ associated with some scalar field ϕ (the "inflaton"). During this time, the quantum fluctuations in ϕ produce classical scalar perturbations, and quantum fluctuations in the spacetime metric produce gravitational waves. If the inflaton potential $V(\phi)$ is given in units of $m_{\rm Pl}^4$, and the

inflaton ϕ is in units of $m_{\rm Pl}$, then the scalar and tensor spectral indices are

$$1 - n_s = (1/8\pi)\,(V'/V)^2 - (1/4\pi)\,(V'/V)', \qquad n_t = -(1/8\pi)\,(V'/V)^2 . \tag{1}$$

The amplitudes can be fixed by their contribution to $C_2^{\rm TT}$, the quadrupole moment of the CMB temperature, $\mathcal{S} \equiv 6\,C_2^{\rm TT,scalar} = 33.2\,[V^3/(V')^2]$, and $\mathcal{T} \equiv 6\,C_2^{\rm TT,tensor} = 9.2\,V$. For the slow-roll conditions to be satisfied, we must have $(1/16\pi)(V'/V)^2 \ll 1$, and $(1/8\pi)(V''/V) \ll 1$, which guarantee that inflation lasts long enough to make the Universe flat and to solve the horizon problem.

When combined with COBE results, current degree-scale–anisotropy and large-scale-structure observations suggest that $\mathcal{T}/\mathcal{S}$ is less than order unity in inflationary models, which restricts $V \lesssim 5 \times 10^{-12}$. Barring strange coincidences, the COBE spectral index and relations above suggest that if slow-roll inflation is right, then scalar and tensor spectra must both be nearly scale invariant ($n_s \simeq 1$ and $n_t \simeq 0$).

3 Temperature Anisotropies

The primary goal of CMB experiments that map the temperature as a function of position on the sky is recovery of the temperature autocorrelation function or angular power spectrum of the CMB. The fractional temperature perturbation $\Delta T(\hat{\mathbf{n}})/T$ in a given direction $\hat{\mathbf{n}}$ can be expanded in spherical harmonics,

$$\frac{\Delta T(\hat{\mathbf{n}})}{T} = \sum_{lm} a^{\rm T}_{(lm)}\, Y_{(lm)}(\hat{\mathbf{n}}), \quad \text{with} \quad a^{\rm T}_{(lm)} = \int d\hat{\mathbf{n}}\, Y^*_{(lm)}(\hat{\mathbf{n}})\, \frac{\Delta T(\hat{\mathbf{n}})}{T}. \tag{2}$$

Statistical isotropy and homogeneity of the Universe imply that these coefficients have expectation values $\left\langle (a^{\rm T}_{(lm)})^* a^{\rm T}_{(l'm')} \right\rangle = C_l^{\rm TT}\,\delta_{ll'}\,\delta_{mm'}$ when averaged over the sky. Roughly speaking, the multipole moments $C_l^{\rm TT}$ measure the mean-square temperature difference between two points separated by an angle $(\theta/1^\circ) \sim 200/l$.

Predictions for the C_l's can be made given a theory for structure formation and the values of several cosmological parameters. Fig. 1 shows predictions for models with primordial adiabatic perturbations. The wriggles come from oscillations in the photon-baryon fluid at the surface of last scatter. Each panel shows the effect of independent variation of one of the cosmological parameters. As illustrated, the height, width, and spacing of the acoustic peaks in the angular spectrum depend on these (and other) cosmological parameters.

These small-angle CMB anisotropies can be used to determine the geometry of the Universe.[6] The angle subtended by the horizon at the surface of last scatter is $\theta_H \sim \Omega^{1/2}\ 1^\circ$, and the peaks in the CMB spectrum are due to causal processes at the surface of last scatter. Therefore, the angles (or values of l) at which the peaks occur determine the geometry of the Universe. This is illustrated in Fig. 1(a) where the CMB spectra for several values of Ω are shown. As illustrated in the other panels, the angular position of the first peak is relatively insensitive to the values of other undetermined (or still imprecisely determined) cosmological parameters such as the baryon density, the Hubble constant, and the cosmological constant (as well as several others not shown such as the spectral indices and amplitudes of the scalar and tensor spectra and the ionization history of the Universe). Therefore, determination of the location of this first acoustic peak should provide a robust measure of the geometry of the Universe.

Fig. 2 shows data from current ground-based and balloon-borne experiments. By fitting the theoretical curves to these points, several groups find that the best fit to the data is found with a total density $\Omega \simeq 1.0$.[7] However, visual inspection of the data points in Fig. 2 clearly indicate that this current determination of the geometry cannot be robust.

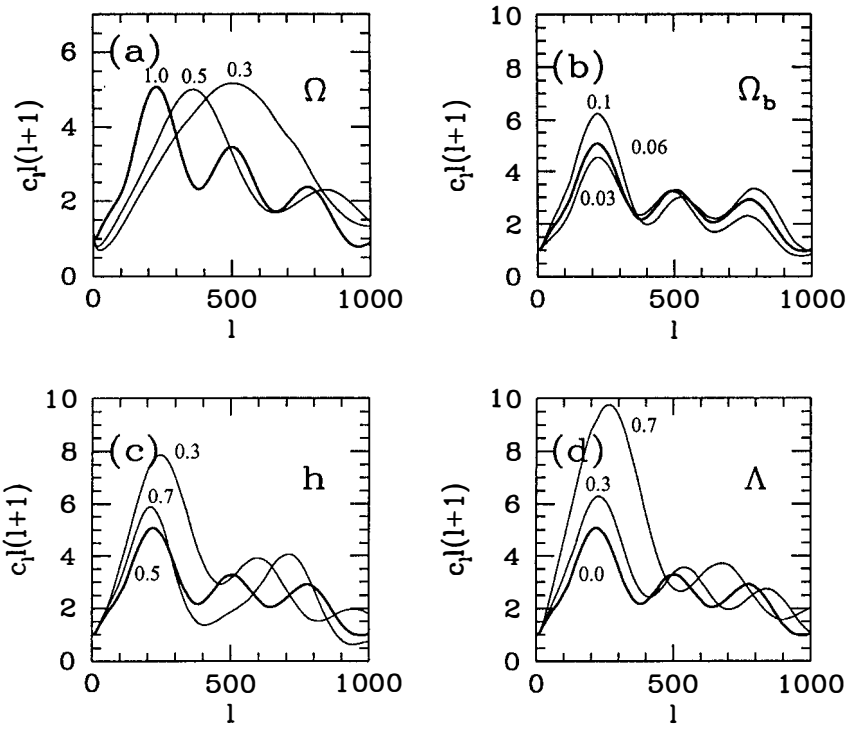

Figure 1: Theoretical predictions for CMB spectra as a function of multipole moment l for models with primordial adiabatic perturbations. In each case, the heavy curve is that for the canonical standard-CDM values, a total density $\Omega = 1$, cosmological constant $\Lambda = 0$, baryon density $\Omega_b = 0.06$, and Hubble parameter $h = 0.5$. Each graph shows the effect of variation of one of these parameters. In (d), $\Omega + \Lambda = 1$.

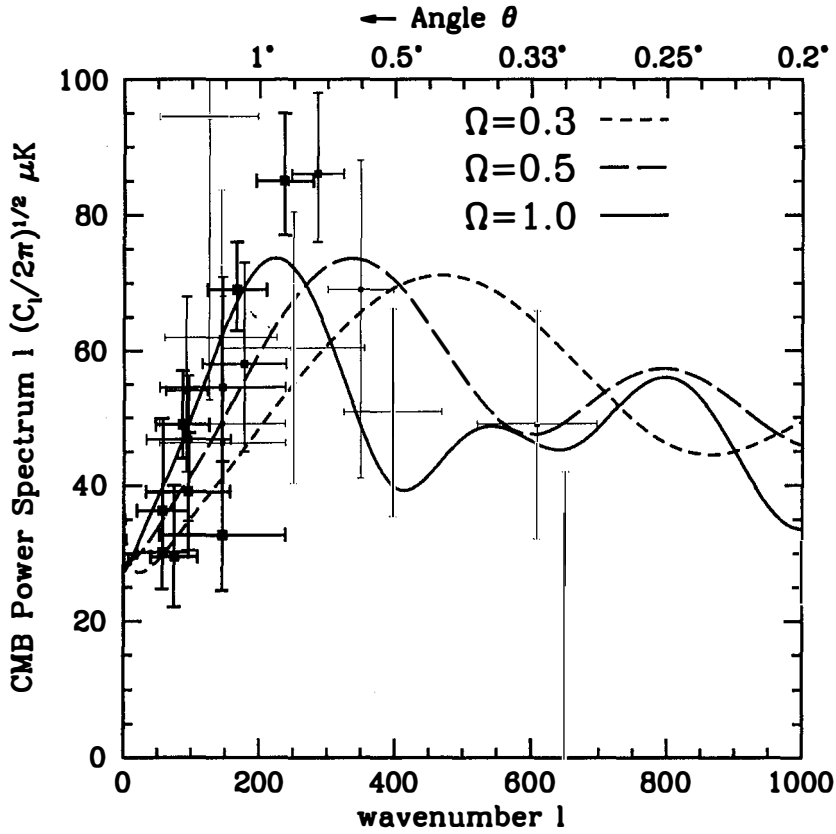

Figure 2: Current CMB data.

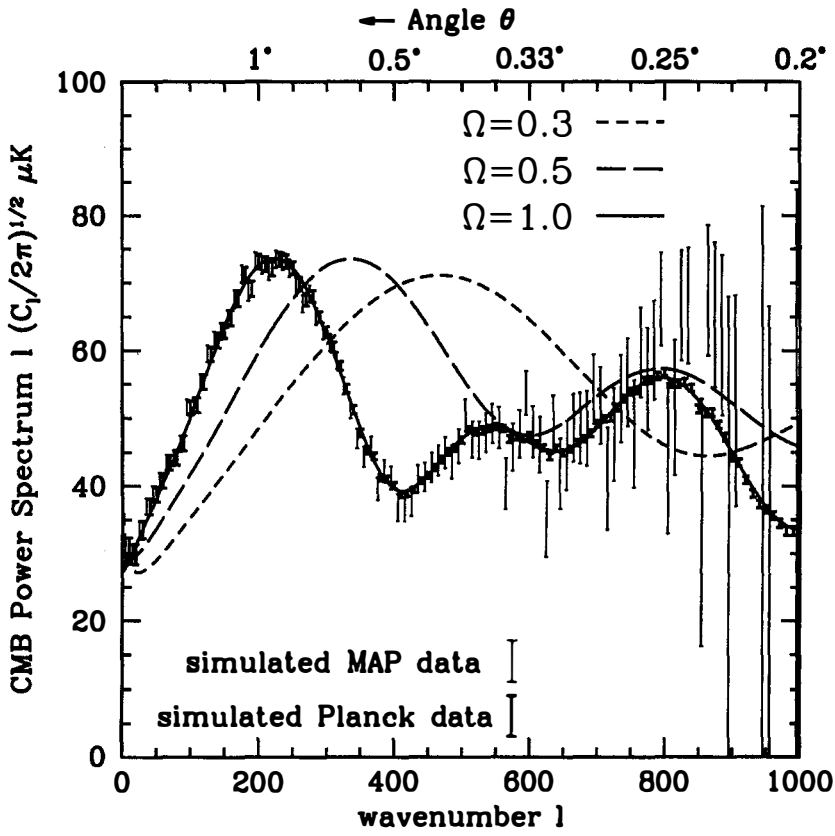

Figure 3: Simulated MAP and Planck data.

In the near future, the precision with which this determination can be made will be improved dramatically. NASA has recently approved the flight of a satellite mission, the Microwave Anisotropy Probe (MAP)[8] in the year 2000 to carry out these measurements, and ESA has approved the flight of a subsequent more precise experiment, the Planck Surveyor.[9] Fig. 3 shows simulated data from MAP and Planck. The heavier points with smaller error bars are those we might expect from Planck and the lighter points with larger error bars are those anticipated for MAP. Even without any sophisticated analysis, it is clear from Fig. 3 that data from either of these experiments will be able to locate the first acoustic peak sufficiently well to discriminate between a flat Universe ($\Omega = 1$) and an open Universe with $\Omega \simeq 0.3 - 0.5$.

By doing what essentially boils down to a calculation of the covariance matrix for such simulated data, it can be shown that these satellite missions may potentially determine Ω to better than 10% *after* marginalizing over all other undetermined parameters (we considered 7 more parameters in addition to the 4 shown in Fig. 1), and better than 1% if the other parameters can be fixed by independent observations or assumption.[10] This would be far more accurate than any traditional determinations of the geometry.

We also found that the CMB should provide values for the cosmological constant and baryon density far more precise than those from traditional observations.[11] If there is more nonrelativistic matter in the Universe than baryons can account for—as suggested by current observations—it will become increasingly clear with future CMB measurements. Subsequent analyses have confirmed these estimates with more accurate numerical calculations.[12]

Although these forecasts relied on the assumptions that adiabatic perturbations were responsible for structure formation and that reionization would not erase CMB anisotropies, these assumptions have become increasingly justifiable in the past few years. As discussed above, the leading alternative theories for structure formation now appear to be in trouble, and recent detections of CMB anisotropy at degree angular separations show that the effects of reionization are small.

The predictions of a nearly scale-free spectrum of primordial adiabatic perturbations will also be further tested with measurements of small-angle CMB anisotropies. The existence and structure of the acoustic peaks shown in Fig. 1 will provide an unmistakable signature of adiabatic perturbations[13] and the spectral index n_s can be determined from fitting the theoretical curves to the data in the same way that the density, cosmological constant, baryon density, and Hubble constant are also fit.[11]

Temperature anisotropies produced by a stochastic gravity-wave background would affect the shape of the angular CMB spectrum, but there is no way to disentangle the scalar and tensor contributions to the CMB anisotropy in a model-independent way. Unless the tensor signal is large, the cosmic variance from the dominant scalar modes will provide an irreducible limit to the sensitivity of a temperature map to a tensor signal.[11]

4 CMB Polarization and Gravitational Waves

Although a CMB temperature map cannot unambiguously distinguish between the density-perturbation and gravity-wave contributions to the CMB, the two can be decomposed in a model-independent fashion with a map of the CMB polarization.[14,15,16] Suppose we measure the linear-polarization "vector" $\vec{P}(\hat{\mathbf{n}})$ at every point $\hat{\mathbf{n}}$ on the sky. Such a vector field can be written as the gradient of a scalar function A plus the curl of a vector field $\vec{B}$: $\vec{P}(\hat{\mathbf{n}}) = \vec{\nabla}A + \vec{\nabla} \times \vec{B}$. The gradient (i.e., curl-free) and curl components can be decomposed by taking the divergence or curl of $\vec{P}(\hat{\mathbf{n}})$ respectively. Density perturbations are scalar metric perturbations, so they have no handedness. They can therefore produce no curl. On the other hand, gravitational waves *do* have a handedness so they can (and we have shown that they do) produce a curl. This therefore provides a way to detect the inflationary stochastic gravity-wave background and thereby test

the relations between the inflationary observables. It should also allow one to determine (or at least constrain in the case of a nondetection) the height of the inflaton potential.

More precisely, the Stokes parameters $Q(\hat{\mathbf{n}})$ and $U(\hat{\mathbf{n}})$ (where Q and U are measured with respect to the polar $\hat{\theta}$ and azimuthal $\hat{\phi}$ axes) which specify the linear polarization in direction $\hat{\mathbf{n}}$ are components of a 2×2 symmetric trace-free (STF) tensor,

$$\mathcal{P}_{ab}(\hat{\mathbf{n}}) = \frac{1}{2} \begin{pmatrix} Q(\hat{\mathbf{n}}) & -U(\hat{\mathbf{n}}) \sin\theta \\ -U(\hat{\mathbf{n}}) \sin\theta & -Q(\hat{\mathbf{n}}) \sin^2\theta \end{pmatrix}, \tag{3}$$

where the subscripts ab are tensor indices. Just as the temperature is expanded in terms of spherical harmonics, the polarization tensor can be expanded,[15]

$$\frac{\mathcal{P}_{ab}(\hat{\mathbf{n}})}{T_0} = \sum_{lm} \left[a^{\mathrm{G}}_{(lm)} Y^{\mathrm{G}}_{(lm)ab}(\hat{\mathbf{n}}) + a^{\mathrm{C}}_{(lm)} Y^{\mathrm{C}}_{(lm)ab}(\hat{\mathbf{n}}) \right], \tag{4}$$

in terms of the tensor spherical harmonics $Y^{\mathrm{G}}_{(lm)ab}$ and $Y^{\mathrm{C}}_{(lm)ab}$, which are a complete basis for the "gradient" (i.e., curl-free) and "curl" components of the tensor field, respectively. The mode amplitudes are given by

$$a^{\mathrm{G}}_{(lm)} = \frac{1}{T_0} \int d\hat{\mathbf{n}}\, \mathcal{P}_{ab}(\hat{\mathbf{n}})\, Y^{\mathrm{G}\,ab\,*}_{(lm)}(\hat{\mathbf{n}}), \qquad a^{\mathrm{C}}_{(lm)} = \frac{1}{T_0} \int d\hat{\mathbf{n}}\, \mathcal{P}_{ab}(\hat{\mathbf{n}})\, Y^{\mathrm{C}\,ab\,*}_{(lm)}(\hat{\mathbf{n}}). \tag{5}$$

Here T_0 is the cosmological mean CMB temperature and Q and U are given in brightness temperature units rather than flux units. Scalar perturbations have no handedness. Therefore, they can produce no curl, so $a^{\mathrm{C}}_{(lm)} = 0$ for scalar modes. On the other hand tensor modes *do* have a handedness, so they produce a non-zero curl, $a^{\mathrm{C}}_{(lm)} \neq 0$.

A given inflationary model predicts that the $a^{\mathrm{X}}_{(lm)}$ are gaussian random variables with zero mean, $\left\langle a^{\mathrm{X}}_{(lm)} \right\rangle = 0$ (for $\mathrm{X}, \mathrm{X}' = \{\mathrm{T}, \mathrm{G}, \mathrm{C}\}$) and covariance $\left\langle \left(a^{\mathrm{X}'}_{(l'm')}\right)^* a^{\mathrm{X}}_{(lm)} \right\rangle = C_l^{\mathrm{XX}'} \delta_{ll'} \delta_{mm'}$. Parity demands that $C_l^{\mathrm{TC}} = C_l^{\mathrm{GC}} = 0$. Therefore the statistics of the CMB temperature-polarization map are completely specified by the four sets of moments, C_l^{TT}, C_l^{TG}, C_l^{GG}, and C_l^{CC}. Also, as stated above, only tensor modes will produce nonzero C_l^{CC}.

To illustrate, Fig. 4 shows the four temperature-polarization power spectra. The dotted curves correspond to a COBE-normalized inflationary model with cold dark matter and no cosmological constant ($\Lambda = 0$), Hubble constant (in units of 100 km sec^{-1} Mpc^{-1}) $h = 0.65$, baryon density $\Omega_b h^2 = 0.024$, scalar spectral index $n_s = 1$, no reionization, and no gravitational waves. The solid curves show the spectra for a COBE-normalized stochastic gravity-wave background with a flat scale-invariant spectrum ($h = 0.65$, $\Omega_b h^2 = 0.024$, and $\Lambda = 0$) in a critical-density Universe. Note that the panel for C_l^{CC} contains no dotted curve since scalar perturbations produce no C polarization component. The dashed curve in the CC panel shows the tensor spectrum for a reionized model with optical depth $\tau = 0.1$ to the surface of last scatter.

As with a temperature map, the sensitivity of a polarization map to gravity waves will be determined by the instrumental noise and fraction of sky covered, and by the angular resolution. Suppose the detector sensitivity is s and the experiment lasts for t_{yr} years with an angular resolution better than 1°. Suppose further that we consider only the CC component of the polarization in our analysis. Then the smallest tensor amplitude $\mathcal{T}_{\mathrm{min}}$ to which the experiment will be sensitive at 1σ is[17]

$$\frac{\mathcal{T}_{\mathrm{min}}}{6 C_2^{\mathrm{TT}}} \simeq 5 \times 10^{-4} \left(\frac{s}{\mu\mathrm{K}\sqrt{\mathrm{sec}}} \right)^2 t_{\mathrm{yr}}^{-1}. \tag{6}$$

Thus, the curl component of a full-sky polarization map is sensitive to inflaton potentials $V \gtrsim 5 \times 10^{-15} t_{\mathrm{yr}}^{-1}\ (s/\mu\mathrm{K}\sqrt{\mathrm{sec}})^2$. Improvement on current constraints with only the curl polarization component requires a detector sensitivity $s \lesssim 40\, t_{\mathrm{yr}}^{1/2}\, \mu\mathrm{K}\sqrt{\mathrm{sec}}$. For comparison, the

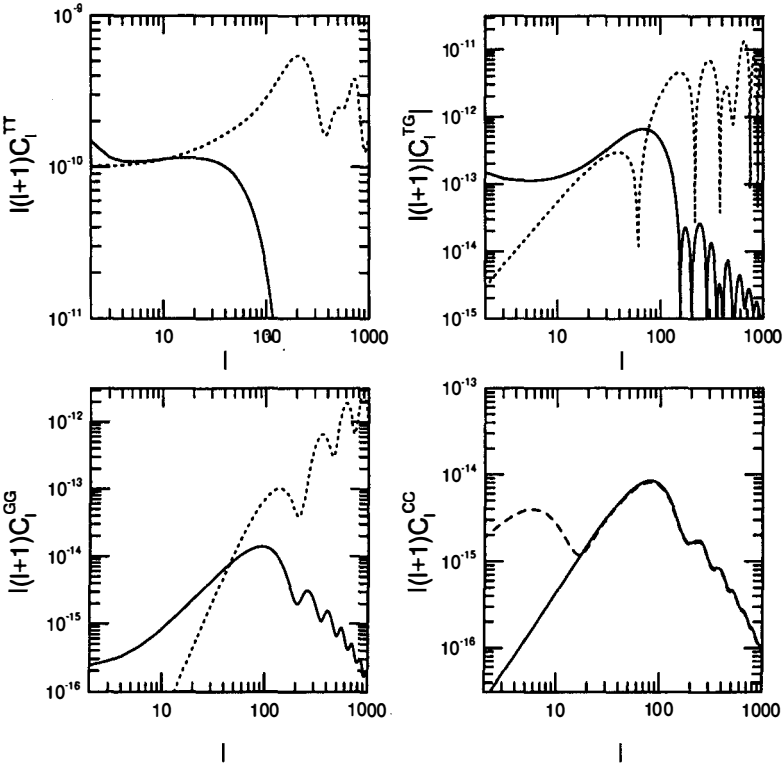

Figure 4: Theoretical predictions for the four nonzero CMB temperature-polarization spectra as a function of multipole moment l. The dashed line in the lower right panel shows a reionized model with optical depth $\tau = 0.1$ to the surface of last scatter.

detector sensitivity of MAP will be $s = \mathcal{O}(100\,\mu\mathrm{K}\sqrt{\mathrm{sec}})$. However, Planck may conceivably get sensitivities around $s = 25\,\mu\mathrm{K}\sqrt{\mathrm{sec}}$.

Eq. 6 is the sensitivity obtained by using only the curl component of the polarization, which provides a model-independent probe of the tensor signal. However, if we are willing to consider specific models for the tensor and scalar spectra, the sensitivity to a tensor signal may be improved somewhat by considering the predictions for the full temperature/polarization auto- and cross-correlation power spectra.[17]

For example, Fig. 5 shows the 1σ sensitivity $\sigma_{\mathcal{T}}$ to the amplitude $\mathcal{T}$ of a flat ($n_t = 0$) tensor spectrum as a function of detector sensitivity s for an experiment which maps the CMB temperature and polarization on the full sky for one year with an angular resolution of 0.5°. The dotted curve shows the results obtained by fitting only the TT moments; the dashed curve shows results obtained by fitting only the CC moments; and the solid curve shows results obtained by fitting all four nonzero sets of moments.

In Fig. 5, we have assumed that the spectra are fit only to $\mathcal{S}$, $\mathcal{T}$, and n_s, and the parameters of the cosmological model are those used in Fig. 5. If one fits to more cosmological parameters (e.g., Ω_b, h, Λ, etc.) as well, the the sensitivity from the temperature moments, important for larger s, is degraded. However, the sensitivity due to the CC component, which controls the total sensitivity for smaller s, is essentially unchanged. Again, this is because the CC signal is very model-independent.

For detectors sensitivities $s \gtrsim 20\,\mu\mathrm{K}\sqrt{\mathrm{sec}}$, the tensor-mode detectability for the three-parameter fit shown in Fig. 5 comes primarily from the temperature map, although polarization does provides some incremental improvement. However, if the data are fit to more cosmological parameters (not shown), the polarization improves the tensor sensitivity even for $s \gtrsim 20\,\mu\mathrm{K}\sqrt{\mathrm{sec}}$. In any case, the sensitivity to tensor modes comes almost entirely from the curl of the polarization for detector sensitivities $s \lesssim 10\,\mu\mathrm{K}\sqrt{\mathrm{sec}}$. Since the value of s for Planck will be somewhat higher, it will likely require a more sensitive future experiment to truly capitalize on the model-independent curl signature of tensor modes.

Finally, it should be noted that even a small amount of reionization will significantly increase the polarization signal at low l,[18] as shown in the CC panel of Fig. 4 for $\tau = 0.1$. With such a level of reionization (which may be expected in CDM models, as discussed in the following Section), the sensitivity to the tensor amplitude is increased by more than a factor of 5 over that in Eq. (6). This level of reionization (if not more) is expected in cold dark matter models,[6,19,20] so if anything, Eq. (6) and Fig. 5 provide conservative estimates.

5 The Ostriker-Vishniac Effect and the Epoch of Reionization

Although most of the matter in CDM models does not undergo gravitational collapse until relatively late in the history of the Universe, some small fraction of the mass is expected to collapse at early times. Ionizing radiation released by this early generation of star and/or galaxy formation will partially reionize the Universe, and these ionized electrons will re-scatter at least some cosmic microwave background (CMB) photons after recombination at a redshift of $z \simeq 1100$. Theoretical uncertainties in the process of star formation and the resulting ionization make precise predictions of the ionization history difficult. Constraints to the shape of the CMB blackbody spectrum and detection of CMB anisotropy at degree angular scales suggest that if reionization occurred, the fraction of CMB photons that re-scattered is small. Still, estimates show that even if small, at least some reionization is expected in CDM models:[6,19,20] for example, the most careful recent calculations suggest a fraction $\tau_r \sim 0.1$ of CMB photons were re-scattered.[20]

Scattering of CMB photons from ionized clouds will lead to anisotropies at arcminute separations below the Silk-damping scale (the Ostriker-Vishniac effect).[21,22] These anisotropies arise

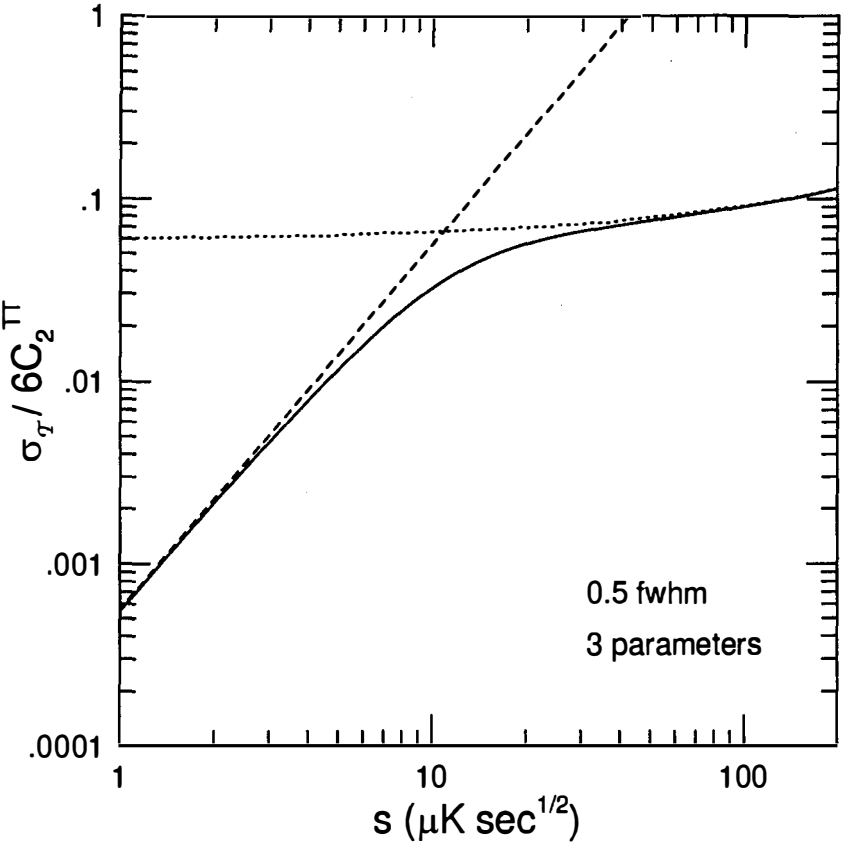

Figure 5: Results for the 1σ sensitivity σ_T to the amplitude T of a flat ($n_t = 0$) tensor spectrum as a function of detector sensitivity s for an experiment which maps the CMB temperature and polarization on the full sky for one year with an angular resolution of 0.5°. The vertical axis is in units of the temperature quadrupole. See text for more details.

at higher order in perturbation theory and are therefore not included in the usual Boltzmann calculations of CMB anisotropy spectra. The level of anisotropy is expected to be small and it has so far eluded detection. However, these anisotropies may be observable with forthcoming CMB interferometry experiments[23] that probe the CMB power spectrum at arcminute scales.

Fig. 6 [22] shows the predicted temperature-anisotropy spectrum from the Ostriker-Vishniac effect for a number of ionization histories. The ionization histories are parameterized by an ionization fraction x_e and a redshift z_r at which the Universe becomes reionized. The optical depth τ to the standard-recombination surface of last scatter can be obtained from these two parameters.

Reionization damps the acoustic peaks in the primary-anisotropy spectrum by $e^{-2\tau}$, as shown in Fig. 6, but this damping is essentially independent of the details of the ionization history. That is, any combination of x_e and z_r that gives the same τ has the same effect on the primary anisotropies. So although MAP and Planck will be able to determine τ from this damping, they will not constrain the epoch of reionization. On the other hand, the secondary anisotropies (the Ostriker-Vishniac anisotropies) produced at smaller angular scales in reionized models *do* depend on the ionization history. For example, although the top and bottom dashed curves in Fig. 6 both have the same optical depth, they have different reionization redshifts ($z_r = 20$ and $z_r = 57$). Therefore, if MAP and Planck determine τ, the amplitude of the Ostriker-Vishniac anisotropy determines the reionization epoch.[22]

In a flat Universe, CDM models normalized to cluster abundances produce rms temperature anisotropies of 0.8–2.4 μK on arcminute angular scales for a constant ionization fraction of unity, whereas an ionization fraction of 0.2 yields rms anisotropies of 0.3–0.8 μK.[22] In an open and/or high-baryon-density Universe, the level of anisotropy is somewhat higher. The signal in some of these models may be detectable with planned interferometry experiments.[22]

6 Discussion

If MAP and Planck find a CMB temperature-anisotropy spectrum consistent with a flat Universe and nearly–scale-free primordial adiabatic perturbations, then the next step will be to isolate the gravity waves with the polarization of the CMB. If inflation has something to do with grand unification, then it is possible that Planck's polarization sensitivity will be sufficient to see the polarization signature of gravity waves. However, it is also quite plausible that the height of the inflaton potential may be low enough to elude detection by Planck. If so, then a subsequent experiment with better sensitivity to polarization will need to be done.

Inflation also predicts that the distribution of primordial density perturbations is gaussian, and this can be tested with CMB temperature maps and with the study of the large-scale distribution of galaxies. Since big-bang nucleosynthesis predicts that the baryon density is $\Omega_b \lesssim 0.1$ and inflation predicts $\Omega = 1$, another prediction of inflation is a significant component of nonbaryonic dark matter. This can be either in the form of vacuum energy (i.e., a cosmological constant), and/or some new elementary particle. Therefore, discovery of particle dark matter could be interpreted as evidence for inflation.

Large-scale galaxy surveys will soon map the distribution of mass in the Universe today, and CMB experiments will shortly determine the mass distribution in the early Universe. The next step will be to fill in the precise history of structure formation in the "dark ages" after recombination but before redshifts of a few. Reconstruction of this epoch of cosmic history will likely require amalgamation of the complementary information provided by a number observations in several wavebands. Detection of the secondary CMB anisotropies at arcminute scales produced by scattering from reionized clouds will provide an indication of the epoch of reionization, and therefore the epoch at which structures first undergo gravitational collapse in the Universe.[22]

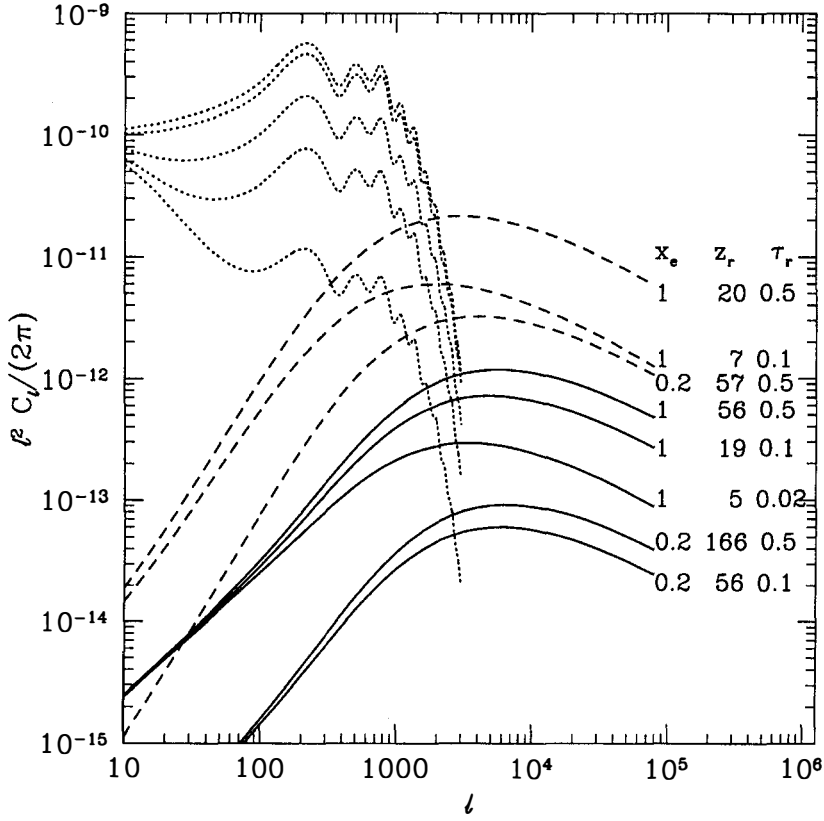

Figure 6: Multipole moments for the Ostriker-Vishniac effect for the COBE-normalized canonical standard-CDM model ($\Omega = 1$, $h = 0.5$, $n = 1$, $\Omega_b h^2 = 0.0125$), for a variety of ionization histories.as listed. We also show predictions for several open high-baryon-density models with the same x_e and τ_r, normalized to the cluster abundance, with dashed curves. The dotted curves show the primary anisotropy for this model for $\tau_r = 0.0$, 0.1, 0.5, 1, and 2, from top to bottom.

Acknowledgments

This work was supported by the U.S. D.O.E. under contract DEFG02-92-ER 40699, NASA NAG5-3091, and the Alfred P. Sloan Foundation at Columbia.

References

1. A.H. Guth, *Phys. Rev.* D **28**, 347 (1981); A.D. Linde, *Phys. Lett.* B **108**, 389 (1982); A. Albrecht and P.J. Steinhardt, *Phys. Rev. Lett.* **48**, 1220 (1982).
2. J.M. Bardeen, P.J. Steinhardt, and M.S. Turner, *Phys. Rev.* D **28**, 679 (1983); A.A. Starobinsky, *Phys. Lett.* B **117**, 175 (1982); A.H. Guth and S.-Y. Pi, *Phys. Rev. Lett.* **49**, 1110 (1982); S.W. Hawking, *Phys. Lett.* B **115**, 295 (1982).
3. L.F. Abbott and M. Wise, *Nucl. Phys.* B **244**, 541 (1984).
4. A.R. Liddle and D. Lyth, *Phys. Lett.* B **291**, 391 (1992); R.L. Davis *et al.*, *Phys. Rev. Lett.* **69**, 1856 (1992); M.S. Turner, *Phys. Rev.* D **48**, 3502 (1993); F. Lucchin, S. Matarrese, and S. Mollerach, *Astrophys. J. Lett.* **401**, L49 (1992); J.E. Lidsey and P. Coles, *Mon. Not. R. Astron. Soc.* **258**, L57 (1992); F.C. Adams *et al.*, *Phys. Rev.* D **47**, 426 (1993); J. Lidsey *et al.*, *Rev. Mod. Phys.* **69**, 373 (1997).
5. U.-L. Pen, U. Seljak, and N. Turok, *Phys. Rev. Lett.* **79**, 1611 (1997); A. Albrecht, R.A. Battye, and J. Robinson, *Phys. Rev. Lett.* **79**, 4736 (1997).
6. M. Kamionkowski, D.N. Spergel, and N. Sugiyama, *Astrophys. J. Lett.* **426**, L57 (1994).
7. C.H. Lineweaver and D. Barbosa, *Astrophys. J.*, in press (1998); S. Hancock *et al.*, astro-ph/9708254.
8. http://map.gsfc.nasa.gov.
9. http://astro.estec.esa.nl/SA-general/Projects/Planck/
10. G. Jungman, M. Kamionkowski, A. Kosowsky, and D.N. Spergel, *Phys. Rev. Lett.* **76**, 1007 (1996).
11. G. Jungman, M. Kamionkowski, A. Kosowsky, and D.N. Spergel, *Phys. Rev.* D **54**, 1332 (1996).
12. J.R. Bond, G. Efstathiou, and M. Tegmark, astro-ph/9702100; M. Zaldarriaga, D.N. Spergel, and U. Seljak, *Astrophys. J.* **488**, 1 (1997).
13. W. Hu and M. White, *Phys. Rev. Lett.* **77**, 1687 (1996).
14. M. Kamionkowski, A. Kosowsky, and A. Stebbins, *Phys. Rev. Lett.* **78**, 2058 (1997).
15. M. Kamionkowski, A. Kosowsky, and A. Stebbins, *Phys. Rev.* D **55**, 7368 (1997).
16. U. Seljak and M. Zaldarriaga, *Phys. Rev. Lett.* **78**, 2054 (1997); M. Zaldarriaga and U. Seljak, *Phys. Rev.* D **55**, 1830 (1997).
17. M. Kamionkowski and A. Kosowsky, *Phys. Rev.* D **67**, 685 (1998).
18. M. Zaldarriaga, *Phys. Rev.* D **55**, 1822 (1997).
19. M. Tegmark, J. Silk, and A. Blanchard, *Astrophys. J.* **420**, 484 (1994).
20. Z. Haiman and A. Loeb, *Astrophys. J.* **483**, 21 (1997).
21. J.P. Ostriker and E.T. Vishniac, *Astrophys. J. Lett.* **306**, L51 (1986); E.T. Vishniac, *Astrophys. J.* **322**, 597 (1987); G. Efstathiou, in *Large-Scale Motions*, ed. V. Rubin and S.J. Coyne (Princeton University Press, Princeton, 1988); S. Dodelson and J.M. Jubas, *Astrophys. J.* **439**, 503 (1995); W. Hu, D. Scott, and J. Silk, *Phys. Rev.* D **49**, 648 (1994); W. Hu and M. White, *Astron. Astrophys.* **315**, 33 (1996).
22. A.H. Jaffe and M. Kamionkowski, astro-ph/9801022, submitted to *Phys. Rev.* D.
23. M. White, J. Carlstrom, and M. Dragovan, astro-ph/9712195.

Probing Cosmic topology using CMB anisotropy

Tarun Souradeep, Dmitry Pogosyan and J. Richard Bond
Canadian Institute for Theoretical Astrophysics,
University of Toronto, ON M5S 3H8, Canada

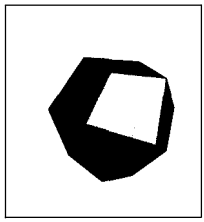

The measurements of CMB anisotropy have opened up a window for probing the global topology of the universe on length scales comparable to and beyond the Hubble radius. We have developed a new method for calculating the CMB anisotropy in models with nontrivial topology and apply it to open universe models with compact spatial topology. We conduct a Bayesian probability analysis for a selection of models which confronts the theoretical pixel-pixel temperature correlation function with the COBE–DMR data. Our results demonstrate that strong constraints on compactness arise: if the universe is small compared to the 'horizon' size, correlations appear in the maps that are irreconcilable with the observations.

The remarkable degree of isotropy of the cosmic microwave background (CMB) points to homogeneous and isotropic Friedmann-Robertson-Walker (FRW) models for the universe. This argument is a purely local one and does not refer to the global topological structure of the universe. In fact, in the absence of spatially inhomogeneous perturbations, a FRW model predicts an isotropic CMB regardless of the global topological structure. However, the observed large scale structure in the universe and CMB anisotropy allude to the existence of small spatially inhomogeneous primordial perturbations. The global topology of the universe does affect the observable properties of the CMB anisotropy. In compact universe models, the finite spatial size usually implies a suppression of the power in large scale perturbations and consequently the CMB anisotropy is suppressed on angular scales above a characteristic angle related to size of the universe. Another signature is the breaking of statistical isotropy in characteristic patterns determined by the photon geodesic structure of the compact manifold.

Much recent astrophysical data suggest the cosmological density parameter, Ω_0, is subcritical.[1] In the absence of a cosmological constant, this would imply a hyperbolic spatial geometry for the universe (commonly referred to as the 'open' universe in cosmological literature). The topologically trivial (simply connected) hyperbolic 3-space, $\mathcal{H}^3$, is non-compact and has infinite size. There are numerous theoretical motivations, however, to favor a spatially compact

universe.[2] To reconcile this with a flat or hyperbolic geometry, consideration of models with non-trivial topology is required. A compact cosmological model is constructed by identifying points on the standard infinite flat or hyperbolic FRW space under the action of a suitable discrete subgroup, Γ, of the full isometry group, G, of the FRW space. The FRW spatial hypersurface is the *universal cover*, tiled by copies of the compact space, $\mathcal{M}$. Any point $\mathbf{x}$ of the compact space has an image $\mathbf{x}_i = \gamma_i \mathbf{x}$ in each tile on the universal cover, where $\gamma_i \in \Gamma$.

For Gaussian perturbations, the angular correlation function, $C(\hat{q}, \hat{q}')$, of the CMB temperature fluctuations in two directions $\hat{q}$ and $\hat{q}'$ in the sky completely encodes the CMB anisotropy predictions of a model. The dominant contribution to the anisotropy in the CMB temperature measured with wide-angle beam ($\theta_{\rm FWHM} \gtrsim 2^\circ\, \Omega_0^{1/2}$) comes from the cosmological metric perturbations through the Sachs-Wolfe effect. The angular correlation function of the CMB anisotropy, $C(\hat{q}, \hat{q}')$, depends on the spatial two point correlation function, $\xi_\Phi \equiv \langle \Phi(\mathbf{x}, \tau_{\rm rec}) \Phi(\mathbf{x}', \tau_{\rm rec}) \rangle$ of the gravitational potential, Φ, on the hypersurface of last scattering.[a] To calculate the spatial correlation function on a compact hyperbolic (CH) manifold, described by the corresponding Γ, we have developed a general technique – the *method of images*, which evades the difficult problem[b] of solving for eigenfunctions of the Laplacian on these manifolds.[3] Using the method of images, the spatial correlation function, ξ_Φ^c, between two points $\mathbf{x}$ and $\mathbf{x}'$ on a compact space of volume $V_\mathcal{M}$ can be expressed as[4]

$$\xi_\Phi^c(\mathbf{x}, \mathbf{x}') = \lim_{r_* \to \infty} \sum_{r_j < r_*} \xi_\Phi^u(r_j) - \frac{4\pi}{V_\mathcal{M}} \int_0^{r_*} dr\, \sinh^2 r\, \xi_\Phi^u(r)\,, \qquad r_j = d(\mathbf{x}, \gamma_j \mathbf{x}')\,. \tag{1}$$

a regularized sum over the correlation function, ξ_Φ^u, on the universal cover evaluated between $\mathbf{x}$ and images $\gamma_i \mathbf{x}'$ of $\mathbf{x}'$. Numerically it suffices to evaluate the above expression up to r_* a few times the curvature radius, d_c, to reach a convergent result. We then integrate ξ_Φ^c along photon trajectories to get $C(\hat{q}, \hat{q}')$ which includes both surface and integrated (ISW) Sachs-Wolfe effects.

The CMB photons can be viewed as propagating to the observer from a 2-sphere of radius, R_H, – the sphere of last scattering (SLS). In contrast to the topologically trivial models, widely separated pixels in compact spaces can still have strong correlations if in the sum over images, eq. (1), one of the images of $\mathbf{x}'$ happens to be close to $\mathbf{x}$. The dependence of the spatial correlations on the anisotropic distribution of images leads to a characteristic statistical anisotropy in the CMB in compact models. These effects are pronounced when the compact space fits well within the SLS, but persist at an observable level even when $V_\mathcal{M}$ is comparable to (or somewhat bigger than) $V_{\rm SLS}$, the volume of SLS. If SLS does not fit completely inside a single tile – a copy of the compact space, the CMB temperature values will be identical along pairs of circles if temperature fluctuations are dominated by the surface terms at the SLS.[5] This pattern of matched circles is one specific manifestation of the angular patterns in $C(\hat{q}, \hat{q}')$.

Figure 1 compares theoretical realizations of the CMB anisotropy in a selection of CH models with the COBE–DMR data. In this work, the six COBE–DMR four-year maps[6] are first compressed into a (A+B)(31+53+90 GHz) weighted-sum map, with the customized Galactic cut advocated by the DMR team. There is no effective loss of information when we do further data compression by using $5.2^\circ \times 5.2^\circ$ pixels.[7] The theory and data maps have been postprocessed so as to facilitate a fair visual comparison. The incompatibility of models with small $V_\mathcal{M}/V_{\rm SLS}$ (SCH-$\Omega_0 = 0.3, 0.6$) is visually obvious: the best fit amplitudes are high which is reflected in the steeper hot and cold features. Although, SCH-$\Omega_0 = 0.9$ and LCH-$\Omega_0 = 0.6$ do not appear grossly inconsistent, the intrinsic anisotropic correlation pattern is at odds with the data.

[a] Other effects which contribute to the CMB anisotropy at smaller angular scales can also be approximated in terms of spatial correlation of quantities defined on the hypersurface of last scattering.[4]

[b] The correlation function is usually computed using a mode function expansion. However, obtaining closed form expressions for eigenfunctions of the Laplacian may not be possible beyond the simplest topologies and even numerical estimation is known to be difficult in CH spaces.

We have carried out a full Bayesian analysis of the probability of the CH models given the COBE–DMR 4yr data. In Table 1 we present the *relative likelihood* of the selected models to that of the infinite, $\mathcal{H}^3$, model with the same Ω_0. (The COBE data alone does not strongly differentiate between the infinite hyperbolic models with different Ω_0.) The anisotropy of the theoretical $C(\hat{q}, \hat{q}')$ causes the likelihood of compact models to vary significantly with the orientation of the space with respect to the sky, depending on how closely the features in the single data realization available match (or mismatch) the pattern in $C(\hat{q}, \hat{q}')$. Some optimal orientations may also have the "ugly" correlation features hidden in the Galactic cut. We analyzed 24 different orientations for each of our models and found that only the model with $V_{\mathcal{M}} > V_{\rm SLS}$ (LCH-$\Omega_0 = 0.8$) cannot be excluded (at one orientation this model is even preferable to standard CDM; this raises a question of the statistical significance of any detection of intrinsic anisotropy of a space when only a single realization of data is available).

Similar conclusions were reached by some of the authors (JRB, DP and I. Sokolov [8]) for flat toroidal models. Comparison of the full angular correlation with COBE data led to a much stronger limit on the compactness of the universe than limits from other methods. [9] The main result of the analysis was that $V_{\rm SLS}/V_{\mathcal{M}} < 0.4$ at 95% *CL* for the equal-sided 3-torus. For non compact 1-torus, the constraint on the most compact dimension is not quite as strong.

In summary, our results demonstrate that the COBE data can put strong constraints on the compact models of the universe. If the universe is small compared to the 'horizon' size, correlations appear in the maps that are irreconcilable with the large angle COBE–DMR data.

Table 1: The Log-likelihoods of the compact hyperbolic models relative to the infinite models with same Ω_0 are listed below. The likelihoods are calculated by comparison with COBE–DMR data. The three columns of Log-likelihood ratios correspond to the best, second best and worst values that we have obtained amongst 24 different rotations of the compact space relative to the sky. The number in brackets gives a convenient, albeit crude, translation to gaussian likelihood. Only the last model can be reconciled with the COBE–DMR data.

Topology	Ω_0	$V_{\rm SLS}/V_{\mathcal{M}}$	Relative Log. Likelihood (Gaussian approx.)		
			Orientation		
			'best'	'second best'	'worst'
$m004(-5,1)$	0.3	153.4	-35.5 (8.4σ)	-35.7 (8.4σ)	-57.9 (10.8σ)
	0.6	19.3	-22.9 (6.8σ)	-23.3 (6.8σ)	-49.4 (9.9σ)
$V_{\mathcal{M}}/d_c^3 = 0.98$	0.9	1.2	-4.4 (3.0σ)	-8.5 (4.1σ)	-37.4 (8.6σ)
$v3543(2,3)$	0.6	2.9	-3.6 (2.7σ)	-5.6 (3.3σ)	-31.0 (7.9σ)
$V_{\mathcal{M}}/d_c^3 = 6.45$	0.8	0.6	2.5 (2.2σ)	-0.8 (1.3σ)	-12.6 (5.0σ)

References

1. Dekel, A., Burnstein, D., & White, S.D.M. 1996, in *Critical Dialogues in Cosmology*, ed. N.Turok, (World Scientific).
2. Ellis, G.F.R. 1971, Gen. Rel. Grav., **2**, 7; Lachieze-Rey, M. & Luminet, J.-P. 1995, Phys. Rep., **25**, 136; Cornish, N. J., Spergel, D. N. & Starkman, G. D. 1996, Phys. Rev. Lett. **77**, 215
3. Bond, J. R., Pogosyan, D. & Souradeep, T. 1998, in: *Proceedings of the XVIIIth Texas Symposium on Relativistic Astrophysics*, ed. A. Olinto, J. Frieman & D. N. Schramm, (World Scientific).
4. Bond, J. R., Pogosyan, D. & Souradeep, T. 1998, Class. Quantum Grav. (in press), *Proc. CWRU conference on 'Cosmology and Topology'*; *ibid.*, preprint.
5. Cornish, N. J., Spergel, D. N. & Starkman, G. D. 1996, preprint gr-qc/9602039.
6. Bennett, C. *et al* 1996, Ap. J. Lett., **464**, L1; and 4-year DMR references therein.
7. Bond, J. R. 1994, Phys. Rev. Lett., **74**, 4369.
8. Bond, J. R. 1997, in *Proc. of the XVIth Moriond Astrophysics Meeting*, ed. F. R. Bouchet *et al.*, (Editions Frontieres, France); Bond, J. R. 1998, Proc. Natl. Acad. Sci. USA, **95**, 35.
9. Sokolov, I.Y. 1993, JETP Lett. **57**, 617; Starobinsky, A.A. 1993, JETP Lett. **57**, 622; Stevens, D., Scott, D. & Silk, J. 1993, Phys. Rev. Lett. **71**, 20; de Oliveira Costa, A. & Smoot, G.F. 1995, Ap.J. **448**, 477; de Oliveira Costa, A., Smoot, G.F. & Starobinsky, A.A. 1996, Ap.J. **468**, 457

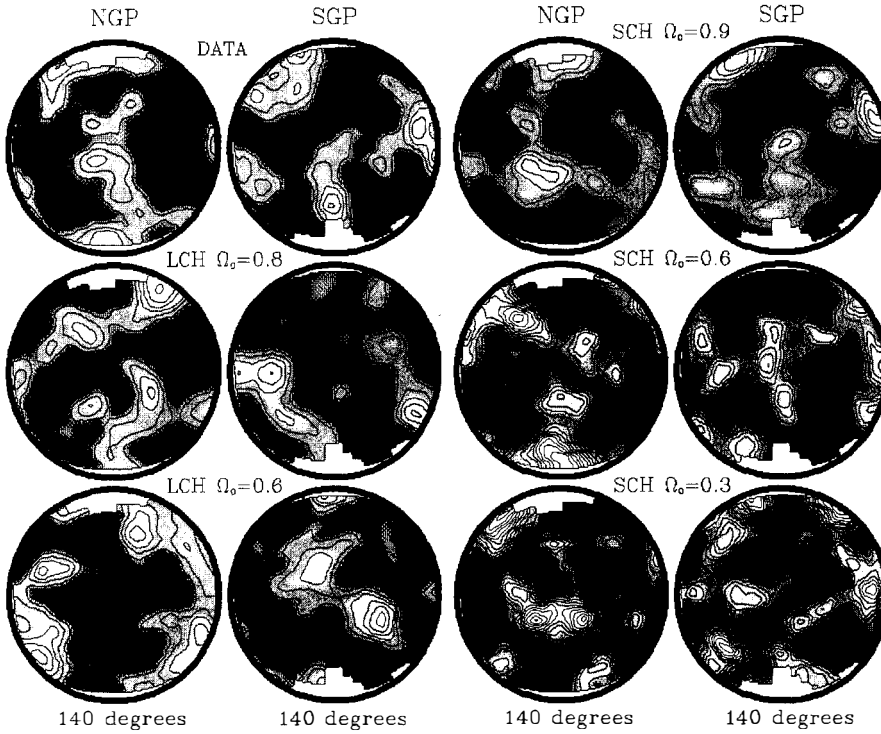

Figure 1: The figure consists of two columns of CMB sky-maps showing a pair of 140° diameter hemispherical caps each, centered on the South (SGP) and North (NGP) Galactic Poles, respectively. The map labeled DATA, shows the COBE-DMR 53+90+31 GHz A+B data after Wiener filtering assuming a standard CDM model, normalized to COBE. The rest of the five maps are one random realization of the CMB anisotropy in two examples of compact hyperbolic (CH) spaces for several values of Ω_0 based on our theoretical calculations of $C(\hat{q}, \hat{q}')$ convolved with the COBE-DMR beam. Both surface and integrated (ISW) Sachs-Wolfe effects have been included in $C(\hat{q}, \hat{q}')$. No noise was added. The power was normalized to best match the COBE data. The theoretical sky was optimally filtered using the COBE experimental noise to facilitate comparison with data. The maps labeled L(arge)CH refer to the CH model $v3543(2,3)$. The right column shows the CMB maps for the S(mall)CH model $m004(-5,1)$. (The model number associated with the topology corresponds to that of the census of CH spaces in the Geometry center, Univ. of Minnesota: SCH is one of the smallest and LCH is one of the largest spaces in the census). LCH with $\Omega_0 = 0.8$ is compatible with the data with a suitable choice of orientation while all the others are ruled out (See Table 1). For all six maps, the average, dipole and quadrupole of the $|b| > 20°$ sky were also removed and a 20° Galactic latitude cut was used, with extra cuts to remove known regions of Galactic emission proposed by the COBE team accounting for the ragged edges. The contours are linearly spaced at 15 μK steps. The maps have been smoothed by a 1.66° Gaussian filter.

TOPOLOGICAL DEFECTS WITH BROKEN SCALE INVARIANCE

Ue-Li Pen
Harvard-Smithsonian Center for Astrophysics

Defect models have recently been declared dead[1], because they predict microwave background and matter fluctuations grossly out of line with what we see. In this talk we apply the fact that many defects are automatically destroyed at the time of radiation-matter transition, thus resurrecting the defects model. Moreover, the resurrected version predicts a cosmological constant, explains the apparent excess of hot clusters and the non-Gaussianity observed in galaxy surveys. If this model is correct, then the MAP and PLANCK missions will not measure what people expect them to (oscillations); rather, they will measure a broad hump.

The traditional class of scale invariant defect models has severe problems[2]. They do not explain the rise in fluctuation amplitude at scales of a few degrees, and the slope of the perturbations is at conflict with the observed matter power spectrum. We show here that global topological defects are generically destroyed at the matter-radiation transition at a cosmic age of 100000 years. In this case, instead of being at great discrepancy with the cosmic microwave background radiation fluctuations, this model in fact correctly explains several hitherto mysterious phenomena. The most recent supernovae search[3,4], concordance arguments[5] and direct angular diameter distance measurements[6] have suggested that the universe is filled with a cosmological constant. Its existence is at best mysterious in most cosmological models. The new defect models, however, predict such a cosmological constant from the COBE observations.

Let us now address the decay of global defects at matter-radiation equality. In modern particle physics, all interactions which are not forbidden actually occur. On this ground, one generically expects couplings between gravity and other quantum fields which are stronger than just the space time curvature. Global fields experience couplings of the form $\epsilon\phi_1^\dagger\phi_2 R$, where ϵ is a dimensionless coupling constant of order unity, and R is the scalar curvature. In the radiation epoch of the universe, $R = 0$, so the coupling has no dynamical effect. But when the universe enters matter domination, this coupling will generally destroy the exact symmetry which gave rise to the defects, and they will collapse coherently. During the onset of collapse, the vacuum energy contributed by the new coupling will boost the power on the largest scales, making the power spectrum more consistent with the observed excess of large scale power. Today there would be no defects remaining. At late times when the cosmological constant begins to dominate, fluctuations decay, thus inducing large scale CMB anisotropies. The COBE detection in this model would be solely due to relatively local, sub-horizon, fluctuations at the ca 100 Mpc scale, whose potential decays at late time through the influence of a cosmological constant. Since linear perturbations do not generate any late time anisotropies in a flat matter dominated universe, the COBE detection in fact predicts a cosmological constant. This is in contrast to inflationary models, where a cosmological constant is disfavoured by the COBE observations[7].

These defect models have two free parameters. One is the symmetry breaking scale ϕ_0, and

the second is its coupling to the Riemann scalar ϵ. From the velocity dispersion in clusters of galaxies we expect $\phi_0/m_{\rm planck} \sim v^2/c^2 \sim 10^{-5}$, which would also be related to the COBE fluctuations. This energy scale suggests that the defect would be relicts of the breaking of the Grand-Unified-Theory in the early universe. A predictive property of this model is the non-Gaussianity of fluctuations. The strongest constraints arises from the statistics of rich clusters[8]. Several clusters with temperatures above 12 keV have been found[9], and a recent cluster with a temperature of 17 keV[10] has been discovered. The existence of these very hot clusters is becoming an enigma for any Gaussian cosmological model. In non-Gaussian defect models, one would expect a larger proportion of high temperature clusters relative to low temperature ones. The recent Las Campanas galaxy survey discovered features in the two dimensional galaxy power spectrum which is inconsistent with Gaussianity[11]. Such signs of non-Gaussianity are generically predicted in these defect models.

In the defect scenario, the small scale CMB experiments MAP and Planck will not measure the multiple oscillations expected from adiabatic perturbations imprinted before the big bang, as predicted by inflation. Instead, the degree scale anisotropies are caused by the incoherent properties of global defects[2]. A sample angular power spectrum in such a scenario is shown in Figure 1. The effect of these broken defects is simulated using CMBFAST[12] by truncating the primordial power at matter-radiation equality, which corresponds to the peak in the power. This prediction is heuristic, since decoherence, vector modes and other complications are only modelled in a simple fashion, but one would expect the qualitative results to remain similar. Without the oscillations, it will be very difficult to reconstruct cosmological parameters accurately. On the other hand, this would be an exciting measurement of fundamental physics and the history of symmetry breaking.

References

1. Watson, A., Science, 278, 574 (1997)
2. Pen, U., Seljak, U. and Turok N., "Power Spectra in Global Defect Theories of Cosmic Structure Formation" *Physical Review Letters*, **79**, 1611-1614 (1997).
3. Glanz, J., Science, 279, 1298 (1998).
4. Perlmutter, S.; Aldering, G.; Della Valle, M.; Deustua, S.; Ellis, R. S.; Fabbro, S.; Fruchter, A.; Goldhaber, G.; Groom, D. E.; Hook, I. M.; Kim, A. G.; Kim, M. Y.; Knop, R. A.; Lidman, C.; Mcmahon, R. G.; Nugent, P.; Pain, R.; Panagia, N.; Pennypacker, C. R.; Ruiz-Lapuente, P.; Schaefer, B.; Walton, N. Nature, 391, 51-54 (1998).
5. Ostriker, J.P. and Steinhardt, P.J., Nature, 377, 600 (1995).
6. Danos, R. and Pen, U., astro-ph/9803058, submitted to ApJL.
7. Bunn, E.F. and Sugiyama, N., ApJ, 446, 49-53 (1995)
8. Chiu, W., Ostriker, J.P. and Strauss, M.A., astro-ph/9708250, "Using Cluster Abundances and Peculiar Velocities to Test the Gaussianity of the Cosmological Density Field".
9. Donahue,M.,Gioia,I.,Luppino,G., Hughes,J.P, & Stocke, J.T. 1997, astro-ph/9707010.
10. Tucker, W., Blanco, P., Rappoport, S., David, L., Fabricant, D., Falco, E.E., Forman, W., Dressler, A., Ramella, M., "1E0657-56: A Contender for the Hottest Known Cluster of Galaxies", astro-ph/9801120.
11. Landy, S.D., Shectman, Stephen A., Lin, H., Kirshner, R.P., Oemler, A.A., Tucker, D., ApJ, 456, 1 (1996).
12. Seljak, U. and Zaldariagga, M., ApJ, 436, 437-444 (1996).

ACKNOWLEDGEMENTS. This work was supported by the Harvard Milton fund. The idea of broken scale invariance from non-minimal coupling is due to Neil Turok. I thank Uros Seljak for helpful discussions.

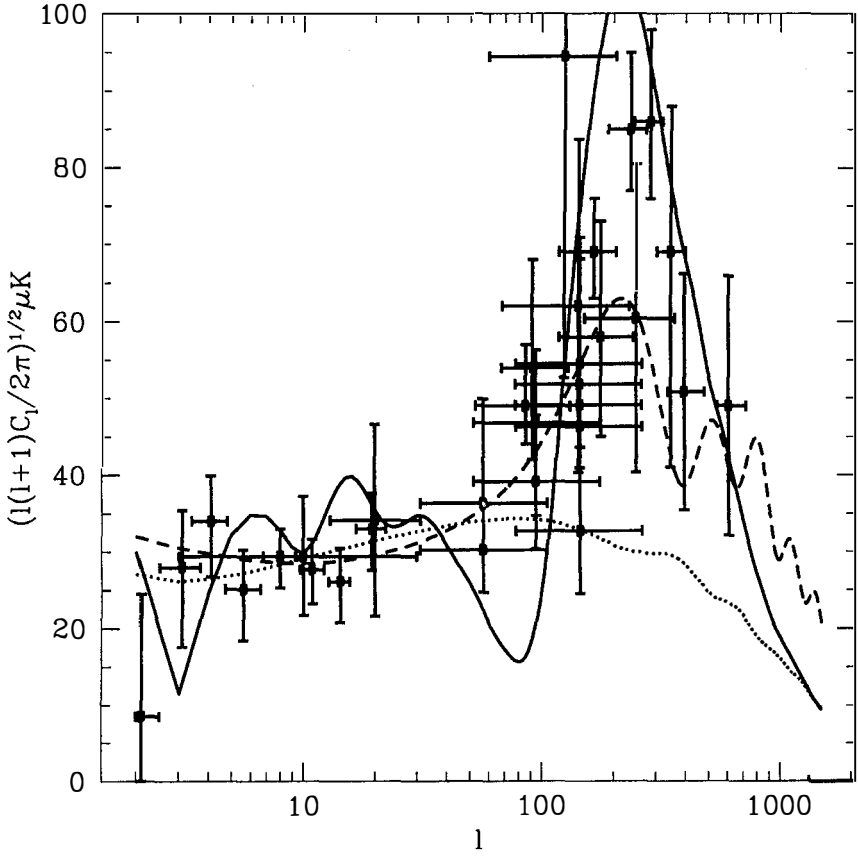

Figure 1: The angular CMB power spectrum. The solid line shows the general prediction of the broken global defect model. It resolves the problems exhibited by scaling defect models (dotted curve). The dashed line is the prediction of the cosmic concordance model of Ostriker and Steinhardt[5]. Overlaid on this plot are the various experimental data points.

COSMIC STRINGS IN A UNIVERSE WITH NON-CRITICAL MATTER DENSITY

R.A. Battye
Department of Applied Mathematics and Theoretical Physics, University of Cambridge, Silver Street, Cambridge CB3 9EW, U.K.

In the light of recent work which suggests that structure formation by cosmic strings in a critical matter density universe require large biases, we discuss the effects of reducing the matter density. Using a full linear Einstein-Boltzmann solver, we compute the cold dark matter density field and the microwave background anisotropies/polarization in a flat universe with a non-zero cosmological constant. We find that universes with $\Omega_\Lambda = 0.7 - 0.8$ give a good fit to the shape of the observed galaxy distribution, albeit with a bias of around 2. This has interesting implications for the anisotropy and polarization of the microwave background. Finally, we discuss the effects of relaxing the assumption that the universe is flat.

The last year has seen enormous progress in pinning down the predictions for structure formation and the microwave background from defect based theories [1,2,3]. When the matter density is critical, it was found that there is an almost generic under production of the power on the largest scales currently observed, with only the most convoluted models achieving a satisfactory amount of power on $100h^{-1}$Mpc scales, usually at the expense of an over production on smaller scales. In ref.[3] this was quantified in terms of the bias required to reconcile the observed galaxy correlations in the baryonic matter with the calculated cold dark matter (CDM) power spectrum on those scales. This was named the b_{100} problem and it was suggested that this bias could be as large as 5. Such a bias is both difficult achieve theoretically and apparently incompatiable with the current observations in flat, critical density universe.

During the past few months many have described defect based scenarios as being 'ruled out'! While this is very much human nature and may even be true, it is important to assess the true scientific implications objectively. A more conservative approach would be to acknowledge the difficulties these models have in fitting the current data with the following provisors : (1) *Deviations from scaling are slight.* It is scaling which relates the contributions on different scales and

hence allows for the possibility of modifying the power spectrum. In ref.[3] an exhaustive study was made of deviations from scaling and it was concluded that only truely radical deviations could hope to rectify the the b_{100} problem. (2) *Deviations from gaussianity are mild.* Defect based theories are inherently non-gaussian, but the superposition of a large number of sources is likely to be gaussian. Since the data is analyzed under the assumption of gaussianity it may be that we may be being mislead. However, preliminary indications are that the string models are almost gaussian on $100h^{-1}$Mpc scales[4]. (3) *The data on* $100h^{-1}$*Mpc is accurate.* On these scales the observed data is dominated by a single survey (APM) and one might suggest that the crucial observations are close to its resolution. Hopefully, future surveys (PSCz, 2DF and SDSS) will improve our confidence in these observations. (4) *Large biases are unacceptable.* I have already commented that there is no evidence for large biases, but some are not totally uncomfortable with this possibility. (5) *The matter density is critical.* All the work was based on a flat cosmology with standard cosmological parameters, although it was shown that variations in the Hubble constant and baryon density could not solve the b_{100} problem. Since a substantial body of current observations suggest that the universe may have a non-zero cosmological constant or be open, it is important that this possibility is investigated. This is the subject of this review based mainly on ref.[5], but backed up by refs.[6,7,8].

We will concentrate on the case of a flat universe with a non-zero cosmological constant, since calculations in an open universe using an accurate linear Einstein-Boltzmann solver would require a substantial technological improvement. However, we will make some qualitative remarks on the open case later. The reduction of matter density will be seen to have two related effects on the CDM power spectrum. Firstly, the shift in the time of equal matter-radiation will effect the shape of the power spectrum in the standard way via the shape parameter $\Gamma \sim \Omega_{\rm m} h$, where $\Omega_{\rm m}$ is the fractional density in matter and the Hubble constant is $H_0 = 100h$ km sec^{-1} Mpc^{-1}. In the case of the standard adiabatic theories, where the perturbations are created around the horizon size, this is estimated to be $\Gamma \approx 0.2 - 0.3$. However, the perturbations are created inside the horizon in defect theories and so the size of perturbations created at the time of equal matter-radiation will be slightly smaller, with the consequence that the required value of Γ is slightly smaller. We find that $\Omega_{\rm m} \approx 0.2 - 0.3$ with $h = 0.5$, that is $\Omega_\Lambda = 0.7 - 0.8$ and $\Gamma \approx 0.1 - 0.15$, gives a particularly good fit to the shape of the data for a pure scaling model.

The other effect is related to the modifications in the scaling regime during the matter-radiation transition. It is well known that the density of strings will be reduce by around a factor of two during this transition and this can have a substantial influence on the power spectrum. It has already been pointed out that radical deviations from scaling can lead to an improvement in b_{100} for a critical matter density universe, but smaller deviations can only effect smaller scales. In a model with a cosmological constant, the time of equal matter-radiation is shifted in such a way that such a small deviation can effect b_{100}. Using the velocity dependent one-scale model[9] to model these deviations, we have computed the CDM power spectrum and the angular power spectra of the micowave background anisotropies and polarization using a modified version of CMBFAST[10], which the includes the scalar, vector and tensor perurbations generic in any defect model. The results are presented in the figure for $\Omega_\lambda = 0.7, 0.8$ and $h = 0.5, \Omega_{\rm b} = 0.05$, along with those for pure scaling[3] and standard CDM.

The first thing to notice is the substantial improvement in the CDM power spectrum relative to the data, although one still requires a bias of around 2. This is still quite large, but the baryon density is now substantial proportion of the total and it may be easier to create a substantial bias, since the baryons are not forced to necessarily trace the CDM. The angular power spectrum of the microwave background anisotropies is also effected in a positive way relative to the current observations. The critical matter density case is not favourable when compared to the data, with the absence of a substantive rise in the power spectrum as suggested, but not yet confirmed, by the data. However, the models with a non-zero cosmological constant do have a substantial rise,

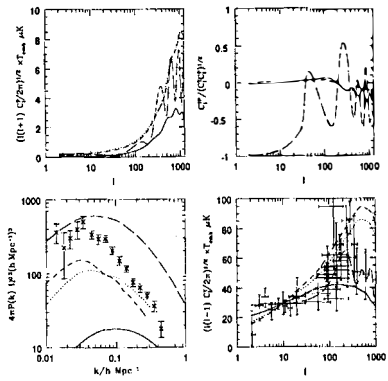

Figure 1: The results of the calculations for the standard scaling source (solid line), $\Omega_\lambda = 0.7$ (dotted line) and $\Omega_\lambda = 0.8$ (short-dashed line), all compared with standard CDM (long-dashed line): (bottom,left) the CDM density field, (bottom,right) the microwave backgorund anisotropies, (top,left) the polarization of the microwave background, (top,right) the cross-correlation of the anisotropy and polarization, relative to the amplitude of the two components.

albeit around $l = 400 - 600$, rather than $l = 200 - 300$ as suggested by the data. The reason for this increase in power on smaller scales is that one has changed the relative normalization between the anisotropy created at the time of last scattering on small scales and that created along the line of sight by the integrated Sachs-Wolfe effect (ISW), which dominate the larger scales, plus the decrease in Ω_m that is known to increase the amount of power on smaller scales. It is not a series of peaks as in the adiabatic case, but a broad peak as has been suggested as the signature of an incoherent source[11]. As one final point on this subject, one should note that too much power on small scales is not likely to be a problem when comparing to the data, since it can be removed easily, in this case by reionization. This would also slightly reduce the bias required to fit the galaxy correlations.

The angular power spectrum of polarization and its cross correlation with the temperature anisotropies are also of interest since future satellite missions, as well as ground based measurements, may measure them. There are a number of interesting signatures for active models which can be seen clearly in this model. Firstly, we should note that the amplitude of the polarization in these models has a maximum rms of $8\mu K$ around $l = 800 - 1000$, but that there are two distinct parts to this, the so called electric, E, and magnetic, B, components. The B-component is only present in the models where there are tensor and vector components to the anisotropies and is still relatively small ($\sim 0.1\mu$K around $l = 100$) in adiabatic models with a substantial tensor component. In the models under consideration here it is much larger, with a maximum rms of around 2μK (note that the standard scaling model [12] has an maximum rms of 1μK), which may be detectable.

The cross correlation between temperature and polarization on scales below the scale of the horizon at last scattering is zero by causality, in contrast to the adiabatic case[13]. In particular it is zero around $l = 100$, when the adiabatic model is strongly anti-correlated. Most interesting, though, from the point of observations is the suppression of the cross correlation on smaller scales, which is a characteristic of the incoherent nature of the source[14,12]. At a very basic level the anisotropy and polarization are two oscillatory functions which are out of phase, $\cos(x)$ and $\sin(x)$ say. To compute the angular power spectra for the anisotropy and polarization one must integrate the square of this oscillatory function multiplied by a structure function, encoding the

precise details of the source. Since this is always positive, one gets the characteristic broad peak in the spectrum. But when one computes the cross correlation, it is the product of the two which multiplies the stucture function and integrates out to be almost zero. However, one can see the that the cross correlation, although suppressed, appears to be consistently negative on small scales, that is, the temperature and polarization are anti-correlated The slighly more subtle reason for this is that there are actually two oscillatory components to the anisotropy, from the intrinsic and Doppler effects, which are responsible for the peaks and troughs in the standard adiabatic spectrum. The Doppler component is out of phase and suppressed relative to the intrinsic, but is of the opposite sign and in phase with the source of the polarization, hence creating a negative cross-correlation.

We have shown that some of the problems of standard defect scenarios in underproducing power in the large scale matter distribution can be remedied by the reduction of the matter density from critical. Although we have concentrated on the case of a flat universe with a non-zero cosmological constant, the general picture that we have presented will also be true for an open universe [6,8], with a couple of simple modifications. Firstly, the bias required to fit the galaxy correlations will be slightly larger. Using the simple formula of ref.[8], one can estimate that this would increase by around a factor of 1.4 for $\Omega_{\rm m} = 0.2$. Also the CMB power spectra will be shifted by the familiar geometric factor, $\Omega_{\rm m}^{-1/2}$, for adiabatic models. Hence, we conclude that the cosmological constant based models have a better chance of fitting the observations, if the current trends are confirmed.

Acknowledgements

I would like to thank Andy Albrecht and James Robinson for their collaboration in the work presented here. I have benefitted substantially from conversations with Neil Turok and particularly Paul Shellard, who first suggested the implications of scaling deviations to me. The computations presented here were done at the UK National Cosmology Supercomputing Centre, supported by PPARC, HEFCE and Silicon Graphics/Cray Research. I am currently supported by Trinity College.

References

1. U.L. Pen, U. Seljak and N .Turok, *Phys. Rev. Lett.* **79**, 1615 (1997).
2. B. Allen, R.R. Caldwell, S. Dodelson, L. Knox, E.P.S. Shellard and A. Stebbins, *Phys. Rev. Lett.* **79**, 2624 (1997).
3. A. Albrecht, R.A. Battye and J. Robinson, *Phys. Rev. Lett.* **79**, 4736 (1997). A. Albrecht, R.A. Battye and J. Robinson, astro-ph/9711121.
4. P.P. Avelino, E.P.S. Shellard, J.H.P. Wu and B. Allen, In prep..
5. R.A. Battye, J. Robinson and A. Albrecht, astro-ph/9711336.
6. P.P Avelino, R.R. Caldwell and C.J.A.P. Martins, *Phys. Rev.* **D56**, 4568 (1997).
7. P. Ferreira, *Phys. Rev. Lett.* **74**, 3522 (1995).
8. P.P. Avelino, E.P.S. Shellard, J.H.P. Wu and B. Allen, astro-ph/9712008.
9. C.J.A.P. Martins and E.P.S. Shellard, *Phys. Rev.* **D54**, 2535 (1996).
10. U. Seljak and M. Zaldarriaga, *Ap. J.* **469**, 437 (1996).
11. A. Albrecht, D. Coulson, P. Ferreira and J. Magueijo, *Phys. Rev. Lett.* **76**, 1413 (1996).
12. U.L. Pen, U. Seljak and N. Turok, *Phys. Rev. Lett.* **79**, 1615 (1997).
13. M. Zaldarriaga and D. Spergel, *Phys. Rev. Lett.* **79**, 2180 (1997).
14. R.A. Battye and D.D. Harari, Unpublished.

EXTRAGALACTIC POINT SOURCES AND THE PLANCK SURVEYOR MISSION

G. DE ZOTTI, L. TOFFOLATTI, G.L. GRANATO
Osservatorio Astronomico di Padova,
Vicolo dell'Osservatorio 5, I-35122 Padova

We review estimates of small scale fluctuations due to extragalactic point sources in the Planck Surveyor frequency bands. While our undestanding of the spectral and evolutionary properties of these sources is far from complete, conservative estimates allow us to confidently conclude that, in the frequency range 100–200 GHz, their contaminating effect is well below the expected anisotropy level of the cosmic microwave background (CMB), down to angular scales of at least $\simeq 10'$. Hence, an accurate subtraction of foreground fluctuations is not critical for the determination of the CMB power spectrum up to multipoles $\ell \simeq 1000$. In any case, Planck's wide frequency coverage will allow to carefully control foreground contributions. On the other hand, the all sky surveys at 9 frequencies, spanning the range 30–900 GHz, will be unique in providing complete samples comprising from several hundreds to many thousands of extragalactic sources, selected in an essentially unexplored frequency region. New classes of sources may be revealed in these data. The familiar "flat"-spectrum radio sources should show spectral features carrying essential information on their physical properties. Crucial information will be provided to understand the nature of radio sources with strongly inverted spectra. Scenarios for the cosmological evolution of galaxies will be extensively tested.

1 Introduction

The multifrequency all-sky maps produced by the Planck Surveyor mission will comprise, in addition to anisotropies which are outgrowths of primordial fluctuations, and whose precision measurements are the main goal of the mission, astrophysical foregrounds, the most important of which, over the frequency range of interest, are those due to emissions in our own Galaxy and to extragalactic radio and mm/sub-mm sources.

We deal here with extragalactic sources, which may be a major limiting factor for experiments, like Planck, aimed at accurately determining the cosmic microwave background (CMB) power spectrum C_ℓ up to multipoles $\ell \sim 2000$, corresponding to angular scales $\theta \sim 5'$. In fact,

a Poisson distribution of sources produce a white noise power spectrum with the same power in all multipoles [47], so that their contribution to fluctuations in a unit logarithmic multipole interval increases with ℓ as $\ell(\ell+1)C_\ell \propto \ell^2$ (for large values of ℓ), while, at least for the standard inflationary models, which are consistent with the available anisotropy detections, the function $\ell(\ell+1)C_\ell$ yielded by primordial CMB fluctuations is approximately constant for $\ell \lesssim 100$, then oscillates and finally decreases quasi exponentially for $\ell \gtrsim 1000$ ($\theta \lesssim 10'$). Hence confusion noise due to discrete sources will dominate at small enough angular scales.

In § 2 we summarize the limitations set by fluctuations due to extragalactic sources on Planck measurements of primordial CMB anisotropies. On the other hand, the multifrequency all sky surveys carried out by the Planck Surveyor mission will provide a very rich database for astrophysical studies; their impact on investigations of physical and evolutionary properties of different classes of extragalactic sources is briefly outlined in § 3. Our main conclusions are presented in § 4.

2 Small scale fluctuations due to extragalactic sources

A detailed discussion of the problem has been recently carried out by Toffolatti et al. [48]. Guiderdoni et al. [24] have worked out semi-analytic models for galaxy evolution in the IR/sub-mm range and have presented predictions for source counts in the Planck/HFI bands, among others. The source confusion noise in the same bands has also been estimated by Blain et al. [3].

Due to the steep increase with frequency of the dust emission spectrum in the mm/sub-mm region (the typical spectral index is $\alpha \simeq -3.5$, $S_\nu \propto \nu^{-\alpha}$), the crossover between radio and dust emission components for essentially all classes of extragalactic sources occurs at wavelengths of a few mm; dust temperatures tend to be higher for distant high luminosity sources, partially compensating the effect of redshift. The minimum in the spectral energy distribution of sources is thus roughly coincident with the CMB intensity peak, making the mm region ideal for mapping primordial anisotropies. A further consequence is that there is an abrupt change in the source populations observed in channels above and below ~ 1 mm: radio sources dominate at longer wavelengths, while in the sub-mm region the Planck instruments will mostly see dusty galaxies.

2.1 Radio sources

Estimates of the confusion noise due to radio sources do not require extrapolations in flux: the available source counts are more than sensitive enough to include any radio source of the familiar steep and "flat"-spectrum classes, likely to cause detectable fluctuations in any of the Planck maps. The real issue is the spectral behaviour since existing surveys extend only up to 8.4 GHz and hence substantial extrapolations in frequency are required.

The results reported by Toffolatti et al. [48] are based on evolutionary models fitting the observed counts, as well as redshift and luminosity distributions, of both steep- and "flat""-spectrum radio sources at several frequencies up to 8.44 GHz. In the Planck channels one has to deal primarily with "flat"-spectrum sources, mostly at substantial redshifts. These sources appear to keep a spectral index $\alpha \sim 0$ up to $\simeq 100$ GHz [28 13]. At higher frequencies a steepening or even a spectral break is generally observed [32]. Considerable uncertainties however remain on the high frequency behaviour of these sources. To allow for this, Toffolatti et al. [48] have considered three different values for the mean spectral index of compact radio sources in the range 20–200 GHz: $\alpha = -0.3$, 0, and 0.3; above 200 GHz a steepening to $\alpha = 0.7$ was assumed.

2.2 Evolving dusty galaxies

We are faced here with the need of substantial extrapolations both in frequency and in flux. In fact, there is a wide gap with the nearest wavelength (60 μm) where the most extensive (yet

relatively shallow) surveys exist. There is a considerable spread in the distribution of dust temperatures, so that the 1.3 mm/60 μm flux ratios of galaxies span about a factor of 10 [7 16 10]. A tentative estimate of the luminosity function of galaxies at mm wavelengths based on a 1.25 mm/60 μm bivariate luminosity distribution has been presented by Franceschini et al. [17]. Furthermore, the observational constraints on evolution of far-IR sources are very poor. IRAS 60 μm counts cover a limited range in flux and are rather uncertain at the faint end [25 22 2].

¿From a theoretical point of view, there is a great deal of uncertainty on the physical processes governing galaxy formation and evolution. Some models assume that the comoving density of galaxies remained constant after their formation, while they evolved in luminosity due to the ageing of stellar populations and the birth of new generations of stars (pure luminosity evolution). On the other hand, according to the hierarchical galaxy formation paradigm, big galaxies are formed by coalescence of large numbers of smaller objects. Furthermore, evolution depends on an impressive number of unknown or poorly known parameters: merging rate, star formation rate, initial mass function, galactic winds, infall, interactions, dust properties, etc.

Although the evolutionary history is highly uncertain, strong evolution is expected in the far-IR/mm region particularly for early type galaxies since during their early phases they must have possessed a substantial metal enriched interstellar medium. This expectation is supported by evidences of large amounts of dust at high redshifts [39 35 27], and by the intensity of the isotropic sub–mm background [40 23 44 26], first discovered by Puget et al. [40]. Moreover, the large, negative K-correction strongly amplifies the evolutionary effects, that may thus be appreciable in the relatively shallow Planck surveys, at least in the highest frequency bands.

Toffolatti et al. [48] adopted the luminosity evolution models by Franceschini et al. [19], updated adding a density evolution up to $z = 2$ of late type galaxies [18]. Their reference model (referred to as updated model C), which entails a dust enshrouded phase during the early evolution of spheroidal systems (early type galaxies and bulges of disk galaxies), provides a good fit to the 60 μm IRAS counts, as recently reassessed by Bertin et al. [2], to the far-IR extragalactic background spectrum, and to the preliminary estimates of the counts at 170 μm [29] and at 850 μm [45].

A different approach, directly plugged in current hierarchical scenarios for galaxy formation, has been taken by Guiderdoni et al. [24] who produced a set of models starting from a description of non-dissipative and dissipative collapses of primordial perturbations. The most extreme of these models exceed, even by an order of magnitude, predictions of the updated model C. An extreme evolution in the far-IR to sub-mm bands is indeed indicated by the most recent estimates [44 26] indicating a very intense far-IR extragalactic background.

The contributions of AGNs to the counts in the Planck high frequency channels are even more uncertain. The detailed estimates by Granato et al. [21] indicate a detection rate of radio quiet AGNs increasing with increasing frequency, from a few units over the whole sky at 217 GHz to a few hundreds at the highest frequencies; in any case, their number is expected to be small compared with the number of far-IR galaxies.

2.3 Fluctuations due to extragalactic sources and CMB anisotropy measurements

Given the performances of the instruments, the Planck experimental accuracy is effectively limited by astrophysical foregrounds. It is true that, on small angular scales ($\theta < 30'$), on average, the instrumental noise may exceed fluctuations due to extragalactic sources particularly if these are subtracted out down to relatively faint flux levels (on larger scales the dominant foreground fluctuations are due to Galactic emission and generally exceed the instrumental noise). However, much lower than average instrumental noise levels, well below the amplitude of extragalactic source fluctuations, will be reached in regions around the ecliptic poles that will be scanned many times; these regions are large enough to allow a careful determination of

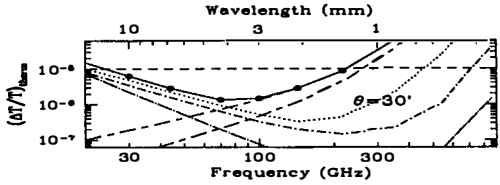

Figure 1: Temperature fluctuations as a function of frequency for an angular scale of 30′. The horizontal dashed line show the expected level of primordial CMB anisotropies. Average contributions from Galactic free-free, synchrotron and dust (for the two possible dust emission spectra mentioned by Kogut et al. [31]) emissions at $|b| > 50°$ are shown by dots/short dashes, dots-long dashes, long/short dashes, respectively. The dotted line gives the contribution of extragalactic sources. The solid line is the total contribution of astrophysical foregrounds to fluctuations; the filled circles on this line correspond to Planck channels.

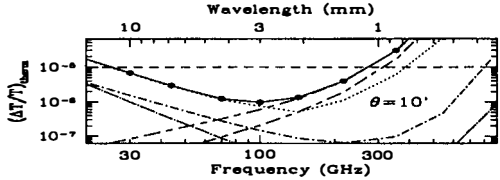

Figure 2: Same as in Fig. 1 but for an angular scale of 10′.

the power spectrum of CMB anisotropies on small scales. On moderate to large angular scales ($\theta \gtrsim 30'$), foreground fluctuations are minimum at frequencies $\simeq 70$ GHz (see Fig. 1) while on smaller scales the minimum moves to $\simeq 100$ GHz (Fig. 2).

In the frequency range 100–200 GHz CMB anisotropies are expected to dominate over foreground fluctuations at least up to $\ell \simeq 1000$. Only a tiny fraction of pixels is expected to be contaminated by extragalactic sources which can be efficiently identified thanks to the multifrequency observations carried out during the mission. If only the brigthest ($S > 1$ Jy) sources are removed, the contribution of clustering to fluctuations is small compared with the Poisson term. However, the effect of clustering may show up in the case of source subtraction down to below 100 mJy, introducing a modest feature in the angular power spectrum at $\theta \sim 20'$ at high frequencies (clustering of galaxies) and $\theta \sim 80'$ at low frequencies (clustering of radio sources).

The separation of CBR fluctuations from those due to extragalactic sources is further eased by the substantial difference between the power spectra of the two components [47]. Also, in principle, it is possible to discriminate fluctuations due to discrete sources from primordial CMB anisotropies on the basis of their quite different angular size, by means of higher resolution observations. Thus, contamination by extragalactic sources does not set a critical limitation to Planck mapping of primordial CMB anisotropies.

3 Studies of extragalactic sources with the Planck Surveyor mission

3.1 "Flat"-spectrum radio sources

According to the estimates by Toffolatti et al. [48] the Planck surveys will provide multifrequency data for a relatively large (from several hundred to a few thousand sources), complete sample

of "flat-"spectrum radio sources (compact radio galaxies, radio loud QSOs, BL Lacs, blazars), allowing investigation of a number of interesting issues.

The available observations of the spectral energy distributions of these sources generally have a gap at mm/sub-mm wavelengths. Those sources which have data in this interval frequently show a dip in the mm region, indicative of a cross-over of two components. This spectral feature, that Planck can observe, carries a good deal of extremely interesting information on the physical properties of sources. For example, in flow models of compact radio sources, the spectrum steepens at a frequency at which the radiative cooling time equals the outflow time [1]; for "hot spots", this typically lies in the millimeter or far-IR part of the spectrum, while, in cocoons or extended regions of lower surface brightness, the break moves down to lower frequencies.

According to the basic model [4 43], which has been supported by a large body of observational evidence, the spectral break frequency, ν_b, at which the synchrotron spectrum steepens, is related to the magnetic field B and to the "synchrotron age" t_s (in Myr) by $\nu_b \simeq 96(30\,\mu\mathrm{G}/B)^3 t_s^{-2}$ GHz. Various evolutionary models of the radio emission spectrum have been proposed based on different assumptions [36] ("one-shot" or continuous injection of relativistic electrons, complete or no isotropization of the pitch-angle distribution). These models strongly differ in the form of the falloff above ν_b. Also, many compact sources are observed to become optically thin at $\nu \gtrsim 10$ GHz. Correspondingly, their spectral index steepens to values ($\alpha \simeq 0.7$) typical of extended, optically thin sources. Thus, the systematic multifrequency study at the Planck frequencies will provide a statistical estimate of the radio source ages and measurements of the high frequency spectral behaviour and of its evolution with cosmic time: these are pieces of information of great physical importance.

In the case of blazars [5] the component dominating at cm wavelengths is rather "quiescent" (variations normally occur on time of years) and has a spectral turnover at $\sim$ 2–5 cm, where the transition between optically thick and optically thin synchrotron emission occurs. At higher frequencies the emission is dominated by a violently variable "flaring" component, which rises and decays on timescales of days to weeks, and has a self-absorption break at mm/sub-mm wavelengths. The mm/sub-mm region is thus crucial to understanding the mechanisms responsible for variability in radio loud active nuclei.

It is known from VLBI studies that the apparently smooth "flat" spectra of compact radio sources are in fact the combination of emissions from a number of components with varying synchrotron self absorption frequencies which are higher for the denser knots. The mm/sub-mm region is unique for studying sub-parsec scale, high density regions, including the radio core [34]. Thus, while lower frequency surveys provide much more detailed information relevant to define *phenomenological* evolution properties, surveys at mm wavelenghts are unique to provide information on the *physical* properties.

Excess far-IR/sub-mm emission, possibly due to dust, is often observed from local radio galaxies [30]. Planck data will allow to assess whether this is a general property of these sources; this would have interesting implications for the presence of interstellar matter in the host galaxies, generally identified with giant ellipticals, which are usually thought to be devoid of interstellar matter.

3.2 Inverted-spectrum radio sources

The predictions of Toffolatti et al. [48] do not explicitly include sources with strongly inverted spectra, peaking at mm wavelengths, that would be either missing from, or strongly underrepresented in low frequency surveys and be very difficult to distinguish spectrally from fluctuations in the CMB [8].

GHz Peaked Spectrum radio sources (GPS) appear to have a fairly flat distribution of peak

frequencies extending out to 15 GHz in the rest frame[38], suggesting the existence of an hitherto unknown population of sources with peak at high frequency [33]. It is very hard to guess how common such sources may be. Snellen [46] exploited the sample of de Vries et al. [9] to estimate a count of $22 \pm 10\,\mathrm{Jy}^{-3/2}\,\mathrm{sr}^{-1}$ for sources having peak frequencies between 1 and 8 GHz and peak flux densities between 2 and 6 Jy. He also found that counts of GPS sources are only slowly decreasing with increasing peak frequency in that range. If indeed the distribution of peak frequencies extends up to several tens GHz keeping relatively flat, it is conceivable that from several tens to hundreds of GPS sources will be detected by the Planck experiment. Thus, although these rare sources will not be a threat for studies of CMB anisotropies, we may expect that the Planck surveys will provide crucial information about their properties. GPS sources are important because they may be the younger stages of radio source evolution [15 41] and may thus provide insight into the genesis and evolution of radio sources; alternatively, they may be sources which are kept very compact by unusual conditions (high density and/or turbulence) in the interstellar medium of the host galaxy [49].

Planck/LFI may also allow to study another very interesting class of radio sources, powered by advection-dominated accretion flows [37 14 12 20]. These may correspond to the final stages of accretion in large elliptical galaxies hosting a massive black hole. Their radio emission is characterized by an inverted spectrum with spectral index $\alpha \sim -0.4$ up to a frequency of 100–200 GHz, followed by fast convergence.

3.3 Evolving dusty galaxies

As shown by Toffolatti et al. [48] and Guiderdoni et al. [24], the Planck high frequency channels will detect the dust emission from a large number of evolving galaxies. A spectacular breakthrough has been achieved in the last couple of years, in the optical/UV, with the long sought detection of large samples of galaxies at $z \sim 3$, allowing to get a direct insight into the history of the cosmic star and metal formation. On the other hand, several lines of evidence indicate that optical/UV data are offering a very incomplete view of the galaxy evolution at high z [23 6 11 42]. Indeed, there are indications that most of the starlight emitted during early phases of the evolution of spheroidal systems may be essentially invisible in the optical-UV region [23 10]. This may not be surprising since active star formation is generally observed to occur in dusty environments. The very strong, negative K-correction due to the steep rise with frequency of the dust emission spectrum in the mm/sub-mm wavelength range, makes this spectral region particularly well suited for detecting high-z galaxies. In fact, models [24] predict that most sources detected in the Planck high frequency channels are at $z \geq 1$; in some cases, substantial tails up to $z \simeq 3$–4 are expected. Planck high frequency surveys may thus provide a wealth of data essential to understand the the cosmic star and metal formation history.

4 Conclusions

Luckily enough, both for galaxies and active galactic nuclei, the crossover between the radio and the dust emission components, determining a minimum in the spectral energy distribution, is roughly coincident with the CMB intensity peak. The dust temperature tends to be higher for bright distant objects, moving the minimum to higher frequencies in the rest frame and thus partially compensating for the effect of redshift. This situation makes the mm region ideal for mapping primordial anisotropies.

Although our understanding of foregrounds at Planck frequencies is far from complete, estimates using worst-case parameters in extrapolating existing measurements to Planck frequencies or angular scales, allow us to safely conclude that, in the frequency range 100-200 GHz, the foreground fluctuations, which are dominated, on small scales ($\theta \lesssim 30'$), by extragalactic sources,

are well below the expected amplitude of CMB anisotropies over much of the sky. Hence, the removal of foreground contamination is not critical for accurate determinations of the power spectrum of CMB anisotropies up to multipoles of at least $\ell \sim 1000$.

On the other hand, while only a small fraction of high Galactic latitude pixels are strongly contaminated by astrophysical foregrounds, the Planck surveys at 9 frequencies will provide sufficiently rich complete samples for astrophysical studies. Spectral information will be provided for "flat"-spectrum radio sources (compact radio galaxies, radio loud QSOs, BL Lacs, blazars) over a frequency region where spectral features carrying essential information on their physical conditions show up (breaks due to energy losses of relativistic electrons, self-absorption turnovers of flaring components, ...). Planck surveys will be unique in providing complete samples of bright radio sources with inverted spectra, essentially undetectable in radio-frequency surveys. Important classes of sources of this kind are GHz peaked spectrum sources, which may be the youngest stages of radio source evolution and may thus provide insight into the genesis of radio sources, and advection dominated sources, corresponding to final stages of accretion in giant elliptical galaxies hosting a massive black hole. The high frequency Planck channels will detect thousands of dusty galaxies, a large fraction of which at substantial redshifts, allowing to extensively test scenarios for galaxy evolution. The increasing evidence that a large, and perhaps dominant fraction, of star formation at high redshifts may be hidden by dust, makes far-IR to sub-mm surveys an essential complement to optical data.

Acknowledgments

GDZ acknowledges enlightening discussions with R. Fanti on GHz peaked sources and with A. Franceschini on advection dominated sources. We have benefited from many years of collaboration on foregrounds with L. Danese, C. Burigana, A. Franceschini, and P. Mazzei. Work supported in part by CNR and ASI.

References

1. Begelman, M.C., Blandford, R.D., Rees, M.J., 1984, Rev. Mod. Phys., 56, 255
2. Bertin, E., Dennefeld, M., Moshir, M., 1997, A&A, 323, 685
3. Blain, A.W., Ivison, R.J., Smail, I., 1998, MNRAS, in press
4. Blandford, R.D., Rees, M.J., 1974, MNRAS, 165, 395
5. Brown, L.M.J., et al., 1989, ApJ, 340, 129
6. Burigana C., Danese L., De Zotti G., Franceschini A., Mazzei P., Toffolatti L., 1997, MNRAS, 287, L17
7. Chini, R., Krügel, E., Lemke, R., Ward-Thompson, D., 1995, A&A, 295, 317
8. Crawford, T., Marr, J., Partridge, R.B., Strauss, M.A., 1996, ApJ, 460, 225
9. de Vries, W.H., Barthel, P.D., O'Dea, C.P., 1997, A&A, 321, 105
10. De Zotti, G., Mazzei, P., Franceschini, A., Danese, L., 1996, in Science with Large Millimeter Arrays, ed. P. Shaver, Springer-Verlag, p. 43
11. De Zotti, G., et al., 1998, in proc. conf. "The young universe: galaxy formation and evolution at intermediate and high redshift", S. D'Odorico, A. Fontana, & E. Giallongo eds, A.S.P. Conference Series, in press
12. Di Matteo, T., Fabian, A.C., 1997, MNRAS, 286, L50
13. Edelson, R.A., 1987, AJ, 94, 1150
14. Fabian, A.C., Rees, M.J., 1995, MNRAS, 277, L55
15. Fanti, C., Fanti, R., Dallacasa, D., Schilizzi, R.T., Spencer, R.E., Stanghellini, C., 1995, A&A, 302, 317
16. Franceschini, A., Andreani, P., 1995, ApJ, 440, L5

17. Franceschini, A., Andreani, P., Danese, L., 1998, MNRAS, in press
18. Franceschini, A., et al., 1997, in proc. ESA symposium "The far infrared and submillimeter universe", ESA SP-401, 159.
19. Franceschini, A., Mazzei, P., De Zotti, G., Danese, L., 1994, ApJ, 427, 140
20. Franceschini, A., Vercellone, S., Fabian, A.C., 1997, MNRAS, submitted
21. Granato, G.L., Danese, L., Franceschini, A., 1997, ApJ, 486, 147
22. Gregorich, D.T., Neugebauer, G., Soifer, B.T., Gunn, J.E., Herter, T.L., 1995, AJ, 110, 259
23. Guiderdoni, B., Bouchet, F.R., Puget, J.-L., Lagache, G., Hivon, E., 1997, Nature, 390, 257
24. Guiderdoni, B., Hivon, E., Bouchet, F.R., Maffei, B., 1998, MNRAS, in press
25. Hacking, P., Houck, J.R., 1987, ApJS, 63, 311
26. Hauser, M., et al., 1998, in preparation
27. Hughes, D.H., Dunlop, J.S., & Rawlings, S. 1997, MNRAS, 289, 766
28. Impey, C.D., Neugebauer, G., 1988, AJ, 95, 307
29. Kawara, K., et al. 1997, in proc. ESA symposium "The far infrared and submillimeter universe", ESA SP-401, 285
30. Knapp, G.R., Patten, B.M., 1991, AJ, 101, 1609
31. Kogut, A., et al., 1994, ApJ, 433, 435
32. Landau, R., et al., 1986, ApJ, 308, 78
33. Lasenby, A.N., 1996, Proc. XVI Moriond Astrophysics Meeting "Microwave Background Anisotropies", eds. F.R. Bouchet, R.
34. Lawrence, A., 1997, Proc. ESA Symp. "The Far Infrared and Submillimeter Universe", ESA SP-401, p. 127
35. Mazzei, P., De Zotti, G., 1996, MNRAS, 279, 535
36. Myers, S.T., Spangler, S.R., 1985, ApJ, 291, 52
37. Narayan, R., Yi, I., 1995, ApJ, 444, 231
38. O'Dea, C.P., Baum, S.A., 1997, AJ, 113, 148
39. Omont, A., et al., 1996, A&A, 315, 1
40. Puget, J.-L., Abergel, A., Bernard, J.-P., Boulanger, F., Burton, W.B., Désert, F.-X., Hartmann, D., 1996, A&A, 308, L5
41. Readhead, A.C.S., Taylor, G.B., Pearson, T.J., Wilkinson, P.N., 1996, ApJ, 460, 634
42. Rowan-Robinson, M., et al., 1997, MNRAS, 289, 490
43. Scheuer, P.A., 1974, MNRAS, 166, 513
44. Schlegel, D.J., Finkbeiner, D.P., Davis, M., 1998, astro-ph/9710327
45. Smail, I., Ivison, R.J., Blain, A.W., 1997, ApJ, 490, L5
46. Snellen, I.A.G., 1997, Ph. D. Thesis, University of Leiden
47. Tegmark, M., Efstathiou, G., 1996, MNRAS, 281, 1297
48. Toffolatti, L., Argüeso-Gómez, F., De Zotti, G., Mazzei, P., Franceschini, A., Danese, L., Burigana, C., 1998, MNRAS, in press
49. van Breugel, W., Miley, G., Heckman, T., 1984, AJ, 89, 5

RISING SPECTRUM FOREGROUND SOURCES

K. GRAINGE and A. EDGE
MRAO, Cavendish Laboratory, Madingley Road, Cambridge, England.
Physics Department, University of Durham, South Road, Durham, England.

We have attempted to use the most appropriate existing survey data to best estimate the contribution of foreground sources with rising spectra. Rising-spectra sources are those which present the greatest challenge for spectral discrimination against the CMB. So far, we have been able to employ surveys at 1.4 and 5GHz with follow up at 15 GHz, plus multifrequency observations with the VLA. Preliminary results indicate of the order of 5 rising sources at 30 GHz per square degree at the 10 mJy level. Of course, higher frequency selection (and simultaneous observation) will improve our knowledge further. This work will be described in greater detail in Edge et al.[1].

1 Introduction

The bulk of the radio emission from AGN is believed to be due to the synchrotron mechanism. The emission can be characterised by a power-law continuum spectrum, $F_\nu \propto \nu^{-\alpha}$, with a typical value of $\alpha \approx 0.7$ if the emitting region is optically thin. However, if the density of the gas is high enough, the relativistic electrons responsible for the emission reabsorb the radiation. Because of this synchrotron self-absorption, lower-frequency emission is preferentially cut out and the spectral shape changes to one of rising flux with higher frequency, with a theoretical limit of $\alpha = -2.5$. Many such sources with peaks in their spectra at around 1 GHz have been found from low frequency surveys. It is quite physically plausible to postulate sources in a more extreme environments whose spectra would peak at much higher frequency, and such sources have indeed been found serendipitously (figure 1). Such a population of high-peak-frequency GPS sources may well dominate the point-source component of contaminating foregrounds for Cosmic Microwave Background (CMB) experiments. Since the CMB emission has an index $\alpha = -2$ below approximately 200 GHz, such sources would be difficult to discriminate spectrally. Therefore it is vital to determine the abundance of these GigaHertz-Peaked Spectrum (GPS)

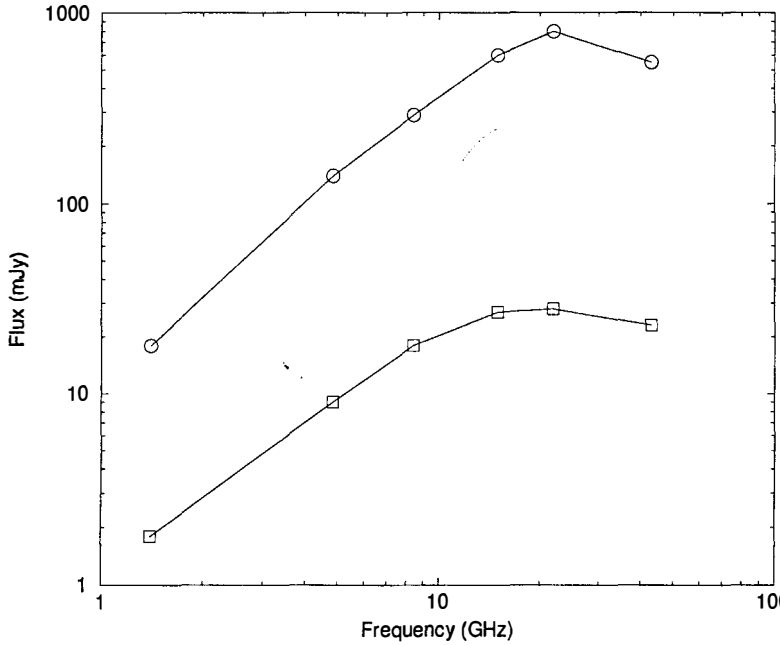

Figure 1: Spectra of the sources RXJ1459+33 (circles) and RXJ0952+51 (squares) measured with the VLA. Both of these sources have highly inverted spectra, although not quite as steep as the theoretical limit of $\alpha = -2.5$, and peak at around 20 GHz. Extrapolating downwards in frequency, even RXJ1459+33 (which has a peak flux of approximately 1 Jy) has a flux less than 1 mJy at 325 MHz; thus it and a population of similar sources will not have been detected in low frequency surveys such as WENSS.

sources in order to estimate the degree of contamination that they introduce to any primordial anistropies which we may hope to detect.

2 Abundance of GigaHertz-Peaked Spectrum Sources

2.1 Previous surveys

Existing samples of GPS sources select their candidates by searching for inverted-source spectra between surveys performed at low frequency. As a result, most of the GPS sources found in such surveys have low peak frequencies. For example, the sample of faint GPS sources from the Westerbork Northern Sky Survey [2] (WENSS) which was selected from surveys at 325 MHz, 609 MHz and 5 GHz contains forty-seven members, but only two of these have peak frequencies greater than 7 GHz. The reason for this is that a GPS source whose peak frequency is higher than that for a source at the same redshift and with the same bolometric luminosity (presumably in a less extreme environment) will have a lower flux at low frequency; hence high peak frequency sources are very much less likely to be detected in low frequency surveys. Therefore in order to determine the number density of GPS sources which peak at a certain frequency one must search for them with surveys conducted at that same frequency.

The majority of the proposed experiments to map the anistropies in the CMB observe at frequencies of 30 GHz and above. Unfortunately, no large-field-of-view surveys exist at these frequencies. Thus the best we can do is to use the highest-frequency surveys available at the moment and include in our sample only those candidates whose spectra are still inverted in follow up observations at higher frequencies; this will give us a lower limit on the number density of GPS sources.

2.2 Our Sample

We selected potential candidates from the VLA NVSS survey at 1.4 GHz and the Greenbank 5 GHz survey over 10% of the northern sky. We imposed a minimum flux limit of 50 mJy at 5 GHz, and further insist that $\alpha < -0.5$ between 1.4 and 5 GHz. This gave us 200 sources. We then made follow up observations of these at 15 GHz using the Ryle Telescope[3] (RT), and selected those with $\alpha < -0.5$ between 5 and 15 GHz, leaving us 55 candidates. These were mapped with the VLA at 6 frequencies – 1.4, 5, 8.4, 15, 22 and 43 GHz and we found that all but 5 were indeed GPS sources with peak frequencies above 10 GHz.

This method has many potential selection biasses. The worst of these is that GPS sources are known to be highly variable, coupled with the asynchronism of the radio observations; the Greenbank survey was made in 1987, the NVSS between 1993 and 1996, and the RT follow up observations in 1997. Therefore it is quite probable that many GPS sources have been rejected by our selection strategy. However, the VLA multi-frequency imaging was done simultaneously, so we can be confident that all 50 members of our sample are indeed GPS sources.

The majority of the GPS sources that we found did not have spectra as extremely inverted as those shown in figure 1, and more typically had spectra similar to that for 0646+448, shown in figure 2. Such spectra can be accounted for as being the result of the superposition of the emission from several unresolved sites with differing environments. Several of these sources had spectra which were still rising at 43 GHz, implying that emission sites with environments extreme enough to give rise to such high peak frequency spectra are physically possible. Furthermore, 0646+448 has been identified with an optical counterpart with redshift 3.398, so in the rest frame the peak of the emission is above 190 GHz.

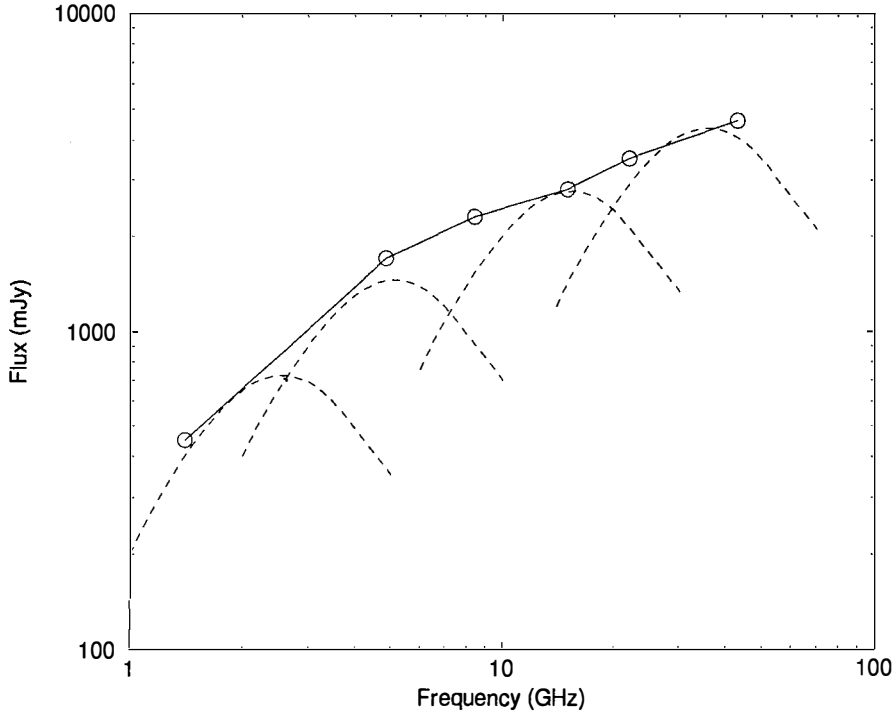

Figure 2: Spectrum of source 0646+448 (solid line) and indictation of how this spectrum could be made up by summing together the emission from several unresolved sites of synchrotron self-absorption, each having a different environment, and so a different peak frequency.

3 Conclusions

We have surveyed 2000 square degrees of the sky and have detected 50 GPS sources with 5 GHz flux higher than 50 mJy whose spectra are still rising above 10 GHz. Due to various selection effects, this figure should be regarded as an lower limit. Assuming a power law of the number density against flux $n(S)dS \propto S^{-1.5}$, we calculate that at 30 GHz we would expect to find on the order of 5 GPS sources per square degree with flux above 10 mJy. This abundance of GPS sources could introduce serious contamination to some of the proposed experiments to map primary anistropies in the CMB; it represents a confusion noise of 5 μK in a $25'$ beam at 30 GHz. There is evidence that physical environments which give rise to synchrotron self-absorption with peak frequency of up to at least 190 GHz do exist, but our present survey is inadequate to estimate the abundances of such sources: a large-field-of-view survey at high frequencies will be required to answer this question.

Acknowledgments

This work was conducted primarily by Alastair Edge and will be described in greater detail in Edge et al.[1].

References

1. A C Edge et al., in prep, 1998.
2. I Snellen, PhD thesis, University of Leiden, 1997.
3. M E Jones in Proc IAU Colloq. 131, ASP Conf. Ser. 19, T Cornwell and R Perley eds, p395, 1991.

LENSED SUBMILLIMETRE-WAVE FOREGROUNDS AND THE CMBR

A.W. BLAIN

Cavendish Laboratory, Madingley Road, Cambridge, CB3 0HE, United Kingdom

Samples of high-redshift galaxies are easy to select in the millimetre/submillimetre (mm/submm) waveband using sensitive telescopes, because their flux density–redshift relations are expected to be flat, and so the selection function is almost redshift-independent at redshifts greater than 0.5. Source counts are expected to be very steep in the mm/submm waveband, and so the magnification bias due to gravitational lensing is expected to be very large, both for lensing by field galaxies and for lensing by clusters. Recent submm-wave observations of lensed images in clusters have constrained the submm-wave counts directly for the first time. In the next ten years our knowledge of galaxy evolution in this waveband will be greatly enhanced by the commissioning of sensitive new instruments and telescopes, including the CMBR imaging space mission *Planck Surveyor*. This paper highlights the important features of gravitational lensing in the submm waveband and discusses the excellent prospects for lens searches using these forthcoming facilities.

1 Distant dusty galaxies

The flux density–redshift relation for distant dusty star-forming and active galaxies in the submm waveband is expected to be approximately flat at redshifts in the range $0.5 \leq z \leq 10$, because of the large negative K–correction obtained when the steep modified thermal dust spectra of these galaxies, which peak in the rest-frame far-infrared waveband, are redshifted into the observed mm/submm waveband.[1] Consequently, the faint submm-wave source counts are expected to be very steep as compared with the faint counts in other wavebands. The surface density of such galaxies at mJy flux densities was uncertain by up to three orders of magnitude[2] until six sources were detected in the fields of two rich clusters of galaxies[3] in 850-μm observations using the SCUBA bolometer array receiver at the James Clerk Maxwell Telescope (JCMT) last year;[4] it is now known to within a factor of about two.[a] The brightest of these sources has now been identified with an obscured AGN/starburst galaxy at $z = 2.803$.[5] These observations allowed the source confusion noise that will affect mm/submm-wave CMBR observations, made by either balloon-borne experiments or the *Planck Surveyor* space mission,[6] to be estimated directly for the first time.[7] Lensing is not expected to modify the predicted source confusion noise significantly.

[a]This work has benefited greatly from the results of observations made using SCUBA at the JCMT in collaboration with Ian Smail, Rob Ivison and Jean-Paul Kneib.

2 Gravitational lensing

Because of the large negative K–correction for galaxies in the submm waveband, the redshift distribution of faint galaxies is expected to extend out to much larger redshifts as compared with other wavebands. Hence the gravitational lensing cross section for a typical source is also expected to be large as compared with that in other wavebands. In addition, the steep submm-wave counts are expected to be associated with a large positive magnification bias[8] over a wide range of flux densities; that is lensing is expected to produce a considerable increase in the surface density of detectable sources. The effects of lensing by both galaxies[8,9] and clusters,[3,10] and the consequences of different world models for the predictions,[11,12] are described in detail elsewhere. In the light of the first observed 850-μm counts[4] realistic estimates of the observability of lensed galaxies using existing and future instruments can be made.[7,10,13] The details of the observations[4] and lensing calculations[3,8,9,11] are not discussed in this short contribution.

The properties of galaxy–galaxy lenses in the field and images lensed by clusters are considered in Sections 3 and 4 respectively. The catalogues of point sources that will be detected in mm/submm-wave CMBR surveys, and especially in the all-sky *Planck Surveyor* survey,[6] will allow large samples of galaxy–galaxy lenses to be compiled, as summarized in Section 5.

3 Galaxy–galaxy lensing

The submm-wave source counts are expected to be steep at observable flux densities, and so the corresponding magnification biases are predicted to be large. Predictions of the counts of both lensed and unlensed galaxies at wavelengths of 850 and 500 μm, based on direct submm-wave observations,[4] and existing models of both the lensing optical depth[8,11] and the evolution of galaxies[2] are shown in Fig. 1. The counts are compared with the 3σ sensitivities of long-term surveys made using a range of existing and future mm/submm-wave telescopes; SCUBA at the 15-m JCMT, a large ground-based interferometer array such as the MMA,[14] the 3.5-m space-borne telescope *FIRST*,[15] and the space-borne all-sky CMBR imaging satellite *Planck Surveyor*.[6] If the curves representing the predicted counts lie above the thin solid line labelled with the name of a particular telescope then that telescope is expected to detect at least one source in the survey. A more detailed description of these instruments and their likely levels of source confusion is given elsewhere.[7]

The ratio of the numbers of lensed to unlensed galaxies with flux densities greater than about 50 mJy – the 3σ sensitivity of the *Planck Surveyor*[6] – is predicted to be greater than 1%, which illustrates the very large magnification bias. The surface density of such lenses is expected to be between about 10^{-2} and $0.1\,\mathrm{deg}^{-2}$. Hence, a large sample of lensed star-forming galaxies[9,13] and quasars[5] could be found in a practical survey using the next generation of submm-wave instruments. The 50-m single-antenna US/Mexican LMT/GTM telescope[16] will also have a formidable performance in a lens search. In a practical *Planck-Surveyor*-based survey[13] up to 10^3 lensed sources could be detected. The inclusion of a population of galactic disks in the population of lensing galaxies[17] can increase the optical depth to high-magnification lensing by a significant factor,[18] and so this remarkably large number of lens detections expected in the *Planck Surveyor* survey may actually be a conservative estimate of the true number.

4 Lensing by clusters

The counts on which the results in this paper are based were determined by submm-wave observations of rich lensing clusters.[4] The large K–corrections for background galaxies ensure that galaxies within the clusters at $z \ll 1$ are unlikely to contaminate the results,[3] and a sample of about 20 sources has now been obtained.[12] The magnification bias factor in the cores of rich

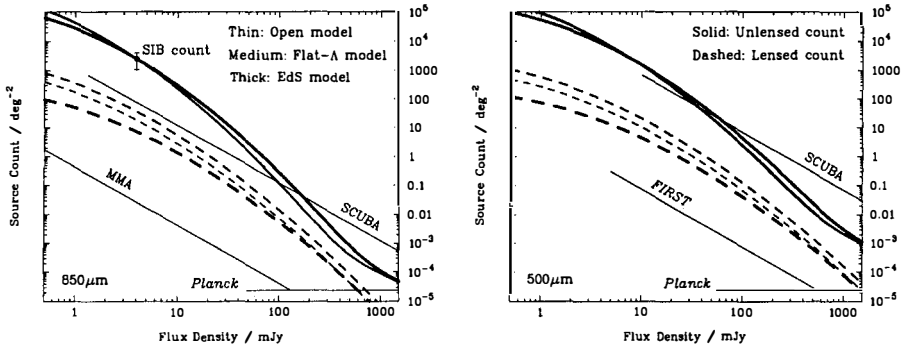

Figure 1: Predicted submm-wave source counts of both lensed (dashed lines) and unlensed (solid lines) galaxies at wavelengths of 850 μm (left) and 500 μm (right) in three different world models. The Einstein–de Sitter (EdS) model is represented by thick curves; the Flat-Λ model, with $\Omega_0 = 0.3$ and $\Omega_\Lambda = 0.7$, is represented by curves of medium thickness, and the Open model, with $\Omega_0 = 0.3$ and $\Omega_\Lambda = 0$, is represented by the thin curves. The counts of unlensed galaxies in the Open and Flat-Λ models are almost indistinguishable; they lie below the counts in the EdS model. The predicted counts are consistent with counts and upper limits to counts derived from current observations made at wavelengths of 850 μm (SIB[4]), 2.8 mm[19] and 175 μm,[20] and with the observed intensity of background radiation.[11] In the standard notation[2] $p = 3$, $z_0 = 7$; in the EdS, Flat-Λ and Open models z_{max} takes the values 2.6, 2.87 and 3.0 respectively. The sensitivities of existing and future instruments are included for comparison. If the counts lie above the lines representing instrumental sensitivities then 3σ detections are expected in a survey. An integration time of 200 h is assumed for a SCUBA survey; 1000 h is assumed for *FIRST*[15] and the MMA.[14] The nominal 14-month *Planck Surveyor*[6] mission is assumed. Hubble's constant $H_0 = 50\,\mathrm{km\,s^{-1}\,Mpc^{-1}}$.

clusters is predicted to be several hundred in the submm waveband, as compared with less than about ten in the optical waveband;[3] and so these observations offer considerable promise both for investigating the history of star and galaxy formation,[21] unbiased by the effects of dust extinction, and the values of cosmological parameters.[11] Lensing is expected to increase the mean flux density and angular separation of point sources in the fields of clusters, which is expected to increase the severity of source confusion noise in the fields of clusters as compared with the field when observed on arcminute scales in the mm/submm waveband.[10] Hence, if a very accurate measurement of the Sunyaev–Zel'dovich effect in clusters[22] is required then the flux density due to confusing point sources may need to be subtracted from these observations, using arcsecond-resolution maps of the cluster obtained using either a large single-antenna telescope[16] or a large interferometer.[14]

5 Lens surveys in the mm/submm waveband

Although the SCUBA camera at the 15-m JCMT is much more sensitive than previous submm-wave instruments, it is not expected to detect a large number of galaxy–galaxy lenses, as shown in the left-hand panel of Fig. 1 and discussed elsewhere.[8] The line represented the sensitivity limit of SCUBA clearly lies above the expected count of lensed sources.

However, the prospects for using future mm/submm-wave telescopes, *FIRST*, *Planck Surveyor*, the MMA and the LMT/GTM to detect and study lensed galaxies and quasars appear to be excellent. In Fig. 1 the lines representing the sensitivity limits of *FIRST*, *Planck Surveyor* and the MMA all lie significantly below the expected counts of lensed sources. The BOLOCAM receiver at the LMT/GTM will operate at wavelengths longer than 1.1 mm, and although not shown in Fig. 1, its performance is expected to be similar to that of the MMA. Mm/submm-wave surveys using these instruments will all produce a large catalogue of sources, with flux

densities in the range 10–100mJy for the space-borne surveys,[9,13] in the range 1–10mJy for the LMT/GTM and potentially at 100-μJy flux densities for the MMA. However, only the MMA has the potential to resolve the multiple image components of a lensed system directly. The sample of sources detected using other telescopes will require high-resolution follow-up imaging using an interferometer array, and final spectroscopic confirmation using large near-infrared/optical telescopes in order to decide whether they are lensed or not. These follow-up observations would require a concerted campaign of observing lasting for several months; however, they are practical.[13] A catalogue containing of order 1000 galaxy–galaxy lenses will be the final product of future mm/submm-wave lens surveys.

6 Conclusions

1. The surface density of distant galaxies in the submm waveband, and therefore the expected surface density of gravitational lenses and the effects of source confusion in future observations, is now known with reasonable accuracy.

2. The *Planck Surveyor* survey and surveys using other forthcoming mm/submm-wave telescopes will produce catalogues of distant sources that will be of great interest for studies of galaxy evolution. Lensed galaxies and quasars will be detected with an efficiency of up to 10% in these surveys, and a sample of order 1000 lenses could be compiled.

References

1. A.W. Blain and M.S. Longair, *MNRAS*, **264**, 509 (1993).
2. A.W. Blain and M.S. Longair, *MNRAS*, **279**, 847 (1996).
3. A.W. Blain, *MNRAS*, **290**, 553 (1997).
4. Ian Smail, R.J. Ivison and A.W. Blain, *ApJ*, **409**, L5 (1997, astro-ph/9708135).
5. R.J. Ivison *et al.*, *MNRAS*, submitted (1998, astro-ph/9712161).
6. M. Bersanelli *et al.*, *COBRAS/SAMBA* (ESA, Paris, 1996).
7. A.W. Blain, R.J. Ivison and Ian Smail, *MNRAS*, submitted (1998, astro-ph/9710003).
8. A.W. Blain, *MNRAS*, **283**, 1340 (1996).
9. A.W. Blain in *The far-infrared and submillimetre universe*, ed. A. Wilson, 175 (ESA, Noordwijk, 1997, astro-ph/9710139).
10. A.W. Blain, *MNRAS*, in press (1998, astro-ph/9801099).
11. A.W. Blain, *MNRAS*, in press (1998, astro-ph/9710160).
12. Ian Smail, R.J. Ivison, A.W. Blain and J.-P. Kneib in preparation.
13. A.W. Blain, *MNRAS*, in press (1998, astro-ph/9801098).
14. R.L. Brown in *Cold gas at high redshift*, eds M. Bremer *et al.*, 411 (Kluwer, Dordrecht, 1996)
15. G. Pilbratt in *The far-infrared and submillimetre universe*, ed. A. Wilson, 7 (ESA, Noordwijk, 1997).
16. F.P. Schloerb in *25 years of millimeter-wave spectroscopy*, eds W.B. Latter *et al.*, 221 (Kluwer, Dordrecht, 1997).
17. Ole Möller and A.W. Blain, *MNRAS*, submitted (1998).
18. A.W. Blain, Ole Möller and Ariyeh H. Maller, *MNRAS*, submitted (1998).
19. D.J. Wilner and M.C.H. Wright, *ApJ*, **488**, L67 (1997).
20. K. Kawara *et al.* in *The far-infrared and submillimetre universe*, ed. A. Wilson, 285 (ESA, Noordwijk, 1997).
21. A.W. Blain, Ian Smail and R.J. Ivison in preparation.
22. A.E. Lange, this volume.

WHY H_0 FROM S-Z + X-RAY WORKS IN PRACTICE

Richard SAUNDERS
Cavendish Laboratory, Madingley Road, Cambridge CB3 0HE, UK.

Various simplifying assumptions are made in the estimation of H_0 via the S-Z (Sunyaev-Zel'dovich) + X-ray route. These are investigated. It is found that uncertainty in the line-of-sight length will likely give an H_0 error of only a few percent with a sample of a dozen clusters, that the use of an isothermal King model rather than a hydrostatic model gives a sysytematic underestimate of perhaps 15 percent at most, that cooling flows and clumping have little effect in practice, and that pressure support by magnetic field appears to make no difference at all.

1 Introduction

The various groups attempting to measure H_0 by combining S-Z (Sunyaev-Zel'dovich) and X-ray observations assume the cluster gas follows an isothermal King model. Although the groups' procedures differ in detail, an outline of ours illustrates what is involved: given the cluster redshift and gas temperature (from X-ray spectroscopy), we fit a King model to the X-ray image and get gas parameters as a function of H_0; we then simulate an S-Z observation of a cluster with these parameters, compare this with the measured S-Z data, and go back and adjust H_0 until we get a good fit. In fitting the King model we allow for cluster ellipticity and assume the core radius along the line of sight is the geometric mean of the two radii in the plane of the sky.

As a result, the different groups get H_0 values for different clusters that now vary by a factor of under two. This lack of discrepancy for such a new method is partly accounted for by the directness of the method, but the agreement seems remarkable given the factors we are taking no account of: the core radius in the line of sight is unknown, the isothermal assumption is unphysical, and we have ignored cooling flows, gas clumping and indeed contributions to pressure from other than the observed gas. In what follows we look at the likely effect on H_0 determination of each of these factors.

The dependence of H_0 on the principal measured quantities is given (see e.g. Jones [1]) by

$$H_0 \propto \frac{T^2 X}{S^2}, \tag{1}$$

where T is the electron temperature, X is the X-ray surface brightness, and S is the S-Z surface brightness. Note that if one changes an assumption then in general *all* the quantities T, X and S change – this is explicitly *not* taken into account in the simulations of Roettiger et al.[2]

2 Effect of unknown line-of-sight core radius

We do not know the line-of-sight core radius for a particular cluster, but we can constrain it from study of clusters which, like the ones we choose for H_0 work, are selected by X-ray luminosity and are thus randomly oriented. We have therefore simulated the effect of our assumption that the unknown core radius is the geometric mean of the other two, as follows:

- we fill a cluster with gas and we pick each of three orthogonal core radii by choosing a number at random between 20 and 120 arcsec – this factor of 6 is much bigger than the ratio of projected radii seen in the X-ray images of the clusters we use, and is thus generous;
- we orient the cluster randomly;
- we simulate its S-Z and X-ray images assuming an H_0 of 50 km s^{-1} Mpc^{-1};
- we analyse these images in the standard way to estimate H_0;
- we repeat all of the above 49 times more.

The results are given in the Figure which shows, for each simulated cluster, the H_0 value obtained and the fractional error in the line-of-sight core radius assumed (i.e. the geometric mean of the two projected onto the sky). The *key* result of this study is however the geometric mean of the H_0 values for all the clusters (taking the geometric mean is the correct way to average H_0 values in a sample): this is 49.2 km s^{-1} Mpc^{-1}, corresponding to an error of under 2 percent even given the extreme factor of 6 range in core radius assumed above. Thus in a real sample of say ten clusters, the resultant error in H_0 from this cause would likely be 4 percent at most.

3 Effect of isothermal approximation

To quantify the effect of the King-model assumption, we have simulated a cluster similar to A2218 assuming the gas to be in the more-physical state of hydrostatic equilibrium. We find that the gas temperature has fallen to about 0.85 of the isothermal value at 3 core radii, and to about 0.65 at 6 radii, and slightly exceeds the isothermal value inside 1.5 core radii – these are consistent with the observed temperature profiles of similar clusters. Now, S-Z and X-ray comparison for H_0 determination is in practice done out to one or a few core radii, and we find that for our A2218 simulation, only 60 percent of the total X-ray luminosity comes from within 3 core radii. So one might be worried – until one reallises that 98 percent of the *projected* X-ray emission, which is what one *actually measures*, comes from within 3 core radii. Thus one doesn't do too badly with a King: assuming H_0 is 50 km s^{-1} Mpc^{-1}, our simulations return 48 if one fits out to 1 core radius and 43 if one fits out to 3. Of course, one can immediately do better by assuming hydrostatic equilibrium in the first place.

4 Massive cooling flows

In another simulation of cluster similar to A2218, we imposed a *massive* cooling flow such that the temperature was 8 keV outside 0.5 core radii but fell sharply to 2 keV inside. This cooling flow is so extreme that one would be bound to notice it anyway. Ignoring it and assuming H_0 is 50 km s^{-1} Mpc^{-1}, performing the standard analysis returned a value of 52 km s^{-1} Mpc^{-1}.

5 Clumping

Consider clumps of gas of lower temperature than the bulk of the gas but in pressure equilibrium with it and thus at higher density. Because the clump pressure is unchanged the S-Z signal is maintained. The density goes up so the X-ray signal goes up, but the *emission-weighted* temperature (which, again, is what one *actually measures*) falls and compensates in the estimation of H_0. We have simulated two cases. In the first, we have modelled a cluster in which, throughout the whole cluster, there are equal volumes of gas with a density contrast of a factor of two. Analysing this on the assumptions of isothermal gas and an H_0 of 50 km s^{-1} Mpc^{-1}, our standard procedure returns $H_0 = 49$. Increasing the density contrast to an extreme factor of 5 (it is very hard to see how this could be done undetectably) returns $H_0 = 43$.

6 Unseen contributions to pressure support

Suppose that part of the pressure support against gravity comes from an extra, non-gaseous, invisible phase such as magnetic field. One might imagine this would lead to major uncertainty for H_0 determination by this route. This is in fact not the case, as the following shows. Take the gas pressure to be a fraction f of the total (gas + magnetic) pressure: $P_{gas} = fP_{total}$. Now the extra magnetic phase does not produce any X-rays, so the emission-weighted temperature T is unchanged. The X-ray surface brightness falls, compared with the case of no magnetic field, to

$$X \propto \int n^2 dl \propto f^2 \int n_N^2 dl = f^2 X_N, \tag{2}$$

where the subscript N denotes the "normal" case of no magnetic field. Likewise the S-Z signal falls:

$$S \propto \int ntdl \propto f \int n_N T dl = f S_N. \tag{3}$$

Now we have

$$H_0 \propto \frac{T^2 X}{S^2} = \frac{T^2 f^2 X_N}{f^2 S_N^2} \tag{4}$$

So the H_0 value obtained is unaffected by the presence of the magnetic pressure support. Remarkable!

7 Conclusions

In examining the effects of the greatly simplifying assumptions currently made in the estimation of H_0 by the S-Z + X-ray route, we find the following.

1. The uncertainty in the line-of-sight depth of a cluster should lead to an error in H_0 of a few percent given a sample of ten clusters.

2. The use of the unphysical isothermal King model leads to a systematic underestimate of H_0 of some 15 percent in the worst case, but this is easily remedied.

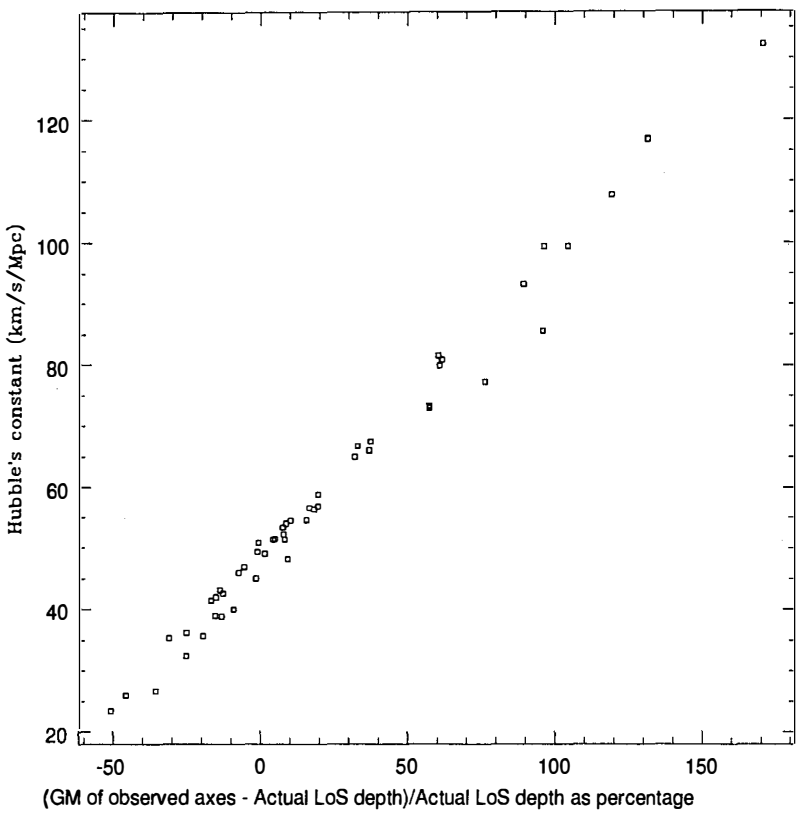

3. Cooling flows are irrelevant and clumping is relatively unimportant, because the changes to X-ray surface brightness are largely compensated by changes to the emission-weighted temperature.

4. Contributions to pressure from unseen phases such as magnetic field do not matter at all.

Acknowledgments

Keith Grainge, Will Grainger, Mike Jones and Alessia Maggi contributed substantially to this work. This work, and the Ryle Telescope project in general, is partly funded by the Particle Physics and Astronomy Research Council.

References

1. Jones M., Astro. Lett. and Communications **32**, 347 (1995)
2. Roettiger, K., et al., Ap.J **482**, 588 (1997)

Fast Determination of the Power Spectrum from Cosmic Microwave Background Sky Maps[a]

Siang Peng Oh, David N. Spergel
Princeton University Observatory, Princeton, NJ 08540, USA

Gary Hinshaw
Goddard Space Flight Center, MD 20771, USA

Abstract

There is enormous potential to advance cosmology from statistical characterizations of cosmic microwave background sky maps. The angular power spectrum of the microwave anisotropy is a particularly important statistic. Existing algorithms for computing the angular power spectrum of a pixelized sky map typically require $O(N^3)$ operations and $O(N^2)$ storage, where N is the number of independent pixels in the map. The *MAP* satellite will produce megapixel maps of the cosmic microwave background temperature at multiple frequencies; thus, existing algorithms are not computationally feasible. We introduce an algorithm that requires $O(N^2)$ operations and $O(N^{3/2})$ storage that can find the minimum variance power spectrum, and present results from an analysis of a simulated two million pixel map. Our algorithm is roughly one million times faster than previous methods, and thus makes feasible an analysis that was hitherto intractable.

1 Introduction

Computing the power spectrum of the CMB maps which the upcoming MAP and PLANCK missions will yield should reveal enormous amounts of information about conditions in the early universe. However, the canonical methods which have been used on the COBE data cannot be extended to these maps: the operations counts scale as $O(N^3)$ and the required memory scales as $O(N^2)$, which for $N \sim few 10^6$ would take several hundred years on a GFlop machine and require terabytes of RAM.

All existing methods employ some variant of likelihood maximisation. In Gaussian models the probability distribution of the power spectrum c_l given the data $\mathbf{x}$ is given by:

$$\mathcal{L}(c_l|\mathbf{x}) = \frac{\exp\left(-\frac{1}{2}\mathbf{x}^T\mathbf{C}^{-1}\mathbf{x}\right)}{(2\pi)^{N/2}(\det\mathbf{C})^{1/2}} \tag{1}$$

where $\mathbf{C} = \mathbf{S} + \mathbf{N}$ is the covariance matrix of the theoretical model, which has both signal($\mathbf{S}$) and noise ($\mathbf{N}$) contributions. An efficient way to maximise the likelihood function $L = -2\ln(\mathcal{L})$ is to first expand it in a Taylor series. One can then use the Newton-Raphson technique (Press et al, 1992) to iteratively solve for the root of the ensuing equations:

$$c_l^{(n+1)} = c_l^{(n)} + \frac{1}{2}\sum_{l'} \mathbf{F}_{ll'}^{-1}\left[\mathbf{x}^T\mathbf{C}^{-1}\mathbf{P}^l\mathbf{C}^{-1}\mathbf{x} - \mathrm{tr}(\mathbf{C}^{-1}\mathbf{P}^l)\right] \tag{2}$$

where

$$\mathbf{P}^l = \frac{\partial\mathbf{C}}{\partial c_l} \tag{3}$$

and we have replaced the second derivative of the likelihood function by its expectation value, the Fisher matrix:

$$\mathbf{F}_{ll'} = \left\langle -\left(\frac{\partial^2}{\partial c_l \partial c_{l'}}\right)\ln\mathcal{L}\right\rangle = \frac{1}{2}\mathrm{tr}(\mathbf{C}^{-1}\mathbf{P}^l\mathbf{C}^{-1}\mathbf{P}^{l'}) \tag{4}$$

Similar results have been obtained by previous authors (Tegmark 1997, Bond et al 1997). Our key advance is in reducing all ostensibly $O(N^3)$ operations to $O(N^2)$ operations:

[a]Work reported by A. Refregier

•$\mathbf{C}^{-1}\mathbf{x}$ Rather than solve this equation exactly via Cholesky techniques, we solve it iteratively via conjugate gradient techniques (Press et al 1992, Barrett et al 1994), which are applicable to symmetric, positive definite linear systems. A good approximate inverse or preconditioner $\tilde{\mathbf{C}}^{-1}$ is essential to reducing the number of iterations required. We find such a preconditioner by exploiting the approximate azimuthal symmetry of the noise pattern on the sky. It requires $O((N/20)^{3/2})$ memory for storage and takes $O((N/20)^2)$ operations to compute. In addition, each iteration of the conjugate gradient technique involves performing matrix multiplies of the form $\mathbf{Cz}$. We speed this up by writing $\mathbf{C}$ as a convolution of diagonal matrices and spherical harmonic transforms. By employing fast spherical harmonic transforms (Muciaccia et al 1997, Driscoll & Healey 1994), we are able to reduce the cost of matrix multiplies to $O(N^{3/2})$, down from $O(N^2)$. The total cost of solving $\mathbf{Cx} = \mathbf{z}$ is $O(n_{iter}N^{3/2})$, where $n_{iter} \sim 6$. As an example, we take $\sim 30s$ to solve the system for a 500 000 pixel map, and $\sim 250s$ to solve the system for a 2 million pixel map, as a single processor job on an SGI Origin 2000.

•$\mathrm{tr}(\mathbf{C}^{-1}\mathbf{P}^l)$ We first compute this term approximately by once again assuming azimuthal symmetry of the noise. We then compute it exactly by generating Monte Carlo realisations of maps and exploiting the fact that

$$\left\langle \mathbf{x}^T\mathbf{C}^{-1}\mathbf{P}^l\mathbf{C}^{-1}\mathbf{x} \right\rangle = \mathrm{tr}(\mathbf{C}^{-1}\mathbf{P}^l) \tag{5}$$

where we have used $\langle \mathbf{x}^T\mathbf{x} \rangle = \mathbf{C}$. The errors obtained by computing the trace term via Monte-Carlos rather than exactly are $\sqrt{(1 + 1/n_{realisations})}$ times larger than the minimum variance errors. Thus, for instance, if we perform 100 Monte-Carlos, our error bars are only 0.5% larger than minimum variance. The total cost of this step is $O(n_{realisations}n_{iter}N^{3/2})$.

•$\mathbf{F}$ Note that only an approximate second derivative is required to converge to the maximum of the likelihood function. The maximum likelihood solution is fully independent of $\mathbf{F}$. We therefore compute $\mathbf{F}$ approximately using the preconditioner $\tilde{\mathbf{C}}^{-1}$ previously computed, which required $O((N/20)^2)$ operations. Once we obtain the maximum likelihood c_ls, we use Monte Carlo simulations to obtain their probability distribution and hence error estimates.

2 Results

Figure 1 shows the initial power spectrum and recovered c_l's for a simulated 2 million pixel map, with a noise level appropriate to a single frequency of *MAP*'s 2 year data. We assume the noise per pixel scales inversely with pixel area. We apply a Galactic plane cut that excludes the region $|b| < 10°$, with an additional 5% of the sky removed at random to simulate the effect of cutting extragalactic point sources. In addition, we assume a 0.21° FWHM beam size.

We used 10 Monte-Carlo simulations to compute $\mathrm{tr}(\mathbf{C}^{-1}\mathbf{P}^l)$. The result converged in 5 iterations in c_l space, running for 10 hours on an 8 processor Origin 2000. We expect an least a further factor of 2 reduction in run-time with more agressive optimization and parallelization of the code. The recovered c_l's $\chi^2/(l_{max} - 1) = 1.08$, in reasonable accordance with the expectation that for a minimum variance technique we should have $\chi^2/l_{max} \sim 1 \pm 1/\sqrt{l_{max}}$ (in fact, since we expect to obtain $(1 + 1/n_{realisations})\chi^2$, we are well within the expected bounds). We find that 67% of the points lie within the 1 σ error band, and 95% of the points lie within the 2 σ error band. Note that the negative c_l's at high l are of no physical consequence. If one is uncomfortable with them, a minimum variance binning at high l could be performed.

Full details on the algorithm are reported in Oh, Spergel & Hinshaw 1998.

Acknowledgments

We have benefited from discussions with Chuck Bennett, Peter Kostelec, Robert Lupton, Bill Press, George Rybicki, Michael Strauss, Max Tegmark and Michael Vogeley. SPO, DNS, and GH are supported by NASA's *MAP* Project.

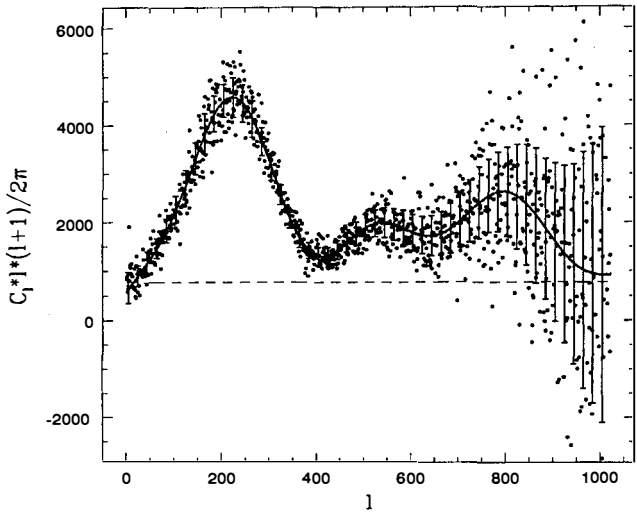

Figure 1: Recovered c_ls for a 2 million pixel map, with representative error bars shown. The dotted line indicates the starting guess.

References

1. Barret,R.,*et al* 1994, Templates for the Solution of Linear Systems: Building Blocks for Iterative Methods (SIAM:Philadelphia).
2. Bond, J.R., Jaffe, A.H., Knox, L., 1997, astro-ph/9708203
3. Driscoll, J.R., & Healy, D.M. 1994, Advances in Applied Mathematics, 15, 202
4. Muciaccia, P.F., Natoli, P., & Vittorio, N. 1997, astro-ph/9703084
5. Oh, S.P., Spergel, D.N., Hinshaw, G., 1998, ApJ, submitted
6. Press, W.H., Teukolsky, S.A., Vetterling, W.T., & Flannery, B.P., 1992, Numerical Recipes: The Art of Scientific Computing, 2nd Ed., (Cambridge: Cambridge University Press)
7. Tegmark, M. 1997, *Phys. Rev.* D, 55, 5895

MOVING GRAVITATIONAL LENS EFFECT

N. AGHANIM, S. PRUNET, O. FORNI
Institut d'Astrophysique Spatiale, Bât. 121, Université XI
91405, Orsay CEDEX, France

& F.R. BOUCHET
Institut d'Astrophysique de Paris, 98 bis Boulevard Arago
75014, Paris, France

We investigate the secondary anisotropies induced by the transverse motions of clusters of galaxies and derive the induced average contribution in three cosmological models.

When a gravitational potential well evolves, after recombination, the extra-time delay the CMB photons suffers to traverse the well induces a secondary anisotropy [1]. The moving gravitational lens effect takes place for an apparent evolution of the potential well: due to the bulk motion of structures across the line of sight. Photons crossing the leading edge of a structure are redshifted (increasing depth of the potential well during the crossing time); while photons crossing the trailing edge of the same structure are blueshifted [4], [5]. The frequency shift due to this transverse motion is directly related to the gravitational deflection angle. The induced secondary anisotropy has a characteristic spatial signature[a] a hot-cold temperature pattern (Fig. 1) with black body spectrum.

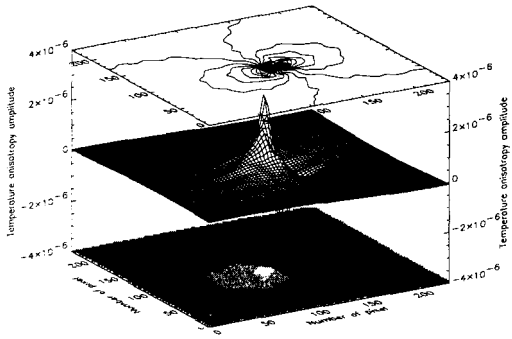

Figure 1: Spatial pattern of a moving lens anisotropy ($M = 10^{15}\ M_\odot$ and $v = 600$ km/s).

[a] Following M. Birkinshaw, we call it the "butterfly effect".

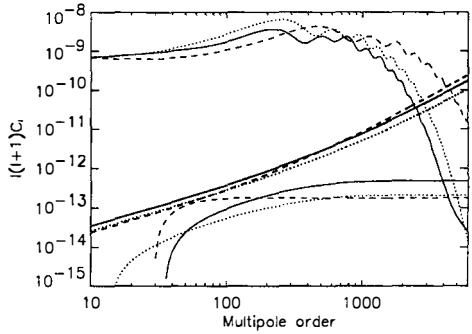

Figure 2: The power spectra for the SCDM model (solid line), OCDM model ($\Omega_0 = 0.3$) (dashed line) and ΛCDM model ($\Lambda = 0.7$ and $\Omega_0 = 0.3$) (dotted line) are shown for the primary fluctuations (CMBFAST code), the SZ kinetic fluctuations (thick lines) and to the butterflies (thin lines).

1 Method and hypotheses

We compute the anisotropies induced by a predicted[2] population of lensing structures (described with the universal profile[3]). We thus simulate maps of the secondary anisotropies (thermal and kinetic Sunyaev-Zel'dovich effect and "butterfly effect"). The velocities are drawn from a Gaussian distribution with its *rms* value derived from initial power spectrum. The positions of the structures (randomly drawn) are recovered thanks to the SZ thermal effect, which is perfectly separated by its spectral signature. We analyse the maps with a wavelet decomposition (with a suitable wavelet) of the remaining signal (SZ kinetic + butterflies + primary CMB). We study three cosmological models.

2 Main results and Conclusions

• The primary CMB anisotropies are dominant in all the cosmological models (for $l < 4000$ in SCDM, $l < 4500$ in ΛCDM and $l < 6000$ in OCDM). The rms contribution of the "butterfly effect" is far below the SZ kinetic and primary anisotropies. This contribution is thus negligible and will not affect the future CMB measurements (Fig. 2).
• We note the point-like l^2 dependence of the power spectrum of the SZ kinetic anisotropies at small scales implying a high level of confusion at these scales.
• We have highlighted[7] the fact that the butterfiies have a very significant spatial signature but we did not succeed in separating them from the SZ kinetic and primary CMB with which there is a spectral confusion. It is even worse at small scales for weak structures for which we do not observe the SZ thermal effect.

References

1. Rees, M.J., Sciama, D.W. *Nature* **511**, 611 (1968)
2. Press, W., Schechter, P. *ApJ* **187**, 425 (1974)
3. Navarro, J.F., Frenk, C.S., White, S.D.M. *ApJ* **462**, 563 (1996)
4. Birkinshaw, M. in *Moving Gravitational lenses*, p. 59, eds. J. Moran, J. Hewitt & K.Y. Lo (Springer-Verlag, Berlin, 1989)
5. Birkinshaw, M., Gull, S.F. *Nature* **302**, 315 (1983)
6. Viana, P.T.P., Liddle, A.R. *M.N.R.A.S.* **281**, 323 (1996)
7. Aghanim, N., Prunet, S., Forni, O., Bouchet, F.R. submitted to *A&A*

MAIN BEAM AND SIDELOBE EFFECTS ON PLANCK OBSERVATIONS

C. BURIGANA[1], N. MANDOLESI[1], L. VALENZIANO[1],
F. VILLA[1], M. BERSANELLI[2] and D. MAINO[3]
[1] *Istituto TeSRE/CNR, Via Gobetti 101, I-40129 Bologna, Italy*
[2] *IFCTR/CNR, Via Bassini 15, I-20133 Milano, Italy*
[3] *SISSA - Intern. School for Advanced Studies, Via Beirut 2-4, I-34014 Trieste, Italy*

The extreme sensitivity of the Planck observations requires that all potential systematic effects are avoided or drastically reduced. Systematic errors can be expected from non-ideal optical performance, receiver instabilities, thermal effects, pointing accuracy. The impact of each effect on the measurements must be properly estimated, and it should be reduced by a careful instrument design and an adequate observational strategy, rather than relying on a-posteriori corrections of their combined effect in the data. We focus here on the effects introduced by beam distortions for the Planck optical design. We point out the main requirements on the primary mirror aperture to achieve the key cosmological goal of 10′ resolution at the "clean" astrophysical window at 100 GHz.

1 Introduction

Future space missions dedicated to the imaging of the cosmic microwave background (CMB), like Planck and MAP, represent a powerful opportunity for cosmology and astrophysics. The nominal angular resolution and sensitivity of the Planck instruments, both at high frequencies (HFI) and low frequencies (LFI), allow to determine the angular power spectrum, C_l, of CMB primordial fluctuations up to multipoles, l, larger than 10^3 (see Vittorio[1] and references therein), i.e. until secondary anisotropies do not largely overwhelm primordial signatures. On the other hand, experiences from the previous CMB experiments as well as a realistic analysis of Planck observational performances indicate that a stringent control of all the systematic effects is crucial to reach the mission objectives. Galactic and extragalactic foregrounds are important sources of astrophysical contaminations at a level that depend on the frequency and angular scale (see De Zotti *et al.* [2] and references therein), but, from the opposite point of view, their study represents an important co-product of the Planck mission. Two complementary approaches have been proposed by both LFI and HFI teams for reducing the impact of instrumental systematic effects on anisotropy measurements: the "hardware" approach, i.e. design mission strategy and instruments in order to minimize all the potential systematic effects, and the "software" approach, i.e. develop data analysis methods to further reduce residual effects in the data. We present here some results of the LFI team studies on the Planck telescope optical performances.

2 The effect of sidelobes and main beam distortions

Optical aberrations make the main (i.e. within few FWHM from the beam centre) beam response somewhat different from the reference case of a pure gaussian, centrally symmetric shape. The

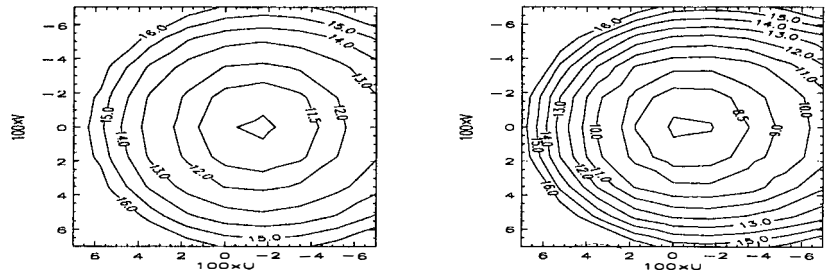

Figure 1: Contour plot of effective angular resolution (in arcmin) for the relevant sky field of view, U–V, in the case of a 1.3 m (left panel) and a 1.75 m (right panel) aperture gregorian telescope.

radiation pattern at large angles from the main beam (sidelobes) is dominated by diffraction effects on the structure edges, that make not negligible the response at large angles from the beam centre. Sidelobes introduce a contamination in sky temperature measured by the main beam due to the contribution of the sky signal entering the outer regions; this effect maybe significant owing to the Galactic emission, depending on the observed sky region, on the frequency and on the shielding efficiency. Further, the behaviour of the radiation pattern at intermediate angular scales from the beam centre has to be carefully considered. The present optical analysis for the "Phase A" Planck telescope is still preliminar but indicates a maximum ratio of about the 10% between the "outer" signal and the "inner" one, to be principally ascribed to the beam response immediately external to the main beam (K. Gorski and E. Hivon, private communication). Main beam distortions may introduce a degradation of the angular resolution and of the sensitivity per resolution element. These two last effects can be seen as orthogonal one each other in the space $\theta - \Delta T$ of angular scales and temperature anisotropy or, equivalently, in the space of $l - C_l$ (Burigana *et al.*[3], Mandolesi *et al.*[4]). For telescopes like that of Planck, the relative importance of main beam distortions and sidelobe effects is controlled by the edge taper (Sletten[5]): reducing its level reduces the sidelobe level and the main beam angular resolution. An edge taper of -30 dB relative to the centre for the central beam has been assumed for the present computations.

The instrument design of the Planck mission calls for multi-frequency focal plane arrays placed at the focus of an off-axis gregorian telescope, in order to achieve proper angular resolution, sensitivity, and spectral coverage. As a consequence, not all the feedhorns can be located very close to the centre of the focal plane, where optical distortions are minimum. This issue is crucial after the recent proposed baseline configuration of the Focal Plane Unit (FPU), a symmetric design with HFI in the central portion of the focal plane and LFI distributed as a ring around it, thus requiring a major effort to minimize the negative effect of beam distortions.

We have used a software, based on the calculations reported by Sletten [5], to compute the beam shapes for three gregorian telescopes with different aperture D: 1.3 m ("Phase A" mirror, see Bersanelli *et al.*[6]), 1.55 m, 1.75 m. A typical beam shape is reported in Villa *et al.*[7]. The contour plots of typical off-axis beams show that the curves of equal response roughly have elliptical shapes, with the centres of the different response level curves somewhat shifted one each other, coupled to localized distortions (spots) at response levels of about -15 dB respect to the centre (see Villa *et al.*[7] and Mandolesi *et al.*[4]). A decrease in the effective beam angular resolution is also evident in the off-axis beam shapes. These features increase with the distance from the optical axis and with the frequency.

In order to evaluate the main beam distortion impact on Planck observations, we have applied a modified version of the fully numerical method described in Burigana *et al.*[3]: a

Table 1: Beam properties at 100 GHz for telescopes of different aperture: W_e (in arcmin) and values (in μK) of the thermodynamic temperature *rms* differences, σ_{th}, measured by "true" beams and corresponding gaussian beams. Results from pairs of beams located at the same U and | V | have been averaged. By averaging over all the feeds we have: $< W_e >= 13.1, 11.0, 9.7$ arcmin and $< \sigma_{th} >= 2.2, 2.1, 2.0\mu$k respectively for the 1.3, 1.55, 1.75 m aperture telescopes.

D →	1.3m		1.55m		1.75m		D →	1.3m		1.55m		1.75m	
Feed	W_e	σ_{th}	W_e	σ_{th}	W_e	σ_{th}	Feed	W_e	σ_{th}	W_e	σ_{th}	W_e	σ_{th}
1	12.00	2.10	10.00	1.70	8.90	2.60							
2 & 17	12.15	3.15	10.25	2.75	9.00	1.90	3 & 16	12.35	2.70	10.45	2.10	9.20	2.10
4 & 15	13.00	2.30	11.00	1.45	9.80	2.70	5 & 14	12.90	2.40	10.90	2.80	9.55	1.75
6 & 13	13.15	2.00	11.00	2.00	9.70	1.90	7 & 12	13.40	2.05	11.20	2.35	9.85	2.00
8 & 11	13.90	1.15	11.65	1.95	10.25	1.85	9 & 10	14.20	2.05	12.05	1.40	10.70	1.70

simulated CMB fluctuations sky (standard CDM, but our results are essentially independent of the assumed model) is convolved with the calculated beams truncated at 1° from the beam centre, as well as with a set of Gaussian beams of widths from 6′ to 17′. The FWHM of the Gaussian beam that gives the smallest sky temperature *rms* difference compared to a given distorted beam can be taken as the effective angular resolution, W_e, of that distorted beam (semi-analytical methods, based on effective window functions, give very similar results, see Mandolesi *et al.* [4]). In addition, this minimum value of *rms* quantifies the typical difference between signals measured by a distorted beam and the *corresponding* gaussian one, i.e. the added noise due to main beam distortions in absence of further reduction through data analysis.

3 Optical performance versus primary mirror aperture

Figure 1 shows our results as contour plots of effective angular resolution over the relevant sky field of view (the U–V plane, the U (V) direction corresponding to the x (y) direction on the FPU – see the figure in Villa *et al.* [7]) for the smallest and largest primary mirrors considered here. Note the symmetry of this effect in the V direction and the large asymmetry in the U direction which strictly reflects the intrinsic asymmetry of the adopted gregorian configuration; the locations of the feedhorns in the focal plane have been designed to take this effect into account (see Villa *et al.* [7] and Mandolesi *et al.* [4]). Table 1 summarize our results for all the 100 GHz beams.

We are able also to quantify one of the most important effects of distorted beams: even observations at the same position on the sky taken by different feeds at a given frequency *cannot be simply averaged together*, being each beam differently distorted, possibly with a different orientation. Figure 2 shows the distributions histogram of differences between the signal measured by the all the 17 LFI 100 GHz feeds (solid lines) at 100 different positions choosen along a typical scan circle on the sky and for two subsets of feeds with quite similar (differences $\lesssim 0.2'$, dotted lines) or quite different ($\sim 2'$, dashed lines) W_e. Unfortunately, this dispersion of the sky temperature measurements cannot be significantly reduced by increasing the telescope aperture. It can be reduced only with a different FPU configuration which allows a location of all the 100 GHz feeds closer to the centre or, hopefully, in the data analysis; nevertheless, all previous experience with CMB data shows that the more and larger are the systematic effects that must be scrubbed from the data in analysis, the more uncertain is the result.

As shown by the evaluations in Figure 1 and Table 1, a larger telescope allows to reach the nominal 10′ resolution; this is due both to the better resolution of the best LFI feed and to the partial reduction of the (absolute) angular resolution degradation between the best and the worst LFI feed in the LFI ring region; in addition, at least a partial reduction of the added noise is obtained. This is due to the better optical performance as well as to the well known geometrical property that larger aperture telescopes lead to beam locations closer to the optical

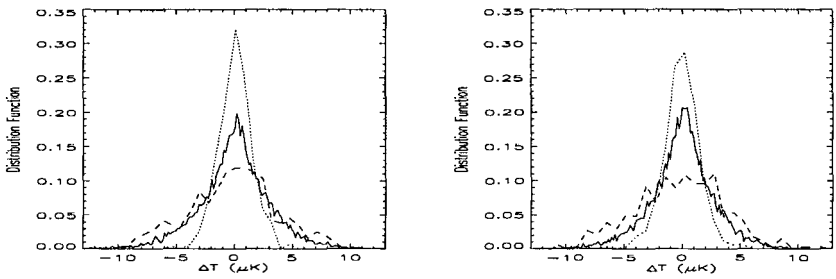

Figure 2: Distribution functions of differences between the signal measured by the LFI 100 GHz feeds and for two subsets of them (see text). [Telescope aperture of 1.3 m (left panel) and of 1.75 m (right panel)].

axis direction, so automatically releasing the issue of the distortions. For example, in the case of 1.3 m aperture telescope the mean 100 GHz beam points at an angle of 3.3° from the optical axis; this angle becames about 2.8° or 2.5° respectively for an aperture of 1.55 m or of 1.75 m.

4 Conclusions

Our results show that the "Phase A" optical design of Planck suffers from large off-axis beam distortions that seriously degrade the beam effective angular resolution and compromise Planck science as well as enormously complicate the data analysis. The "Phase A" telescope and the present FPU arrangement yields a $\sim$ 30 percent degradation of the LFI effective angular resolution, and is therefore not acceptable.

Our analysis shows that these deficiencies can be reduced by enlarging the primary mirror (hopefully up to 1.75 m aperture), using an edge taper of about $-(30 \div 35)$ dB and optimizing the shapes of the primary and secondary. Such a telescope would have little thermal and structural impact on the mission design. Moreover, possible elimination of the need for a large radiation shield may result in net mass savings to ESA compared to the "Phase A" design. It would be more prudent and advantageous to build a larger telescope for Planck that minimizes the beam distortions (particularly for what concerns the impact on the angular resolution) and/or to locate the LFI feeds at 100 GHz closer to the centre (so minimizing the dispersion of the sky temperature measurements too) than to try the reduction of these distortion effects during the data analysis only.

Acknowledgments

It is a pleasure to thank K. Gorski, P. Guzzi, E. Hivon, C. Lawrence, M. Malaspina, J. Tauber, L. Wade and M. White for useful discussions.

References

1. N. Vittorio, this Conference, (1998).
2. G. De Zotti *et al.*, this Conference, (1998).
3. C. Burigana *et al.*, A&A, in press (1998).
4. N. Mandolesi *et al.*, Int. Rep. TeSRE/CNR 199 (1997).
5. C.J. Sletten, Reflector and Lens Antennas, Artech House (1988).
6. M. Bersanelli *et al.*, ESA, COBRAS/SAMBA Rep. Phase A Study, D/SCI(96)3, (1996).
7. F. Villa *et al.*, this Conference, (1998).

SYNCHROTRON EMISSION FROM THE GALAXY

R.D. DAVIES and A. WILKINSON
Department of Physics & Astronomy, Jodrell Bank, University of Manchester
Manchester M13 9PL, England

Galactic synchrotron emission is a potentially confusing foreground, both in total power and in polarization, to the Cosmic Microwave Background Radiation. It also contains much physical information in its own right. This review examines the amplitude, angular power spectrum and frequency spectrum of the synchrotron emission as derived from the presently available de-striped maps. There are as yet no maps at arcminute resolution at frequencies above 2.4 GHz. This incomplete information is supplemented with data from supernovae, which are thought to be the progenitors of the loops and spurs found in the Galactic emission. The possible variations of the frequency spectral index from pixel to pixel are highlighted. The relative contributions of free-free and synchrotron radiation are compared, and it is concluded that the free-free contribution may be smaller than had been predicted by COBE. New high resolution polarization surveys of the Galactic plane suggest detail on all scales so far observed. At high latitudes the large percentage polarisation means that the foreground contamination of the polarised CMB signal will be more serious than for the unpolarized radiation.

1 Introduction

Galactic emission at radio wavelengths is important to understand in its own right. Moreover it is crucial to be able to quantify and remove this component as a foreground to the cosmic microwave background (CMB). Both synchrotron and free-free emission contribute to this foreground, with the synchrotron emission dominating at low frequencies ($\leq$1 GHz).

The synchrotron emissivity is a function of both the relativistic (cosmic ray) density and the local magnetic field strength. The luminosity at frequency ν is given by

$$I(\nu) = const\ LN_0B^{(p+1)/2}\nu^{-(p-1)/2} \quad (1)$$

where N_0 is the density of relativistic electrons, L is the emission depth, B is the magnetic field and the relativistic electron energy spectrum[22] is given by $dN/dE = N_0E^{-p}$. The radio spectral

index is $\alpha = (p-1)/2$ in energy terms or $2+\alpha$ when expressed as a brightness temperature $T_B \propto \nu^{-(2+\alpha)} = \nu^{-\beta}$. Within the interstellar magnetic field of 2 to 5 microgauss, emission at GHz frequencies is characteristically from relativistic electrons with an energy of 1 to 10 GeV. Both B and N_0, as well as p, will vary from point to point in the Galactic disk and nearby halo. The cosmic ray electrons are thought to originate mainly in supernovae then diffuse outwards in the expanding remnant. Structure will be formed in the remnant as it collides with the non-uniform ambient medium. The magnetic field will be likewise amplified in compression regions and vary in strength and direction. The net effect is to produce elongated synchrotron emission structures on a wide range of scales. The spectral index of the emission will vary with position for two reasons. Firstly the electron spectral index varies from one supernova to another and secondly the spectrum steepens ($\Delta p = +1$) with time due to radiation energy loss thus giving an age-dependent spectral index.

This paper will describe the synchrotron features in and near the Galactic plane which are believed to give rise to the structures seen at higher galactic latitudes. All-sky and large area surveys are assessed to give information about the amplitude and spectrum of the high latitude emission which is a potential confusing foreground to the CMB. Comments are given about the role of synchrotron polarization and of free-free emission.

2 Large area surveys at low frequencies

Radio surveys at frequencies less than 2 GHz are dominated by synchrotron emission. The well-known survey by Haslam et al. [7] at 408 MHz is the only all-sky map available. Large-area surveys with careful attention to baselines and calibration have also been made at 1420 MHz [15] and most recently at 2326 MHz [9]. All these investigations have been made with FWHP beamwidths of less than 1°. Before these surveys can be used to derive the angular power spectrum and the emission (frequency) spectral index, it is necessary to remove the baseline stripes [2] in the most commonly used radio maps at 408 and 1420 MHz. These stripes contain power on angular scales of a few to ten degrees. Lasenby [12] has used the 408 and 1420 MHz surveys to estimate the spatial power spectrum of the high latitude region surveyd by the Tenerife CMB experiments; he found an angular power spectrum somewhat flatter than the l^{-3} law derived for HI and for IRAS far infrared emission.

The spectral index of Galactic synchrotron emission can be readily determined at frequencies less than 1 GHz where the observational baselevel uncertainty is much less than the total Galactic emission. Lasenby [12] used data covering the range 38 to 1420 MHz to determine the spectral index variation over the northern sky. Clear variations in spectral index of at least 0.3 about a mean value of 2.7 were found. There was a steepening in the spectral index at higher frequencies in the brighter features such as the loops and some SNRs. Up to 1420 MHz, no such steepening was found in the regions of weaker emission. At higher Galactic latitudes where no reliable zero level is available at 1420 MHz, an estimate can be made of the spectral index of local features by using the T-T technique. The de-striped 408 and 1420 MHz maps gave spectral indices of β = 2.8 to 3.2 in the northern galactic pole regions [2].

The de-striped 408 MHz map shows there are substantial areas (100° × 50° in RA × Dec) in both the northern and southern skies which are devoid of appreciable synchrotron structure and can be used for CMB studies. The Tenerife experiments have been based on the northern low emissivity band centred on Dec = 40°, RA = 130° to 250° where the rms Galactic emission in a 5° beam is $\leq 4\mu$K at 33 GHz [7].

3 What we know from SNRs

Supernovae are probably the progenitors of the main structures in the Galactic radio emission at intermediate latitudes. The supernova remnants (SNRs) are the easily recognisable early stages of the expansion phenomenon. A supernova releases about 10^{51} ergs into the interstellar medium (ISM). This passes through the free expansion phase, then after it has encountered its own mass in the ISM it moves into the Sedov (adiabatic) phase. The SNR shock ultimately disappears when the expansion velocity slows to the local sound velocity. This process takes 10^5 to 10^6 years to reach the point where the remnant is not clearly recognizable as a single entity but will still give rise to synchrotron emission from the residual CR electrons and magnetic fields.

An examination of statistics and structure of SNRs will give some indication of the properties of the emission from their residual structures. Firstly, it is possible to recognise the various evolutionary phases in the SNR phenomenon in individual remnants. Objects like Cas A and the Crab Nebula (500 to 1000 years old) are in the early free expansion stage while the Cygnus Loop (15 to 20,000 years old) is losing energy in multiple shocks. Secondly, the statistics of the spectral index of the integrated emission show a spread of α of ± 0.1 about the mean value of 0.7 [18], with some objects such as the Crab Nebula ($\alpha = 0.3$) having more extreme indices. This spread will presumably result in a spread in the spectral indices of their residual structures.

The Cygnus Loop provides an excellent case study of an SNR in its late phase of evolution. High sensitivity maps of arcmin resolutions are available at a range of frequencies. This remnant is 3.°5 x 2.°5 (30 pc $\times$ 20 pc) in diameter lying at l = 74°, b = -8.°5 and at a distance of 500-800 pc. The 1.4 GHz synthesis map by Leahy, Roger and Ballantyne [13] made with a 1x1 arcmin^2 beam shows both filamentary and diffuse structure on angular scales from a few to 30 arcmins. By comparing maps at 0.408 and 2.695 GHz Green [6] finds significant variations (0.3) in spectral index between the major features of the remnant.

4 What we know from spurs and loops

Large features with a synchrotron spectrum extend far from the Galactic plane. The most prominent of these are the spurs and loops which describe small circles on the sky with diameters in the range 60° to 120° [1]. Because of their association with HI and, in some cases, with X-ray emission, they are believed to be low surface brightness counterparts of the brighter SNRs seen at lower latitudes. Other more diffuse structure at higher latitudes may be even older remnants. Reich and Reich [16] find that the Loops I (the North Polar Spur) and II have a steeper spectrum than the average Galactic emission. Between 408 MHz and 1420 MHz these two loops have temperature spectral indices of 2.93 and 2.85 respectively. Using T-T plots Davies, Watson and Gutierrez [2] derived a spectral index of $\beta = 3.2$ for the brightest part of Loop I. Lawson et al.[12] claim that most of the large structures seen on the maps are related to Loops I and III suggesting that they are the evidence of diffusive shock acceleration of the CR electrons derived from the supernova. They derive a distance for Loop I of 130 $\pm$ 75 pc and a radius of 115 $\pm$ 68 pc; Loop III is thought to be of similar size.

A revealing high sensitivity survey of a substantial part of the southern Galactic plane (l = 238° to 365°, b = -5° to +5°) has been made with a resolution of 10 arcmin at 2.4 GHz by Duncan et al. [3]. These authors found a large amount of structure and detail including many low surface brightness loops and spurs. They also list over 30 possible SNR candidates, a number of which have angular diameters of about 10°. Many of the spurs can be traced even further from the plane in the 2.326 GHz survey of Jonas, Baarth and Nicolson [9]. The spectral index of these new spurs has still to be determined.

5 Higher frequency surveys at Jodrell Bank and Tenerife

It is important to make Galactic surveys at intermediate and high latitudes at frequencies closer to those at which the CMB structure is being investigated. Because of the variation of spectral index from one region to another, the structure at 408 MHz will be quite different from that at 10 or 30 GHz. Two separate experiments have been established to address this problem. The first is a high sensitivity short baseline interferometer operating at 5 GHz at Jodrell Bank[14](Fig. 1). By making observations at a range of baselines the point source and the Galactic contribution to the microwave background can be separated. After correction for the point sources the Galactic emission at 5 GHz can be compared with the published 408 MHz survey. The spectral index of Galactic features in the survey was found to be about 3.0 at intermediate and higher Galactic latitudes.

The 10, 15 and 33 GHz beamswitching radiometers at Teide Observatory Tenerife are scaled to give the same resolution (5° FWHP beamswitched ±8°). Comparison of the surveys at the three frequencies should allow the Galactic emission to be separated from the intrinsic CMB component. Observations already available from this experiment can constrain the Galactic contribution at 33 GHz. The observed rms fluctuation level at 10 GHz in the Dec = +40° scan between RA = 160° and 230° is 29 +20/-30 μK[7]. This rms level will include both a Galactic and CMB contribution. Using a 2σ upper limit and subtracting quadratically the detected CMB signal (54 μK) we derive an upper limit for the Galactic emission at 10 GHz of 43 μK. This would produce an upper limit at 33 GHz of 2 μK if it were synchrotron with $\beta = 3.0$ and an upper limit of 4 μK if it were free-free emission with $\beta = 2.1$. Hancock et al.[7] derive a spectral index for Galactic emission at the 3 frequencies of $\beta = 3.1$.

6 Synchrotron versus free-free

Free-free emission is not easily identified at radio frequencies except near the Galactic plane. At higher latitudes it must be separated from synchrotron emission by virtue of its different spectral index. At higher frequencies where free-free emission might be expected to exceed the synchrotron component, the signals are weak and the survey zero levels are indeterminate. Most of the information on the thermal electron content currently available at intermediate and higher frequencies comes from Hα surveys. This diffuse Hα emission is thought to be a good tracer of diffuse free-free emission since both are emitted by the same ionized medium and both intensities are proportional to emission measure ($EM = ne^2dl$), the line of sight integral of the free electron density squared. Major Hα structures are a feature of the well-known Local (Gould Belt) System which extends some 40° from the plane at positive b in the Galactic centre and at negative b in the anticentre. Other Hα features are known to extend 15° to 20° from the plane [19].

The intermediate latitude Hα distribution may be modelled (Reynolds 1992) as a layer parallel to the Galactic plane with a half-thickness intensity of 1.2 Rayleigh (R). The rms variation in this Hα emission is about 0.6R on degree scales. In the context of the present discussion 1R will give a brightness temperature of about 10 μK at 45 GHz. Further information about angular structure in the Hα emission can be derived from the North Celestial Pole (NCP) study by Gaustad et al.[5]. Veeraraghavan & Davies[22] used this material to derive a spatial power spectrum on angular scales of 10 arcmin to a few degrees. The spatial power law index is -2.3 ± 0.1 over this range with an rms amplitude of $0.12cosec(b)$ Rayleighs on 10 arcmin scales. This level is consistent with the limits derived from the Tenerife experiments and indicates that the free-free rms brightness becomes comparable with the synchrotron value at about 20 GHz where it would comprise 10 to 20 percent of the CMB fluctuation amplitude. Kogut et al.[10] compared the COBE DMR maps with the DIRBE maps and claimed a correlation between free-free and

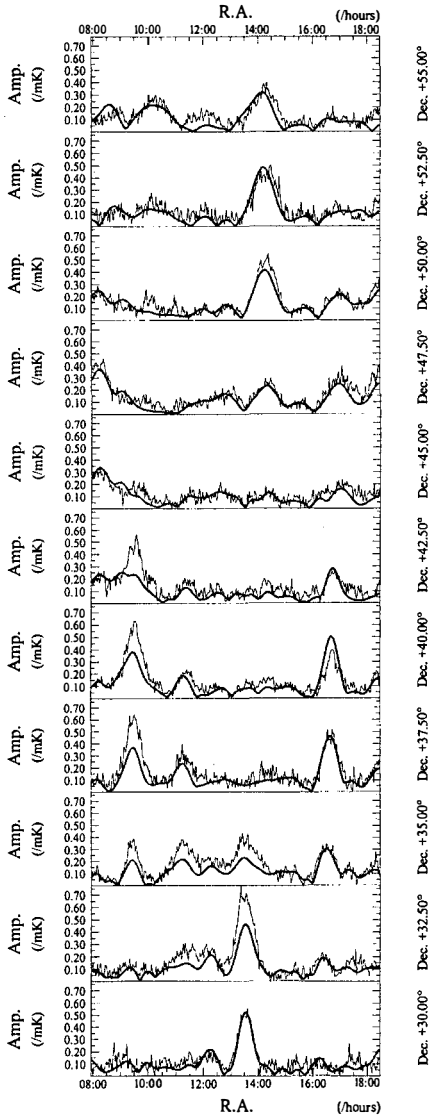

Figure 1: Comparison of 5 GHz interferometer narrow spacing (baseline 12 wavelengths) data with the Greenbank point source survey (dark line). The differences are due to source variability or Galactic synchrotron emission.

dust emission. They obtained free-free levels somewhat higher (in a 7° beam) than measured more directly in the Tenerife experiments.

6.1 A note on polarization

Extensive surveys of the polarization of Galactic synchrotron polarization have been made at frequencies up to 1-2 GHz. Significant polarized signals are found over most of the surveyed sky. The percentage polarization increases with frequency indicating the presence of a Faraday rotating medium with a rotation measure of 8 rad m^{-2} [20]. The mean polarization amplitude at 1400 MHz lies between 20 and 30 % at higher ($|b| \geq 30°$) Galactic latitudes as seen in an 0.°6 beam. The polarization degree in Loop I reaches ~72 % at higher Galactic latitudes. This is close to the theoretical upper limit where the fractional polarization is given by

$$\pi = \frac{3\beta - 3}{3\beta - 1} \tag{2}$$

where β is the temperature spectral index. The other loops have maximum polarization in the range 30-50 %.

A detailed study of the polarization of the Cygnus Loop has been made at 1.4 GHz by Leahy, Roger & Ballantyne[13]. They find that the bright filaments have the B field aligned along their length with a maximum polarization in the remnant of 39 percent and a mean value of 7 percent. The lower values of polarization in some areas are most likely due to depolarization in the Faraday screen of the object which has a rotation measure of -20 to -35 rad m^{-2}. The 5 GHz map of Kundu & Becker [11] shows a fractional polarization of 25 percent over the southern half of the source.

The 2.4 GHz Galactic plane survey by Duncan et al. [4] shows considerable complex structure with their 10 arcmin beam. Bright, extended regions of polarization emission of the order of 5° across include the Vela SNR and a large structure appearing to the north of Sgr A. A quasi-uniform weak component of patchy polarization is seen over the length of the survey.

Theory indicates that the CMB radiation will be polarized at a level of 5 to 10 percent. On the other hand the synchrotron emission can be 30 percent polarized at 1.4 GHz and probably higher at higher frequencies. Accordingly this foreground Galactic polarization must be considered more seriously than the total power case when measuring CMB polarization. A foreground feature which is 10 percent of an intrinsic CMB feature may have polarization which is 30 to 50 percent of the polarized intensity of the feature.

Acknowledgments

AW would like to acknowledge the receipt of a Daphne Jackson Research Fellowship, sponsored by PPARC.

References

1. Berkhuijsen E.M., Haslam C.G.T., Salter C.J., *Astr. Astrophys.* **14**, 252 (1971).
2. Davies R.D., Watson R.A., Gutierrez C.M., *Mon. Not. R. astr. Soc.* **278**, 925 (1996).
3. Duncan A.R., Stewart R.T., Haynes R.F., Jones K.L., *Mon. Not. R. astr. Soc.* **277**, 36 (1995).
4. Duncan A.R., Haynes R.F., Jones K.L, Stewart R.T., *Mon. Not. R. astr. Soc.* **291**, 279 (1997).
5. Gaustad J., McCullough P., van Buren D., *Pub.Astron.Soc.Pacific* **108**, 351 (1996).
6. Green D., *Astron. J.* **100**, 1927 (1990).

7. Hancock S. Davies, R.D., Lasenby, A.N. Guttierrez, C.M., Watson, R.A., Rebolo. R. and Beckman, J.E., *Nature* **367**, 333 (1994).
8. Haslam C.G.T., Salter C.J., Stoffel H., Wilson W.E., *Astr. Astrophys. Suppl.* **?47**, 1 (1982).
9. Jonas J.L., Baart E.E., Nicolson G.D., *Mon.Not.R.ast.Soc.* in press, 1998.
10. Kogut A. et al., *Astrophys. J.* **460**, 1 (1996).
11. Kundu M.R., Becker R.H., *Astron. J.* **77**, 459 (1972).
12. Lawson K.D., Mayer C.J., Osborn J.L., Parkinson M.L., *Mon. Not. R. astr. Soc.* **225**, 307 (1987).
13. Leahy D.A., Roger R.S., Ballantyne D., aj **114**, 2081 (1997).
14. Melhuish S.J. et al., *Mon. Not. R. astr. Soc.* **286**, 48 (1997).
15. Reich P., Reich W., *Astr. Astrophys. Suppl.* **63**, 205 (1986).
16. Reich P., Reich W., *Astr. Astrophys. Suppl.* **74**, 7 (1988).
17. Reynolds J., *Astrophys. J.* **392**, L35 (1992).
18. Reynolds S., *Galactic and Extragalactic Radio Astronomy*, (Springer-Verlag, Berlin, 1988).
19. Sivan,J.P, *Astr. Astrophys. Suppl.* **16**, 163 (1974).
20. Spoelstra T.A.T., *Astr. Astrophys.* **135**, 238 (1984).
21. Veeraraghavan S., Davies R.D., *Particle Physics and the Early Universe* eds. Bately R., Jones M.E., Green D.A., (CUP, 1997).
22. Verschuur G.L., Kellermann K.I., *Galactic and Extragalactic Radio Astronomy*, (Springer-Verlag, Berlin,1988).

Galactic Free-free Emission and Hα

J.G. Bartlett[1] & P. Amram[2]
[1] *Observatoire de Strasbourg, 11 rue de l'Université, 67000 Strasbourg, France*
[2] *IGRAP, Observatoire de Marseille, 2 Place Le Verrier, 13248 Marseille Cedex 4, France*

We review present understanding of Galactic free–free emission and its possible importance to CMB fluctuation measurements. Current results, from both "direct" observations in the microwave band and from Hα studies, suggest that this foreground does not represent a serious obstacle to mapping the CMB; however, this is based on limited information and we emphasize the need for more exhaustive studies. We also present some preliminary results based on our recent Hα observations near the South Pole CMB data sets. The fluctuation amplitude seen in Hα indicates that the detected CMB fluctuations are not significantly contaminated by free–free emission, at least if the diffuse gas is at a temperature of $T \sim 10^4$ K.

1 Galactic Free–free Emission

The three main sources of microwave emission from our Galaxy are synchrotron radiation, thermal dust emission and bremsstrahlung (free-free emission). Among these three, bremsstrahlung poses the greatest difficulty for cosmic microwave background (CMB) observations for two reasons: 1/ it dominates over the frequency range where the total Galactic emission is minimal, and hence where the majority of CMB experiments are performed, and 2/ it dominates *only* over a small range of frequencies (see Fig. 3 of Kogut et al. 1996a). Thus, it is the principal Galactic contaminant of many CMB experiments, but it cannot be traced by observing at either much higher or lower frequencies. For example, the dust and synchrotron foregrounds may be mapped in the infrared and radio, respectively. Such maps prove very useful for foreground control and elimination. There exists, nevertheless, a tracer of Galactic bremsstrahlung – Hydrogen Hα in emission, which is produced by the same warm ionized medium (WIM) responsible for the bremsstrahlung. Unfortunately, there is at present no full–sky map available in Hα. In what follows, we review what is known about Galactic free–free emission, with an emphasis on implications for CMB experiments. We will first consider "direct" observations of the foreground in the microwave band (from CMB work) and then consider in detail studies based on the Hα

line. An excellent recent review of the subject has been given by Smoot (1998). To focus the discussion, we will center it on two primary questions: 1/ How well correlated are dust and free–free emissions? 2/ Might there be a hot component of the interstellar medium (ISM) producing Galactic free–free emission which could violate limits based on a simple interpretation of current Hα observations?

1.1 Direct Observations of Bremsstrahlung

A summary of direct observations of Galactic bremsstrahlung in terms of equivalent brightness temperature variations at 40 GHz (Q–band) – ΔT_{ff} – is given in Table 1. All these results come from CMB experiments. The three DMR maps, obtained at 31.5, 53 and 90 GHz, have been combined to optimize a signal with the spectral dependence of free–free emission, $\sim \nu^{-2}$ (Kogut et al. 1996a, 1996b) (this has been done for all three Galactic emissions; the maps are available at `http://nssdca.gsfc.nasa.gov/astro/cobe/cobe_home.html`). Unfortunately, the signal–to–noise in the resulting free–free map is too low to follow in detail the distribution of Galactic bremsstrahlung. Nevertheless, based on the COBE 4 year results, Kogut et al. (1996b) constrain the brightness fluctuations due to bremsstrahlung to $\Delta T_{ff} = 9 \pm 7 \mu$K. This provides a 95% upper limit of $\Delta T_{ff} < 23 \mu$K on the *total* Galactic free–free emission. For comparison, the extracted CMB fluctuation amplitude (brightness variations at 10^o) is $29 \pm 1 \mu$K (Banday et al. 1997).

In order to boost the signal–to–noise, Kogut et al. (1996b) also searched for galactic emission by cross–correlating the three DMR and the DIRBE 140 micron maps, finding a significant result. The spectral characteristics of the correlated signal are those of a combination of dust and free–free emission, with the free–free contributing $\Delta T_{ff} = 12 \pm 5 \mu$K. Within the errors, this is consistent with the above upper limit, but it does leave room for a non–correlated component of the same amplitude.

Table 1: Summary of Direct Free–Free Constraints

reference	resolution	patch size	ΔT_{ff} at 40 GHz	comments
Kogut et al. 1996b:				
(DMR/DIRBE)	10^o	$\|b\| > 20^o$	$12 \pm 5 \mu$K	dust correlated
(DMR)			$9 \pm 7 \mu$K	total emission
de Oliveira–Costa et al. 1997 (Saskatoon)	1^o	$7.5^o \times 7.5^o$	$17.5 \pm 9.5 \mu$K	dust correlated no spectral info.
Leitch et al. 1997 (OVRO 5.5 & 40 m)	0.3^o	$DEC = 88^o$	$\sim 27 \mu$K	total emission

Oliveira–Costa et al. (1997) performed a similar analysis on the Saskatoon data, cross–correlating the CMB results with the DIRBE far infrared maps. They marginally detect a non–zero correlation with an amplitude consistent with that found by Kogut et al. (1996b), extending the free–free/dust correlation down to angular scales of $\sim 1^\circ$ (the COBE results are restricted to $>7^o$). These results raise the first question posed in the introduction: Just how well does dust emission trace Galactic bremsstrahlung? The COBE and Saskatoon analyses demonstrate the existence of a free–free component correlated with Galactic dust emission, but it should be remembered that the possibility of an equally important, non–correlated component remains. The angular power spectrum of the dust–correlated component is $P(l) \sim l^{-3}$ (Kogut et al. 1996b), showing a rapid fall–off towards small angular scales. This power spectrum is not at all surprising – it is simply the power spectrum already observed for the dust distribution (Gautier et al. 1992; Wright 1998). It is worth noting that such a power spectrum implies that the true sky variance remains roughly constant towards small scales, but that estimates

of this variance in restricted patches of sky may be "pulled" far from the true variance by the important correlations on scales equal to the patch size; in other words, the uncertainty on the estimate will be larger than that deduced by assuming $N_{\rm pixel}$ independent measurements of the sky brightness. This should be kept in mind when interpreting the estimates given in the tables.

Complicating matters somewhat is a recent result reported by Leitch et al. (1997). Using the OVRO 5.5 and 40 meter telescopes at frequencies of 32 and 14.5 GHz, they find a large signal in a ring at constant declination around the North Celestial Pole (Saskatoon region) with the spectral characteristics of free–free emission. The corresponding 40 GHz amplitude on an angular scale of $0^o.3$ is $\Delta T_{ff} \sim 27\mu$K, slightly larger than the upper limits imposed on larger scales by the previous observations or by the extrapolation of the dust power spectrum. This result could indicate the emergence on smaller scales of an important bremsstrahlung component uncorrelated with dust. We return to this point below when discussing the Hα results.

1.2 Hα Studies

The ionized gas responsible for the free–free emission is also a source of line emission, in particular Hydrogen Hα. This optical line, at 6563 angstroms, may thus be used to trace the gas distribution and, hence, map the free–free foreground (Lyα would do the same, but absorption is a serious problem). In the following, we present simplified versions of the various formulae; a more detailed treatment can be found in Valls–Gabaud (1998). The Hα intensity, usually expressed in terms of Rayleighs (R= 2.41×10^{-7}ergs/cm^2/s/ster), is given by

$$I_\alpha = (0.36\ \mathrm{R}) \left(\frac{EM}{\mathrm{cm}^{-6}\ \mathrm{pc}}\right) T_4^{-0.9} \tag{1}$$

where $T_4 \equiv T/(10^4\ \mathrm{K})$ and EM represents the emission measure. This expression is valid for temperatures $T_4 \leq 2.6$ (Leitch et al. 1997). Free–free emission depends on the same quantities (given here for pure Hydrogen and in the limit as $h\nu/kT \to 0$):

$$T_{ff} = \frac{(5.43\,\mu\mathrm{K})}{\nu_{10}^2 T_4^{1/2}} \left(\frac{EM}{\mathrm{cm}^{-6}\ \mathrm{pc}}\right) g_{ff} \tag{2}$$

where the observation frequency is $\nu = \nu_{10} 10^{10}$ GHz and g_{ff} is the thermally averaged gaunt factor:

$$g_{ff} = 4.69(1 + 0.176 \ln T_4 - 0.118 \ln \nu_{10}) \tag{3}$$

The relation between the line and free–free emissions is particularly simple due to the fact that both depend primarily on the emission measure. Combining Eqs. (1)and (2) yields

$$T_{ff} = (15\ \mu\mathrm{K}) g_{ff} T_4^{0.4} \nu_{10}^{-2} \left(\frac{I_\alpha}{\mathrm{R}}\right) \tag{4}$$

Note that this is an expression for the absolute free–free intensity, T_{ff}, to be distinguished from its variation, ΔT_{ff}.

Table 2: Hα Results

reference	resolution	patch size	ΔT_{ff} at 40 GHz	comments
Reynolds et al. 1990	$0^o.8$	diverse pointings	$\sim 10\ \mu$K	Fabry–Perot
Reynolds et al. 1992	$0^o.8$	$12^o \times 10^o$	$\sim 10\ \mu$K	Fabry–Perot
Gaustad et al. 1996	$0^o.1 - 1^o$	$7^o \times 7^o$	$< 5\ \mu$K	broad–band
Simonetti et al. 1996	1^o	diam $= 30^o$	$< 5\ \mu$K	broad–band
Marcelin et al. 1998	$0^o.5$	24 pointings	$< 5\ \mu$K	Fabry–Perot

The ideal would therefore be to have a sensitive all–sky map in Hα to control the free–free foreground; this does not at present exist. For many years, R. Reynolds has been carrying out Hα observations of the Galaxy with a double Fabry–Perot spectrometer (needed to separate Galactic $H\alpha$ from the much larger geocoronal Hα emission). A good review of these results and a summary of what is known about the distribution of the WIM is given by Reynolds (1990). For the essential, the gas seems to be distributed above and below the Galactic Plane with a characteristic scale height of $\sim$ 1 kpc. It is thought that the gas has a temperature close to $T_4 = 1$. These conclusions are the result of diverse, pointed observations (a rough picture of the gas distribution is given in Reynolds 1990). A significant improvement will soon come from the WhaM survey (Reynolds et al. 1998), an effort to map the northern sky in Hα at a resolution of 1° (the WhaM web page is a very useful source of information – `http://www.astro.wisc.edu/wham/WhaM.html`).

A rough summary of current results from Hα is given in Table 2, where we have assumed $T_4 = 1$. We note that the small–scale observations are essentially upper limits, but that Reynolds actually sees fluctuations at $\sim$ 2 R. From this compilation, it would seem that the variations on small scales are not very large and should not pose a problem for CMB experiments, which are expecting signals in the range $30 - 100\mu$K. An important caveat is always that, up till now, these observations cover a rather small fraction of sky. The last entry, Marcelin et al. (1998), is discussed below.

The Gaustad et al. (1996) and Simonetti et al. (1996) observations cover the Saskatoon area (North Celestial Pole). They are based narrow band filters instead of the high resolution spectrographs used by Reynolds et al. and Marcelin et al. This means that they are unable to extract the geocoronal from the Galactic signal, implying that only upper limits on $H\alpha$ fluctuations can be deduced. Their strict limits argue against a significant level of contamination in the CMB results from Saskatoon. However, as already mentioned, Leitch et al. (1997) report a detection of a much stronger signal *within the same region.* As pointed out by Leitch et al., this discrepancy could be explained by the presence of a hot component of the ISM, say around $T \sim 10^6$ K (see Eq. [4]), bringing up the second question posed in the introduction. It is important to realize that this temperature corresponds to the virial temperature of the Galactic halo; thus, we could be seeing some evidence for a hot medium in the halo of our Galaxy, or perhaps in the Local Group. This possibility may be constrained by X–ray observations, as discussed by Smoot (1998).

Attempting to clarify the nature of the dust/free–free relation, Kogut (1997) compared the Reynolds et al. (1992) patch with the DIRBE maps and found a significant correlation. This is the best way to try and answer our first question concerning the dust/free–free correlation, because the Hα gives information on the total free–free emission. Looking at Kogut's figure 2, it is clear that there remains a significant variation around the regression line. This could represent a non–correlated component of bremsstrahlung contributing a signal perhaps as large as the correlated component. If so, dust emission would not be sufficient to trace and remove all of the free–free foreground.

2 A New Fabry-Perot Hα Study

In this section, we present our recent observations in Hα taken near the South Pole CMB data sets. For a complete description of the instrument, see Amram et al. (1991).

2.1 Observations

The observations were made from the ESO site at La Silla (Chile) in November 1996 with a 36 cm telescope equipped with a scanning Fabry–Perot interferometer. The field of view is

$38' \times 38'$, the spectral sampling step was either 5 km s^{-1} or 2.5 km s^{-1} (i.e. 0.10 Å or 0.05 Å), depending on the scanning process adopted (24 or 48 channels over the free spectral range of 115 km s^{-1}, i.e. 2.5 Å, of the Fabry–Perot interferometer). The lines passing through the 8 Å FWHM filter were: the Galactic Hα line we are looking for, the geocoronal Hα emission and the OH night–sky line at 6568.78 Å. These two parasitic lines are brighter than the Galactic Hα line we are looking for, the geocoronal line being typically twice as bright as the OH line and 10 times brighter than the Galactic line. In order to compare the Galactic Hα emission fluctuations with the South Pole CMB results (Schuster et al. 1993; Gundersen et al. 1995), we selected fields at declinations of $-63°$ and $-62°$. Our fields were separated by 15 mn in right ascension, which is about $1°45'$ on the sky, thus offering a fair coverage of each exposed band. We observed 19 fields at $-62°$ (from $\alpha = 23^h50$ to $\alpha = 4^h20$) and 5 fields at $-63°$ (from $\alpha = 1^h35$ to $\alpha = 2^h50$). Some of these fields were observed twice, on different nights, to check the reproducibility of our measurements. The observing conditions were fairly good, and a standard 2^h exposure time was adopted.

2.2 Data reduction

Due to the "wrap–around" nature of the FSR (Free Spectral Range) of the Fabry-Perot interferometer (FSR=2.52 Å), the OH night sky line at 6568.78 Å appears closer to the Hα lines (geocoronal and Galactic) than it actually is, with an apparent separation of only 1 Å with respect to Hα_o (see Fig. 1). The motion of the earth around the sun and the motion of the sun in the galaxy were combined in such a manner that the separation between the Galactic and geocoronal Hα lines remained approximately constant, around 0.5 Å, along the bands of sky observed in November. The extraction of Galactic Hα emission is not easy, since it is typically 10 times fainter than the parasitic lines, whose width (FWHM around 0.35Å) and shape (not far from gaussian) also tend to bury the Galactic signal in their wings. To improve the signal–to–noise ratio and the spectral resolution, we selected a $30'$ diameter disk centered on the interference rings observed in each field. The Hα emission profile obtained for each observed field is thus the addition of the profiles of all pixels (about 31000) found within $15'$ from the center of the field.

The OH night–sky line at 6568.78 Å is in fact the sum of two close components of the same intensity, one at 6568.77 Å and the other at 6568.78 Å. More complicated is the case of the geocoronal emission line, with not less than seven fine structure transitions. The two main components, produced by Lyman β resonance excitation, are found at 6562.73 Å and 6562.78 Å, with 2:1 ratio (Yelle & Roesler 1985). However, these two components were insufficient when we decomposed our observed profiles, a residual remaining systematically at 6562.92 Å. This is due to cascade excitation which is particularly strong for the 7th component at 6562.92 Å (Nossal 1994). Although the cascade contribution is not accurately known, it proved satisfactory to use the Meier Model cited in Nossal's thesis, adding a component at 6562.92 Å with a 1:6 ratio compared with the brightest component at 6562.73 Å.

After subtraction of the night–sky lines, a residual was found at the expected velocity for Galactic Hα emission, that is to say, around zero in V_{LSR} (radial velocity in the local standard of rest), and with the expected width, around 35 km s^{-1}, according to Reynolds (1990). Fig. 1 shows an example of a profile decomposition for one of our fields, together with the gaussian fit of the Galactic emission below. The width of the gaussian was left as a free parameter and adjusted automatically for the best fit. This width was typically found to vary between 25 an 50 km s^{-1}. The absolute calibration in intensity was made by observing the HII region N11E in the Large Magellanic Cloud (Caplan & Deharveng 1985).

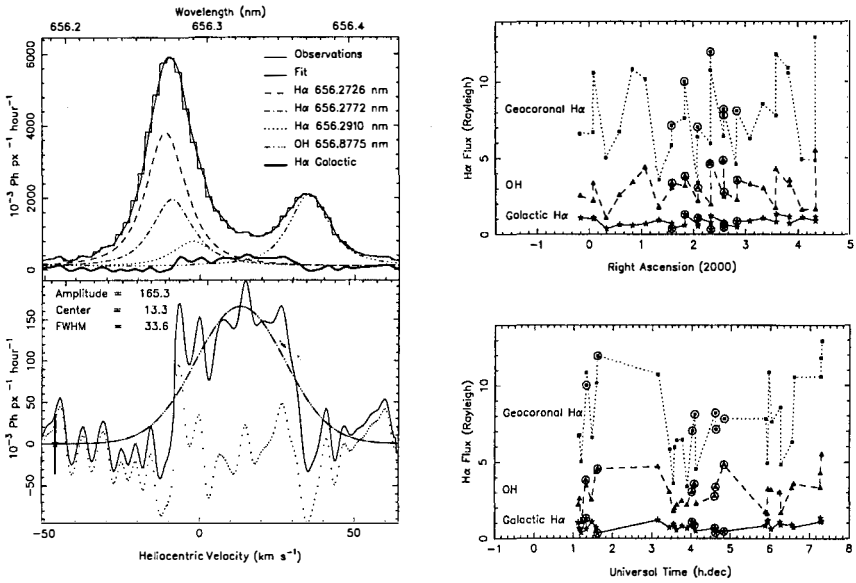

Figure 1: LEFT: -Top- Example of the decomposition of the observed line profile into geocoronal Hα emission (3 components) and OH night-sky line. The remaining signal (thick line) shows the Galactic Hα emission. -Bottom- Best fit of the same Galactic Hα emission, amplified 20 times, by a gaussian. The shift with respect to 0 km s^{-1} heliocentric velocity is explained by the motion of the sun with respect to the LSR. RIGHT: Geocoronal Hα (squares + dotted), OH (triangles + dashed) and Galactic Hα (stars + solid) line intensities as a function of -Top- right ascension (2000); -Bottom- mean observing time (UT). The effect of the solar depression angle is visible. Circled symbols represent the fields at a declination -63°; the other fields are at declination -62°.

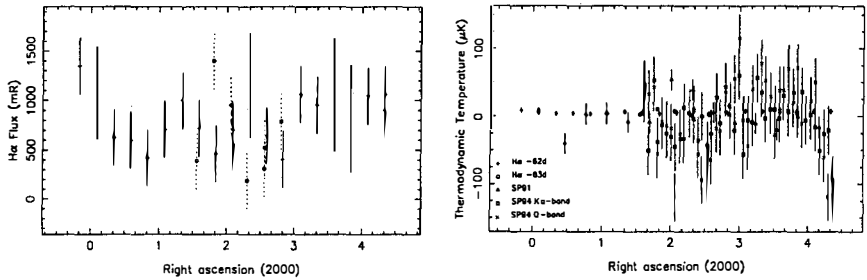

Figure 2: LEFT: Solid error bars: H α intensities measured at declination $-62°$. Dotted error bars: H α intensities measured at declination $-63°$. RIGHT: Comparison of the South Pole results with the free-free emission signal deduced from our Hα observations.

2.3 Results

We find that the Galactic Hα emission along the observed bands, at $-62°$ and $-63°$, varies between 0.2 R and 1.4 R, in agreement with intensity values measured by Reynolds (1990) in the northern hemisphere far from the galactic plane. Fig. 2 shows the measured intensity for the Galactic Hα emission along the two declination bands. The error bars are the average *rms* difference between the signal and the fitted gaussian, found to be 0.35 Rayleigh. Reynolds (1990) gives intensities of the Galactic Hα emission with an uncertainty of 0.4 Rayleigh.

Fig. 2 suggests that the overall variations are faint and that the galactic Hα emission varies smoothly along the two bands of sky we observed. For a gas with $T_4 = 1$, the magnitude of the implied temperature variations at CMB frequencies is much smaller than observed in the South Pole data sets. A visual comparison is made in the right-hand panel of Figure 2, where we compare the *total* Hα intensity with the CMB *differences.*

3 Summary

To summarize the current status of our understanding of Galactic free-free emission, we would say that although there is *no indication* of fluctuations large enough to pose serious difficulties for CMB observations, the observational constraints remain weak. A critical interpretation of the results in the tables would be that the limit on large scale free-free fluctuations is the same order as the CMB amplitude on these same scales (at 40 GHz). On smaller scales, observations in $H\alpha$ have not turned up any signs of large amplitude variations, but those based on high resolution spectrographs are few and cover only a small percentage of the sky. There does appear to be a dust/free-free correlation on all angular scales, but there is room, and perhaps tentative indications of, an equally important non-correlated component (question #1 posed in the introduction). And then there is the puzzeling result from Leitch et al. (1997), perhaps pointing to a hot phase of the ISM which could, due to lack of sensitivity, escape many of the present $H\alpha$ limits (question #2 posed in the introduction).

Obviously, CMB observations at higher frequencies, where much of the effort is now being concentrated, will suffer less from any possible free-free contamination, and the many of the next generation CMB experiments have a wide spectral coverage to aid the removal of foregrounds. Even given the above critical viewpoint, it would be a surprise to discover free-free emission presenting an important difficulty for all planned CMB experiments, at least in terms of measuring the variance, or power spectrum, from the early Universe. Foregrounds will, however, be much more important for higher order statistics looking for non-gaussian signatures. In such

cases, the non–gaussian foregrounds will have to be removed to high precision. A sensitive, high spectral resolution Hα survey of the entire sky would be of great value in the context of the above considerations.

We have also reported some results from our recent Hα observations taken with a Fabry–Perot system at La Silla. The data cover two bands along which the South Pole data sets show significant fluctuations in CMB brightness. The observed Hα fluctuations indicate that the CMB results in this region are not significantly contaminated by free–free emission (assuming a gas with $T_4 = 1$).

4 Acknowledgments

We would like to thank M. Marcelin, D. Valls–Gabaud and A. Blanchard for letting us present results based on our joint observations; the work presented here is the result of many long discussions together. We also thank G. Smoot for encouragement and many helpful conversations. A thanks also goes to the organizers for an extremely enjoyable and interesting meeting.

References

1. P. Amram, J. Boulesteix, Y.M. Georgelin, Y.P. Georgelin, A. Laval, Le Coarer E., M. Marcelin, M. Rosado, The Messenger 64, 44 (1991).
2. A.J. Banday, K.M. Górski, C.L. Bennett, G. Hinshaw, A. Kogut, C. Lineweaver, G.F. Smoot & L. Tenorio, ApJ 475, 393 (1997)
3. J. Caplan, L. Deharveng, A&A Suppl. Ser., 62, 63 (1985)
4. J.E. Gaustad, P.R. McCullough and D. Van Buren, PASP 108, 351 (1996)
5. T.N. Gautier, F. Boulanger, M. Pérault and J.L. Puget, AJ 103, 1313 (1992)
6. J.O. Gundersen, M. Lim, J. Staren et al., ApJ 443, L57 (1995)
7. A. Kogut, AJ 114, 1127 (1997)
8. A. Kogut , A.J. Banday, C.L. Bennett, K.M. Górski, G. Hinshaw and W.T. Reach, ApJ 460, 1 (1996a)
9. A. Kogut, A.J. Banday, C.L. Bennett, K.M. Górski, G. Hinshaw, G.F. Smoot, and E.L. Wright, ApJ 464, L5 (1996b)
10. E.M. Leitch, A.C.S. Readhead, T.J. Pearson and S.T. Myers, ApJ 486, L23 (1997)
11. M. Marcelin, P. Amram, J.G. Bartlett, D. Valls–Gabaud & A. Blanchard, submitted to A&A (1998)
12. Nossal, PhD. thesis, University of Wisconsin, Madison (1994)
13. A. de Oliveira–Costa, A. Kogut, M.J. Devlin, C. B. Netterfield, L.A. Page and E.J. Wollack, ApJ 482, L17 (1997)
14. R.J. Reynolds in "The Galactic and Extragalactic Background Radiation", Eds. S. Bowyer & C. Leinert, 157 (1990)
15. R.J. Reynolds, ApJ 392, L35 (1992)
16. R.J. Reynolds, S.L. Tufte, L.M. haffner, K. Jaehnig and J.W. Percival to be published in Publications of the Astronomical Society of Australia (can be found on the WhaM web page) (1998)
17. J. Schuster, T. Gaier, J. Gundersen, P. Meinhold, T. Koch, M. Seiffert, C.A. Wuensche & P. Lubin, ApJ 412, L47 (1993)
18. J.H. Simonetti, B. Dennison and Topasna, ApJ 458, L1 (1996)
19. G.F. Smoot, astro–ph/9801121 (1998)
20. E.L. Wright, ApJ 496, 1 (1998)
21. D. Valls–Gabaud, PASA, 15, in press (1998)
22. R.V. Yelle & F.L. Roesler, J. Geophys. Res. 90,7568 (1985)

Galactic dust polarized emission at high latitudes and CMB polarization

S. K. Sethi[2], S. Prunet[1], F.R. Bouchet[2]
[1]*IAS, bât. 121, 91405 Orsay*
[2]*IAP, 98bis Boulevard Arago, 75014 Paris*

We estimate the dust polarized emission in our galaxy at high galactic latitudes, which is the dominant foreground for measuring CMB polarization using the high frequency instrument (HFI) aboard Planck surveyor. We compare it with the level of CMB polarization and conclude that, for angular scales $\leq 1^\circ$, the scalar-induced CMB polarization and temperature-polarization cross-correlation are much larger than the foreground level at $\nu \simeq 100$ GHz. The tensor-induced signals seem to be at best comparable to the foreground level.

1 Introduction

The forthcoming satellite CMB projects MAP and Planck surveyor hold great promise for detecting the CMB polarization. A major stumbling block this detection is the unknown level of galactic polarized foregrounds. In this paper, we attempt to estimate the level of dust polarized emission at high galactic latitudes. We model this emission using the three-dimensional HI maps of the Leiden/Dwingeloo survey at high galactic latitudes and the fact that the dust emission, for a wide range of wavelengths, has a tight correlation with the HI emission maps of this survey [1]. Assuming the dust grains to be oblate with axis ratio $\simeq 2/3$, which recent studies support [2], we determine the intrinsic dust polarized emissivity. The distribution of magnetic field with respect to the dust grain distribution is quite uncertain, we thus consider three extreme cases (to be described below).

2 Method

From the HI maps of Leiden/Dwingloo survey[3] one can construct a statistical model of the three-dimensional dust distribution using the relation between the optical depth for dust emission τ

at $\lambda = 250\,\mu$m and the HI column density $N_{\rm HI}$ [1]:

$$\frac{\tau}{N_{\rm HI}} = 10^{-25}\,{\rm cm}^2 \tag{1}$$

Boulanger *et al.* [1] also showed that the galactic dust emission spectrum can be well fitted with a Planck spectrum with temperature = 17.5 K with emissivity proportional to ν^2. We use this spectral dependence of dust emission throughout this paper. The $N_{\rm HI}$–τ correlation remains good for $N_{HI} \leq 5 \times 10^{20}\,{\rm cm}^{-2}$ which is typical for high galactic latitudes.

As our aim is to construct two-dimensional maps of polarized component of dust emission from these three-dimensional maps of unpolarized emission, we need the following information: (a) the intrinsic dust polarized emissivity, which depends on the type and shape of the grain, (b) the strength and direction of magnetic field in the diffuse cloud, and (c) the polarization reduction factor.

Intrinsic polarized emissivity. The galactic distribution of dust grains can be well understood by the silicate/graphite model, with the volume fraction of graphites between 0.25 and 0.5 of the silicates in the total grain volume [4]. Assuming spheroidal grains, Hildebrand and Dragovan [2] showed that the grains are oblate with the ratio of axis $\simeq 2/3$. Assuming no reduction of polarization, the intrinsic polarized emissivity is $\simeq 30\%$ in this case.

Magnetic field. The dust grains align themselves with the magnetic field. To estimate the reduction of polarization from smearing along any line of sight, one needs to know the direction and strength of the magnetic field. There is great uncertainty in the direction of the magnetic field relative to dust distribution as the observational evidence show contradictory indications [5,6]. Therefore, we consider three extreme cases:

(1) The magnetic field is aligned with the major axis of the structure. This case is relevant for dust filaments aligned with the field.

(2) The magnetic field lies in the plane perpendicular to the major axis of the structure, with its direction random in that plane (valid e.g. for helicoidal field around filaments)

(3) The magnetic field has the same direction throughout the three-dimensional map.

Also we assume, as recent observations and theoretical estimates show, that the the dust grains are aligned with the magnetic field independent of the strength of the magnetic field.

Polarization reduction factor. The reduction of intrinsic polarized emissivity due to projection on the sky can be written as [4]:

$$\Phi = RF\cos^2\gamma, \tag{2}$$

where R is the Rayleigh reduction factor which gives the reduction of polarization due to the inclination of grain axes about the direction of the magnetic field. As discussed above, we assume perfect alignment of the dust grains with the magnetic field and therefore take $R = 1$ throughout. The $\cos^2\gamma$ factor accounts for the projection of the direction of polarization on the plane of the sky. Using the three-dimensional maps, we calculate this factor by first estimating, for every pixel, the direction of the structure by finding the direction of minimum gradient in the nearest 27 pixels in the four nearest velocity templates, which are taken as slices in 3-dimensional space. After finding the direction of dust structure with respect to the plane of the velocity template, the direction of magnetic field can be fixed for Case (1) and (2) of the magnetic field distribution. The $\cos^2\gamma$ term (γ being the angle between the direction of magnetic field and the plane of the velocity template) can then be easily computed; and by multiplying by this factor, the projected distribution of polarized emission is evaluated for every velocity template. This procedure is used to construct the projected distribution of the Stoke's parameters for the first two cases of the magnetic field distribution. For the third case (the magnetic field having the same direction

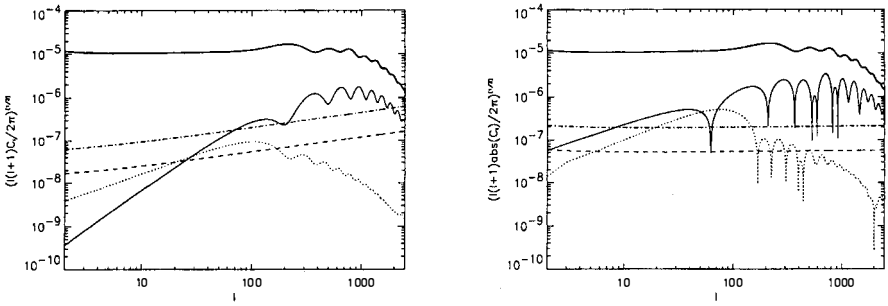

Figure 1: Left Panel: The power spectra of dust polarized emission is compared with the theoretical predictions for CMB polarization. The scalar and tensor-induced E-mode power spectra (*solid* and *dotted* lines respectively) are plotted against the dust polarized power spectra at 143 GHz and 217 GHz (the *dashed* and *dot-dashed* lines, respectively). The CMB temperature power spectrum is shown for comparison (*thick solid* line). The power spectra are plotted in the units of $\Delta T/T$. Right Panel: Same as the left panel for the ET cross-correlation

everywhere), we assume, for simplicity, $\cos^2\gamma = 0.5$. F term is the reduction of polarization from summing the contribution of different directions of polarization along any line of sight [7]. This factor is estimated directly by vectorially adding the contribution from every velocity template along a line of sight.

3 Results

3.1 Angular distribution of dust polarized emission and comparison with CMB power spectra

We construct two-dimensional 15°x15° maps between latitudes 30° and 75° using the methods described in the last section, and take the Fourier transform of these maps to obtain the power spectra of the Stoke's parameters. For a comparison with the CMB polarized component, it is convenient to define variables E and B [10], which are linear combinations of the usual Stoke's parameters in Fourier space. It is because B always vanishes for the scalar-induced CMB polarization. Also the cross-correlation of B with all the other variables vanishes.

In terms of these variables, the estimated power spectra and the cross-correlation of dust polarized emission can approximately be fitted by:

$$C_E(\ell) = 8.9 \times 10^{-4} \ell^{-1.3}\ (\mu\mathrm{K})^2 \quad (3)$$

$$C_B(\ell) = 1.0 \times 10^{-3} \ell^{-1.4}\ (\mu\mathrm{K})^2 \quad (4)$$

$$C_{ET}(\ell) = 1.7 \times 10^{-2} \ell^{-1.95}\ (\mu\mathrm{K})^2. \quad (5)$$

The power spectra are normalized at 100 GHz and are for the maps between galactic latitudes 30° and 45° (where the level of contamination is the highest) for Case (1) of the magnetic field distribution. The other two cases of magnetic field distribution result in smaller or comparable level of foregrounds at $\ell \geq 200$ (for details, see Prunet *et al* [8]).

We plot these against the scalar and tensor induced CMB power spectra for various variables in Fig. 1 and 2. The cosmological model we adopted to compute the CMB spectra is a flat, tilted CDM model, which generates tensor-induced B-mode polarization, with scalar spectral index $n_s = 0.9$. We take the tensor spectral index $n_t = 1 - n_s = 0.1$ with scalar to tensor quadrupole ratio of $7(1 - n_s)$. The CMB power spectra were computed using the CMB Boltzmann code CMBFAST [10].

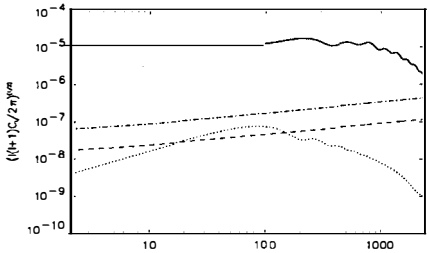

Figure 2: Same as Fig. 1 for B-mode power spectra.

In Fig. 1, the scalar-induced E-mode CMB power spectrum is seen to be above the level of dust contamination for $\ell \gtrsim 200$ for the two HFI frequency channels at 143 GHz and 217 GHz. However the tensor-induced E-mode CMB fluctuations, which in any case constitute a small part of the E-mode signal, are likely to be swamped by the foreground contamination. The detection of B-mode anisotropies is more interesting as it would unambiguously determine the presence of tensor-induced component in CMB fluctuations[9,11,12]. As seen in Fig. 2 the B-mode power spectrum is at best comparable to the foreground level in a small ℓ-range. Fig 1 shows that the CMB ET cross-correlation power spectrum from scalar perturbations is more than an order of magnitude above the level of foreground contamination, at least for $\ell \gtrsim 100$ while the tensor-induced ET cross-correlation remains below the foreground signal.

As the foregrounds differ from CMB in both ν- and ℓ-dependence, the level of foreground contamination can be substantially reduced even in the presence of noise[13,14]. The extension of this technique to include polarization and temperature-polarization cross-correlation, and how it can be used to quantify errors on various power spectra, is described in a companion paper in this volume[15].

References

1. F. Boulanger *et al.* , A & A **312**, 256 (1996)
2. R. H. Hildebrand and M. Dragovan, ApJ **450**, 663 (1995)
3. D. Hartmann and W. B. Burton, Atlas of Galactic HI emission, Cambridge University Press (1995)
4. H. M. Lee and B. T. Draine,ApJ **290**, 211 (1985)
5. P. C. Myers and A. A. Goodman, ApJ **373**, 509 (1991)
6. A. A. Goodman, P. Bastien, F. Menard, and P. C. Myers, ApJ **359**, 363 (1990)
7. B. J. Burn, MNRAS **133**, 67 (1966)
8. S. Prunet, S. K. Sethi, and F. R. Bouchet, submitted for publication
9. U. Seljak, ApJ **482**, 6 (1997)
10. U. Seljak and M. Zaldarriaga,ApJ **469**, 437 (1996)
11. M. Kamionkowski and A. Kosowsky, astro-ph/9705219
12. M. Zaldarriaga and U. Seljak, astro-ph/9609170
13. F. R. Bouchet *et al.* , Space Science Rev. 74, 37(1995).
14. M. Tegmark and G. Efstathiou, ApJ **281**, 1297 (1996).
15. S. Prunet, S. K. Sethi, and F. R. Bouchet, this volume.

Multi-frequency Wiener filtering of CMB data with polarization and estimation of cosmological parameters

S. Prunet[1], S.K. Sethi[2], F.R. Bouchet[2]
[1]*IAS, bât. 121, 91405 Orsay*
[2]*IAP, 98bis Boulevard Arago, 75014 Paris*

We present a method of subtracting the foreground contamination for the measurement of CMB polarization. We calculate the resultant errors on CMB polarization and temperature-polarization cross correlation power spectra for the high frequency instrument (HFI) aboard Planck Surveyor, and estimate the corresponding errors on cosmological parameters

1 Introduction

The upcoming satellite CMB experiment Planck surveyor offers an unprecedented opportunity to measure CMB polarization. A major hurdle in extracting the primary CMB signal from data, apart from noise, is galactic and extragalactic foregrounds. However, as the foregrounds differ from CMB in both frequency dependence and spatial distribution, one can hope to reduce their level in a multi-frequency CMB experiment. A multi-frequency Wiener filtering method to implement this scheme was developed [1,2] and applied to cleaning the simulated CMB temperature map by Bouchet *et al.* [1]. They showed that the residual contamination after cleaning the map is much smaller than the CMB primary signal, and therefore the foregrounds may not be a major obstacle in the extraction of CMB temperature angular power spectrum. However, as the CMB polarization signal is expected to be one to two orders of magnitudes below the temperature signal, it is likely to be comparable to both the experimental noise and the level of foregrounds. Sethi *et al.* [3] modelled and estimated the level of dust polarized emission at high galactic latitudes. Dust polarization is expected to be the dominant contaminant for measuring CMB polarization using Planck HFI.

In this paper, we extend the multi-frequency Wiener filtering method to include the polarization and temperature-polarization cross-correlation. The aim of this exercise is to quantify errors in estimating various power spectra and consequently the errors in cosmological parameters. Our results are relevant for Planck HFI.

2 Multi-frequency Wiener filtering on CMB data

Let us denote the observed data at different frequencies as, y^i_ν, where ν indicates the frequency of the instrumental channel, and i the nature of the observed field (temperature T and E-mode polarization[5]). y^i_ν, for a given i, takes contributions from various galactic and extragalactic sources, apart from the primary CMB signal and instrumental noise. Let us call x^j_p the contribution of the field j due to process p, this is the quantity we want to recover from the observational data y^i_ν. We assume that there is a linear relation between them. In multipole space, it can be expressed as:

$$y^i_\nu(l,m) = A^{ij}_{\nu p}(l,m) x^j_p(l,m) + b^i_\nu(l,m) \tag{1}$$

where $A^{ij}_{\nu p}$ is the instrument response kernel, and b^i_ν is the detector noise level per pixel for the full mission time (all repeated indices are summed over).

The problem is now how to construct an optimal estimator $\hat{x}^j_p$. We chose this estimator to be linear in the observed data:

$$\hat{x}^i_p = W^{ij}_{p\nu} y^j_\nu \tag{2}$$

The reconstruction error for a given field and process is given by $|(\hat{x}^i_p - x^i_p)^2| \equiv (\varepsilon^i_p)^2$. $W^{ij}_{p\nu}$ is chosen so as to make the variance of the reconstruction error minimal. The derivatives of the error with respect to the filters coefficients $W^{ic}_{p\mu}$ should then be zero. This condition can be expressed as:

$$A^{ck}_{\mu p'} W^{il}_{p\nu'} A^{lm}_{\nu' p''} \langle x^k_{p'} x^m_{p''} \rangle + W^{ib}_{p\nu'} \langle b^c_\mu b^b_{\nu'} \rangle = A^{ck}_{\mu p'} \langle x^k_{p'} x^i_p \rangle. \tag{3}$$

2.1 *Implementation of foregrounds removal*

Eq. (3) is valid for the general case in which various processes, fields, and corresponding instrumental noises could be correlated. We consider here only uncorrelated processes and noises between different fields and channels. We allow for the correlation between the two fields T and E. With these conditions, Eq. (3) can be written as a system of four matrix equations which can be solved by substitution.

Bouchet *et al.* [1] defined a quantity called the 'quality factor' to understand the quality of extraction of the signal corresponding to a given process. A straightforward generalisation of the quality factor, valid for multiple fields, can be written as:

$$Q^{ij}_{pp'} = \frac{\langle \hat{x}^i_p \hat{x}^j_{p'} \rangle}{\langle x^i_p x^j_{p'} \rangle} = W^{ik}_{p\nu} A^{kl}_{\nu p''} \langle x^l_{p''} x^j_{p'} \rangle \tag{4}$$

where we have used Eq. (3) to write the second equality. $\mathbf{Q}^{11}$ and $\mathbf{Q}^{22}$ can readily be interpreted as the quality of the reconstruction of temperature and polarization maps, respectively. It should be noted that in the presence of cross-correlations, the quality factor of either field is better than the case without cross-correlations. Though the reconstruction of temperature maps is only slightly changed by cross-correlation term, the quality of polarization reconstruction gets a big boost from the presence of temperature-polarization cross-correlation. However the meaning of term $\mathbf{Q}^{21}$ (and $\mathbf{Q}^{12}$) is not apparent. Much of the contribution to $\mathbf{Q}^{12}$ comes from the term with $\mathbf{W}^{11}$, and therefore it is very close to the quality factor for the extraction of temperature and is nearly independent of the polarization noise. It is not surprising as it merely tells us that to optimally reconstruct the cross-correlation one needs to throw out the noisy data, i.e. the polarization. However, the quantity of interest for us is the error in the extraction of the power spectrum of cross-correlation, which should not be confused with $\mathbf{Q}^{12}$. To get a real idea of the error bars of the different spectra, we must define estimators of those power spectra from the filtered data, and compute their covariance.

2.2 *Unbiased estimators of power spectra*

$\hat{x}^i_p$ (Eq. (2)) is the data obtained after performing Wiener filtering on the multi-frequency maps. Our aim in this section is to use this data to write an unbiased estimator of the true

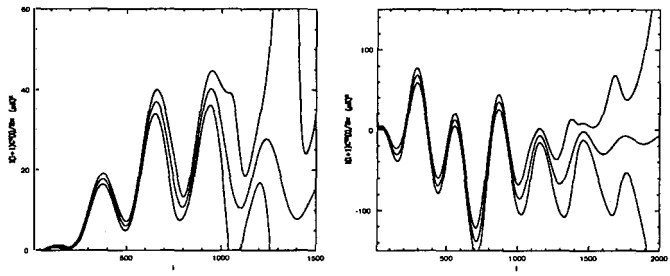

Figure 1: Power spectra and 1σ errors for the E-mode polarization and the temperature-polarization cross-correlation respectively.

power spectrum x_p^i. The average power spectrum of $\hat{x}_p^i$ can be written as:

$$\langle \hat{x}_p^i \hat{x}_{p'}^i \rangle = W_{p\nu}^{ij} W_{p\nu'}^{il} \left[A_{\nu p'}^{jk} A_{\nu' p''}^{lm} \langle x_p^i x_{p'}^i \rangle + \langle b_\nu^j b_{\nu'}^l \rangle \right] \tag{5}$$

This can be expanded to give:

$$\langle \hat{x}_p^i \hat{x}_p^j \rangle = (Z_p^{ij} C_p^{ij} + b_p^{ij}) = Q_p^{ij} C_p^{ij} \tag{6}$$

Here $\{i, j\}$ stand for T and E. b_p^{ij} are generalized versions of the instrumental noise, containing contributions of the noise from different channels as well as some power leakage of the other processes and the other fields. We then define unbiased estimators of the spectra:

$$\hat{C}_p^{ij} = \frac{1}{Z_p^{ij}} \left(\frac{1}{2\ell+1} \sum_m \| \hat{x}_p^i(m) \hat{x}_p^j(m) \| - b_p^{ij} \right) \tag{7}$$

and compute their covariances:

$$Cov(\hat{C}_p^{TT}) = \frac{2}{2\ell+1} \left(C_p^{TT} Q_p^{11} / Z_p^{11} \right)^2 \tag{8}$$

$$Cov(\hat{C}_p^{EE}) = \frac{2}{2\ell+1} \left(C_p^{EE} Q_p^{22} / Z_p^{22} \right)^2 \tag{9}$$

$$Cov(\hat{C}_p^{TE}) = \frac{1}{2\ell+1} \frac{((Q_p^{12})^2 (C_p^{TE})^2 + Q_p^{11} Q_p^{22} C_p^{TT} C_p^{TE})}{(Z_p^{12})^2} \tag{10}$$

It has been assumed that both CMB and foregrounds are Gaussian fields in the computation of covariances. In Fig. 1 we show the E-mode polarization and ET cross-correlation power spectra for sCDM model and the expected 1σ errors on their measurement using the specifications of Planck HFI. Apart from polarized dust, an additional contribution to polarized foregrounds from 40% polarized synchrotron emission has been assumed. As the synchrotron foreground is subdominant at HFI frequencies, it doesn't affect our results. However, it is expected to be the major foreground for MAP and Planck low frequency instrument (LFI).

3 Errors on cosmological parameters

The unbiased estimators defined above and their covariances can be used to estimate the precision we expect on the measurement of cosmological parameters once the foregrounds are filtered out for any desired experiment.

3.1 Fisher Matrix

The Fisher matrix is defined as an average value of the second derivatives of the logarithm of the Likelihood function with respect to the cosmological parameters, taken at the maximum

Table 1: Errors on cosmological parameters. $\Delta\Omega_\Lambda$ is given in absolute value.

Parameters	C_2	h	Ω_b	Ω_Λ	τ	n_s	n_t	T/S
Model	$796(\mu K)^2$	0.5	0.05	0.0	0.05	0.99	0.01	0.1
Worst case	3.72 %	1.11 %	1.93 %	0.032	28.3 %	0.40 %	538 %	78.0 %
Best channel	2.5 %	1.07 %	1.87 %	0.031	2.74 %	0.38 %	453 %	67.6 %
Wiener	1.98 %	0.23 %	0.34 %	$6.6\,10^{-3}$	19.7 %	0.10 %	242 %	27.0 %

likelihood point:

$$F_{ij} = \left\langle \frac{\partial^2 \mathcal{L}}{\partial\theta_i \partial\theta_j} \right\rangle_{\Theta=\Theta_0} \tag{11}$$

One can take this matrix as an estimate of the covariance matrix of the cosmological parameters. Following Zaldarriaga *et al.* [4] we generalize the Fisher matrix approach to the polarized case. It can be written as:

$$F_{ij} = \sum_{\ell=2}^{+\infty} \sum_{X,Y} \frac{\partial C_\ell^X}{\partial\theta_i} \mathrm{Cov}^{-1}\left(\mathrm{C}_\ell^X, \mathrm{C}_\ell^Y\right) \frac{\partial C_\ell^Y}{\partial\theta_j} \tag{12}$$

where $\mathrm{Cov}(\mathrm{C}_\ell^X, \mathrm{C}_\ell^Y)$ stands for the covariance matrix of the power spectra estimators, and $\{X, Y\} \in \{T, E, TE\}$. We will then use the covariances computed for the unbiased estimators defined in the previous section to take into account the foregrounds removal in the error bars computation.

With the present specifications of Planck HFI, our results are shown in Table 1 for a variant of CDM model. The best channel case corresponds to $\nu = 143\,\mathrm{GHz}$ channel with no foregrounds and the worst case corresponds to the same channel with foregrounds added as noise. As is clearly seen, significant improvement on parameter estimation can be achieved if the foregrounds are removed using the Wiener filtering technique discussed in previous sections, except for the optical depth to the last scattering surface τ. An accurate determination of such small values of τ depends on the level of CMB polarization at $\ell \leq 10$, which in our case is dominated by polarized foregrounds which cannot be easily removed. And therefore, a careful analysis of polarized foregrounds at large scales is necessary to determine such a small value of τ. The different power spectra were computed with the CMB Boltzmann code CMBFAST [6].

References

1. F. R. Bouchet *et al.* , Space Science Rev. 74, 37(1995).
2. M. Tegmark and G. Efstathiou, ApJ **281**, 1297 (1996).
3. S. K. Sethi, S. Prunet, and F. R. Bouchet, this volume.
4. M. Zaldarriaga, D. N. Spergel, and U. Seljak, ApJ **488**, 1 (1997).
5. U. Seljak, ApJ **482**, 6 (1997).
6. U. Seljak and M. Zaldarriaga,ApJ **469**, 437 (1996)

MEASURING THE COSMIC MICROWAVE BACKGROUND AT 3 CM

S. T. STAGGS
Department of Physics: Joseph Henry Laboratories
Princeton, New Jersey 08544-0708, USA

No deviations from a blackbody curve have yet been measured in the cosmic microwave background (CMB) spectrum. The University of Chicago and Princeton recently collaborated on a balloon-borne experiment to measure the CMB temperature at 3 cm, a wavelength longer than those probed by the COBE FIRAS. The preliminary result has been published; [1] this paper summarizes the current state of the experiment.

1 Introduction

The most obvious distinguishing feature of the CMB is its impressive blandness, or lack of features. Once the isotropic blackbody nature of this omnipresent radiation is interpreted as reflecting an early thermalized state of the universe, any small perturbations must be explained. The explanation for the scales and amplitudes of perturbations in the *spatial* distribution of the CMB photons is famous for its potential to constrain models of structure formation. Similarly, any small perturbations in the *frequency* spectrum would require explanations which might provide new insights on the history of the universe. Possible types of spectral distortions are described most recently by Stebbins [2] (and references therein).

2 Observations and Discussion

The CMB spectrum at wavelengths between 1 cm and 0.5 mm was measured very accurately by the COBE/FIRAS; [3] no distortions were found at the level of a few parts in 10^5. The CMB temperature as measured by FIRAS is $2.726 \pm .004$ K (see Fixsen et al. 1996 [3] for interpretation of the error).

Recently, Princeton and the University of Chicago set out to make a measurement *complementary* to the FIRAS data, by considering a longer wavelength. The results are reported in

Staggs et al. 1996:[1] we measured $T_{CMB} = 2.730 \pm 0.014$ K at 3 cm, the most precise measurement yet made of T_{CMB} at a frequency lower than those probed by FIRAS and the UBC/COBRA rocket.[4] The instrument was a balloon-borne radiometer with its front end within 100 mK of thermal equilibrium with the sky signal; all the optics were cold (< 5 K) except for the ground-screens which contributed about 3 mK. A mechanical waveguide switch alternately coupled a low-noise HEMT amplifier to a good blackbody (at 2.749 K most of the time) and to the corrugated horn antenna which observed the sky with a 15° beam. The instrument observed at a 40° zenith angle and rotated 360° in azimuth every few minutes. The radiometer offset is about 10 mK; the raw signal difference we measure between the sky and the 2.749 K cold load is only 12 mK, illustrative of the fact that all systematic corrections are small.

The error on our published result is very conservative and we are working to refine our estimate of it. The final error is dominated by three roughly equal ($\approx$ 10 mK) effects: the ground pickup, the loss in the corrugated horn, and the radiometer offset. In the past year, we characterized the beam pattern of the gondola, including its ground screens, to high accuracy, substantially reducing one of the three errors. New calculations of the loss in corrugated horns, coupled with recent lab measurements on the conductivity of the particular alloy of aluminum from which our horn is constructed (7075), should allow us to reduce the second of the three errors. What remains is completion of lab tests to determine the source of the radiometer offset, which would allow us to lower our estimate of its error. Such tests are underway.

Acknowledgments

I am grateful for the collaboration of David Wilkinson, Norman Jarosik, and Stephan Meyer on the balloon-borne experiment described here. I also acknowledge the excellent help of Matthew Hedman, Eugenio Ortiz, and Lisbeth Vazquez in measuring the gondola beam pattern. Finally, I thank Stuart Bradley and Lyman Page for testing corrugated horns' loss.

References

1. Staggs, S. T., Jarosik, N.C., Meyer, S. S., & Wilkinson, D. T. 1996, *Astrophys. J.*, 473, L1
2. Stebbins, A. 1997, proceedings of NATO ASI "The Cosmic Microwave Background," Strasbourg; also available as *astro-ph* 9705178
3. Fixsen, D. J., Cheng, E. S., Gales, J. M., Mather, J.C., Shafer, R.A., & Wright, E. L. 1996, *Astrophys. J.*, 486, 623
4. Gush, H., M. Halpern & E. Wishnow 1990, *Phys. Rev. Lett.*, 65, 537

MULTIFRACTAL ANALYSIS OF THE 4-YR COBE DMR EXPERIMENT

J. M DIEGO[1,2], E. MARTINEZ-GONZALEZ[1], J. L. SANZ[1]
S. MOLLERACH[3], V. MARTINEZ[3]
1 IFCA, Departamento de Astrofísica, Facultad de Ciencias, Avda. Los Castros, s/n, Santander 39005, SPAIN
2 Departamento de Física Moderna, Facultad de Ciencias, Avda. Los Castros, s/n, Santander 39005, SPAIN
3 Departamento de Astronomia y Astrofísica, Universidad de Valencia, Valencia 46100, SPAIN

In this work we apply the multifractal analysis to the four-year COBE-DMR data an we obtain the spectrum of fractal dimensions. We prove the viability of this method with this kind of data and the capacity of such a method when one is interested in the obtention of cosmological parameters such as the quadrupole normalization value Q_{rms-PS} and the spectral index n. We estimate the most probable model that best fit the data and we compare this result with those given by other methods.

1 The method

There are several reasons why a multifractal analysis is an interesting alternative to the standard ones. First of all, we do not need to assume any gaussian property for the temperature. Second, this method works with moments of any order, not only two or three. Also this method considers the fluctuations of temperature at all scales, searching for scaling properties predicted by the *Sachs-Wolfe* effect produced by a scale-free power spectrum of density fluctuations.
We briefly describe how the method works. For a more exhaustive description of the method, a straightforward presentation can be found, for example in the book *Fractals* (Feder 1988).
One starts with a CMB map (like the 53+90 GHz combination map of the COBE-DMR 4 year data set). We substract the monopole and dipole, and we apply a mask that takes care of the regions of the sky dominated by galactic emission. There are 3881 remainig pixels. Upon this data one has to form a grid of boxes $\delta \times \delta$ where we define the measure $\mu_i(\delta)$. In our case the measure is simply the sum of the absolute temperatures over the pixels in the $Box_i(\delta \times \delta)$.

Those mesures corresponding to boxes afected by the mask (boxes with voids inside) are propely weighted by an area realation. The resulting measure must be normalized in a subsequent step. Now we can define the next quantity called the generalized box-counting partition function.

$$Z(q,\delta) = \sum_{i=1}^{N_{boxes}(\delta)} \mu_i(\delta)^q \tag{1}$$

where $N_{boxes}(\delta)$ is the number of boxes (or cells) needed to cover the map when the grid with resolution δ is used.
Variying δ (for a fixed q) and if we represent $\ln Z(q,\delta)$ vs $\ln \delta$ trough this variation we will see something like a straight line that corresponds to the fact that we have a scaling in the measure (one line for each q). Adjusting this curve to a straight line we can obtain the slope $-\tau(q)$.
Now appears the most atractive quantity for our interest. The generalized fractal dimensions:

$$D(q) = \frac{\tau(q)}{1-q} \tag{2}$$

If we are able to find the slope of the curves (one per q) $\ln Z(q,\delta)$ vs $\ln \delta$ trough a linear regression, then we can obtain $\tau(q)$ and $D(q)$. It can be proved (Feder 1985) that the quantities q and $\tau(q)$ can be related trough a Legendre transformation with other two very interesting quantities. These are α and $f(\alpha)$. These relations are:

$$\alpha(q) = -\frac{d\tau(q)}{dq} \tag{3}$$

$$f(\alpha) = q\alpha(q) + \tau(q) \tag{4}$$

Once one has $\tau(q)$, obtain $\alpha(q)$ and $f(\alpha)$ using eq. [3] and [4] is straightforward.

In fig.1 we present the shape of this curves for the 53+90 GHz map.

There are plotted $D(q)$, $\alpha(q)$, and $f(\alpha)$. A narrow $f(\alpha)$ curve means a very homogeneous data and an asymmetric $f(\alpha)$, or equivalently $f(q)$ *could* mean that the signal is non gaussian. A more detailled discussion about the shape of this curves can be found in a coming paper that describes more precisely this work (Diego et al. 1998). Now we use these curves as a parametrization of the data and we apply a likelihood analysis in order to find the parameters Q_{rms-PS} and n that best fit the data.

2 Likelihood analysis

We based our analysis on the study of the behaviour of the $D(q)$ curve as a function of the quadrupole normalization value Q_{rms-PS} and the spectral index n. Using this curve we can parametrize the data and reduce the total information of one sky map (one temperature per pixel) to one single curve : $D(q)$.
We make Monte Carlo simulations of the CMB for a scale-free model with a power spectrum given by $P(k) \propto k^n$ and with variance C_l in the shperical armonics parameters a_{lm} (Bond and Efstathiou 1987).
We project this maps into the COBE pixelization and we change the quadrupole normalization Q_{rms} and the spectral index n. Later the instrumental noise is added to the simulations.
But there is other effect that must be taken into account, the cosmic variance. Several simulations, all they with exactly the same parameters set, looks different due to the random nature of the coefficients a_{lm}, that are directly related with the power spectrum C_l. To treat conveniently this effect we perform a great number of simulations for each value of Q_{rms-PS} and

then we compare the medium $D(q)$ curve of these simulations with the single one $D(q)$ curve corresponding to the COBE data.
Making use of a maximun likelihood method one can determine what is the best fit of the simulations (signal + noise) to the COBE data.
We tested the power of the likelihood in order to fit the parameters Q_{rms-PS} and n by means of simulated maps (like the COBE maps) but with a known value of Q_{rms-PS} and n and then using these maps as the original COBE maps and extracting later the values of Q_{rms-PS} and n. The conclusion was that this method gets the input parameters with errors (1σ level) of a few percent. So, the likelihood method accurately renders the Q_{rms-PS} and n values with a relatively small uncertainty when a simulation is used as the data.
When we are using the real data instead of one simulation the situation is something different. In fact we obtain through a likelihood analysis an important degeneration betwen the models that best fit the real data. There is a degeneration in the n parameter that is the same result that is sistematically found by other methods but in this case this degeneracy is something bigger. We think that this is due to the low signal to noise ratio of our signal (about 2). This method shows a high sensitivity to the presence or not of noise. A single fluctuation below or upon the mean can be growed up when we are using high exponents q and this sistematically affects to the scaling laws in $\ln Z$ vs. $\log \delta$. Apart this degeneration we found the tipical anticorrelation in the two parameters Q_{rms-PS} and n.
There is another paper (Mollerach et al. 1998) which analize the same data but from a different point of view. That work studies the roughnes of the last scattering surface considered as a fractal and the result is quite similar to the previous one presented here.

3 Conclusions

The multifractal analysis is an appropiate tool when very homogeneous signals are involved and shows an important sensitivity to small changes in the data. But this characteristic that could in principle be considered as an important advantage becomes a problem when spurious signals (like noise or galactic emission) are involved. In fact, the asymmetry observed in the $f(q)$ curve for the COBE data is not present for the average value of the models. This assimetry which can be assigned to spurious contributions, limits the applicability of the method. This assimetry could be produced by the presence of an important fluctuation in the map, even one single pixel could explain it! Maybe the noise is the reason of this fluctuation or maybe some contaminated pixels by galactic emission and not extracted with the mask, or maybe the temperatures are not gaussian ... This opens an interesting question that will be addressed in the future.
In the particular case that a likelihood analysis is needed, this method is also an interesting alternative because there is not assumption about the gaussianity of the temperatures and instead we only make use of the gaussian distribution of the $D(q)$ curves for each parameter q that is not a so strong condition upon the data like the former.

References

1. Bond, J. R., and Efstathiou, G. 1987, MNRAS, 226, 655
2. Diego, J. M., Martínez-González, E., Sanz, J.L, Mollerach, S., and Martínez, V., preprint.
3. Feder, J. 1988, Fractals, Plenum Press, New York, 233 Spring Street, New York, N.Y. 10013
4. Mollerach, S., Martínez, V., Paredes, S., Diego, J. M., Martínez-González, E., and Sanz, J.L. preprint.

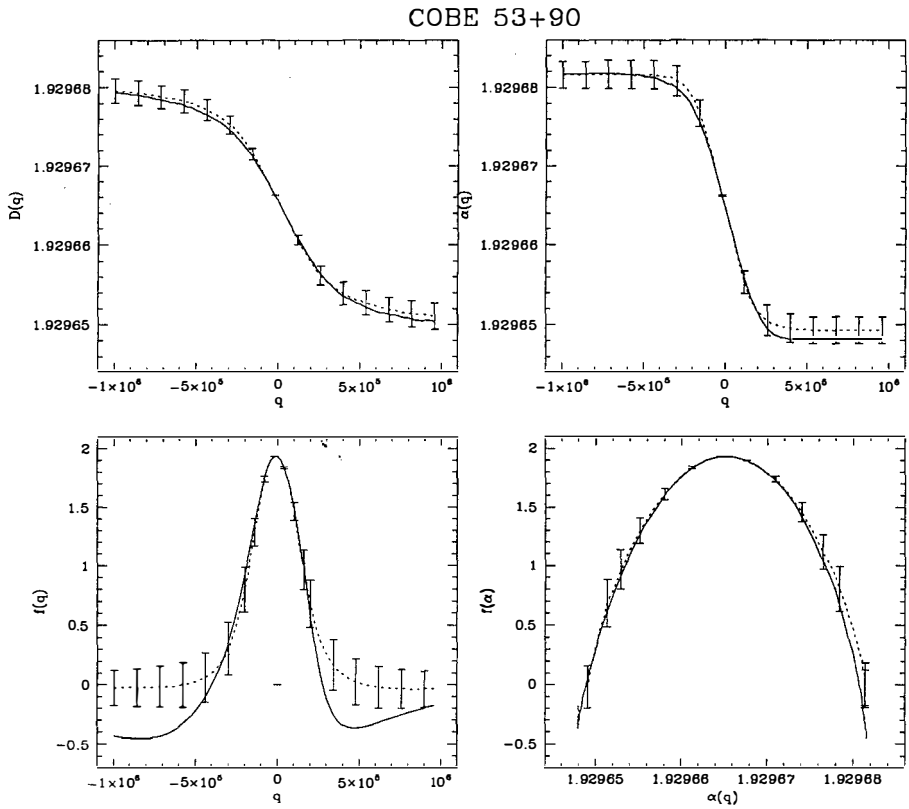

Figure 1: From top to bottom and from left to right: $D(q)$, $\alpha(q)$, $f(q)$, and $f(\alpha)$ for the COBE-DMR data (solid line). In the plot is also showed the corresponding curves with its error bars (1 σ) for the model with $Q_{rms-PS} = 15.0\ \mu k$ and $n = 1.2$ (dotted line).

THEORETICAL PREDICTIONS OF CMB ANISOTROPIES GENERATED BY SCALING SEEDS VERSUS CURRENT OBSERVATIONAL DATA

M. SAKELLARIADOU[1,2 a]
R. DURRER[1], M. KUNZ[1], C. LINEWEAVER[3]
[1] *Département de Physique Théorique, Université de Genève, 24 quai Ernest Ansermet, CH-1211 Genève 4, Switzerland.*
[2] *Institut für Theoretische Physik, Universität Bern, Sidlerstrasse 5, CH-3012 Bern, Switzerland.*
[3] *School of Physics, UNSW, Sydney, Australia.*

We calculate angular power spectra of cosmic microwave background anisotropies induced by scaling seeds, constrained by energy momentum conservation. Motivated by global topological defects, we concentrate on the regions of parameter space found in (A) the $\mathcal{O}(4)$ texture models and (B) the large-N limit of $\mathcal{O}(N)$ models. We then use χ^2 fitting to compare the obtained theoretical predictions to recent flat-band power measurements of the CMB.

The origin of the large scale structure in the universe is an important open problem in cosmology, currently addressed by two families of models. Initial density perturbations can either be due to *freezing in* of quantum fluctuations during an inflationary era, or they may be induced by *seeds*, defined as any non-uniformly distributed form of energy, which contributes only a small fraction to the total energy density of the universe and which interacts with the cosmic fluid only gravitationally. Our aim here[1] is to investigate whether a generic class of seed induced perturbations with a purely scalar component, constrained just by energy momentum conservation and scaling arguments, can be ruled out by present observations of CMB anisotropies. As a further step, we plan to investigate how vector and tensor modes are constrained by the current data. The models we consider are motivated by topological defects, which can be formed naturally during a symmetry-breaking phase transition in the early universe.

[a] Talk given by Mairi Sakellariadou

We characterize the scalar part of the energy momentum tensor of the seeds by four *seed functions*, f_ρ, f_p, f_v, f_π, defined by [2,3]

$$\Theta_{00} = M^2 f_\rho \ ; \ \Theta_{i0} = M^2 f_{v,i} \ ; \ \Theta_{ij} = M^2[\{f_p - (1/3)\Delta f_\pi\}\gamma_{ij} + f_{\pi|ij}] \ , \tag{1}$$

where Δ denotes the Laplacian and $|$ the covariant derivative with respect to the metric γ of the three space; M is a typical *mass*, or energy scale, of the seeds. The gravitational strength of the seeds is characterized by the dimensionless parameter $\epsilon \equiv 4\pi G M^2$. The seed functions satisfy the covariant conservation equations [3]

$$\dot{f}_\rho - \Delta f_v + (\dot{a}/a)(f_\rho + 3f_p) = 0 \tag{2}$$

$$\dot{f}_v + 2(\dot{a}/a) f_v - f_p - (2/3)\Delta f_\pi = 0 \ ; \tag{3}$$

a denotes the cosmic scale factor, dot stands for derivative with respect to conformal time t.

We define *scaling seeds* to be sources for which the power spectra $\langle |f_\bullet|^2 \rangle (k,t)$ are, up to an overall power of t determined by dimensional reasons, functions of $x = kt$ only. Thus, the power spectra of the functions $f_\bullet$ can be given in the form [1]

$$\langle |f_\rho|^2 \rangle = t^{-1} \ F_1^2(x) \quad ; \quad \langle |f_p|^2 \rangle = t^{-1} \ F_2^2(x) \ ;$$
$$\langle |f_v|^2 \rangle = t \ F_3^2(x) \quad ; \quad \langle |f_\pi|^2 \rangle = t^3 \ F_4^2(x) \ . \tag{4}$$

We further require that the sources decay on sub-horizon scales. Such models imply, on large angular scales, a scale-invariant Harrison-Zel'dovich spectrum. Guided by numerical simulations and simple physical considerations, we write [1]

$$F_1 = \frac{A_1}{1 + \alpha_1 x^{n_1}} \ ; \ F_3 = \frac{A_3}{1 + \alpha_3 x^{n_1}} \tag{5}$$

while F_2 and F_4 are determined by energy momentum conservation, Eqs. (2,3). The gravitational action of the seeds is determined by the induced Bardeen potentials, which contain contributions from the seeds, as well as the matter and radiation fluids. For each model parametrized by $(A_1, \alpha_1, n_1, A_3, \alpha_3, n_3)$, we calculate[4] the induced CMB anisotropies, once the fluid perturbations and the Bardeen potentials are determined. To solve the system of the perturbation equations, we approximate the random variables $f_\bullet$ by the square root of their power spectra.

We investigate scaling seed models in the context of a flat cold dark matter universe [1]. In particular, we consider two types of models. In the first one we choose $n_1 = 2$, $n_3 = 4$; a choice supported by numerical simulations of global textures [5]; we refer to this first type of scaling seed models as model A. Inspired by analytical results in the large-N limit of $\sigma(N)$ models [6], we set, in what we refer to as model B, $n_1 = 5/2$ and $n_3 = 7/2$. We set the arbitrary normalization by fixing $A_1 = 1$, and we vary $A_3 (= A_3/A_1)$. We further reduce [1] the remaining 3-dimensional parameter space $(A_3, \alpha_1, \alpha_3)$ to 2-dimensions (A_3, α_1), by setting $\alpha_3 = \alpha_1/2$. Choosing $\alpha_3 = 2\alpha_1$, leads to qualitatively similar results. In the parameter space we explore, we vary [1] $-1.0 \leq A_3 \leq +1.0$ for model A and $-1.2 \leq A_3 \leq +0.5$ for model B. For α_1 we choose the parameter range $0.01 \leq \alpha_1 \leq 2.0$ for model A and $0.001 \leq \alpha_1 \leq 0.141$ for model B. We normalize the power spectra at $\ell = 10$ by fitting to the data.

We use [1] χ^2 fitting, to compare our models to recent flat-band power measurements of the CMB. We plot our data along with the best-fit power spectra for models A and B in Fig. 1.

Fig. 2 is a contour plot in the $\alpha_1 - A_3$ plane for model A; Fig. 3 is the analogous one for model B. There are 32 data points and 28 degrees of freedom (28 = 32 - 2 (fitted defect parameters) - 1 (normalization) - 1 (sliding Saskatoon absolute calibration)). Model A yields [1] a χ^2 minimum value $\chi^2_{\rm min} = 21.2$; model B yields [1] $\chi^2_{\rm min} = 27.1$. Therefore, our fits are quite reasonable.

To interpret our χ^2 fits, we note that if perturbations decay fast enough, the height of the first acoustic peak is determined by $f_\rho + 3f_p \sim A_1/4$, while the Sachs-Wolfe plateau is fixed by

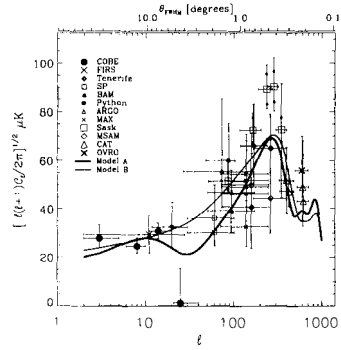

Figure 1: Flat-band power measurements. The best-fit models of two scaling seed models are also shown: one most relevant to model A (Fig. 2) and the other for model B (Fig. 3).

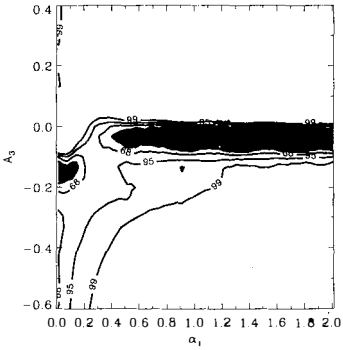

Figure 2: χ^2-fit of model A to the CMB data. The "X" marks the χ^2_{min}; the grey area is the $(\chi^2_{min}+1)$, $\sim 1\sigma$-likelihood region. Contours marked "68", "95" and "99" refer to goodness-of-fit contours.

A_4. Thus, χ^2 is not expected to be very sensitive to α. This is indeed the case [1] for $\alpha_1 \gtrsim 0.4$ (Fig. 2.) in model A, and for $\alpha_1 \gtrsim 0.03$ (Fig. 3) in model B. Fig. 2 shows the χ^2 fit of model A to the CMB data. Small negative values of A_3 ($-0.1 \leq A_3 \leq 0$) are preferred[1]. For $\alpha_1 \gtrsim 0.4$ the result does not depend strongly on α_1. For smaller values of α_1 ($\alpha_1 \lesssim 0.2$), the seed functions decay slower, implying that somewhat larger values of $|A_3|$ are preferred, since the acoustic peaks are already enhanced[1]. Fig. 3 is the model B analog of Fig. 2. Also here, a positive A_3 is excluded for $\alpha_1 \gtrsim 0.01$. A value of $A_3 \sim -0.1$ is generically preferred[1]. Since the χ^2 *landscape* within the parameter range explored in Figs. 2, 3 is rather flat, values within the "68" contour are reasonably compatible with current data[1].

As it was first shown [7], and later confirmed by full numerical simulations [8], the full texture models — i.e., including scalar, vector and tensor modes — have acoustic peaks which are substantially too low to fit the observational data. To briefly explain this result, let us note the following: Numerical simulations of $\mathcal{O}(4)$-textures give [9], in the matter dominated era, $A_1 \sim 4, \alpha_1 \sim 0.012$ and $A_3 \sim 0.37, \alpha_3 \sim 0.05$. The scalar contribution to the SW plateau is $\sim 1.1\epsilon^2$ at $\ell \approx 10$ and the height of the first acoustic peak is about $\sim 5\epsilon^2$. Full simulations, which include vector and tensor modes[5], lead to an amplitude of the SW contribution on the

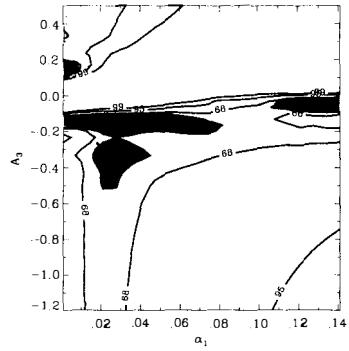

Figure 3: Same as previous figure except here we are fitting model B to the data.

order of $\ell(\ell+1)C_\ell \sim 8^{+4}_{-2}\epsilon^2$. Therefore the vector and tensor parts contribute more than $\sim 80\%$ to the SW plateau, while they are not expected to influence the acoustic peaks.

Our analysis shows[1] that present observations of CMB anisotropies cannot rule out a generic class of seed induced perturbations with a purely scalar component, constrained just by energy momentum conservation and scaling arguments. As a second step, one should include vector and tensor contributions and investigate whether generic scaling seeds, with all three components, constrained from just energy momentum conservation, are compatible with current data. Recently, topological defect models have been found[7,8], for which the Sachs-Wolfe plateau is dominated by vector and tensor modes, leading to power spectra which cannot fit the data. Thus, such topological defect models are ruled out. Finally, one should study whether scaling seed induced perturbations, which are compatible with current observational data, represent a *realistic topological defect model.*

Acknowledgments

M.S. would like to thank the organizers of the *XXXIIIrd Rencontres de Moriond* on *Fundamental Parameters in Cosmology*, for inviting her to present this work.

References

1. R. Durrer, M. Kunz, C. Lineweaver and M. Sakellariadou, *Phys. Rev. Lett.* **79**, 5198 (1997).
2. R. Durrer, *Phys. Rev.* **D42**, 2533 (1990).
3. R. Durrer, *Fund. of Cosmic Physics* **15**, 209 (1994).
4. R. Durrer and M. Sakellariadou, *Phys. Rev.* **D56**, 4480, 1997.
5. R. Durrer and Z. Zhou, *Phys. Rev.* **D53**, 5394 (1996).
6. M. Kunz and R. Durrer, *Phys. Rev.* **D55**, 451 (1997).
7. R. Durrer, A. Gangui and M. Sakellariadou, *Phys. Rev. Lett.* **76**, 579 (1996).
8. U. Pen, U. Seljak and N. Turok "Power Spectra in Global Defect Theories of Cosmic Structure Formation", astro-ph/97004165 (1997).
9. M. Kunz and R. Durrer, in preparation.

CMB ANISOTROPY MEASUREMENTS USING STRATOSPHERIC BALLOONS

P. DE BERNARDIS, S. MASI
Department of Physics, University of Rome La Sapienza,
P.le A. Moro 2, 00185 Roma, Italy

We review the topic of Cosmic Microwave Background Anisotropy measurements carried out by means of balloon-borne telescopes. After a short description of the experimental methodology, we outline the peculiar problems of these experiments, and we describe the main results obtained and the perspects for future developments.

1 Stratospheric Balloons and CMB Anisotropy Measurements

1.1 Stratospheric Balloons

Stratospheric balloons are space carriers offering flights at 30-40 Km altitude, for payloads with mass up to 2500 Kg, with reasonable cost and short development time scales. The available time at float ranges between a few hours and a couple of weeks. The intrinsic payload stability is of the order of a few arcminutes. The observable elevations are between 0° and 65° (or up to the zenith placing the payload on top of the balloon).

The team of NASA-NSBF (USA) offers 6-48 hours flights over North America and 1-2 weeks flights in Artic and Antarctic (Long Duration Balloons). The team of CNES (France) offers balloon flights of a few hours over France and up to 60 hours in Sweden. The team of ASI (Italy) offers 20-40 hours transmediterranean flights from Sicily to Spain. Balloon flights are also carried out by teams in Russia, Brazil, Japan and in China.

Infrared mongolfieres[1] have been used for ultra long duration flights of lightweight payloads ($\sim$ 50 Kg). Superpressure balloons are being developed, providing in the near future ultra-long ($\sim$ 3 months) balloon flights for medium-mass payloads.

1.2 *CMB measurements from Stratospheric Balloons*

The main advantage of placing a CMB telescope on a stratospheric balloon is a large reduction of the atmospheric brightness (temperature) and noise. This effect is wavelength dependent. The advantage is huge for observation wavelengths above 100 GHz, while it is not too important for wavelenghts below 40 GHz, where longer observation time and easier access to the experiment favour high mountain observations. For wide band bolometric receivers the balloon environment offers an additional advantage, since the reduced radiation background permits to reach a lower temperature of the sensor, thus increasing significantly its sensitivity.

A generic instrument for the measurement of CMB anisotropies is composed by the following main subsystems: the gondola, usually an aluminum or carbon fiber tubolar lightweight structure with an inner frame (containing the telescope, the receiver and a star sensor for attitude reconstruction) and an outer frame containing the elevation mechanism for the inner frame, the azimuth mechanism and a pivot to rotate the entire payload with respect to the flight chain, the data processing and storage electronics and lithium batteries to power the system. The space agency provides the uplink and downlink telemetry and the navigation hardware (GPS, altitude sensors, ballast, balloon valves etc..).

Placing the telescope below a stratospheric balloon has a number of disadvantages. Interactivity with the experiment is greatly reduced, and the duration of the measurement is only a few hours for normal balloon flights. So all the tests for systematic effects must be planned in advance, with great care, and inserted in the flight sequence, taking advantage of the increased sensitivity of balloon systems to perform quicker test. Also, the balance between time devoted to integration, time for calibration, and tests for systematics must be optimized. Long Duration Ballooning offers unique extensive possibilities of systematics tests.

The telescope must point/scan the sky regions selected for calibration and observations. Pointing a telescope attached to a stratospheric balloon is much more difficult than pointing a ground based telescope, and also more difficult than pointing a satellite, due to the presence of gravity and of perturbations induced by the residual atmosphere. A huge effort has been paid by X-ray and IR astronomers to develop Attitude Control Systems (ACS) suitable for balloon borne experiments[2 3 4 5 6]. These systems are based on gyroscopes, magnetometers and star cameras as sensors, and on motorized high inertia flywheels as actuators to control the payload motion. Receiver calibration is usually achieved observing a planet. The performance of the ACS should be good enough to provide a pointing stability of at least FWHM/20, with the additional necessity of making good raster scans for beam shape and calibration purposes. An advantage of balloon experiments with respect to ground based experiments is the possibility of measuring the large scale dipole anisotropy of the CMB, which provides a calibrator with the same spectrum of the (sub-)degree scale anisotropies. In this case, the ACS should be able to rotate the experiment over 360° in azimuth, with a scan speed large enough to mantain the dipole signal inside the useful electrical bandwidth of the instrument and with negligible pendulations. Due to atmospheric inhomogeneity and sidelobes spillover, this calibration mode is practically impossible for ground-based experiments.

The balloon - flight chain - payload system is a pendulum. The balloon drifts with the stratospheric jet-stream. Inhomogeneities in the wind can excite pendulations of the system, which has three main pendulation modes: a rigid pendulation of the system (period $\sim 30s$); a pendulation of the payload in opposition with the balloon (period $\sim 10s$), and a pendulation of the gondola around the pivoting point (period o a few s). Pendulations of the experiment can also be induced by the attitude control system itself, due to the non-diagonal nature of the inertia tensor of the payload and to static and dynamic unbalancing of the flywheels. Pendulations modulate the residual atmospheric brightness, thus producing a periodic signal in the receiver. If $I_{ATM}(e,\nu)$ is the atmospheric brightness, $E(\nu)$ is the spectral efficiency, and e is the beam

elevation, pendulations Δe produce brightness fluctuations equivalent to CMB temperature fluctuations, of the order of

$$\frac{\Delta T_{CMB}}{\Delta e} = \frac{T_{CMB}}{\tan e} \frac{\int I_{ATM}(e,\nu) E(\nu) d\nu}{\int B(T_{CMB},\nu) \frac{xe^x}{e^x-1} E(\nu) d\nu}$$

Bolometric systems are prone to this problem, since their spectral efficiency is intrinsically quite wide, and the $E(\nu)$ is defined by means of suitable blocking / mesh filters. In fig.1 we compare the spectrum of the atmosphere to the spectrum of the CMB anisotropy as seen through a suitable filters chain defining a 90 GHz nominal bandpass. The pendulation induced signal can be reduced to $\sim 1 \mu K/arcmin$ with extreme care in the quality and choiche of the receiver filters, and with good performance of the ACS (pendulations lower than a few arcmin peak to peak).

Radio Frequency interference due to powerful telemetry transmitters is difficult to fight, especially for the ultrasensitive bolometric microwave receivers used for CMB anisotropy research. To understand the extent of the problem, one should notice that the telemetry transmitters have a power of a few W at a frequency of a few GHz, while the CMB receivers have a sensitivity of the order of 10^{-17} W at a frequency only 100 times higher. Extensive filtering of the signal lines exiting the receiver and wavelength selection / filtering on the optical path of the receiver must be carefully optimized.

The problem of sidelobes rejection is common to all the CMB experiments. These experiments try to detect $10 \mu K$ signals embedded in a 300K environment. Balloon experiments cannot take advantage of drift scans, due to the very long integration time required by such an observation mode. Very clean (low sidelobes) off-axis telescopes and shielding systems have been developed [6 7 8]. The problem is more severe for long wavelength HEMT-based recievers. Measurements of the same sky patches carried out at different locations during the balloon flight are the only way to test for sidelobes contamination in the cosmological data. In this respect balloon experiments cannot compete with the planned lagrangian point space missions [9 10]. Anyway, no evidence for spillover contamination has been found in sensitive balloon-borne CMB surveys.

Balloon borne experiments devoted to CMB anisotropy (recent, ongoing and planned) are listed in table 1. The general trend is towards higher angular resolution. Sub-degree resolutions allow to detect the acoustic peaks in the power spectrum of CMB anisotropy, inferring cosmological parameters, and testing for gaussian versus non gaussian CMB fluctuations. The detectability of higher ℓ acoustic peaks depends on both the angular resolution and noise performance of the instrument. In general, a beam FWHM smaller than 20 arcmin is required to start to make a reasonable ℓ-space spectroscopy of the acoustic peaks. 10 arcmin FWHM beams are optimal.

First generation experiments made statistical samples of the sky temperature fluctuations ΔT_i. Second generation experiments are making maps of the CMB temperature field $\Delta T(RA, dec)$, thus producing a lot more information. Transition from the first to the second generation of experiments has been possible because of the development of new detectors: Spider-web bolometers and sensitive HEMTs receivers. The two techniques are in competition. Also, the map making experiments are based on scanning techniques rather than on pointed observations.

1.3 Bolometers versus HEMTs

High Electron Mobility Transistors (HEMTs) are used to make sensitive, wide band (10 GHz), coherent detectors[11]. They work up to 50 GHz, with good noise performances: $NET_{CMB} \sim 500 \mu K\sqrt{s}$ is the state of the art for the noise figure. These devices work at reasonable cryogenic temperatures (4 K) and feature high speed and high rejection of out of band radiation. As a result, they are quite insensitive to atmospheric emission and fluctuations. Also, the fast response

allows for fast scans of the sky, with tendency towards large sky coverage. Working at relatively low frequencies, they need large telescopes to get a given beamsize: getting a diffraction limited beam of 10 arcmin FWHM at 40 GHz requires a 3 m diameter telescope. At higher frequencies (up to 150 GHz), coherent detection systems use SIS junctions as mixers between CMB radiation and radiation from a stable local oscillator. The down-converted intermediate frequency signal is amplified by low noise cryogenic HEMTs and detected.

Cryogenic Bolometers are used to make incoherent, wide band (30-100 GHz) detectors, operating at frequencies higher than 90 GHz with extremely low noise : $NET_{CMB} \sim 100\ \mu K\sqrt{s}$ is the state of the art. They need very low temperatures (0.3K-0.1K), so require complex cryogenic systems, which must be expecially rugged in the case of balloon-borne experiments [12 13 14 15]. Being thermal detectors, feature slow response (tens of ms) and are sensitive to the load from the radiative background. The telescope emissivity needs to be really low, and spillover from ambient temperature blackbody radiation can significantly degrade the bolometer performances. Moreover, bolometers need sophisticated out of band radiation rejection / filtering techniques [16 17]. Working at higher frequencies, they feature higher angular resolution for the same telescope size: a 0.9 m diameter telescope at 150 GHz already produces a diffraction limited beam of 10 arcmin FWHM. Bolometers are sensitive to any kind of energy deposited in the sensing element. Ionization by cosmic rays (mainly protons) in the stratosphere represents an annoying source of excess noise in bolometric receivers. The problem has been only recently solved with the development of web-like absorbers[18], which feature negligible cross section for cosmic rays while mantaining full sensitivity to CMB photons and reduced heat capacity, resulting in quicker response.

1.4 Sky scan techniques

The first generation of experiments performed chopped measurements. The beam direction was moved periodically in the sky, thus allowing synchronous detection. The signal to noise ratio was improved spending a long integration time for each selected observed direction. The measured quantities are $\Delta T_{meas,i} = \frac{1}{\tau}\int_0^\tau \Delta T(\vec{x}(t))R(t)dt$ and the mean square value of the measured signals was compared to the theoretical $< \Delta T^2 >= \sum_\ell \frac{2\ell+1}{4\pi} c_\ell w_\ell$. Here the window function w_ℓ depends on the beam shape and on the details of the modulation performed by the chopper and of the demodulation performed by the signal processing electronics in the receiver. For example, for a total power gaussian beam experiment $w_\ell = \exp[-\frac{1}{2}\ell(\ell+1)\sigma_B^2]$, while for a square wave chop with peak to peak amplitude α, $w_\ell = 2[1 - P_\ell(\cos\alpha)]\exp[-\frac{1}{2}\ell(\ell+1)\sigma_B^2]$. The results of these experiments are one or a few (if multiple window functions can be obtained from the signals processing) data points in the CMB anisotropy power spectrum. Typical combined analysis of results from these experiments can be found e.g. in [19 20 21].

The second, new generation of experiments performs scan measurements. The telescope beam scans the sky at constant speed. Different spherical harmonic components of the CMB temperature field produce different electrical frequencies in the detector. This experimental approach requires extremely low detector noise and extremely high system stability. ℓ-space spectroscopy is possible using a scanning instrument and an averaging signal analyzer. The procedure to get power spectra from these data is outlined in [22]. Sky maps can also be recovered from the time ordered scan data. However, drifts and $1/f$ noise project in the map in a non-trivial way, producing the characteristic striping well known for the IRAS and DIRBE maps. The best way to reduce this effect in the data analysis is a hot important topic [23 24 25 26 27 28], since the same problem will be present in the data from the future satellite missions MAP and Planck. It must be stressed that scanning balloon experiments represent the only available test-bed for studying and reducing the effect, experimenting on both the hardware and the software. From the experimentalist point of view, the first problem is to setup the scan so that the CMB

information is encoded in a frequency band matching the electrical band of the detection system, and as far as possible from system noise and disturbances. Assuming a scan at constant zenith angle Θ, the temperature fluctuations of the CMB along the scan can be expressed as a Fourier series $T(\Theta,\phi) = \sum_m \alpha_m e^{im\phi}$. If the azimuthal scan rate is $\dot{\phi}$, the m-th component of the CMB signal (which has a mean square amplitude $\Gamma_m =< \alpha_m \alpha_m^* >$) will produce in the detector a signal at the electrical frequency $f = \dot{\phi} m/2\pi$. So a frequency analysis of the detector signal can be performed to get m-space spectroscopy of the CMB anisotropy. Moreover, the 1-D m-space spectrum Γ_m is related in a simple way[22] to the 2-D ℓ-space power spectrum c_ℓ of the CMB: $\Gamma_m = \sum_{\ell=|m|}^{\infty} c_\ell B_\ell^2 P_{\ell m}^2(\Theta)$. This relationship is valid for scans along full circles; shorter scans on circle sections have a lower ℓ-space resolution. All the spherical harmonics components of the CMB with $\ell > m$ contribute to the detector signal at frequency $m\dot{\phi}/2\pi$. If ℓ_{min} is the lowest spherical harmonic of interest, the experimentalist will setup the scan in such a way that noise in the system is confined at frequencies lower than $f_{min} = \ell_{min}\dot{\phi}/2\pi$. This condition is stricter for the HEMT based receivers, which feature higher 1/f noise knee. On the other hand, if the highest spherical harmonics of interest is ℓ_{max} (which depends on the beam size of the experiment), the scan speed should be adjusted so that the frequency $f_{max} = \ell_{max}\dot{\phi}/2\pi$ is lower than the high frequency cut-off of the experiment. This condition is quite strict for bolometric receivers, which feature $\sim$ 10 ms thermal time constants. HEMT based experiments can afford faster scan rates, but good tradeoffs are also possible with bolometer based systems, which, in addition, feature a lower general noise level. The situation is depicted in fig.2, where we plot the typical noise spectrum for a balloon borne CMB experiment, resulting from 1/f and white noise from the detector and the atmosphere and broadened lines from pendulation-induced atmospheric noise. We also plot in fig.2 the transfer function of the bolometer and the frequency spectrum of the CMB signal, as encoded by the scanning procedure and by the beam of the instrument. For beam sizes of the order of 20 arcmin, scan speeds of the order of 3 deg/s, and bolometer time constants below 100 ms, all the interesting CMB anisotropy information can be encoded in the lowest noise frequency band of the system.

2 A small zoo of balloon-borne CMB anisotropy experiments

In the following we summarize the highlights of several recent, ongoing and planned Balloon measurements of the CMB anisotropy at sub-degree scales (see table 1 for a synoptic and for references). It is evident that widely different approaches are used, mainly because different laboratories developed and optimized in their past different detection and processing techniques, and also because we do not know too well the observable to be measured and the related systematic effects.

• Flown experiments:

ARGO is a first-generation experiment, developed at the University of Rome La Sapienza, ENEA Frascati and IROE-CNR Firenze, and flown in 1993. The experiment features a 1.2m cassegrain telescope with wobbling secondary, resulting in a 0.8° FWHM beam chopped by 1.4° p-p. The large throughput bolometric receiver had four detectors with bands centered at 2.0, 1.2, 0.8, 0.5 mm. CMB anisotropy was detected in the 2.0 and 1.2 mm bands in the regions of Hercules and Aries/Taurus, with S/N of the order of one per pixel (on $\sim$ 200 independent pixels). Spectral ratios and comparisons with local contaminants templates were essential to asses the cosmic nature of the detected fluctuations, excluding local contaminations.

BAM is a first generation experiment developed by the British Columbia group and flown in 1995. It features a cryogenic differential Fourier Transform Spectrometer with two bolometric receivers, in the focus of an off axis 1.65 m telescope, resulting in two beams 42 arcmin FWHM on the sky separated by 3.6°. Analysis of the rapid-scan interferograms provides the useful CMB data in five spectral bands (from 93 to 276 GHz), plus important checks for systematics.

A problem in a memory chip reduced the time available for data taking during the flight. CMB anisotropy was detected in a set of 10 sky directions. A new flight of the payload is scheduled for May 1998.

BOOMERanG is a second generation experiment, developed by a collaboration headed by University of Rome La Sapienza and Caltech, with contributions from ENEA, IROE-CNR, QMWC, UCSB, U.Mass. It was flown two times in August 1997 with a total power bolometric receiver and a 1.3 m off-axis telescope, producing four 20 arcmin FWHM pixels at 150 GHz and two 30 arcmin FWHM pixels at 90 GHz. The flight demonstrated the outstanding performances of system, mainly the low background on the bolometers, the extremely low level of the sidelobes, and the absence of excess noise in the total power bolometers readout. The system performed 40^o wide azimuth scans (forward-back with a rounded triangle waveform), covering a $5^o \times 80^o$ region in Cetus, Aquarius, Capricornus. The system was calibrated in flight observing Jupiter and the CMB Dipole. Custom spider-web bolometers reduced drastically the rate of cosmic ray events (down to about 60 events in the full flight). Excess noise is limited to very low frequencies, unimportant for CMB anisotropy signals. The data analysis is currently in progress. This flight represents also a qualification of the payload for the long duration flight to be done at the end of this year (see below).

HACME is a second generation HEMT experiment developed by the group of University of California at Santa Barbara. It features 39, 41 and 43 GHz receivers with $\sim 500\mu K\sqrt{s}$ noise. The gregorian telescope produces 46 arcmin FWHM beams. The most interesting feature of the experiment is a rotating flat mirror mounted in front of the telescope. The flat is tilted 2.5 degrees relative to its spin axis, and spins at 2.5 Hz. So the beam scans the sky on 5^o diameter circles, thus pushing toward large sky coverage, with very well cross-linked scans. The beam elevation changes along the circle, but the low frequency makes the resulting atmospheric signal negligible. Also, any residual atmospheric signal at the spin frequency is well outside the signal frequency band occupied by the degree/scale CMB anisotropy. It was flown two times in 1996, observing about 5000 independent pixels. The disadvantage of this scan technique is the very short integration time per pixel. Maps recovered from the time ordered data are already published [28], but the sensitivity is not high enough to pick-up by-eye cosmic structures from the maps. The statistical analysis of the data is in progress.

MAX/ACME is a first generation experiment, developed by a collaboration between the University of California at Berkeley and the University of California at Santa Barbara. It has been flown five times since 1989. It features a 1.3 m Gregorian telescope with wobbling secondary mirror and several multiband bolometric receivers, resulting in $\sim 0.5^o$ FWHM beamsize at wavelengths between 3.3 and 0.8 mm. MAX detected CMB anisotropies in 7 different sky regions, with $\Delta T/T$ ranging from $(1.2^{+0.4}_{-0.3}) \times 10^{-5}$ to $(2.9^{+4.3}_{-1.8}) \times 10^{-5}$. Spectral arguments, taking advantage of the multiband nature of the system, allow to reject the hypothesis of Galactic contamination of the data. All these detections may be consistent with coming from a single parent population.

MSAM is a first generation experiment, flown in 1992, 1994, 1995, developed by a collaboration headed by University of Chicago and NASA/Goddard SFC. It features a 1.4 m off-axis Gregorian telescope with a nutating secondary. The cryogenic bolometric receiver has four wavelength bands between 2.0 and 0.42 mm. The instrument had a resolution of $\sim 0.5^o$ and sampled a ring centered on the NCP. Data from the different wavelenght bands were combined to create separate CMB and dust channels, thus rejecting local contamination of the cosmological data. Repeated measurements of the same sky regions in different flights reproduced the same anisotropy detection of the CMB, which is also consistent with the measurements of the ground-based Saskatoon experiment on the same NCP ring. The second phase of the MSAM experiment, flown in 1997, used an adiabatic demagnetization refrigerator to cool five detectors at 0.1K.

QMAP is a HEMT-based second generation experiment developed at Princeton and University of Pennsylvania. It is basically the Saskatoon experiment[29] mounted on a balloon platform: a chopping flat is mounted in front of an off-axis 1 m primary, feeding two Q-band (39 arcmin FWHM, 8 GHz bandwidth), one K-band (54 arcmin FWHM, 8 GHz bandwidth) and one D-band (20 arcmin FWHM) receivers. The elevation of the beam is 41^o, and the chop sweep at 4.4 Hz was 10^o or 20^o depending on the flight. The azimuth scan of the gondola produced a second level of chop with 10^o amplitude, centered on the NCP. The system has been flown in 1996 and 1997, and observed about 700 independent pixels in the NCP region. The data analysis is in progress.

• Experiments to be flown:

BEAST is a scaled-up version of HACME, developed by UCSB with contributions from JPL, CNR-Bologna, CNR-Milano, EFEI-INPE (Brazil). The instrument has a 2.2 m lightweigth primary, with 7 Q-band detectors ($275\mu K\sqrt{s}$ noise, 19 arcmin FWHM beam) and 2 Ka-band detectors ($180\mu K\sqrt{s}$ noise, 26 arcmin FWHM beam). Using a spinning flat in front of the primary, all pixels scan on 10^o circles at 5 Hz, while the telescope is swept through different azimuth angles depending on the mission. The LDB version of BEAST will cover about 4000 square degrees, with final sensitivity of about 70 μK per 10 arcminutes pixel. A second LDB flight will have 10 additional W-band (90 GHz) receivers ($500\mu K\sqrt{s}$ noise, 9 arcmin FWHM beam). The test flight will be in 1998 and the LDB flights are planned for 1998 and 1999. ACE is the lightweight Ultra Long Duration version of BEAST, planned for 100 days flights.

BOOMERanG LDB is the long duration flight of BOOMERanG N.A., currently planned for the Antarctic flight in 1998. The LDB hardware, including the long duration ^3He cryostat, the spider web bolometers, the ACS sensors and actuators, the sun shield system and the fully automated flight programmer / data logger, has been tested successfully in the August 1997 flight. The experiment will feature an improved focal plane, with 16 detectors: four 90 GHz bolometers ($75\mu K\sqrt{s}$ noise, 20 arcmin FWHM beam) and four three-band photometers ($90\mu K\sqrt{s}$ @ 150 GHz, $120\mu K\sqrt{s}$ @ 220 GHz, plus a 450 GHz dust monitor, all with 12 arcmin FWHM beam). The experiment will scan the Orologium region, the lowest dust contrast region in the sky, which happens to be opposite to the Sun in the Antarctic summer. The scan strategy and focal plane setup provide several confirmation levels for the detected signals. At short times (few seconds), the detected signal should reproduce in the second detector of the same row, and both the detectors should see in time-reverse in the back-scan the structure seen in the forward-scan; a few minutes later the second row of detectors should see the same structure. All this should reproduce the day after, with only a slight sky rotation, which becomes significant at the end of the flight. The forecast for the final sensitivity of 15 μK per 20 arcminutes pixel at 90 GHz and 25 μK per 12 arcminutes pixel at 150 GHz, with a sky coverage of 2500 square degrees.

MAXIMA is developed by the University of California at Berkeley, with contributions from Caltech, QMW, Universita' di Roma La Sapienza, IROE-CNR Firenze. A 1.5 m off axis primary feeds an array receiver with 14 bolometers (8 at 150 GHz, 3 at 240 GHz, 3 at 420 GHz). All the detectors have a 11 arcmin FWHM. Sky chop is obtained by nutating the lightweight carbon-fiber primary mirror, thus obtaining a 4 deg/s, 6^o amplitude scan of the beam. In addition, a slower azimuth slew of the gondola (50^o p-p) will produce a significant sky coverage. Two partially overlapping regions will be scanned in a regular 6 hours north-America flight, in order to check for systematics and make easier the map reconstruction. The experiment is expected to map about 26000 independent pixels, with final sensitivity of $\sim 24\mu K$/pixel at 150 GHz and $\sim 66\mu K$/pixel at 240 GHz. The flight of MAXIMA will be in spring 1998.

TOP-HAT is a new-generation payload mounted on-top of the balloon, and designed for Long Duration Ballooning. The system is developed at NASA-Goddard and Bartol, U. of Chicago, U. of W. at Madison. The peculiar location of the payload features better ground

shields and absence of signals reflected from the balloon, allowing observations near the zenith. The disadvantages are a stricter weight limit, a complex ACS and the difficult recovery of the payload after test flights. The experiment has a low sidelobes Cassegrain telescope with a single pixel receiver (5 bands from 150 to 630 GHz, 20 arcmin FWHM beam). The test flight of TopHat Pointer (planned for the spring of 1998) will cover the same NCP region observed by MSAM and Saskatoon, with improved sensitivity and high frequency coverage. In the LDB flight (1999), the telescope, tipped 12 degrees off the zenith, spins observing a 24 deg circle. Sky rotation allows the system to map 1800 square degrees of sky and about 20000 independent pixels.

3 Conclusions

Ballooning for CMB Anisotropy measurements is a very active field worlwide. The activity is growing, for two main scientific reasons:

1) High frequency (>90 GHz) and high angular resolution ($\sim$ 10 arcmin FWHM) measurements are possible and effective.

2) These measurements complement the forthcoming data from MAP and are a very important test-bed for Planck technologies.

Moreover, good science is being produced, and promises for important results (like the ℓ-space spectroscopy of the acoustic peaks, or detection/falsification of non-gaussian statistics for the CMB fluctuations) are quite convincing.

As an example relevant for this conference, we can mention the fact that determination of several cosmological parameters is possible with very good accuracy from LDB experiments. For example, if all the systematics effects are properly removed, a single LDB experiment with 12 arcmin FWHM beams, 16 total power bolometric detectors with sensitivity of 80 $\mu K\sqrt{s}$, 10 days of observing time spent over a $50^o \times 50^o$ sky region, can measure the power spectrum of the CMB anisotropies with very good accouracy [30]. Fits can be done on the measured power spectrum [31], allowing to recover Ω_{tot} with a 3% error, Ω_Λ with 6% error, Ω_B with 1% error, n scalar with 18% error, H_o with 1% error, $Q_{rms,PS}$ with 4% error. Here the errors for any parameter make no assumptions about the value of the other parameters. These measurement errors can be significantly reduced if one or more of the cosmological parameters are constrained by other observations or fixed by assumptions.

Acknowledgments

This work has been supported by Programma Nazionale Ricerche in Antartide, Agenzia Spaziale Italiana, Universita' di Roma "La Sapienza". We thank M. Devlin, S. Hanany, P. Meinhold, B. Netterfield, J. Ruhl for providing us with informations about several ongoing and planned experiments.

References

1. Malaterre P., *Adv. Space Res.* **5**, 23 (1985).
2. Hoffman W.F., Fazio G.G., Harper D.A., *Adv. Space Res.* **5**, 117 (1985).
3. Meinhold P. R., et al. APJ **406**, 12 (1993)
4. Fixen D.J., et al. *Astrophys. J.* **470**, 63 (1996)
5. Lamarre J.M. et al., *Infrared Phys.* **35**, 277 (1994)
6. M.L. Fischer, et al. *Astrophys. J.* **388**, 242 (1992)
7. Gervasi M. et al. *Appl. Optics* **in press**, AO-013847 (1998)
8. N. Martin et al., Proc. SPIE **86**, 2807 (1996).
9. http://astro.estec.esa.nl/SA-general/Projects/Planck/

10. http://map.gsfc.nasa.gov/
11. Pospieszalski M.W., et al., IEEE MTTT-S **Digest**, 1253 (1990)
12. Cheng E.S., et al., *Rev. Sci. Instr.* **67**, 4008 (1996)
13. P. Palumbo, et al. *Cryogenics* **34**, 1001 (1994)
14. A. Benoit, Proc. of ESA Symposium, ESA SP-400, 1997
15. S. Masi, et al. *Cryogenics* **37**, 000 (1998)
16. Page L.A., et al., *Appl. Optics* **33**, 1 (1994)
17. Holzapfel W.L. et al., astro-ph/9702222 (1997)
18. Maukopf P., et al., *Appl. Optics* **36**, 765 (1997)
19. P. de Bernardis, et al, *Astrophys. J.* **480**, 1D (1997)
20. Webster M., et al, Astro-ph 9802109
21. Ratra B., et al, *Astrophys. J.* **481**, 2234 (1997)
22. J. Delabrouille, K. M. Gorski, E. Hivon, astro-ph/9710349
23. E. L. Wright, et al., *Astrophys. J.* **458**, L53 (1996)
24. M. A. Janssen, et al., astro-ph/9602009
25. E. L. Wright, astro-ph/9612006
26. G. F. Smoot, astro-ph/9704193
27. Tegmark M., *Phys. Rev.* D **56**, 4514 (1997)
28. Tegmark M., et al., astro-ph/9711076
29. Netterfield C.B., *Astrophys. J.* **474**, 47 (1997)
30. Masi S. et al., in Topological Defects in Cosmology, F. Melchiorri and M. Signore eds, World Scientific, 1997.
31. Andrew Jaffe, Arthur Kosowsky, Lloyd Knox, private communication, 1996.

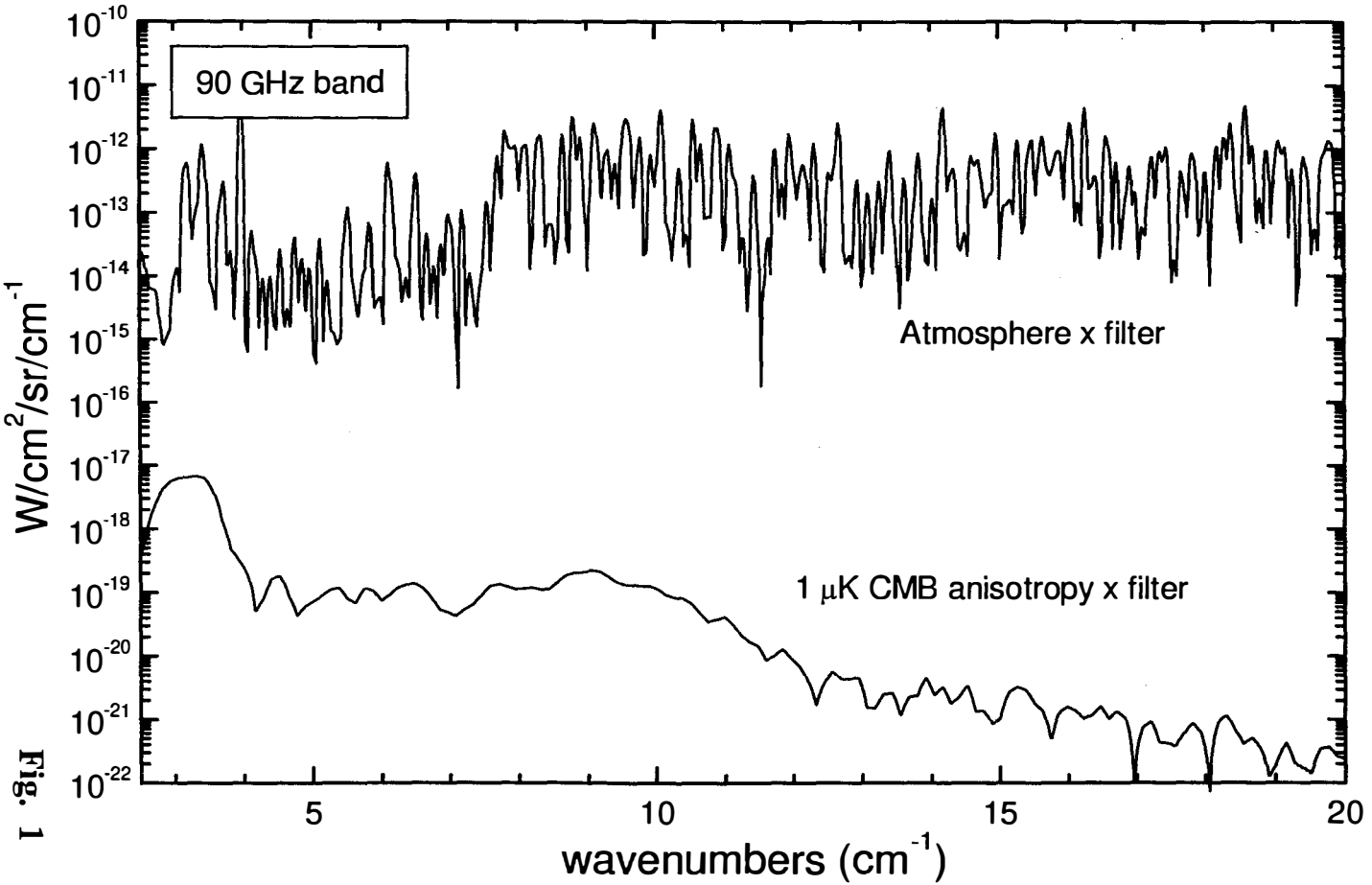
90 GHz band
Atmosphere x filter
1 μK CMB anisotropy x filter
W/cm²/sr/cm⁻¹
wavenumbers (cm⁻¹)
10⁻¹⁰
10⁻¹¹
10⁻¹²
10⁻¹³
10⁻¹⁴
10⁻¹⁵
10⁻¹⁶
10⁻¹⁷
10⁻¹⁸
10⁻¹⁹
10⁻²⁰
10⁻²¹
10⁻²²
5
10
15
20

Fig. 1

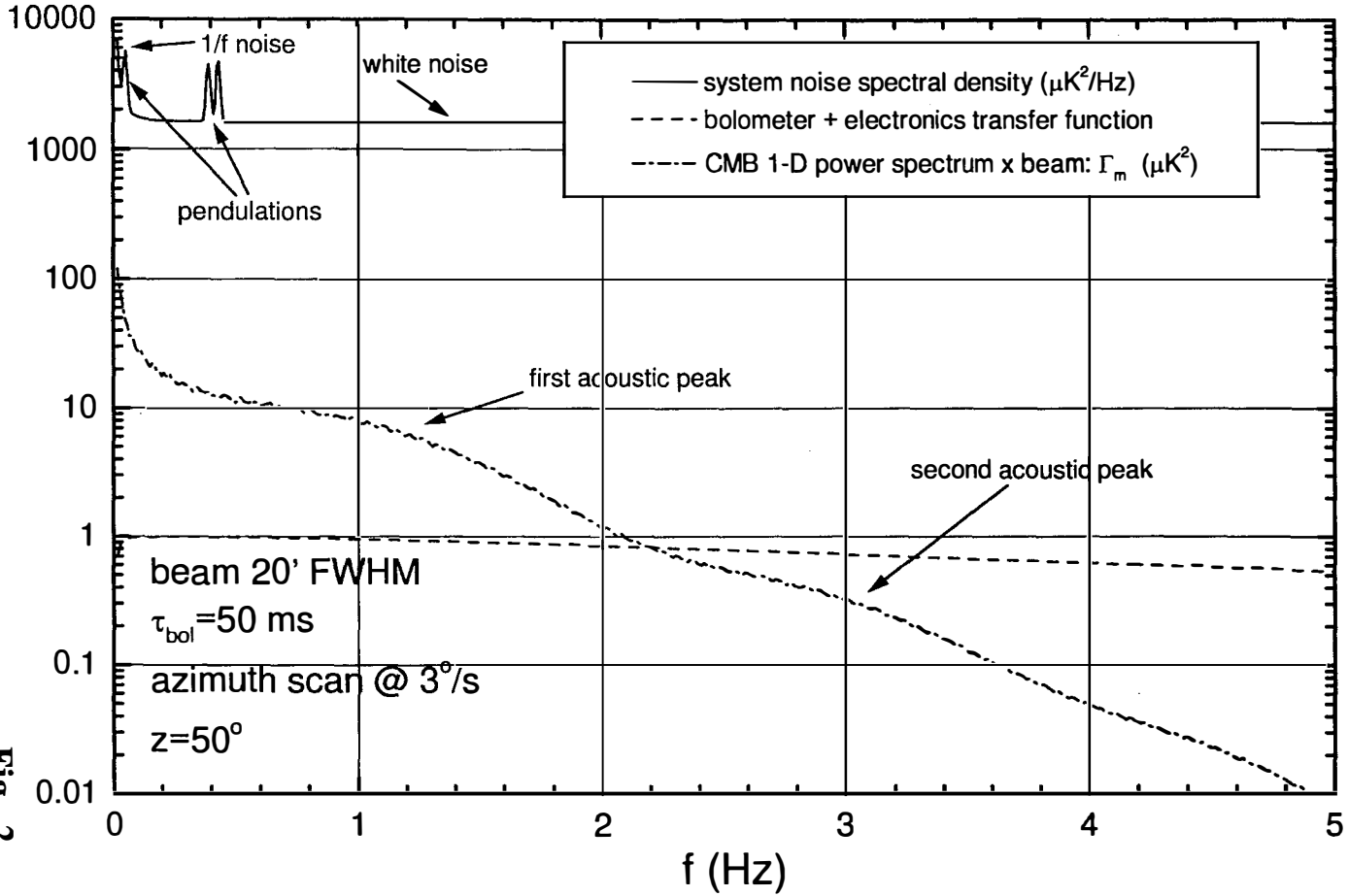
10000
1000
100
10
1
0.1
0.01
0
1
2
3
4
5
f (Hz)
1/f noise
white noise
pendulations
first acoustic peak
second acoustic peak
system noise spectral density (μK²/Hz)
bolometer + electronics transfer function
CMB 1-D power spectrum x beam: Γm (μK²)
beam 20' FWHM
τbol=50 ms
azimuth scan @ 3°/s
z=50°

Fig. 2

	Experiment	Ref.	Technology	Bands (GHz) #detectors	Beam FWHM (arcmin)	Sky Chop - p-p - form	Scan	Data
Recent	ARGO	2	BOLOs	150+270+490+600 / 4	53	WS - 1.4° - S	AZ - SI	~200 differences
	BOOMERanG NA	3	BOLOs	90+150 / 6	22	TP	AZ - 2°/s	~2000 ind.pix.
	BAM	4	BOLOs	Interf. 111 to 255 / 2	42	DIFF - 3.6°	AZ - SI	10 differences
	HACME	5	HEMT	39+41+43/3	46	SF - 5°- TP	C	~5000 ind.pix.
	MAX / ACME	6	BOLOs	105+180+270+420 / 4	30	WS - 1.4° - S	AZ 4° sine	~300 differences
	MSAM I	7	BOLOs	170+280+500+680 / 4	37	WS - 40' - 3F	AZ - slow	~40 differences
	MSAM II	8	BOLOs	70+90+120+150+170/ 5	20	WS - 40' - 3F	AZ - slow	under analysis
	QMAP	9	HEMT	30+40 / 3(x2 polar.)	54+39	CF - 10°/20° - S	AZ 10° sine	~700 ind.pix.
Future	ACE (ULDB)	10	HEMT	90 / lots	9	SF – 10° - TP	C	~200000 ind.pix.
	BEAST I (LDB)	11	HEMT	30+40 / 9	25+19	SF – 10° - TP	C	~36000 ind.pix
	BEAST II (LDB)	11	HEMT	30+40+90 /19	25+19+9	SF – 10° - TP	AZ – 120°	~140000 ind.pix.
	BOOMERanG (LDB)	12	BOLOs	90+150+240+400 / 16	20-12	TP	AZ - 2°/s –120°	~66000 ind.pix.
	MAXIMA	13	BOLOs	150+240+420 / 14	11	WP -6° sawtooth	AZ – 7° sine	~26000 ind.pix.
	TOP-HAT	14	BOLOs	70+90+120+150+170/ 5	20	WS - 40' - 3F	AZ - slow	~500 ind.pix.
	TOP-HAT (LDB)	14	BOLOs	170+280+420+500+630 / 5	20	TP	AZ - S	~20000 ind.pix.

Notes: Sky Chop: WS = Wobbling Secondary; TP = Total Power; CF = Chopping Flat; SF = Spinning Flat; S = sine wave chop; T = triangle chop; 3F = three fields. Scan: AZ = azimuth scan by means of payload rotation; SI = step and integrate; slow = slow rotation; C = circle; S = spin at constant elevation

References: ***2*** - P. de Bernardis et al. Astron. Astrophys., 271, 683, (1993); P.de Bernardis, et al., Ap.J.Lett., 422 , L33, (1994); P. de Bernardis, et al., Ap.J.Lett., 433 , L1, (1994). ***3*** - Lange et al. SPACE SCIENCE REVIEWS, 74, 1-2, (1995); de Bernardis et al. In MICROWAVE BACKGROUD ANISOTROPIES, pg. 155, Bouchet et al editors, ed. Frontieres (1996); Masi S. et al., in "Topological Defects in Cosmology", M. Signore and F. Melchiorri editors, World Scientific, (1997) ***4*** – Tucker et al. Ap.J., 475: L73-L76, (1997) ***5*** – Meinhold P. Private communication; Tegmark M., et al. Astro-PH 9711076 ***6*** –M.L. Fischer, et al.. Ap.J. 388, 242 (1992); D.C. Alsop, et al, Ap.J., 395, 317 (1992); J. Gundersen, et al, Ap.J.L, 413,L1 (1993); M. Devlin et al., Ap.J, 444, 226 (1995); M.J. Devlin, et al. Ap. J.L., 430, 1 (1994); A.C. Clapp, et al., Ap.J. L., 433:57-60, (1994); M.A. Lim, et al., astro-ph/9605142; S. T. Tanaka et al., astro-ph/9512067. ***7*** – D. J. Fixsen, E. S. et al., Ap.J. 470 63 (1996); E. S. Cheng, et al., Ap.J. 488 L59 (1997); M. S. Kowitt et al., Ap.J. 482 17 (1997); E. S. Cheng et al., Ap.J. 456 L71 (1996); E. S. Cheng, et al., Ap.J. 422 L37 (1994). ***8*** – http://cobi.gsfc.nasa.gov/msam-tophat.html. ***9*** – Devlin M., private communication, 1998 ***10*** –***11***- Meinhold P., private communication ***12*** – de Bernardis P., private communication ***13*** – Hanany S. et al. . In MICROWAVE BACKGROUD ANISOTROPIES, pg. 143, Bouchet et al editors, ed. Frontieres (1996); Lee A. et al. pg.149 same proceedings. ***14*** – S. Cheng, in J. L. Sanz et al., eds., Present and Future of the Cosmic Microwave Background, Lecture Notes in Physics 429 76 (New York: Springer-Verlag) (1994); M. S. Kowitt et al., Astrophys. Lett. Commun. 32 273 (1995).

REVIEW OF GROUND-BASED CMB EXPERIMENTS

A.N. LASENBY, A.W. JONES and Y. DABROWSKI
Mullard Radio Astronomy Observatory, Madingley Road, Cambridge CB3 0HE, England

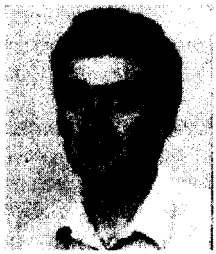

We present in this paper a brief review of Ground-Based Cosmic Microwave Background (CMB) experiments. We first recall the main experimental problems and adopted solutions. We then review the Tenerife experiments, giving an update together with some new results. Then results and problems from other experiments are highlighted including IAC-Bartol, Python, Saskatoon, Mobile Anisotropy Telecope (MAT) and the Owen Valley Radio Observatory (OVRO) experiments. We next move on to the future ground experiments, in particular new interferometers such as the Very Small Array (VSA), the Cosmic Background Imager (CBI) and the Degree Angular Scale Interferometer (DASI/VCA). To finish, very recent work is presented on joint likelihood analysis for estimation of cosmological parameters where both CMB results and Large Scale Structure (LSS) surveys are considered.

1 Experimental Problems and Solutions

1.1 The Contaminants

From the ground, the detection of Cosmic Microwave Background (CMB) anisotropy at the level $\Delta T/T \sim 10^{-5}$ is a challenging problem and a wide range of experimental difficulties occur when conceiving and building an experiment. We will focus here particularly on the problem caused by the contamination of foreground sources and the solutions that have been adopted to fight against them. The anisotropic components that are of essential interest on angular scales of approximately $1/2 - 1$ degree are: (i) The galactic dust emission which becomes significant at high frequencies (typically > 100 GHz). (ii) The galactic thermal (free-free) emission and non-thermal (synchrotron) radiation which are significant at frequencies lower than typically ~ 30 GHz. (iii) The presence of point-like sources. (iv) The dominating source of contamination is the atmospheric emission, in particular at frequencies higher than ~ 10 GHz.

1.2 The Solutions

A natural solution is to run the experiment at a suitable frequency so that the contaminants are kept low. There exists a window between $\sim$ 10 and $\sim$ 40 GHz where both atmospheric and galactic emissions should be lower than the typical CMB flux. For example, the Tenerife experiments are running at 10, 15 and 33 GHz and the Cambridge Cosmic Anisotropy Telescope (CAT) at 15 GHz. However, in order to reach the level of accuracy needed, spectral discrimination of foregrounds using multi-frequency data is necessary (see for example M.P. Hobson, this volume). Concerning point (iv), three basic techniques, which are all still being used, have been developed in order to fight against the atmospheric emission problem:

The Tenerife experiments are using the *switched beam* method. In this case the telescope switches rapidly between two or more beams so that a differential measurement can be made between two different patches of the sky, allowing one to filter out the atmospheric variations.

A more modern and flexible version of the switched beam method is the *scanned beam* method (e.g. Saskatoon and Python telescopes). These systems have a single receiver in front of which a continuously moving mirror allows scanning of different patches of the sky. The motion pattern of the mirror can be re-synthesised by software. This technique provides a great flexibility regarding the angular-scale of the observations. The Saskatoon telescope has been very successful in using this system.

Finally, an alternative to differential measurement is the use of interferometric techniques. Here, the output signals from each of the baseline horns are cross-correlated so that the Fourier coefficients of the sky are measured. In this fashion one can very efficiently remove the atmospheric component in order to reconstruct a cleaned temperature map of the CMB. The Cosmic Anisotropy Telescope (CAT) operating in Cambridge has proved this method to be very successful, giving great expectations for the Very Small Array (VSA) currently being built and tested in Cambridge (jointly with Jodrell Bank) for siting in Tenerife. American projects such as the Cosmic Background Imager (CBI) and the Very Compact Array (VCA/DASI) are also planning to use this technique.

2 The Tenerife Experiments

[Project collaborators: Rod Davies (P.I.), Carlos Gutiérrez, Bob Watson, Rafa Rebolo]

2.1 Drift Scan Experiments

Due to the stability of the atmosphere and its transparency [1], the Izaña observatory of the Tenerife island is becoming very popular for cm/mm observations of the CMB (e.g. Tenerife experiments, IAC-Bartol, VSA). The three Tenerife experiments (10, 15 and 33 GHz) are each composed of two horns using the switched beam technology (angular resolution $\sim$ 5 degrees). The observations take advantage of the Earth rotation and consist of scanning a band of the sky at a constant declination. The scans have to be repeated over several days in order to achieve sufficient accuracy. See e.g. Davies *et al.* [1] (1996) for a complete description.

The first detection at Tenerife (Dec+40°), which dates back to 1994 [2,3], clearly reveals common structures between the three independent scans at 10, 15 and 33 GHz. The consistency between the three channels gave confidence that, for the first time, identifiable individual features in the CMB were detected [4]. Subsequently this was confirmed by comparing directly to the COBE DMR data [5,6]. Bunn, Hoffman and Silk [7] (1996) have applied a Wiener filter to the COBE DMR data in order to perform a prediction for the Tenerife experiments over the region $35° < \mathrm{Dec} < 45°$. Assuming a CDM model, the COBE angular resolution has been improved in order to match the Tenerife experiments' resolution. The prediction has been observationally verified [8], giving great confidence that the revealed features are indeed tracing out the seed structures present in the early universe.

2.2 *Latest results*

There is now enough data to perform a 2-D sky reconstruction [9] for the 10 GHz and 15 GHz experiments (33 GHz to follow shortly). 8 separate declination scans have been performed of the full range in RA from Dec+27.5° up to Dec+45° in steps of 2.5°. This allows the reconstruction with reasonable accuracy of a strip in the sky of 90° × 17.5° in an area away from major point sources and the Galactic plane. The crucial aspect in obtaining accurate results is, first of all, to allow for atmospheric correlations between the different scans. Secondly, and probably more importantly, to be aware that the maps are sensitive to unresolved discrete radio sources (typically of the Jy level in the Tenerife field) in addition to the CMB. Special analysis has been performed in order to remove these sources which have to be monitored continuously since they are variable on the time scales involved. This monitoring task is done in collaboration with M. and H. Aller (Michigan) who have a data-bank of information on these sources.

The 10 GHz 2-D map is likely to include a significant galactic contribution; however it is believed that this contribution is negligible for the 15 GHz map which reveals intrinsic Microwave Background anisotropies on 5 degrees scale. Likelihood analysis on the reconstructed 15 GHz 2-D map is in preparation and will be published shortly. Previous results [3] are: $\delta T = [l(l+1)C_l/(2\pi)]^{1/2} = 34^{+15}_{-9}$ μK at $l \sim 18$ (see Table 1 and Figure 1). The next step concerning the data analysis is to use the Maximum Entropy Method for frequency separation on the spherical sky, in conjunction with all sky maps such as the Haslam 408 MHz [10], IRAS, Jodrell Bank (5 GHz) and COBE. The resulting frequency information will allow us to separate very accurately components such as synchrotron, free-free, dust and CMB (see M.P. Hobson, this volume), which is an exciting prospect.

3 Updates and Results on Various Experiments

3.1 *IAC-Bartol*

This experiment runs with four individual channels (91, 142, 230 and 272 GHz) and is also located in Tenerife where the dry atmosphere is required for such high frequencies. This novel system is using bolometers which are coupled to a 45 cm diameter telescope. The angular resolution is approximately 2° (see elsewhere [11,12,13] for instrument details and preliminary results).

This switched beam system has performed observations at constant declination (Dec+40°), overlapping one of the drift scans of the Tenerife experiments. Atmospheric correlation techniques between the different channels have been applied in order to remove the strong atmospheric component present in the three lowest channels [14]. This atmospheric contaminant is believed to be accurately removed and the galactic synchrotron and free-free emissions are likely to be negligible at these frequencies. On the other hand, the galactic dust emission has been corrected using DIRBE and COBE DMR maps. Finally, the contamination by point-like sources was removed by multi-frequency analysis on known and unknown sources. The results obtained are $\delta T = 113^{+66}_{-60}$ μK at $l \sim 33$ and $\delta T = 55^{+27}_{-22}$ μK at $l \sim 53$ (see Table 1 and Figure 1). One can notice that the $l \sim 33$ point is well off the expected value, however, tests show that the atmospheric component is still very high in this δT value. The $l \sim 53$ point seems to be in better agreement with results from the Saskatoon or Python experiments.

3.2 *Python*

This experiment is using a single bolometer mounted on a 75cm telescope and operating at the single frequency of 90GHz with a 0.75° FWHM beam. Python is located at the Amundsen-Scott South Pole Station in Antarctica. It is performing extremely well in terms of mapping rather large regions of the sky (currently 22° × 5.5°). Three seasons of observations have been analysed

Table 1: Some Current Ground Based Experiments

Experiment	Frequency	Angular Scale	Site/Type	l	δT
Tenerife	10, 15, 33 GHz	$\sim 5°$	Tenerife (Switched Beam)	18^{+9}_{-7}	34^{+15}_{-9}
IAC-Bartol	91, 142, 230 and 272 GHz	$\sim 2°$	Tenerife (Switched beam)	33^{+24}_{-13} 53^{+22}_{-13}	113^{+66}_{-60} 55^{+27}_{-22}
Python III	90 GHz	0.75°	South Pole (Scanned Beam)	87^{+18}_{-38}	60^{+15}_{-13}
Python I, II & III				170^{+69}_{-50} 139^{+99}_{-34}	66^{+17}_{-16} 63^{+15}_{-14}
Saskatoon	6/12 channels between 26 and 46 GHz	$0.5° - 3°$	Canada (Scanned Beam)	87^{+39}_{-29} 166^{+30}_{-43} 237^{+29}_{-41} 286^{+24}_{-38} 349^{+44}_{-41}	49^{+6}_{-5} 69^{+7}_{-6} 85^{+10}_{-8} 86^{+12}_{-10} 69^{+19}_{-28}
OVRO	14.56 and 32 GHz	$\sim 0.1° - 0.4°$	Owens Valley (Switched)	589^{+167}_{-228}	$56^{+8.6}_{-6.5}$

so far (Python I[15], Python II[16] and Python III[17]). In addition to the power-spectrum results of Python III (see Table 1 and Figure 1), the combined analysis of Python I, II & III gives an estimate of the power-spectrum angular spectral index [17]: $m = 0.16^{+0.2}_{-0.18}$ which is consistent with a flat-band power model (i.e. $m = 0$).

A point where the Python experiment differs from all the others is its single frequency measurement. All the experiments discussed here are using either widely spaced frequencies (e.g. Tenerife experiments, COBE) or closely patched bands of different frequencies (e.g. the interferometers discussed in Section 4). As mentioned above, multi-frequency analysis allows identification and correction of the contaminanting component. However, near the pole, the atmospheric emission is believed to be small, while at 90 GHz the galactic dust contribution is estimated to be as small as $\sim 2\mu K$. On the other hand, 17 known point-like sources are present in the Python field, which are estimated to give a 2% effect in the final result. The brightest source may contribute up to 50 μK in a single beam and ideally source removal using information from a separate telescope at the same frequency is required. Python IV and V data have already been taken and the analysis should provide power-spectrum estimations very shortly; see Kovac *et al.*[18] (1997) for details about the IV$^{\text{th}}$ season.

3.3 Saskatoon current status

The Saskatoon experiment is a scanned beam system which operates with 6 or 12 independent channels at frequencies between 26 and 46 GHz. The observations cover the North Celestial Pole with angular scales from 0.5° to 3°. The experiment has been running from 1993 to 1995 and details of the instrument as well as early results can be found elsewhere[20,21]. To find more details about the data analysis and recent results, see for example Wollack *et al.*[22] (1997), Netterfield *et al.*[23] (1997) and Tegmark *et al.*[24] (1997).

The 5 Saskatoon results (see Table 1) are crucial in constraining the position of the first Doppler peak (see Figure 1) and therefore the cosmological parameters. The overall flux calibration of the Saskatoon data was known to have a ±14% error, affecting significantly estimates of Hubble's parameter (H_0) for example. However, recent work from Leitch *et al.* (private communication) who carried out joint observations of Cassiopea A and Jupiter, allows the reduction

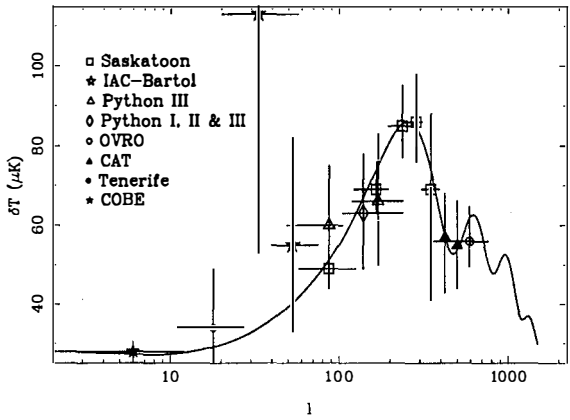

Figure 1: Plot of the CMB Power Spectrum. The data points are those presented in Table 1 and the overlaid standard CDM curve is for the parameters estimated in Section 5. the COBE data point is the 4-Year COBE DMR result (Bennett *et al* [19]. 1996) and the CAT points are given in J. Baker (this volume).

of this uncertainty. The latest calibration is now known with an estimated error of $\sim 4\%$.

Recent work on the foreground analysis of the Saskatoon field has been carried out by Oliveira-Costa *et al.* [25] (1997). These authors found no significant contamination by point-like sources. However, they report a marginal correlation between the DIRBE 100 μm and Saskatoon Q-Band maps which is likely to be caused by galactic free-free emission. This contamination is estimated to cause previous CMB results to be over-estimated by a factor of 1.02.

3.4 Mobile Anisotropy Telescope

The Mobile Anisotropy Telescope (MAT) is using the same optics and technology as Saskatoon at a high-altitude site in Chile (Atacama plateau at 5200m). This site is believed to be one of the best sites in the world for millimetre measurements and is now becoming popular for other experiments (e.g. CBI) because of its dry weather. The experiment is mounted on a mobile trailer which will be towed up to the plateau for observations and maintenance. The relevant point where MAT differs from the Saskatoon experiment is the presence of an extra channel operating at 140 GHz. This will greatly improve the resolution and should provide results well over the first Doppler peak. Data has already been taken over the last few months at 140 GHz and is currently being analysed. See the MAT www-page [26] for a full description of the project.

3.5 Owens Valley Radio Observatory

The Owens Valley Radio Observatory (OVRO) telescopes have been used since 1993 for observation of the CMB at 32 GHz and 14.5 GHz. The RING40M experiment uses the 40-meter telescope (14.5 GHz channel) while the RING5M experiment is mounted on the 5.5-meter telescope (32 GHz channel). Both experiments have an angular resolution of $\sim 0.12°$. Details about these experiments can be found in Readhead *et al.* [27] (1989) or in Myers *et al.* [28] (1993) for example.

36 fields at Dec+88°, each separated by 22 arcmin, have been observed around the North Galactic Pole. Using these data, Leitch *et al.* [29] report an anomalous component of Galactic emission. Some further work on the same data (Leitch *et al*, private communication) gives the following estimate for the CMB component: $\delta T = 56^{+8.6}_{-6.5}$ μK at $l \sim 589$. As seen on Figure 1,

Table 2: Future Ground Based Experiments

Experiment	Frequency	Angular Scale	Site/Type	Date
VSA	26 to 36 GHz	$0.25° - 2°$	Tenerife (14 element interferometer)	1999
CBI	26 to 36 GHz	$0.07° - 0.3°$	Chile (13 element interferometer)	1999
DASI	26 to 36 GHz	$0.25° - 1.4°$	South Pole (13 element interferometer)	1999

this new OVRO result seems to agree well with the CAT estimations and therefore helps in constraining the position of the first Doppler peak. Further details of this measurement should be available shortly.

4 Ground Based Interferometers

As seen in Section 1.2, interferometers allow accurate removal of the atmospheric component. Therefore special ground sites are not always necessary in order to perform sensitive measurements. For example, the 3 element interferometer Cosmic Anisotropy Telescope (CAT) is currently operating in Cambridge, UK [30]. A full discussion of the CAT current status is given by J. Baker (this volume) and results, including the new CAT2 points, are plotted in Figure 1.

The Very Small Array (VSA) is currently being built and tested in Cambridge for siting in Tenerife and should be observing in late 1999. The 14 elements of the interferometer will operate from 26 to 36 GHz and cover angular scales from 0.25° to 2° (see Table 2). The results will consist of 9 independent bins regularly spaced from $l \sim 150$ to $l \sim 900$ on the Power Spectrum diagram [31]. This will give significant information on the second Doppler peak, while the first peak will be constrained accurately enough to estimate the total density Ω and Hubble's constant H_0, with a 10% error. The VSA current status is discussed in this volume by M.E. Jones.

There are two other interferometer projects which will complement the work done with the VSA: The Cosmic Background Imager (CBI), to be operated from Chile by a CalTech team [32] and The Degree Angular Scale Interferometer [33,34] (DASI) – formerly Very Compact Array (VCA) – which will be operated at the South Pole (University of Chicago & CARA). They both share the same design (13 element interferometers) and the same correlator operating from 26 to 36 GHz (see Table 2). However the size of the baselines differ between CBI and DASI so that CBI will cover angular scales from 4 to 20 arcmin while DASI will cover the range between 15 arcmin and 1.4° (similar to the VSA).

All three of these interferometric experiments (VSA, CBI and DASI) should be in operation by the end of 1999.

5 Joining CMB and Large Scale Structures Data

As mentioned earlier, by comparing the observed CMB Power Spectrum with predictions from cosmological models one can estimate cosmological parameters[3,35,36]. In an independent manner, similar predictions can be achieved by comparing Large Scale Structure (LSS) surveys with cosmological models[37,38,39]. Recently, Webster *et al.*[40] propose to use full likelihood calculations in order to join CMB and LSS predictions. They use results from various independent CMB experiments together with the IRAS 1.2 Jy galaxy redshift survey and parametrise a set of spatially flat models. Because the CMB and LSS predictions are degenerate with respect to different parameters (roughly: Ω_m vs Ω_Λ for CMB; H_0 and Ω_m vs $b_{\rm iras}$ for LSS), the combined data likelihood analysis allows the authors to break these degeneracies, giving remarkable parameter

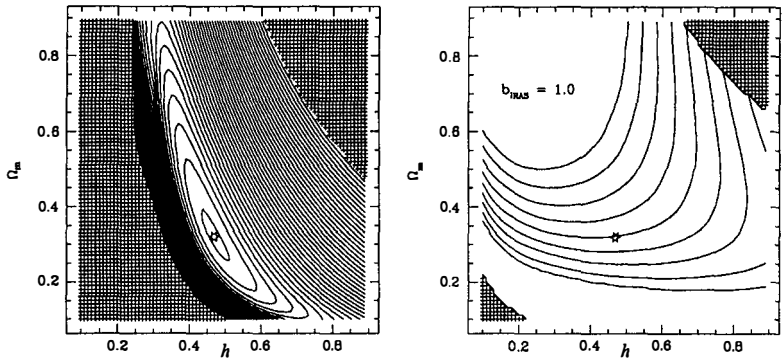

Figure 2: Plots on the (Ω_m,h) plane, where $h = H_0/100$ km s^{-1}. Left: Likelihood contours defining the optimum values for (Ω_m,h). Right: $b_{\rm iras}$ contours with corresponding optimal value for $b_{\rm iras} = 1$.

predictions. We note that Ω_m is the overall *matter* density. A preliminary result of the joint likelihood calculations is given in Figure 2 showing a well-defined peak for Ω_m and H_0, together with the corresponding optimal value for the IRAS light-to-mass bias ($b_{\rm iras}$).

The preliminary best fit results from the two data sets joint analysis on all the free parameters are [40] (marginalised error bars for 95% confidence): $\Omega_m = 0.32 \pm 0.08$, $\Omega_b = 0.061 \pm 0.013$, $H_0 = 47 \pm 6$ km s^{-1} Mpc^{-1}, $b_{\rm iras} = 1.04 \pm 0.06$ and $\sigma_8 = 0.78 \pm 0.1$, where Ω_b is the baryonic density and σ_8 is the variance measured in a 8 Mpc radius sphere.

6 Conclusion

Ground-based CMB experiments are already providing significant constraints on cosmological models, particularly the interferometers and future ground-based experiments, will sharpen these up considerably. Although full-sky high resolution satellite experiments like Planck Surveyor will eventually provide definite answers for the CMB, the ability of ground-based experiments to go deep on selected patches, and the controllability and accessibility of such experiments, mean that they will have a very important role for some years to come.

References

1. R.D. Davies, C.M. Gutiérrez, J. Hopkins, S.J. Melhuish, R.A. Watson, R.J. Hoyland, R. Rebolo, A.N. Lasenby and S. Hancock, MNRAS **278**, 883 (1996).
2. S. Hancock, R.D. Davies, A.N. Lasenby, C.M.G. Delacruz, R.A. Watson, R. Rebolo and J.E. Beckman, Nature **367**, 333 (1994).
3. S. Hancock, C.M. Gutiérrez, R.D. Davies, A.N. Lasenby, G. Rocha, R. Rebolo, R.A. Watson and M. Tegmark, MNRAS **289**, 505 (1997).
4. A.N. Lasenby, S. Hancock, R.D. Davies, C.M.G. Delacruz, R.A. Watson and R. Rebolo, A.L.& COMM **32**, 191 (1995)
5. C.H. Lineweaver, S. Hancock, G.F. Smoot, A.N. Lasenby, R.D. Davies, A.J. Banday, C.M.G. Delacruz, R.A. Watson and R. Rebolo, ApJ **448**, 482 (1995).
6. S. Hancock, A.N. Lasenby, C.M.G Delacruz, R.D. Davies, R.A. Watson and R. Rebolo, A.L.& COMM **32**, 201 (1995).
7. E.F. Bunn, Y. Hoffman and J. Silk, ApJ **464**, 1 (1996).

8. C.M. Gutierrez, S. Hancock, R.D. Davies, R. Rebolo, R.A. Watson, R.J. Hoyland, A.N. Lasenby and A.W. Jones, ApJ **480**, L83 (1997).
9. A.W. Jones, S. Hancock, A.N. Lasenby, R.D. Davies, C.M. Gutiérrez, G. Rocha, R.A. Watson and R. Rebolo, MNRAS **294**, 582 (1998).
10. C.G.T. Haslam, H. Stoffel, C.J. Salter and W.E. Wilson, A&A Supp. S. **47**, 1 (1982).
11. L. Piccirillo, Rev. Sci. Instr. **62**, 1293 (1991).
12. L. Piccirillo and P. Calisse, ApJ **411**, 529 (1993).
13. L. Piccirillo et al., ApJ **475**, L77 (1997).
14. B. Femenia, R. Rebolo, C.M. Gutiérrez, M. Limon and L. Piccirillo, ApJ, in press, astro-ph/9711225 (1998).
15. M. Dragovan, J.E. Ruhl, G. Novak, S.R. Platt, B. Crone, R. Pernic and J.B. Peterson, ApJ **427**, L67 (1994).
16. J.E. Ruhl, M. Dragovan, S.R. Platt, J. Kovac and G. Novak, ApJ **453**, L1 (1995).
17. S.R. Platt, J. Kovac, M. Dragovan, J.B. Peterson and J.E. Ruhl, ApJ **475**, L1 (1997).
18. J. Kovac, M. Dragovan and D.A. Schleuning, BAAS **191**, 112 (1997).
19. C.L. Bennett, A. Banday, K.M. Górski, G. Hinshaw, P. Jackson, P. Keegstra, A. Kogut, G.F. Smoot, D.T. Wilkinson and E.L. Wright, ApJ **464**, L1 (1996).
20. E.J. Wollack, N.C. Jaroski, C.B. Netterfield, L.A. Page and D. Wilkinson, ApJ **419**, L49 (1993).
21. E.J. Wollack, M.J. Devlin, N.C. Jaroski, C.B. Netterfield, L. Page and D. Wilkinson, Tech. Rep. Princ. Univ, 01/1996 (1996).
22. E.J. Wollack, M.J. Devlin, N.C. Jaroski, C.B. Netterfield, L. Page and D. Wilkinson, ApJ **476**, 440 (1997).
23. C.B. Netterfield, M.J. Devlin, N.C. Jaroski, L. Page and E.J. Wollack, ApJ **474**, 47 (1997).
24. M. Tegmark, A. Oliveirà-Costa, M.J. Devlin, C.B. Netterfield, L. Page and E.J Wollack, ApJ **474**, L77 (1997).
25. A. Oliveira-Costa, A. Kogut, M.J. Devlin, C.B. Netterfield, L. Page and E.J. Wollack, ApJ **482**, L17 (1997).
26. T. Herbig, http://tyger.princeton.edu/~th/mat/mat.html
27. A.C.S. Readhead, C.R. Lawrence, S.T. Myers, W.L.W. Sargent, H.E. Hardebeck and A.T. Moffet, ApJ **346**, 566 (1989).
28. S.T. Myers, A.C.S. Readhead and C.R. Lawrence, ApJ **405**, 8 (1993).
29. E.M. Leitch, A.C.S. Readhead, T.J. Pearson and S.T Myers, ApJ **486**, L23 (1997).
30. P.F. Scott, R. Saunders, G. Pooley, C. Osullivan, A.N. Lasenby, M. Jones, M.P. Hobson, P.J. Duffettsmith and J. Baker, ApJ **461**, L1 (1996).
31. M.E. Jones, in *Microwave Background Anisotropies (1996)*, F.R. Bouchet, R. Gispert, B. Guiderdoni and J. Tran Thanh Van, editors, Editions Frontières, Paris (1997).
32. T.J. Pearson, http://astro.caltech.edu/~tjp/CBI/
33. M. White, J.E. Carlstrom and M. Dragovan, Submitted to ApJ, astro-ph/9712195 (1997).
34. A.A. Stark, J.E. Carlstrom, F.P. Israel, K.M. Menten, J.B. Peterson, T.G. Phillips, G. Sironi and C.K. Walker, pre-print, astro-ph/9802326 (1998).
35. S. Hancock, G. Rocha, A.N. Lasenby and C.M. Gutiérrez, MNRAS **294**, L1 (1998).
36. C.H Lineweaver, D. Barbosa, A. Blanchard and J.G. Bartlett, A&A **322**, 365 (1997).
37. J.A. Willick, M.A. Strauss, A. Dekel and T. Kolatt, ApJ **486**, 629 (1997).
38. K.B. Fisher and A. Nusser, MNRAS **279**, L1 (1996).
39. A.F. Heavens and A.N. Taylor, MNRAS **275**, 483 (1995).
40. M. Webster, M.P. Hobson, A.N. Lasenby, O. Lahav and G. Rocha, ApJ.L, in press, astro-ph/9802109 (1998).

DETECTION OF CMB ANISOTROPIES IN A SECOND FIELD WITH CAT

JOANNE BAKER
Mullard Radio Astronomy Observatory, Cavendish Laboratory,
Madingley Road, Cambridge CB3 0HE, UK

The Cambridge Cosmic Anisotropy Telescope (CAT) has been used to image a $2^\circ \times 2^\circ$ region of sky at frequencies near 15 GHz; this is the second such region to be imaged with CAT. After removal of discrete foreground radio sources, structure is detected in the images on scales of about half a degree. A Bayesian analysis finds that the fluctuations are consistent with arising mostly in the cosmic microwave background (CMB) radiation. The average power in CMB fluctuations is estimated to be $\Delta T/T = 2.1^{+0.4}_{-0.5} \times 10^{-5}$ for scales corresponding to an average spherical harmonic multipole of $l = 422$. Due to possible Galactic contamination, an upper limit of $\Delta T/T < 2.0 \times 10^{-5}$ in CMB power is given for a bin with centroid $l = 615$. New limits, with the inclusion of the latest CAT2 data, on the values of H_0 and Ω are determined.

1 Introduction

Observations of spatial fluctuations in the cosmic microwave background (CMB) radiation are fundamental to our understanding of structure formation. The Cosmic Anisotropy Telescope (CAT), a three-element interferometer operating at frequencies around 15 GHz, probes these fluctuations on angular scales of about half a degree. CAT was the first experiment to produce images of the CMB sky at this high resolution. Observations on half-degree scales are critical for determining the angular scale of the first acoustic peak[1], and thus provide powerful constraints on basic cosmological parameters including H_0 and Ω.

This contribution describes the observations with CAT of a $2^\circ \times 2^\circ$ area of sky, the second such field observed with CAT. Detection of CMB fluctuations in the first CAT field was described by Scott et al. [2] (Paper I). The cosmological implications of the two CAT detections are examined briefly.

2 Observations of the CAT2 Field

Observations have been made of a field centred at the position 17 00 00 +64 30 00 (B1950), which we call 'CAT2'. To minimise the effects of foreground contamination, the field was chosen to be relatively free from strong radio sources at frequencies up to 5 GHz[3] lie at high Galactic latitude ($b > 30°$) and away from known Galactic features (e.g. the N. Galactic spur).

In periods during 1995 March – 1997 June, the CAT2 field was observed with CAT at three frequencies, 13.5, 15.5 and 16.5 GHz, in arrays with baselines scaled with frequency. The resulting synthesised beams have a FWHM of 22′. Amplitude and phase calibration was carried out daily with observations of Cas A — uncertainties in flux scaling are less than 10%.

The CAT2 data were reduced in the same manner described for the first field[4] and analysed using standard AIPS tasks. Excessively noisy data (reflecting periods of poor weather) were excluded completely from the analysis, as were individual visibilities whose amplitudes exceeded the mean by more than 3σ. In total, about 40% of the data were excluded by these criteria, leaving 370, 310 and 1340 hours of good data at 13.5, 15.5 and 16.5 GHz respectively.

3 Source Subtraction

Radio sources contributing significant flux to the CAT2 image were identified and subsequently monitored at 15 GHz using the Ryle Telescope (RT). The RT has much higher resolution than CAT — its synthesised beam FWHM for this kind of observation is about 30″. The CAT2 field was scanned with the RT in raster mode yielding 29 sources with flux densities greater than 4.5 mJy (i.e. 3σ) at 15 GHz in the central 2°×2°. Flux densities at 13.5 and 16.5 GHz were extrapolated using spectral information obtained from lower frequency (i.e. 5 GHz and 1.4 GHz) surveys. After scaling the source flux densities by the position-dependent primary beam attenuation factor, the corresponding flux densities were subtracted as point sources from the raw visibility data. Totals of 33 mJy at 13.5, 27 mJy at 15.5 and 20 mJy at 16.5 GHz were subtracted.

The resulting source-subtracted images each show excess signal in the central 2°×2°, falling away at larger radii as expected from the antenna envelope beam. At the three frequencies, excess powers above the intrinsic noise level in the central 2°×2° area of 7.8 ± 1.0, 8.2 ± 1.0 and 8.3 ± 0.5 mJy/beam rms were found for the source-subtracted 13.5, 15.5 and 16.5 GHz images respectively. No excess signal remains when data in the two orthogonal polarisations are subtracted from one another, confirming the astronomical origin of the structures.

The 16.5-GHz image is shown in Figure 1; note the instrumental response has not been removed. The structures in the image are generally of low significance, except for a strong negative feature centred at position 17 05 48 +64 49 30 (B1950) reaching −40 mJy (i.e. 5σ). This feature can be seen in the images at all three frequencies (both before and after source subtraction), and in different time cuts, and its spectrum is consistent with that of CMB radiation. The presence of a 5σ dip in the CAT2 image does not in itself provide strong enough evidence for non-Gaussianity of the CMB fluctuations — observations of more fields would be needed to measure the probability of seeing such a feature. On the scales sampled by CAT, it is unlikely that the 5σ dip is caused by a Sunyaev-Zel'dovich (S–Z) effect towards a single massive cluster, as no known clusters lie in this direction on the sky. Any cluster which might produce such an effect would have to be nearby (subtending a large angle on the sky, filling the CAT beam) and/or very massive to produce such a strong signature. The strongest S–Z decrements measured towards nearby clusters at 15 GHz with the RT are about −1mJy on arcminute scales, which would increase to about −20mJy or so once integrated over an extended mass distribution with the CAT resolution of about 10′. A central portion of the CAT2 field has been observed with ROSAT and no X-ray emission (as would be expected to arise in a massive cluster) is seen

in the direction of the negative feature, although it lies close to the edge of the PSPC field. However, we note that two $z \approx 0.2$ X-ray-detected clusters lie in the central 10′ of the CAT2 field [5] — neither is apparent in the CAT images. Also, no obvious Galactic structures at this position were visible in IRAS 100μm or H I maps.

4 Determination of the CMB Component

Due to the limited range of baselines and resulting sparse sampling of the $u-v$ plane by CAT, a statistical likelihood analysis of the raw data was employed to estimate the relative contributions of CMB and Galactic components given the spectral information. A Bayesian likelihood method was used, as in Paper I, as described by Hobson, Lasenby and Jones [6]. This method uses the complex visibility data directly in the calculation of the likelihood function to avoid artifacts generated by Fourier transforming the data to make a map.

As described in Paper I, power was estimated in two independent annular bins centred on spherical harmonic multipole values of $l = 410$ and $l = 590$ and with widths equivalent to the diameter of the antenna function, thus together spanning the range $l \approx 330 - 680$. The noise-weighted centroid positions for data in each bin are $l = 422$ and $l = 615$. CMB and Galactic signals were modelled as independent Gaussian distributions with a power-law spectrum ($S \propto \nu^{\alpha}$), the CMB with a fixed spectral index of +2 in flux density and the Galactic spectral index variable between 0 and -1 (as expected for Galactic free-free and synchrotron emission).

After marginalising over the Galactic parameters, this analysis confirmed that the bulk of power in the 16.5 GHz map (Fig. 1) arises from CMB fluctuations. The CMB component was clearly distinguished in the Bayesian analysis from possible Galactic contamination in the $l = 422$ bin: $\Delta T/T = 2.1^{+0.4}_{-0.5} \times 10^{-5}$ was estimated for the CMB signal, compared with only $\Delta T/T = 0.8^{+0.5}_{-0.8} \times 10^{-5}$ for any Galactic component. The uncertainties quoted are 1σ values. The CMB–Galaxy separation was less certain in the $l = 615$ bin — a Galactic contribution of $\Delta T/T = 1.0^{+0.7}_{-1.0} \times 10^{-5}$ was given by the likelihood analysis, which is equivalent to an upper limit for the marginalised CMB power of $\Delta T/T < 2.0 \times 10^{-5}$ (1σ) in the $l = 615$ bin.

5 Cosmological Implications

The average values of $\Delta T/T$ in the CAT2 field are within the 1σ limits quoted for the CAT1 result, reinforcing the apparent turndown in CMB power on scales less than $\sim 1^{\circ}$ seen with CAT1.

To estimate the constraints on various cosmological parameters imposed by the new CAT data, we compared a range of models (satisfying Big Bang nucleosynthesis constraints) with the latest data from all CMB experiments over scales 10° to 10′ (G. Rocha 1998, private communication) using the method of Rocha & Hancock [7]. To summarise, the marginalised probability distributions obtained by varying all parameters (including Λ and n) favoured $0.4 < \Omega_{\Lambda} < 0.7$ and $30 < H_0 < 55$ (1σ ranges). If $\Lambda = 0$ and $n = 1$ are specified, then the marginalised probability distributions change little, i.e. $0.5 < \Omega_0 < 1.0$ and $30 < H_0 < 70$. The model-fitting procedures and results will be described in full elsewhere.

6 Conclusions

We have imaged a 2°×2° patch of CMB sky at 13-17 GHz with the CAT; this is the second field observed by CAT. Significant anisotropies are detected in the CAT2 field with an average power of $\Delta T/T = 2.1^{+0.4}_{-0.5} \times 10^{-5}$ for the $l = 422$ bin, and $\Delta T/T < 2.0 \times 10^{-5}$ for $l = 615$ (Galactic contamination). This new result agrees remarkably well with the first detection made by CAT

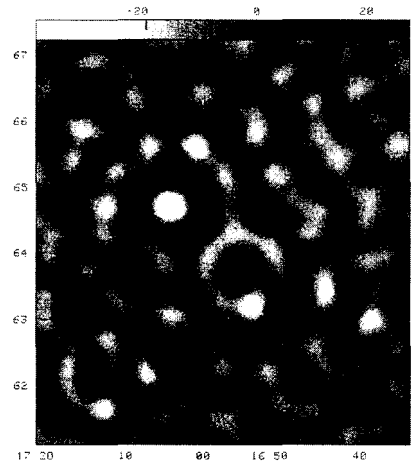

Figure 1: CAT2 image at 16.5 GHz after discrete radio sources have been subtracted. Note that the instrumental response has not been deconvolved. The primary beam of CAT has FWHM of 2°. RA and Dec (B1950) are labelled; the greyscale is marked (mJy/bm).

in a completely different area of sky. Together with other CMB data over a range of angular scales, the inclusion of the CAT2 detection restricts the likely range of cosmological parameters $0.4 < \Omega_0 < 1.0$ and $30 < H_0 < 70$.

Acknowledgments

Graca Rocha carried out the cosmological modelling including the new CAT2 data. Many people at MRAO are involved with CAT: Mike Hobson, Mike Jones, Anthony Lasenby, Guy Pooley, Richard Saunders, Paul Scott, Liz Waldram and others. Financial support for CAT from PPARC is gratefully acknowledged.

References

1. Hancock S. & Rocha G., 1996, in *Microwave background anisotropies*, eds F. Bouchet et al., Procs 31st Rencontre de Moriond, (Editions Frontiers), p179
2. Scott P.F. et al., 1996, ApJL, 461, L1
3. Condon J.J., Broderick J.J. & Seielstad G.A., 1989, AJ, 97, 1064
4. O'Sullivan C. et al., 1995, MNRAS, 274, 861
5. Vikhlinin A. et al., 1998, ApJ, in press (astro-ph/9803099)
6. Hobson M.P., Lasenby A.N. & Jones M.E., 1995, MNRAS, 275, 863
7. Rocha G. & Hancock S., 1996, in *Microwave background anisotropies*, eds F. Bouchet et al., Procs 31st Rencontre de Moriond, (Editions Frontiers), p189

THE VERY SMALL ARRAY: STATUS REPORT

Michael. E. JONES & P. F. SCOTT
Cavendish Laboratory, Madingley Road, Cambridge CB3 0HE, UK.

We are contructing an interferometric telescope, the Very Small Array, to study the cosmic microwave background on angular scales 0.2–4.5°. The physical layout and electronic design of the telescope are optimised to give maximum protection from systematic effects, while still providing sufficient sensitivity to make high signal-to-noise images. A prototype single baseline is currently being tested, with scientific results expected during 2000.

1 Introduction

It is widely accepted that the majority of the cosmological results that might be obtained from the cosmic microwave background (CMB) will come from accurate measurements of the CMB power spectrum over the region of the accoustic peaks, that is in the range $100 < l < 2000$ (where l is the spherical harmonic multipole). We have therefore been constructing an instrument, the Very Small Array (VSA), to measure the power spectrum (and provide images) in precisely this angular range. We have argued previously[1] that interferometers are very well suited for ground-based CMB measurements, given their relative immunity to the atmosphere and other systematic effects compared with switched-beam experiments. Here we will describe some of the more detailed design considerations of the array, and review the progress of the project so far.

2 The VSA—vital statistics

The VSA will consist of an array of 14 antennas, operating in the 26–36 GHz band. The size of the antennas is determined by the largest angular scale we wish to observe: $l = 100$ corresponds to an angular scale of 3°.6, or an interferometer baseline of 16 wavelengths. Our antennas have a clear aperture of 143 mm, ie about 15 wavelengths in the centre of the band. The number of antennas is fixed simply by the cost and complexity of the whole telescope—the more simultaneous baselines present, the better. In order to measure the smallest angular

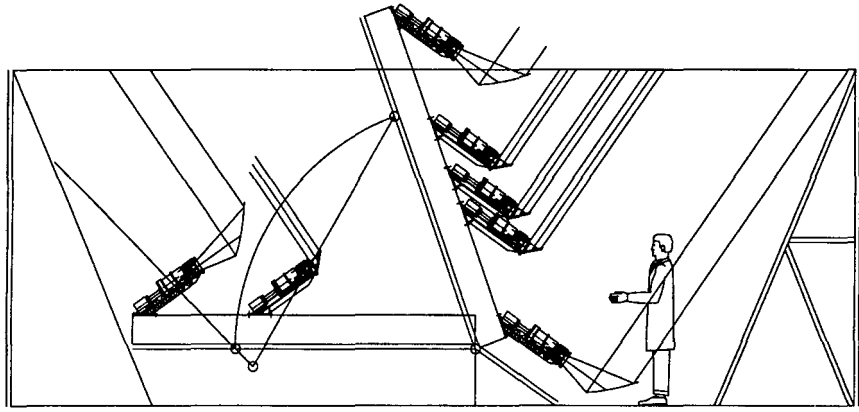

Figure 1: Sketch of VSA layout showing both large and small antennas, and the two extreme positions of the tip-table.

scales ($l = 2000$ corresponds to a baseline of 320λ) without compromising the fraction of the synthesised aperture that is filled, we will also use alternative antennas about 2.25 time larger.

Using the best available front-end amplifiers (a design kindly supplied by NRAO), an observing bandwidth of 1.5 GHz (limited by bandwidth smearing), and a site with good transparency and stability at 30 GHz (Teide Observatory, Tenerife), we should obtain maps with 7 μK sensitivity per 30′ (12′) pixel over a 4°.5 (2°) field in 300 hours observation, using the smaller (larger) antennas.

3 Design considerations

3.1 Tracking arrangement

One of the main advantages of interferometers is *fringe rotation.* That is, because the rotation of the earth constantly changes the relative path from the source to each antenna, the complex visibility due to the source is phase modulated at a rate that depends on the baseline vector and the direction to the source. Synchronous detection at this frequency results in all spurious signals, due to eg crosstalk, atmospheric emission, or bright sources in far sidelobes, being attenuated by factors which can be very large (easily 25 dB). However, this is only true if the antennas are mounted so that the relative path does change, e.g. if the antennas are fixed to the ground and track individually.

A conflicting requirement is that the antennas be very closely packed. The sensitivity of a synthesised aperture is degraded compared to a single aperture with the same beam by the fraction of the aperture that is filled. For an array of N antennas of size d, aperture efficiency η and maximum baseline D, this factor is roughly $f = \eta N(D/d)^2$. It is much easier to pack antennas very closely if they do not move relative to each other.

We therefore need a design in which the antennas can be packed closely in two dimensions, yet have a large change of relative path as they track. They must also, of course, have excellent sidelobe performance (the Sun is about 90 dB more powerful than the final noise level) and be free from crosstalk.

The design we have selected (Fig. 1) achieves these goals by using the the conical horn-reflector antenna (CHRA) design[2] already used successfully on the Cosmic Anisotropy Telescope[3], with a modified mounting arrangement. The antennas are mounted on a table, with the horn

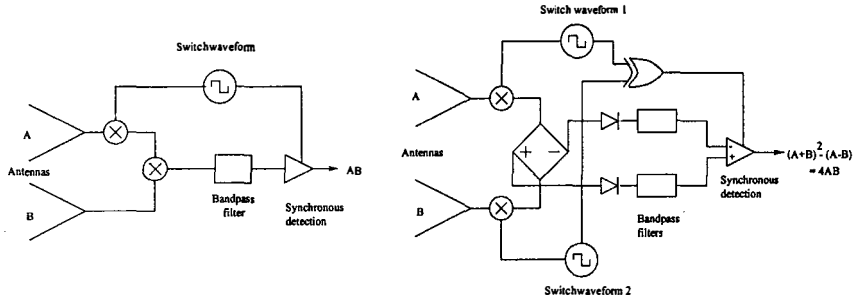

Figure 2: (Left) Simple multiplying interferometer. (Right) Plus-minus correlator as used in the VSA. This is insensitive gain fluctuations in either input.

axis in a vertical N-S plane. Tracking in the E-W direction is obtained by rotating the mirror about the optic axis of the horn; in the N-S direction, by tipping the table about a horizontal E-W axis. Restricting the E-W tracking range of the mirror to $\pm 35°$ allows E-W packing of the antennas as close as 1.3 aperture diameters. The antennas are mounted on the table with the horn axis at 35° to the table top; this allows arbitrarily close packing of the antennas in the N-S direction. Tipping the table by up to 70° achieves a zenith angle coverage of $\pm 35°$ in the N-S direction. Most of the tracking motion is individual to the antennas, with only a small motion of the table (none when observing at the celestial equator). This results in a fringe rate almost as high as for a fully individually-mounted array.

The antennas themselves have sidelobe levels of better than -50 dB at angles $> 30°$ from the main beam, thanks to careful control of the boundary conditions (using corrugations) at the edges of the diffracting aperture. When combined with the shadowing effect of the table and interferometer effects (fringe rotation and bandwidth smearing) this should allow daytime operation for all but very close directions to the Sun.

3.2 Correlator design

The correlator has to be free from systematics, and insensitive to influences such as receiver gain instability. A digital corelator is out of the question, given the bandwidth required (> 1 GHz). A simple analogue multiplier, such as a double-balanced mixer, is sensitive to gain fluctuations in either input. The design we are using, which was also used in the CAT, is based on Ryle's phase-switching correlator[4]. In Ryle's original design, the signal from one antenna has a 180°-phase switch inserted, and the signals from the two antennas are then added. The power of the sum signal is then detected, and the component at the phase-switch freqency amplified. After integration, only a term proportional to the product of the two signals remains, and it is relatively insensitive to gain variations in either side.

In the VSA correlator (Fig. 2), both the sum and difference are squared, and their difference taken, before detection at the switch frequency. This directly removes fluctuations in the total power of each antenna, providing a further protection against low-frequency noise due to the receivers or the atmosphere.

This correlator design has excellent performance, but is expensive and bulky, especially given that we further protect against systematics by housing each correlator unit in a separate earthed box. This means that we can only afford to build one frequency channel. However, we need to observe at more than one frequency in order to separate the CMB signal from the Galactic signal. In making such spectral-index observations, it is a great advantage to have well-matched aperture-plane coverage at each frequency. By observing sequentially at each frequency, we can

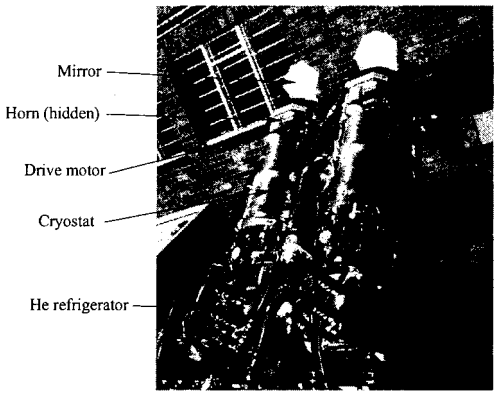

Figure 3: Two prototype VSA antennas under test.

re-scale the array each time to provide identical aperture-plane coverage. This would not be possible with simultaneous observation in widely-spaced observing bands.

4 Project status

The project was given funding in July 1996, and at the time of writing (March 1998), two complete antennas, with all their associated backend and correlator, have been built and are being tested (Fig. 3). Assembly of the complete telescope (in Cambridge) will proceed during 1998, and it is hoped to ship the array to Tenerife during 1999, with science observations beginning shortly thereafter.

Acknowledgments

The VSA is a collaborative project between the Cavendish Laboratory (Cambridge University), the Nuffield Radio Astronomy Laboratories (Manchester University), and the Instituto de Astrofisica de Canarias; many people at all three institutions are responsible for the work described here. The VSA is funded by the Particle Physics and Astronomy Research Council.

References

1. Jones M.E., in *Microwave Background Anisotropies*, ed. Bouchet F.R., Gispert R., Guideroni B., Tran Thanh Van J., (Editions Fronteires, 1997).
2. Yassin G., Robson M. Duffet-Smith P.J., IEEE Trans. Antenn. Prop. **41**, 357 (1993).
3. Robson M., Yassin G., Woan G., Wilson D.M.A., Scott P.F., Lasenby A.N., Kenderdine S., Duffet-Smith P.J., A&A **277**, 314 (1993)
4. Ryle M., Proc. Roy. Soc. A. **211**, 351 (1952)

TOPOLOGICAL ANALYSIS OF HIGH–RESOLUTION CMB MAPS [a]

B.D. WANDELT, E. HIVON, K.M. GORSKI,
Theoretical Astrophysics Centre (TAC), Juliane Maries Vej 30,
2100 Copenhagen Ø, Denmark

We report the development of numerical tools for the topological analysis of sub–degree resolution, all–sky maps. Software to be released in the HEALFAST (V0.9) package defines neighbour relationships for the HEALPIX tessellation of the sphere. We apply this routine to a fast extrema search which scales strictly linearly in the number of pixels, N_p. We also present a highly efficient algorithm for simulating the gradient vector and curvature tensor fields "on–the–fly" with the temperature map, needing only of order $N_p \log_2 N_p$ more operations.

1 Introduction

The Microwave Anisotropy Probe (MAP) and the Planck Surveyor satellite missions promise to produce high–resolution full sky maps of the Cosmic Microwave Background (CMB) within the next decade. These maps will contain a great deal of cosmologically relevant information and therefore present a tremendous opportunity for doing high–precision cosmology. Owing to the unprecedented wealth of data, this opportunity brings with it the challenge of developing tools which help extract this information in manageable processing time.

Much attention has been given to the problem of estimating the angular power–spectrum of CMB anisotropies. To illustrate the difficulties one is facing, we note that even choosing the fastest presently available algorithm and allowing for parallelisation and technological advance, the estimation of the angular power–spectrum C_l of CMB anisotropies will take $\gtrsim 6$ years [1] for future million pixel maps.

While the C_l spectrum is the statistic of choice for a large class of cosmological models where the primordial fluctuations are Gaussian distributed, the possibility remains that another physical mechanism produced structure in the universe. In this case the CMB maps will almost certainly be non–Gaussian and contain more information than merely the power on different angular scales. Failing this, non–linear gravitational effects and foregrounds will produce detectable non–Gaussian signals.

Even for Gaussian maps, it has been shown that extrema statistics capture information about cosmological parameters and their theory is well developed [2,3,4,5]. The importance of studying these and other topological properties of CMB temperature and polarisation has been noted by

[a] Full size, full colour images can be downloaded from *http://www.tac.dk/~wandelt*

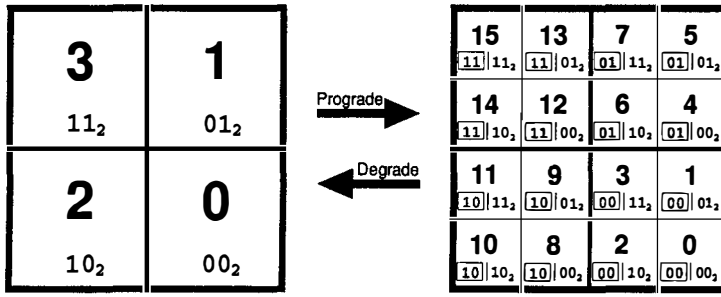

Figure 1: Quadtree pixel numbering. The coarsely pixelised coordinate patch on the left consists of four pixels. Two bits suffice to label the pixels. To increase the resolution, every pixel splits into 4 daughter pixels shown on the right. These daughters inherit the pixel number of their parent (boxed) and acquire two new bits to give the new pixel number. Several such coordinate patches are joined at the boundaries to cover the sphere. All pixels carry a prefix (here omitted for clarity) which identifies which patch they belong to.

several authors [6]. Extrema have the advantage that they dominate the noise and are therefore very robust. As a consequence they have been among the first scientific results reported from recent CMB observations (one of them even at this conference [7]!).

The aim of this talk is to present tools which allow the implementation of a wide range of data analysis and processing techniques on the sphere.

2 Tools

2.1 Neighbour relationships on the sphere

Finding neighbours of a given pixel is essential for performing many local operations on digitised data, such as finding extrema, saddle points and zero crossings, finite differencing, extraction of patches, real-space filtering *etc.* While next-neighbour relationships are trivially defined on a lattice in the plane, on the sphere it is necessary to match distinct coordinate patches. Further, in a spherical topology the number of next-neighbours is not the same for all pixels.

We base our methods on the HEALPIX tessellation of the sphere [8]. However, even when a pixelisation of the sphere is given, we must still decide how to number the pixels. We choose the hierarchical, quadtree numbering scheme illustrated in Figure 1. This scheme is well-known and was used for the COBE pixelisation. Its main advantages for finding next-neighbours are that

- a neighbour can be found by direct operation on the binary representation of the pixel number which is computationally very cheap (finding all next-neighbours of 12×10^6 pixels takes less than 10 seconds [b]);
- the algorithm is manifestly resolution independent owing to the self-similarity of the numbering scheme;
- once an algorithm exists that finds next-neighbours, it can easily be extended to find a whole neighbourhood of a pixel by first degrading, then finding next-neighbours and then prograding.

A disadvantage is that in its implementation the boundary matching of coordinate patches has to be customised for the chosen pixelisation scheme. But even here the symmetries of the

[b] All timings are "wall clock" for a single SGI R10000 194MHz processor.

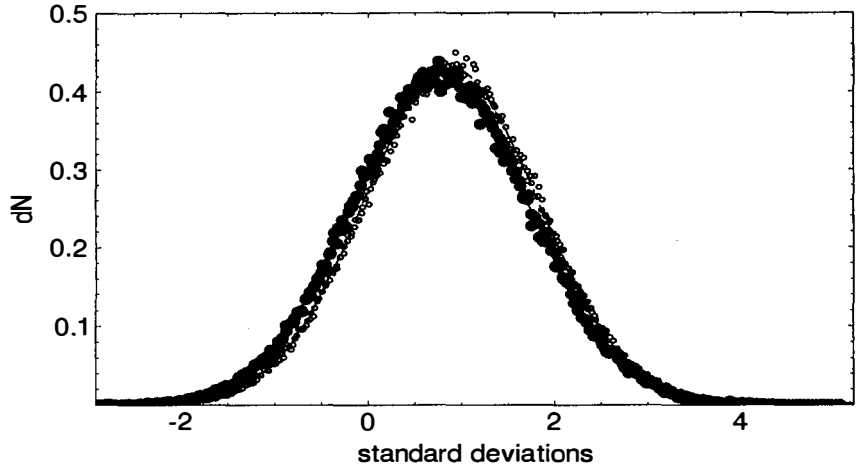

Figure 2: Probability density for finding a maximum (minimum) above (below) a certain excursion level. The minima distributions have been flipped over to coincide with the maxima distributions. Open dots are found from one realization of an $\Omega = .2$ map, filled dots are for standard CDM. Lines show the theoretically expected distributions (solid: SCDM, dashed: OCDM).

quadtree are useful. For example, if two patches like the one on the right of Figure 1 were joined side by side, neighbours of pixels at the joining edge can be found by inverting all even bits of their pixel number, *e.g.*, $4 = \underline{0}1\underline{0}0_2 \leftrightarrow 14 = \underline{1}1\underline{1}0_2$. This and analogous prescriptions generalise to arbitrary resolution.

As an example application, we show in Figure 2 the theoretical prediction and our numerical results for an extrema search in a "standard" CDM and an open model with $\Omega = 0.2$ ($H_0 = 50$km/s/Mpc, $\Omega_b = 0.05$ for both, $\theta_{FWHM} = 10'$ and zero noise). While it is clear that these probability distributions contain much less information than the anisotropy spectrum (they form a 3 parameter family if the total number of pixels is counted), the distributions shown clearly distinguish the two models. We stress that this is a realistic situation, since we used data only from one map.

This example do not even begin to explore the possibilities of these methods. By just measuring the probability distribution of excursion of an extremum from the mean, we are throwing away valuable scale and phase information. A more careful analysis will reveal more about the specific advantages of topological analyses of CMB maps.

2.2 Map simulation and computation of derivative fields

The derivative fields of a map are important for the study of the properties of its stationary points. A Fast Spherical Harmonics Transform code exists for the synthesis of Gaussian HEALPIX temperature maps with a given C_l spectrum [9]. A priori, generating the derivative fields would take just as long for each component as the map generation itself. The time limiting factor for map generation is the calculation of the associated Legendre polynomials $P_l^m(\cos\theta)$ for each ring of constant co–latitude θ. We exploit this fact by calculating the derivative fields at the same time as the temperature map and exploiting the following differential relations:

$$\begin{aligned} \frac{\partial}{\partial\phi}Y_{lm}(\theta,\phi) &= imY_{lm}(\theta,\phi) \\ \frac{\partial}{\partial\theta}Y_{lm}(\theta,\phi) &= -m\cot\theta Y_{lm}(\theta,\phi) - \sqrt{l(l+1)-m(m-1)}Y_{lm-1}(\theta,\phi)e^{i\phi} \\ \frac{\partial^2}{\partial\theta^2}Y_{lm}(\theta,\phi) &= -\left(\left[l(l+1)-\frac{m^2}{\sin^2\theta}\right]+\cot\theta\frac{\partial}{\partial\theta}\right)Y_{lm}(\theta,\phi) \end{aligned} \qquad (1)$$

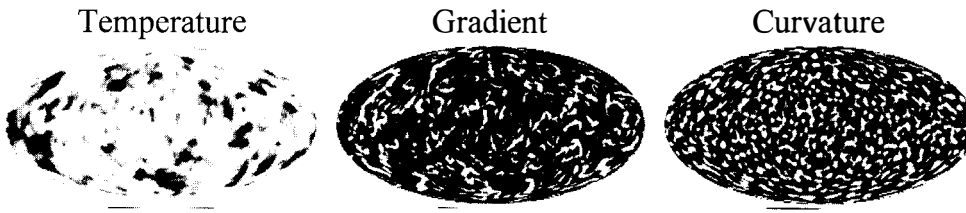

Figure 3: From left to right: the temperature, the square of the gradient vector and the trace of the curvature tensor for a standard CDM sky smoothed at 5 degrees for easier visualisation.

In this way, only five more Fast Fourier Transforms have to be computed for each ring on the sphere, with the total added cost scaling as $N_p \log_2 N_p$. For a map with $N_p = 12.6 \times 10^6$ pixels, this amounts to an added 15 minutes of wall clock computation time for all five derivative components compared with 20 minutes for the temperature alone. In Figure 3 we display temperature anisotropies, the square norm of the gradient vector $|\nabla_i T|^2 = \frac{1}{sin^2\theta}(\frac{\partial}{\partial\phi}T)^2 + (\frac{\partial}{\partial\theta}T)^2$ and the trace of the curvature tensor $\mathrm{Tr}(\lambda_{ij}) = \frac{1}{sin^2\theta}\frac{\partial^2}{\partial\phi^2}T + \frac{\partial^2}{\partial\theta^2}T$, for the standard CDM model.

3 Conclusions

In this talk we presented tools which are generally applicable for the analysis of topological properties of maps on the sphere such as the detection of extrema, saddle points and zero crossings of a function, even though they can be used more generally for any kind of local analysis of spherical data sets. The computational time required for all sky computations scales strictly as the number of pixels in the map, N_p. Further, we extend existing simulation tools for Gaussian fields to generate not only temperature maps but also the associated gradient vector and the curvature tensor fields, with the extra computational cost scaling as $N_p \log_2 N_p$.

Acknowledgments

This work was supported by Dansk Grundforskningsfond through its funding for TAC.

References

1. J. Borrill, preprint, astro-ph/9712121.
2. M. Sazhin, *M.N.R.A.S.* **216**, 25P (1985).
3. J.R. Bond and G. Efstathiou, *M.N.R.A.S.* **226**, 655 (1987).
4. N. Vittorio and R. Juszkiewicz, *Ap. J.* **314**, L29 (1987).
5. R.B. Barreiro *et al.*, *Ap. J.* **478**, 1 (1997).
6. M. Sazhin and Toporenskii *Astr. Lett.* **22**, 791 (1996); P. Arbuzov *et al.*, Int. J. Mod. Phys. D **6**, 409 (1997); P. Arbuzov *et al.*, Int. J. Mod. Phys. D **6**, 515 (1997); P.D. Naselsky and D.I. Novikov, preprint, astro-ph/9801285.
7. J. Baker, in this volume.
8. K.M. Gorski, in preparation.
9. E. Hivon and K.M. Gorski, in preparation.

The effect of point sources on satellite observations of the CMB

M.P. Hobson[1], R.B. Barreiro[2,3], L. Toffolatti[4,5], A.N. Lasenby[1], J.L. Sanz[2], A.W. Jones[1] and F.R. Bouchet[6]

[1] *MRAO, Cavendish Laboratory, Madingley Road, Cambridge CB3 0HE, UK*
[2] *Instituto de Física de Cantabria (CSIC-UC), Av. de Los Castros s/n, 39005 Santander, SPAIN*
[3] *Dep. de Física Moderna, Universidad de Cantabria, Av. de Los Castros s/n, 39005 Santander, SPAIN*
[4] *Osservatorio Astronomico, Vicolo dell'Osservatorio 5, 35122 Padova, ITALY*
[5] *Dep. de Física, Universidad de Oviedo, Av. Calvo Sotelo s/n, 33007 Oviedo, SPAIN*
[6] *Institut d'Astrophysique de Paris, 98 bis Boulevard Arago, 75014 Paris, FRANCE*

We study the effect of extragalactic point sources on future satellite observations of the cosmic microwave background (CMB). In order to separate the contributions due to different foreground components, a maximum-entropy method is applied to simulated observations by the Planck Surveyor satellite. In addition to point sources, the simulations include emission from the CMB and the kinetic and thermal Sunyaev-Zel'dovich (SZ) effects from galaxy clusters, as well as Galactic dust, free-free and synchrotron emission. We find that the main input components are faithfully recovered and, in particular, that the quality of the CMB reconstruction is only slightly reduced by the presence of point sources.

1 Introduction

The maps produced by the MAP and Planck Surveyor satellites will contain contributions from the CMB and various foreground components, most notably Galactic dust, free-free and synchrotron emission, as well as the kinetic and thermal SZ effects from galaxy clusters. In addition to these six main components, significant contamination from extragalatic points sources is also expected. It is therefore clear that in order to obtain maps of the CMB anisotropies alone, it is necessary to separate the emission due to these various components.

In a previous paper, Hobson et al. (1998a, hereafter HJLB) use a non-linear maximum-entropy method (MEM) to separate the emission due to the six different components listed above from simulated Planck Surveyor observations of a 10×10-degree field (see Bouchet et al. 1997; Gispert & Bouchet 1997). It was found that faithful reconstructions may be produced not

only of the CMB anisotropies but also the kinetic and thermal SZ effects from massive clusters and the Galactic components. The analysis presented in HJLB does not, however, include the effect of extragalactic point sources, since no reliable simulations were available at that time.

Here we apply a generalised version of the MEM separation algorithm to simulated Planck Surveyor observations that also include a population of point sources. The simulated maps of the point sources used were created for each Planck Surveyor observing frequency using the updated number counts in each frequency band predicted by Toffolatti et al. (1997). These predictions are based on the Danese et al. (1987) model for the evolution of radio selected sources (adopting an average spectral index $\alpha = 0$ for compact sources up to $\simeq$200 GHz and a break to $\alpha = 0.7$ at higher frequencies) and on the model C of Franceschini et al. (1994), updated by Burigana et al. (1997) to account for the isotropic sub-mm component estimated by Puget et al. (1996). The point source map at each frequency has been produced by Poisson distributing all the sources in the $10^{-5} < S(\nu) < 10$ Jy flux range. Unless sources are identified and subtracted down to faint flux limits, the contribution of clustered sources to the CMB anisotropies is generally found to be small in comparison with the Poisson term. As discussed by Toffolatti et al. (1997), far-IR selected sources should dominate the number counts of bright objects at frequencies $\nu > 300$ GHz, whereas radio selected sources should dominate at lower frequencies. The two underlying parent populations are largely different and uncorrelated, consisting of normal spirals and starburst galaxies in the far-IR and mostly compact AGN, blazars and quasars in the radio.

In our approach, we do not remove any contaminated pixels from the simulated data. Instead we consider the point sources as an additional contribution to the 'noise' and allow the generalised MEM algorithm to reconstruct the CMB and foreground emission in the presence of these sources. The method for addressing the effect of point sources within the existing MEM formalism is given in Hobson et al. (1998b), together with a full description of the results.

2 Analysis of simulated observations

Clearly, the quality of the reconstructions will depend on our prior knowledge of the input components. Following HJLB, we assume that the spectral behaviour of the components is accurately known, but we consider two extreme cases relating to our knowledge of the power spectra of the input components and the confusion noise due to point sources.

2.1 Reconstructions with full power spectrum information

As our first case, we assume knowledge of the azimuthally-averaged power spectra of all six main input components, together with the azimuthally-averaged cross power spectra between these components. We also assume that the noise covariance matrix is fully specified as follows. In addition to the (diagonal) part of the noise matrix due to the instrumental noise, we calculate an empirical estimate of the contribution (to the diagonal and off-diagonal elements) of the point sources. This estimate is calculated directly from 10 independent realisations of the point source maps at each of the 10 Planck frequency channels.

We find that the main input components are faithfully reconstructed, except for a few contaminated pixels containing the brightest point sources. Perhaps most notable is the fact that nearly all of the contaminating points sources present in the data maps are *not* present in the reconstructions. In particular, the CMBR is reproduced extremely accurately and is virtually indistinguishable from the true input map. As we might expect, the Galactic dust emission is also accurately recovered and contains none of the numerous point sources present in the high-frequency data maps. The free-free emission, which is highly correlated with the dust, is also reconstructed reasonably accurately and displays no evidence of point source contamination. The recovery of the synchrotron emission is, however, somewhat poorer. Although the main

Table 1: The rms residual per 4.5 arcmin FWHM Gaussian beam (in μK) of the MEM reconstructions in presence and absence of point sources, assuming full power spectrum information.

Component	$e_{\rm rms}$ no sources	$e_{\rm rms}$ with sources
CMB	5.90	7.50
Kinetic SZ	0.85	0.86
Thermal SZ	3.90	4.40
Dust	1.60	3.80
Free-Free	0.30	0.38
Synchrotron	0.05	0.06

features of this input map are recovered, the reconstruction contains obvious residual points sources. Perhaps most impressive is the reconstruction of the thermal SZ effect, since the MEM algorithm is successful in reproducing the effect in most of the bright clusters and misidentifies only a few point sources as clusters; these appear mostly as large negative features at the reference frequency of 300GHz. The kinetic SZ effect has is reconstructed in a number of clusters having bright thermal SZ effects. In fact, the quality of reconstructions is similar to that obtained in the absence of point sources, as discussed by HJLB. In Table 1 we compare the rms residuals, $e_{\rm rms}$, per 4.5 arcmin FWHM Gaussian beam, of the reconstructions with those obtained by HJLB in the absence of point sources.

2.2 Reconstructions with no power spectrum information

For our second case, we take the opposite view to that adopted above and assume that almost no power spectrum information is available. This corresponds to assuming a flat (white-noise) power spectrum for each component out to the highest measured Fourier mode. The levels of the flat power spectra are chosen so that the total power in each component is approximately that observed in the input maps. Furthermore, the noise covariance matrix contains only the diagonal contribution from the instrumental noise, and no attempt is made to address the effects of the point source contamination.

In this case, it is most encouraging that the CMB reconstruction is still very accurate, even for this very pessimistic scenario. Once again the reconstruction is, at least by eye, almost indistinguishable from the true input map. The Galactic dust component is also accurately recovered and contains very few of the point sources present in the high-frequency channel maps. The thermal SZ effect is also recovered, but only in the brightest clusters, and the reconstrucion also contains numerous misidentified point sources that appear as sharp negative features. The reconstructions of the remaining three components are very poor. In particular, the kinetic SZ reconstruction has simply defaulted to zero in the absence of any useful data, whereas the reconstructions of the Galactic free-free and synchrotron emission are heavily contaminated with point sources and no obvious features in the true input maps are recovered. In Table 2 we compare the rms of the residuals for these reconstructions with the corresponding results obtained by HJLB in the absence of point sources.

3 Discussion and conclusions

We study the effect of point sources on the reconstruction of CMB anisotropies and foreground emission from simulated Planck satellite observations, using a generalised version of the maximum-entropy formalism developed in Hobson et al. (1998a). The resulting reconstructions show that, even in the presence of contaminating point sources, the CMB emission can still be recovered with an accuracy of about 9 μK per 4.5 arcmin FWHM Gaussian beam, even for

Table 2: The rms residuals per 4.5 arcmin FWHM Gaussian beam (in μK) of the MEM reconstructions in presence and absence of point sources, assuming no power spectrum information.

Component	e_{rms} no sources	e_{rms} with sources
CMB	6.10	8.70
Kinetic SZ	0.85	0.85
Thermal SZ	4.35	5.80
Dust	1.90	4.80
Free-Free	0.44	1.60
Synchrotron	0.07	0.23

the pessimistic scenario in which we assume no prior information about the covariance structure of the sky emission. Depending on our prior knowledge of the power spectra of the CMB and foregrounds, it is still possible in the presence of point sources to obtain accurate reconstructions of the thermal SZ effect from clusters and the Galactic dust, free-free and synchrotron emission. The kinetic SZ effect may also be recovered in cluster that have a large thermal effect.

Acknowledgements

JLS and RBB acknowledge financial support from the Spanish DGES, project PB95-1132-C02-02, CICYT, project ESP96-2798-E and from Comisión Mixta Caja Cantabria-Universidad de Cantabria. RBB acknowledges a Spanish M.E.C. Ph.D. scholarship and expresses her gratitude to the Mullard Radio Astromomy Observatory for its hospitality during her stay there. We thank E. Martínez-González, L. Cayón, and F. Argüeso-Gómez for their useful comments. MPH also thanks Youri Dabrowski for translating the abstract into French.

References

1. Bouchet F.R., Gispert R., Boulanger F., Puget J.L., 1997, in Bouchet F.R., Gispert R., Guideroni B., Tran Thanh Van J., eds, Proc. 36th Moriond Astrophysics Meeting, Microwave Anisotropies. Editions Frontière, Gif-sur-Yvette, p. 481
2. Burigana C., Danese L., De Zotti G., Francheschini A., Mazzei P., Toffolatti L., 1997, MNRAS, 287, L17
3. Danese L., De Zotti G., Francheschini A., Bersanelli M., Toffolatti L., 1987, ApJ, 318, L15
4. Francheschini A., Mazzei P., De Zotti G., Danese L., 1994, ApJ, 427, 140
5. Gispert R., Bouchet F.R., 1997, in Bouchet F.R., Gispert R., Guideroni B., Tran Thanh Van J., eds, Proc. 36th Moriond Astrophysics Meeting, Microwave Anisotropies. Editions Frontière, Gif-sur-Yvette, p. 503
6. Hobson M.P., Jones A.W., Lasenby A.N., Bouchet,F.R., 1998a, MNRAS, submitted (HJLB)
7. Hobson M.P., Barreiro R.B., Toffolatti L., Lasenby A.N., Sanz J.L. Jones A.W., Bouchet F.R., 1998b, in preparation
8. Puget J.-L., Abergel A., Bernard J.-P., Boulanger F., Burton W.B., Désert F.-X., Hartmann D., 1996, A&A, 308, L5
9. Toffolatti L., Argüeso Gómez F., De Zotti G., Mazzei P., Francheschini A., Danese L., Burigana C., 1998, MNRAS, submitted

ELECTRONIC INTRACLUSTER GAS TEMPERATURE DETERMINATION WITH SZ MEASUREMENTS

E. POINTECOUTEAU & M. GIARD
CESR/CNRS, 9 av. du Colonel Roche, 31400 Toulouse, France

Interpretation of S.Z. data on clusters of galaxies requires the knowledge of the electronic temperatureof the gas. Up to know the X-ray data have provided this temperature with an accuracy between 0.5 to 3 keV. Independently of the X-ray data, we show that the Sunyaev-Zeldovich effect at millimeter and submillimeter wavelengths can be used to to determine the electronic temperature. We have simulated SZ observations on the line of sight of a galaxies cluster using the Planck Surveyor and the FIRST future space missions characteristics. We have restored the physical clusters parameters using exact SZ calculations. For an 8 keV cluster, the electronic temperature has been restored with an accuracy between 1.2 to 4 keV, depending of its redshift. This new method may be the only way to estimate the intracluster gas temperature in case of distant clusters, that will be out of reach of the future X-ray space missions.

1 Observations of the intracluster gas

The physical studies of the intracluster medium need to know about its thermal properties, indeed the electronic temperature of the hot intracluster gas must be known. The two ways to observe the hot ionised intracluster gas are the Bremmsstrahlung emission at X-ray wavelengths and the interaction with the cosmic microwave background (hereafter CMB), the Sunyaev-Zeldovich effect (Sunyaev & Zeldovich [1], hereafter SZ effect), from submillimeter to centimeter wavelengths. Up to know the electronic temperature, T_e, has been provided by X-ray data, with an accuracy between 0.5 to 4. keV and for instance Hattori et al. [2] have estimated the electronic temperature fo the AXJ2029 galaxies cluster to $8.6^{+4.0}_{-3.6}$ with the ASCA satellite.

The Bremmsstrahlung emission is proportional to the squared electronic density integrated over the line of sight ($\propto \int T_e^{1/2}(l) n_e^2(l) dl$), where the SZ effect is directly proportional to the electronic density integrated over the line of sight ($\propto \int T_e(l) n_e(l) dl$). As shown on Fig 1a,

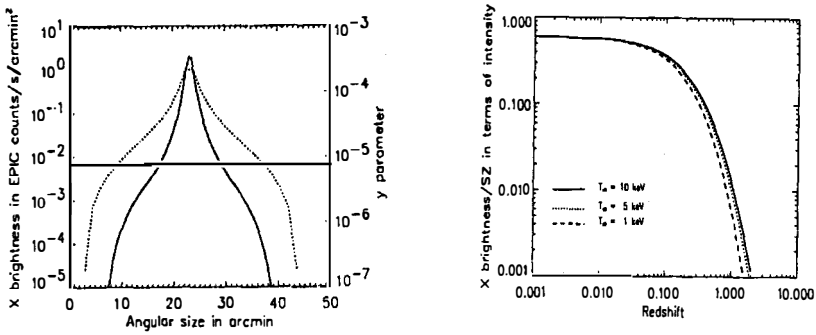

Figure 1: (a-left) Profiles of a 4 keV cluster in the X-ray brigthness (solid line) and the Compton y parameter (dashed line) using a King profile with a core radius, $R_{core} = 0.3$ Mpc, a central density $n_e = 2 \times 10^{-2}$. The cluster is viewed at a redshift of $z = 0.2$ and is cut-off at $20 \times R_{core}$ for the virialized gas. (b-right) Redshift versus the ratio of the X-ray and the SZ brigthnesses. (from Bersanelli et al. [10]).

in the case of a virialized cluster with spherical symmetry, the X-ray profile of the cluster is more peaked than the SZ one, because the X-ray emission is more sensitive to the high density regions. If the intracluster medium is not density homogeneous, the two domains of wavelengths will show two differents components of the gas. The dilution of radiations in the increasing volume of the expending universe makes the X-ray brigthness decreasing as $(1+z)^3$. On the opposite, the SZ brigthness is independent of the redshift, so that it will be adequate to study high redshift clusters that will remain out of reach from X-ray instruments (see Fig. 1b). All these reasons led us to study the possibility to determine the intracluster gas temperature using SZ measurements.

2 Electronic temperature determination

2.1 Exact SZ spectra

Up to now, most of the SZ detections have been performed at radio wavelengths. The data analysis has most often used the analytical expression of the SZ effect, which is a solution of the Kompaneet's equation (a the second order Boltzmann's equation approximation). For millimeter measurements and mostly for submillimeter ones, this expression is insufficient. Indeed, taking into account the plasma temperature ($10^6 - 10^8$ K), the thermal electron velocity distribution is weakly relativistic. This makes the shape of the SZ spectrum different from the one obtained with an approximative analytic treatment.

Previous work on this subject have been made by Wright [3] and Fabbri [4], for analytical corrections; Rephaeli [5], Stebbins [6], Challinor & Lasenby [7] and Itoh et al. [8] for expensions with high order terms and semi analytical calculations. However, we have obtained exact SZ spectra from a simple Monte Carlo integration of the Boltzmann's equation (see Eq. 1):

$$\frac{\partial I_\nu}{\partial s} = n_e \int d\beta \int d\Omega \, p_e(\beta) \frac{d\sigma}{d\Omega} [\, I_\nu(\nu_1) - I_\nu(\nu))] \qquad (1)$$

Where $\frac{d\sigma}{d\Omega}$, the exact differential cross section and $\frac{\nu_1}{\nu}$, the exact frequency shift have to be used. (For more details on the calculations see Pointecouteau et al. [9]). These exact spectra are available on our ftp site: ftp.cesr.fr/pub/astrophysique/sz/.

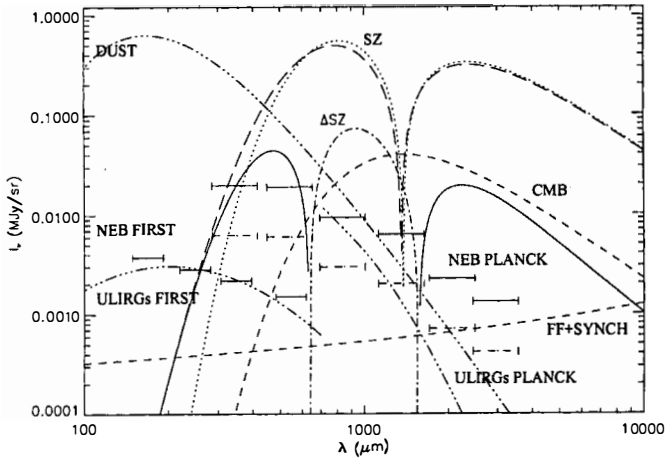

Figure 2: The temperature effect in the thermal SZ effect (ΔSZ=difference between exact and approximation calculation): solid line for the positive part and dotted-dashed line for the negative part. The exact SZ effect (long dash line) and the analytical approximation (dotted line) are overplotted. ($T_e = 8$ keV, $Y_{center} = 3 \times 10^{-4}$). Other contributions have been plotted: The CMB at the level of $\Delta T/T = 30 \times 10^{-6}$, the galactic free-free plus synchrotron emission respectively normalized at the level of 7μK and 4μK at 53 GHz (dashed lines). The galactic dust (with $T_d = 17.5$ K , $n = 2$ and normalized to 0.3 MJy/sr at 100 μm) and the background infrared galaxies beam to beam fluctuations (3 dot-dashed lines). (The background galaxies fluctuations are plotted as two curves, for the Planck and for the FIRST channels, as described in the text.). Horizontal bars represent the Plank and the FIRST sensitivities levels . (Dashed bars for the high sensitivity regions of the Planck survey.).

2.2 Planck/First simulations for electronic temperature determination

Now, using these exact spectra as emission model for clusters SZ brigthness, we have simulated observations on a cluster line of sight of the future space missions, Planck Surveyor and FIRST, using their technical characteristics (Bersanelli et al. [10], Beckwith et al. [11]). Foreground and Background contributions have been added to the SZ brigthness, diluted in the beam of the instrument, for an $y_{center} = 3 \times 10^{-4}$, $T_e = 8$ keV and $R_{core} = 0.3$ Mpc cluster in a $Omega \times h^2 = 0.147$. The galactic dust emission, with a $T_d = 17.5$ K temperature and a $n = 2$ emissivity index (Boulanger et al. [12]), and normalized to 0.3 MJy/sr at 100μm according to the IRAS high galactic latitudes data. The rms level of the emissivity index variability was taken to 0.2 in agreement with the PRONAOS experiment high galactic latitudes data (Bernard private communication). The contribution of the background luminous infrared Galaxies has been obtained by integrating the Log N-Log S sources counts from Guiderdoni et al. [13]. (S^2 was integrated up to $\Omega \times N(S > S_m) = 0.1$). The CMB fluctuation, fixed to a $\Delta T/T = 30 \times 10^{-6}$ level (eg. $\Delta v_p \sim 500$ km/s in term of cluster peculiar velocity.). The galactic free-free and synchrotron emissions have been added too. And finally Instrumental noise, including the nominal mission sensitivity and a 1% relative calibration noise, has been added to the total brigthness. All contribution levels have been plotted on Fig. 2.

The simulations have been fitted with a model including a thermal SZ component, the CMB contribution and the galactic dust emission. y_{center}, the Comptonization parameter, T_e, the gas temperature, ΔT_{CMB}, the CMB temperature fluctuations, the galactic dust level and n, its emissivity index were the free parameters. We have estimated the errors obtained on the restored parameters from the statistics of multiple simulations plus fits. For the electronic temperature,

Table 1: 1 σ statistical error on the gas temperature determination for different configurations. For Planck alone, P1: nominal integration time. P2:10×nominal integration time. For Planck/FIRST, P1/F: Planck's nominal integration time and First deep survey (DS) for FIRST. P2/F: Planck 10×nominal time and First deep survey.

ΔT_e (keV)	P1	P2	P1/F	P2/F
z=0.1	3.1	2.2	1.4	1.2
z=1.	-	4.2	4.3	3.9

the results for a $z = 0.1$ and a $z = 1.$ cluster are summerized in table 1 for different instrumental configurations.

3 Conclusion

The accuracy obtained on the T_e determination is of the same order than the X-ray one. The errors are essentially due to the impossibility to properly modelise the background infrared galaxies emission at submillimeter wavelength. Nevertheless, as it is a new method, X-ray independent, to determine T_e, and, as it allows to estimate T_e with an accuracy between 1.2 to 4 keV, depending of the sources redshift, it seems essential to be able to apply it with Planck and FIRST in a few years. It will give comparative determination with X-ray ones and it will be the only way to estimate T_e for sources with faint or no X-ray counterpart, as those detected by Jones et al. [14] and Richards et al. [15]. Moreover, if determinations can be done on several clusters, a better accuracy on the average cluster gas temperature can be obtained, which can yield to constraints on the formation of the large scale structures.

References

1. Sunyaev, R.A., Zeldovich, Ya.B., Comments Astrophys. Space Phys., 4, 173, 1972
2. Hattori, M., et al., *Nat.* **388**, 146 (1997).
3. Wright, E.L., Ap J **232**, 348 (1979).
4. Fabbri, R., *A&SS* **77**, 529 (1981)
5. Rephaeli, Y., Ap J **445**, 33 (1995).
6. Stebbins, A., astro-ph/9709065, 1997
7. Challinor, A. & Lasenby, A., astro-ph/9711028, 1997
8. Itoh et al., astro-ph/9712289
9. Pointecouteau, E., Giard, M., Barret, D., ApJ submitted, 1998
10. Bersanelli, M.et al., COBRA/SAMBA ESA report, 1996
11. Beckwith, S., et al., FIRST Red book, ESA report, 1993
12. Boulanger, F., et al., *Astron. Astrophys.* **312**, 256 (1996).
13. Guiderdoni, B., et al., *M. N. R. A. S.*, in press
14. Jones, M.E., et al., Ap J **479**, L1 (1997).
15. Richards, E., et al., *Astron. J.* **113**, 1475 (1997).

MAP - THE MICROWAVE ANISOTOPY PROBE

N. JAROSIK, M. LIMON, L. PAGE, D. SPERGEL, D. WILKINSON
Princeton University

C. BENNETT, G. HINSHAW, A. KOGUT, J. MATHER
Goddard Space Flight Center

M. HALPERN
University of British Columbia

S. MEYER
University of Chicago

G. TUCKER
Brown University

E. WOLLACK
National Radio Astronomy Observatory

E. WRIGHT
UCLA

The Microwave Anisotropy Probe (MAP) is a NASA sponsored MIDEX mission which will produce a full sky map of the anisotropy of the Cosmic Microwave Background Radiation. It will observe in five frequency bands spanning 20 – 106 GHz and will achieve an angular resolution of $0.^{\circ}21$ in the highest frequency band. The instrument is differential in design in order to minimize systematic effects and will observe for two years from the Earth-Sun L2 point. MAP is scheduled for launch in the fall of 2000.

1 Introduction

1.1 Background

MAP is the second mission in NASA's Medium Class Explorer (MIDEX) program and was selected for start in March of 1996. The MIDEX program is targeted towards high value space science and astrophysics missions at low cost but potentially high risk. The MAP collaboration includes Goddard Space Flight Center (GSFC), Princeton University, the University of British Columbia, the University of Chicago, UCLA, Brown University and the National Radio Astronomy Observatory. GSFC has primary responsibility for the spacecraft bus and systems while Princeton University is primarily responsible for the instrument.

Table 1: MAP Instrument Specifications

Frequency (GHz)	20-25	28-37	35-46	53- 69	82-106
Resolution (FWHM)	0.°93	0.°68	0.°47	0.°35	0.°21
Number of channels	4	4	8	8	16
noise (per 0.°3 x 0.°3 pixel, channels combined) μK	26	31	27	35	35

1.2 Scientific Goals

The ultimate goal of the MAP project is to both determine the values of many of the fundamental cosmological parameters and to develop an understanding of the processes by which early galaxies formed. The MAP team decided that the best means to this end was to produce a set of high sensitivity, high angular resolution maps of both the intensity and the polarization of the Cosmic Microwave Background Radiation (CMBR). It was also realized that the usefulness of such measurements is often not limited by the intrinsic angular resolution and sensitivity of the instrument, but instead by systematic effects produced either by foreground sources, or instabilities in the instrument itself. The ultimate design of MAP is a result of numerous studies in which the trade-offs between sensitivity, angular resolution and systematic errors were weighed against each other, while trying to maximize the scientific return of the project within the constraints of cost and schedule inherent in the MIDEX program. As a result many of the observatory's systems are single string, although selected redundancy has been added in high risk areas where mass and cost permit. The remainder of this paper will describe the observatory design and specifications, as well as give a brief summary of the current status of the project.

2 The Instrument

2.1 Overview

MAP is a differential instrument using High Electron Mobility Transistor (HEMT) amplifiers as the heart of the receiver system. [1] The receivers' input amplifiers are passively cooled to approximately 95 K in order to lower their noise and hence increase the sensitivity of the instrument. Two back-to-back Gregorian telescopes feed two focal planes, each comprised of an array of 10 corrugated feed horns. The instrument observes the sky in five frequency bands spanning 20–106 GHz (see Table 1.) The two telescopes are pointed so that they observe spots located symmetrically 70.°5 from the spin axis of the spacecraft (see Figure 1.) MAP will be launched on a Delta booster and will observe from the Earth-Sun L2 point. Table 1 summarizes the major aspects of the instrument's performance.

2.2 Scan Pattern

Since the outputs of the MAP radiometers correspond to temperature differences between spots on the sky, whereas the final data products are maps of the temperature and polarization distribution of the CMBR, the choice of a scan pattern is very important to allow for an accurate reconstruction of the temperature and polarization maps. The selected scan pattern is shown in Figure 1. The satellite rotates about its spin axis with a period of approximately 2.2 minutes, measuring a small annular region indicated by the dashed circle. Simultaneously the spin axis of the satellite is precessed 22.°5 about the anti-Sun line with an approximate 1 hour period. The sky coverage resulting from 1 hour of observations is represented by the solid lines in the pattern at the top of Figure 1. The MAP scan stategy covers appoximately 30% of the celestial

sphere every hour, and the scan lines of the data set are highly interconnected, both of which are crucial for reconstruction of the temperature and polarization maps with minimal systematic errors. Since the anti-Sun line about which the spin axis of the observatory precesses sweeps out a line through the ecliptic plane as the Earth circles the Sun, this scan pattern covers the entire celestial sphere, allowing production of a full sky map every six months. By observing from the Earth-Sun L2 point, and generally looking in the anti-Sun direction, the largest sources of potential foreground contamination, the Earth, Sun and moon, are all located on the same side of the spacecraft, far from the lines of sight of the telescopes.

2.3 Optics

The MAP optics consist of back-to-back Gregorian telescopes with shaped primaries. The mirrors and truss work are fabricated from composites and the reflecting surfaces of the mirrors are coated with evaporated aluminum. The horns which collect the radiation in the focal plane are corrugated in design and are machined from aluminum. In all except the lowest frequency band (where the entire horn is machined), the mode converter section of the horn consists of an electroformed copper section. The entire optical system is also passively cooled to $\approx$ 70K to minimize its emission and hence reduce any potential systematic errors.

2.4 Radiometers

The MAP radiometers are based on cryogenic microwave HEMT amplifiers developed at NRAO. The radiometers are differential in design and utilize solid state (PIN diode) phase switches to effect the switching. A major consideration in choosing a radiometer design was the ability to use as many standard commercially available components as possible, to minimize development cost and time. Despite the loss of sensitivity by a factor of $\sqrt{2}$ as compared to total power radiometers, a differential design was selected to minimize potential systematic effects produced by the low frequency gain fluctuations of the HEMT amplifiers.[2,3] The input amplifier stages are cooled to $\approx$ 95K by a large radiator located between the back-to-back primary reflectors. The outputs of these amplifiers are connected to the inputs of additional ambient temperature ($\approx$ 300K) amplifiers by lengths of stainless steel waveguide which provide the needed thermal isolation between the cold and warm radiometer sections. The warm components include amplifiers, phase switches, hybrid tees, filters and detectors. The phase switch toggles at 2.5 kHz producing AC signals in the detector outputs proportional to the difference between the sky temperatures observed by the two telescopes. The signals are passed to the instument's analog electronics unit where they are demodulated and sampled.

3 Mission Overview

3.1 Spacecraft Operations

After launch the MAP satellite trajectory will consist of 2–5 'phasing loops' to position the observatory for a lunar swingby and a subsequent cruise to Earth-Sun L2. MAP should reach its observing station approximately three months after launch at which time it should be in a stable enough condition to begin observations. Data downlinks are scheduled to occur once a day and last from $\frac{1}{2}$ to $1\frac{1}{2}$ hour. During these periods the instrument is still operating in its normal observing mode, however the data being collected during these periods are tagged to indicate the possiblity of contaminations from the telemetry transmission. The nominal mission duration is two years at L2, during which time the entire sky will be observed four times. Once MAP has reached its observing station, fuel usage is minimal, so there will be enough consumables on board to extend the duration of the mission should the opportunity arise.

3.2 Map Making and Calibrations

The radiometers are continuously calibrated from the CMBR dipole, and an absolute calibration is obtained from the annual modulation of this dipole by the Earth's motion about the Sun. The exact pointing and profiles of the main beams will be measured in flight using observations of Jupiter. The instrument's far sidelobe response will be measured using a mock-up of the satellite at Princeton University, and the results compared with theoretical models. The final maps are produced from the time stream data by an iterative technique, which can be accomplished with several days of computing with current processors. Figure 2 shows how well MAP should be able to determine the band power spectra based on two years of observations. The shaded region is the uncertainty in the recovered band power, assuming a sky coverage of 66% to allow for removal of the Galactic plane. The curves plotted correspond to a standard CDM model (solid), a highly reionized CDM model (dot-dash), an open CDM model with $\Omega_0 = 0.2$ (dotted) and a primordial baryon isocurvature (PBI) model (dashed). These results were obtained using only the data for the three highest frequency channels since it is expected that the lower frequency channels will contain substantial Galactic contamination.

4 Current Status

Since selected for start in 1996 several changes have been made to MAP's design. Two of the more significant changes are that the angular resolution in the highest frequency band (82 – 106 GHz) has been improved from $0.^{\circ}31$ to $0.^{\circ}21$, and a redundant transponder has been added. The flight radiometers are in production and have achieved the expected sensitivity. It is expected that MAP will be launched in the fall of 2000, approximately $4\frac{1}{2}$ years after the program's start. Further information in available from the MAP web page at *http://map.gsfc.nasa.gov.*

References

1. M.W. Pospieszalski *et al.*, *Proc. 1995 IEEE MTT-S Int. Microwave Symp.* **45**, 1121 (1995).
2. N. Jarosik, *IEEE Transactions on Microwave Theory and Technique* **44**, 193 (1996).
3. E. Wollack, *Rev. of Sci. Instruments* **66**, 4305 (1995).

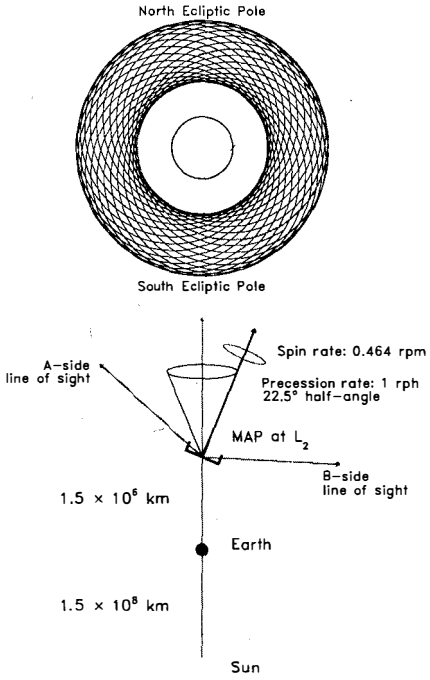

Figure 1: MAP Scan Strategy

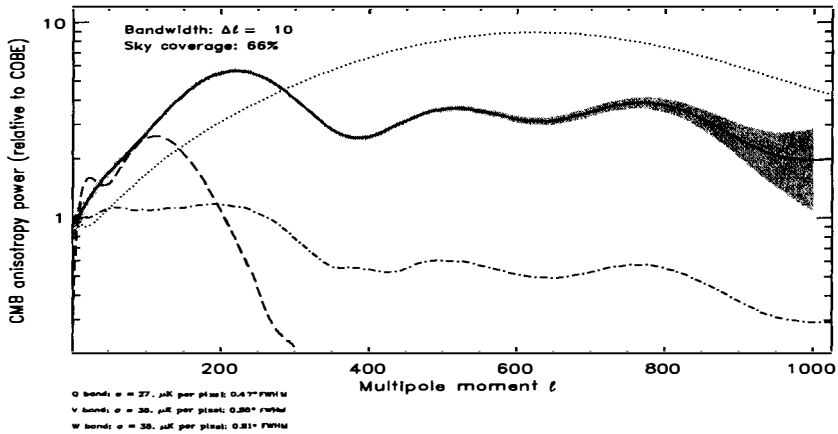

Figure 2: MAP Expected C_ℓ coverage

The Current Status of Planck

J. A. Tauber
Astrophysics Division, Space Science Dpt., European Space Agency
Keplerlaan 1, 2201AZ Noordwijk, The Netherlands

The current status and near-future milestones of the Planck mission within the Scientific Programme of the European Space Agency are described. The main technical changes and advances in the payload definition since the selection of COBRAS/SAMBA (as Planck was previously called) in late 1996 are also described.

1 Introduction

In late 1996, the European Space Agency (ESA) selected the COBRAS/SAMBA [1] mission as the third Medium-Sized Mission of ESA's Horizon 2000 Scientific Programme. COBRAS/SAMBA was designed to image the anisotropies of the Cosmic Background Radiation Field over the whole sky, with unprecedented sensitivity and angular resolution, and was expected to provide a major source of information relevant to several cosmological and astrophysical issues, such as testing theories of the early universe and the origin of cosmic structure, in particular allowing the determination of fundamental cosmological parameters to very high accuracy. At the time of selection, COBRAS/SAMBA was scheduled for launch in 2004. In early 1997, COBRAS/SAMBA was renamed *Planck* in honor of the German scientist Max Planck (1858-1947), Nobel Prize for Physics in 1918.

Since that time, budgetary pressures within ESA's scientific programme have forced a reconsideration of the original implementation plan for Planck. Currently three implementation scenarios are being considered; in any of these scenarios the intention of ESA is to keep the cost of FIRST and Planck together within the cap for a Cornerstone mission minus 10% :

1. The baseline scenario is to combine Planck with ESA's Far Infrared and Submillimetre Telescope (FIRST) [2], i.e. to put both payloads on a single spacecraft bus and operate them sequentially (Fig. 1a). In this so-called "merged" configuration, FIRST/Planck satellite would be launched on a dedicated Ariane 5 rocket.

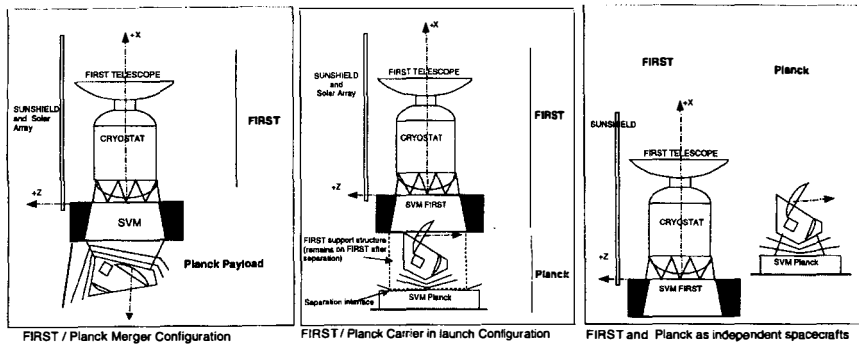

Figure 1: Options being considered for the FIRST and Planck missions.

2. An alternative scenario is for FIRST and Planck to remain stand-alone missions (Fig. 1c). In this configuration Planck would most probably be launched in a Soyouz-Fregat rocket.

3. A third possibility is for FIRST and Planck to be launched together, but to separate during the transfer to the final orbit, and thereafter to be operated independently. This solution is often referred to as the "Carrier", due to the launch configuration of the two spacecraft (Fig. 1b).

After in-house evaluation of these options, ESA commissioned two parallel industrial studies (by Matra Marconi Space in Toulouse, and Aerospatiale in Cannes) to assess in detail their technical feasibility and cost. The technical activities began in September 1997 and were finished in February 1998; as a result of the studies, it is now established that all three solutions are technically feasible. The costing activities will be completed in March 1998.

In parallel to the industrial studies, ESA issued to the scientific community in October 1997 an Announcement of Oppportunity requesting proposals to provide instruments for both Planck and FIRST. Potential proposers were asked to assume that FIRST and Planck would be merged (as in the first scenario above), and that FIRST/Planck would be launched at the end of 2005. Proposals have been duly received in February 1998, and are at the time of writing (Feb. 1998) undergoing an evaluation process.

ESA's intention is to make a decision on the implementation scenario for Planck and FIRST by late May, once all the information deriving from the industrial studies and the instrument proposals has been gathered and analyzed. At the same time, the instrument Principal Investigators will be selected; during the second half of 1998, the instrument proposals will be reiterated in order to make any modifications required by the particular implementation scenario chosen. This process will end in early 1999, when the instrument complement will be finally approved by ESA's Space Programme Committee.

2 Planck vs COBRAS/SAMBA

Since COBRAS/SAMBA was selected, work has continued on the detailed definition of the model payload. At the same time, the new industrial studies have developed new spacecraft configurations. Overall many changes have occurred to the mission. Here are briefly described some of the most important ones, namely those that affect scientific performance in some way. The changes described here will occur irrespective of the implementation scenario chosen.

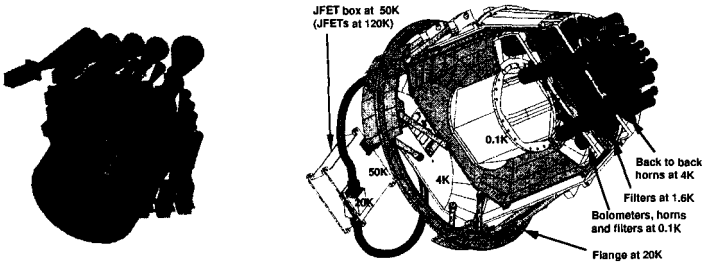

Figure 2: The new focal plane layout of the LFI (on the left) and the HFI (on the right). The two pictures are not to the same scale. The LFI horns (at 20 K) are located in a ring around the HFI.

2.1 Instruments

The model payload of COBRAS/SAMBA included two instruments, referred to as the Low Frequency Instrument (LFI) and High Frequency Instrument (HFI). The LFI consisted of an array of 56 tuned radio receivers grouped into four channels between 30 and 125 GHz, and was passively cooled to a physical temperature of $\sim$100 K. The HFI consisted in total of 56 bolometers divided among 5 channels between 140 and 850 GHz; the bolometers were actively cooled to 0.1 K. A significant problem for COBRAS/SAMBA was the fact that the sensitivity of LFI channels was much poorer (by a factor of $\sim$30) near 125 GHz than the sensitivity of the HFI channel near the same frequency. In order to maximize the effectiveness of Planck's outstanding asset (its very wide frequency range), it was imperative to improve this situation. While something was gained by rearranging the detector distribution and limiting the maximum frequency of LFI to 100 GHz, it was clear that in order to gain a significant factor in sensitivity it would be necessary to cool the LFI detectors to temperatures near $\sim$20 K. The first step in this direction was to reduce by a factor of $\sim$10 the heat dissipation of the LFI in the focal plane. The only way to achieve this was to split the full receiver chains into two parts, one "front-end" in the focal plane, and a "back-end" at 300 K linked to the front-end by means of waveguides. While the existence of waveguide-linked boxes introduces significant complexity to the design of the payload, it was required as the only way to improve the sensitivity of the LFI at critical frequencies. With the siginificantly reduced dissipation it became technically possible to actively cool the front-end down to 20 K.

The introduction of an active cooler for the LFI (the baseline for which is a Joule-Thomson loop driven by a H_2 sorption compressor) in parallel to the already complex cooling system for HFI, necessitated a rationalization of the overall active cooling system. The HFI in COBRAS/SAMBA required a 20 K stage which was provided by a Stirling cooler. In view of the LFI situation, it is now possible for both instruments to share a single cooler, which provides both cooling to 20 K for the LFI detectors, and a first stage at 20 K for the HFI cooling chain (which ultimately leads to 0.1 K). The cooler type chosen for this purpose is the H_2 sorption cooler, two copies of which must be installed to provide redundancy.

The preliminary focal plane layout of both instruments in COBRAS/SAMBA was improved to a more realistic configuration for Planck. For various technical reasons it was found best to place the HFI in the center of the focal plane, while the LFI horns are situated in a circle around the HFI (see Figure 2). This creates some problems for the LFI in terms of optical aberrations due to its off-axis location, however these problems have been quantified and judged acceptable.

Straylight is a major concern for Planck, and extensive simulation has been carried out in the past year to quantify this problem more carefully than was done for COBRAS/SAMBA. A

specific problem has been identified in the telescope configuration due to spillover past the top of the primary mirror; while the COBRAS/SAMBA configuration is marginally within specs, this is such a critical area that it was felt required to increase the margins by installing a reflecting baffle over the top edge of the primary. This baffle will not improve the angular resolution quoted for COBRAS/SAMBA, which is defined by the taper in the horn angular pattern rather than the size of the primary. The projected geometric aperture of the telescope (including the baffle) is now 1.5 m.

It has become clear in the past year that the ability to measure the polarization of the CMB would improve considerably the scientific output of the mission, and therefore effort has been devoted to assess the possibility of making such measurements. The LFI detectors are intrinsically sensitive to linear polarization, and thus the ability to measure more Stokes parameters depends only on orienting the horns appropriately. For the HFI the situation is more tricky since the bolometers are incoherent detectors: in order to measure polarization, it is required to build into the optical system polarizing filters, which introduce some loss. Although there are still many uncertainties (control and knowledge of the cross-polar angular pattern, polarization of the foreground emission, straylight contamination, etc etc) which at the moment make difficult a prediction of the sensitivity of the system to the polarized component of the CMB (predicted to be at ~5% of the CMB fluctuation), the scientific potential is large enough that it is acceptable to add some loss to the measurement of the CMB fluctuation itself. Therefore some of the HFI detectors will be equipped with polarizers, and in the coming year more simulations will be carried out to refine the estimated sensitivity to polarization.

A summary of the characteristics and best current estimate of the performance of the model instruments of Planck is given in Table 1. The performance of the flight instruments can only be assessed after the proposal selection process is completed, but is expected to be close to that of the model payload.

Table 1. Planck Model Payload Characteristics

Telescope	1.5 m. (proj. apert.) Gregorian; shared focal plane; $\epsilon_{system} \sim 1\%$									
	Viewing direction offset 80°-85° from spin axis									
Instrument	LFI				HFI					
Center Frequency (GHz)	30	44	70	100	100	143	217	353	545	857
Detector Technology	HEMT radio receivers				Bolometers					
Detector Temperature	~20 K				~0.1 K					
Cooling Requirements	H_1 sorption cooler				H_2 sorption + 4K J-T stage + Dilution					
Number of Detectors	4	6	12	34	4	12	12	6	8	6
Bandwidth ($\Delta\nu/\nu$)	0.2	0.2	0.2	0.2	0.25	0.25	0.25	0.25	0.25	0.25
Angular Resolution (arcmin)	33	23	14	12	10.7	8.0	5.5	5.0	5.0	5.0
Average $\Delta T/T$ per pixel (12 mos., 1σ, 10^{-6} units)	1.6	2.4	3.6	4.3	1.7	2.0	4.3	14.4	147.0	6670
Sensitive to linear pol.	yes	yes	yes	yes	no	yes	yes	no	yes	no

2.2 Operations

COBRAS/SAMBA was designed to share an Ariane launch with a second passenger; therefore it would have been launched into Geostationary Transfer Orbit, from where it would have cruised under its own power to its final orbit around the 2nd Lagrangian point of the Earth-Sun system (L2). Planck will either share its launch with FIRST (which is also destined for L2), or will have an independent launch. In either case Planck will be launched directly into a trajectory towards L2, either by Ariane 5 or Soyouz-Fregat. An important advantage of the rather tortuous trajectory of COBRAS/SAMBA was that the Moon and Earth would have been

observable by Planck during the transfer; this would have enabled a very accurate measurement of the beam patterns of individual horns, and made easier the removal of straylight signals from later observations. This advantage is lost to Planck; however simulations indicate that adequate knowledge of the beam patterns will be achieved by Planck by dedicated manoeuvers designed to sweep the far sidelobes past bright sources of emission (such as the Sun).

In the case of the current baseline scenario, in which FIRST and Planck share a single spacecraft bus, the scientific operations of each payload will be carried out sequentially. The "Science Management Plan of the Combined FIRST and Planck mission" [3] requires that the entire Planck observation programme is carried out in the early part of the FIRST/Planck mission. Furthermore it states that Planck and FIRST will share the observation time of the combined FIRST/Planck mission according to the following schedule:

1. Satellite commissioning and performance verification phases (TBD months)
2. Predefined science demonstration (0.5 to maximum 1 month)
3. Planck first full sky survey (6 to maximum 7.5 months)
4. FIRST key programmes (7 to maximum 8 months)
5. Planck second full sky survey (6 to maximum 7.5 months)
6. FIRST observations until end of in-orbit phase.

The "Science demonstration phase" will be used by Planck to experiment with various observing strategies before the start of the first sky survey. A major spacecraft manoeuver is required at the time of injection into the orbit around L2 (~7 months after launch), and would imply interruption of any observations which may have started during the transfer phase. Therefore, for continuity and stability reasons, the first Planck sky survey will not begin before that manoeuver is completed, whereas FIRST may be able to take advantage of early observing. With this proviso, the above schedule will be adhered to, and it is expected that the Planck programme will be completed approximately 2 years after launch.

3 Conclusions

Since its selection in late 1996, the programmatic situation of Planck has been uncertain. However, the decision on its form of implementation is expected soon (June 1998), with final confirmation of the payload instruments in February of 1999. Therefore, the Planck programme should be able to start its development phase at the end of 1998 or early 1999 at the most.

On the other hand, the technical maturity of the Planck payload has improved considerably since 1996. The model instruments now offer improved performance as compared to COBRAS/SAMBA, and a correspondingly enhanced scientific return. This improvement should be realizable in any of the implementation scenarios currently being considered.

The future therefore looks bright for the fulfillment of the scientific objectives of Planck, the most ambitious and sophisticated Cosmic Microwave Background experiment ever planned or attempted.

Acknowledgments

I gratefully acknowledge the hard work of many individuals in the scientific community over the past 4 years on the definition of the Planck instruments and mission concept. The work of the ESA FIRST/Planck project team is similarly acknowledged.

References

1. J. Tauber, in *Proc. XVI Moriond Astrophysics Meeting on Microwave Background Anisotropies*, ed. F.R. Bouchet & R. Gispert (Frontières, Gif-sur-Yvette, 1997), pp. 57-66. Also see *http://astro.estec.esa.nl/Planck*.
2. G. Pilbratt, in *Proc. of the ESA Symposium on The Far Infra Red and Submillimetre Universe*, (ESA SP-401, 1997), pp 7-12. Also see *http://astro.estec.esa.nl/First*.
3. ESA/SPC(97)34, Rev. 1.

STUDIES ON THE OPTICAL CHARACTERISTICS OF THE PLANCK TELESCOPE

F. VILLA[1], L. VALENZIANO[1], C. BURIGANA[1], N. MANDOLESI[1], M. BERSANELLI[2]
[1] *Istituto TeSRE-CNR, via Gobetti 101, I-40129 Bologna, Italy*
[2] *IFCTR-CNR, via Bassini 15, I-20133 Milano, Italy*

The next generation of satellite missions, like Planck and MAP, require large telescopes coupled to detector arrays to measure CMB anisotropies at small angular scales. The careful prediction of the optical performances of such telescopes plays a crucial role for the optimization of the optical configuration and for the evaluation of associated systematic effects. A brief review of the optical calculations for the Planck telescope is presented. Results are used to evaluate the optical distortions and to optimize the location of the Planck/LFI (Low Frequency Instrument) feedhorns.

1 Optical Calculations

The properties of the radiation pattern have been calculated for three optical configurations of the Planck telescope. The first one is the STANDARD configuration assumed during the "Phase A" study[1]. The second and third, called ENLARGED.1550 and ENLARGED.1750, are proposed to improve the optical quality of the Planck telescope, by increasing the aperture diameter (from 1.3m to 1.55m and 1.75m respectively), maintaining the same secondary reflector and the same equivalent focal ratio. All the configurations are "Gregorian off-axis telescopes": the incident wave is scattered by the primary parabolic mirror to the secondary ellipsoidal mirror and then to the focal region where the detectors are located[4]. The secondary reflector axis is tilted at 14 degrees with respect to the parabola axis in order to minimize the beam distortions at the center of the focal region. For each configuration, we calculated the position and the shape of the focal surface (i.e. the surface of maximum directivity)[6]. Geometrical optics approximation has been used: circular bundles of rays from the rim of the primary mirror are propagated through the telescope optics. The points at which the bundles converge to the minimum size (in least-square sense) trace the focal surface and also give the correspondence between angles from the optical axis and the linear displacements in the focal surface, often referred as the plate scale (that depends on the effective focal length of the telescope).

These results are used as input to calculate the response of the telescopes on the sky[7] (the beam pattern). A FORTRAN code, based on the Physical Optics (PO) and Geometrical Optics (GO) techniques, has been implemented to calculate the response as a function of the view direction on the sky[5]. Given the position of the detector (a corrugated feedhorn) in the focal region and the corresponding view direction with respect to the chief ray, the integration of the currents on the aperture surface of the main reflector is calculated in order to obtain the Far Field radiation pattern. For each configuration, the response of the telescope in a regular elevation-azimuth grid on the sky that covers the field of view has been obtained. The evaluation of the

distortion as a function of the detector position on the focal surface has been used to optimize the location (in the focal region) and the pointing direction of each feed. We have also taken into account the physical size of the feedhorns and of the receivers, as well as the HFI focal box located in the central region.

2 Conclusion

Optical calculations have been used to optimize the LFI FPU assembling and to predict the sistematic effects of the optics. We notice that the STANDARD optical design of Planck suffers from beam distortion effects which lead to a large degradation of the effective angular resolution of the beams [3]. The new arrangement of the Focal Plane Unit (FPU), with HFI in the center and LFI around it, is not ideal from the LFI point of view [2].

In order to recover the nominal LFI (and presumably HFI) Planck angular resolution introduced by beam distortions at an acceptable level, a larger primary mirror is demanded.

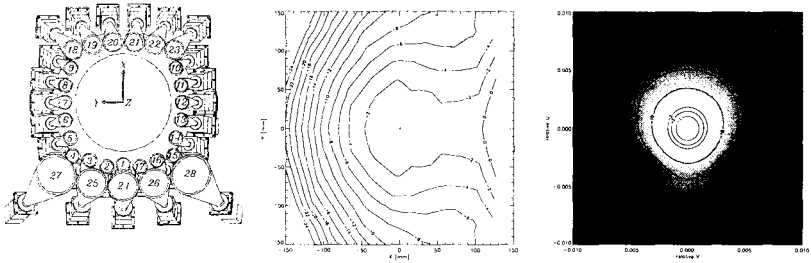

Figure 1: Left panel: new Focal Plane Assembling Unit. The feeds from 1 to 17 are at 100 GHz. The other feeds are working at 70 GHz (18-23) , at 44 GHz (24-26) and at 30 GHz (28-29). Middle panel: contour plot of the focal surface of the STANDARD telescope design. It is worth noticing that the focal surface is not a plane. Right panel: example of the beam simulation calculated at 100 GHz for the LFI feedhorn # 1 and the STANDARD configuration.

References

1. Bersanelli M. *et al*, COBRAS/SAMBA Report on the Phase A Study, ESA, D/SCI(96)3, (1996)
2. Burigana C. *et al*, this conference, (1998)
3. Mandolesi N. *et al*, Int Rep. TeSRE/CNR 199, On the Planck effective Angular Resolution, (1997)
4. Nielsen P.H. & Pontoppidan K., Design & analysis of the COBRAS/SAMBA telescope, TICRA Rep. S-699-02, (1996)
5. Sletten C.J., Reflector and Lens Antennas - Analysis and Design Using Personal Computers, Artech House, (1988)
6. Valenziano L. *et al*, Int. Rep. TeSRE/CNR, Focal Surface Evaluation for the Planck Telescope, (1997 in preparation)
7. Villa F. *et al*, Int. Rep. TeSRE/CNR, Main Beam Simulations for the Planck Telescope, (1997 in preparation)

CMB ANISOTROPIES ON CIRCULAR SCANS

J. Delabrouille, R. Gispert and J.-L. Puget
Institut d'Astrophysique Spatiale, CNRS & Université Paris XI, bât 121, 91405 Orsay Cedex, France

We address the problem of map-making with data from the PLANCK SURVEYOR High Frequency Instrument, with an emphasis on the understanding and modelling of instrumental effects, and in particular that of sidelobe straylight.

1 CMB mapping: A complex problem

The goal of a CMB satellite experiment as PLANCK SURVEYOR is a precise measurement of the temperature of the microwave sky, $T(\vec{n})$, as a function of direction $\vec{n}$. Data samples obtained with the experiment, however, are not directly quantities of interest, but rather depend in a complex way on sky temperature, on the instrument, and on the scan strategy.

1.1 Model of the measurement

The complex process of radiation detection and signal production which relates the detected signal to the temperature field on the sky may be modelled, for a given detector, by:

$$s(t) = h(t) \star \left[\eta(t) \int \mathrm{d}\nu \left(b(\nu,t) + H_{\text{filters}}(\nu) \int_{(4\pi)} \mathrm{d}\Omega L_\nu(\mathrm{R}_t(\vec{n})) T(\vec{n}) \right) \right] + n(t) \qquad (1)$$

$h(t)$ is a global impulse response of the detector and electronics, $\eta(t)$ is the detector efficiency, assumed to be (possibly) slowly time dependent, $H_{\text{filters}}(\nu)$ is the transmission of the filters which set the frequency band of observation, $L_\nu(\vec{n})$ the frequency-dependent radiation pattern of the antenna (including all optical elements), R_t a time-dependent rotation which reflects the scan strategy, and $T(\vec{n})$ the temperature on the sky which one wishes to measure. Randomness in the process of detection (in photon arrivals, in electronic processes in the detectors) is represented by a noise term, $n(t)$. Finally, $b(\nu,t)$ is a self-emission term, due to radiation from instrumental parts (filters, slightly emissive mirrors...) impinging on the detectors.

We have written equation 1 in terms of continuous functions $s(t)$ and $T(\vec{n})$. In the following, we will use sampled and pixelised versions s_k and T_p when convenient. The problems of digitalisation and pixelisation, interesting by themselves, are left out of this discussion.

1.2 Data Processing

For optimal mapping of the CMB anisotropies, it is necessary to optimise mission parameters and options (optimisation of $h(t)$, $H_{\rm filters}(\nu)$, $L_\nu(\vec{n})$, R_t...) as well as methods of data processing for recovering sky temperature maps from $s(t)$. The traditionnal approach of data processing in the context of CMB mapping consists in modelling the measurement as $s_k = A_{ki} y_i + n_k$ where s_k is the vector of signal samples (measurements), A a linear operator, $y_i = (T_{\rm pixel}, X_i)$ a vector of quantities to be determined from the data set, where $T_{\rm pixel}$ are sky temperatures in a set of pixels, and X_i other quantities contributing to the signal. n_k is a vector of noise realisations. If we assume that the noise autocorrelation matrix $N = \langle n\, n^T \rangle$ is known, then the inversion can be performed by computing the estimator:

$$\hat{y} = [A^T N^{-1} A]^{-1} A^T N^{-1} s_k \tag{2}$$

This method, in principle, produces the best unbiased estimate of the sky. It is in essence the one that has been used by the DMR team [1]. It suffers, however, from a few drawbacks that make it impractical for PLANCK. The first is the size of the linear system to be manipulated (a few million pixels on the sky, and a few billion samples per detector for a 1-year mission). The second is that it is not clear *a priori* that a relevant set of parameters X_i can be identified and the remaining noise correlation matrix estimated reliably so that the measurement can be meaningfully modelled by a linear equation connecting s_k to y_i.

We propose a way of analysing the PLANCK data which relies more specifically on the properties of the PLANCK scanning. The PLANCK satellite is spun at $f_{\rm spin} = 1\,\mathrm{rpm}$ (0.0167 Hz) around a spin axis, which is moved in 5 arcminute steps every 2 hours or so in order to follow the apparent yearly motion of the sun and keep the spin axis roughly anti-solar. Because of this, the data reduction (for one detector) can be decomposed into 2 steps: for a given, fixed, spin-axis position, about 120 consecutive scans can be averaged into one single ring, after what about 4000 rings (for a one year mission, for one detector) need to be reconnected into a map of the sky. The first step (obtaining rings from data streams) reduces the amount of data samples by a factor of 120 in a non-destructive way and filters out efficiently all non-synchronous systematic effects. Scan-synchronous effects, which can not be identified or removed in the first step, can be taken care of in a second step of map reconstruction from a set of rings (from all detectors in a channel, eventually).

2 From data streams to rings

The first step of our analysis is to build a single ring of data using a set of $N_{\rm turns} = 120$ consecutive scans. A plot of the expected distribution of the power of the signal as a function of frequency is shown on figure 1. Signal and scan-synchronous systematics have a line spectrum concentrated at harmonics of the spinning frequency $f_{\rm spin}$. The rejection of non-synchronous signals is possible by building a numerical filter which keeps harmonics of the spinning frequency and filters out other frequencies. Simple co-addition of samples is one such filter, but it is not necessarily optimal. Another option involves multiplication of the signal by a weighting function (apodisation) prior to co-addition and computation of Fourier modes. The filter should be adapted to the shape of the noise spectrum and the location of non-synchronous systematic lines. Its efficiency, whatever the method, is limited by the finite size of the observation window. The resolution in frequency around each harmonic is of the order of $f_{\rm spin}/N_{\rm turns}$.

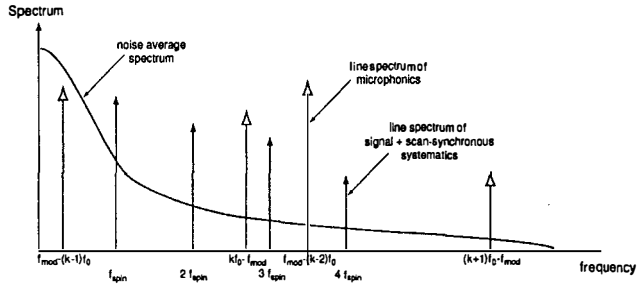

Figure 1: Schematic spectra of signal, noise and systematics for periodic scanning, after demodulation. This spectrum is representative of what is expected for the PLANCK HFI for one spin-axis position. Possible contribution of microphonics due to periodic vibrations yields, after demodulation, a non-synchronous line spectrum.

Scan synchronous effects, or quasi synchronous noise which cannot be separated from the signal by the filter due to insufficient resolution, cannot be removed from the useful astrophysical signal at this stage. Such signals include those induced by scan-synchronous temperature fluctuations of the payload, and sidelobe effects.

An additionnal use of the analysis on rings is the possibility to compare the spectra of the cosmological signal to that of the noise [2]. This is a precious tool for the optimisation of instrument and mission parameters.

3 Map-making from a set of rings

Assume we now want to reconnect the set of PLANCK rings into a map. When the main beam of the instrument comes back to a given pixel of the sky, we get a redundant measurement of the same useful astrophysical quantity in a different instrumental configuration. Such redundancies help identifying scan-synchronous effects reprojected on each ring by comparing measurements obtained at crossing points between different rings.

As an illustration of issues related to the identification and subtraction of scan-synchronous effects, we will discuss the problem of sidelobe straylight. The measurement sample s_k from the detector at a time t_k can be represented, in sampled form, as

$$s_k = u_k + \sum_i L_i T_{\rm sky}(p_k(i)) + n_k \quad (3)$$

$$= u_k + M_{kip} L_i T_p + n_k \quad (4)$$

It has been assumed that the (two-dimensional, band-averaged) sidelobe antenna pattern and the (band-averaged) sky have been pixelised into one dimensional vectors L_i and T_p repectively. The notation used in equation 3, supposes that for each satellite orientation there is an unambiguous correspondance between sky pixels and antenna pattern pixels, represented by the map $p_k(i)$, but this constraining assumption is not necessary when the notation of equation 4 are used. u_k is the useful temperature fluctuation in the main beam, and n_k the noise (here assumed to be white noise).

The anisotropies we want to measure do not generate significant sidelobe signals. Only bright features (galactic plane, dipole) contribute significantly. A numerical estimate of the sidelobe contribution shows in particular that the Galaxy may generate significant (above noise levels) sidelobe signals, especially in the highest frequency channels.

The absolute temperature of these bright regions of the sky will be measured extremely precisely by PLANCK (to a relative accuracy of the order of 10^{-2} to 10^{-3} at least) because noise and systematic effects of any kind (after first-order correction) will be much lower in amplitude than the corresponding signals (which have amplitudes of a few millikelvin). Therefore, equation 4 can be rewritten as $s_k = u_k + A_{ki}L_i + n_k$, where $A_{ki} = M_{kip}T_p$ is a $N_k \times N_i$ known matrix, which depends only on the absolute temperature of the sky and on the scan strategy. A possible method to solve the system for u_k and L_i simultaneously is an iterative one:

a- We first get an estimate of the CMB anisotropies on the sky by standard methods (for instance averaging measurements), neglecting sidelobe effects (or after first-order sidelobe correction using prior knowledge of the antenna pattern). This yields a first order map $\widehat{\Delta T}(\theta, \phi)$.

b- An estimator $\widehat{u_k}$ of u_k is computed for each sample k by $\widehat{u_k} = \Delta T_1(\theta_k, \phi_k)$, where (θ_k, ϕ_k) defines the direction of pointing of the main beam for sample k. Differences $\widehat{\delta_k} = s_k - \widehat{u_k}$ are computed.

c- The system $\widehat{\delta_k} = A_{ki}L_i$ is solved for an estimator $\widehat{L_i}$ of L_i. If the noise is white, the solution is simply $L_i = [A^T A]^{-1} A^T \widehat{\delta_k}$.

d- The process is iterated with a new estimate of δ_k obtained by correcting for the estimated sidelobe effects using the estimator of L_i.

There are two important conditions for this prescription to work in practice. The first is that the size of the system be small enough that several iterations can be effectively computed. The second is that matrix $[A^T A]$ be regular. The fulfillment of the first condition is insured by the low spatial frequency character of the sources of sidelobe signal, which have significant angular sizes of at least one degree, but usually much more (galactic emission, CMB dipole). Using a model of the sky obtained from extrapolations of the DIRBE data and the DMR dipole templates in the PLANCK SURVEYOR wavebands, and several models of PLANCK SURVEYOR sidelobes obtained by numerical simulations, we have shown that there is no significant difference between convolution signals calculated using half a degree and three degree resolution maps. It is therefore not necessary, for sidelobe correction, to pixelise the lobe with pixels smaller than a few degrees. The size of vector L_i is then a few thousand entries only. The fulfillment of the second condition has been checked with the use of numerical simulations. For the PLANCK scan strategy, using as a sky template the galactic emission as measured by DIRBE, we have shown that matrix $[A^T A]$ is indeed regular, which means that the galactic plane can be used as a source to map the sidelobes. This is very useful in particular for the highest frequency channels of PLANCK where the sidelobe contamination from galactic dust is the largest.

4 Conclusion

We have shown that the scan strategy of PLANCK SURVEYOR along rings on the sky allows to decompose the problem of converting data streams into CMB anisotropy maps in two independent steps. This makes the problem tractable numerically, and helps in analysing and monitoring the impact of systematic effects. In particular, a promising method for the identification and removal of sidelobe signals has been developped.

References

1. M. Janssen and S. Gulkis in *The infrared and submillimeter sky after COBE; Proceedings of the NATO ASI*, Les Houches, France, Mar 20-30, 1991 (A93-51701 22-90)
2. J. Delabrouille, K. Górski and E. Hivon, MNRAS **in press**, astro-ph/9710349 (1997)

LARGE SCALE PROPERTIES OF THE FAR-INFRARED BACKGROUND

L. POPA[1] and C. BURIGANA[2]
[1] *Institute of Space Sciences, R-76900, Bucharest-Magurele, Romania*
[2] *Istituto TESRE, Consiglio Nazionale delle Ricerche, Via Gobetti 101, I-40129 Bologna, Italy*

We have analyzed COBE/*FIRAS* maps searching for an isotropic foreground at submillimetre wavelengths by exploiting the map correlation properties without requiring additional data sets to subtract the contribution of the Galaxy. We claim that the *rms* brightness is given by $(\nu I_\nu)_{rms} \simeq 4 \times (\lambda/400\mu\mathrm{m})^{-3.1}\mathrm{nWm}^{-2}\mathrm{sr}^{-1}$ for $\lambda \geq 400\mu$m. The genus distributions of the diffuse light maps are consistent with a random gaussian field with a coherence angle $\sim 5°.9$, in agreement with COBE-*DMR*. Also, in agreement with the indications inferred from galaxy catalogues, at angular scales ranging from few degrees to few tens of degrees we find a steepening of the angular autocorrelation function with respect to the behaviour derived from galaxy surveys at smaller angular scales. These evidences strongly support the extragalactic origin of the detected residual far-infrared background.

1 Introduction

The far-infrared and millimetre background originates from a variety of discrete sources and diffuse emissions, from our galaxy and external galaxies; just a small fraction is coming from distant faint galaxies. The cosmic far-infrared and millimetre background (CFIR/*mm*) should contain informations on the re-processing of the star light by dust produced during the early phases of stellar evolution in the galaxies (Mazzei & De Zotti [1]), the evolution function of the galaxies (Franceschini *et al.* [3]) and their clustering pattern, related to the primordial power spectrum of the density field (Bond *et al.* [2]).

Recently Puget *et al.*[4] claimed the existence of a cosmic far-infrared background component in *FIRAS* data in the 400-800μm range, with a spectrum that indicates the possible presence of sources at high redshift. Also, an isotropic component with similar spectral shape was found in *FIRAS* data by Fixsen *et al.* [5], at an intensity level in agreement within a factor of $\simeq 1.5$ with that obtained by Puget *et al.*[4]. Upper limits of the dark sky surface intensity from COBE-*FIRAS* maps have been also derived by Shafer *et al.*[6] by a technique that analyses for spatially correlated errors in the *FIRAS* data.

We have recently analysed the COBE-*FIRAS* data (Burigana & Popa [7]) tooking the advantage of their continuous spectral coverage in the relevant spectral window between ~300 and ~1500 GHz that permits the foregrounds removal and in the same time the measurement of the angular autocorrelation function. The method based on the correlation properties of the diffuse light was also successfully applied in V (Shectman [8]) and UV (Martin & Bowyer [9]) bands and by the *DIRBE* team (Kashlinsky [10], Kashlinsky *et al.* [11]).

The contribution to the CFIR/*mm* from early type of galaxies is expected to exibit angular correlations that reflect their spatial correlations (Shectman [8]; Cole *et al.* [12]). In the context

of Gaussian fluctuations models, the power spectrum $P(k)$ or equivalently the spatial galaxy correlation function $\xi(r)$ define the statistical properties of the density field. They are related through $\xi(r) = 1/(2\pi^2)\int_0^\infty P(k) j_0(kr) k^2 dk$, where $j_n(x)$ is n-th order Bessel function. The angular autocorrelation function C(ϑ) is related with $\xi(r)$ via the Limber equation (Peebles[13], Kashlinsky *et al.*[11]):

$$C(\vartheta) = \int_0^\infty A_\vartheta(z) \left(\frac{d\nu I_\nu}{dz}\right)^2 \Psi^2(z)(1+z)^2\sqrt{1+\Omega z}\, dz, \qquad (1)$$

where it was assumed a null cosmological constant Λ and the small angle approximation ($\vartheta \ll 1$); Ω is the density in units of the critical density; $\Psi(z)$ is a function that accounts for the evolution of the clustering pattern and is defined to be unity at $z = 0$; $A_\vartheta(z)$ relates directly to $\xi(r)$ (Kashlinsky[10]) through: $A_\vartheta(z) = 2R_H^{-1}\int_0^\infty \xi\sqrt{u^2 + [x(z)\vartheta/(1+z)]^2}du$, where $x(z)$ is the comoving distance, $R_H = cH_0^{-1}$, H_0 being the Hubble constant, and $u = cdt/dz$.
After the convolution with the *FIRAS* beam that has FWHM $\tau = 7°$, the autocorrelation function at zero-lag $C(0)$ can be written as (Kashlinsky *et al.*[11]):

$$C(0) = \int_0^\infty A_\tau(z) \left(\frac{d\nu I_\nu}{dz}\right)^2 \Psi^2(z)(1+z)^2\sqrt{1+\Omega z}dz, \qquad (2)$$

where $A_\tau(z) = (1/(2\pi R_H))\int_0^\infty P_0(k) k\, W(kx(z)\tau/(1+z))\, dk$, $P_0(k)$ is the power spectrum of the galaxy clustering at the present epoch, and $W(x) = (3j_1(x)/x)^2$ is the beam window function; the small angle approximation allows to separate the angular dependence of the correlation function from the integral in eq. (2) (nevertheless this factorization works quite well also to $\vartheta \sim 30°$, Peebles[13]).
Eq. (2) can be used to place an upper limit on the *rms* brightness of the diffuse light field:

$$(\nu I_\nu)_{z,rms} = \int_0^\infty (d\nu I_\nu/dz)^2 \Psi^2(z)(1+z)^2\sqrt{1+\Omega z}\, dz \le \sqrt{C(0)/min(A_\tau(z))}\,. \qquad (3)$$

The analysis of the two-point correlation function obtained from APM galaxy catalogue (Maddox *et al.*[20]) shows at small angular scales a power law dependence of the correlation function, $C(\vartheta) \propto \vartheta^{-\gamma}$, with a spectral index $\gamma \simeq 0.7$, which implies $\xi(r) \approx r^{-1-\gamma}$ and $P(k) \approx k^{\gamma-2}$ (Kashlinsky[10], Baugh & Efstathiou[14]).

2 Data analysis and foregrounds removal

FIRAS is a four-port (two input, two output) Michelson Interferometer (COBE-*FIRAS* Explanatory Supplement[15]). For the purpose of this work we took the data from LLSS (30-660 GHz) and RHSS (60-2880 GHz) modes which produce spectra with a resolution of 4.2 GHz and 16.9 GHz respectively. The data cover 95% of the sky with an angular resolution $FWHM = 7°$. There are 6144 pixels in the maps with a pixel separation angle about 2°.6; each pixel in the sky consists of a spectrum with 34 and 166 points for LLSS and RHSS modes respectively.

For each pixel we fit the spectra in the considered frequency range with different components. *i)* A monopole spectrum modelled with a Planck function $B_\nu(T_0)$ at a temperature of $T_0 = 2.728(\pm 0.009$K at the 1σ level, Mather *et al.*[16], Fixsen *et al.*[5]). *ii)* A dipole spectrum fitted by the derivative of the Planck function as in Fixsen *et al.*[5] and Shafer *et al.*[6]. *iii)* The contribution of the galactic dust described by using a spectral model with two modified blackbodies (for "cold" and "warm" galactic dust) and a ν^2 emissivity law (Reach *et al.*[17]), that we found to give the best description of our data in terms of the χ^2. The spectral lines were fitted and removed using the appropriate data files containing the spectral intensities and line shapes. *iv)* The contribution of the Zodiacal light was modelled for each *FIRAS* pixel by taking the 25μm *DIRBE* latitude profile scaled by $0.167(\nu/100\mu\text{m})^{-3}$ (Reach *et al.*[17]; Puget *et al.*[4]).

The residual spectra obtained for each pixel are characterized by a number of bright discrete sources that must be eliminated. We have used for this purpose the wavelets filtering of the spectra (Press *et al.*[18]). We have tested different clipping thresholds. The choice of threshold values of 2.5 and 4.6 respectively for LLSS and RHSS maps allows to have a distribution of the residual intensities, after the mean has been subtracted, close to a gaussian distribution and a *rms* surface intensity value at each frequency above the corresponding *FIRAS* instrumental noise. The residuals obtained in this way were used to construct weighted averaged maps over the frequency window considered for both LLSS and RHSS. In this way the correlations existing between adiacent frequency channels are reduced.

We have analysed the topological structure of the maps to test if their fluctuations reflect Gaussian density perturbations with random phases, as expected if their origin is cosmological. We have examined the distribution of spots with the intensity above same threshold and found that the histograms are skew, with a clear gaussian shape. We have then computed another useful topological discriminator, the number of genus defined as the excursion regions enclosed by isobrightness contours (Gott *et al.*[19]). The found shapes of the genus distributions are typical for a random Gaussian field with a coherence angle $\vartheta_c = 5°.9$, in good agreement with the results based on the analysis of temperature correlation function of *DMR* data.

3 Results and discussion

The upper limits on the fluctuations of CFIB/*mm*, calculated here as the *rms* surface intensity at each frequency, offer a powerful test of any model of its sources. We analysed the frequency dependence of $\sqrt{C(0)}$ for different fields: two $20° \times 20°$ regions centred on the ecliptic poles, a $10° \times 10°$ field around the Lockman region, two fields at $b > 60°$ and $b < -60°$, and the entire maps LLSS and RHSS excluding the pixels within $|b| \leq 10°$. The results from all the investigated fields are in good agreement on each other and we find a high isotropy of the $\sqrt{C(0)}$. Figure 1 compares our results with the previous results in terms of νI_ν versus λ. Translated in upper limits for $(\nu I_\nu)_{rms}$, for $\lambda \geq 400\mu$m, the frequency dependence of $\sqrt{C(0)}$ implies:

$$\sqrt{min A_\tau(z)} \times (\nu I_\nu)_{rms} \leq (3.64 \pm 0.02) \times \left(\frac{\lambda}{400\mu\mathrm{m}}\right)^{-3.1\pm0.01} \mathrm{nWm^{-2}sr^{-1}}\,. \qquad (4)$$

Although our approach is in principle devoted to find upper limits for $(\nu I_\nu)_{rms}$, we refitted the experimental spectra by adding a new component with the same frequency dependence found for $\sqrt{C(0)}$, in order to give an estimate of the residual brigthness. From the entire maps ($|b| \geq 10°$) we have found $(\nu I_\nu)_{rms} = (1.18 \pm 0.01)\sqrt{C(0)}$.

The high isotropy of this component can be interpreted in terms of emission by a galactic halo at high distance from the galactic centre (Fixsen *et al.*[5]) or in terms of integrated emission from distant galaxies (Puget *et al.*[4]) with a bulk of star formation rate at relevant redshift. To distinguish between these two possibilities, we have derived the angular autocorrelations function $C(\vartheta)$ of submillimetre diffuse light in ten frequency windows of 100 GHz width by averaging over the frequency the LLSS and RHSS maps. In the angular range $2.6° < \vartheta \lesssim 30°$ power law approximations $[C(\vartheta) \propto \vartheta^{-\gamma}]$ fit quite well the data. Our uncertainty in the determination of the spectral index γ at each band is relatively large and we find a spreading of its value with the wavelength, ranging γ from 1.2 to 3.2 (including 1σ error), with a possible steepening of the angular autocorrelation function with the frequency.

In spite of these uncertainties, our result is substantially in agreement with the evidence of a steepening of the galaxy angular autocorrelation function at scales larger than few degrees, found from the Lick survey and from the APM catalogue (Maddox *et al.*[20,21], Baugh & Efstathiou[14]). This evidence further supports the extragalactic origin of the detected diffuse light like that predicted by the model of Franceschini *et al.*[3] which takes into account the galaxies luminosity

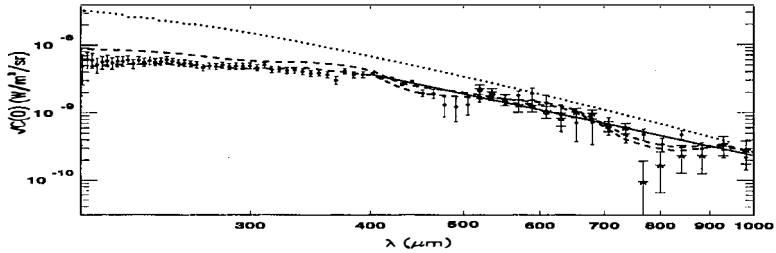

Figure 1: $\sqrt{C(0)}$ as a function of wavelength for LLSS (stars) and RHSS (filled points) [error bars at the 1σ level] and our corresponding power law best fit for $\lambda \geq 400\mu$m (solid line); upper limit from Shafer *et al.*[6] (dotted line); the residual brightness found by Puget *et al.*[4] (dashed lines) without (upper curve) and with (lower curve) subtraction for ionized gas.

evolution. The level and the power law dependence of this extragalactic component constraint the redshift (2.1–3.8) and the metallicity production rate of this active phase of star formation rate and dust reprocessing (Burigana *et al.*[22]) with implications for the level of discrete source fluctuations (Toffolatti *et al.*[23]) at millimetre and sub-millimetre wavelengths.

References

1. P. Mazzei and G. De Zotti, MNRAS 279, 535 (1996).
2. J.R. Bond *et al.*, ApJ 306, 428 (1986).
3. A. Franceschini *et al.*, ApJ 427, 140 (1994).
4. J.L. Puget *et al.*, A&A 308, 5 (1996).
5. D.J. Fixsen *et al.*, ApJ 473, 576 (1996).
6. R.A. Shafer *et al.*, preprint submitted to ApJ (1997).
7. C. Burigana and L. Popa, A&A, in press (1998).
8. S. Shectman, ApJ 188, 233 (1974).
9. C. Martin and S. Bowyer, ApJ 338, 677 (1989).
10. A. Kashlinsky, ApJ 399, L1 (1992).
11. A. Kashlinsky *et al.*, ApJ 470, 681 (1996).
12. S. Cole *et al.*, ApJ 385, 9 (1992).
13. P.J.E. Peebles, "Large Scale Structure of the Universs", Princeton Univ. Press (1980).
14. C.M. Baugh and G. Efstathiou, MNRAS 265, 145 (1993).
15. COBE-*FIRAS* Expl. Suppl., ed. J.C. Mather *et al.*, COBE Ref. Pub. No.95-C (1995).
16. J. Mather *et al.*, ApJ 420, 439 (1994).
17. W.T. Reach *et al.*, ApJ 451, 188 (1995).
18. W. Press *et al.*, "Numerical Recipes in Fortran", Cambridge Univ. Press (1992).
19. J.R. Gott *et al.*, ApJ 352, 1 (1990).
20. S. Maddox *et al.*, MNRAS 242, 43 (1990).
21. S. Maddox *et al.*, MNRAS 283, 1227 (1996).
22. C. Burigana *et al.*, MNRAS 287, L17 (1997).
23. L. Toffolatti *et al.*, MNRAS, in press (preprint astro-ph/9711085) (1997).

NEW APPROACHES TO MEASURE FUNDAMENTAL PARAMETERS

Testing Ω_0 from Clusters: Low and High Redshift

A. BLANCHARD, J.BARTLETT, R.SADAT
Observatoire astronomique de Strasbourg, ULP, CNRS, UMR 7550,
11, rue de l'université, 67 000 Strasbourg, France

Galaxy clusters properties provide some of the most stringent constraints on models of galaxy formation, essentially because clusters are rare objects and, hence, their properties are sensitive to the underlying density fluctuations. I briefly discuss how cluster can be used to constrain cosmological parameters and how a self-consistent modeling of X-ray clusters can be build, including their evolution properties, in a way to match available observations. Such a modeling is over-constrained, and therefore is rather robust. This offers an interesting way to constrain the amplitude of mass fluctuations: the amplitude from clusters on a scale of $8h^{-1}\Omega_0^{-1/3}$ Mpc is independent of the spectrum (but σ_8 is not). The shape of power spectrum can be usefully constrained in critical model, ruling out the standard CDM spectrum and favors CDM like spectrum with $\Gamma \leq 0.3$. An other interesting aspect is the redshift evolution of the properties of clusters: measurement of this evolution is able to allow one to determine the mean density of the universe. Preliminary applications of this test on X-ray clusters provide evidence for a high density universe.

1 Cosmological constraints from X-ray clusters

1.1 The M/L ratio.

This is the historical way to determine the mean density of the universe from clusters. The basic idea is to have an estimate of the mass of a cluster and a measure of the light in the same region the ratio of these two quantities in solar units is called the mass to light ratio, M/L. Provide that we know reasonably well the amount of light ρ_L we can estimate the mass density of the universe, by assuming the M/L ratio to be universal:

$$\rho_m = M/L\rho_L \tag{1}$$

Equivalently this can be expressed in term of the density parameter of the universe:

$$\Omega_0 = \frac{M/L}{(M/L)_c} \tag{2}$$

Typical value for the M/L are $300 - 600h$, while the typical $(M/L)_c$ are of the order of $1500h$, leading to $\Omega_0 \approx 0.3$. Those number suffer from uncertainties however: the analysis of Coma by White et al. (1993) leads to $M/L \approx 600h$ and Zucca et al. (1998) found a higher luminosity density than previously known leading to $(M/L)_c \approx 1000h$. This gives an interesting high value of $\Omega_0 \approx 0.6$. However, the M/L argument should be corrected for stellar population: clusters contain essentially early type galaxies, while the field is dominated by late type. This may contributes to a 50% change. However this raises doubts on the whole argument: one can worry in which band is Eq. 1 giving the right estimate? Is it safe to consider that the fraction of the universe in a stellar form (representing probably less than $\Omega_* \sim 0.01$) is universal, when ones knows that the stellar population varies from place to place, and that there are some indications that the luminosity function varies either? The possibility that the M/L in clusters may not be representative of the universe (also may be because our mass estimates are incorrect) has been advocated in the biased picture. It is interesting to notice that many cosmologists were much more reluctant to the idea of an antibias. However the argument on stellar population provides an argument for it...

1.2 Gas in clusters

In a similar way to the previous analysis we can estimate the value of the $M_{\rm gas}/L$ ratio. Again the analysis of the Coma cluster gives :

$$M_{\rm gas}/L \sim 30h^{-1/2} \tag{3}$$

which leads to :

$$\Omega_{\rm gas} \sim 0.03h^{-3/2} \tag{4}$$

This value is interestingly close to the nucleosynthesis value:

$$\Omega_{\rm bbn} \sim 0.0144h^{-2}\left(\frac{\eta_{10}}{4}\right) \tag{5}$$

White et al. (1993) have estimated the ratio of baryonic matter to dark matter in the Coma cluster and point out that its value was inconsistent with primordial nucleosynthesis in a $\Omega_0 = 1$ universe. The argument is the following. The baryonic fraction, *assuming* the dark matter to be non-baryonic, in a cluster is typically:

$$f_{\rm b} \sim 0.06h^{-2}\left(\frac{\eta_{10}}{4}\right) \tag{6}$$

(Evrard, 1997). This is expected to be of the order of:

$$f_{\rm bbn} \sim \frac{\Omega_{bbn}}{\Omega_0} \tag{7}$$

With the above value of $\Omega_{\rm bbn}$, this leads to :

$$\Omega_0 \sim 0.24h^{-1/2}\left(\frac{\eta_{10}}{4}\right) \tag{8}$$

apparently inconsistent with $\Omega_0 = 1$, unless ones advocates a high η_{10}, marginally consistent with the low Deuterium recently claimed and a low Hubble constant, $h \sim 0.35$, (Bartlett et al., 1995).

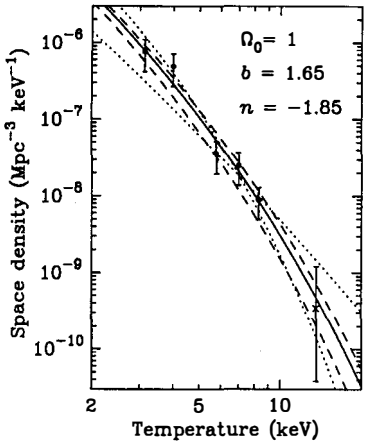

Figure 1: Temperature distribution function. The circles are the data points from Henry & Arnaud (1992) (these values are the original ones, which may need to be revised accordingly to Henry (1997)), while the cross figures A2163. The continuous line is the best fitting model $n = -1.85$ and $b = 1.65$, the other lines represents models at the two sigma level.

2 Constraining the Primordial Power Spectrum

The abundance of clusters can be fruitfully used to constraint cosmological scenario. We refer the reader to J.Bartlett (1997) for a recent review on the subject.

The way to constrain the power spectrum relies on the Press and Schechter formula which seems to fit extremely well the mass function as determined from numerical simulations. Furtheremore, numerical simulations (see for instance Evrard, Metzler & Navarro 1996) show that the temperature of the gas in a cluster is tighly related to its virial mass:

$$T = 4M_{15}^{2/3}(1+z)\mathrm{keV} \tag{9}$$

M_{15} should be understood as the mass enclosed in a spherical region with a contrast density given by the spherical model (in the case $\Omega_0 = 1$ this value is 178, for the open cases, see the appendix of Oukbir and Blanchard, 1997, OB97 hereafter). This mass-temperature relation is unsensitive to the cosmological background density. In this approach, the only uncertainty may come from the procedure used to identify clusters: quite often the PS formula is checked against the friend of friend algorithm while the PS objects are defined by a spherical overdensity. Both definitions seem to lead to the same mass function anyway (Borgani et al., 1998).

The temperature mass relation can be established in a simple way from the hydrostatic equilibrium equation, leading to a temperature 20% larger than Eq. ??. The knowledge of the temperature function and of the temperature-mass relation allows one to compare models to observations and to infer the best parameters of the models. An example of this fitting procedure is presented in figure 1 in the case $\Omega_0 = 1$. An alternative approach consist to normalize the models to the luminosity function which needs the additional knowledge of the luminosity-temperature relation. Such a procedure has been followed by Mathiesen & Evrard (1997) for

instance. Oukbir, Blanchard & Bartlett 1997 (OBB97 hereafter) have shown that such a procedure should lead to similar results basically because the temperature distribution function given by Henry and Arnaud (1991) is consistent with the luminosity function, derived from EMSS, but also with those derived from ROSAT, provide that one uses the observed relation between luminosity and temperature.

3 Redshift evolution

One of the most exciting possibility is the perspective first outlined by Oukbir and Blanchard (1992): the evolution of the abundance of X-ray clusters is a probe of the mean density of the universe.

More recenttly, OB97 showed that the evolution of the number of clusters at a given mass for models which are normalized to present-day abundance of X-ray clusters does not depend on the spectrum but is sensitive to Ω_0. A direct application of this test requires the knowledge of the temperature distribution function at high redshift. A quantity which was not available until very recently. Henry (1997) has presented a first tentative application of this test on the basis of 10 clusters. OB97 have proposed an alternative method to measure Ω_0 from existing data, by using the evolution of the $L_x - T_x$ relation. This is based on the fact that in order to reproduce the redshift distribution of the EMSS X-ray clusters, OB97 found that it was necessary to introduce an evolving $L_x - T_x$ relation:

$$L_x \approx 0.05 T_x^3 (1+z)^\beta \tag{10}$$

(L_x being in units of 10^{44} erg/s and T_X in keV) with an evolution which sensitively varies with Ω_0:

$$\beta \sim 4.\Omega_0 - 3. \tag{11}$$

Therefore the measure of β may provide an estimate of Ω_0, althought realistic uncertainty on the relation between β and Ω_0. Similar conclusions have been reached by Reichert et al. (1998) and Borgani et al (1998), the latter using ROSAT distribution function. This last work is a very interesting confirmation as it comes from an independent survey.

number counts

An interesting test of the models self-consistency is to compute the number counts. This number counts were *predicted* by OB97 before any publications of the observed ROSAT counts. This predicted counts are presented on figure 2, with comparison with some of the available data. As one can see from figure 2, our predictions are in good agreement with data. Mathiesen & Evrard (1997) have fitted number counts and have basically confirmed our results, although they get a steeper relation between β and Ω_0.

4 Applications of the test

The first measurments of Ω_0 based on the redshift evolution of the number density of X-ray clusters has been provided by Henry (1997) and by Sadat et al (1998). Eke et al. (1998) have reanalysed the data of Henry (1997) and reached essentially identical conclusion. Carlberg et al. (1997) and Fan et al (1997) apply a similar measurement based on velocity dispersion. The result obtained by these groups are somewhat different, ranging from $\Omega_0 \sim 0.3$ (Carlberg et al., 1997; Fan et al, 1997) to $\Omega_0 \sim 0.85$(Sadat et al., 1998). Blanchard and Bartlett (1998) have adressed the difference between those results, and showed that the data used by Carlberg et al.

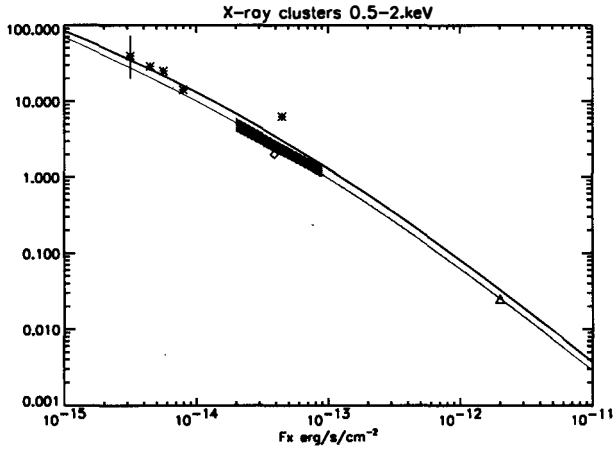

Figure 2: Predicted number counts by OB97 and OBB97 compared to some published numbers. The number counts at the fainter flux (stars) comes from McHardy et al. (1997).

(1997) and Fan et al (1997) were consistent with a high Ω_0. Henry's analysis and its revised version by Eke et al. (1998) provides a convincing evidence for an intermediate value $\Omega_0 \sim 0.5$. However, in practice this test is delicate : in order to reach a meaningful conclusion, one has to be sure that the temperature has been properly estimated at both low and high redshift. This is far from being reached, as one is looking for differences which are of the order of a factor of two (between redshift 0.1 to 0.3). For instance, the number of 4 keV clusters found by Henry and Arnaud (1992) in their first analysis was nearly ten times higher than what was found by Edge and Steward (1991). More recently the analysis of Eke et al (1998) differs from White, Efstathiou & Frenk (1993) by a factor of 5. Therefore. it is likely that the primary source of difference in these analyses comes from using different abundances of clusters and it is premature to conclude given the present-day uncertainties. However, one may use a different approach based on the evolution of the luminosity function. In principle this quantity is not well understood from theoretical point of view, and therefore its use could be misleading if some evolution goes in it. On the other hand using the luminosity function is easier in order to undertand the selection criteria and it offers a more robust statistics. Blanchard and Bartlett (1998) have computed the number evolution of clusters at a given bolometric luminosity ($L_{bol} \approx 8.10^{44}$ erg/s/cm^2). From a comparison of the luminosity function at $z = 0.66$ to the local one (assuming $z = 0.$) they found that the number of clusters has changed by a factor of nearly six. This is the strongest evidence for evolution in the cluster population. During this conference, several others groups have shown similar results based on ROSAT distant clusters. Sadat et al. (1998) found an evidence for a slightly positive evolution in $L_x - T_x$: $\beta = 0.5 \pm 0.5$. Therefore the observed decrease in the number of clusters at a given bolometric luminosity is a direct evidence for a decrease in the number of clusters at a fixed temparture. This data suggest that the number of ~ 5 keV clusters have increased be factor of at least 5 since the epoch $Z = 0.66$. The advantage of this comparison has to be outlined once again: we compared clusters with identical bolometric luminosities which are expected to be clusters with identical temperature in the absence of evolution in $L_x - Tx$. Assuming $\sigma_8 = 0.6\Omega^{0.5}$ leads to $\Omega = 0.75$, in agreement with Sadat et al. (1998), under the asumption of no evolution ($\sigma_8 = 0.5\Omega^{0.5}$ would lead to $\Omega \approx 0.6$). The values they got are 13% higher because of the small positive evolution found in the observed $L_x - T_x$.

5 Conclusion

The new cosmological test of the mean density of the universe proposed by Oukbir and Blanchard (1992) based on the evolution in the number density of X-ray clusters can potentially offer a reliable answer: this test is based on a dynamical estimate of the mean density of the universe as a whole and is therefore likely to be free of the problems encountered by standard methods. First estimates by different groups have led to relatively high value of the density parameter in the range 0.45 to 0.85, which are consistent between each other at the 2σ level. It is likely that more detailled analysis, as well as more well-controlled high-Z clusters samples will allow rapidly a better measurement. It might also be that we will discover a new kind of systematics which forbids to perform this test in an usefull way... However, this step has not yet been reached until now!

Acknowledgments

There are too many other collegues that we would like to thank here for discussion on this question. One of us, AB, want however to thank M. Arnaud for her patience in answering all his questions on various aspects of X-ray observations of clusters during these last years.

References

1. J., Bartlett, *From Quantum Fluctuations to Cosmological Structures*, D., Valls-Gabaud, M.A.Hendry, P.Molaro, K.Chamcham, *A.S.P. Conf. Ser.*, **vol. 126**, p 365, (1997).
2. J., Bartlett, A., Blanchard J., Silk, M.S., Turner *Science*, **267**, 980 (1995)
3. A., Blanchard, J., Bartlett, *A&A* , in press (1998).
4. S., Borgani, P., Rosati, P., Tozzi, C., Norman, 1998, *ApJ*, submitted.
5. V., Eke, S., Cole, C.S.F., Frenk, *MNRAS* **282**, 263 (1996).
6. V., Eke et al., astro-ph/9802350
7. A.E., Evrard, astro-ph/9701148
8. X., Fan, N.A., Bahcall, R., Cen, *ApJ* **490**, L123 (1997)
9. J.P, Henry, K.A., Arnaud *ApJ* **372**, 410 (1991)
10. J.P, Henry,*ApJ* **489**, L1 (1997)
11. I.M., McHardy et al., astro-ph/9703163
12. B,. Mathiesen, A. E., Evrard, astro-ph/9703176.
13. J., Oukbir, A., Blanchard *A&A* **262**, L21 (1992)
14. J., Oukbir, A., Blanchard *A&A* **317**, 10 (1997)
15. J., Oukbir, A., J.G., Bartlett, Blanchard, *A&A* **320**, 365 (1997)
16. Reichart et al, 1998, astro-ph/9802153
17. R., Sadat, A., Blanchard 1998, J., Oukbir, *A&A* **329**, 21 (1998)
18. S.D.M., White, G., Efstathiou, C.S.F., Frenk *MNRAS* **262**, 1023 (1993).
19. S.D.M., White, J.F., Navarro, A.E., Evrard *Nature* **366**, 429 (1993)
20. H. Zucca *et al*, *A&A* , in press (1998).

The $\Omega_M - \Omega_\Lambda$ Constraint from CNOC Clusters

R. G. Carlberg[1,2,8], H. K. C. Yee[1,2], E. Ellingson[1,3], S. L. Morris[1,4], H. Lin[1,2], M. Sawicki[1,2], D. Patton[1,6], G. Wirth[1,6], R. Abraham[1,4,5], P. Gravel[1,2], C. J. Pritchet[1,6], T. Smecker-Hane[1,4,7] D. Schade[4], F. D. A. Hartwick[6] J. E. Hesser[4], J. B. Hutchings[4], & J. B. Oke[4]

[1] *Visiting Astronomer, Canada-France-Hawaii Telescope, which is operated by the National Research Council of Canada, le Centre National de Recherche Scientifique, and the University of Hawaii.* [2] *Department of Astronomy, University of Toronto, Toronto ON, M5S 3H8 Canada.* [3] *Center for Astrophysics & Space Astronomy, University of Colorado, CO 80309, USA.* [4] *Dominion Astrophysical Observatory, Herzberg Institute of Astrophysics, National Research Council of Canada, 5071 West Saanich Road, Victoria, BC, V8X 4M6, Canada.* [5] *Institute of Astronomy, Madingley Road, Cambridge CB3 OHA, UK.* [6] *Department of Physics & Astronomy, University of Victoria, Victoria, BC, V8W 3P6, Canada.* [7] *Department of Physics & Astronomy, University of California, Irvine, CA 92717, USA.* [8] *on leave at: Carnegie Observatories, 813 Santa Barbara Street, Pasadena, CA 91101, USA.*

The CNOC redshift survey of galaxy clusters measures Ω_M from $\Omega_e(z) = M/L \times j/\rho_c$ which can be applied on a cluster-by-cluster basis. The mass-to-light ratios, M/L, are estimated from rich galaxy clusters, corrected to the field population over the $0.18 \leq z \leq 0.55$ range. Since the luminosity density depends on cosmological volumes, the resulting $\Omega_e(z)$ has a strong dependence on cosmology which allows us to place the results in the $\Omega_M - \Omega_\Lambda$ plane. The resulting Ω_M declines if $\Omega_\Lambda > 0$ and we find that $\Omega_\Lambda < 1.5$.

1 Introduction

In the Friedmann-Robertson-Walker solution for the structure of the universe the geometry and future of the expansion uniquely depend on the mean mass density, ρ_0, and a possible cosmological constant. It is a statement of arithmetic[16] that at redshift zero $\Omega_M \equiv \rho_0/\rho_c = M/L \times j/\rho_c$, where M/L is the average mass-to-light ratio of the universe and ρ_c/j is the closure mass-to-light ratio, with j being the luminosity density of the universe. Estimates of the value of Ω_M have a long history with a substantial range of cited results[2]. Both the "Dicke coincidence" and inflationary cosmology would suggest that $\Omega_M = 1$. The main thrust of our survey is to clearly discriminate between $\Omega_M = 1$ and the classical, possibly biased, indicators

that $\Omega_M \simeq 0.2$.

Rich galaxy clusters are the largest collapsed regions in the universe and are ideal to make an estimate of the cluster M/L which can be corrected to the value which should apply to the field as a whole. To use clusters to estimate self-consistently the global Ω_M we must, as a minimum, perform four operations.

- Measure the total gravitational mass within some radius.
- Sum the luminosities of the visible galaxies within the same radius.
- Measure the field luminosity density at the cluster redshift.
- Understand the differential luminosity and density evolution between the clusters and the field.

2 Survey Design

The Canadian Network for Observational Cosmology (CNOC) designed observations to make a conclusive measurement of Ω_M using clusters[20]. The clusters are selected from the X-ray surveys, primarily the Einstein Medium Sensitivity Survey[12,13,11], which has a well defined flux-volume relation. The spectroscopic sample, roughly one in two on the average, is drawn from a photometric sample which goes nearly 2 magnitudes deeper, thereby allowing an accurate measurement of the selection function. The sample contains 16 clusters spread from redshift 0.18 to 0.55, meaning that evolutionary effects are readily visible, and any mistakes in differential corrections should be more readily detectable. For each cluster, galaxies are sampled all the way from cluster cores to the distant field. This allows testing the accuracy of the virial mass estimator and the understanding of the differential evolution process. We introduce some improvements to the classical estimates of the velocity dispersion and virial radius estimators, which have somewhat better statistical properties. A critical element is to assess the errors in these measurements. The random errors are relatively straightforward and are evaluated using either the statistical jackknife or bootstrap methods[10], which follow the entire complex chain of analysis from catalogue to result. The data are designed to correct from the M/L values of clusters to the field M/L.

3 Results

We find[6] that $\Omega_M = 0.19 \pm 0.06$ (in a $\Omega_\Lambda = 0$ cosmology, which is the formal 1σ error. In deriving this result we apply a variety of corrections and tests of the assumptions.

- The clusters have statistically identical M/L values, once corrected for evolution[5].
- High luminosity cluster and field galaxies are evolving at a comparable rate with redshift, approximately one magnitude per unit redshift.
- Cluster galaxies have no excess star formation with respect to the field[1,3].
- Cluster galaxies are 0.1 and 0.3 magnitudes fainter than similar field galaxies[6,18,19,14].
- The virial mass overestimates the true mass of a cluster by about 15%, which can be attributed to the neglect of the surface term in the virial equation[6].
- There is no significant change of M/L with radius within the cluster[6].
- The mass field of the clusters is remarkably well described by the NFW[15] profile, both in shape and scale radius[8].
- The evolution of the number of clusters per unit volume is very slow, in accord with the PS[17] predictions for a low density universe[7].
- The clusters have statistically identical efficiencies of converting gas into stars, which is consistent with the value in the field[9].

These results rule out $\Omega_M = 1$ in any component with a velocity dispersion less than about 1000 $\mathrm{km\,s^{-1}}$.

4 Ω_Λ dependence

The luminosity density, j, contains the cosmological volume element which has a very strong cosmology dependence. The cosmological dependence of the $\Omega_e(z)$ can be illustrated by expanding the cosmological terms to first order in the redshift, z,

$$\Omega_e(z) \simeq \Omega_M[1 + \frac{3}{4}(\Omega_M^i - \Omega_M + 2\Omega_\Lambda)z], \quad (1)$$

where Ω_M and Ω_Λ are the true values and Ω_M^i with $\Lambda = 0$ is the cosmological model assumed for the sake of the calculation[4]. If there is a non-zero Λ then $\Omega_e(z)$ will vary with redshift. The available data are the CNOC1 cluster M/L values and the 3000 galaxies of the preliminary CNOC2[21] field sample for j. To provide a well defined $\Omega_e(z)$ we limit both the field and cluster galaxy luminosities at $M_r^{k,e} \leq -19.5$ mag, which provides a volume limited sample over the entire redshift range. A crucial advantage is of using high luminosity galaxies alone is that they are known to have a low average star formation rate and evolve slowly with redshift, hence their differential corrections are small, and reasonably well determined[6]. The results are displayed in Figure 1. The fairly narrow redshift range available does not provide a very good limit on Ω_Λ, although values $\Omega_\Lambda > 1.5$ are ruled out. The power of this error ellipse is to use it in conjunction with other data, such as the SNIa results which provide complementary constraints on the $\Omega_M - \Omega_\Lambda$ pair.

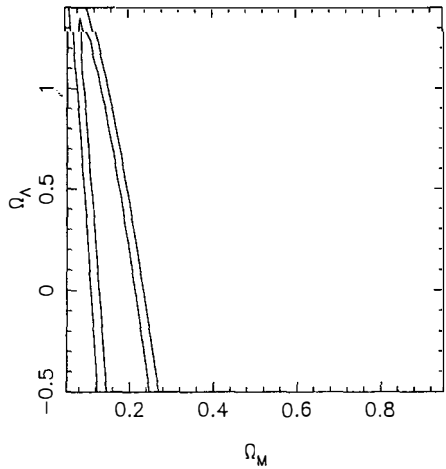

Figure 1: The CNOC1 cluster M/L values combined with the CNOC2 measurements of j for $M_r^{k,e} \leq -19.5$ mag galaxies, gives an $\Omega_e(z)$ which leads to the plotted χ^2 (68% and 90% confidence) contours.

The limit on the $\Omega_M - \Omega_\Lambda$ pair in Figure 1 has been corrected for known systematic errors which are redshift independent scale errors in luminosity and mass. The high luminosity galaxies in both the cluster and field populations are evolving at a statistically identical rate with redshift, which is close passive evolution. If the cluster galaxies are becoming more like the field with redshift (*i. e.* the Butcher-Oemler effect, which is partially shared with the field), so that they need less brightening to be corrected to the field, then that would raise the estimated Ω_Λ, although the correction is so small that the correction would be $\Delta\Omega_\Lambda \simeq 0.3$ over this redshift interval. The results are completely insensitive to galaxy merging that produces no new stars. The data indicate that there is no excess star formation in cluster galaxies over the observed redshift range, with galaxies fading as they join the cluster[6,3]. The fact that evolution of the

high luminosity field galaxies is very slow and consistent with pure luminosity evolution[6] (Lin, *et al.* in preparation) gives us confidence that the results are reasonably well understood. It will be very useful to have data that extends to both higher and lower redshift, which would allow a measurement of Ω_Λ and better constraints on any potential systematic errors.

References

1. Abraham, R. G., Smecker-Hane, T. A., Hutchings, J. B., Carlberg, R. G., Yee, H. K. C., Ellingson, E., Morris, S. L., Oke, J. B., & Rigler, M. 1996, ApJ, 471, 694
2. Bahcall, N. A., Lubin, L. M., & Dorman, V. 1995, ApJ(Lett), 447, L81
3. Balogh, M. L., Morris, S. L., Yee, H. K. C., Carlberg, R. G., & Ellingson, E. 1997, ApJ 488, L75
4. Carlberg, R. G. 1997, ApJ, submitted (astroph/9708054)
5. Carlberg, R. G., Yee, H. K. C., Ellingson, E., Abraham, R., Gravel, P., Morris, S. L., & Pritchet, C. J. 1996, ApJ, 462, 32
6. Carlberg, R. G., Yee, H. K. C., & Ellingson, E. 1997, ApJ, 478, 462
7. Carlberg, R. G., Morris, S. L., Yee, H. K. C., & Ellingson, E. 1997b, ApJ(Lett), 479, L19
8. Carlberg, R. G., Yee, H. K. C., Ellingson, E., Morris, S. L., Abraham, R., Gravel, P., Pritchet, C. J., Smecker-Hane, T., Hartwick, F. D. A., Hesser, J. E., Hutchings, J. B., & Oke, J. B. 1997, ApJ(Lett), 485, L13
9. Carlberg, R. G., Yee, H. K. C., Ellingson, E., Morris, S. L., Abraham, R., Gravel, P., Pritchet, C. J., Smecker-Hane, T., Hartwick, F. D. A., Hesser, J. E., Hutchings, J. B., & Oke, J. B. 1997, ApJ, submitted
10. Efron, B. & Tibshirani, R. 1986, *Statistical Science*, 1, 54
11. Gioia, I. M. & Luppino, G. A. 1994, ApJS, 94, 583
12. Gioia, I. M., Maccacaro, T., Schild, R. E., Wolter, Stocke, J. T., Morris, S. L., & Henry, J. P. 1990, ApJS, 72, 567
13. Henry, J. P., Gioia, I. M., Maccacaro, T., Morris, S. L., Stocke, J. T., & Wolter, A. 1992, ApJ, 386, 408
14. Lin, H., Yee., H. K. C., Carlberg, R. G., & Ellingson, E. 1997, ApJ, 475, 494
15. Navarro, J. F., Frenk, C. S. & White, S. D. M. 1997, ApJ, 490, 493
16. Oort, J. H. 1958, in *La Structure et L'Évolution de L'Univers*, Onzième Conseil de Physique, ed. R. Stoops (Solvay: Bruxelles) p. 163
17. Press, W. H. & Schechter, P. 1974, ApJ, 187, 425
18. Schade, D., Carlberg, R. G., Yee, H. K. C., López-Cruz, O. & Ellingson, E. 1996a, ApJ(Lett), 464, L63
19. Schade, D., Carlberg, R. G., Yee, H. K. C., López-Cruz, O. & Ellingson, E. 1996b, ApJ(Lett), 465, L103
20. Yee, H. K. C., Ellingson, E. & Carlberg, R. G. 1996, ApJS, 102, 269
21. Yee, H. K. C., Sawicki, M. J., Carlberg, R. G., Morris, S. L., Patton, D. R., Wirth, G. D., Shepherd, C. W., Ellingson, E., Schade, D., & Marzke, R. 1997 in *Redshift Surveys in the 21st Century*, JD11 at the 23rd IAU General Assembly (astro-ph/971036)

TESTING Ω_0 WITH X–RAY CLUSTERS: A PHYSICAL APPROACH

PAOLO TOZZI
II Università di Roma
E-mail tozzi@roma2.infn.it

The X-ray emission from clusters of galaxies is one of the most pursued observational probe to investigate the distribution of dark matter and the related density parameter Ω_0. The crucial link to derive the statistics of observables from a dynamical theory is constituted by the physics for the diffuse baryons (or ICP) responsible of the X–ray emission. Here we propose a physical model for the ICP which leads to a definite L–T relation. Then we perform a physical–based cosmological test, pointing out three cold dark matter universes: a Tilted critical CDM, a flat CDM with $\Omega_0 = 0.3$, and an Open CDM with $\Omega_0 = 0.5$, which are discussed on the basis of the RDCS survey.

1 Introduction

Groups and clusters of galaxies constitute cosmic structures sufficiently close to equilibrium and with sufficient density contrast ($\delta \approx 2\,10^2$ inside the virial radius R) as to yield definite observables. They are dominated by dark matter (hereafter DM), while the baryon fraction is observed to be less than 20%. The great majority of these baryons are in the form of *diffuse plasma* (ICP) with densities $n \sim 10^{-3}$ cm^{-3} and virial temperatures $kT \sim 5$ keV, and are responsible for powerful X-ray luminosities $L \sim 10^{44}$ erg/s by optically thin thermal bremsstrahlung. As the plasma is a good tracer of the potential wells, much better than member galaxies, the X–ray emission is a powerful tool to investigate the mass distribution out to moderate and high redshifts. The ICP temperature directly probes the height of the potential well, with the baryons in the role of mere tracers; on the other hand, the luminosity with its strong dependence on density ($L \propto n^2$) reliably probes the baryonic content and distribution. Statistically, an average L–T correlation is observed along with substantial scatter, and this provides the crucial link to relate the X-ray luminosity functions with the underlying statistics of the DM.

A physical model for the diffuse baryons is difficult to achieve. In fact, the simple self similar model (Kaiser 1986), which assumes the ICP amount to be proportional to the DM's at all z and M, leads to a relation $L \propto T^2$, conflicting with the observed correlation for rich clusters. The latter is close to $L \propto T^{3.5}$ (David et al. 1993; Mushotzky & Scharf 1997). Here we propose a physical model for baryons, which leads to a prediction for the L–T relation (see Cavaliere, Menci & Tozzi 1997, CMT97) and allows a non parametrical approach to the search for cosmological parameters. The results, presented in §3, are a synthesis from Cavaliere, Menci & Tozzi (1998, CMT98).

2 A physical model for the ICP

Respect to the self-similar model, we indicate the missing ingredient in the stellar energy feedback by supernovae. We assume that such non gravitational heating is efficient in depleting the potential wells of the clusters progenitors, at $z \simeq 1 \div 2$, and in pre-heating the intergalactic medium to temperatures in the range $T_1 = 0.1 \div 0.8$ keV, as recently observed in the outer cluster atmosphere (Henriksen & White 1996).

We describe clusters evolution as a sequence of hierarchical merging episodes of the DM halos; the history of such episodes is followed in the framework of the hierarchical clustering by Monte Carlo simulations based on merging trees consistent with the Press & Schechter (1974) statistics. In the ICP, shocks of various strengths (depending on the temperature ratio between the accreted gas and the plasma in the main progenitor) are associated to such merging events. The shocks provide the boundary conditions for the ICP to re-adjust to a new hydrostatic equilibrium.

2.1 Hydrodynamical equilibrium

In the framework of the hierarchical clustering it is possible to check the assumption of equilibrium. Roettiger, Stone & Mushotzky (1997) showed that after a major merging event, i.e., with a mass ratio less than 2.5, the non thermal contribution to the pressure is negligible after two Gyrs from the epoch of merging. Adopting this as a conservative rule to identify *disturbed* clusters at redshift $z = 0$, we find that the fraction of such clusters (for which the hydrodynamical equilibrium does not fully apply) is always less than 20% in most CDM universes.

The next step is computing the disposition of the ICP in equilibrium in a DM potential well. Then we simply use the hydrostatic equilibrium equation $(dP/dr)/n = -GM(< r)/r^2$, where $n(r)$ is the gas density profile, $M(< r)$ is the mass contained within the radius r (dominated by DM) and P is the pressure. To solve the equation we need the boundary condition, i.e., the density of the gas at the virial radius $n(R)$, and the state equation, that we write for a polytropic gas as $P \propto T n^\gamma$, where γ is the polytropic index treated as a free parameter. The resulting profile is:

$$n(r) = n(R)\Big[1 + \beta\Big(\frac{\gamma - 1}{\gamma}\Big)\Big(\phi(R) - \phi(r)\Big)\Big]^{1/(\gamma-1)}, \qquad (1)$$

where $\phi \equiv V/\sigma_r$ is the adimensional gravitational potential, and $\beta \equiv \mu m_H \sigma_r / kT_2$, with σ_r the line-of-sight velocity dispersion of the DM particles. Here T_2 is ICP the temperature inside the virial radius. The above equation can be considered a generalized β-model (Cavaliere & Fusco-Femiano 1978), which reconduces to the usual isothermal case for $\gamma \to 1$. Thus, before computing the ICP distribution, we need the boundary condition $n(R)$.

2.2 Physics of shocks

We expect the inflowing gas (with velocity v_1) to become supersonic close to R. In fact, many hydrodynamical simulations (see, e.g., Takizawa & Mineshige 1997) show shocks to form, to convert most of the bulk energy into thermal energy, and to expand slowly remaining close to the virial radius. So we take R as the shock position, and focus on nearly static conditions inside, with the internal bulk velocity $v_2 << v_1$.

The post-shock state is set by conservations across the shock not only of the energy, but also of mass and momentum, as described by the Rankine-Hugoniot conditions (see Landau & Lifshitz 1959). These provide at the boundary the temperature jump T_2/T_1, and the corresponding density jump $g \equiv n(R)/n_1$, which reads:

$$g\Big(\frac{T_2}{T_1}\Big) = 2\Big(1 - \frac{T_1}{T_2}\Big) + \Big[4\Big(1 - \frac{T_1}{T_2}\Big)^2 + \frac{T_1}{T_2}\Big]^{1/2} \qquad (2)$$

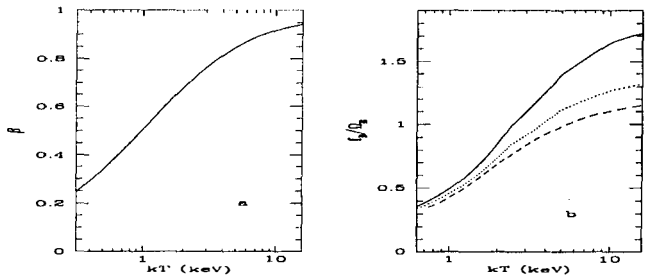

Figure 1: a) *The $\beta(T)$ parameter entering equation 1. b) Baryonic fraction respect to the universal value Ω_B for different values of γ. Continuous line: $\gamma = 1$; dotted line: $\gamma = 1.1$; dashed line: $\gamma = 1.2$.*

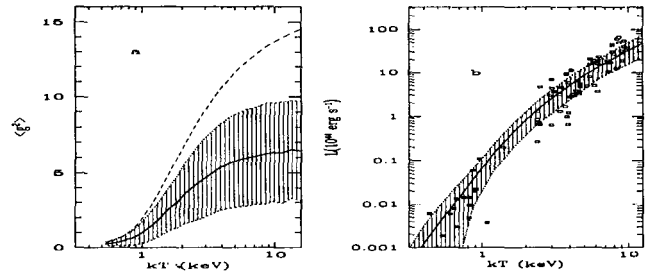

Figure 2: a) *The factor $\langle g^2 \rangle$ averaged over merging histories (solid line) with 96% confidence level (shaded region). The non-averaged g is plotted for comparison (dashed line). b) Predicted L–T relation. Data by David et al. (1993) for clusters (open squares) and Ponman et al. (1996) for groups (solid squares).*

for a plasma with three degrees of freedom. Here n_1 is the baryon density external to the virial radius, and it is assumed to be unbiased respect to the universal value, i.e., $n_1 = \Omega_B \rho$ where ρ is the total density. Eq. 2 includes both *weak* shocks (with $T_2 \approx T_1$, appropriate for small groups accreting preheated gas, or for rich clusters accreting comparable clumps), and *strong* shocks (appropriate to "cold inflow" as in rich clusters accreting small clumps and diffuse gas). Given the nearly static post-shock condition $v_2 << v_1$, it is possible to show that in the case of strong shocks $kT_2 \approx -V(R)/3 + 3kT_1/2$ holds, where the second term is the contribution from non gravitational energy input (CMT98). This leads to a factor $\beta(T)$ which decline from ~ 1 for rich clusters, to ~ 0.4 for poor groups, where the nuclear competes with the gravitational energy (see fig. 1a). A specific gas profile depends on the choiche for the potential well (in the following we use forms given by Navarro, Frenk & White (1996), but this is not mandatory). A general result is that the corresponding baryonic fraction lowers down with the mass scale by a factor of three from clusters to groups (see fig. 1b).

2.3 The L-T correlation

The X-ray luminosity of a cluster with temperature profile $T(r)$ and density profile $n(r)$ can be written:

$$L \propto \langle g^2(T) \rangle \int d^3r \, \frac{n^2(r)}{n^2(R)} \, T^{1/2}(r) \, , \tag{3}$$

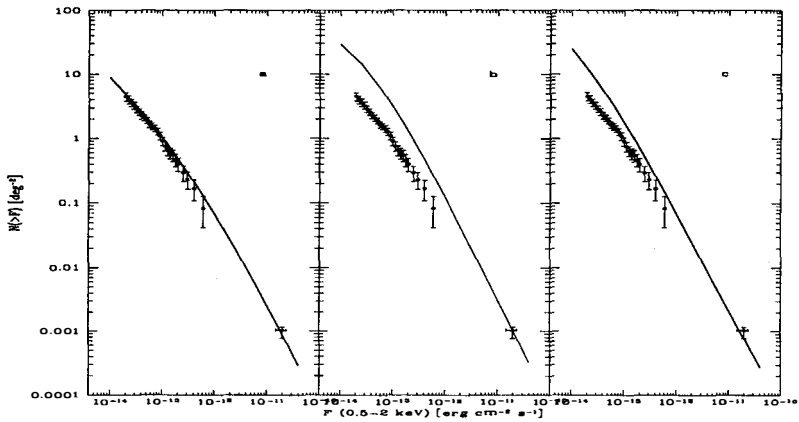

Figure 3: *Predicted counts for TCDM (a), OCDM (b) and ΛCDM (c). Data by Rosati et al. (1998), and Piccinotti et al. (1982) for the point at high fluxes.*

where the statistical effect of the merging histories has to be taken into account. In fact, for a cluster or a group of a given mass (or temperature), the effective compression factor squared $\langle g^2 \rangle$ is obtained upon averaging eq. 2 over the sequence of the DM merging events; in such events, T_2 is the virial temperature of the receiving structure, and T_1 is the higher between the stellar preheating temperature and the virial value prevailing in the clump being accreted. The averaged $\langle g^2 \rangle$ is lower than the g^2 computed with a single temperature T_1, because in many events the accreted gas has a temperature higher than the preheating value. In addition, an intrinsic *variance* is generated from the merging histories (see fig. 2a).

In agreement with the observations, the *shape* of the average $L - T$ relation flattens from $L \propto T^5$ at the group scale (where the nuclear energy from stellar preheating competes with the gravitational energy) to $L \propto T^3$ at the rich cluster scales (see fig. 2b). At larger temperatures the shape asymptotes to $L \propto T^2$, the self-similar scaling of pure gravity. Notice the intrinsic *scatter* due to the variance in the dynamical merging histories, but amplified by the n^2 dependence of L. The average normalization rises like $\rho^{1/2}(z)$, where ρ is the effective external mass density which increases as $(1+z)^2$ in filamentary large scale structures hosting most groups and clusters (see Cavaliere & Menci 1997). We check that the shape of the L–T relation is little affected by changes of γ (we assume a fiducial value $\gamma = 1.2$, see CMT98).

3 A physical based cosmological test

We adopt the Press & Schechter rendition of the hierarchical clustering. For each CDM universe we first check agreement with local constraints on the luminosity function $N(L)$ and on the temperature function $N(T)$; then the test is performed on the flux counts $N(> F)$ in the ROSAT band, which include the effect of the evolution (the higher z sample of RDCS by Rosati et al. 1998). While the normalization σ_8 is fixed by the constraints from COBE for a given CDM spectrum, the predictions for the faint counts are sensitive to Ω_0.

We focus on three popular CDM universes. The first is the critical TCDM, for which we adopt the tilted spectrum with primordial index $n_p = 0.8$, with amplitude $\sigma_8 = 0.66\,(1 \pm 0.08)$, and with a high baryonic fraction $\Omega_B = 0.15$ (the Hubble constant is $h = 0.5$). The tilt is

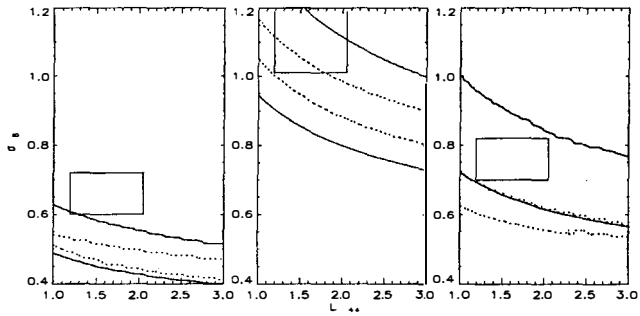

Figure 4: *The 99% confidence contours for both the computed local luminosity function (solid lines) and the computed number counts (dotted lines), in the $L_{44} - \sigma_8$ plane ($L_{44} = L_o/10^{44}$ erg/s). The boxes indicate ± 1 standard deviations in σ_8 (corresponding to the COBE uncertainty) and in L_{44}. a) TCDM, consistent with the counts within 2 standard deviations below σ_8; b) ΛCDM; c) OCDM ($\Omega_o = 0.5$).*

chosen so as to minimize one of the main problems of the Standard CDM, namely, the excess of small-scale power. The high baryon fraction is chosen to solve the so called "baryonic crisis" (White et al. 1993). We note that the slope of predicted counts is sufficiently *flat* to fit both the bright and the faint data by lowering σ_8 to within the COBE uncertainty (in fig. 3a we adopt $\sigma_8 = 0.6$).

The second is an open CDM universe. After Liddle et al. (1996), we focus first on the representative OCDM cosmogony, with $\Omega_o = 0.5$, $h = 0.65$ with $\Omega_B = 0.07$, which yield $\sigma_8 = 0.76\,(1 \pm 0.08)$. It is seen that the counts show excesses over the data. The underlying reason is that in open cosmologies long lines of sight and slow dynamical evolution conspire to yield a slope of the counts too *steep* to account for both faint and bright counts.

The third universe (ΛCDM) has a flat geometry with $\Omega_o = 0.3$ and $\Omega_\lambda = 0.7$, $\Omega_B = 0.05$ and $h = 0.7$. The normalization is $\sigma_8 = 1.1\,(1 \pm 0.08)$. In this intermediate condition faint counts are higher respect to TCDM, yet lower than in the $\Omega_o \approx 0.5$ case, to yield a moderate excess (fig. 3c).

For a synthetic presentation, we also show in fig. 4 the effects of varying σ_8 and the normalization of the $L-T$ relation, i.e., the average luminosity L_{44} corresponding to 4.5 keV. In TCDM and in ΛCDM the counts are consistent with the observations on considering the uncertainties in the present COBE normalization and the intrinsic uncertainty in the L-T relation, while, on the other hand, in OCDM the counts are inconsistent with local data by a significant excess.

4 Discussion and conclusion

We proposed a physical-based approach to cosmological tests with clusters of galaxies. We describe the X–ray emission from clusters with a specific model for the diffuse baryons. In this sense this approach is alternative to the parametrical approach (see Borgani this meeting).

The results of our model depend on two parameters, the external temperature T_1 and density n_1, which are *not* free. Specifically, we use for T_1 the range $0.1 \div 0.8$ keV provided by the stellar preheating. The value of n_1 for rich clusters is related to the DM density by the universal baryonic fraction. Thus we compute the expression of the bolometric luminosity for a given temperature. The average of the square of the density jump factor $\langle g^2 \rangle$ over the merging histories coupled with $\beta(T)$ is what gives to the statistical $L - T$ correlation the curved shape shown in fig. 2b. In addition, our approach predicts an intrinsic *variance* of dynamical origin due to the

different merging histories, and built in the factor g^2.

With the ICP state so described, we proceeded to constrain the cosmological parameters. After the observations by Rosati et al. (1998), we have computed the X-ray observables for groups and clusters of galaxies. On the basis of local data, the set of acceptable CDM universes is restricted to three disjoint domains: $\Omega = 1$ for the Tilted CDM with high baryon content; $\Omega_o \simeq 0.5$ for standard CDM; $\Omega_o \approx 0.3$ for CDM in flat geometry. However, only the TCDM and the ΛCDM universes give acceptable faint counts. As an overall remark, a common feature of all the above universes is constituted by some excess in the counts. This may indicate some non–trivial incompleteness in the canonical hierarchical clustering, worth keeping under scrutiny. We recall that in the adiabatic models for the ICP (Evrard & Henry 1991, Kaiser 1991) the evolution of the $L-T$ relation is reduced or even negative, thus alleviating the excess. However, the anti–evolution required in OCDM would be very difficult to justify (the adiabatic models are largely discussed in CMT98).

Now the question is: to what extent enlarging the data base on X–ray clusters will help in further constraining cosmology? We argue that the variance intrinsic to the hierarchical clustering, and amplified by the ICP emissivity, sets an effective limitation. Richer, faint surveys will hardly provide a sharper insight into cosmology unless one reduces both the uncertainty concerning σ_8 and the larger one concerning L_o. However, we stress that such efforts will find soon a more proper aim than constraining Ω_o. This is because MAP, and subsequently PLANCK, will accurately measure on still linear scales not only the perturbation power spectrum but also directly Ω_o. Once the cosmological framework has been fixed, the study of groups and clusters in X-rays will resume its proper course, that is, the physics of systems of intermediate complexity which is comprised of the DM and of the ICP component.

Acknowledgments

The author acknowledge partial founding by the Training Mobility Research Programme.

1. Cavaliere, A., Menci, N. 1997, ApJ, **480**, 132
2. Cavaliere, A., Menci, N., Tozzi, P. 1997, ApJL **484**, 1 (CMT97)
3. Cavaliere, A., Menci, N., Tozzi, P. 1998, ApJ accepted, [astro-ph/9802185] (CMT98)
4. Cavaliere, A., & Fusco–Femiano, R. 1978, A&A, **70**, 677
5. David, L.P., Slyz, A., Jones, C., Forman, W., Vrtilek, S.D., & Arnaud, K.A. 1993, ApJ, **412**, 479
6. Evrard, A.E., Henry, J.P. 1991, ApJ, **383**, 95
7. Henriksen, M.J., & White, R.E. 1996, ApJ, **465**, 515
8. Kaiser, N. 1986, MNRAS, **222**, 323
9. Kaiser, N. 1991, ApJ, **383**, 104
10. Landau, L.D., Lifshitz, E.M. 1959, *Fluid Mechanics* (London, Pergamon Press), p. 329
11. Liddle, A.R., Lyth, D.H., Roberts, D., & Viana, P.T.P. 1996, MNRAS, **278**, 644
12. Mushotzky, R.F., & Scharf, C.A. 1997, ApJ, **482**, 13
13. Navarro, J.F., Frenk, C.S., & White, S.D.M. 1996, ApJ, **462**, 563
14. Piccinotti, G., Mushotzky, R.F., Boldt, E.A., Holt, S.S., Marshall, F.E., Serlemitsos, P.J., & Shafer, R.A. 1982, ApJ, **253**, 485
15. Ponman, T.J., Bourner, P.D.J., Ebeling, H., Böhringer, H. 1996, MNRAS, **283**, 690
16. Press, W.H., & Schechter, P. 1974, ApJ, **187**, 425
17. Roettiger, K., Stone, J.M, & Mushotzky, R.F. 1997, preprint [astro-ph/9708043]
18. Rosati, P., Della Ceca, R., Norman, C., & Giacconi, R. 1998, ApJ, **492**, L21
19. Takizawa, M., & Mineshige, S. 1997, preprint [astro/ph 9702047]
20. White, S.D.M., Navarro, J.F., Frenk, C.S., & Evrard, A.E. 1993, Nature, **366**, 429

EVOLUTION OF THE CLUSTER ABUNDANCE FROM THE RDCS

Stefano BORGANI
INFN–Sez. di Perugia, via A. Pascoli 10, I-06100 Perugia, Italy

The Rosat Deep Cluster Survey provides a robust determination of cluster number counts, redshift distribution and X–ray luminosity function out to $z \simeq 0.8$. Based on a Press–Schechter approach for the mass function of galaxy clusters, I use such observational results to constrain the power–spectrum of density fluctuations, the cosmic density parameter and the thermodynamics of the intra–cluster medium (ICM).

1 Introduction

Galaxy clusters are the largest bound cosmic structures, arising from rare high peaks of the initial density fluctuation field. For this reason, their number density is very sensitive to the global statistical properties of the cosmic matter fluctuation field. Indeed, their local ($z \lesssim 0.1$) abundance has been already used as a stringent constraint for cosmological models. Independent analyses have shown that $\sigma_8 \Omega_0^{\gamma(\Omega_0)} \simeq (0.5 - 0.7)$, where Ω_0 is the density parameter, σ_8 the r.m.s. fluctuation amplitude within a sphere of $8\,h^{-1}$Mpc ($h = H_0/100 \mathrm{km\,s^{-1}\ Mpc^{-1}}$) radius and $\gamma(\Omega_0) \simeq 0.4 - 0.6$, depending on the cosmological model [1,2]. Furthermore, the increasing availability of data on clusters at higher redshift, $z \simeq 0.3$–0.5, should provide a handle on the required density parameter which best reproduces the evolution of the cluster abundance and, therefore, offers a unique possibility to break the degeneracy between Ω_0 and σ_8 [3,4].

The Rosat Deep Cluster Survey (RDCS) by Rosati et al. (see ref. [5] for a description of the sample) provides a complete sample of clusters identified in the *ROSAT* PSPC archive and spectroscopically confirmed out to a redshift of $z \simeq 0.85$. It represents to date the deepest statistical cluster sample and, therefore, it is particularly well suited to probe the evolution of the cluster abundance. In the following we will outline the main results of our comparison between the RDCS sample and the predictions of cosmological models. To this purpose, we will use the evolving X–ray luminosity function (XLF), the number counts $n(S)$ and the redshift distribution $n(z)$. A complete description of our analysis is deserved to a more detailed paper[6]

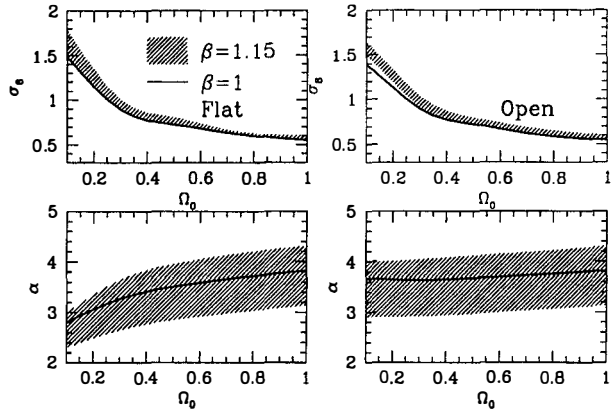

Figure 1: Constraints at the 90% c.l.from the local XLF on σ_8 (upper panels) and α (lower panels), for both flat (left panels) and open (right panels) models.

2 The Analysis

Our approach is based on the Press-Schechter [7] prescription to compute the comoving number density of virialized halos at redshift z:

$$\frac{dn}{dM} = \sqrt{\frac{2}{\pi}} \frac{\bar{\rho}}{M^2} \frac{\delta_c(z)}{\sigma_M} \left| \frac{d\log\sigma_M}{d\log M} \right| \exp\left(-\frac{\delta_c(z)^2}{2\sigma_M^2} \right) . \quad (1)$$

Here $\bar{\rho}$ and σ_M are the present-day average matter density and r.m.s. fluctuation at the mass scale M, respectively, while $\delta_c(z)$ is the linear-theory overdensity extrapolated at the present time for a uniform spherical fluctuation collapsing at redshift z.

As for the power-spectrum, which determines σ_M, we assume the expression $P(k) = A\,k\,T^2(k)$. We fix the normalization A according to the 4-year *COBE* CMB anisotropy data, while

$$T(q) = \frac{\ln(1+2.34q)}{2.34q} \left[1 + 3.89q + (16.1q)^2 + (5.46q)^3 + (6.71q)^4 \right]^{-1/4} . \quad (2)$$

Here $q = k/h\Gamma$, where Γ the shape parameter, which specifies the value of σ_8 through the *COBE* normalization, once Ω_0 is fixed.

The conversion from cluster masses to luminosities in the *ROSAT* band [0.5-2.0] keV is realized as follows: **(a)** convert mass into temperature by assuming virialization, isothermal gas and taking $\beta = 1.15$ for the ratio between kinetic energy of dark matter and gas thermal energy [8]; **(b)** convert temperature into bolometric luminosity according to $L_{bol} \propto T^{\alpha}(1+z)^A$; **(c)** compute the bolometric correction to the [0.5-2.0] keV band by using a Raymond-Smith code with $\mu = 0.3$ for the average metallicity of the ICM.

Having adopted this procedure, we have four parameters which we should fit to the data. Two of them, σ_8 (or, equivalently, Γ) and Ω_0, specify the cosmological model, while the other two, α and A, characterize the thermodynamics of the ICM. Firstly, we will use the local XLF from RDCS, along with that by Ebeling et al. [9] at $L_X > 10^{44}\,\mathrm{erg\,s^{-1}}$, to constrain σ_8 and α. Secondly, we will use the XLF at $z > 0$ from RDCS and from EMSS [12], the RDCS number counts $n(S)$ and redshift distribution $n(z)$ to constrain the evolutionary parameters, namely Ω_0 and A. We note here that $n(S)$ alone for RDCS has been recently used to put constraints on cosmological models [10,11].

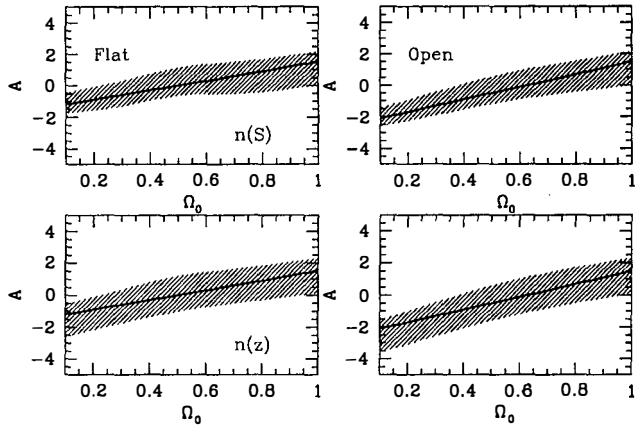

Figure 2: Constraints at the 90% c.l. on the Ω_0–A plane from number counts (upper panels) and redshift distribution (lower panels).

3 Results

We show in Figure 1 the 90% c.l. constraints for σ_8 and α for both flat and open models coming from the local XLF, obtained by means of a χ^2 minimization procedure. Also shown as solid lines are the best fitting parameters in case we take $\beta = 1$. As for the σ_8–Ω_0 scaling, we find $\sigma_8 \Omega_0^{\gamma(\Omega_0)} = (0.58 \pm 0.02)$, with $\gamma(\Omega_0) = 0.47 - 0.16\Omega_0$ for flat models and $\gamma(\Omega_0) = 0.53 - 0.27\Omega_0$ for open models, thus in fair agreement with similar constraints coming from the local X–ray temperature function [1] as well as from the optical virial analysis of nearby galaxy clusters. As for the parameter α, it turns out that agreement with results about the local L_{bol}–T relation [13] is found, within the large observational scatter, for most of the values of Ω_0.

In Figure 2 we plot the constraints on the Ω_0–A plane from the number counts and the redshift distribution. As a general result, we point out that $n(S)$ and $n(z)$ provides completely consistent results, with the former being slightly more constraining in the low–Ω_0 regime. As expected, the more rapid fluctuation evolution in high–Ω_0 models favors a positive evolution of the L_{bol}–T relation in order to account for the presence of a remarkable amount of clusters at high redshift or low fluxes. Such constraints can be roughly represented through the relations $A = (3\Omega_0 - 1.5) \pm 1.0$ for flat models and $A = (4\Omega_0 - 2.5) \pm 1.0$ for open models, thus consistent with the result by Sadat et al.[14] from the analysis of the EMSS redshift distribution. Such results imply that both better observational data about the evolution of the L_{bol}–T relation and a larger X–ray flux–limited cluster sample are required in order to place more stringent constraints on the density parameter.

Acknowledgments

The Author wish to thank his the people who collaborated with him in the analysis presented here. They are: Colin Norman, Piero Rosati and Paolo Tozzi.

References

1. V.R. Eke, S. Cole and C.S. Frenk, MNRAS **282**, 263 (1996)

2. M. Girardi, S. Borgani, G. Giuricin, F. Mardirossian and M. Mezzetti Astrophys. J. Lett. „ s (u)bmitted (1998)
3. R.G. Carlberg, S.L. Morris, H.K.C. Yee and E. Ellingson Astrophys. J. **479**, L19 (1997)
4. V.R. Eke, S. Cole, C.S. Frenk and J.P. Henry, preprint astro–ph/9802350 (1998)
5. P. Rosati, R. Della Ceca, C. Norman and R. Giacconi, *Astrophys. J. Lett.* 492 L21 (1997)
6. S. Borgani, P. Rosati, P. Tozzi and C. Norman, Astrophys. J. ,, s (u)bmitted (1998)
7. W.H. Press and P. Schechter, Astrophys. J. **187**, 425 (1974)
8. G.L. Bryan and M.L. Norman, A **s**, t (r)ophys. J. 495 80 (1998)
9. H. Ebeling, A.C. Edge, A.C. Fabian, S.W. Allen, C.S. Crawford and H. Böhringer, Astrophys. J. **479**, L101 (1997)
10. B. Mathiesen and A.G. Evrard, *MNRAS* in press (1997), *preprint* astro-ph/9703076
11. T. Kitayama, Y. Suto, *Astrophys. J.* 490 557 (1997)
12. Gioia I.M., Henry J.P., Maccacaro T., Morris S.L., Stocke J.T., Wolter A., 1990, ApJ, 356, L35
13. D.A. White, C. Jones and W Forman, MNRAS **292**, 419 (()1997)
14. R. Sadat, A. Blanchard and J. Oukbir, *Astron. Astrophys.* **329**, 21 (1998)

THE EFFECTS OF LARGE SCALE STRUCTURE ON CLUSTER SUBSTRUCTURE AND CLUSTER TEMPERATURE DISTRIBUTIONS

W. FORMAN, M. MARKEVITCH & H. DONNELLY
Harvard-Smithsonian Center for Astrophysics, 60 Garden St.
Cambridge, MA 02138, USA

We discuss the relationships between cluster structure and large scale structures, such as filaments, using A85 as an example. As predicted by numerical simulations, the small scale structures in clusters are co-aligned with the much larger filamentary structures in which clusters are embedded and from which they formed. Also, we describe the ASCA temperature profiles for a sample of clusters and show that all clusters exhibit a similar temperature profile. We compare the observations to numerical simulations.

1 Why Clusters of Galaxies?

Clusters of galaxies are a small, but significant fraction of the mass of the Universe and their properties make them ideal cosmological probes. As the largest, most massive collapsed systems, clusters are "young" and have dynamical time-scales at most a few times smaller than the age of the Universe. Therefore, their properties should reflect the initial conditions of the environment from which they formed. In this contribution, we discuss two cluster topics. First we describe the relationship between cluster structure and the larger filamentary environment from which they formed and continue to grow via accretion. Second, we discuss cluster temperature profiles as derived from ASCA observations.

2 Cluster Morphology and Substructure – A85

Because clusters are "young" systems, they should "remember" the environment from which they formed. Observations suggest that clusters do "remember" their environment; they grow by infall of matter in preferential directions defined by the surrounding large scale structure. One cluster that clearly shows the substructure-large scale structure relationship is A85.

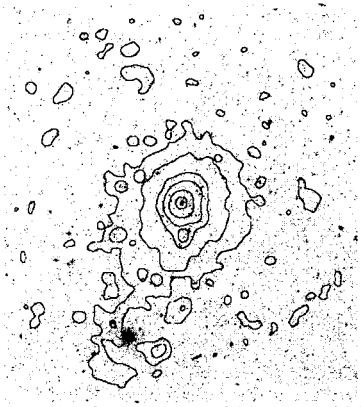

Fig. 1 – Optical image of A85 with ROSAT PSPC isophotes superposed. The energy band used is 0.4-2.0 keV and the image has been smoothed with a 60″ Gaussian. Emission extending to the south and south-east is clearly visible.

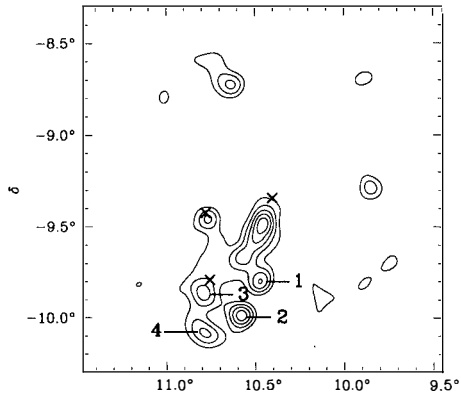

Fig. 2 – Residual X-ray emission obtained after subtracting the smooth emission derived from the north half of the image, as described in the text. The crosses indicate the centers of the three clusters A85, A87 and A89. The numbers correspond to individual sources.

A85 is a bright, relatively nearby ($z = 0.0555$), cooling flow cluster (see Durret et al. [1] for a detailed discussion of the material presented below). The ROSAT PSPC image, shown in Fig. 1, clearly shows emission peaked on the cD at the cluster center with cluster emission extending to large radii. Also, we see a second smaller region of extended emission approximately 10′ south of A85 (720 kpc, projected on the sky). In addition to these features, there is excess emission towards the south-east, extending almost to the edge of the PSPC FOV. The emission to the southeast is concentrated in a narrow range of position angles, approximately between 135° and 180° (counter clockwise from north).

To further explore the properties of the A85 emission, Fig. 2 shows an image of the "asymmetric" X-ray emission to the south-east of A85 (generated by subtracting a radial profile generated of the northern half of the image and then normalizing by the original image). The surface brightness enhancement to the south is clearly visible and the position angle of the emission shifts in angle towards the southeast as one proceeds further away from the cluster center.

The ASCA spectral data suggest that matter is infalling into A85 at the present epoch. The ASCA temperature map [2] shows a temperature enhancement just north of the southern subcluster, suggesting that the galaxies, gas, and dark matter forming the subcluster, are presently infalling into the main cluster and interacting with the surrounding material. The observed temperature increase could be produced by compression of the X-ray emitting gas caused by the infalling clump.

The position angle defined by the X-ray features is seen optically at a variety of scales. First, the galaxy distribution in A85 is elongated towards PA$\simeq$ 160° and the major axis of the central cD galaxy itself is elongated along the same direction. Remarkably, the X-ray and optical features within the cluster are co-aligned with a much larger structure extending from northwest to southeast and including A70, A85 and A89, A87, A91, the NGC 255 group and A106.[3] Such a structure extends over more than 5° on the sky, corresponding to a linear distance of 28 Mpc at the redshift of A85. This is obviously a lower limit, since the filament may be inclined to the line of sight.

Alignments and merger effects shown for A85 and observed in other clusters (e.g., Centaurus

shows similar alignments and merger effects[4]) confirm the predictions from numerical simulations which suggest that clusters should accrete matter from a few preferred directions, defined by filamentary structures, and that the accretion can persist over cosmologically long times.[5] Thus, it should not be surprising to see common alignments between central galaxy major axes, infalling subclusters and surrounding groups, and even on the scale of neighboring clusters.[6] The present observations suggest that future observations should allow detailed comparisons between large scale numerical simulations and cluster properties.

3 Cluster Temperature Profiles

Prior to the launch of ASCA with its broad energy band, it had been difficult to measure the temperature distributions of rich, and therefore, hot clusters. A recent study provides temperature maps for a flux limited sample of 26 nearby ($0.04 < z < 0.09$) clusters.[2] Of these 26 clusters, 9 exhibited strong merger activity. The remaining clusters exhibited reasonable azimuthal symmetry and were used to generate radial temperature profiles (for details of the ASCA cluster study see Markevitch et al.[2]).

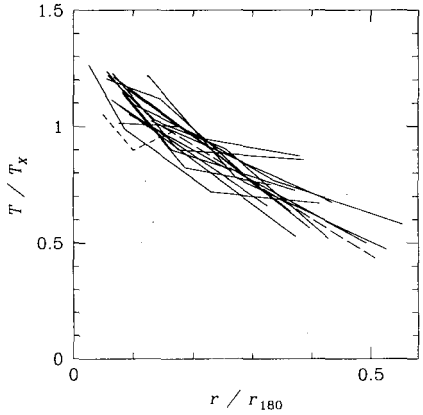

Fig. 3 –
Temperature profiles for non-merging clusters derived from ASCA observations[2] The temperatures are normalized to the cluster mean; the radii are normalized to the virial radius (see text). Uncertainties are not given for clarity. The dashed lines are for AWM7 and A2163. All profiles are observed to decrease by almost a factor of 2 at half the virial radius. The scatter is remarkably small and lies within the uncertainties.

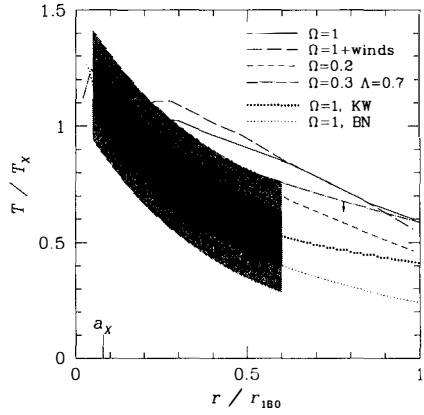

Fig. 4 – Comparison of observed and model cluster temperature profiles. The central (dark band) approximately corresponds to the scatter of the temperature values in Fig. 3, while the larger grey band includes most of their 90% uncertainties. Six theoretical profiles are shown (see Markevitch et al.[2] for details). The figure suggests that detailed temperature profiles may be able to distinguish among cosmological models.

The ASCA cluster temperature profiles are shown in Fig. 3 with all temperatures normalized to the cluster mean. The profiles are shown as a function of radius in units of the estimated virial radius, r_{180}, the radius at which the mean cluster density is 180 times the closure density. The observed temperature profiles are different in angular (detector) coordinates, but are similar in such physical units.

The single most important characteristic of Fig. 3 is the clear temperature decline seen in *all* the clusters. The temperature decline is significant, with temperatures decreasing by

almost a factor of 2. In Fig. 4 the observed profiles are compared to several different numerical simulations.[7,8,9,10] While still only suggestive, the comparison of observations and simulations indicates that future, more accurate observations may be able to differentiate among models of cluster formation.

In addition to providing a better understanding of clusters, the observed temperature profiles are important for computing cluster masses and baryon fractions. Most previous work has assumed that the cluster gas is isothermal. The observed temperature profiles, compared to the isothermal assumption imply 1) larger masses at small radii and 2) smaller masses at large radii. As emphasized for A2256, the smaller masses at large radii strengthen the argument in favor of a low Ω universe.[11]

Finally, we comment on the implications of a universal temperature profile for a universal mass profile. The gravitating mass, M in a cluster within a radius r, can be expressed in terms of the observed temperature and gas mass distributions as:

$$M(<r) \propto T_{gas}(r) \left(\frac{d \ln \rho_{gas}}{d \ln r} + \frac{d \ln T_{gas}}{d \ln r} \right) r \qquad (1)$$

where T_{gas} is the gas temperature and ρ_{gas} is the gas density. We have already noted the remarkable similarity of cluster gas temperature profiles. The gas density profiles are also remarkably similar. If the gas density distribution is characterized as $\rho \propto [1 + (r/a)^2]^{-3\beta/2}$ where a is a characteristic radius, then two-thirds of a sample of 85 clusters have gas profiles characterized by $\beta = 0.6 \pm 0.1$.[12] Thus, very similar temperature and density profiles indicate that clusters may indeed have a universal mass profile, as suggested by numerical simulations.

4 Conclusions

We have presented observations of A85 which show that cluster substructure reflects the large scale structure around them with alignments on scales from tens of kpc to tens of Mpc. Finally, we discussed ASCA temperature profiles which suggest that clusters, not undergoing major mergers, may have very similar temperature distributions when scaled to a meaningful physical radius. The similar temperature profiles, combined with similar gas density distributions, further suggest that clusters may be described by a universal mass profile.

We thank the Smithsonian Institution and NASA Grant NAG5-3065 for supporting the research reported here.

References

1. F. Durret, W. Forman, D. Gerbal, C. Jones, A. Vikhlinin A&A in press , (1998).
2. M. Markevitch, W. Forman, C. Sarazin, A. Vikhlinin ApJ in press , (1998; astroph 9711289)
3. E. Slezak, F. Durret, J. Guibert, C. Lobo A&AS in press , (1998; astroph 9710103)
4. E. Churazov, M. Gilfanov, W. Forman, C. Jones ApJ in press , (1998; astroph 9802166)
5. J. Colberg, S. White, A. Jenkins, F. Pearce MNRAS submitted , (1997; astroph 9711040)
6. M. West, C. Jones, W. Forman ApJ **451**, L5 (1995)
7. A. Evrard, C. Metzler, J. Navarro ApJ **469**, 494 (1996)
8. V. Eke, J. Navarro, C. Frenk MNRAS submitted , (1997; astroph 9708070)
9. N. Katz, S. White ApJ **412**, 455 (1993)
10. G. Bryan, M. Norman ASP Conference Series **123**, (1997; astroph 9710186)
11. M. Markevitch, A. Vikhlinin ApJ **474**, 84 (1997)
12. C. Jones, W. Forman ApJ submitted , (1998)

CLUSTERS, COSMOLOGY, AND AXAF

C. JONES, A. VIKHLININ, & B. MCNAMARA
Harvard-Smithsonian Center for Astrophysics, 60 Garden St.
Cambridge, MA 02138, USA

We summarize results from a recently completed ROSAT survey of distant clusters of galaxies. The large solid angle of this ROSAT survey allows a test of previously reported cluster evolution. We confirm there is significant negative cluster evolution for very luminous clusters, i.e., at high redshifts there are fewer luminous clusters than at the present epoch. Also, we compare cluster core radii from the ROSAT survey with those measured from the Einstein survey of nearby clusters and find no evolution in cluster core radii. Finally, we summarize the capabilities of AXAF, emphasizing in particular its extremely high angular resolution.

1 Clusters of Galaxies As Cosmological Probes

Clusters are complex, multi-component systems with hundreds of galaxies, a hot (10^7 to 10^8K) intracluster medium (ICM), and dark matter evolving in tightly coupled ways. Only a few percent of the mass in clusters lies in the optical galaxies. In rich clusters, most of the luminous baryonic mass (about 25% of the total cluster mass) is in the hot ICM [1,2].

Cluster properties are functions both of the processes operating within them and of the underlying cosmology. As Alain Blanchard (this volume) discusses, clusters are ideal for testing cosmological models. First, clusters are very luminous and are observed both optically and in X-rays to significant distances ($z \approx 1$). Second, since clusters have dynamical timescales which are a significant fraction of the age of the Universe, we observe them at different evolutionary stages. Also since cluster dynamical timescales are long, the imprint of the initial conditions has not yet been completely erased. Third, since clusters are massive objects, they form only from rare peaks in the underlying density field, in the standard scenario, so their properties are sensitive to cosmological parameters. Numerical simulations show that many cluster properties including mass and temperature functions, X-ray luminosity functions, radial mass and temperature distributions, mean cluster properties as a function of redshift, and the characteristics of substructure can differentiate among cosmological models. For example, for standard biased

Table 1: Comparison of Cluster Surveys

Survey	Sq. deg	Sample Definition	Results
EMSS [10]	>130	Einstein IPC	Evolution – deficit of $L_x > 5 \times 10^{44}$ clusters at $z > 0.3$
Rosati et al. [16]	33	PSPC > 15 ksec	No detected evolution using 70 clusters
WARPS [17]	16	PSPC > 8 ksec	No detected evolution using 46 clusters
SHARC [18]	17	PSPC > 10 ksec	No detected evolution using 35 clusters
RIXOS [19]			Strong evolution using 13 clusters
McHardy et al. [20]	0.2	110 ksec pointing	$\sim$ 6 possible clusters (2 extended)
Vikhlinin et al. [12]	160	PSPC > 2 ksec	Significant evolution for $L_x > 3 \times 10^{44}$ at $z > 0.3$ with 203 clusters

CDM, a flat open model with $\Omega = 0.3$ and $\Lambda = 0.7$, and an open CDM model, the expected number of hot (>7 keV) clusters, per square degree at $z = 0.8$, is in the ratio of 1:60:300. [3]

Clusters are unique because of their size. They are sufficiently large that an inventory of their components should be representative of cold matter in the Universe. A massive, rich cluster with $M_{\rm total} \sim 10^{15} M_\odot$ forms from a density perturbation of radius $\sim$ 15 Mpc. Hence, determining baryon fractions in clusters provides the cosmological baryon fraction, provided the processes responsible for the hot gas distribution are modeled adequately. Combining measurements of the cluster baryon fraction with nucleosynthesis calculations provides an upper bound on the total mass density in the Universe. The large baryonic fraction in the hot X-ray gas has led to the so-called "baryon catastrophe" with its implications for a low Ω universe [4,2].

2 The Evolution in X-rays of Distant Clusters

Of all methods for detecting distant clusters, X-ray surveys are the least sensitive to projection, because the X-ray emission is proportional to the square of the density of the hot gas, which must be compressed in a deep potential well for us to detect it. It is noteworthy that unlike optical surveys, X-ray surveys have the possibility of finding interesting objects such as "fossil" clusters in which almost all galaxies have merged to form a cD galaxy [5], and hypothetical "failed" clusters in which galaxy formation was suppressed [6]. To date, the largest published sample of distant X-ray selected clusters is that from the Einstein EMSS [7,8]. However, because of the relatively high flux limit, the EMSS sample contains only 6 clusters at $z > 0.5$.

Selecting distant cluster samples from various ROSAT surveys is being pursued by several different groups. Table 1 summarizes these results, and the earlier EMSS work. Note that because of the small area survey in all but one ROSAT survey [9], most surveys cannot study the luminosity function of distant clusters above 3×10^{44} ergs s^{-1}, where the deficit of high redshift EMSS clusters was reported [10]. Figure 1 shows the $\log N - \log S$ distribution for clusters from the ROSAT and Einstein analyses.

The Vikhlinin et al. source catalog includes 203 optically confirmed clusters, and thus is one of the largest X-ray selected samples, comparable in number to the ROSAT All-Sky Survey sample of nearby clusters. [11] Cluster candidates are selected as extended X-ray sources using the wavelet decomposition technique and are then identified through optical observations, which show that 91% of our sources are clusters. We also measured cluster core-radii for fixed $\beta = 0.67$. We then used this sample to search for cluster X-ray luminosity and core radius evolution [12].

Based on the area sampled in the Vikhlinin et al. catalog, for a model with no evolution, we expect 9.3 luminous ($L_x > 3 \times 10^{44}$ ergs s^{-1}) clusters at redshifts $z > 0.3$. We observe at most two such clusters. Such a deviation is significant at more than 99.5% confidence. For the negative evolution observed in the EMSS, we predict only 2–3 clusters, in agreement with the observed number. Thus we are able to test, and confirm, the EMSS evolution results, even with

the incomplete redshift data currently in hand.

We also can compare the observed and predicted number of lower-luminosity clusters at high redshift. At $z > 0.4$, we find 18 clusters with luminosities from 1 to $3 \times L^{44}$ ergs s^{-1}, compared with 22.2 predicted by the no-evolution model. Thus, the evolution in this interval is certainly different from that of the high L_x clusters. The absence of evolution in yet lower luminosity clusters is supported by the analysis of the $\log N - \log S$ distribution (Fig. 1), from which Vikhlinin et al. find that the cluster volume emissivity, dominated by low-luminosity objects, does not evolve. The low-L_x results are generally in agreement with other ROSAT surveys listed in Table 1. The observed evolution can be reproduced by a model in which the characteristic luminosity decreases with redshift, but the comoving number density of clusters increases. Such models arise naturally in the hierarchical cluster formation scenario [13].

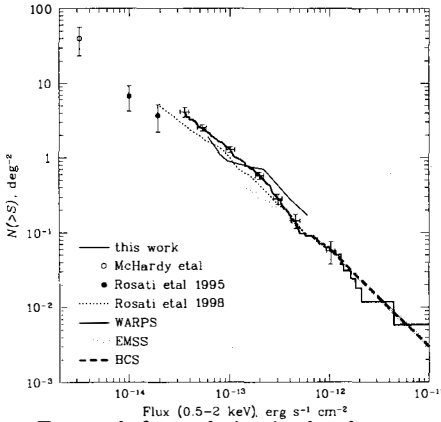

Fig. 1 – The $\log N - \log S$ relation (see Vikhlinin et al. [9] for details) is shown as the heavy solid histogram with several individual points including error bars. Vertical error bars represent the uncertainty in the number of clusters, while horizontal error bars correspond to a possible systematic uncertainty in flux. Good agreement is found between different samples.

To search for evolution in the cluster core radii, Vikhlinin et al. [12] compared the radius distribution for distant, $z > 0.4$, clusters and for nearby clusters in the Einstein sample. [14] This comparison shows that the core radius distributions for distant and nearby clusters are remarkably similar. The median radius is 240 ± 14 kpc for nearby clusters, and 210 ± 14 kpc ($q_0 = 0.5$) or 230 ± 16 kpc ($q_0 = 0$) for distant clusters. Some models predict a much stronger evolution in core radii. For example, in some self-similar models, the cluster radius grows by a factor of ~ 2 from $z = 0.4$ to the present, while hydrodynamic simulations with $\Omega + \Lambda = 1$ show a factor of 1.5 growth [13,15].

3 The AXAF Mission

The past twenty years have been a "Golden Age" for astronomy with the development of new telescopes, detectors, and accessibility to space. For X-ray astronomy, this period has been characterized by the maturing of imaging optics including Einstein, with its few arc second imaging capability, ROSAT with its wide-field, and ASCA with its broad energy-band. This "Golden Age" will continue with the launches of AXAF in 1998 with its sub arc second angular resolution and XMM in 1999 with its moderate spatial resolution and large collecting area. These observatories will provide unprecedented opportunities for investigations in nearly every area of astrophysics, from the study of black holes, to the enrichment of the ICM with heavy elements from supernovae, to the cosmological evolution of quasars and clusters of galaxies.

AXAF will carry the highest resolution X-ray mirror ever flown and a suite of advanced imaging and spectroscopic instruments designed to study sources of cosmic X-ray emission in

the energy range from 0.1 to 10 keV. In angular resolution, spectral resolution, and sensitivity, AXAF will provide very significant advances over previous X-ray missions. AXAF's major advances in high resolution imaging and spectroscopy also required what is arguably the most extensive ground calibration of any X-ray mission.

Two instruments can be placed in the AXAF focal plane – the HRC built at SAO, and ACIS from Penn State/MIT. Each is comprised of an "imager" as well as a spectroscopic readout. AXAF's sensitivity comes in part from its collecting area (the effective area for ACIS peaks at $\sim$700 cm^2), but primarily from the high spatial resolution of the telescope, which has an expected on-orbit FWHM of $\sim$0.3″, not including aspect blurring.

AXAF carries two sets of transmission gratings, the High Energy Transmission Gratings (HETG from MIT) and the Low Energy Transmission Gratings (LETG from Utrecht/MPE). When inserted in the converging beam behind the AXAF mirror assembly, the gratings disperse the X-rays, forming spectra that are read out with the appropriate imaging detector at the focal plane. Both gratings achieve resolving powers of 100 to 1000 for point sources and are optimized to cover the energy range of 0.4-8 keV (HETG) and 0.09-3 keV (LETG), with total effective areas ranging from 10-200 cm^2. The gratings will permit detailed spectroscopy and plasma diagnostics for a wide variety of sources.

We thank the Smithsonian Institution and NASA NAG5-3064 for supporting this research.

References

1. L. David, K. Arnaud, W. Forman, C. Jones ApJ **356**, 32 (1990)
2. L. David, C. Jones, W. Forman ApJ **445**, 578 (1995)
3. P. Viana, A. Liddle MNRAS **281**, 323 (1996)
4. S. White, J. Navarro, A. Evrard, C. Frenk Nature **366**, 429 (1993)
5. T. Ponman, D. Allan, L. Jones, M. Merrifield, I. McHardy, H. Lehto, G. Luppino Nature **369**, 462 (1994)
6. W. Tucker, H. Tananbaum, R. Remillard ApJ **444**, 532 (1995)
7. I. Gioia, T. Maccacaro, R. Schild, A. Wolter, J. Stocke, S. Morris, J.P. Henry ApJS **72**, 567 (1990)
8. J. Stocke, S. Morris, I. Gioia, T. Maccacaro, R. Schild, A. Wolter, T. Fleming, J.P. Henry, ApJS **76**, 813 (1991)
9. A. Vikhlinin, B. McNamara, W. Forman, C. Jones, H. Quintana, A. Hornstrup ApJ **502**, (1998 astro-ph/9803099)
10. J.P. Henry, I. Gioia, T. Maccacaro, S. Morris, J. Stocke, A. Wolter ApJ **386**, 408 (1992)
11. H. Ebeling, A. Edge, A.C. Fabian, S. Allen, C. Crawford, H. Böhringer ApJ Letters **479**, 101 (1997)
12. A. Vikhlinin, B. McNamara, W. Forman, C. Jones, H. Quintana, A. Hornstrup ApJ Letters in press astro-ph/9803101 , (1998)
13. N. Kaiser MNRAS **222**, 323 (1986)
14. C. Jones, W. Forman ApJ submitted , (1998).
15. R. Cen, J. Ostriker ApJ Letters **429**, 4 (1994)
16. P. Rosati, R. Della Ceca, C. Norman, R. Giacconi ApJ Letters **492**, 21 (1998)
17. L. Jones, C. Scharf, E. Perlman, H. Ebeling, G. Wegner, M. Malkan Proc. 'Röntgenstrahlung from the Universe', eds. Zimmermann, H. U., Trümper, J., and Yorke, H., MPE Report 263 591 1995
18. C. Collins, D. Burke, A. Romer, R. Sharples, R. Nichol ApJ Letters **479**, 117 (1997)
19. F. Castander et al. Nature **377**, 39 (1995)
20. I. McHardy et al. MNRAS, in press; astro-ph/9703163 , (1997)

COSMOLOGY AND CLUSTERS OF GALAXIES WITH XMM, THE X-RAY MULTI-MIRROR MISSION

M. ARNAUD
CEA/Service dAstrophysique, CE Saclay,
91191 gif sur Yvette Cedex, FRANCE

We present the payload and performances of the X-ray Multi-mirror Mission (XMM), with emphasis on its unique capabilities for cosmological studies of galaxy clusters. The exceptional sensitivity of XMM, associated with good spectroscopic imaging capabilities, will allow the detection and observations of clusters out to cosmological distances ($z > 1$) and very accurate determination of the gas temperature and abundances distributions in more nearby ones. These are key data to determine precisely the dark matter content of these objects and to understand how they form and evolve. We will thus be able to put new independent constraints on cosmological scenario of large structure formation and on associated parameters like the density of the Universe and the shape and normalisation of the initial fluctuations spectrum.

1 The XMM satellite: payload and performances

The XMM (X-ray Multi-mirror Mission) satellite [1] is the second cornerstone of the ESA long-term Science Programme. This facility-class X–ray observatory will be launched in 1999, on a 48 h orbit, with an expected lifetime of 10 years. The specificity of XMM lies in the exceptional collecting area of its X–ray telescopes. XMM is also unique in that it allows simultaneously non dispersive spectroscopic imaging and high resolution dispersive spectroscopy, together with a study of the UV/optical properties of the X-ray source via the coaligned Optical Monitor (OM).

The XMM payload consists in three grazing incidence telescopes of 7.5 meters focal length, with a total effective area of $\sim$ 4500 cm^2 at 2 keV and of $\sim$ 1750 cm^2 at 8 keV. The spatial resolution will be 15" (Half Power Diameter) at the focus of each camera, with a field of view of 30' in diameter. The focal instruments of the X–ray telescopes are of two types (see Fig. 1):

- 2 reflection grating systems for high resolution spectroscopy ($\Delta E/E = 0.1 - 0.3\%$) in the 0.3–2 keV range, placed behind two of the telescopes (RGS experiment).

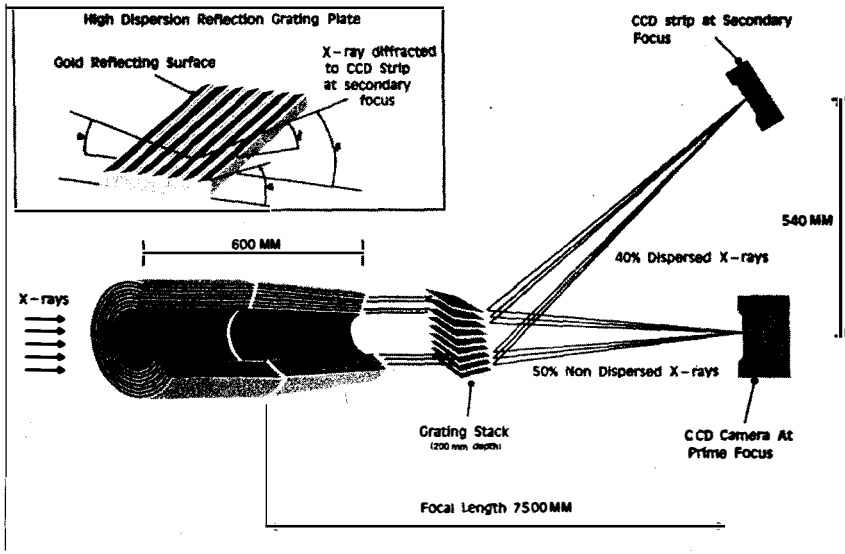

Figure 1: Two of the XMM telescopes are equipped with the RGS experiment. After collection by the mirror module (58 Wolter shells) about 40% of the light is dispersed by a Reflection Grating Array, while a similar amount is focused to the EPIC camera. The diffracted beam is imaged by a CCD camera on the Rowland circle for high resolution spectroscopy. In the third telescope, all the light is collected by the EPIC CCD experiment. The Figure was reproduced from ESA SP-1097.

- 3 CCD cameras placed at the primary focal plane of the three telescopes allowing medium-resolution spectro-imagery in the energy range between 0.1 and 12 keV ($\Delta E = 60 - 140$ eV). Each camera carries a mosaic of CCDs, in order to cover the telescope field of view. Those three cameras constitute the EPIC experiment.

The Optical Monitor consists of a 30 cm Ritchey-Chretien telescope with a MIC detector at the focus (1600 -5500 Å, $17' \times 17'$ Field of view, pixel size of $\sim 1''$).

With a factor ~ 10 increase in effective area as compared to ASCA, and a much improved spatial resolution, better than ROSAT/PSPC, XMM will supersede all the previous X-ray satellites. Two other major X-ray satellites will be launched around the turn of the century: AXAF by NASA (USA) in November 1998 and ASTRO-E by ISAS (Japan, in collaboration with USA) in 2000. XMM, AXAF and ASTRO-E have complementary capabilities: an order of magnitude better spatial resolution of AXAF as compared to XMM, at the expense of collecting area; high resolution non dispersive spectroscopy with ASTRO-E (see Fig. 2).

A more detailed description of XMM, together with a list of XMM publications, can be found on the ESA web site at http://astro.estec.esa.nl/XMM.

2 XMM performances and cluster observations

The X-ray emitting hot intra-cluster medium (ICM) is the main baryonic component of galaxy clusters. X-ray imagery observations provide the gas density distribution, while the determination of the temperature profiles and abundance gradients requires spatially resolved X-ray spectroscopy. From X-ray observations we can derive the heavy element, gas mass and entropy distribution and measure the gravitational potential, through the hydrostatic equation, and thus

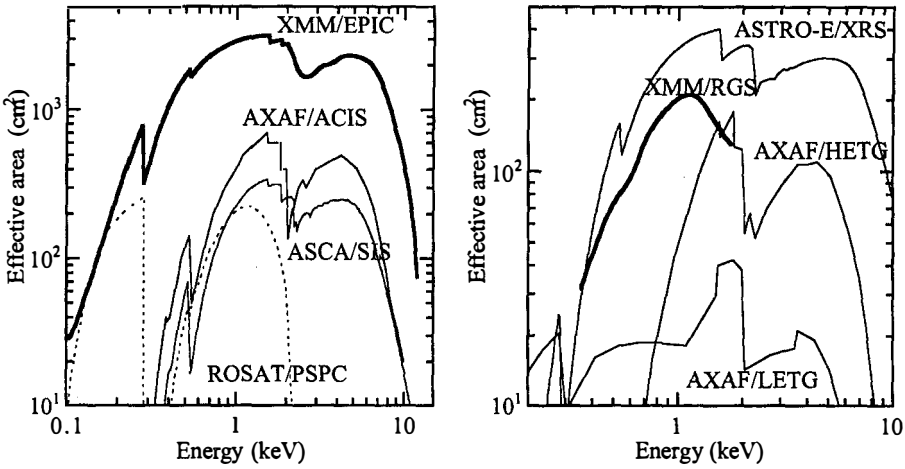

Figure 2: **Left**: Imaging spectroscopy capability of XMM, ROSAT, ASCA and AXAF. The total effective area of XMM/EPIC is compared to the effective area of AXAF/ACIS and ASCA/SIS (CCD cameras) and ROSAT/PSPC (Position Sensitive Proportional counter). XMM/EPIC will combine the spectral resolution of ASCA/SIS with a spatial resolution better than the ROSAT/PSPC, while covering the entire 0.1–10 keV energy range and providing a factor $\sim 5-10$ larger effective area. On the other hand AXAF will provide unprecedently high angular resolution (better than 1"). **Right**: Same for high resolution spectroscopy experiments. The XMM/RGS has a factor about 10 greater effective area than AXAF/HETG but a factor about 2 lower resolving power, as a consequence of the telescope effective area and resolution. AXAF also provides high resolution dispersive spectroscopy at high energy. The definitive improvement in sensitivity will come with the ASTRO-E observatory which will be equipped with a micro-calorimeter array (ASTRO-E/XRS). This non-dispersive device has an efficiency close to 1 over the whole energy range, and is not limited to the observation of point sources.

the total mass content and distribution. All these are key quantities for cosmological studies as discussed in Sect. 3.

Cluster parameters span a very large dynamical range and the large collecting area of XMM is crucial for that reason, all the more as X-ray emission scales as the square of the gas density. XMM/EPIC will permit to probe the external part of the clusters (up to virial radius) where the surface brightness has typically dropped by 3 order of magnitudes from its central peak value. It will enable us to study complete samples of clusters, where poor clusters exhibit a luminosity typically 1000 times lower than the rich clusters. It will also give a unique access to the early Universe clusters, the flux of which can be decreased by ~ 3000 with respect to nearby clusters of same luminosity (when comparing z = 1 to z = 0.0232, the redshift of Coma), and thus to the evolution and formation of clusters (see Fig 3).

The spatial resolution and field of view of XMM/EPIC are well suited to clusters. They will be resolved at all redshift, the half-power diameter of 15" translating to a dimension less than 110 kpc, smaller than the typical core radius. The field of view will enable full coverage of clusters at $z > 0.15$ (assuming a typical virial radius of 3 Mpc and $H_0 = 50$).

The extended energy coverage, up to 12 keV, is necessary to constrain the continuum spectrum of clusters and determine accurately the temperature, that can reach 15 keV. In addition the good energy resolution, combined with the high effective area, will permit precise abundance determinations.

It must be emphasized that XMM has well matched spatial resolution/collecting area performances for extended sources; this is needed to fully take advantage of the improvement in resolution, that required a commensurate increase in sensitivity to get enough photons per bin.

3 XMM and cosmological parameters

Several issues, related to the determination of the cosmological parameters, will benefit from XMM through cluster studies. This includes constraints on the density parameter Ω of the Universe, the initial fluctuation spectrum, the Hubble constant and q_0 parameter. For the determination of these last two parameters through combined X-ray/SZ observations I refer the reader to the review of A. Lange (see these proceedings).

3.1 The baryonic mass fraction and the density parameter of the Universe

The density parameter Ω of the Universe can be constrained [2] by the baryon (essentially gas) mass fraction in clusters, combined with the limit on the baryonic density in the Universe derived from primordial nycleosynthesis. The large gas mass fraction, $f_{\rm gas} \sim 20 - 30\%$, derived recently in several cluster sample studies [3], favors low values of Ω, typically $\Omega = 0.2 h_{50}^{-1/2}$. This is the so-called "baryonic catastrophy". However large uncertainties remain.

If the gas distribution has been mapped with unprecedented precision with ROSAT up to large radii, there are still open issues like the possible clumpiness of the gas and the presence of a multi-phase gas. They need to be solved to be fully confident in the gas mass estimates. AXAF (exceptional spatial resolution) and ASTRO-E (high sensitivity high resolution spectroscopy) are probably the best instruments for these respective issues.

Present day satellites like ROSAT and ASCA only provide very crude information on temperature distribution. The hydrostatic equation relates the total mass enclosed in a given radius to the pressure gradient at that radius. The determination of the total mass distribution thus requires very precise measurements of the temperature profiles. Moreover, an estimate of the total cluster mass, without making further assumptions on the shape of the potential at large scale, requires in principle to extend the measurements up to the virial radius. Furthermore the physics around the virial radius is essentially unknown. Numerical simulations [4] predicts non equipartition between the ionic and electron temperatures in the vicinity of the outer shock and the presence of hot gas beyond the virial radius due to conduction. This has impact on the determination of the total mass and on our understanding of cluster gravitational collapse, and needs to be observationally checked.

XMM, with its exceptional sensitivity and its good spatial resolution, will be the best instrument to measure accurately the temperature profile in clusters and probe the external parts and thus estimate precisely the total mass of cluster. For example we will be able to measure in 50 ksec the temperature profile of a massive ($L_X = 10^{45}$ ergs/s), medium distant (z=0.3) cluster with a 20% precision at 5 core radii (1 core radius wide bin). Comparison with independent weak lensing estimates for such moderate redshift clusters will permit to assess the validity of the X-ray mass determination. We will thus determine if there is indeed a "baryonic catastrophy". Moreover the gas entropy distribution, the relative distribution of the gas and dark matter and the abundance gradients measured by XMM will constrain the thermodynamics history of the gas (gravitational heating due to initial gravitational collapses and by shocks induced by mergers, additional heating by galactic winds) and thus the formation and evolution of clusters.

3.2 The cosmological history of clusters, the density of the Universe and the initial fluctuation spectrum

In the standard hierarchical models of structure formation, bound objects arise from the collapse of initial density fluctuations that grow under the influence of gravity. In such theories, the build-up of structures occurs through continous mergers of smaller previously collapsed structures. This formation process is going on now at cluster scale, as indicated by the observed variety of dynamical states of these objects. Therefore constraints on such cosmological models

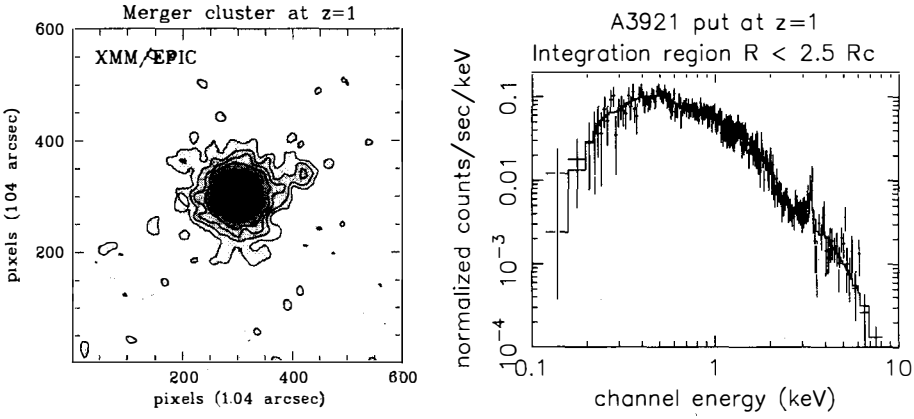

Figure 3: Simulation (J.L.Sauvageot, SAp) of the XMM/EPIC observation of a merger cluster at z=1. The exposure time is 100 ksec. The characteristics of this cluster are those of A3921[5]: its total luminosity is 5 10^{44}ergs/s and the main cluster is accreting a sub-cluster located 1 Mpc away from its center. The sub-cluster is 10 times less luminous than the main cluster. **left**: Simulated image of the cluster as seen by the central EPIC/MOS CCD. Note that the sub-cluster is perfectly resolved and detected. **Right**: Simulated EPIC spectrum. The temperature is determined with a precision better than 10%.

can be inferred from statistical studies of the cluster population properties and its evolution with time.

Many analytical and numerical calculations show that the present rate of cluster growth depends strongly on the density parameter Ω of the Universe. This cosmological parameter can thus be constrained in principle from the frequency of substructures in the present day cluster population [6], provided that subclustering is a reliable indicator of youth or recent accretion and that 'substructure' is suitably quantified. In practice recent attempts to constrain Ω from statistical studies of cluster X-ray spatial morphologies[7] have yielded some contradictory results and the reliability of this method is debated [8]. It is essential that we understand better the physics of merger events (in particular the intracluster medium relaxation timescale) and their effect on observable cluster properties.

Hydrodynamic simulations of cluster evolution[9] indicate that the evolutionary state of clusters should be much better characterized by the temperature structure than by the surface brightness structure. The high sensitivity and good spatial and spectral resolution of XMM will allow a major step forward in our ability to investigate merger events and in our understanding of cluster formation. With XMM it will possible for the first time, to obtain unblurred temperature maps of nearby and medium redshift clusters (as discussed above) and to detect merger events at high redshift (see Fig 3). AXAF will provide the high resolution structure information on bright clusters, that XMM will not be able to give.

Similarly the present day cluster mass distribution and its evolution is a strong cosmological constrain [10] (see the review of A.Blanchard, these proceedings). The number of clusters per unit of mass at a given redshift, N(m,z) can be computed from the initial density fluctuation spectrum, that can be thus constrained from comparison with local observations. On the other hand the evolution of the high mass end of the mass function strongly depends on the value of Ω. Unfortunatly it is difficult to measure directly the mass, M, and one has to use indirect related quantities like the temperature, kT, or even the luminosity L_X. Furthermore only the local

temperature function is presently known and we have only crude information on the evolution of the luminosity function (through cluster X-ray surveys).

To make significant progress it is essential to do more sensitive X-ray surveys, as possible with XMM, and thus obtain larger samples, extending to higher redshift. For instance XMM will serendipitously detect 1000 clusters/yr with $F_X[0.5-10keV] > 10^{-14} erg/s/cm^2$. It is also important to obtain accurate mass function at least for nearby redshift clusters (i.e measure their mass, see above) and obtain as accurate as possible temperature estimates for distant clusters. Note that XMM will be able to measure the mean temperature of medium luminosity, $z = 1$ clusters (see Fig 3) and detect and resolve $z = 2$ clusters, with crude (at $\sim 20\%$) estimate of kT if they are very luminous ($L_X > 10^{45}$ ergs/s for $\sim 100ksec$ exposures). Equally important will be the capability of XMM to measure and understand the scaling between M, kT and L_X. For instance numerical simulation of cluster formation predicts universal scaling law for the potential shape and for the relationship between cluster mean temperature and total mass, that could be cheked with XMM. The kT-L_X relation is likely to strongly depnds on the detailed thermodynamical history of the ICM, which we will be able to assess with XMM.

4 Conclusion

Galaxy clusters occupy a unique position in the hierarchical scenario of structure formation, as their population is still forming today. Their observed properties depend on cosmological initial conditions, but also on the detailed physical mechanisms at work within them (gravitational relaxation, heating and cooling...). Thus clusters can put important constraints on cosmological parameters, providing that we understand how they form as individual objects and then evolve. This requires spectroscopic information, yielding temperature and abundances distribution, on a cluster sample, that covers a wide mass and redshift domains. XMM with its superior sensitivity and good spatial and spectral resolution will be the best facility to perform such studies.

Finally I would like to emphasize that we shall soon benefit from a unique opportunity for cosmological studies, with complementary observatories: the X-ray satellites XMM, AXAF, ASTRO-E (formation and evolution of clusters), MEGACAM (weak lensing and distribution of the dark matter) and PLANCK Surveyor (cosmological parameters from CMB, SZ effect). Equally important is the development of the numerical simulations of large structures formation and cluster inner evolution.

References

1. D.Lumb, H.Eggel, R.Lainé, A.Peacock, Proceedings of the SPIEE v2808, 1996, p.326. See also the serie of papers on XMM in these proceedings.
2. White S.D.M., Frenk C.S., 1991, ApJ, 379, 52
3. Evrard A.E., 1997, MNRAS, 292, 289
4. Chieze, J.P., Alimi, J., Teyssier, R., 1998, ApJ, 495, 630
5. M. Arnaud M., R. Rothenflug R., D. Neumann D., Böhringer H., Yamashita.K., 1997, A&A submitted
6. Richstone D., Loeb A., Turner E.L., 1992, ApJ, 393, 477
7. Buote D., Xu G., 1997, MNRAS, 284, 439
8. Nakamura F.E., Hattori M., Mineshige S., 1995, A&A, 302, 649
9. Schindler S., Müller E., 1993, A&A, 272, 137
10. Oukbir J., Blanchard, A., 1997, A&A, 317, 1

THE XMM MEDIUM DEEP SURVEY

Marguerite PIERRE (mpierre@cea.fr)
DAPNIA/CEA Service d'Astrophysique,
XMM Survey Science Center,
CE Saclay, F-91191 Gif sur Yvette, France

In the context of the XMM Guaranteed Time, we have defined a survey covering 25 square degrees down to a sensitivity of $\sim 10^{-14}$ erg/s/cm^2. This will enable us to investigate in a unique way large scale structures out to $z \sim 1-2$.

1 X-ray large scale structures and XMM

High galactic latitude fields observed at medium sensitivity in X-ray (10^{-14} erg/s/cm^2) contain essentially two types of sources: AGN (pointlike) and galaxy clusters (extended). Mapping a large area is thus potentially extremely relevant to understand the distribution of the deep potential wells of the universe as well as that of QSOs (which is still an enigma). Numerous complementary applications are possible in connection with surveys at other wavelengths such as the Sunyaev-Zel'dovich effect and optical weak lensing analyses.

Thanks to its very large collecting area and good spatial resolution ($\sim$ 12"), XMM is the ideal instrument for mapping large scale structures in the X-ray band. It will be able to flag galaxy clusters as extended sources out to $z \sim 1-2$.

2 The XMM Medium Deep Survey

The project has been designed by teams belonging to the XMM consortiums in association with optical surveys. The total covered area will be $5^o \times 5^o$ with exposure times of 20 ks. From this, we expect some 300 clusters out to $z \sim 2$ and 10 times as many AGNs or QSOs, probably much further away. Fig. 1 shows a simulated high-z cluster spectrum observed with the EPIC instrument and Fig. 2, the expected cluster redshift distribution.

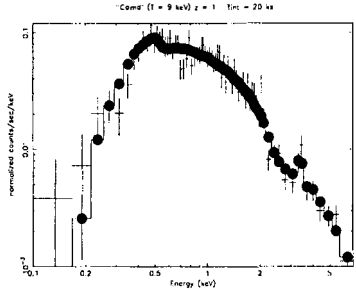

Figure 1: Simulated XMM/EPIC spectrum of a Coma-like cluster (T = 9 keV, $L_X = 10^{45}$ erg/s), located at $z = 1$, observed during 20 ks and assuming that 60% of the total flux has been used for the spectrum; overlaid is the corresponding model. Such a spectrum enables a temperature and a redshift determination to within 15-20% and 5-10 % respectively.

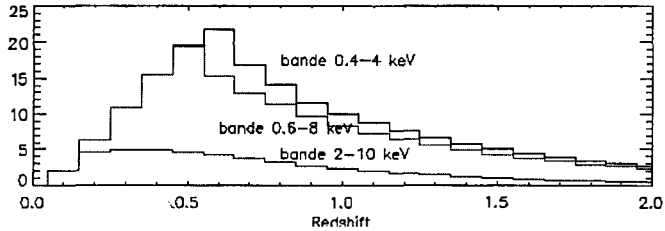

Figure 2: Expected cluster population to be seen by XMM, for a 15 sq. deg. area observed during 20 ks and assuming the canonical value of 250 kpc for the cluster core radii and no evolution of the cluster luminosity function up to the considered redshifts. Detection has been performed in three energy bands at the 5σ level which corresponds to $\sim 10^{-14}$ erg/s/cm^2 in the [2-10] keV band. With this configuration, we expect more than 300 clusters in total for a 25 sq. deg. area: 1/3 of them being located beyond $z \geq 1$ with a distribution peaking at $z = 0.6$. Alternatively, if a 3 σ detection is assumed with $R_c = 100$ kpc, which is representative of cooling flow clusters (or of small groups), the number of detected objects could exceed 500 with a distribution centered around $z = 0.8$.

The XMDS consortium consists of:

CE Saclay, XMM/SSC (M.Pierre)
IFCTR Milan, XMM/EPIC (D. Maccagni)
Uni. Liège, XMM/OM (J.Surdej)
CE Saclay, CFHT/MEGACAM (L. Vigroux), optical imaging
LAS Marseille, VLT/VIRMOS (O. Lefèvre), optical spectroscopy

3 Reference

http://astro.estec.esa.nl/XMM/xmm.html

PROBING THE HOT IGM WITH AXAF

CLAUDE R. CANIZARES & TAOTAO FANG
Department of Physics & Center for Space Rsearch,
Massachusetts Institute of Technology,
Cambridge MA USA 02136

The transmission grating spectrometers on AXAF have sufficient sensitivity and energy resolution to detect resonance X-ray absorption lines in the spectra of distant quasars. Such lines would be produced in an ionized, and somewhat chemically enriched component of the inter-galactic medium. The bulk of the baryonic content of the universe at redshifts $\leq 2-3$ could be in this form and would thus be revealed by AXAF.

The Advanced X-ray Astrophysics Facility (AXAF)[a], now scheduled for launch in late 1998, will carry two transmission grating spectrometers that give unprecedented energy resolution and good sensitivity over 0.07-8 keV. These are the Low Energy[1] and High Energy Transmission Gratings[2] (LETG and HETG)[b], each of which is optimized for a portion of the energy band, and each of which can achieve resolving powers of up to $E/\Delta E \approx 1000$.

We plan to use AXAF's spectroscopic capability to probe the hot component of the intergalactic medium (IGM). This is an analog of the well established studies of cooler IGM material through UV and optical spectroscopy, which have revealed the Lyman α forest, damped Ly α clouds, metal line systems, etc. As in those studies, we will be looking for spectral features imposed by the intervening material on the X-ray continuum of distant quasars.

In the X-ray band, the features of interest are resonance lines from highly ionized heavy elements, some of which are listed in Table 1. Several of these (marked with an asterix) are the Ly α lines of hydrogenic species, whose energy is 13.6 Z^2 eV (where Z is the atomic number). Some other K lines of He-like alpha elements and L lines of Ne-like to H-like Fe may also be of interest. In principle, absorption edges from bound-free transitions of heavy elements in any

[a] http://asc.harvard.edu
[b] for HETG see http://space.mit.edu/HETG, for LETG see http://www.rosat.mpe-garching.mpg.de/axaf

Table 1: Table 1. Resonant X-ray Absorption Lines (* denotes Ly α lines of hydrogenic ions)

Ion	E (keV)	Ion	E (keV)
OVII	0.57	MgXII*	1.47
OVIII*	0.65	SiXIII	1.87
FeXVII	0.83	SiXIV*	2.01
NeIX	0.92	FeXXV	6.70
NeX*	1.02	FeXXVI*	6.97
MgXI	1.35		

ionization stage should also be present, but in practice the optical depths for edges are likely to be too small.[3]

The sensitivity of the AXAF spctrometers is such that we will readily detect absorption lines with equivalent widths comparable to our spectral resolution element of $\approx 1eV$ (or $10^{-2}A$) at 1 keV. One might push as much as an order of magnitude lower in selected observations. To produce such a feature requires a column density of the appropriate ion of $\approx 10^{16} cm^{-2}$ which in turn implies hydrogen column densities of $\approx 2 \times 10^{20} f_{ion}^{-1} [A/A(Fe)_{\odot}]^{-1}$, where f_{ion} is the ionization fraction and $A/A(Fe)_{\odot}$ is the element abundance relative to the solar value for Fe. To put this in an astrophysical context, it would suffice to have 3×10^{12} $M_{\odot}$ spread over a sphere of radius 0.5 Mpc if it had 0.3 solar abundance; this would correspond to a density 2.5×10^{-4}, or an overdensity of 50 times critical at the present epoch.

Thus AXAF spectrometers will probe any moderately dense regions along the line of sight containing material that is both ionized and somewhat enriched with heavy elements. Ionization could be either collisional or radiative, corresponding to thermal plasma with tempratures above $\approx 3 \times 10^6 K$ or ionization parameters $\xi \geq 0.1$, respectively.

There is good reason to believe that ionized, chemically enriched regions not only exist, but may well represent most of the baryonic content of the universe at redshifts less than 2-3.[4,5] Standard big bang nucleosynthesis predicts baryon densities of $\Omega_B \approx 0.1 - 0.3$, and recent estimates of the number and density of Ly α clouds at high redshift are consistent with this value. But Ω_B in stars or cool clouds at lower redshift is less than 0.004 (values quoted are for $H_o = 70 km\ s^{-1}\ Mpc^{-1}$). Scaling from groups and clusters of galaxies supports the hypothesis that, at lower redshift, most of the baryons are in the form of hot plasma. It is also plausible that this plasma is at least moderately enriched with heavy elements.[5,6,7] Even at high z, the Ly α clouds appear to have metalicities as high as ≈ 0.1 solar.[8]

It is instructive to consider the densest clouds seen in the optical/UV, namely damped Ly α systems (DLA). These have hydrogen column densities approaching $10^{21} cm^{-2} s^{-1}$ and metalicities 10% of solar. [9] We estimate that the X-ray background, though highly uncertain, is ten times too weak to photoionize a typical DLA sufficiently to give detectable X-ray lines.[10] On the other hand, it may well be that the clouds are also ionized by shocks and/or by a local source of photoionizing radiation, as suggested by the detection of OVI lines.[11] In that case the DLA could be seen in X-rays as well.

Observationally, rather than focus on the few DLA quasars already detected in X-rays, we have chosen to take an approach that simply maximizes the sensitivity to randomly distributed X-ray absorbers. During the first several months of the AXAF mission, we will observe the brighest X-ray quasars with $z \geq 2$, 0836+7104 and 2149-304. Lower redshift abosrbers will be probed by several observations of more local quasars and BL Lac objects.

Although our program is something of a fishing expedition, it has the considerable potential

of providing an entirely new probe of the IGM and of revealing the bulk of the baryons in the universe.

Acknowledgments

This work supported in part by NASA contract NAS8-38249

References

1. P. Predehl, H. Kraus, H. W. Brauninger, W. Burkert, G. Kettenring & H. Lochbihler, *SPIE Proceedings* 1743, 475 (1992
2. T.H. Markert, C.R. Canizares, D. Dewey, M. McGuirk, C. Pak & M.L. Schattenburg, *SPIE Proceedings* 2280, 168 (1994)
3. P. Shapiro & J. Bahcall *Astrophys. J.* 241, (1980), K.S. O'Flaherty & P. Jackson *Astrophys. J.* 479, 673 (1997)
4. E. Giallongo, S. Cristiani, S. D'Odorico, A. Fontana & S. Savaglio in *13th IAP Colloquium: Structure and Evolution of the Intergalactic Medium from QSO Absorption Line Systems* ed. P. Petitjean & S. Charlot in press
5. M. Fukugita, C. Hogan & P.J.E. Peebles preprint astro-ph/9712020 (1997)
6. P. Salucci & M. Persic preprint astro-ph/9601018 (1996)
7. A. Renzini in *The Young Universe* ed. S. D'Odorico *et al.* Astron. Soc. Pacific. Conf. Series in press (astro-ph/9801209)
8. C. Steidel, M. Dickinson, D. Meyer, K. Adelberger & K. Sembach *Astrophys. J.* 480, 568 (1997)
9. L. Lu, W. Sargent, T. Barlow, C. Churcill & S. Vogt *Astrophys. J. Supp.* 107, 475 (1996)
10. T. Fang & C. Canizares *Bull. Amer. Astron. Soc.* 191, 122.06 (1997), C. Canizares & T. Fang in *13th IAP Colloquium: Structure and Evolution of the Intergalactic Medium from QSO Absorption Line Systems* ed. P. Petitjean & S. Charlot in press
11. L. Lu and B. Savage *Astrophys. J.* 403, 127 (1993), S. Burles and D. Tytler *Astrophys. J.* 460, 584 (1996)

HIGH-REDSHIFT QUASARS AS PROBES OF PRIMORDIAL LARGE-SCALE STRUCTURE AND GALAXY FORMATION

S.G. DJORGOVSKI
Palomar Observatory, Caltech, Pasadena, CA 91125, USA

Several arguments suggest that quasars at $z > 4$ may be in the cores of future giant ellipticals, and forming at the very highest peaks of the primordial density field. A strong bias-driven primordial clustering is then expected in these fields, which are naturally interpreted as the cores of future rich clusters. High-redshift quasars can thus be used as markers of some of the earliest galaxy formation sites. Recent discoveries of (proto)galaxy companions of $z > 4$ quasars, and hints of strong clustering among high-z quasars give some support to this idea. The frequency of companions is much higher than is expected for a general field, or the upper limits for comparable redshifts in the HDF. Clustering of quasars themselves at $z > 3$ or 4 may reflect the primordial large-scale structure.

1 Introduction

Primeval galaxies (PGs) have now been found, in a variety of forms and environments, using a variety of techniques: narrow-band Lyα imaging [1], Lyman-break method [2], as DLA absorbers [3], as quasar companions [4,5], as gravitationally lensed objects [6], etc. Statistical studies of the HDF [7] have outlined a global history of galaxy formation in the general field. Moreover, we are starting to see evidence [8] for large-scale structure formation at high redshifts, i.e., $z > 3$.

However, any single discovery method may bias the sample of objects found, and formative histories of galaxies in different environments may vary substantially. For example, galaxies in rich clusters are likely to start forming earlier than in the general field, and studies of galaxy formation in the field may have missed possible rare active spots associated with rich protoclusters. Diverse and complementary paths towards discoveries of first galaxies are still very much worth pursuing. Our group is pursuing the use of quasars at $z > 4$ as markers of the early galaxy formation sites, by looking for PGs associated and/or clustered with quasar host galaxies themselves ($z_{gal} \approx z_{QSO}$).

It is now believed that galaxy formation is an extended series of processes, which may have a broad peak at $z \sim 2-3$. However, it is of a considerable importance to catch the *first* galaxy-size structures forming at high redshifts, i.e., the very onset of massive galaxy formation.

Any galaxies at $z > 4$ must be still very young, simply on account of the timing: they can be at most a few percent of the present galaxian age, or $\sim 0.5-1$ Gyr, for any reasonable cosmology. The evolutionary status of galaxies at $z \sim 2$ or 3 is more ambiguous, with possible physical ages up to $\sim 2-3$ Gyr, or $\sim 10-20\%$ of their present age. Going to $z > 4$ removes this age ambiguity.

We are conducting an observational program to discover and study such protogalaxies in the earliest stages of formation, clustered with the known quasars at $z > 4$. This pushes beyond the territory now explored in the HDF and elsewhere, at the epochs when the universe was only a few percent of its present age.

2 Quasars as Cores of Massive Protogalaxies

There is currently very little known about normal galaxies and their progenitors at $z > 4$. While the current theoretical belief[9] is that some subgalactic structures ($M \sim 10^6-10^8 M_\odot$) may start forming at $z \sim 6-10$, more massive ($M \sim 10^{11}-10^{12} M_\odot$) progenitors of normal galaxies today are unlikely to be in place before $z \sim 4-5$.

Some of these first massive protogalaxies may be the hosts of quasars at $z > 4$. While AGNs by themselves are problematic as a probe of galaxy formation and evolution, they may still provide useful pointers to the sites of early galaxy formation. The relation between high-z AGN and galaxy formation remains unclear. The comoving density of quasars seems to track very well the inferred history of star formation in galaxies[7], and both follow the merger rate evolution predicted by hierarchical structure formation scenarios. The same kind of processes, dissipative merging and infall, may be an important trigger of both star formation and the AGN activity.

Indeed, most or all ellipticals and massive bulges at $z \sim 0$ seem to contain central massive dark objects suggestive of an earlier quasar phase[10]. Masses of these putative "dead quasars" also correlate with the luminous old stellar mass of the host galaxy, again suggestive that they formed at about the same time and through the same sequence of early dissipative merging and starbursts.

The very existence of numerous quasars at $z > 4$ poses a timing problem, and it is likely that they are situated in the massive parent structures (future host galaxies) which are among the first objects to form[11]. Furthermore, high metallicities (up to $10 \times Z_\odot$!) observed in $z > 4$ quasars[12] are indicative of a considerable chemical evolution involving several generations of massive stars in a system massive enough to retain and recycle their nucleosynthesis products, e.g., comparable to the cores of giant ellipticals. Metallicities and abundance patterns in the intracluster x-ray gas at lower redshifts are also suggestive of an early, rapid star formation and enrichment phase in the rich cluster progenitors at high redshifts[13].

It is perfectly possible that *every* young elliptical or a massive bulge undergoes an early quasar phase as it is forming the bulk of its stars. While quasar activity can happen at any redshift if there is a central engine in place and a supply of fuel available, the situation at high redshifts is special: these objects must be young on account of the short time scales. Quasars at $z > 4$ can thus be naturally interpreted as being in the cores of future massive ellipticals.

In general, the most massive density peaks in the early universe are likely to be strongly clustered[14] and thus the first galaxies may be forming in the cores of future rich clusters. It then makes sense to look for other galaxies with or without AGN, forming in the immediate vicinity of known $z > 4$ quasars.

3 Quasar Clustering at z > 3

There is a possibility that some quasar-marked protoclusters at high redshifts have already been discovered. Schneider, Schmidt & Gunn (SSG) [15] present the results of a grism search for quasars at $2.7 < z < 4.9$, covering 61.47 deg^2. In this volume, they define a *complete* sample of 90 quasars, which they used to measure the evolution of the quasar luminosity function. However, they have found something remarkable: among their complete sample of 90 quasars, there are *3 close pairs*, all at $z > 3$: PC 0951+4637 A+B: $\langle z \rangle = 3.223$, $\Delta z = 0.005$, $\Delta\theta = 410$"; PC 1314+4748 A+B: $\langle z \rangle = 3.355$, $\Delta z = 0.004$, $\Delta\theta = 364$"; and PC 1643+4631 A+B: $\langle z \rangle = 3.810$, $\Delta z = 0.041$, $\Delta\theta = 198$".

The corresponding comoving separations are $\sim 3 - 5$ Mpc, i.e., comparable to the sizes of galaxy clusters. The volume covered by the SSG survey is huge, and for each quasar pair, the probability of a random occurrence in this volume is $\sim$ a few $\times 10^{-5}$. The pairs are detected independently. Thus, the joint probability of finding 3 pairs this close in this survey is $P \sim 10^{-13}$! This clearly cannot be due to a chance. Assuming a standard power-law clustering with slope $\gamma = -1.8$, the implied comoving clustering length is of the order of $50h^{-1}$ Mpc, i.e., comparable to that of the richest Abell clusters today. It thus appears very likely that these quasar pairs mark sites of rich protoclusters of galaxies.

While sporadic evidence for clustering of quasars at high redshifts has been presented in the past, this was the first time that a complete and well-defined sample of quasars was available for this purpose, enabling meaningful statistical arguments. Clustering of absorbers and their companion galaxies has also been detected in several instances, and of Lyman-break galaxies as well: we know that some large scale structure is in place at $z \sim 2 - 3$.

Studies of the clustering of quasars for the entire SSG sample have been done by two groups [16,17]. Both have found some evidence for clustering, which is dominated by these pairs. Previous studies of quasar clustering (typically out to $z \sim 2$ or so) have generally found that their clustering amplitude decreases with redshift, presumably reflecting the growth of the large-scale structure [18]. Here we seem to see the reversal of this trend: a sudden (and perhaps rather dramatic) increase in the clustering strength of quasars at $z > 3$. Similar effect was also found by La Franca et al. [19], in an analysis of a completely independent sample of objects at somewhat lower redshifts.

This can be interpreted as an evidence for biasing: these quasar pairs may be marking some of the highest peaks of the density field at that epoch, probably marking the regions which will evolve into rich galaxy clusters today.

We searched for other objects at the same redshifts in these quasar-pair fields using narrow-band imaging centered on the redshifted Lyα line to select star-forming galaxies and faint AGN at the same redshifts. Our preliminary spectroscopic follow-up confirmed several objects, including both Lyα emission galaxies, and previously unknown, faint quasars [20]. These findings are certainly consistent with the idea that these quasar pairs may be marking sites of future rich clusters [21].

It then makes sense to push to even higher redshifts, and look for objects clustered with known quasars at $z > 4$.

4 New Discoveries of Quasar Companions at z > 4

This approach has been proven to work. The first galaxy discovered at $z > 3$ was a quasar companion (PKS 1614+051 at $z = 3.215$) [4], and many other examples have been found since then at $z \sim 2 - 3$. This method is now starting to yield non-AGN galaxies at $z > 4$.

A galaxy companion of BR 1202–0725 at $z = 4.695$ has been discovered independently and at the same time by two groups [22,5], and confirmed spectroscopically [23]. No high-ionization lines

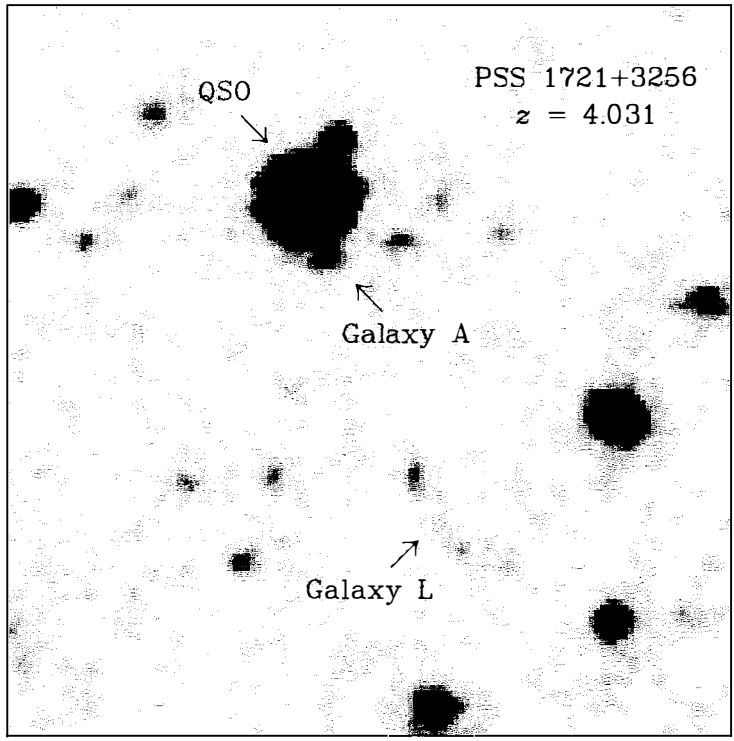

Figure 1: Deep R band Keck image of the field of PSS 1721+3256, a quasar at $z = 4.031$. The field shown is 27.5 arcsec square. Galaxy L is an $R \approx 25^m$ object at the QSO redshift; galaxy A is probably also at the same redshift.

detected in its spectrum, but the close proximity of this object to the QSO suggests that its strong Lyα emission may be powered by the QSO radiation field, rather than by star formation. Furthermore, a dusty companion object has been found in the same field [24,25]. Two companion galaxies were also found [26] in the field of the quasar BR 2237–0607 at $z = 4.55$.

There are now several other cases. For example, we have recently found [20] an apparently normal galaxy companion of the quasar PSS 1721+3256 at $z = 4.031$ (Fig. 1). It is an $R \approx 25^m$ galaxy seen 13 arcsec in projection from the QSO (corresponding to ~ 450 comoving kpc, or ~ 90 proper kpc at that redshift, for a reasonable range of cosmologies), sufficiently far as to be relatively unaffected by the QSO radiation field. Its inferred continuum luminosity is $\sim L_*$, and its spectrum (Fig. 2) shows no trace of an AGN: no high ionization lines, relatively weak Lyα (an order of magnitude less than the companion of BR1202–0725) with $W_{\lambda\, rest} \approx 25$ Å. The inferred star formation rate, both from the Lyα emission line and the UV continuum at $\lambda_{rest} = 1500$Å, is SFR ≈ 4 to $5\ M_\odot$/yr. Its properties are then exactly what one may expect from a PG powered by a mild star formation. Another possible Lyα companion galaxy in the same field (galaxy A) awaits a further spectroscopic confirmation.

Another very interesting case is PSS 0030+1702 at $z = 4.305$ (Fig. 3). The QSO has at least

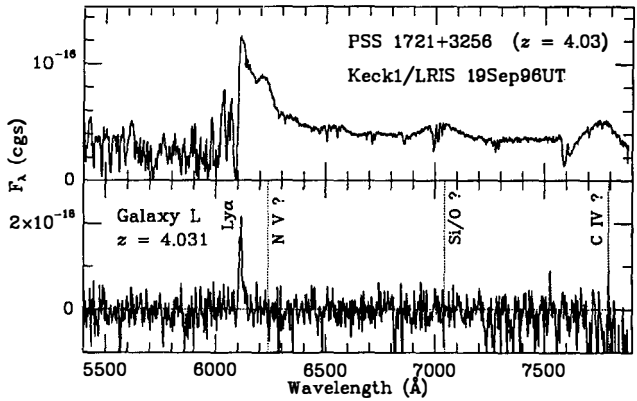

Figure 2: Keck spectra of the quasar PSS 1721+3256 and its companion galaxy L at $z = 4.031$. Note the complete absence of high-ionization lines in the galaxy's spectrum, suggesting that it is powered by star formation, rather than by an AGN.

one, and possibly two Lyα companion galaxies within 10 arcsec from the line of sight [20]. Their observed parameters are similar to those of the galaxy companion of PSS 1721+3256, described above: no high-ionization lines in their spectra, relatively weak Lyα, continuum luminosity $\sim 1 - 1.5\ L_*$, SFR $\sim 10 \pm 5\ M_\odot$/yr (both from the Lyα line, and the UV continuum flux). We also conclude that these objects are most likely powered by star formation.

We have also found [20] similar cases of protogalaxy companions of quasars PSS 0117+1552 at $z = 4.275$, PSS 0248+1802 at $z = 4.465$, PSS 1048+4407 at $z = 4.45$, PSS 1057+4555 at $z = 4.12$, PSS 1253-0228 at $z = 4.01$, and GB 1713+2148 at $z = 4.01$; several other cases which require more observations at this point. Overall, the intrinsic properties of these quasar companion galaxies (their luminosities, SFR, etc.) are very similar to those of the Lyman-break selected populaton at $z \sim 3$, except of course for their special environments and higher look-back times.

In addition to these galaxies where we actually detect (presumably starlight) continuum, we sometimes see pure Lyα emission line nebulæ within a few arcsec from the quasars, with no detectable continuum at all. One example is PSS 0030+1702. The Lyα flux from the nebula exactly what may be expected from photoionization by the QSO, with $L_{Ly\alpha} \approx 2 \times 10^{43}$ erg/s. These nebulæ may be parts of still gaseous protogalaxy hosts of the quasars themselves. We can thus see and *distinguish* both the objects powered by the neighboring QSO, and objects which by all signs appear to be "normal" PGs in their vicinity.

5 Evidence for Protoclusters in Highly Biased Regions?

The median projected separations of these objects from the quasars are $\sim 100h^{-1}$ comoving kpc, an order of magnitude less than the comoving r.m.s. separation of L_* galaxies today, but comparable to that in the rich cluster cores. The frequency of QSO companion galaxies at $z > 4$ also appears to be an order of magnitude higher than in the comparable QSO samples at $z \sim 2 - 3$, the peak merging epoch; galaxy interactions alone are thus probably not the

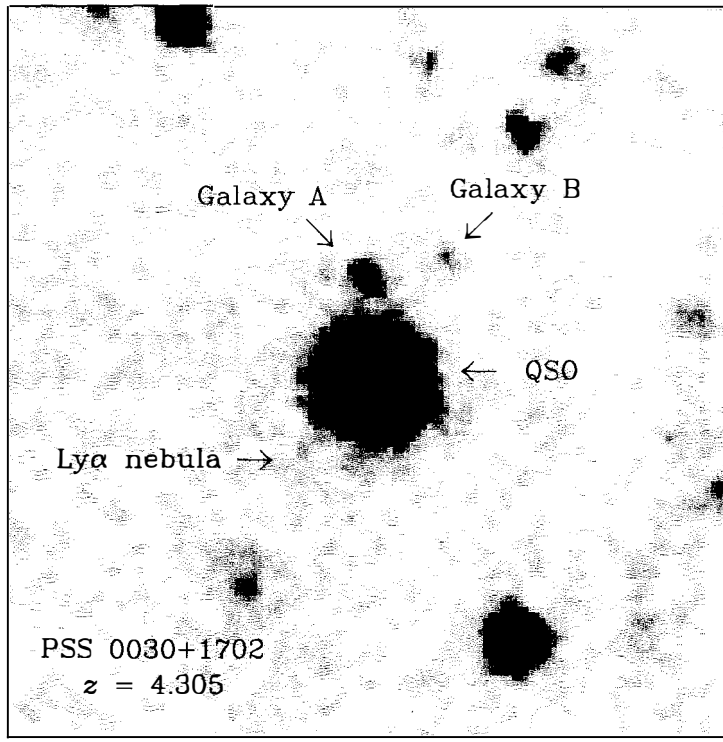

Figure 3: Deep R band Keck image of the field of the quasar PSS 0030+1702, at $z = 4.305$. The field shown is 27.5 arcsec square. Galaxy A is an $R \approx 24^{m}$ object at the QSO redshift; galaxy B ($R \approx 25^{m}$) may also be at the same redshift. There is a pure Lyα line emission nebula on the opposite side of the quasar, probably a part of the still gaseous QSO host galaxy ionized by its UV emission.

whole story here. The implied average star formation density rate in these regions is some 2 or 3 orders of magnitude higher than expected from the limits estimated for these redshifts [7] for *field* galaxies.

While this is still very preliminary, this "excess" may be an observable manifestation of biasing, i.e., the expected clustering of the highest density peaks. A generic expectation in most models of galaxy formation, including the standard CDM cosmogony, is that first objects forming at high redshifts should be strongly clustered: they would presumably form in the highest peaks of the density field, which are clustered *ab initio* [14,27]. The same explanation applies to the redshift "spikes" at $z \sim 3 - 3.5$ found by Steidel et al. [8]. What we are finding may be even denser, and thus much rarer peaks at $z > 4$. Because they are rare, we use quasars as markers of sites where some structure is already forming, in order to increase our chances. Doing a "pure deep field" approach at these redshifts would be much harder and less likely to succed than at $z \sim 3$. These are obviously very special (highly biased) spots in the early universe.

Quasars at $z > 4$ may thus be interpreted as being in the metal-rich cores of young, massive ellipticals, and possibly mark sites of future rich clusters of galaxies. The discoveries of their companion galaxies may support this idea: these may be "normal" PGs in the cores of future rich clusters, in the earliest stages of formation. These are obviously very special spots in the early universe, and they present a great opportunity to study galaxy and cluster formation, in an enviroment deliberately different from the general field (e.g., the HDF).

On an even larger scale, there may be some evidence for excess power on supercluster scales, as probed by quasars at $z > 4$ (Fig. 4). While the numbers of objects are still relatively small, we are finding an unexpectedly large frequency of QSO pairs and triplets (and even one quartet!) with typical comoving separations of $\sim 100h^{-1}$ Mpc [20]. The statistical significance of this effect is still difficult to quantify, due to the heterogeneity of some of the data, and the patchy sky coverage. The effect may be spurious, e.g., due to the variable depth of the QSO surveys or other selection effects, or it could be real. If it is real, it may be due to the actual clustering of quasars, or to some other physical effect, e.g., a patchy gravitational magnification by the foreground large-scale structure.

If this is a real clustering signal, its implications would be profound. It would be the first detection of a primordial large-scale structure, seen by its highest, highly biased peaks containing quasars, only a few hundred physical Mpc away from the CMBR photosphere. As the data improve, both for the QSO samples and the CMBR measurements, it would be intriguing to see if any correlation can be found between these quasar-marked structures and the CMBR fluctuations behind them.

Further work is needed in order to better establish and quantify these findings. If the evidence holds, it would represent a powerful confirmation of our basic ideas about biased galaxy formation. In any case, we are begining to probe the earliest phases of galaxy and large-scale structure formation at high redshifts.

Acknowledgments

Various parts of this work are done in collaboration with S. Odewahn, R. Gal, R. de Carvalho, L. Ferrarese, M. Pahre, K. Banas, and several others; their efforts and contributions are gratefully acknowledged. I also wish to thank the staff of Palomar and Keck observatories for their expert help during many observing runs. This work was supported in part by the Bressler Foundation and the Norris Foundation. I thank the organizers for a partial travel support.

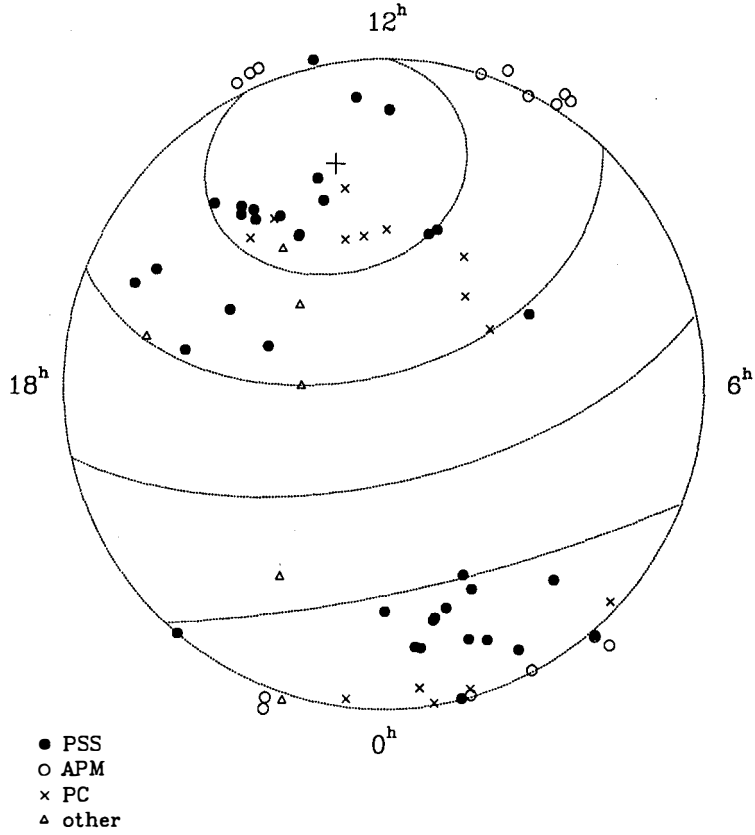

Figure 4: The distribution of known $z > 4$ quasars (as of May 1998) on the northern and equatorial sky. The majority are from the uniform, but still very incomplete Palomar DPOSS survey (PSS)[28,20]; others are from the APM survey [29], from the Palomar transit surveys (PC) [15], and a few others selected in radio, x-rays, colors, or serendipity. Several close pairs and triplets are seen, sometimes with components found by independent surveys. The dotted lines indicate the circles of equal Galactic latitude, $b_{II} = -30°, 0°, +30°$, and $+60°$, and the cross marks the North Galactic pole.

References

1. Cowie, L., & Hu, E. *Astron. J.* **115**, 1319 (1998).
2. Steidel, C., Giavalisco, M., Pettini, M., Dickinson, M., & Adelberger, K. *Astrophys. J. Lett.* **462**, L17 (1996).
3. Djorgovski, S., Pahre, M., Bechtold, J., & Elston, R. *Nature* **382**, 234 (1996).
4. Djorgovski, S., Spinrad, H., McCarthy, P., & Strauss, M. *Astrophys. J. Lett.* **299**, L1 (1985).
5. Hu, E., McMahon, R., & Egami, E. *Astrophys. J. Lett.* **459**, L53 (1996).
6. Franx, M., Illingworth, G., Kelson, D., van Dokkum, P., & Tran, K. *Astrophys. J. Lett.* **486**, L75 (1997).
7. Madau, P., Ferguson, H., Dickinson, M., Giavalisco, M., Steidel, C., & Fruchter, A. *Mon. Not. R. Astron. Soc.* **283**, 1388 (1999).
8. Steidel, C., Adelberger, K., Dickinson, M., Pettini, M., & Kellogg, M. *Astrophys. J.* **492**, 428 (1998).
9. Miralda-Escude, J., & Rees, M. *Astrophys. J. Lett.* **478**, L57 (1997).
10. Kormendy, J., & Richstone, D. *Ann. Rev. Astron. Astrophys.* **33**, 581 (1995).
11. Turner, E. *Astron. J.* **101**, 5 (1991).
12. Hamann, F., & Ferland, G. *Astrophys. J.* **418**, 11 (1993).
13. Loewenstein, M., & Mushotzky, R. *Astrophys. J.* **466**, 695 (1996).
14. Kaiser, N. *Astrophys. J. Lett.* **284**, L9 (1984).
15. Schneider, D., Schmidt, M., & Gunn, J. *Astron. J.* **107**, 1245 (1994).
16. Stephens, A., Schneider, D., Schmidt, M., Gunn, J., & Weinberg, D. *Astron. J.* **114**, 41 (1997).
17. Kundic, T. *Astrophys. J.* **482**, 631 (1997).
18. Hartwick, F.D.A., & Schade, D. *Ann. Rev. Astron. Astrophys.* **28**, 437 (1990).
19. La Franca, F., Andreani, P., & Cristiani, S. *Astrophys. J.* **?**, in press (1998).
20. Djorgovski, S.G., et al., in preparation (1998).
21. Djorgovski, S., Thompson, D., & Smith, J.D. in *First Light in the Universe*, eds. B. Rocca-Volmerange et al., Gif sur Yvette: Editions Frontières, p. 67 (1993).
22. Djorgovski, S.G., in *Science with the VLT*, eds. J.R. Walsh & I.J. Danziger, Berlin: Springer Verlag, p. 351 (1995).
23. Petitjean, P., Pecontal, E., Vals-Gabaud, D., & Charlot, S. *Nature* **380**, 411 (1996).
24. Omont, A., Petitjean, P., Guilloteau, S., McMahon, R., Solomon, P., & Pecontal, E. *Nature* **382**, 428 (1996).
25. Ohta, K., Yamada, T., Nakanishi, K., Kohno, K,. Akiyama, M., & Kawabe, R. *Nature* **382**, 426 (1996).
26. Hu, E., & McMahon, R. *Nature* **382**, 231 (1996).
27. Efstathiou, G., & Rees, M. *Mon. Not. R. Astron. Soc.* **230**, P5 (1988).
28. Kennefick, J.D., Djorgovski, S.G., & de Carvalho, R. *Astron. J.* **110**, 2553 (1995).
29. McMahon, R., Irwin, M., & Hazard, C., in preparation (2001).

GLOBAL COSMOLOGICAL PARAMETERS MEASURED USING CLASSICAL DOUBLE RADIO SOURCES

RUTH A. DALY, ERICK J. GUERRA, & LIN WAN
Department of Physics, Princeton University, Princeton NJ 08544, USA

Fourteen classical double radio galaxies with redshifts between zero and two were used to determine the cosmological parameters Ω_m, Ω_Λ, and Ω_k, where these are the normalized values of the mean mass density, cosmological constant, and space curvature at the present epoch. A low value of Ω_m is obtained, and $\Omega_m = 1$ is ruled out with 97.5 % confidence. The low value of Ω_m determined using the radio source method described here is also indicated by several independent tests. Thus, it appears that either a cosmological constant, or space curvature, is significant at the present epoch. This means that the universe is undergoing, or has recently undergone, a transition away from a state of matter domination and into a state where either a cosmological constant or space curvature is determining the expansion rate of the universe. The low value of Ω_m presented here and by Guerra & Daly (1998) means that we can state with 97.5 % confidence that the universe will continue to expand forever.

1 Introduction

The structure and fate of the universe can be described by the cosmological parameters Ω_m, Λ, and k, where Ω_m is the average density of matter in the universe at the present time divided by the critical density, Λ is the current value of the cosmological constant (generally, though not always, taken to be time-independent), and k describes the global geometry of the universe. The normalized values of Λ and k are denoted Ω_Λ, and Ω_k (e.g. Peebles 1993). Assuming that any relativistic component, such as the microwave background radiation, has a negligible contribution to the total mass-energy density at the present time, the following equation must be satisfied: $\Omega_m + \Omega_\Lambda + \Omega_k = 1$.

As originally discussed by Dicke (1970), and later by Peebles (1993), each term evolves differently with redshift, so it is unlikely that two terms will be comparable at any given time. However, if $\Omega_m < 1$, then, the universe is undergoing a transition away from a state of matter

domination into a state where either space curvature or the cosmological constant is dominant. Following Dicke's argument, it is rather unlikely that all three terms will be significant at the present time.

The cosmological parameters can only be believably determined when several independent methods of estimating the parameters all yield similar values, both within each category of test, and comparing results from different categories. At present, there are three main categories of estimates of Ω_m: (1) local, low-redshift dynamical tests; (2) tests that depend on the coordinate distance to high-redshift sources through the angular size distance or the luminosity distance; and (3) tests using the fluctuations of the microwave background radiation on different angular scales. At the present time, values of Ω_m have been determined using methods (1) and (2); results obtained using method (1) are mentioned below. Method (2) has been applied to radio galaxies with redshifts between zero and two by Daly (1994, 1995), Guerra & Daly (1996, 1998), and is applied here to radio sources with redshifts between zero and two. Method (2) has also been applied to supernovae by Garnavich *et al.* (1998) and Perlmutter *et al.* (1998), who study sources to a redshift of about one. At some point in the future, there may be independent constraints from measurements of fluctuations of the microwave background radiation on different angular scales.

Several local, low-redshift estimates of Ω_m indicate that it is significantly less than unity (Hudson *et al.* 1995; Shaya, Peebles, & Tully 1995; Carlberg *et al.* 1997; Bahcall & Fan 1998). These tests are interesting and important, though they are all subject to caveats. Many depend on whether the mass is distributed like the light, known as "biasing," and many local measurements only indicate the amount of mass that is clustered on the scales of galaxies and clusters of galaxies. The concordance of many local, low-redshift tests suggests that the amount of mass that clusters with galaxies is significantly less than the critical value.

Estimates of cosmological parameters that utilize the coordinate distance to sources at high redshift (category [2] defined above), such as tests involving angular size distance or luminosity distance, are fundamentally different from local, low-redshift tests. The value of Ω_m estimated through the coordinate distance, the angular size distance, or the luminosity distance, is truly the global value of Ω_m. The test is independent of any biasing of matter relative to light, of how or whether the mass is clustered, of the nature of the dark matter (e.g. baryonic, cold dark matter, hot dark matter, etc.), and of the origin of fluctuations that lead to galaxy formation (e.g. cosmic strings, textures, adiabatic or isocurvature fluctuations, etc.).

Two tests currently being used to determine global cosmological parameters through the coordinate distance to high-redshift sources (category [2] defined above) are the radio source method, and the supernova method.

2 The Radio Source Method

A new way in which powerful classical double radio sources can be used to determine global cosmological parameters is described in detail by Daly (1994, 1995), and Guerra & Daly (1996, 1998). The idea is to use two independent measures of the average size of a given radio source, where the size is measured by the separation of the two radio hot spots. The two measures depend on the angular size distance to the source in different ways, so equating them allows a determination of the coordinate distance to the source, which in turn can be used to determine values for cosmological parameters.

Powerful classical radio sources form an unusually homogeneous population, and the average size, or separation between the two radio hot spots, of the sources at any given redshift exhibits a rather small dispersion. One measure of the average size of a given source is $< D >$, the average size of similar sources at the same redshift. Another measure of the average size of a source is $D_* = v_L \, t_*$, where v_L is the average rate of growth of that source, and t_* is the total time for

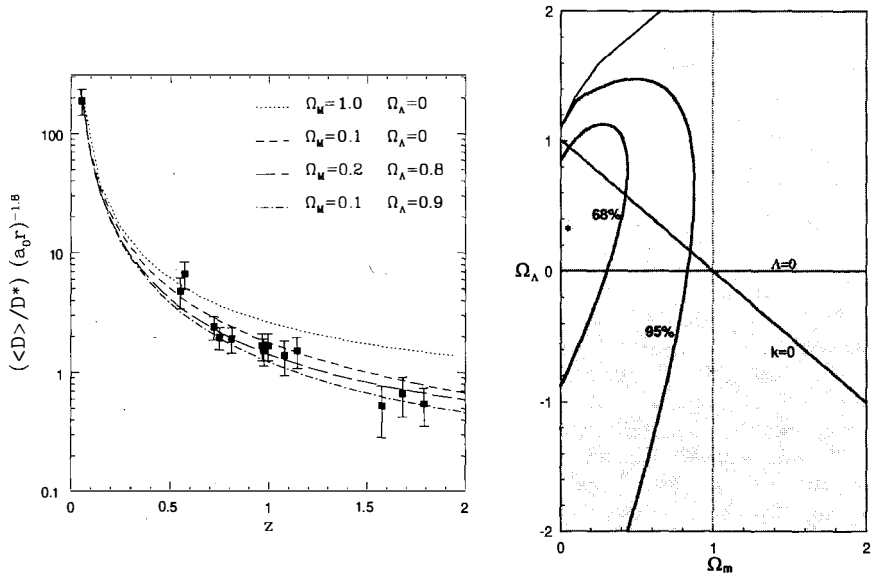

Figure 1: The data are compared with expectations in different cosmological models on the left hand panel. Note how well the data track the curves expected in a low density universe all the way from a redshift of zero to a redshift of about 2. The one-dimensional confidence contours on the parameters Ω_m and Ω_Λ are shown on the right hand panel; one and two sigma constraints on either parameter can be obtained by projecting onto the appropriate axis. A universe with $\Omega_m = 1$ is ruled out with 97.5 % confidence. Lines indicating zero space curvature, zero cosmological constant, and $\Omega_m = 1$ are drawn on figure 1b. The location of the minimum of the reduced χ^2 is indicated by a star.

which the highly collimated outflows of that source are powered by the AGN; this outflow leads to the large scale radio emission. Several observational properties of powerful classical double radio sources can be explained by setting $t_* \propto L_j^{-\beta/3}$ (Daly 1994). Given this parameterization, it is straight-forward to show that $D_* \propto (B_L a_L)^{-2\beta/3} v_L^{(1-\beta/3)}$, where B_L and a_L are the magnetic field strength and width of the radio lobe, located just behind the radio hot spot. Each of these parameters, B_L, a_L, and v_L can be determined using radio data (e.g. Wellman, Daly, & Wan 1997). The best fit value of β is about 2, in which case $D_* \propto (B_L a_L)^{-4/3} v_L^{1/3}$, as discussed in detail by Guerra & Daly (1998).

3 Results

Clearly, $< D >$ for sources at a given redshift is proportional to the angular size distance, luminosity distance, or coordinate distance $(a_o r)$ to the sources. For $\beta \simeq 2$, $D_* \propto (a_o r)^{-0.8}$, so the ratio $< D > /D_* \propto (a_o r)^{1.8}$. For the correct choice of cosmological parameters, the ratio $< D > /D_* = 1$, at all redshifts. Thus, one way to compare the data with the cosmological models is to compare $(< D > /D_*)(a_o r)^{-1.8}$ with the curves $(a_o r)^{-1.8}$ assuming different values for the cosmological parameters. This is shown in figure 1a. It is clear that a low value of Ω_m is favored, and $\Omega_m = 1$ does not fit the data well at all. In fact, it is shown in figure 1b that $\Omega_m = 1$ is ruled out with 97.5 % confidence.

Allowing for error bars on all quantities, the best fit values of the cosmological parameters

are: $\Omega_m = 0.2^{+0.3}_{-0.2}$ assuming zero space curvature ($k = 0$, $\Omega_\Lambda = 1 - \Omega_m$), and $\Omega_m = -0.1^{+0.5}_{-0.4}$ assuming zero cosmological constant ($\Lambda = 0$, $\Omega_k = 1 - \Omega_m$). These values can be obtained by projecting the one-dimensional fits, shown in figure 1b, onto their respective axes. Allowing Ω_Λ and Ω_k to vary simultaneously, the confidence levels for each parameter are shown on figure 1b in such a way that the one and two sigma constraints on each can be obtained by projecting onto the appropriate axis.

4 Discussion

The constraints on cosmological parameters obtained here arise primarily from the relative position of the data points as a function of redshift, and are not sensitive to any particular point, or to the normalization of the curves (which is left as a free parameter in the fits). For example, if the one low-redshift point near $z = 0$ is excluded, the results do not change (see Guerra & Daly 1998). It is clear from figure 1a that the radio source model is working extremely well; the data fall right along the cosmological curves all the way from zero redshift to a redshift of about two. It is clear from figure 1b that, given this data, it is very unlikely that $\Omega_m = 1$.

The results presented here are very similar to those obtained by the supernovae groups. Any potential problems, such as dust extinction or evolution, are completely different for the two methods. The fact that they yield nearly identical results suggests that both are correct. In addition, the low value of Ω_m obtained using this method agrees with the low values indicated by local dynamical tests, which further suggests that Ω_m is low, and the universe will continue to expand forever.

We are in the process of obtaining radio information on 67 additional radio galaxies with redshifts between zero and two. With these additional sources we will be able to constrain cosmological parameters to very high accuracy.

Acknowledgments

It is a pleasure to thank Rick Perley and Ruth Durrer for helpful conversations. This work was supported in part by the US National Science Foundation, the Independent College Fund of New Jersey, and a grant from Mark M. Wheeler III.

References

1. N. A. Bahcall & X. Fan, *BAAS* **191**, 95.02 (1998).
2. R. G. Carlberg *et al.*, *ApJ* **485**, L13 (1997).
3. R. A. Daly, *ApJ* **426**, 38 (1994).
4. R. A. Daly, *ApJ* **454**, 580 (1995).
5. R. H. Dicke, *Gravitation and the Universe*, (American Philosophical Society, Philadelphia, 1970), p. 62.
6. P. Garnavich *et al.*, *ApJ* **493**, L53 (1998).
7. E. J. Guerra & R. A. Daly, in *Cygnus A: Study of a Radio Galaxy*, eds. C. Carilli & D. Harris (Cambridge University Press, Cambridge, 1996).
8. E. J. Guerra & R. A. Daly, *ApJ* **493**, 536 (1998).
9. M. J. Hudson *et al.*, *MNRAS* **274**, 305 (1995).
10. P. J. E. Peebles, *Principles of Physical Cosmology*, (Princeton University Press, Princeton, 1993), p. 312.
11. S. Perlmutter *et al.*, *Nature* **391**, 51 (1998).
12. E. J. Shaya, P. J. E. Peebles, & R. B. Tully, *ApJ* **454**, 15 (1995).
13. G. F. Wellman, R. A. Daly, & L. Wan, *ApJ* **480**, 96 (1997).

SHORT REVIEW ON NON-BARYONIC DARK MATTER SEARCHES (MOSTLY CRYOGENIC EXPERIMENTS)

MAURICE CHAPELLIER
Service de Physique de l'État Condensé, DRECAM, CEA Saclay
91191 Gif-sur-Yvette, France

We present the basic ideas in the cryogenic detection of Dark Matter , a promising method to detect WIMPs in the halo of our galaxy. Preliminary results are shown and a few existing experiments are briefly commented.

Qui vit sans folie n'est pas si sage qu'il croit.
François, duc de La Rochefoucault

1 What are we searching for?

As widely describes in many review papers [1,2], Dark Matter appears to be required in the Universe to account for the observed masses which cannot be only baryonic , the latter beeing constrained by nucleosynthesis to $\Omega_b \leq 0.1$. Furthermore Cold Dark Matter (CDM) seems a requested ingredient for galaxies formation. We take for granted that a large part of the rotation curves around galaxies are due to the gravitationaly trapped CDM. In our galaxy, this give an upper limit of 0.3 to 0.5 $\mathrm{GeV/cm^3}$, four orders of magnitude bigger than the closure density in the Universe. These particles stand in a nearly non rotating spherical halo, extended far away from the luminous part of the galaxy. As a consequence of the galaxy's rotation and the trapping, these particles have a speed distribution which is maxwellian with a mean velocity around 300 km/s. Our preferred candidate is a WIMP, the Lightest Stable Particle of the Supersymmetric family, a neutralino which is an (unknown) mixture of a photino, 2 higgsinos and a zino. The masses should be between 40 to a few hundred GeV, other masses are excluded (following reasonable assumptions) by LEP experiments. This particle has a weak interaction of two types, one is spin independant, a coherent vectorial coupling which give a cross section $\sigma^c_W \propto A^2$ where A is the number of nucleon of the target. The other type is an axial coupling,

spin dependant with $\sigma^a_W \propto C\lambda_s J(J+1)$ where C is a hadronic matrix, λ_s is a Lande factor and J is the spin of the nuclei. The effect of the interaction is an elastic recoil of the nucleus. The maxwellian distribution lead $\frac{dN}{dE_r}$ to be exponential with an average energy given by:

$$< E_r >= 2 \text{ keV} \frac{m_N}{1 \text{ GeV}} \left(\frac{m_W}{m_W + m_N}\right)^2 \quad (1)$$

Remarks:

1. in most situations, due to the $\propto A^2$, σ^c_W is much bigger than σ^a_W. If the particle has a purely axial coupling, the rate will be very low;
2. the highest calculated rate for the coherent coupling range from 1 to 10 events per kg.day
3. the maximum transfer energy is given by a nucleus with $m_N \sim m_W$. For this reason, germanium is well suited for the expected mass of the WIMPs.

As a consequence, we need massive detectors with a low threshold, and a very serious protection and rejection against surrounding radioactivity[a].

2 A possible approach

1. The experiments take place in an underground laboratory to suppress most of the cosmic rays and rapid neutrons. As an example to work in Fréjus tunnel reduces the muons flux to 4 muons/m^2/day (a factor $\sim 2.10^6$ lower than at sea level), the rapid neutron flux to 4.10^{-6}/cm^2/s
2. In the underground laboratory, the experiment is located in a clean lead/copper castle with a gazeous pure nitrogen flux, to suppress the radioactivity from the rocks and outer materials and the radon gas (^{40}K, U and Th chains)
3. Inside the castle, we have a low radioactivity, very low temperature apparatus to cool a pur insulating crystal : because the heat capacity decreases as T3, the temperature rise of the crystal is a sensitive measurement of any deposition of energy, including that of a WIMPs. As an example the rise in temperature of one mole of Ge (73g) cooled at T=10 mK is ΔT=40 μK for an energy deposition of 10 keV. The ratio ΔT/T is pretty well measured with appropriate thermometers and cold electronics.
4. Even so, the rate of spurious counting is still too large. The last trick is to use another parameter which is the ionisation produce by the particle.Because the recoil (Wimp.. or rapid neutrons) induce an ionisation four time lower than standard ionisation radiation, such a measurement provides in principle a good discrimination. Unluckily only a very few materials are suited for this type of measurement, Ge and Si being so far the only crystals pur enough to allow the collection of electrons and holes in a very low temperature experiment. Let us remark that the collection has to be done in a moderate electric applied voltage (less than 10 V) which adds extra heat making more difficult the discrimination.

3 Example of results

We show in figure 1 a biplot heat versus ionisation with an applied voltage of -6 V for a diode made out of 70 g Ge from the Edelweiss collaboration. A clear separation is seen between recoil

[a]Three interesting numbers illustrate this point : a 70kg human beeing emits 8000 antineutrinos/s coming from b decay of his 14C and 40K ; in average, 7000 atoms of radon are emitted per m2/s of concrete or ground and 1kg of garden soil contains 107 atoms of Pu.

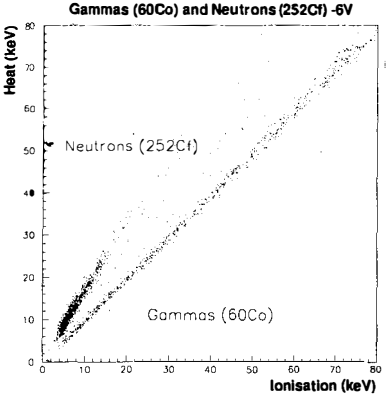

Figure 1: Biplot heat versus ionisation, with an applied voltage of -6 V. A clear separation between recoils and gamma is seen.

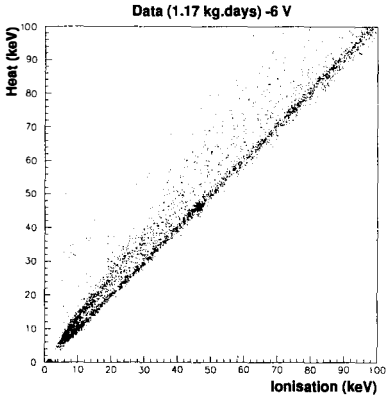

Figure 2: Same plot as in figure 1 but during a long time, with no source. A spurious surface population appears.

and gamma events. But when we make no sources and long run counting, a third unexpected population appears showing a lack of charge collection (figure 2). This is attributed [3] to surface events for which the initial diffusion of charges to the nearby electrode prior to drift causes some loss in the number of counted charges. To use this type of results to produce an exclusion plot, we first show in figure 3 the number of events versus the charge phonon ratio.

We then retain only the lower half of the recoil spectrum thereby eliminating most of the electron recoil events. The results after preliminary treatment of signals is shown in figure 4 and compared with the classical Ge, an experiment still better for high masses (see [4] and a forthcoming paper of Edelweiss collaboration for more details). Similar results were obtained by the CDMS collaboration [5] .

4 Other types of experiments

A large cryogenic experiment (CRESST collaboration) with saphir crystal, very good threshold and resolution is installed in the Gran Sasso laboratory. It will best cover low masses, but so far no discrimination is feasable. It will need extreme purity in all materials [6]. HDMS collaboration has in preparation a classical Ge detector surrounded by a well type Ge acting as a veto [7]. This should permit a reduction of the background by a factor 20.

A massive room temperature detector has been realized with NaI scintillators, and a claim of a possible annual modulation was presented in [8]. This experiment suffer from obvious systematic errors which are strongly criticized in [9]. It is a general matter that in this type of experiments surface events would suffer some singularity. For the same reasons, disperses samples as superheated superconducting granules or freon dropplets will therefore be difficult to handle properly. An other possible Dark Matter candidate is the axion, introduced to explain the CP violation. A pretty experiment [10] has recently excluded masses in the range 2.9-3.3 meV.

5 Conclusion

Cryogenics experiments with rejection seem to offer, for the time beeing with only a few nuclei, a good possibility to detect the LSP. One should notice that in very large experiments of the

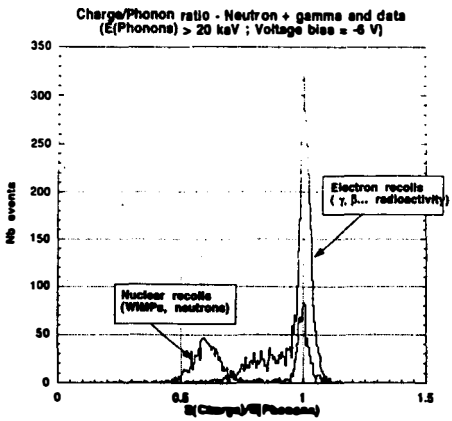

Figure 3: Biplot heat versus ionisation, with an applied voltage of -6 V. A clear separation between recoils and gamma is seen.

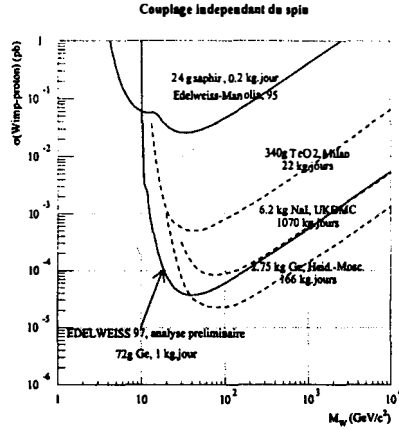

Figure 4: Preliminary exclusion plot for a coherent coupling, and a comparison with the classical Ge from Heidelberg-Moscow.

future LHC, this particle will be detected only as a missing energy and momentum, similarly to the neutrino in the β decay.

References

1. G. Jungman, M. Kamionkowski, K. Griest *Physics Reports* **267**, 195 (1996)
2. L. Mosca *Survey in High Energy Physics* 9, 275 (1996)
3. T. Shutt *et al. Proc. 7th International Workshop on Low Temperature Detectors* (1997) 224
4. P. Di Stefano, EDELWEISS *in Proceedings of TAUP 97*
5. D. Akerib *et al.* astro-ph/97120343 30/12/97
6. M. Sisti *at al. in Proceedings of the 7th International Workshop on Low Temperature Detectors* (1997) 232
7. V. Bednyakov *et al.* hep-ph/9606261
8. R. Bernabei *et al.* preprint ROM 2F / 97 / 33
9. G. Gerbier, J. Mallet, L. Mosca, C. Tao astro-ph/9710181
10. C. Hagmann *et al. Phys. Rev. Lett.* **80**, 2043 (1998)

Microlensing : thème et variations. A review

Marc MONIEZ
Laboratoire de l'Accélérateur Linéaire, IN2P3-CNRS, Université de Paris-Sud, B.P. 34, F-91898 Orsay Cedex, France

Abstract

Microlensing is probably one of the most promising new observational method of the decade. Four experimental dedicated setups are now monitoring the luminosity of millions of stars in order to search for gravitational microlensing by unseen objects. Two international networks continuously follow in real time the most interesting microlensing events discovered by the search systems. It has been demonstrated that the investigations accessible to microlensing range from the galactic dark matter problem to the search for extrasolar planets

1 Introduction

B. Paczyński [27] first pointed out the possibility of using the gravitational microlensing effect to detect massive compact objects of the galactic halo in the direction of the Magellanic Clouds. In september 1993, three teams, EROS [12], MACHO [3] and OGLE[35] have discovered the first microlensing events in the directions of the Large Magellanic Cloud and the Galactic Center. Since the first discoveries, microlensing searches have entered an industrial era, and hundreds of such effects have been detected in several directions, namely the Magellanic Clouds (LMC and SMC), the Galactic Center (GC), and the galactic spiral arms (GSA).

Microlensing search was first intended to study the contribution of massive compact objects to the galactic dark halo. Important constraints have been obtained by the MACHO and EROS teams on this issue.

The search for microlensing in the galactic center was intended to study the galactic bulge and bar structures through the optical depth measurements. The present results are somewhat surprising because the optical depth in the direction of the galactic center is found to be significantly larger than the one expected in most galactic models.

The specific networks PLANET and GMAN have been setup in order to continuously monitor the possible microlensing effects, as soon as they are suspected by MACHO, OGLE or EROS. The main purpose of these networks is to search for anomalous microlensing events,

and therefore to use the phenomenon as a tool to probe the target star and the deflector and get informations not accessible by other means, like planet detection and stellar profiles.

2 microlensing basics

The microlensing effect occurs if a massive object passes close enough to the line of sight of a star, temporarily magnifying its light (see fig. 1). In the case of a single point-like object acting as a deflector on a single point-like source, the apparent amplification of the source luminosity at a given time t is determined by

$$A(t) = \frac{u(t)^2 + 2}{u(t)\sqrt{u(t)^2 + 4}}\,, \tag{1}$$

where $u(t)$ is the distance between the undeflected line of sight and the deflecting object, expressed in units of the "Einstein Radius"

$$R_E = \sqrt{\frac{4GM}{c^2}\, Lx(1-x)} \simeq 970 \times \sqrt{\frac{M}{M_\odot}} \times \sqrt{\frac{L}{10\ Kpc}} \times \frac{\sqrt{x(1-x)}}{0.5} \times R_\odot \tag{2}$$

Here G is the gravitational constant, L is the distance to the source, xL is the distance to the deflector and M its mass. In eq. (1), a singularity occurs when $u(t) = 0$. The amplification of an idealized point-like source would be infinite at this position, and the image would be a ring with a radius equal to the Einstein radius. When projected on the transverse plane of the deflector, the set of positions where a point-like source would undergo an infinite magnification is called the caustic curve, and the corresponding image is called the critical curve. For simple microlensing, the caustic curve is the single point corresponding to the direction of the deflector, and the critical curve is the Einstein ring.

The motion of the deflector relative to the line of sight to the source makes the magnification vary with time: for deflectors of masses within the interval $[10^{-7}, 1]M_\odot$ located in the halo, time scales range typically from hours to months for a significant variation in the magnification of a source in the Large Magellanic Cloud (LMC). Assuming a deflector moving at a constant apparent transverse speed V_T, reaching its minimum distance to the undeflected line of sight (impact parameter) u_{min} at time t_0, $u(t)$ is given by $u(t) = \sqrt{u_{min}^2 + ((t-t_0)/\Delta t)^2}$. $\Delta t = \frac{R_E}{V_T}$ the "lensing time scale" is the only measurable parameter bringing useful information on the deflector in this case (simple microlensing).

For a source in the LMC ($L = 55kpc$), it can be expressed as:

$$\Delta t(days) = 91 \times \left[\frac{V_T}{200km/s}\right]^{-1} \times \left[\frac{M}{M_\odot}\right]^{\frac{1}{2}} \times \frac{[x(1-x)]^{\frac{1}{2}}}{0.5} \tag{3}$$

2.1 microlensing event characteristics

The simple microlensing effect (point-like source and point-like deflector with uniform relative motion with respect to the line of sight) has some very characteristic features which allow to discriminate it from any known intrinsic stellar variability :

- The event is singular in the history of the source (as well as of the deflector).
- The gravitational origin of the effect implies that the magnification is independent of the colour.
- The magnification is a known function of time, depending on only 3 parameters (u_{min}, t_0, Δt), with a symmetrical shape.
- As the geometric configuration of the source-deflector system is random, the impact parameters of the events have to be uniformly distributed. This allows the prediction of the theoretical maximum amplification distribution which, corrected for microlensing detection efficiency, can be compared with the observed one.
- The passive role of the lensed stars implies that their population should be representative of the monitored sample, particularly with respect to the observed colour and magnitude distributions.

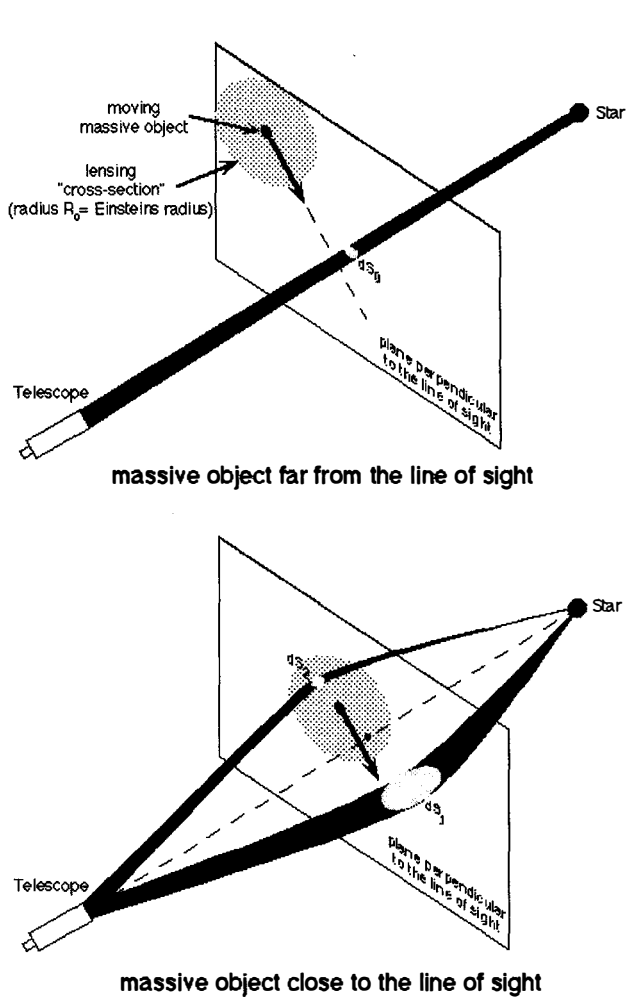

Figure 1: *Principle of the microlensing effect. The magnification A is given by* $A = \frac{dS_1+dS_2}{dS}$

2.2 *Optical depth and event rate*

The probability for a given star to be amplified by a factor larger than 1.34 ($u = 1$) at a given time, is the probability for its line of sight to intercept the Einstein disk of radius R_E of one of the deflectors. This probability is called the optical depth τ. When events are detected, the *measured* optical depth is estimated from

$$\tau = \frac{1}{N_{obs} T_{obs}} \frac{\pi}{2} \sum_{events} \frac{\Delta t}{\epsilon(\Delta t)}$$

where N_{obs} is the number of monitored stars in the target, T_{obs} is the duration of the observation period and $\epsilon(\Delta t)$ is the detection efficiency of the microlensing events with a time scale Δt, relative to the events with impact parameter $u_0 < 1$ and time of maximum within the observation period. The event rate corrected for the observation efficiency is computed to be $\Gamma = 1/(N_{obs} T_{obs}) \times \Sigma_{events}(1/\epsilon(\Delta t))$.

Assuming a standard isothermal halo model for the galactic halo [14], the optical depth is estimated to be about 4.5×10^{-7} up to the LMC. Assuming that all deflectors have the same mass M, the rate per star for microlensing effects with amplifications greater than a threshold amplification A_T (corresponding to an impact parameter $u_{min} = u_T$) has been calculated to be $1.6\ 10^{-6}\ u_T \sqrt{M_\odot / M}\ yr^{-1}$ in the direction of LMC [17 20].

2.3 *Beyond standard microlensing*

The simple microlensing approximation can be broken in many different ways : double lens, extended source, deviations from the uniform movement due to the rotation of the earth around the sun (parallax effect), to the orbit of the source around the center of mass of a multiple system, or to a similar orbit of the acting deflector. All these anomalies have already been observed and examples will be shown in sect. 4.4. The interest of these "exotics" is due to the extremely valuable extra-information that can be obtained from any specific situation (more constraints on the lensing configuration, or informations on the source or on the deflector...).

3 The setups dedicated to microlensing search

3.1 *The experimental detection of microlensing events*

All the running observationnal setups have in common the fact that they aim at monitoring the largest possible field of view, with the shortest time-sampling. They all make use of wide field CCD-cameras, mounted on one meter class telescopes. Data analysis are also based on the same principles : Firstly, light curves (i.e. flux versus time curves) for catalogued stars or for pixels are extracted from the raw data, using automatic astrometric and photometric alignment procedures, secondly each light curve is subjected to a microlensing search algorithm based on the expected characteristics of the events. Three types of experiments can be distinguished. The two first could be called "discovery experiments" whereas the third could be considered as "follow-up experiments".

3.2 *The discovery experiments based on star monitoring*

Four dedicated setups (EROS, MACHO, OGLE and MOA) are now searching for microlensing, looking for specific patterns in the light curves of several million stars.

- EROS : Expérience de Recherche d'Objets Sombres

  After a first phase which started in 1990, using photographic plates and a specially designed 16 CCDs camera [13 11], the EROS team uses the MARLY telescope (1 meter diameter, f/5) installed at La Silla observatory since july 1996, with a dichroic beam-splitter allowing simultaneous imaging in an EROS-blue and EROS-red wide pass-bands of a $0.7°(\alpha) \times 1.4°(\delta)$ field. Photons are collected by two cameras equipped with 2×4 $2K \times 2K$ LORAL CCDs. The pixel size is 0.6 arcsec, and the median global seeing is 2 arcsec. Fig 2 displays the positions of all the fields monitored for microlensing

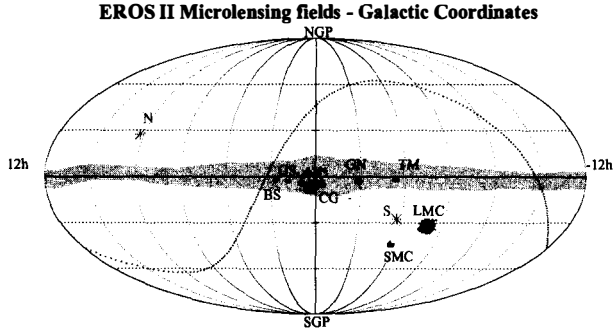

Figure 2: *Map of the fields monitored by EROS for microlensing search. CG = Galactic Center, BS = β Scuti, GS = γ Scuti, GN = γ Normæand TM = θ Muscæ.*

search. Exposure times range typically from 2 to 5 minutes and have been optimized to maximize the global significance of the photometric measurements taken during microlensing amplifications (compromise between the number of measurements and their precision). Since july 1996, EROS monitors fields in the Magellanic Clouds (LMC and SMC), in the Galactic Center (GC), and more specifically in the direction of the galactic spiral arms (GSA).

- MACHO : MAssive Compact Halo Objects
  Since june 1992 the MACHO team uses a 1.27 m (F/3.9) dedicated telescope, also equipped with a dichroic beamsplitter and two cameras of 2 × 2 mosaics of $2K \times 2K$ LORAL CCDs [21 34]. This setup, installed at Mount Stromlo (Australia), allows simultaneous blue and red band photometry, and covers a field of $0.7°(\alpha) \times 0.7°(\delta)$ with a pixel size of 0.62 arcsec. The Magellanic Clouds as well as the Galactic Center are monitored for microlensing searches (see one of the exotic candidates discovered by MACHO and monitored by the follow-up networks on figure 3).
- OGLE : Optical Gravitational Lensing Experiment
  After a first phase started in 1992, making use of a 1m (F/7) telescope in Las Campanas (Chile) to monitor the Galactic Center (see figure 4), the OGLE team has built his own dedicated instrument, using a 1.3 meter (F/9.2) telescope, equipped with a thin CCD camera of $2K \times 2K$ pixels and a filter wheel with standard UBVRI filters installed [37]. The system operates in driftscan mode, with the telescope drifting in declination at a rate of a few arc seconds per time second. Then a single image covers a field of $0.25°(\alpha) \times 0.9°(\delta)$ with a pixel of 0.4 arcsec. The first target monitored with this new setup is LMC.
- MOA : Microlensing Observations in Astronomy.
  This team has started microlensing searches on a 0.6 telescope, located at mount John Observatory (New-Zealand), equipped with an array of 3 × 3 non-buttable $1K \times 1K$ CCDs. They have monitored an average of around one million stars in the directions of the Magellanic Clouds since 1996.

3.3 The discovery experiments based on pixel monitoring

Two teams, AGAPE (Andromeda Gravitational Amplification Pixel Experiment [10]) and VATT Microlensing Survey of M31 (Vatican Advanced Technology Telescope [15]) are monitoring pixels instead of individual stars. Those surveys take advantage of the large number

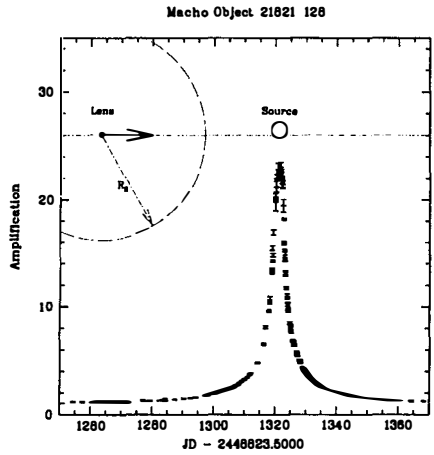

Figure 3: *Light curve of a microlensing candidate found by MACHO in the direction of the Galactic Bulge. The lens/source configuration is indicated. Here, the event has been carefully monitored and the measurements are sensitive to the finite size of the source.*

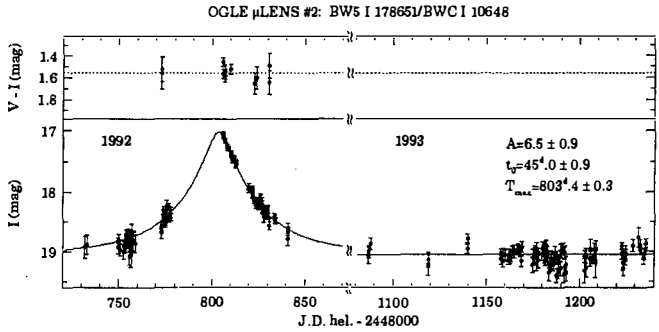

Figure 4: *Light curve of the OGLE#2 microlensing candidate found in the direction of the Galactic Center.*

of underlying stars participating to the flux of a single pixel, of which one could potentially undergo a strong microlensing effect, and then temporarily emerge from a continuum. This technique can improve the sensitivity to microlensing signal in the directions monitored by the previous experiments [25] [26]. But the most promising issue is the possibility to search for microlensing in directions where the stars are not resolved, like M31. The AGAPE and VATT teams both use 2 meter class non-dedicated telescopes equipped with large CCDs. The MEGA (Microlensing Exploration of the Galaxy and Andromeda) survey has also started to use the KPNO 4-meter and Isaac Newton telescopes in the purpose of studying the variations of the optical depth around the center of M31. Now those teams are about to be able to detect events [24] [38].

3.4 The follow-up experiments

Two networks (PLANET and GMAN) are able to monitor the most interesting candidates found by the other experiments, which have now reached the capability of on-line detection needed to start alerts well before the end of the lensing process. PLANET and GMAN use one meter class telescopes all around the world, to be able to monitor the candidates 24 hours a day. Wide field of view is not needed here, but a precise photometry has to be performed, which needs longer exposures and finer images, compared with the discovery experiments. In some cases, spectrometry has also been performed at various amplification stages.

- PLANET : Probing Lensing Anomalies NETwork
  The primary goal of PLANET [29] [30] is the study of microlensing anomalies – departures from an achromatic point-source, point-lens approximation light curve – through multi-band, rapidly-sampled photometry. The strategy of intensive monitoring allows to get fine structure on hourly time scales. The resolution of sharp caustic crossing in binary events, which last a few days, but peak in a few hours, allows to much more tightly constrain the parameters of binary lens models. Four observatories are now involved in the collaboration.
- GMAN : Global Microlensing Alert Network
  Like PLANET, this network uses telescopes from 5 different observatories to precisely monitor exotic microlensing events [18].

4 Review on the observational results

4.1 Microlensing signal

Of order of 100 events have been found in the GC, about 10 in the direction of LMC, 1 in the direction of SMC, and a few towards the spiral arms. All the previously described event characteristics have been checked (Sect. 2.1.), and fig. 5 [5] illustrates one of the statistical tests that the event sample should satisfy (uniformity of the impact parameter distribution, taking into account efficiencies).

4.2 Microlensing and the galactic dark matter problem

The microlensing searches in the LMC and SMC [28] [8] directions are mainly sensitive to the component of the galactic dark halo made of massive compact objects, because the corresponding lines of sight do not intercept regions with large densities of visible stars. The null result in the short-duration event search obtained by the EROS 1 CCD experiment [32] sensitive to events of a few hours, and the specific spike analysis of the MACHO data [6], allows to put very stringent combined limits on the contribution of light compact objects to the galactic halo. As shown on fig 6, a significant contribution of objects in the mass interval $[10^{-7}, 10^{-3}]M_{\odot}$ is now excluded [1]. The long-duration microlensing events detected in LMC-SMC by EROS [9] and MACHO [5] indicate a possible contribution of heavier objects (with an average of $0.5M_{\odot}$) at the level of 50% to the mass of the galactic halo. The hypothesis of a strong contribution of self-lensing (i.e. lensing by objects belonging to the LMC/SMC themselves), which would led to lower the part of dark matter component made of compact

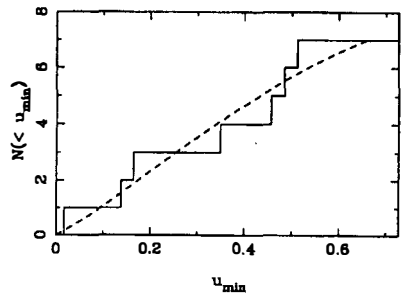

Figure 5: *Cumulative distribution of the reconstructed impact parameter for 7 LMC-events (MACHO). The dotted curve shows the expected distribution.*

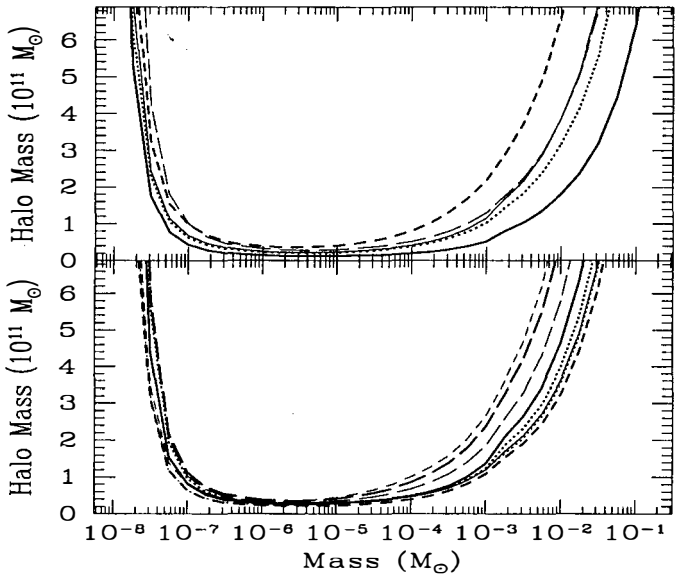

Figure 6: *Combined EROS+MACHO upper limit on the contribution of compact objects to the halo mass, as a function of their mass. Each marker corresponds to a halo model. The mass of a standard spherical and isothermal halo would be* $4 \times 10^{11} M_{\odot}$.

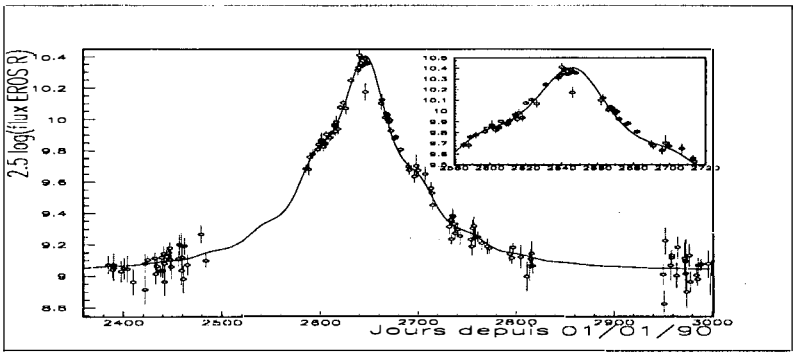

Figure 7: *Red light-curve of one of the microlensing candidates found by EROS far from the direction of the Galactic Center (similar curve in blue not shown here). The line corresponds to the best fit for the microlensing of a binary source.*

objects, is still controversial [22]. The global conclusion of those results is that at least 50% of the galactic dark matter is made of something different than massive compact objects.

4.3 Microlensing and the galactic structure

Of order of hundred events have been identified in the direction of the Galactic Center by MACHO [7], OGLE [36] and DUO [2]. The measured optical depth is in clear excess of the expected one, if one does not account for a bar elongated towards a direction close to the sun. Fig. 8 shows the measured value of the optical depth, compared with the expected contributions from the Halo, the Disk, and the combination of a bulge with a bar. Note that the latter contribution is not symmetrical with respect to the galactic center, due to the elongation of the bar. The average duration of the events towards the galactic center is 21 *days*, corresponding to an average deflector mass of $0.15 M_{\odot}$ if all lenses are in the disk, or $0.20 M_{\odot}$ if all lenses are in the bulge/bar [23] [17].

EROS has detected 3 long-duration events ($\sim$ 80 *days*, see one of them on fig. 7) in 2 directions situated far away from the galactic center ($\sim -20°$ *to* $30°$ of galactic longitude, see fig. 2 and 8) [16]. Of course, it has to be noticed that the corresponding optical depths plotted on fig. 8 are only indicative, because they are based on very few observations.

4.4 Exotics : Microlensing as an astrophysical probe

The power of the discovery experiments associated with the followup networks has allowed the discovery of some very exciting deviations to the simple microlensing [39].

- In the case of a double lens, the expected amplification can exhibit very different features than in the simple approximation, because the caustic curve is no more a single point. The effective maximum amplification when the target star goes through the caustic curve is in practice limited by the light distribution at the stellar surface, and can even change with the colour. The search for multiple lenses made of a main star surrounded by a planetary system is now considered as the most promising way to undoubtly discover new extra-solar planets, and as *the only way* to discover earth-like planets. Fig. 9 shows an example of a binary lens as measured by MACHO and the CTIO telescope [31].
- As the source is not point-like, the correct way to estimate the magnification of a star by microlensing is to integrate the lensing effect over the star's surface. If the radius of the star is not negligible with respect to the impact parameter of a microlensing effect, then the magnification curve is distorted from the simple approximation. In

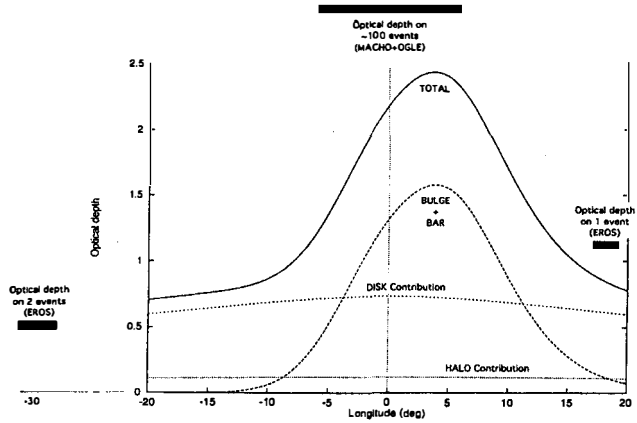

Figure 8: *The expected variation of the optical depth with the galactic longitude, for lines of sight in the galactic plane* [23]. *The contribution of the different galactic component is shown (see text). The bars show rough estimates of the observed optical depths.*

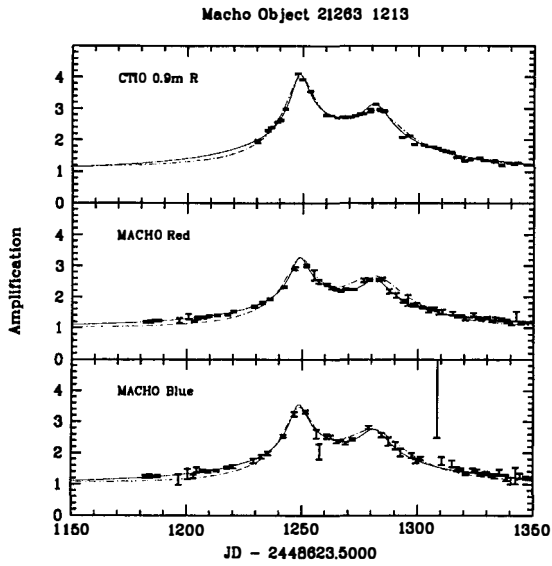

Figure 9: *Light curves of a binary-lens microlensing event discovered by MACHO and also measured at the CTIO. The dotted curves correspond to a (less good) fit of a binary-source instead of a binary-lens.*

particular, the maximum amplification is limited, and chromatic effects can occur if the light distribution on the star's surface depends on the wavelength. This effect was measurable on the candidate of fig. 3 [31] [30].

- The distance between the deflector and the line of sight (observer-source) depends on the trajectory of the deflector as well as on the trajectories of the exremities of the observer-source line. A single deflector moves uniformly over a straight line, but if the deflector is a part of a multiple system, it also orbits around the center of gravity, thus affecting the amplification versus time curve.
- If the variation of the Earth's velocity rotating component around the sun is not negligible with respect to the transverse speed of the deflector, then the apparent trajectory of the deflector with respect to the line of sight is a cycloid. The resulting amplification versus time curve would be affected by this parallax effect. This effect is more easily observable for long duration events (several months), for which the change in the Earth velocity is important [4].
- Similarly, a rotation of the source around the center-of-mass of a multiple system would also induce a Xallarap effect (mirror of parallax) with a characteristic time given by the period of the rotation of the source [33] (see example on fig. 7 [16]).
- The detected light may also have a composite origin : a multiple system may be lensed, with different amplifications for each component depending on the impact parameters, or with only one component being amplified [33]. The latter case is equivalent to the configuration of a single amplified star, blended by another star close to the line of sight (distant or not).

5 Conclusion

Microlensing is now a mature domain. It has already rendered valuable services to science for the dark matter problem and for the galactic structure. More precision is expected soon with the increasing statistics. The microlensing phenomenon also acts as an unhoped-for natural telescope, which has made possible for the first time the resolution of star-profiles, and great hope to detect extra-solar planets is now justified. Last but not least, the huge data-bases built by the dedicated experiments have already contributed to a better knowledge of variable stars like the cepheids. Much more serendipitious results can be expected in the future. Ambitious projects exists to develop this new field, like a satellite project to measure parallaxes [19]. New ways to analyse data are also explored. Anyhow, very important results are expected from high statistics available soon.

References

1. Afonso C. et al. 1998, Astro-ph/980382
2. Alard C., Guibert J., Bienayme O. et al. 1995a, *Messenger 80, 31*
3. Alcock C., Akerlof C.W., Allsman R.A. et al. 1993, Nat 365, 621
4. Alcock C., Allsman R.A., Alves D. et al. 1995b, ApJ, 454 , L125
5. Alcock C., Allsman R.A., Alves D. et al. 1996a, submitted to ApJ
6. Alcock C., Allsman et al. 1996b, ApJ, 471, 774
7. Alcock C., Allsman R.A., Alves D. et al. 1997a, ApJ, 479, 119
8. Alcock C. et al. 1997b, Astro-ph/9708190
9. Ansari R., Cavalier F., Moniez M. et al. 1996, A&A 314, 94
10. Ansari R. et al., 1997, A&A, 324, 843
11. Arnaud M., Aubourg E., Bareyre P. et al. 1994, Exp. Ast., 4, 265 (I) & 279 (II)
12. Aubourg E., Bareyre P., Bréhin S. et al. 1993a, Nat 365, 623
13. Aubourg E., Bareyre P., Bréhin S. et al. 1993b, *Messenger* 72, 20
14. Caldwell, J.A.R. & Ostriker, J.P. 1981, ApJ 251, 61
15. Crotts A.P.S., Tomaney A.B., 1996, ApJ, 473, L87
16. Derue F. et al., 1998, in proc. 4th Int. Workshop on Grav. Microl. Surveys.
17. De Rujula A., Jetzer Ph. and Massó E., 1991, MNRAS 250,348 ; 1992, A&A 254, 99

18. GMAN coll., 1998, in proc. 4th Int. Workshop on Grav. Microl. Surveys.
19. Gould, A. 1995, ApJ 441, L21
20. Griest, K. 1991, ApJ 366, 412
21. Hart, J. et al., 1996,PASP,108,220
22. HongSheng Z., 1998, in proc. 4th Int. Workshop on Grav. Microl. Surveys.
23. Jetzer Ph., 1998, in proc. 4th Int. Workshop on Grav. Microl. Surveys
24. Le Du Y., 1998, in proc. 4th Int. Workshop on Grav. Microl. Surveys
25. Melchior A.L. et al., 1997, astro-ph/9710194, submitted to A&A.
26. Melchior A.L. et al., 1998, astro-ph/9804321, submitted to A&A.
27. Paczyński, B. 1986, ApJ 304, 1
28. Palanque-Delabrouille N. et al., 1998, A&A, 332,1
29. PLANET coll., 1997, astro-ph/9610128.
30. PLANET coll., 1998, in proc. 4th Int. Workshop on Grav. Microl. Surveys.
31. Pratt M. et al., AAS Meeting 187, San Antonio, Texas, January 1996.
32. Renault C. et al., 1998, A&A, 324, 69L
33. Sazhin M. V., Cherepashchuk A. M., 1994, Astron. Lett., Vol. 20, No. 5, 523
34. Stubbs C. et al., 1993, SPIE, 1900, 192
35. Udalski A., Szymański M., Kaluzny J. et al. 1993, Act. Astr. 43, 289
36. Udalski A., Szymański M., Stanek K.Z. et al. 1994a, Act. Astr. 44, 165
37. Udalski A. et al., 1997, Acta Astron, 47, 319
38. Uglesich R., 1998, in proc. 4th Int. Workshop on Grav. Microl. Surveys.
39. See proc. 4th Int. Workshop on Grav. Microl. Surveys for examples of each deviation discussed here.

Comparison of the SFI Peculiar Velocities with the IRAS 1.2 Jy Gravity Field

Adi Nusser[1] and Luiz N. da Costa[2]
[1] *Max-Planck-Institut für Astrophysik, Karl-Schwarzschild-Str. 1, D-85749 Garching, Germany*
[2] *European Southern Observatory, Karl-Schwarzschild Str. 2, D-85748 Garching, Germany*

We present a comparison between the peculiar velocity fields measured from a recently completed I-band Tully-Fisher survey of field spirals (SFI) and that derived from the *IRAS* 1.2 Jy redshift survey galaxy distribution. The analysis is based on the expansion of these data in redshift space using smooth orthonormal functions and is performed using low and high resolution expansions, with an effective smoothing scale which increases almost linearly with redshift. The effective smoothing scales at 3000 km s^{-1} are 1500 km s^{-1} and 1000 km s^{-1} for the low and high resolution filters. The agreement between the high and low resolution SFI velocity maps is excellent. The general features in the filtered SFI and *IRAS* velocity fields agree remarkably well within 6000 km s^{-1}. This good agreement between the fields allows us to determine the parameter $\beta = \Omega^{0.6}/b$, where Ω is the cosmological density parameter and b is the linear biasing factor. ¿From a likelihood analysis on the SFI and *IRAS* modes we find that $\beta = 0.6 \pm 0.1$ independently of the resolution of the modal expansion. For this value of β, the residual fields for the two filters show no systematic variations within 6000 km s^{-1}. Most remarkable is the lack of any coherent, redshift dependent dipole flow in the residual field.

1 Introduction

Measurements of the peculiar motions of galaxies in the nearby universe represent one of the most powerful tools currently available to probe mass fluctuations on large scales ($\lesssim 100 h^{-1} Mpc$). Furthermore, in conjunction with redshift surveys, the relationship between the distribution of luminous and dark matter can be investigated. Work on this subject has led to some puzzling results, primarily because most earlier work was based on relatively sparse and inhomogeneous set of galaxies with measured peculiar velocities. Recently, the observational situation has dramatically improved with the completion of large Tully-Fisher (TF) redshift-distance surveys in both hemispheres. The most notable are the Mathewson, Ford & Buchhorn (1992, MFB92) survey in the southern hemisphere, and the I-band TF distance survey of spiral galaxies in the field (SFI survey, Haynes *et al.* 1998a) and in clusters (SCI survey, Giovanelli *et al.* 1997a).

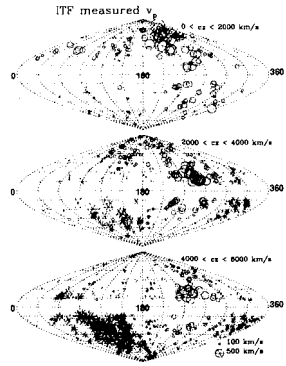

Figure 1: The sky projection in galactic coordinates as seen in the LG frame of the ITF velocity field for the SFI galaxies. In figures 1-3, open circles indicate infall and crosses outflow. The size of the symbols scales with the velocity amplitude.

These TF surveys have been used to construct two largely independent all-sky redshift-distance catalogs: the Mark III catalog, which is a compilation of all available field and cluster data (Willick *et al.* 1997) and the "SFI catalog" which combines field galaxies from the SFI survey with a pruned version of the MFB92 data, appropriately converted to the SFI magnitude and width scale (Giovanelli *et al.* 1997). Details on the SFI sample selection and the final SFI catalog of peculiar velocities will be presented elsewhere (Haynes *et al.* 1998).

2 The SFI and *IRAS* Velocity Fields

In linear theory, the velocity field is related to gravity by the parameter $\beta = \Omega^{0.6}/b$. We compare the underlying peculiar velocity field from the SFI data with the velocity field predicted from the gravity field computed from the *IRAS* galaxy redshift distribution. We apply the above method to the 1114 galaxies within a redshift of 6000 km s^{-1} extracted from the SFI catalog used by da Costa *et al.* (1996). The SFI survey corresponds to about 70% of the sample and covers the northern hemisphere and part of the southern hemisphere, extending to $\delta \sim -25°$. In the southern hemisphere the sample is complemented by galaxies from the MFB92 data set.

We will present results for a smoothing corresponding to $l_{max} = 3, n_{max} = 3$ with 40 modes in total. The inverse TF parameters we obtain after the modal expansion are, $(\gamma, \eta_0 = -0.117, -2.47)$. Given an assumed value for β, we apply the method of Nusser & Davis (1994) to generate maps of velocity fields from the distribution of the *IRAS* galaxies in space. This method generates velocity fields non-iteratively in redshift space. As input to this method, a density field is provided by smoothing the *IRAS* galaxy distribution with a Gaussian window of width equal to half the mean particle separation at a given redshift. The *IRAS* fields are then expanded in the same orthogonal set of basis functions as employed for the SFI velocities. The *IRAS* and SFI velocities are guaranteed to have the same resolution because the original smoothing of the *IRAS* density field is small compared to the resolution of the modal expansion.

The resulting fit to the measured SFI velocity field is shown in figures 1, in redshift shells 2000 km s^{-1} thick. The infall to Virgo ($l = 284°, b = 74°$) dominates the nearby SFI flow. Other features like Ursa Major and Fornax are poorly sampled by the SFI. In the middle panel, the field exhibits a dipole pattern corresponding to the reflex motion of the Local Group with infalling galaxies in the Hydra-Centaurus direction and an outward flow in the Perseus-Pisces direction,

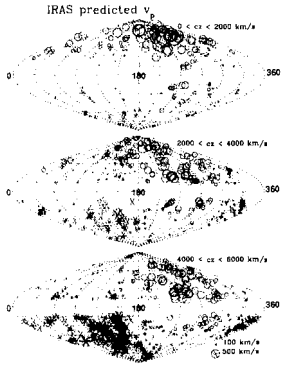

Figure 2: The velocity field derived from the *IRAS* galaxies with $\beta = 0.6$

as seen in the LG restframe, which is even stronger in the most distant shell. We show in figure 2 the *IRAS* field reconstructed with $\beta = 0.6$. The overall agreement is remarkable with only a few nearby galaxies giving large residuals. Most encouraging is the absence of large regions of coherent residuals and the absence of systematic residuals such as the dipole residual seen in previous analysis at intermediate and distant redshift shells (DNW). Moreover, the amplitude of the residuals is close to that obtained by DNW in the analysis of mock catalogs.

3 Summary

We have compared the observed SFI peculiar velocity field with that predicted from the galaxy distribution of the *IRAS* galaxies. We have found good agreement between the two fields for $\beta = 0.6 \pm 0.1$ with no dependence on depth. The good agreement between the fields is consistent with the galaxy distribution being closely related to that of the dark matter by means of a scale independent biasing factor, and with the hypothesis that the TF relation does not depend strongly on environment. The results presented here demonstrate the importance of all-sky homogeneous measurements of peculiar velocities. Current samples are still too small and sparse to allow them to be used to explore smaller scales ($500 - 1500$ km s^{-1}) where non-linear effects become important. Future samples should aim at a higher sampling rate and uniform sky coverage.

Acknowledgments

We thank W. Freudling, R.Giovanelli, M.P.Haynes, J.Salzer and G.Wegner for permission to use results from our mutual project prior to publication.

References

1. Davis, M., Nusser, A. & Willick, J., 1996, ApJ, 473, 22 (DNW)
2. Dekel, A., Bertschinger, E. Yahil, A., Strauss, M, Davis, M. & Huchra, J., 1993, ApJ 412, 1
3. Fisher, K. B. , Davis, M., Strauss, M., Yahil, A. & Huchra, J., 1994, MNRAS 267, 927
4. Fisher, K.B., Lahav, O., Hoffman, Y., Lynden-Bell, D. & Zaroubi, S., 1995, MNRAS 272, 885

5. Giovanelli, R., Haynes, M.P., Herter, T., Vogt, N., Salzer, J.J., Wegner, G., da Costa, L.N. & Freudling, W. 1997a, AJ 113, 22
6. Haynes, M. P. *et al.* 1998b, *in preparation*
7. Mathewson, D.S., Ford, V.L. and Buchhorn, M. 1992, ApJS 81, 413 (MFB92)
8. Nusser, A. & Davis, M., 1994, ApJ, 421, L1
9. Nusser, A. & Davis, M., 1995, MNRAS, 276, 1391 (ND95)
10. Willick, J.A., Strauss, M.A., Dekel, A & Kollat, T., 1997, ApJ, 486, 629

LARGE-SCALE DENSITY–VELOCITY RELATIONS

M.J. CHODOROWSKI
Copernicus Astronomical Center, Bartycka 18, 00–716 Warsaw, Poland

I present recent progress in theoretical modelling of cosmological density–velocity relations in the weakly nonlinear regime. The relations are local, based on rigorous perturbation theory and include the effects of smoothing of the density and the velocity fields. For small smoothing scales, they can be improved by slight adjustments based on N-body results. The relations can be useful for density–velocity comparisons, yielding a fair estimate of Ω and offering a method for disentangling Ω and bias.

1 Introduction

In the gravitational instability paradigm for the formation of structure in the Universe, the peculiar motions of galaxies are tightly related to the large-scale mass distribution. The comparison between the density and the velocity fields can serve as a test of the gravitational instability hypothesis and as a method for estimating the cosmological parameter Ω (Dekel *et al.* [7]). In linear theory, the relation between the density and the velocity fields is

$$\delta(\mathbf{x}) = -f(\Omega)^{-1}\nabla\cdot\mathbf{v}(\mathbf{x})\,, \tag{1}$$

where $f(\Omega) \simeq \Omega^{0.6}$. The relation between the density contrast and the velocity divergence is thus linear and local.

This equation is applicable only when the density fluctuations are small compared to unity, $\sigma_\delta^2 \equiv \langle\delta^2\rangle \ll 1$. However, sampling of galaxies in current redshift surveys and random errors in the peculiar velocity data enable reliable dynamical analysis at smoothing scales down to a few h^{-1} Mpc, where fluctuations already exceed the regime of applicability of linear theory. On the other hand, even at scales as small as a few h^{-1} Mpc, 'typical' (rms) fluctuations are still not in excess of unity.[a] One could thus hope that to construct the relation between the fields in question, perturbation theory can be effectively used.

In perturbation theory, one approximates the evolved density contrast as a sum of terms δ_j, each corresponding to the j^{th} order in perturbation theory,

$$\delta = \delta_1 + \delta_2 + \delta_3 + \dots\,. \tag{2}$$

Similarly, defining a variable θ proportional to the velocity divergence,

$$\theta = -f(\Omega)^{-1}\nabla\cdot\mathbf{v}\,, \tag{3}$$

we can expand it in a perturbative series,

$$\theta = \theta_1 + \theta_2 + \theta_3 + \dots\,. \tag{4}$$

[a] For a Gaussian smoothing function, commonly used in the density–velocity comparisons.

The solutions for δ_j and θ_j were obtained more than a decade ago (Fry [8], Goroff *et al.* [9]). In general, the j^{th} order solution is of the order of $(\delta_1)^j \sim \sigma_\delta^j$. In the weakly nonlinear regime, i.e., when $\sigma_\delta < 1$, which is our case, we may hope the perturbative series to converge rapidly.

Linear theory is nothing but perturbation theory truncated at the lowest, i.e. the first order. A natural way of extending the linear relation (1) is to include higher-order contributions to the density contrast and the velocity divergence. Unfortunately, these contributions are non-local, hence the nonlinear density vs velocity-divergence relation (DVDR) *at a given point* has a scatter. Therefore, as a local estimator of the density from the velocity divergence we adopt the conditional mean, i.e., the mean density *given* the velocity divergence.

The calculation of the conditional moments is a statistical problem. To compute mean δ given θ, $\langle\delta\rangle|_\theta$, we need the joint probability distribution function (PDF) $p(\delta,\theta)$. Under an assumption of Gaussian initial conditions, adopted in this work, this function is initially a bivariate Gaussian (degenerated, since $\delta_1 = \theta_1$). Subsequent nonlinear gravitational evolution, however, drives the PDF away from its initial shape. Our problem here is to calculate it in the weakly nonlinear regime.

Mathematically, a PDF is given by the inverse Fourier transform of its characteristic function Φ, which in turn is related to the cumulant generating function $\mathcal{K}$ by the equation $\Phi = \exp[\mathcal{K}]$. The cumulants, κ_{mn}, from which $\mathcal{K}$ is constructed,

$$\mathcal{K}(it,is) = \sum_{(m,n)\neq(0,0)}^{\infty} \frac{\kappa_{mn}}{m!n!}(it)^m(is)^n\,, \tag{5}$$

are the *connected* (reduced) part of the joint moments of δ and θ, $\kappa_{mn} = \langle\delta^m\theta^n\rangle_{\rm conn}$. We introduce $\mathcal{K}$ because in the weakly nonlinear regime, the cumulants obey a scaling hierarchy in σ_δ such that the series (5) is a power series in σ_δ (even in the case of the standard variables $\mu \equiv \delta/\sigma_\delta$ and $\nu \equiv \theta/\sigma_\theta$). Therefore, truncating (5) at order p we neglect contributions which are $\mathcal{O}(\sigma_\delta^{p+1})$. This yields the truncated PDF and in turn the weakly nonlinear DVDR up to a given order in perturbation theory.

2 Results

Up to third order (Chodorowski & Lokas [3]) we have

$$\langle\delta\rangle|_\theta = a_1\theta + a_2(\theta^2 - \sigma_\theta^2) + a_3\theta^3\,, \tag{6}$$

where σ_θ^2 is the variance of the velocity divergence field. The reverse relation (Chodorowski *et al.* [5]) is

$$\langle\theta\rangle|_\delta = r_1\delta + r_2(\delta^2 - \sigma_\delta^2) + r_3\delta^3 \tag{7}$$

(an extension of a second-order formula by Bernardeau [1]). Because the DVDR has a scatter, expression (7) cannot in general be obtained by direct inversion of expression (6). In density–density comparisons, one reconstructs the mass density field from the observed velocity field and compares it to the observed galaxy density field. In velocity–velocity comparisons, one reconstructs (under some assumptions about bias) the velocity field from the observed galaxy density field and compares to the observed velocity field. Formula (6) is thus relevant for density–density comparisons, while formula (7) is relevant for velocity–velocity comparisons. Indeed, for irrotational flows the velocity field can readily be recovered from its divergence given some boundary conditions at large distances,

$$\mathbf{v}(\mathbf{x}) = \frac{f(\Omega)}{4\pi}\int \mathrm{d}^3x'\theta(\mathbf{x}')\frac{\mathbf{x}'-\mathbf{x}}{|\mathbf{x}'-\mathbf{x}|^3}\,. \tag{8}$$

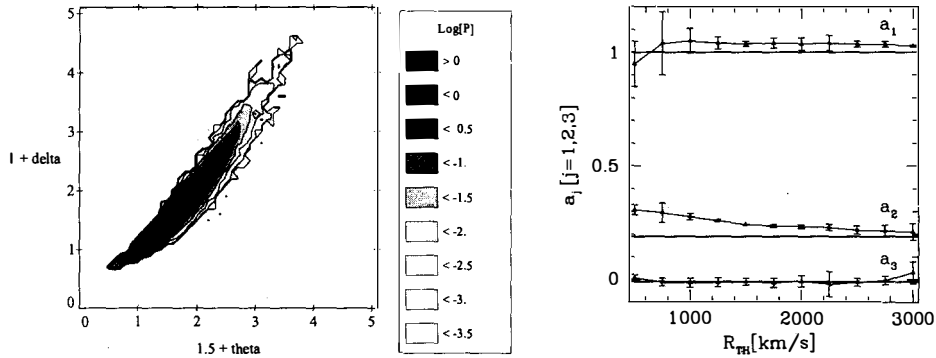

Figure 1: Left: joint probability distribution function for the density contrast (δ) and the velocity divergence (θ) from an N-body simulation by Chodorowski *et al.*,[6] shown against $1+\delta$ and $1.5+\theta$. Right: the coefficients a_j (see eq. [6]), as functions of the smoothing scale, from N-body simulations by Chodorowski & Stompor.[4] Simulation results are shown as thin curves; third order perturbation theory predictions are shown as thick lines. The simulations are for power-law power spectra with the spectral index n equal to -1.5 (left) and -1 (right). A top-hat smoothing function is used.

The coefficients a_j and r_j are the previrialization-, skewness-, and kurtosis-like combinations of the joint moments of δ and θ. Calculations of the reduced moments have already become a small industry in perturbation theory. For Gaussian smoothing, the related moments for δ and for θ (separately) were computed by Łokas *et al.*[10] and Łokas *et al.*[11] The coefficients a_j and r_j, though constructed from the joint moments, possess similar mathematical structure and were computed in an analogous way.[3,5]

Chodorowski *et al.*[5] also calculated the scatter in the DVDR and found it to be relatively small.[b] Nevertheless, one can try to further reduce the variance of density estimators by including off-diagonal components of the velocity deformation tensor. Indeed, including the shear of the velocity field reduces the scatter in the density–velocity relation.[12,2]

3 Tests against N-body simulations

Perturbative expressions for density–velocity relations should be checked against N-body simulations, in order to assess their range of applicability. The results of the simulations by Chodorowski *et al.*[6] and Chodorowski & Stompor[4] (see Figure 1) can be summarized as follows:

- *For large smoothing scales* ($\sigma_\delta \ll 1$), the numerical coefficients a_j and r_j converge to the predicted values. (In this sense, the predicted DVDRs are 'asymptotically unbiased'.)
- *For smoothing scales as small as a few megaparsecs* ($\sigma_\delta \lesssim 1$),
  - The numerical coefficients slightly, but systematically, deviate from predicted values. (Apparently, higher–than third–order contributions become significant.)
  - On the other hand, third-order polynomials, with fitted coefficients, provide excellent fits to N-body data. (Higher-order contributions modify the values of the coefficients for $j = 1, 2, 3$, but do not significantly induce non-zero values for $j > 3$.)

[b] The ratio of the scatter to the rms fluctuation of the density field, σ_δ, vanishes in the limit $\sigma_\delta \to 0$, as expected.

4 Implications for the value of Ω

For the sake of simplicity, here we will consider only second-order corrections to the linear relation (1). Neglecting third-order terms in equation (7) yields

$$\theta = \delta - a_2(\delta^2 - \sigma_\delta^2) \tag{9}$$

($r_2 = -a_2$, $0.2 < a_2 < 0.3$ [5,3]). Assuming linear bias between the galaxy density field, δ_g, and the mass density field, $\delta_g = b\delta$, we can express the relation in terms of the observable quantities $\nabla \cdot \mathbf{v}$ and δ_g,

$$-\nabla \cdot \mathbf{v} = \beta\delta_g - a_2 b^{-1}\beta\delta_g^2 \,. \tag{10}$$

Here, $\beta(\Omega, b) \equiv f(\Omega)/b$ and we also neglect the offset in the relation. We see that the quadratic correction has the opposite sign to the linear term. It implies that the linear relation overestimates the predicted velocities. Hence, in order to match the observed ones, a lower value of β is needed. In effect, *applying linear theory biases the estimate of Ω low* (cf. Strauss & Willick [13]).

Note that the two coefficients of the binomial in δ_g on the RHS of equation (10) are different combinations of β and b, or $f(\Omega)$ and b. This offers a way to solve for Ω and b separately. [3]

5 Summary

The weakly nonlinear estimators of density from velocity, and vice versa, presented here,

- are asymptotically unbiased;
- for smaller smoothing scales, can be improved by slight adjustments from N-body data;
- should be used in density–density and velocity–velocity comparisons, in order not to bias the estimate of Ω low;
- offer a method for disentangling Ω and bias.

Acknowledgments

This research has been supported in part by the Polish State Committee for Scientific Research grants No. 2.P03D.008.13 and 2.P03D.004.13.

References

1. F. Bernardeau, ApJ **390**, L61 (1992).
2. M.J. Chodorowski, MNRAS **292**, 695 (1997).
3. M.J. Chodorowski and E.L. Łokas, MNRAS **287**, 591 (1997).
4. M.J. Chodorowski and R. Stompor, in preparation.
5. M.J. Chodorowski, E.L. Łokas, A. Pollo and A. Nusser, preprint astro-ph/9802050.
6. M.J. Chodorowski, E.L. Łokas, F. Bernardeau and A. Kudlicki, in preparation.
7. A. Dekel, E. Bertschinger, A. Yahil, M. Strauss, M. Davis and J. Huchra, ApJ **412**, 1 (1993).
8. J.N. Fry, ApJ **279**, 499 (1984).
9. M.H. Goroff, B. Grinstein, S.-J. Rey and M.B Wise, ApJ **311**, 6 (1986).
10. E.L. Łokas, R. Juszkiewicz, D.H. Weinberg and F.R. Bouchet, MNRAS **274**, 730 (1995).
11. E.L. Łokas, R. Juszkiewicz, F.R. Bouchet and E. Hivon, ApJ **467**, 1 (1996).
12. P.J. Mancinelli and A. Yahil, ApJ **452**, 75 (1995).
13. M.A. Strauss and J.A. Willick, Phys. Rep. **261**, 271 (1995).

WHAT SHOULD BE THE GEOMETRY OF A GALAXY CATALOG?

S. COLOMBI
Institut d'Astrophysique de Paris, CNRS,
F-75014 Paris, France

I study the effect of the geometry of the catalog on the cosmic error related to the measurement of the second order factorial moment F_2 of count-in-cells in a redshift survey. For doing that, I compute the next to leading order contribution to edge effects which is proportional to the perimeter of the catalog. As an application, I derive a preliminary sampling strategy for the future deep redshift survey VIRMOS.

1 The cosmic error

1.1 The general framework

One way of deriving an optimal sampling strategy for building a redshift survey consists of minimizing the cosmic error on the measurement on an observable [3]. Here I concentrate on the second order factorial moment of counts-in-cells, $F_2 \equiv \langle N(N-1) \rangle$. This quantity is indirectly related to the more traditional two-point correlation function $\xi(r)$ through $F_2 = \bar{N}^2(1+\bar{\xi})$ where $\bar{N}$ is the average count in a cell and $\bar{\xi}$ is the double average integral of ξ over a cell.

Szapudi & Colombi [8] (hereafter SC) computed analytically the cosmic error on factorial moments of counts-in-cells to leading order in v/V, where v is the volume of the considered cell and V the survey volume. They found it could be disentangled into three components: the finite volume error due to the fluctuations of the underlying random field at wavelengths larger than the size of the catalogue; the shot noise error due to the incomplete sampling of the underlying smooth field with a finite number of galaxies; and the edge effects due to the fact that galaxies near the edges of the catalog receive less statistical weight than those far from the boundaries.

The leading order in v/V calculation of SC depends on the geometry of the catalog only through finite volume effects. Here we are going to compute next to leading order corrections, which are proportional to the perimeter $A = \partial V$ of the catalog [7,9] and thus strongly depend on the geometry.

1.2 *Effects of the geometry*

In the general case (see SC for details), the generating function for the cosmic error writes for a statistically homogeneous catalog (without selection effects)

$$E(x,y) = \frac{1}{\hat{V}^2}\int_{\hat{V}} d^3r_1 d^3r_2 \left[P_{r_{12}}(x,y) - P(x)P(y)\right], \tag{1}$$

where $\hat{V}$ is the volume occupied by cells *included* in the catalog, $P(x)$ the generating function for counts and $P_{r_{12}}(x,y)$ is the generating function for bicounts ($r_{12} \equiv |\boldsymbol{r}_1 - \boldsymbol{r}_2|$). The cosmic error on the factorial moment of order k is then $(\Delta F_k/F_k)^2 = (\partial/\partial x)^k(\partial/\partial y)^k E(x+1,y+1)|_{x=y=0}$. This integral can be split into two components[1,8] according to whether the two cells at positions $\boldsymbol{r}_1$ and $\boldsymbol{r}_2$ overlap or not.

The overlapping term, $E_{\rm OV}(x,y)$, corresponds to the edge effect and shot noise contributions. Let $\delta\hat{V}$ being the volume containing points outside $\hat{V}$ but at distance less than 2ℓ from $\hat{V}$. We can then rewrite $E_{\rm OV}$ as

$$E_{\rm OV}(x,y) = \frac{1}{\hat{V}^2}\int_{\hat{V}} d^3r_1 \left[\int_{\hat{V}+\delta\hat{V}, r_{12}\le 2\ell} d^3r_2 F(r_{12}) - \int_{\delta\hat{V}, r_{12}\le 2\ell} d^3r_2 F(r_{12})\right], \tag{2}$$

with the short hand notation $F(r_{12}) = P_{r_{12}}(x,y) - P(x)P(y)$. Assuming that the size of the cell is sufficiently small so that one can neglect the local curvature of the perimeter of $\hat{V}$, $\hat{A} \equiv \partial\hat{V}$, and after integrating by part in the appropriate system of coordinates, one obtains

$$E_{\rm OV}(x,y) \simeq \frac{1}{\hat{V}}\int_0^{2\ell} 4\pi r^2 dr F(r) - \frac{\hat{A}}{4\hat{V}^2}\int_0^{2\ell} 4\pi r^3 dr F(r). \tag{3}$$

At leading order in v/V the first integral in this equation reduces to the edge plus discreteness effect contribution computed by SC. The term proportional to $\hat{A}$ is the next order correction. To some extent, one expects higher order corrections than that to be rather small if the catalog has a reasonable shape (i.e. not too many corners, or not a microbe like or fractal like geometry), which implies that eq. (3) should be quite accurate even for the largest possible cells included in the catalog.

Integrals in eq. (3) can be easily computed numerically as was done in SC for the first order term. More details will be given elsewhere[2]. As we can see, the next to leading order correction is proportional to the perimeter of the survey. Minimizing it implies a survey as compact as possible.

2 Study of a design strategy for the VIRMOS redshift survey

One of the components of the VIRMOS project is a deep magnitude limited redshift survey of $\sim 10^5$ galaxies with $I_{\rm AB} < 22$ covering a small part of the sky, that we will suppose to be four fields of $\sim 4^{\circ 2}$. One of the goals of this survey consists of measuring the evolution of the two-point correlation function, $\xi(r,z)$ with redshift z, for $0 \lesssim z \lesssim 1.2$. Given the expected number density of galaxies on the sky for $I_{\rm AB} < 22$, a complete catalog (with full sampling) would cover $\sim 4^{\circ 2}$. The issue we want to address here is the following: given the above constraints, what should be the geometry of this catalog, and what should be the fraction of galaxies to sample on the sky? The total available area indeed allows a sparse sampling with a factor as small as 1/4 in terms of number density. Moreover the shape of the fields remains to be designed although it should be rectangular for observational convenience.

As we shall use in what follows, one simple way to measure function $\xi(r,z)$ is to consider several subsamples S_i, each containing galaxies at positions $z \in [z_i - \Delta z_i, z_i + \Delta z_i]$. The bin Δz_i should be thin enough for evolution effects to be negligible in S_i and sufficiently wide in

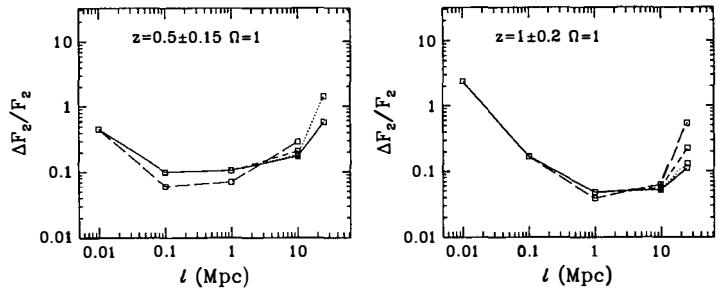

Figure 1: The effect of the shape of the catalog on the cosmic error on the measurement of $F_2 = \bar{N}^2(1+\bar{\xi})$ for the future VIRMOS redshift survey, assuming sCDM. The cosmic error on F_2 is shown as a function of the cell size ℓ for two slices in redshift and for the case $\Omega = 1$. The solid line, dots, dashes correspond to a rectangular field of constant area but varying shape, respectively $2° \times 2°$, $3° \times 1.33°$ and $4° \times 1°$. The long dashes correspond to a catalog with 4 fields of $1° \times 1°$ regularly spaced on a circle making a 45° angle with the galactic plane.

order to have a large enough number of objects, $N_{\mathrm{obj},i}$, in S_i. A simple reasoning using linear perturbation theory shows that $\Delta z_i \propto 1 + z_i$ is a reasonable choice. We consider $i \leq 2$, $z_1 = 0.5$, $\delta z_1 = 0.15$, $z_2 = 1$, $\delta z_2 = 0.2$, which implies, using some models of galaxy formation for number counts as functions of redshift [2], that $N_{\mathrm{obj},1} \simeq 35000$ and $N_{\mathrm{obj},2} = 20000$.

Instead of function ξ, we consider here the factorial moment F_2. To compute the cosmic error, we need a model for clustering up to order 4, and assumptions for the geometry of the universe. To compute two-point statistics, we use the non-linear ansatz of Hamilton *et al.* [5]. We consider two models, open unbiased Cold Dark Matter (oCDM) with density parameter $\Omega = 0.2$ and Hubble constant $H_0 = 75$ km/s/Mpc, and flat standard unbiased CDM (sCDM) ($\Omega = 1$, $H_0 = 50$ km/s/Mpc). Both these models are normalized so that the variance of the underlying galaxy distribution in a sphere of radius $8\,h^{-1}$ Mpc is unity at present time. For higher order statistics, we use the measurements of cumulants on the APM by Gaztañaga [4].

Figure 1 illustrates how the shape of the catalog can influence the cosmic error. As we see, the compact geometry gives the best results for estimating F_2 at large scales because in this regime edge effects dominate. For intermediate scales, the "sparse" geometry, consisting of using several smaller but compact fields spread out on the sky, is the best. Indeed, in that regime, finite volume effects which require large sky coverage are dominant [3]. At small scales, discreteness effects dominate and they do not depend on geometry in that regime.

Figure 2 shows the effects of a sparse sampling strategy [6] which might be technically easier to achieve than full sampling. Such a strategy, consisting in randomly sampling a fraction $f < 1$ of galaxies in the sky, allows a larger sky coverage, so finite volume effects are reduced, as well as edge effects if compactness is preserved. The price to pay however, is an increase of discreteness effects. This is clearly illustrated by figure 2 which shows that a sparse sampling strategy looks reasonable (slightly better in most cases) compared to full sampling at least if one considers all the galaxies in the catalog. The expected errors on the measurement of F_2 are of order 10% or less on a wide dynamic range both for full and sparse sampling.

Of course in the case one wants to study the evolution of clustering by galaxy type separately, the number of object per redshift slice decreases. Then sparse sampling strategy becomes limited, particularly at high redshift. Also as discussed in Colombi *et al.* [3], if one is interested in higher order statistics more sensitive to discreteness effects, a sparse sampling strategy would do probably worse than full sampling.

Note finally that this discussion concerns the factorial moment of order 2, F_2, measured from count-in-cells and for which it is impossible to correct for edge effects [3]. Things would

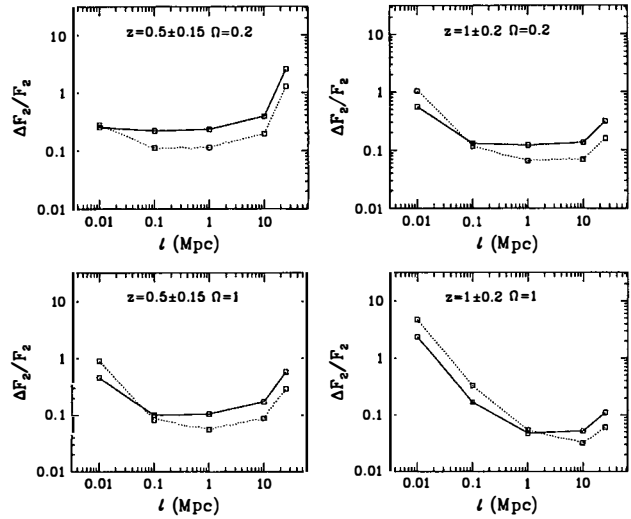

Figure 2: The effect of a sparse sampling strategy on the future VIRSMOS redshift survey, for measuring F_2. The cosmic error on F_2 is shown as a function of scale for two slices in redshift and for two values of Ω (oCDM and sCDM). The solid lines correspond to full sampling on a $2^\circ \times 2^\circ$ square field and the dots correspond to sparse sampling with a factor 1/4 on four $2^\circ \times 2^\circ$ fields regularly spaced on a circle making a 45° angle with the galactic plane.

be obviously different for the two-point correlation function ξ_2 for which edge effects can be corrected for, and would be less significant. Given the accuracy of our calculations, we expect the orders of magnitude given here to be correct within a factor 2 or so, the only difference for ξ being that the increase on the right hand side of the curves in figures 1 and 2 would be slightly shifted to the right.

Acknowledgments

The results presented here are part of a paper in preparation [2]. I would like to thank my collaborators, S. Charlot, J. Devriendt, M. Fioc and I. Szapudi, and O. Le Fèvre and Y. Mellier for introducing me to the VIRMOS survey issues.

References

1. Colombi S., Bouchet F.R. and Schaeffer R., *Astrophysical Journ.* **96**, 401 (1995)
2. Colombi S., Charlot S., Devriendt J., Fioc M. and Szapudi I., in preparation
3. Colombi S., Szapudi I. and Szalay A., *Month. Not. of the Roy. Astr. Soc.*, in press
4. Gaztañaga E., *Month. Not. of the Roy. Astr. Soc.* **286**, 913 (1994)
5. Hamilton A.J.S., Kumar P., Lu E. and Matthews A., *Astrophysical Journ. Lett.* **374**, 1 (1991)
6. Kaiser N., *Month. Not. of the Roy. Astr. Soc.* **219**, 785 (1986)
7. Ripley B. D., *Statistical Inference for Spatial Processes* (Cambridge Univ. Press, Cambridge, 1988)
8. Szapudi I. and Colombi S., *Astrophysical Journ.* **470**, 131 (1996)
9. Szapudi I. and Szalay A., *Astrophysical Journ. Lett.* **494**, 41 (1998)

COSMIC COMPLEMENTARITY: COMBINING CMB AND SUPERNOVA OBSERVATIONS

MAX TEGMARK[a], DANIEL J. EISENSTEIN & WAYNE HU[b]
Institute for Advanced Study, Princeton, NJ 08540
max@ias.edu, eisenstein@ias.edu, whu@ias.edu

We compute the accuracy with which Ω_m and Ω_Λ can be measured by combining future SN Ia and CMB experiments, deriving a handy expression for the SN Ia Fisher information matrix. The two data sets are found to be highly complementary: a joint analysis reduces the error bars by more than an order of magnitude compared to a separate analysis of either data set.

1 Introduction

It may be possible to measure cosmological parameters with great accuracy using upcoming cosmic microwave background (CMB) experiments [1,2,3], galaxy surveys [4,5,6] and supernova Ia searches [7,8,9]. However, no single type of measurement alone can constrain all parameters, as it will inevitably suffer from so-called *degeneracies* in which particular combinations of changes in parameters leave the result essentially unaffected [2,3,10,11]. Fortunately, different types of cosmological measurements are often highly complementary, breaking each other's degeneracies and combining to give much more accurate measurements than any one could give alone. For example, CMB measurements are highly complementary to galaxy surveys [4,6,12,13,14]. The topic of this paper is the well-known[3,4,15] complementarity between CMB and SN Ia for measuring the large-scale geometry of spacetime, given by the density parameters Ω_m for matter and Ω_Λ for vacuum density (cosmological constant).

The accuracy with which Ω_m and Ω_Λ can be measured from a SN Ia survey was first computed by Goobar & Perlmutter[7] and subsequently by making χ^2-fits to real data[8,9,15]. Here we present the first calculation of the *Fisher information matrix* $\mathbf{F}$ for SN surveys, which has the advantage of explicitly showing how the accuracy depends on the survey details. We then compare this with CMB information.

[a] Hubble Fellow
[b] Sloan Fellow

2 The supernova Fisher Matrix

The Fisher information matrix[16] quantifies the information content about Ω_m and Ω_Λ. $\mathbf{F}^{-1}$ gives the best attainable 2×2 covariance matrix for the measurement errors on these parameters, illustrated by the error ellipses in Figure 1b. $\mathbf{F}$ also allows the SN Ia results to be combined with those from the CMB, since if independent experiments are analyzed jointly, their Fisher information matrices simply add.

Suppose that N type Ia supernovae at redshifts $z_1,...,z_N$ have been been observed to have magnitudes $m_1,...,m_N$. These measurements can be modeled as[7]

$$m_n = 5\log_{10}[H_0 d_L(z_n,\Omega_m,\Omega_\Lambda)] + m_0 + \epsilon_n, \tag{1}$$

where m_0 is a constant independent of Ω_m, Ω_Λ and H_0 and ϵ_n is a random term with zero mean ($\langle\epsilon_n\rangle = 0$) including measurement errors, errors in extinction correction and intrinsic scatter in the "standard candle" luminosity. The luminosity distance is

$$H_0 d_L = (1+z)\frac{S(\kappa I)}{\kappa}, \quad I(z;\Omega_m,\Omega_\Lambda) = \int_0^z A(z')^{-1/2}dz', \tag{2}$$

$$A(z) \equiv (1+z')^2(1+\Omega_m z') - z'(2+z')\Omega_\Lambda, \tag{3}$$

where $S(x) \equiv \sinh x$, x and $\sin x$ for open ($\Omega_m+\Omega_\Lambda<1$), flat ($\Omega_m+\Omega_\Lambda=1$) and closed ($\Omega_m+\Omega_\Lambda>1$) universes, respectively. $\kappa \equiv \sqrt{|1-\Omega_m-\Omega_\Lambda|}$. Grouping the measured data m_n into an N-dimensional vector $\mathbf{m}$ and assuming that the errors ϵ_n have a Gaussian distribution, the Fisher matrix is given by[16]

$$\mathbf{F}_{ij} = \frac{1}{2}\mathrm{tr}\left[\mathbf{C}^{-1}\mathbf{C}_{,i}\,\mathbf{C}^{-1}\mathbf{C}_{,j}\right] + \boldsymbol{\mu}_{,i}^t\,\mathbf{C}^{-1}\boldsymbol{\mu}_{,j}, \tag{4}$$

where $\boldsymbol{\mu} \equiv \langle\mathbf{m}\rangle$ is the mean and $\mathbf{C} \equiv \langle\mathbf{m}\mathbf{m}^t\rangle - \boldsymbol{\mu}\boldsymbol{\mu}^t$ is the covariance matrix of $\mathbf{m}$. Commas denote derivatives, so $\boldsymbol{\mu}_{,i} \equiv \partial\boldsymbol{\mu}/\partial\Omega_i$, $i = m$ or Λ. For simplicity, we will assume that

$$\mathbf{C}_{ij} = \delta_{ij}(\Delta m)^2, \tag{5}$$

i.e., that all the magnitude errors ϵ_i are uncorrelated and have the same standard deviation Δm, including systematic errors. Our treatment below is readily generalized to arbitrary error models $\mathbf{C}$. Since $\mathbf{C}_{,i}=0$, all the information about Ω_m and Ω_Λ comes from the second term in equation (4). Differentiating equation (1) thus gives

$$\mathbf{F}_{ij} = \frac{1}{\Delta m^2}\sum_{n=1}^{N} w_i(z_n)w_j(z_n), \tag{6}$$

where

$$w_i(z) \equiv \left(\frac{5}{\ln 10}\right)\left\{\frac{\kappa S'[\kappa I(z)]}{S[\kappa I(z)]}\left[\frac{\partial I}{\partial\theta_i} - \frac{I(z)}{2\kappa^2}\right] + \frac{1}{2\kappa^2}\right\}, \tag{7}$$

$$\frac{\partial I}{\partial\Omega_m}(z) = -\frac{1}{2}\int_0^z \frac{z'(1+z')^2}{A(z')^{3/2}}dz', \qquad \frac{\partial I}{\partial\Omega_\Lambda}(z) = \frac{1}{2}\int_0^z \frac{z'(2+z')}{A(z')^{3/2}}dz'. \tag{8}$$

The expression in braces approaches $I^{-1}\partial I/\partial\theta_i - I^2/6$ as $\kappa\to0$. It is instructive to rewrite equation (6) as

$$\mathbf{F}_{ij} = \frac{N}{(\Delta m)^2}\int_0^\infty f(z)w_i(z)w_j(z)dz, \tag{9}$$

where the SN Ia redshift distribution is given by $f(z) = \frac{1}{N}\sum_{n=1}^{N}\delta(z-z_n)$. The contribution to $\mathbf{F}$ from each redshift can thus be split into two factors, one reflecting the quality of the data

Table 1: Attainable error bars $\Delta\Omega_i$ for various combinations of data sets. The rows correspond to using CMB alone and three forecasts (pessimistic, middle-of-the-road, and optimistic) for available SN Ia data in five years time. The CMB columns correspond to the upcoming MAP and Planck satellite missions without (−) and with (+) polarization information. Planck+ is seen to improve over the "No CMB" column by over an order of magnitude, and the difference is even greater between the "Opt" and "No SN" rows. The "No SN" row is overly conservative, since gravitational lensing breaks the CMB degeneracy somewhat[11] but this lensing information is dwarfed by the SN Ia in the other rows.

					No CMB		MAP−		MAP+		Planck−		Planck+	
SN Ia	N	Δm	$\bar{z}$	Δz	$\Delta\Omega_m$	$\Delta\Omega_\Lambda$	$\Delta\Omega_m$	$\Delta\Omega_\Lambda$	$\Delta\Omega_m$	$\Delta\Omega_\Lambda$	$\Delta\Omega_m$	$\Delta\Omega_\Lambda$	$\Delta\Omega_m$	$\Delta\Omega_\Lambda$
No SN	0	-	-	-	∞	∞	3.6	3.2	2.0	1.8	3.0	2.6	.63	.54
Pess	100	0.5	0.55	0.2	.81	1.1	.12	.12	.12	.10	.12	.10	.11	.10
Mid	200	0.3	0.65	0.3	.22	.34	.06	.08	.05	.05	.05	.04	.04	.04
Opt	400	0.2	0.70	0.4	.08	.14	.04	.07	.02	.03	.02	.02	.02	.02

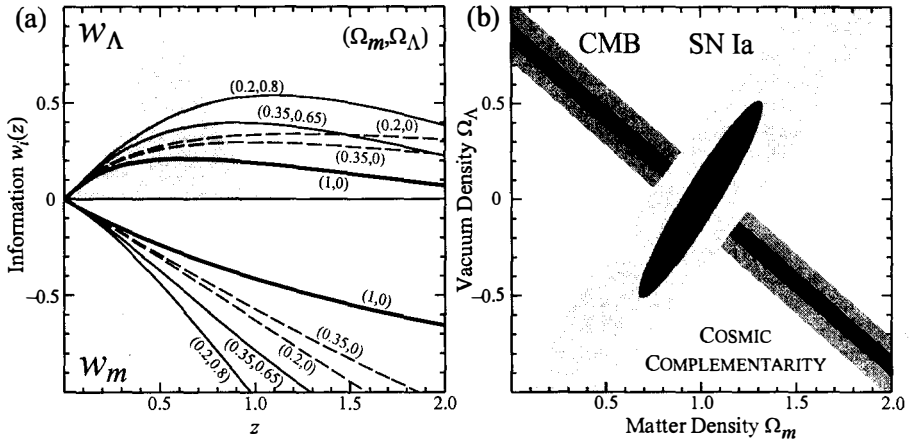

Figure 1: Figure 1a (left) shows the weight functions w_Λ (positive) and w_m (negative) for standard CDM, two open ($\Omega_\Lambda = 0$) models and two flat ($\Omega_\Lambda = 1 - \Omega_m$) models. The Fisher matrix element $\mathbf{F}_{ij}$ is computed by simply integrating the product of the curves w_i and w_j and a redshift distribution f such as the shaded one. Figure 1b (right) shows the 68% confidence regions obtained from the three hypothetical SN Ia data sets specified in Table 1, which are intended to be best-case, middle-of-the-road and worst-case scenarios for what might be available in five years time. Four corresponding ellipses for upcoming CMB experiments are also shown, based on a full 12-parameter analysis described elsewhere[14]. The assumed fiducial model is COBE-normalized CDM with $\Omega_m = 1$, $\Omega_\Lambda = 0$, $\Omega_b = 0.05$, $\Omega_\nu = 0.05$ and $h = 0.5$. Combining the CMB and SN Ia data shrinks the error region to the overlap of the two corresponding ellipses: for instance, the tiny black ellipse in the center is for a joint analysis of the optimistic SN Ia case with polarized Planck data.

set $(Nf[z]/\Delta m^2)$ and the other incorporating the effects of cosmology (the weight functions w_i). The functions w_i are plotted in Figure 1a for a variety of cosmological models. If all the observed supernovae were at the same redshift z, then the resulting 2×2 Fisher matrix $\mathbf{F}_{ij} \propto w_i(z)w_j(z)$ would have rank 1, *i.e.*, be singular. The vanishing eigenvalue would correspond to the eigenvector $(w_\Omega, -w_\Lambda)$. Physically, this is because there is more than one way of fitting a single measured quantity $d_L(z)$ by varying two parameters (Ω_m and Ω_Λ). The corresponding ellipse in Figure 1b would be infinitely long, with slope $-w_\Omega/w_\Lambda$, the ratio of the magnitudes of the Ω_m and Ω_Λ curves in Figure 1a at that redshift. The SN Ia ellipses plotted in Figure 1b correspond to a range of redshifts, with f being a Gaussian of mean $\bar{z}$ and standard deviation Δz given by Table 1. This breaks the degeneracy only marginally, leaving the SN ellipses quite

skinny, since the ratios w_Ω/w_Λ in Figure 1a are seen to vary only weakly with z.

3 Conclusions

In conclusion, we have derived a handy expression for the SN Ia Fisher information matrix and combined it with the Fisher matrix of the CMB. Whereas two identical data sets only give a measly factor of $\sqrt{2}$ improvement in error bars when combined, the gain factor was found to exceed 10 in this case. This "cosmic complementarity" is due to the fortuitous fact that although either data set alone suffers from a serious degeneracy problem, the directions in which they are insensitive (in which the ellipses in Figure 1b are elongated) are almost orthogonal. This is because the CMB probes the redshift-distance relationship via the location of the Doppler peaks, depending mainly on $\Omega_m + \Omega_\Lambda$ for standard CDM, whereas the SN Ia probe the redshift-luminosity relation, measuring roughly $\Omega_m - \Omega_\Lambda$. The complementarity remains just as striking for the more general cosmological models plotted in Figure 1a—both the CMB and SN Ia ellipses simply rotate somewhat in these cases, but remain very skinny and almost perpendicular.

The potential power of upcoming CMB measurements has led to a widespread feeling that they will completely dominate cosmological parameter estimation, leaving other types of experiments making only marginal contributions. Because of cosmic complementarity, of which the present paper gives but one example out of many, this view is misleading: two data sets combined can be much more useful than either one alone.

Acknowledgments

We thank Alex Kim, Saul Perlmutter, Adam Riess and Martin White for useful discussions. MT was supported by NASA though grant NAG5-6034 and a Hubble Fellowship, HF-01084.01-96A, awarded by STScI, which is operated by AURA, Inc. under NASA contract NAS5-26555. DJE and WH were supported by NSF PHY-9513835. WH was additionally supported by a Sloan Fellowship and the W. M. Keck Foundation.

References

1. G. Jungman, M. Kamionkowski, A. Kosowsky and D. N. Spergel, *Phys. Rev. D* **54**, 1332 (1996).
2. J. R. Bond, G. Efstathiou and M. Tegmark, *MNRAS* **291**, L33 (1997).
3. M. Zaldarriaga, D. Spergel and U. Seljak, *ApJ* **488**, 1 (1997).
4. M. Tegmark, *Phys. Rev. Lett.* **79**, 3806 (1997).
5. D. M. Goldberg and M. A. Strauss, *ApJ* **495**, 29 (1998).
6. W. Hu, D. J. Eisenstein and M. Tegmark, preprint astro-ph/9712057 (1988).
7. A. Goobar and S. Perlmutter, *ApJ* **450**, 14 (1995).
8. S. Perlmutter *et al.*, *Nature* **391**, 51 (1998).
9. P. M. Garnavich *et al.*, *ApJL* **493**, L53 (1998).
10. J. R. Bond *et al.*, *Phys. Rev. Lett.* **72**, 13 (1994).
11. R. B. Metcalf and J. Silk, preprint astro-ph/9708059 (1998).
12. E. Gawiser and J. Silk 1998, in preparation.
13. M. Webster *et al.*, preprint astro-ph/9802109 (1998).
14. D. J. Eisenstein, W. Hu and M. Tegmark 1998, in preparation.
15. M. White, preprint astro-ph/9802295 (1998).
16. M. Tegmark, A. N. Taylor and A. F. Heavens, *ApJ* **480**, 22 (1997).

WEAK LENSING EFFECTS TO PROBE THE COSMOLOGICAL PARAMETERS

F. Bernardeau[1], Y. Mellier[2,3] & L. van Waerbeke[4,5]
[1] *Service Physique Théorique, CE de Saclay, F-91191 Gif-sur-Yvette Cedex, France*
[2] *Institut d'Astrophysique de Paris,98bis Boulevard Arago,75014 Paris, France*
[3] *Observatoire de Paris (DEMIRM), 61 Av. de l'Observatoire, 75014 Paris, France.*
[4] *Max-Planck-Institut für Astrophysik, 85740 Garching, Germany*
[5] *CITA, 60 St George St., Toronto, ON M5S 3H8, Canada*

The use of gravitational distortion effects is revealing a very precious mean of probing the mass concentrations in the Universe. Any mass concentrations is indeed detectable with such a mean irrespectively of its apparent luminosity.
Weak lensing effects are shown to be measurable at all scales, from galaxy clusters to large-scale structures of the Universe. We stress that projected mass maps of the large-scale structures of significant size should be available soon. With them, it will be possible to constrain some fundamental cosmological parameters such as the amplitude and shape of the power spectrum or the density parameter of the Universe, Ω_0, with a remarkable accuracy.

1 The gravitational lens effects

1.1 The physical mechanisms

The physical mechanisms of gravitational lenses are well known since the foundation of General Relativity. All gravitational potentials deflect passing photons with an angle fraction per unit length, $\partial\alpha/\partial s$, proportional to the gradient of the gravitational potential ϕ with, $\partial\alpha/\partial s = -2\nabla_\perp\phi$, where the gradient of the potential is taken in the plane orthogonal to the direction of propagation[17,19].

The direct result of this light bending is a displacement of the angular positions of sources on the image plane. The apparent position, $\boldsymbol{\gamma}^I$, is moved from the position in the source plane, $\boldsymbol{\gamma}^S$, with,

$$\boldsymbol{\gamma}^I = \boldsymbol{\gamma}^S + \boldsymbol{\xi}(\boldsymbol{\gamma}^I) \quad with \quad \boldsymbol{\xi}(\boldsymbol{\gamma}^I) = -2\frac{D_{LS}}{D_{OS}\,D_{OL}}\nabla_{\boldsymbol{\gamma}}\Phi, \tag{1}$$

where D_{LS} is the angular distance between the lenses and the sources, D_{OS} is the angular distance to the source plane, and ∇_γ is the angular derivative of the potential. Depending on the magnitude of the lens effect, different regimes are considered (see Fig. 1):

- The strong regime is such that several light path are possible between the sources and the observer. It thus induces multiple images, and the images of background galaxies are often extremely distorted: this is the regime of the giant arcs.

- The regime of arclets correspond to a case where there are no multiple images although a significant distortion of the background objects can be observed.

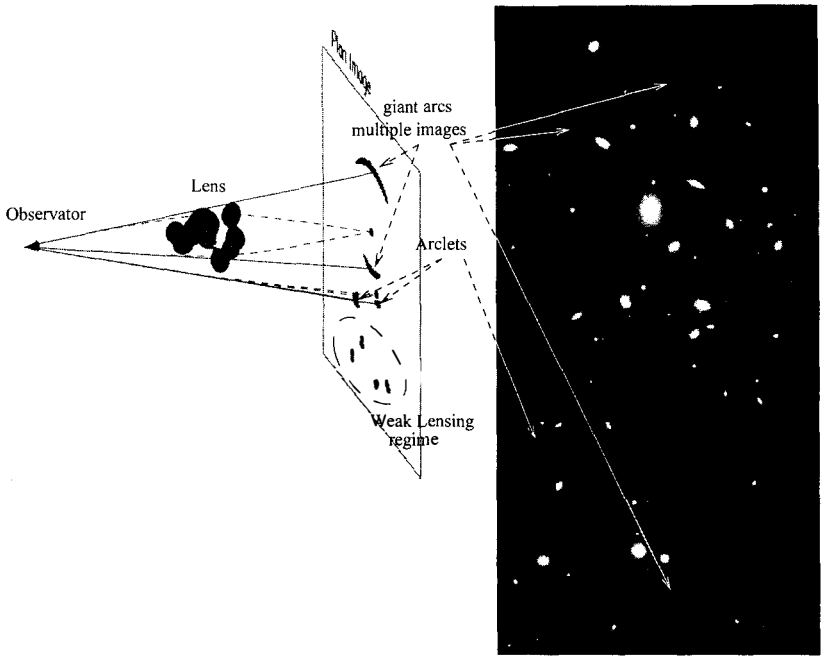

Figure 1: A sketch of the lens effects. Three regimes can be distinguished. The cluster on the right is an HST/STScI image of A2218.

- The weak lensing regime corresponds to cases of modest distortion (typically a few %). Such effect cannot be detected with a single object and therefore should be measured in a statistical way, by averages over a large number of background galaxies.

1.2 The weak lensing regime

In all cases the displacement field is not directly observable. In the weak lensing regime, the deformation only is measurable. For slightly extended objects such as background galaxies the deformation in shape is induced by the variations of the displacement field. More precisely it can be described by the amplification matrix $\mathcal{A}$ that gives the linear transform law between the source and the image plane. Its inverse, $\mathcal{A}^{-1}$, is given by the derivatives of the displacement with respect to the apparent position,

$$\mathcal{A}^{-1} \equiv \frac{\partial \gamma_i^S}{\partial \gamma_j^I} = \delta_{ij} - 2\frac{D_{LS}}{D_{OS}\,D_{OL}}\phi_{,ij}. \tag{2}$$

Usually the components of $\mathcal{A}^{-1}$ are written,

$$\mathcal{A}^{-1} = \begin{pmatrix} 1-\kappa-\gamma_1 & -\gamma_2 \\ -\gamma_2 & 1-\kappa+\gamma_1 \end{pmatrix}, \tag{3}$$

taking advantage of the fact that it is a symmetric matrix. The components of this matrix are expressed in terms of the convergence, κ, (a scalar field) and the shear, γ (a pseudo vector field) with

$$\kappa = \frac{1}{2}\nabla^2\phi; \quad \gamma_1 = \frac{1}{2}(\varphi_{,11} - \varphi_{,22})\,; \quad \gamma_2 = \varphi_{,12}, \quad \textit{with} \quad \varphi = 2\frac{D_{LS}}{D_{OS}\,D_{OL}}\phi. \tag{4}$$

The convergence describes the linear change of size and the shear describes the deformation. The consequences of such a transform can be decomposed in two aspects:

- The magnification effect. Lenses induce a change of size of the objects. As the surface brightness is not changed by this effect, the change of surface induces a direct magnification effect, μ. This magnification is directly related to the determinant of $\mathcal{A}$ so that,

$$\mu = \det(\mathcal{A}) = 1/\left[(1-\kappa)^2 - \gamma^2\right]. \tag{5}$$

- The distortion effect. Lenses also induce a change of shape of the background objects. The eigenvalues of the matrix $\mathcal{A}^{-1}$ determine the direction and amplitude of such a deformation.

2 The magnification effect

In the weak lensing regime, the observational consequences of the magnification effect is a combination of a change the apparent area of the objects, that makes their detection easier, and their dilution (the total area is enlarged as well). The mean local number density of galaxies is then related to the slope of the galaxy counts, α, through

$$n(\gamma) = n_g\, \mu^{2.5\alpha-1} \quad with \quad \alpha = \frac{d\log N}{dm}, \tag{6}$$

where m is the apparent magnitude (in a given band) and n_g is the mean number density of galaxies in the absence of lenses. Whether the number density of galaxies increases or decreases in magnified area thus depends on α and consequently on the selected population of objects.

Such an effect has been advocated[8,9] as a way to detect the lens effect. In general this method suffers from the fact that the background galaxies have intrinsic number density fluctuations. It is therefore more appropriate for mapping the mass fluctuations in galaxy clusters where the magnification effect is large enough to dominate these. In galaxy clusters it is a cheap way to map the mass profiles. More sophisticated analysis allow even to have access to the cosmological constant Λ by probing the extension of the depletion area[6].

3 The distortion effect

3.1 The galaxy shape matrices to measure the distortion field

The distortion effects change the shape of the background objects. The objects appear elongated along the eigenvalues of the amplification matrix. When background objects are only moderately extended (this excludes the case of arcs), their shapes can be described by the matrix,

$$\mathcal{S} \equiv \int d^2\theta\, \theta_i\, \theta_j\, \mathcal{I}(\theta) / \int d^2\theta\, \theta^2\, \mathcal{I}(\theta)/2. \tag{7}$$

It is easy to relate the shape matrix in the source plane to the one in the image plane. This is obtained by a simple change of variable that uses the fact that the surface brightness of the objects is not changed. It implies

$$\mathcal{S}^S = \frac{\mathcal{A}^{-1}\cdot\mathcal{S}^I\cdot\mathcal{A}^{-1}}{\det(\mathcal{A}^{-1})}. \tag{8}$$

By averaging over the shape matrices in the source plane, assuming the intrinsic shape fluctuations are not correlated, one can get the value of $\mathcal{A}^{-1}/\sqrt{\det\mathcal{A}^{-1}}$. The combination we have access to is totally independent of the amplification factor. As a consequence, the quantity which is measurable is the distortion field, $g = \gamma/(1-\kappa)$. This quantity identifies with γ only in the limit of very weak lensing (i.e. when $\kappa \ll 1$).

3.2 The construction of the projected mass density

The elaboration of methods for reconstructing mass maps from distortion fields is not a trivial issue. In a pioneering paper, Kaiser & Squires (1992) showed that this is indeed possible, at least in the weak lensing regime. It was further extended in many ways. Bartelmann, Schneider and his collaborators[1,18,21,22,23] have worked in detail on the edge effects, the possibility of having adaptive smoothing procedures, the use of maximum entropy method etc... This is particularly important when structures of different sizes and contrasts are present at the same time. Finally Kaiser[13] exhibited the relation between the local convergence and the distortion field g which is valid in all regimes. This relation reads

$$\nabla \log(1-\kappa) = \begin{pmatrix} 1-g_1 & g_2 \\ g_2 & 1+g_1 \end{pmatrix}^{-1} \cdot \begin{pmatrix} \partial_1 & \partial_2 \\ -\partial_2 & \partial_1 \end{pmatrix} \cdot \begin{pmatrix} g_1 \\ g_2 \end{pmatrix}. \tag{9}$$

This is a non-linear and non-local relationship.

The first reconstruction of a mass map of a galaxy cluster has been done on MS1224 by Fahlman et al.[10]. Many other reconstructions have now been done or are under preparation.

4 The weak lenses as a probe of the Large-Scale Structures

The idea of probing the large-scale structures with gravitational effects is very attractive. The gravitational survey offers indeed a unique way of probing the mass concentrations in the Universe since it can provide us with mass maps of the Universe that are free of any bias. Its interpretations in terms of cosmological parameters would then be straightforward and independent on hypothesis on galaxy or cluster formation schemes.

4.1 The expected amplitude of the signal

Are the effects from large-scale structures measurable? It depends on the number density of background objects for which the shape matrices are measurable. In current deep galaxy survey the typical mean number density of objects is about 50 arcmin^{-2}. The precision of the measured distortion at the degree scale is then about 10^{-3}. This number is to be compared with the expected amplitude of the signal coming from the large-scale structures. Computations[4,16,12] show that a signal at the percent level is expected (for sources at redshifts of about 1). This makes such detection a priori possible with a signal to noise ratio around 10 (provided the instrumental noise can be controlled down to such a low level).

4.2 What can we learn from such effects?

The relation between the convergence and the local density contrasts in the local universe can be derived easily in the Born approximation,

$$\kappa(\gamma) = -\frac{3}{2}\Omega_0 \int dz_s\, n(z_s) \int d\chi\, \frac{D(\chi_s,\chi)\, D(\chi_s)}{D(\chi)}\, \delta_{mass}(\chi,\gamma)\,(1+z), \tag{10}$$

where χ is the distance along the line of sight, D are the angular distances and δ_{mass} is the local density contrast. From this equation it is obvious that the amplitude of κ is directly proportional of the density fluctuation amplitude and that the two point correlation function of the κ field is related to the shape of the density power spectrum. In the following we parameterize its amplitude with σ_8 that gives the r.m.s. of the density contrast in a sphere of radius $8\,h^{-1}$Mpc. The relation (10) also shows that κ depends on the cosmological parameters. This dependence appears in different places. Indeed the relation between the redshifts (by which the distances of

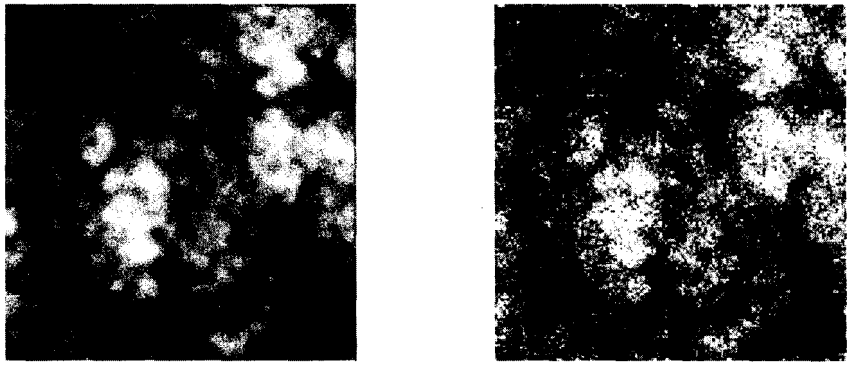

Figure 2: Example of reconstruction of a convergence map. The map on the left panel is a 5×5 square degrees simulated map. The map on the right panel is the reconstructed map obtained after a realistic measurement noise has been introduced in each pixel. At small scale, a Poisson noise is dominating, but the large-scale structures are well recovered (figure from van Waerbeke et al. 1998).

the background objects will be estimated) and the distances are Ω and Λ dependent, as well as the relation between the distances χ and D (these latter are equal in case of a flat background, $\Omega_0 + \Lambda = 1$). The dominant dependence on the cosmological parameters is however due to the overall Ω_0 factor.

The result for the width of the distribution is the following,

$$\langle \kappa_\theta^2 \rangle^{1/2} \approx 0.01 \; \sigma_8 \; \Omega_0^{0.8} \; z_s^{0.75} \; \left(\frac{\theta}{1\,\mathrm{deg}} \right)^{-(n+2)/2} \tag{11}$$

To be noticed is the dependence on the redshift of the sources. It is understandable since the further away the sources are, the more numerous the lenses that can be detected are and the more efficient the detection is. This was noticed by Villumsen[27] who pointed out that the Ω_0 dependence is roughly given by the Ω value at the redshift of the sources. These results are slightly affected by the introduction of the non-linear effects in the shape of the power spectrum[16,11].

A question that arises is whether it is possible to separate the amplitude of the power spectrum from the cosmological parameters. A simple examination of the equation (10) shows that it should be because, for a given value of σ_κ, the density field is more strongly evolved into the non-linear regime when Ω_0 is low.

The consequences of this are two fold. The nonlinearities change the angular scale at which the non-linear dynamics starts to amplify the growth of structures. This effect was more particularly investigated by Jain & Seljak[11] (see also the contribution of B. Jain in these proceedings) who showed that the emergence of the nonlinear regime is apparent in the shape of the angular two-point function. This effect is however quite subtle since it might reveal difficult to separate from peculiarities in the shape of the initial power spectrum.

The other aspect is that nonlinear effects induce non-Gaussian features due to mode couplings. The importance of this effect was first stressed by Bernardeau et al.[3] who showed that the probability distribution function of the local filtered convergence is expected to exhibit a non-zero skewness. The perturbation theory (which is valid a priori at large scale) gives the

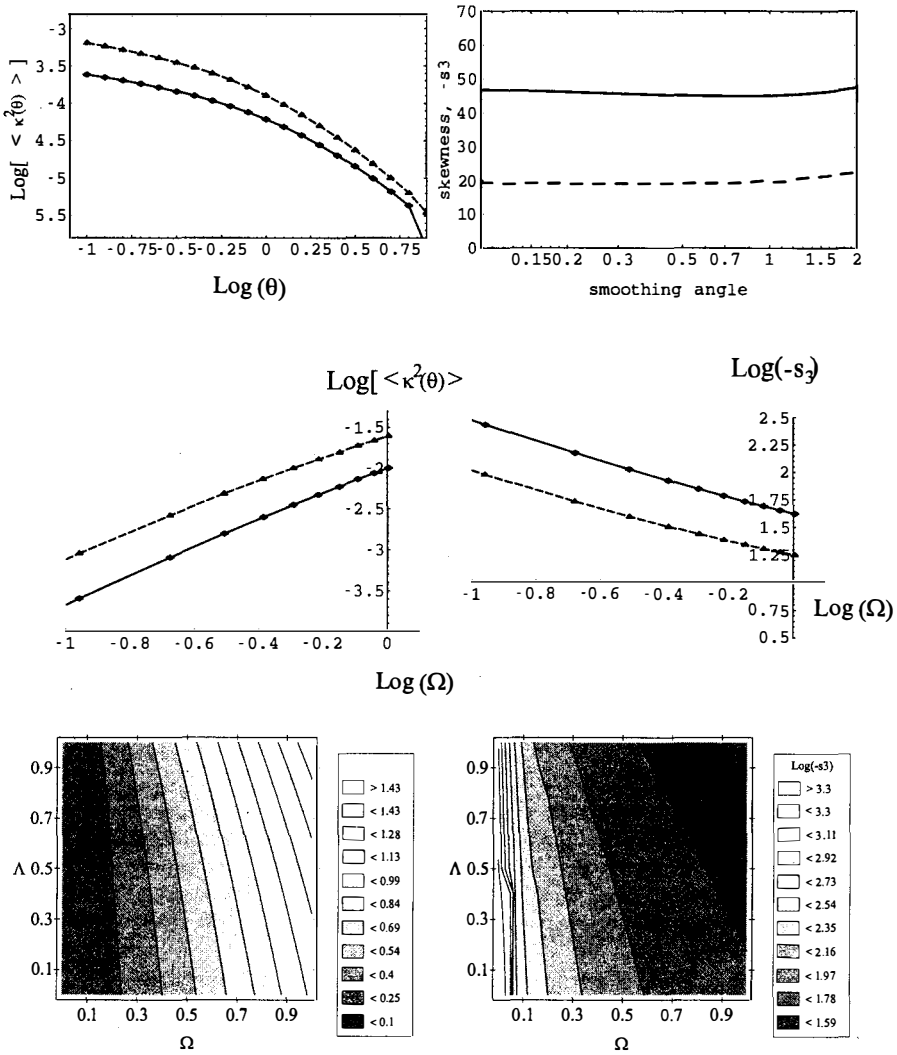

Figure 3: Perturbation Theory results[2] obtained for the width (left panels) and skewness (right panels) of the probability distribution function of the local convergence. The results are plotted as a function of the angular scale in the top panels, of Ω_0 in the middle ones. The solid lines correspond to source redshifts of 1, and the dashed lines to redshifts of 2. In the bottom panels the iso-values of the width and the skewness are plotted in the Ω_0-Λ plane (for source redshifts of 1). It shows that the dependence on Ω_0 is slightly degenerate with Λ.

following result,

$$s_3(\theta) \equiv \frac{\langle \kappa_\theta^3 \rangle}{\langle \kappa_\theta^2 \rangle^2} = -40\ \Omega_0^{-0.8}\ z_s^{-1.35}. \tag{12}$$

The origin of this skewness is relatively simple to understand: as the density field enters the non-linear regime the large mass concentrations tend to acquire a large density contrast in a small volume. This induces rare occurrences of large negative convergences. The under-dense regions tend on the other hand to occupy a large fraction of the volume, but can induce only moderate positive convergences. This mechanism is clearly visible on the maps of figure (2). When the mean source redshift grows the skewness diminishes since the addition of independent layers of large-scale structures tend to dilute the non-Gaussianity.

The validity of Eq. (12) has been confirmed numerically by Gaztañaga & Bernardeau[7], who showed it is valid for scales above a few tens of arcmins. A non-zero skewness has also been observed in the numerical experiment of Jain et al. (see also the contribution of Seljak in these proceedings).

Large angular convergence maps can therefore provide new means for constraining fundamental cosmological parameters. Recent numerical results[29] show that in maps of 5×5 square degrees it is reasonable to expect a precision of a few percent on the normalization and about 10% on the cosmological density parameter.

4.3 The prospects

From an observational point of view, the investigation of the large-scale structures of the Universe with gravitational lenses is in a very preliminary stage. After an early claim by Villumsen[26], a direct evidence of the detection distortion signal of gravitational origin has been reported recently by Schneider et al[20].

There are at present many studies, either theoretical or numerical, that aim to examine all possible systematic errors[5,15], to optimize the data analysis concepts[28] and the scientific interpretations of the resulting mass maps[2,3,24,29]. A few observational surveys are now emerging,

- the ESO key program jointly done by MPA and IAP;
- the DESCART project, part of the scientific program of the wide field CCD camera to be installed at the CFHT.

Acknowledgments

FB thanks IAP and LvW thanks Observatoire Midi-Pyrénées for hospitality.

References

1. Bartelmann, M., Narayan, R., Seitz, S. & Schneider, P., 1996, *Astrophys. J.* **464**, 115
2. Bernardeau, F. astro-ph/9802243
3. Bernardeau, F., van Waerbeke, L. & Mellier, Y. 1997, *Astr. & Astrophys.* **324**, 15
4. Blandford, R. D., Saust, A. B., Brainerd, T. G., Villumsen, J. V. 1991, *Mon. Not. R. astr. Soc.* **251**, 600
5. Bonnet, H. & Mellier, Y. 1995 *Astr. & Astrophys.* **303**, 331
6. Fort, B., Mellier, Y. & Dantel-Fort, F. 1997, *Astr. & Astrophys.* **321**, 353
7. Gaztañaga, E. & Bernardeau, F. 1998, *Astr. & Astrophys.* **331**, 829
8. Broadhurst, T. (1995) SISSA preprint astro-ph/9511150.
9. Broadhurst, T., Taylor, A.N., Peacock, J. (1995) *Astrophys. J.* **438**, 49
10. Fahlman, G., Kaiser, N., Squires, G., Woods, D. 1994, *Astrophys. J.* **437**, 56

11. Jain, B., Seljak, U. 1997, *Astrophys. J.* **484**, 560
12. Kaiser, N. 1992 *Astrophys. J.* **388**, L72
13. Kaiser, N. 1995 *Astrophys. J.* **439**, 1
14. Kaiser, N. & Squires, G. 1993 *Astrophys. J.* **404**, 441
15. Kaiser, N., Squires, G. & Broadhurst, T. 1995 *Astrophys. J.* **449**, 460
16. Miralda-Escudé, J. 1991 *Astrophys. J.* **380**, 1
17. Sachs, R. K. 1961, *Proc. Roc. Soc. London* A**264**, 309
18. Schneider, P. 1995, *Astr. & Astrophys.* **302**, 639
19. Schneider, P., Ehlers, J., Falco, E. E. 1992, *Gravitational Lenses*, Springer.
20. Schneider, P., Van Waerbeke, L., Mellier, Y., Jain, B., Seitz, S., Fort, B. 1997, astro-ph/9705122.
21. Seitz, C., Schneider, P., 1995 *Astr. & Astrophys.* **297**, 247
22. Seitz, S., Schneider, P., 1996 *Astr. & Astrophys.* **305**, 388
23. Seitz, S., Schneider, P., Bartelmann, M., astro-ph/9803038
24. Seljak, U. astro-ph/9711124
25. Squires, G. & Kaiser, N. 1996, *Astrophys. J.* **473**, 65
26. Villumsen, J. V., astro-ph/9507007
27. Villumsen, J. V. 1996, *Mon. Not. R. astr. Soc.* **281**, 369
28. van Waerbeke, L., Mellier, Schneider, P., Fort, B. & Mathez, G. 1997 *Astr. & Astrophys.* **317**, 303
29. van Waerbeke, L., Bernardeau, F. & Mellier, Y. 1998, in preparation

NUMERICAL INVESTIGATIONS OF WEAK LENSING BY LARGE-SCALE STRUCTURE

Bhuvnesh Jain [1], Uroš Seljak [2], Simon White [3]
[1] *Dept. of Physics, Johns Hopkins University, Baltimore, MD 21218, USA*
[2] *Harvard Smithsonian Center For Astrophysics, Cambridge, MA 02138, USA*
[3] *Max-Planck-Institut für Astrophysik, Garching 85740, GERMANY*

We use numerical simulations of ray tracing through N-body simulations to investigate weak lensing by large-scale structure. These are needed for testing the analytic predictions of two-point correlators, to set error estimates on them and to investigate nonlinear gravitational effects in the weak lensing maps. On scales larger than 1 degree gaussian statistics suffice and can be used to estimate the sampling, noise and aliasing errors on the measured power spectrum. For this case we describe a minimum variance inversion procedure from the 2-d to 3-d power spectrum and discuss a sparse sampling strategy which optimizes the signal to noise on the power spectrum. On degree scales and smaller the shear and convergence statistics lie in the nonlinear regime and have a non-gaussian distribution. For this regime ray tracing simulations are useful to provide reliable error estimates and calibration of the measurements. We show how the skewness and kurtosis can in principle be used to probe the mean density in the universe, but are sensitive to sampling errors and require large observed areas. The probability distribution function is likely to be more useful as a tool to investigate nonlinear effects. In particular, it shows striking differences between models with different values of the mean density Ω_m.

1 Introduction

Weak lensing by large-scale structure (LSS) shears the images of distant galaxies. The first calculations of weak lensing by LSS (Blandford et al. 1991; Miralda-Escude 1991; Kaiser 1992), based on the pioneering work of Gunn (1967), showed that lensing would induce coherent ellipticities of order 1% over regions of order one degree on the sky. Recently several authors have extended this work to probe semi-analytically the possibility of measuring the mass power spectrum and cosmological parameters from the second and third moments of the induced ellipticity or convergence (e.g. Bernardeau et al. 1997; Jain and Seljak 1997; Schneider et al. 1997).

The analytical work cited above suggested that nonlinear evolution of the density perturbations that provide the lensing effect can significantly alter the predicted signal. It enhances the power spectrum on scales below one degree and makes the probability distribution function (pdf) of the ellipticity and convergence non-Gaussian. We have carried out numerical simulations of ray tracing through N-body simulation data to compute the fully nonlinear moments and pdf. Details of the method and results are presented in a forthcoming paper; here we summarize the method and present some highlights of the results in Figures 1-5. We also discuss reconstruction of the dark matter power spectrum and error estimation using the gaussian approximation.

2 Ray Tracing Method

The dark matter distribution obtained from N-body simulations of different models of structure formation is projected on to 2-dimensional planes lying between the observer and source galaxies. Typically we use galaxies at $z \sim 1$ with $\sim 20 - 30$ planes. We propagate $\sim 10^6$ light rays through these planes by computing the deflections due to the matter at every plane. Fast Fourier Transforms are used to compute gradients of the potential that provide the shear tensor at each plane. The outcome of the simulation is a map of the shear and convergence on square patches of side length $1 - 5°$. Several realizations for each model are needed to compute reliable statistics on scales ranging from $1'$ to $1°$. Figure 1 shows the shear map from two cold dark matter models with shape paratemeter $\Gamma = 0.2$, one with $\Omega_m = 1$ (upper panel) and the other with $\Omega_m = 0.3$ (lower panel).

Numerical resolution on small scales is limited primarily by (i) the force softening used in the N-body simulations, and, (ii) by the finite size of the grid used to compute FFT's and to propagate the light rays. We have chosen grid spacings in order to avail of the full resolution provided by the N-body simulations. The simulations used, adaptive P^3M simulations with 256^3 particles, were carried out using codes kindly made available by the Virgo consortium (e.g. Jenkins et al. 1997) and have previously been analyzed in the strong lensing regime by Bartelmann et al. (1998). These, coupled with ray tracing on a 2048^2 grid, provide us with small scale resolution down to $\lesssim 0.5'$, well into the nonlinear regime for weak lensing. On large scales the finite number of transverse modes of the density field at any redshift leads to fluctuations that must be averaged using several realizations of the ray tracing as well as the N-body simulation for a given model. We have used an ensemble of PM simulations to get reliable statistics on large scales.

In the weak lensing regime, the magnification and induced ellipticity are given by linear combinations of the Jacobian matrix of the mapping from the source to the image plane. The Jacobian matrix is defined by

$$\Phi_{ij} \equiv \frac{\partial \delta\theta_i}{\partial \theta_j} \tag{1}$$

where $\delta\theta_i$ is the $i-$th component of the perturbation due to lensing of the angular position on the source plane, and θ_j is the $j-$th component of the position on the image plane. The convergence is defined as $\kappa = -(\Phi_{11}+\Phi_{22})/2$, while the two components of the shear are $\gamma_1 = -(\Phi_{11}-\Phi_{22})/2$ and $\gamma_2 = -\Phi_{12}$. The convergence κ can be reconstructed from the measured shear γ_1, γ_2, up to a constant which depends on the mean density in the survey area. If the survey is sufficiently large and there is little power on scales larger than the survey, this error can be neglected.

3 Results of Simulations

There are strong features due to the nonlinear clustering of the dark matter as shown in Figure 1. Collapsed halos produce tangential patterns of shear around them, while quasilinear filamentary structures are also visible. The two cosmological models show qualitative differences in the

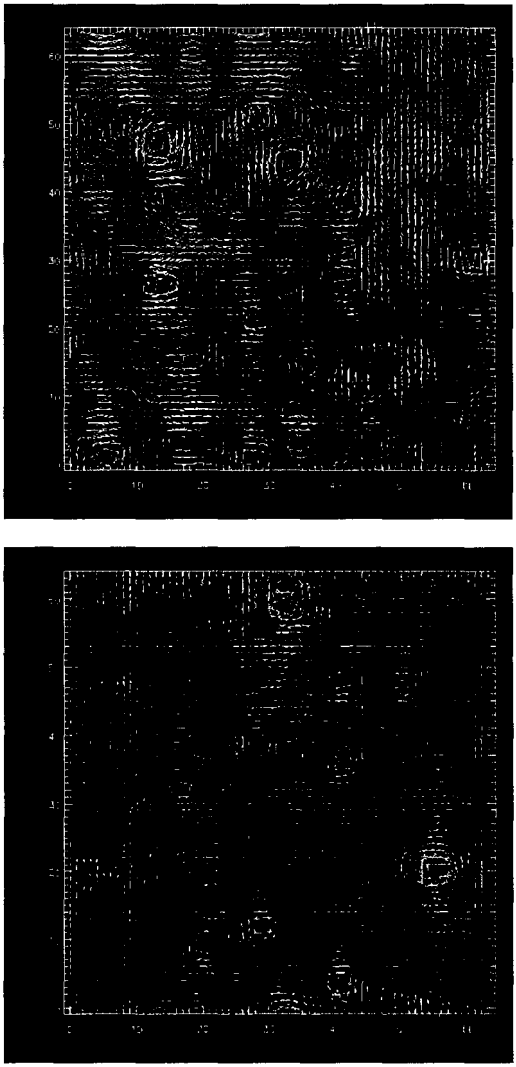

Figure 1: The shear pattern on a 1° field for an Einstein-de Sitter model (upper panel) and an open model (lower panel) with $\Omega_m = 0.3$. The rms shear in these fields is about 2%. The open model produces a shear pattern dominated mostly by halos of clusters or groups. The Einstein-de Sitter model has a lower normalization ($\sigma_8 = 0.6$) compared to the open model ($\sigma_8 = 0.85$) and evolves more rapidly with redshift – this leads to a smaller fraction of the mass being part of massive collapsed halos. The qualitative differences between the models are reflected in the statistical measures shown in the following figures.

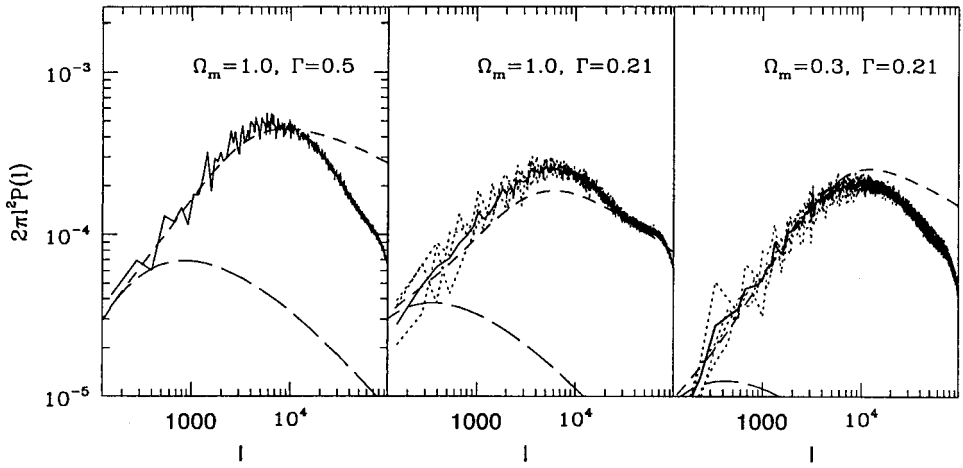

Figure 2: The dimensionless power spectrum of κ and γ. For the cosmological model indicated by Ω_m and Γ in the panel, the power spectrum from ray tracing is compared with the linear (long-dashed) and nonlinear analytical (short-dashed) predictions. The dotted curves in two of the panels show measurements from individual realizations while the solid curves are the mean spectra. The angular wavenumber l is given in inverse radians - the smallest l plotted corresponds to modes with wavelength of order $L \simeq 2.5°$, where L is the side-length of the field. Note that the decline in the N-body power spectrum at $l > 10^4$ is because of the limited resolution.

shear pattern, with the open model being far more dominated by halos and lacking irregular or filamentary structures. Figure 2 shows the power spectrum of the convergence (essentially identical to that of the shear) for 3 cosmological models. The amplitude of the convergence is enhanced by a factor of several compared to linear theory on small scales, as seen from the difference between the measured spectrum and the one predicted from linear theory. For a square field 2.5° on a side essentially all the modes have become nonlinear. The analytical nonlinear spectrum (from Jain and Seljak 1997) agrees adequately (to about 20%) with the measured one over more than 2 orders of magnitude. On the smallest scales, the measured spectrum is suppressed due to resolution effects. For the middle panel there are differences with the analytic prediction caused by too small a simulation box ($85h^{-1}$Mpc). We ran several PM simulations and found that for models with a lot of large scale power simulation boxes of size $200h^{-1}$Mpc are needed for an adequate treatment of the large scale modes. The results from these simulations agree well with the analytic predictions.

Figure 3 shows the skewness and kurtosis of the convergence. The skewness on scales $\lesssim 10'$ is larger than the perturbation theory predictions shown by the dashed lines. The ratio of the skewness for the open and $\Omega_m = 1$ models shows that it is a sensitive probe of matter density Ω_m (Bernardeau et al. 1997), but for a proper calibration one has to resort to N-body simulations. The kurtosis shows the same trend of increasing with decreasing Ω_m. However the skewness and kurtosis are sensitive to the sampling variance and therefore require a large survey area for a robust measurement.

We also investigate the one-point pdf of the convergence and shear to assess its sensitivity to different model parameters. One example is shown in Figure 4, where the pdf of κ is compared with that of the 3-dimensional overdensity $\delta = (\rho - \bar{\rho})/\bar{\rho}$. The comparison illustrates a key difference: whereas the pdf of δ is fully determined by the smoothed variance (for a given shape of the power spectrum), that of κ is sensitive to Ω_m as well. The sensitiviy of the pdf and higher moments to Ω_m arises because the relative deflection of photons is determined by the projected

matter density, not the relative overdensity. Particularly robust is the difference between the mean convergence, tracing the mean projected density, and the smallest negative convergence, tracing empty regions of the universe. In this case empty voids in an open universe produce a smaller de-magnification relative to the mean than in an $\Omega_m = 1$ universe. This shows up as a less negative cut-off in the pdf in Figure 4 and, unlike the moments of pdf, is independent of the amplitude and shape of the power spectrum on sufficiently small scales. This difference at large negative κ as well as differences in the positive tail account for the sensitivity of the pdf to Ω_m. A detailed analysis of the pdf in the presence of noise will be given in a future publication.

4 Power Spectrum Estimation

The first measure we want to extract from the observed data is the power spectrum in the presence of noise. On large scales (above one degree) the data are gaussian distributed and there is a well defined strategy to measure the power spectrum, which at the same time also provides the sampling and noise error estimate (Seljak 1997). On small scales the optimal weighting of the data is less critical, but one needs to use the N-body simulations to measure the sampling variance and mode-mode correlations.

On almost all the scales from a few arcminutes to several degrees the signal to noise in the power spectrum is much larger than unity for a survey of degree size and flux limit of I=25-26 (Jain & Seljak 1997). This suggests sparse sampling (Kaiser 1997), where the survey area is not fully covered, so that for a given amount of observing time the area can be increased (thereby reducing the sampling variance), while the density of galaxies is decreased (increasing the noise variance). If there was only noise then one could devise an optimal sampling strategy by equating the noise and sampling variance terms in the error matrix for the power spectrum. In practice however there is an additional noise term arising from the small scale modes that are not well measured. This aliasing term (see Seljak 1997 for its explicit form) is really a signal, but if those modes are not sufficiently well sampled, then they cannot be reconstructed and therefore act as noise. This additional power has to be added to the usual noise. If the sampling is sufficiently sparse, then this term dominates over the usual noise. Since its amplitude depends on the amount of small scale power one has to measure it first before subtracting its contribution.

This leads to the following adaptive sparse sampling strategy: first one measures the power on small scales using a filled survey. Once this power is measured to sufficient accuracy one can start to sparsely sample the sky, moving from smaller to larger and larger scales. At each step one minimizes the variance, which amounts to equating the sampling variance to the noise+aliasing variance, the later being estimated using the measured power on smaller scales. If the amount of small scale power is small one can afford very spase sampling, otherwise only modest sparse sampling can be used. In either case the formalism allows for an optimal sampling strategy which is adaptive in the sense that if the slope of the power spectrum changes as a function of scale so does the sampling fraction.

A $10^\circ \times 10^\circ$ field which is sparsely sampled gives a 2-d power spectrum shown in figure 5a. Usually one is more interested in a 3-d power spectrum and would therefore like to invert the 2-d to a 3-d spectrum. In general the 2-d power spectrum at some l mode receives contributions from a wide range of 3-d k modes, with the window peaking at $l \sim kr$, where r is half the distance between the observer and the source galaxies. Conversely each 3-d spectral bin estimate will receive contributions from a range of 2-d spectral bins, appropriately weighted with the window so that 2-d bins close to the peak of the window have a larger weight than those far in the tails. In addition, one must also appropriately weight the 2-d estimators themselves using the corresponding covariance matrix. If a given 2-d bin has large sampling or noise variance then it should be downweighted appropriately. The complete formalism is presented in Seljak (1997). Figure 5b shows for the $10^\circ \times 10^\circ$ sparsely sampled field the 3-d reconstructed power spectrum.

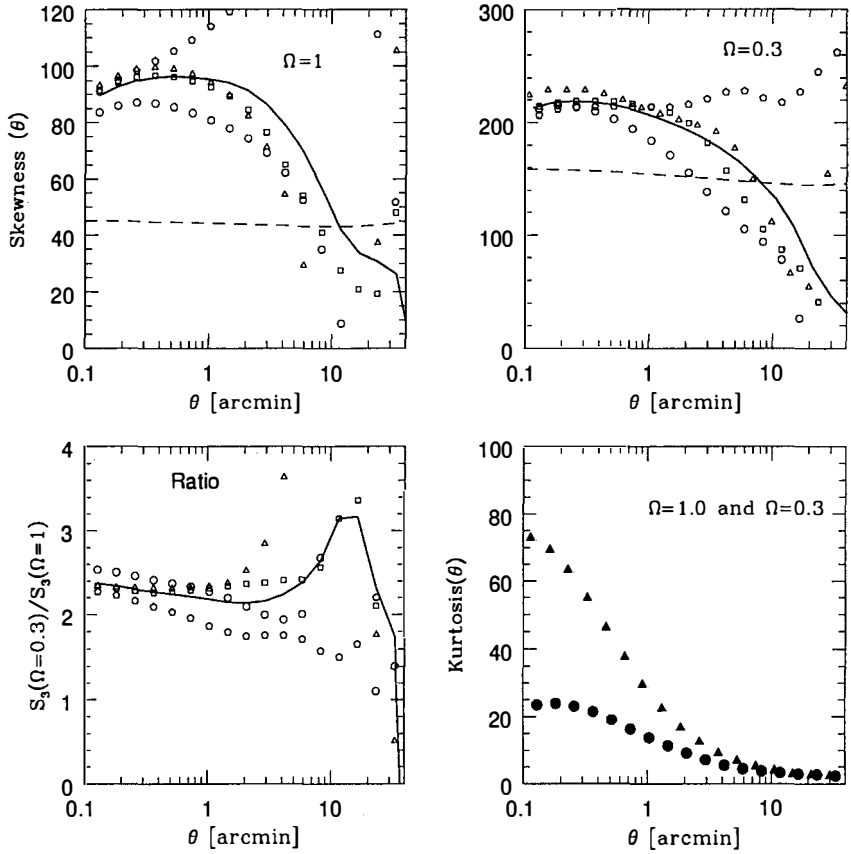

Figure 3: The skewness $S_3(\theta)$ of κ versus θ for low and high Ω_m models. The symbols in the upper panels show the skewness measured from four different realizations of the ray tracing. The solid line is the average over these realizations, while the dashed line is the prediction from perturbation theory. The lower left panel shows the ratio of the skewness for $\Omega_m = 0.3$ and $\Omega_m = 1$, again for the different realizations and their average. The lower right panel shows the kurtosis of κ for the $\Omega_m = 0.3$ model (triangles) and the $\Omega_m = 1$ model (circles).

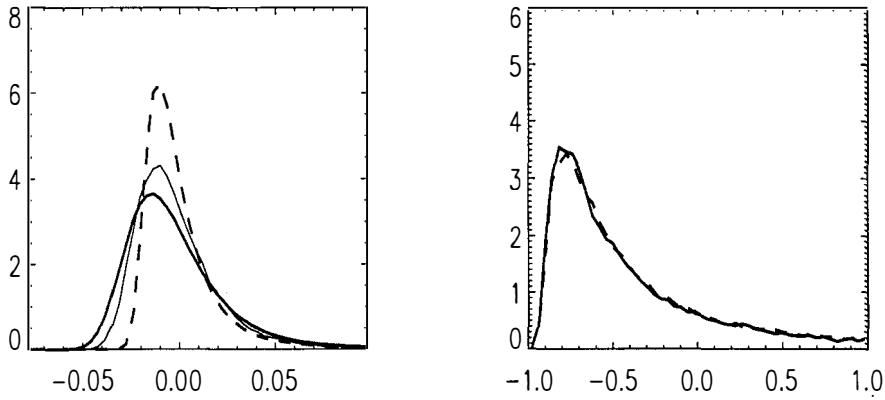

Figure 4: The probability distribution function (pdf) of κ and of δ, the 3-dimensional over-density. The left panel show the pdf of κ for the open (dashed) model and the Einstein-de Sitter (solid) model. The thick solid curve uses the same smoothing scale as the dashed curve, 0.4′. The thin solid curve is for a smoothing scale of 1.6′ which has the same rms as the dashed curve. The right panel shows the pdf of the 3-dimensional density for the same two models, smoothed on a scale of 2.7 h^{-1} Mpc. The rms for the two models is nearly the same. A comparison of the two panels shows that the rms completely dictates the pdf for δ (for the same shape of the power spectrum), while the pdf of κ differs with Ω_m even if the rms is the same.

The reconstructed 3-d bins are strongly correlated because of the window. This explains why the variance on individual estimators is smaller than in the 2-d case – the estimators were essentially averaged over a wider range in k. This causes no problems if the power spectrum is smooth; however, fine details such as bumps and peaks cannot be accurately resolved with weak lensing data because of the smoothing. Note that we have assumed gaussian sampling variance, which becomes invalid on small scales ($k > 0.5hMpc^{-1}$) and will increase the errors in that regime.

Acknowledgments

The high resolution simulations in this paper were carried out using codes made available by the Virgo consortium. We thank Joerg Colberg for help in accessing this data and Ed Bertschinger for making available his PM N-body code. We are grateful to Matthias Bartelmann, Ue-Li Pen, Peter Schneider and Alex Szalay for useful discussions.

References

1. Bartelmann, M. et al. 1998, A&A, 330, 1
2. Bernardeau, F., van Waerbeke, L., & Mellier, Y. 1997, A&A, 322, 1
3. Blandford, R. D., Saust, A. B., Brainerd, T. G., & Villumsen, J. V. 1991, MNRAS, 251, 600
4. Gunn, J. E. 1967, ApJ, 147, 61
5. Jain, B., & Seljak, U., 1997, ApJ, 484, 560
6. Jenkins, A. et al. (The Virgo Consortium) 1997, astro-ph/9709010

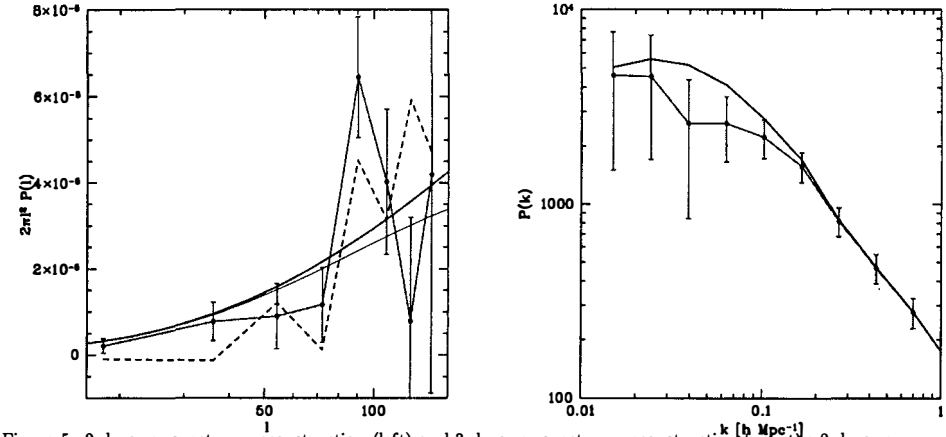

Figure 5: 2-d power spectrum reconstruction (left) and 3-d power spectrum reconstruction from the 2-d power spectrum (right). Both are for simulated 100 square degree sparsely (1 in 4) sampled data with a density of 2×10^5 galaxies per square degree. The thick and thin solid lines on the left are for the nonlinear and linear power spectrum, respectively, while the dashed line is the power spectrum with 45° rotation. The latter should vanish in a perfect survey if weak lensing signal is generated by gravity. If the sampling is sparse aliasing mixes power into this combination. The amount of aliasing can be estimated once the true power is measured, in which case on can verify the assumption of weak lensing signal generated by gravity. On the right the solid line is the nonlinear 3-d power spectrum. A survey of this size can reconstruct the power spectrum up to the turnover scale.

7. Kaiser, N. 1992, ApJ, 388, 272
8. Kaiser, N. 1998, ApJ, in press, astro-ph/9610120
9. Miralda-Escude, J. 1991, ApJ, 380, 1
10. Schneider, P. et al. 1997, astro-ph/9708143
11. Seljak, U. 1997, astro-ph/9711124

WEAK GRAVITATIONAL LENSING AND FOREGROUND-BACKGROUND CORRELATIONS

J. L. SANZ, N. BENITEZ, E. MARTINEZ-GONZALEZ
IFCA, Facultad de Ciencias, Av. de los Castros s.n., 39005-Santander, Spain

We study, in the framework of weak gravitational lensing, the correlations between the amplification or polarization of background and foreground sources. For the crosscorrelation of the background magnification and foreground matter distribution the maximum is at zero lag and the amplitude remains above a few percent for scales below 1′ whereas the crosscorrelation of the background polarization and foreground matter distribution presents a maximum of the order of 1% at a non null-angle in the range $\simeq 0.4' - 1'$. We apply these results to estimate the quasar-galaxy correlation function ω_{qg} due to weak lensing

1 The lensing vector

We will consider the propagation of photons from a source at redshift z_e to the observer ($z = 0$), the universe being a perturbed Friedmann model with vanishing pressure. For scalar perturbations, the metric in the conformal Newtonian gauge is given in terms of the scale factor $a(\tau)$ and a single potential $\phi(\tau, \vec{x})$, that satisfies the Poisson equation, as follows (Martí nez-González et al. 1997)

$$ds^2 = a^2(\tau)[-(1+2\phi)d\tau^2 + (1-2\phi)\gamma^{-2}\delta_{ij}dx^i dx^j], \tag{1}$$

$\gamma = 1 + \frac{k}{4}\vec{x}^2$, we take units such that $c = 8\pi G = a_o = 2H_o^{-1} = 1$ and $k/(4 \mid 1 - \Omega \mid) = 0, -1, +1$ denote the flat, open and closed Friedmann universe.
Assuming a perturbation scheme ("weak lensing"), the null geodesic equation for the previous metric can be integrated in the form $\vec{x} = \lambda\vec{n} + \vec{\epsilon}$, where $\vec{n}$ is the direction of observation and λ is the distance to the photon in the background metric. The perturbation $\vec{\epsilon}$ can be decomposed in a term parallel to the direction of observation $\vec{n}$ and a term, $\vec{\alpha}_\perp$, ortoghonal to such a direction. The last term is given by

$$\vec{\alpha}_\perp = 2\int_0^\lambda d\lambda' W(\lambda, \lambda')\vec{\nabla}_\perp\phi(\lambda', \vec{x} = \lambda'\vec{n}) \tag{2}$$

where $W(\lambda, \lambda')$ is a window function

$$a(\lambda) = \frac{(1-\lambda)^2}{1 + k\lambda^2/4}, \quad W(\lambda, \lambda') = (\lambda - \lambda')\frac{1 + k\lambda\lambda'/4}{1 + k\lambda'^2/4}. \tag{3}$$

For photons that are propagated from a source at redshift z (distance λ) to the observer($z_o = 0$ or $\lambda_o = 0$), the lensing vector $\vec{\beta}$ is defined in the usual way: $\vec{\beta} \equiv \vec{n} - (\vec{x} - \vec{x}_o)|\vec{x} - \vec{x_o}|^{-1}$. Thus we find: $\vec{\beta} = \lambda^{-1}\vec{\alpha}_\perp(\lambda)$.

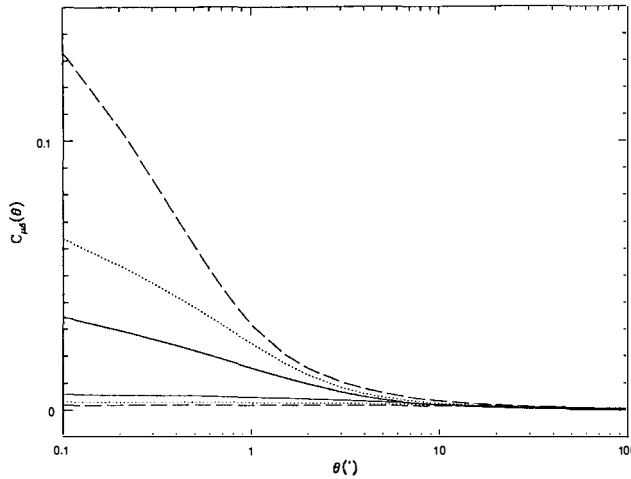

Figure 1: $C_{\mu\delta}(\theta)$ for a foreground population peaked at $z_f = 0.2$ and a background one at $z_b = 1$ and for three values of Ω: 1 (solid), 0.3 (dotted) and 0.1 (dashed). The three bottom lines represent the linear contribution for the same Ω values.

2 Correlations between background and foreground sources

Let us assume a population of background sources (e.g. quasars or galaxies), placed at different distances λ with a distribution $R_b(\lambda)$ ($\int_0^1 d\lambda R_b(\lambda) = 1$). Then, we can define the integrated lensing vector $\vec{\beta}(\vec{n}) = \int_0^1 d\lambda R_b(\lambda)\vec{\beta}(\lambda, \vec{n})$ and taking into account equations (2,3) we obtain: $\vec{\beta}(\vec{n}) = \vec{D}S, D^i \equiv (\delta^{ij} - n^i n^j)\frac{\partial}{\partial n^j}$, where

$$S(\vec{n}) \equiv 2\int_0^1 d\lambda T_b(\lambda)\phi(\lambda, \vec{x} = \lambda\vec{n}), \quad T_b(\lambda) \equiv \frac{1}{\lambda}\int_\lambda^1 d\lambda' \frac{1}{\lambda'} R_b(\lambda') W(\lambda', \lambda). \tag{4}$$

If we take the derivative along the plane orthogonal to the direction of observation $\vec{n}$, we get the convergence tensor $\theta_{ij} \equiv D_j\beta_i = D_j D_i S$ which can be decomposed in the form ($h_{ij} \equiv \delta_{ij} - n_i n_j$)

$$\theta_{ij} = \kappa h_{ij} + p_{ij}, \quad \kappa(\vec{n}) = \frac{1}{2}h^{ij}\theta_{ij}, \quad p_{ij}(\vec{n}) = \theta_{ij} - \kappa h_{ij} \tag{5}$$

For weak lensing, the convergence scalar $\kappa(\vec{n})$ is related to the magnification by $\mu(\vec{n}) = 1 + 2\kappa(\vec{n})$. Moreover, the polarization components in the plane orthogonal to $\vec{n}$ can be defined in the standard way $p_1 \equiv p_{11} - p_{22}, p_2 \equiv 2p_{12}$ and the complex polarization is $p \equiv p_1 + ip_2$. So, we can define the scalar polarization $p^2 \equiv pp* = 2p_{ij}p^{ij}$.

Let us consider a second population of foreground sources (e.g. galaxies) placed at different distances λ with a distribution $R_f(\lambda)$ ($\int_0^1 d\lambda R_f(\lambda) = 1$). If $\delta(\lambda, \vec{x})$ represents the density fluctuation (that satisfies the Poisson equation $(\nabla^2 + 3k)\phi = \frac{1}{2}\rho_b a^2 \delta$), we shall assume that there is a constant bias factor b relating the number fluctuation, $\frac{\delta N}{N}$, and such an overdensity. Then, we can define the integrated overdensity $\delta(\vec{n}) = \int_0^1 d\lambda R_f(\lambda)\delta(\lambda, \vec{n})$.

We get the following crosscorrelations (Sanz et al. 1997)

$$C_{\mu\delta}(\theta) \equiv 2\langle\kappa(\vec{n})\delta(\vec{n}')\rangle = A_0, \quad C_{p\delta}(\theta) \equiv \langle p(\vec{n})\delta(\vec{n}')\rangle = A_2, \tag{6}$$

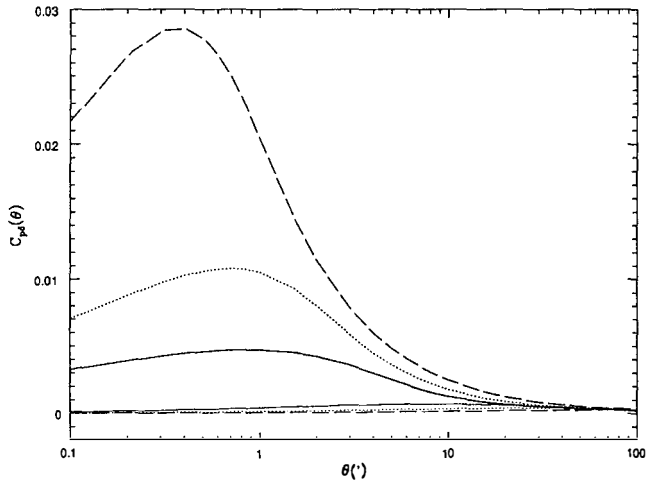

Figure 2: $C_{p\delta}(\theta)$ for a foreground population peaked at $z_f = 0.3$ and a background one at $z_b = 1$ and for three values of Ω: 1 (solid), 0.3 (dotted) and 0.1 (dashed). The three bottom lines represent the linear contribution for the same Ω values.

$$A_i \equiv \frac{6\Omega}{\pi} \int_0^1 d\lambda T_b(\lambda) R_f(\lambda) (\frac{\lambda}{1-\lambda})^2 \int_0^\infty dk k P(\lambda, k) J_i(ks\theta) \tag{7}$$

where J_i is the Bessel function of 1st kind. The power spectrum $P(\lambda, k)$ is defined by: $\langle \delta_{\vec{k}}(a) \delta^*_{\vec{k}'}(a) \rangle \equiv P(a,k)\delta^3(\vec{k} - \vec{k}')$. For such a calculation see Martí nez-Gónzalez et al.(1997).

We assume a CDM model with a primordial Harrison-Zeldovich spectrum, a Hubble parameter $h = 0.5$ and flat and open universe models. We use the normalization $\sigma_8 = 0.6, 1, 1.4$ for universes with $\Omega = 1, 0.3, 0.1$ following Viana and Liddle (1996), this is based on cluster abundances. For the nonlinear evolution of the power spectrum we use the recently improved fitting formula given by Peacock and Dodds (1996).

For the redshift distributions of the background and foreground sources we consider a Dirac delta distribution peaked at λ_b and λ_f respectively. The crosscorrelation $C_{\mu\delta}(\theta)$ for a population of background sources peaked at $z_b = 1$ and another of foreground lenses at $z_f = 0.2$ (Fig 1) has a maximum at zero lag and rapidly decreases for scales above a few arcmin. The amplitude is always above a few percent for scales $\leq 1'$ and at these scales the linear contribution is negligible compared to the nonlinear one for all the Ω values. We also remark that $C_{\mu\delta}$ increases when Ω decreases whereas considering only the linear contribution the situation is reversed.

The crosscorrelation between the polarization of a background source population peaked at $z_b = 1$ and the matter density fluctuations peaked at $z_f = 0.3$, $C_{p\delta}(\theta)$, has a maximum value in the angular range $0.4' - 1'$ and this scale is smaller for low Ω models (Fig 2). As in the case of $C_{\mu\delta}$, the linear contribution is negligible; however, it peaks at a much larger angle of $\sim 10'$ as a consequence of the much larger scales which contribute to the linear level. Including the nonlinear evolution, a correlation of $\sim 1\%$ can be expected at angular scales $\leq 1'$ for realistic models of structure formation.

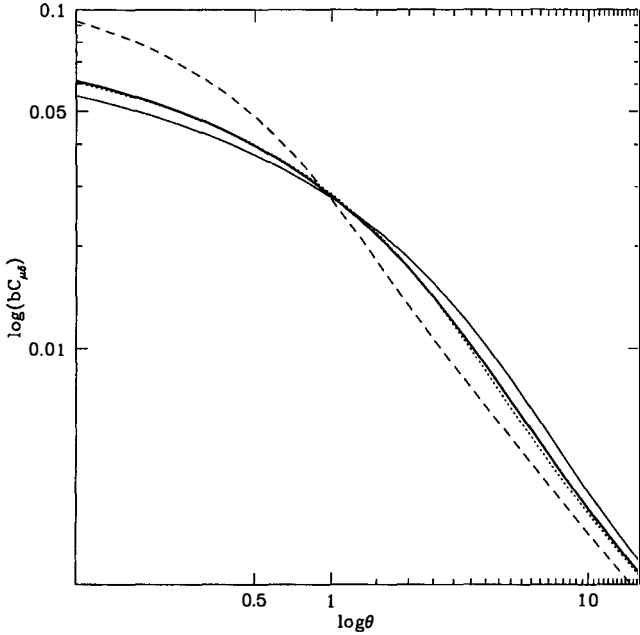

Figure 3: The product $bC_{\mu\delta}$ for galaxy and quasar populations at respectively $z_g = 0.15, z_q = 1.4$ for several values of Ω (Ω, 1 (dotted line), 0.3 (dashed line) and 0.1 (thin solid line). The thick solid line is the "average" $bC_{\mu\delta}$. The dependence of b and $C_{\mu\delta}$ with Ω cancel and $bC_{\mu\delta}$ depends very weakly on Ω.

3 The quasar-galaxy correlation function

One the most obvious applications of the theory outlined above is to calculate the expected correlation ω_{qg} between high-redshift quasars and foreground galaxies. This correlation is given in the weak lensing regime by (Bartelmann 1995)

$$\omega_{qg}(\theta) = b(\alpha_e - 1)C_{\mu\delta} \tag{8}$$

The results of $C_{\mu\delta}$ from the previous section has been normalized to the cluster abundance $\sigma_8 = 0.6\Omega^{-0.34+0.28\Omega-0.13\Omega^2}$. For consistency we normalize the biasing factor as $b = \sigma_8^{-1}$.

The variation of b and of the amplitude of $C_{\mu\delta}$ with Ω somehow cancel and unlike $C_{\mu\delta}$, the product $bC_{\mu\delta}$ depends very weakly on Ω, as it is shown in Fig 3, where we plot $bC_{\mu\delta}$ calculated using delta-functions for the galaxy and quasar distributions with $z_g = 0.15, z_q = 1.4$. These values are representative of typical quasar and galaxy samples. We see that there are two different regimes for ω_{qg}, one at small scales $\theta \leq 1'$ and the other at larger scales, $\theta > 2'$.

The dependence of ω_{qg} on Ω at small scales can be approximated as

$$\omega_{qg} \approx A_s \log\theta + B_s$$

This fit is valid for $0.1' < \theta < 1'$. $A_s = -0.029\Omega^{0.37\log\Omega}$ and B_s (which is equal to the value of ω_{qg} at $1'$) is practically constant, $B_s = 0.029 \pm 0.02$. We see that A_s quickly drops as Ω grows,

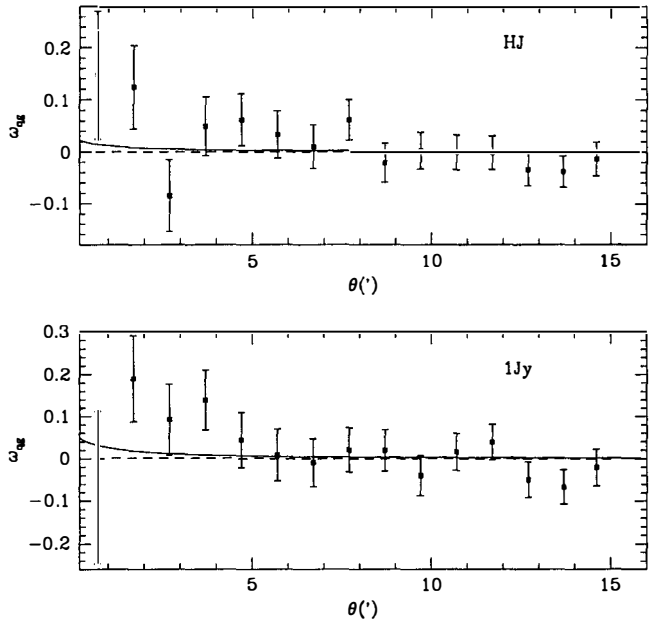

Figure 4: The observed ω_{qg} (square dots) for the 0.5Jy and 1Jy samples (Benítez et al. 1998). The solid line is the theoretical estimation of ω_{qg} as calculated in the text using a value of $\Omega = 0.4$, corresponding to the "average" $bC_{\mu\delta}$ of Fig 3.

although the amplitude of the variation is small, $A_s = 2.34$ at $\Omega = 0.1$ and $A_s = 1$ for a flat universe.

The value of $(\alpha - 1)$ is ≈ 1.5 for optically selected bright quasars, and ≈ 1 for a radio-loud sample as the 1Jy (Benítez et al. 1998). Thus, the expected correlation amplitude at small scales is just a few percents, several times below the observed value of ω_{qg} (Fig 4). In Benítez et al. 1998 we show that this discrepancy can be solved if we take into account the scale dependence of the biasing factor b.

References

1. Bartelman, M. A&A **298**, 661 (1995).
2. Benítez, N., Martínez-González, Sanz, J.L. 1998, in preparation.
3. Dolag, K. & Bartelmann, M., A&A **298**, 661 (1995).
4. Martínez-González, E., Sanz, J.L. and Cayón, L. ApJ **484**, 1 (1997).
5. Peacock, J.A. & Dodds, S.J.MNRAS **280**, L19 (1996)
6. Sanz, J.L., Martínez-González, E. and Benítez, N. MNRAS **291**, 418 (1997)
7. Viana, P.T.P. & LiddleA.R. MNRAS, 281 (323)1996

Cluster Mass Profile from Combined Strong and Weak Lensing

Hanadi M. AbdelSalam, Prasenjit Saha
Astrophysics, Department of Physics, Keble Road, Oxford OX1 3RH, UK

Liliya L. R. Williams
Institute of Astronomy, Madingley Road, Cambridge CB3 0HA, UK

We present a new non-parametric method for reconstructing the two dimensional mass maps of galaxy clusters from their lensing effects on background galaxies. The method combines constraints from the strong and weak lensing regimes in a linear fashion and breaks the "mass-sheet degeneracy" that has long plagued the weak lensing techniques. The feasibility of the method is demonstrated by applying it to the spectacular lensing cluster Abell 2218.

1 Introduction

Gravitational lensing provides a unique way to determine the mass distribution of galaxy clusters. It does not rely on any assumption about the dynamical state and the nature of the matter in clusters. There are two distinct methods for reconstructing cluster mass distribution from their gravitational lensing effect. The first method works only on the strong lensing regime (giant arcs and multiple images) and it requires fitting simple parametrized profiles to individual cluster-sized galaxies [5]. The second method is non-parametric and uses the statistical distortion or shear field of the cluster to trace its mass distribution [4]. Both methods suffer some sort of non-uniqueness problem. However, the method we are to describe is non-parametric and uses constraints from both multiply imaged systems and single arclets and naturally overcomes the systematic effects of the aforementioned traditional methods.

2 Outline of the Method

The method is based on a pixellated mass distribution for the cluster lens [1]. For example, the ij-th pixel is a square tile with a surface mass density κ_{ij} in units of the critical density $\Sigma_{crit} = \frac{c^2}{4\pi G} D_d$. For a source at an unlensed position β, the appropriately scaled time-delay in the direction θ is

$$\tau(\theta) = \frac{1}{2}(\theta - \beta)^2 - \frac{D_{ds}}{D_s} \sum_{ij} \kappa_{ij} \psi_{ij}(\theta), \tag{1}$$

where

$$\psi_{ij}(\theta) = \frac{1}{\pi} \int_{ij} \ln |\theta - \theta'| d^2\theta' \tag{2}$$

is the coefficient of the deflection potential at θ due to the ij-th pixel only. Thus the contribution of the ij-th pixel to the lens potential is $\kappa_{ij}\psi_{ij}$.
Lensing observations in galaxy cluster provide us with the following information:

- Positions of multiple images on the sky, i.e $\nabla\tau(\theta) = 0$.
- Orientations and elongation of singly-imaged arclets, for example magnification in direction θ'_x is at least k times that along perpendicular direction θ'_y, then

$$k\left|\frac{\partial^2}{\partial\theta'^2_{x'}}\tau(\theta)\right| \leq \left|\frac{\partial^2}{\partial\theta'^2_{y'}}\tau(\theta)\right|. \tag{3}$$

Both observations provide us with linear constraint equations on the unknowns β and κ_{ij}. Mass maps are then reconstructed by use of quadratic programming to minimize M/L variations while satisfying the lensing constraints exactly. So we minimize

$$\sum_{ij}\left[\kappa_{ij} - L_{ij}\sum_{i'j'}\kappa_{i'j'}\right]^2 + \epsilon^4\sum_{ij}(\nabla^2\kappa_{ij})^2, \tag{4}$$

where L_{ij} is the light distribution of the cluster and ϵ is a smoothing parameter. Errors in the mass distribution are estimated using Monte-Carlo simulations over the light distribution.

3 Breaking the mass-sheet-degeneracy

According to equation (1) the lens equation reads

$$\beta = \theta - \frac{D_{ds}}{D_s}\sum_{ij}\kappa_{ij}\nabla\psi_{ij}(\theta). \tag{5}$$

The invariant transformation

$$\sum_{ij}\kappa_{ij}\nabla\psi_{ij}(\theta) \rightarrow \frac{D_s}{D_{ds}}(1-a)\theta + a\sum_{ij}\kappa_{ij}\nabla\psi_{ij}(\theta), \qquad \beta \rightarrow a\beta \tag{6}$$

where a is a constant, physically amount to rescaling the surface mass density and adding a sheet of constant mass. The transformation (6) leaves the observed image properties encoded in equation (5) unchanged. This invariance or the "mass-sheet degeneracy" can be easily broken by having at least two different source redshifts at the same time.

4 Mass Profile of Abell 2218

The results from applying the method to the inner regions of Abell 2218 enclosed by the frame of the WFPC2/HST image is shown in Figure 1. Our mass map revealed that the cluster is clearly bimodal with several detailed sub-structures that are not necessarily associated with light but are strongly required by the lensing data [see Fig. 1, left panel]. The error estimates are shown as contour plot of the fractional uncertainties in the mass distribution [see Fig. 1, right panel]. Zooming in to the region of the secondary peak shows that there is more mass in the direction of nearby fainter galaxies implying that there is a M/L discrepancy between cluster galaxies [see Fig. 1, left panel]. It is also found that the primary mass and light peaks are offset by about $10''(\simeq 33h_{50}^{-1}\mathrm{kpc})$ [see Fig. 1, right panel].
These M/L discrepancy and the offset are found to be strongly robust with pixel size, pixel shape [2] and light distribution [see AbdelSalam *et al.* 1998b for more details].

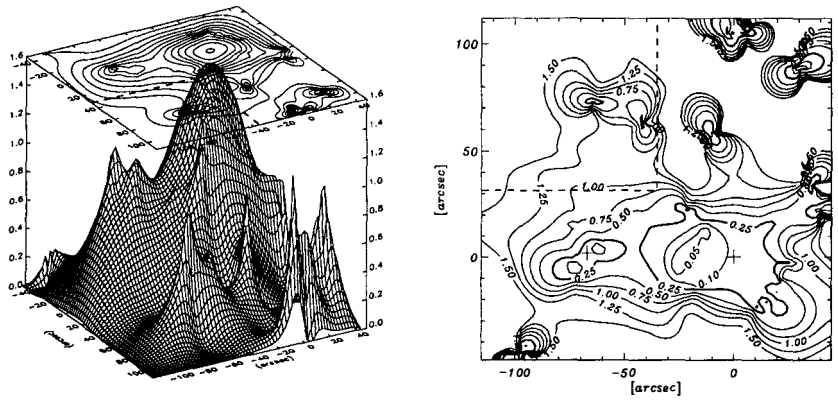

Figure 1: **Left:** Mass distribution of Abell 2218 in units of the critical density Σ_{crit}. The total mass enclosed by the HST image is $2.75 \times 10^{14} h_{50}^{-1} M_{\odot}$. **Right:** The Fractional uncertainties in the mass map, with the two cross signs marking the two light peaks in the cluster.

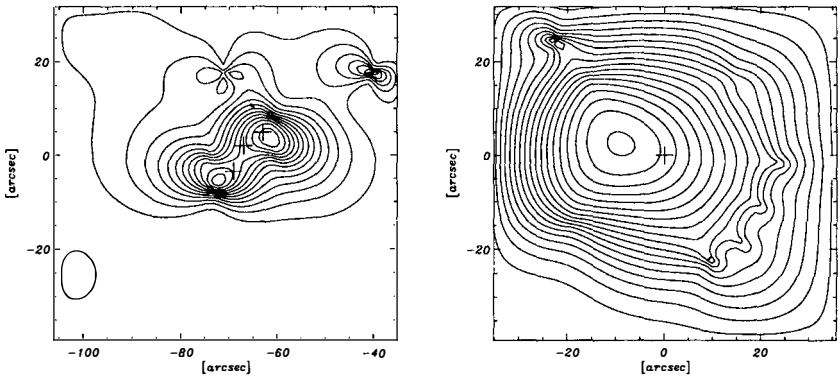

Figure 2: **Left:** Mass map using smaller pixels of the region of the secondary peak. The crosses mark the 3 optically visible galaxies. **Right:** Zooming in to region of the primary peak with the cross marking the centre of the dominant cD galaxy, and the mass map is seen to be offset from it by $10''$.

5 Lensing versus X-ray

On comparing our lensing mass estimates for A2218 with those from the X-ray mass models, we find that estimates from lensing are at least 2.5 times that from the X-ray model by Allen 1998[3][see Fig. 2].

This discrepancy confirms an earlier result by Miralda-Escudé & Babul 1995. They attributed the discrepancy to turbulent motion, projection effects and a multi-phased hot gas or the X-ray gas is not in thermal equilibrium. It is possible that this discrepancy provide a valuable hint about the dynamical state of A2218 and similar rich clusters that are still undergoing a merging phase.

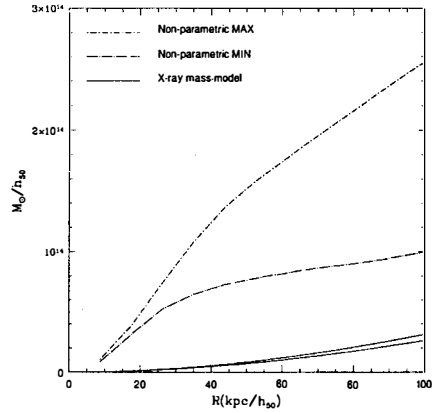

Figure 3: The range of the radial mass profile for A2218 allowed by lensing, and the mass profile from an X-ray model for the same cluster by Allen 1998.

6 Concluding Remarks

We have described a new elegant method for reconstructing the surface mass profile of a cluster from combined combined strong and weak lensing, and applies it to Abell 2218. The reconstructed mass map of A2218 revealed an unprecedented level of detail. In particular, the offset between the primary mass peak and the light peak and the M/L discrepancy between galaxy-sized components. We have also found that mass estimates from lensing are at least 2.5 times that from X-ray emitting gas models.

Acknowledgements

HMA would like to thank the organizers of the XXXIIIrd Recontres de Moriond: "Fundamental Parameters in Cosmology" for their kind hospitality.

References

1. AbdelSalam, H.M., Saha, P. and Williams, L.L.R., 1998a, *MNRAS*, **294**, 734
2. AbdelSalam, H.M., Saha, P. and Williams, L.L.R., 1998b, *in preparation*
3. Allen, S.W., 1998, *MNRAS, in press*, astro-ph/9710217
4. Kaiser, N. and Squires, G. 1993, *ApJ*, **404**, 441
5. Kneib, J.-P., Ellis, R., Smail, I., Couch, W.J., Sharples,R.M., 1996, *ApJ*, **471**, 643
6. Mirald-Escudé, J. and Babul, A., 1995, *ApJ*, **449**, 18

WEAK LENSING AROUND CLUSTERS TO CONSTRAIN Ω and Λ.

L. GAUTRET
DEMIRM, Observatoire de Paris,
61 Av. de l'Observatoire, 75014 Paris, France

In the weak lensing regime, a cluster induces elliptical distortion on background galaxies. This so-called shear depends on the cosmology (Ω, Λ) through the lensing factor $\omega = \frac{Dls}{Dos}$, lever arm of the lens regarding to the position of the distorded source. Making the most of the recent advances in determining galaxy redshifts from multicolor photometry, the method presented here to constrain the cosmological parameters is based on the construction of a purely geometrical operator $G(\Omega, \Lambda)$ directly from the data: the ellipticities of triplets of neighbouring background galaxies. The idea governing the structure of G is to get rid of the dependency on the mass profile of the cluster as well of any systematic coming from the intrinsic source ellipticities. Built as the average of 3-3 determinants on many triplets, G is linear regarding to every source of noise which therefore vanish in $1/\sqrt{N}$ if N is the total number of observed distorded galaxies. Simulations lead to the encouraging result that a very significant constraint on (Ω, Λ) can be reached : $\Lambda^{+0.05}_{-0.07}$ in the case $\Omega + \Lambda = 1$ or $\Omega^{+0.07}_{-0.07}$ in the case $\Lambda = 0$, at a 70 % confidence level, from the observations of about 500 clusters with the VLT instrument FORS (about 150 nights of observations). Therefore the main issue about the existence of the cosmoligical constant could be definitely settled with an even shorter program of observations (about 10 nights).

1 Introduction

Weak gravitational lensing effects are now well understood and detected: see for example Fort & Mellier [1]. With the very promising results of photometric redshifts determination (see Brunner *et al.* [3], Hogg *et al.* [4]), it becomes possible to introduce a new refinement in the weak lensing investigations: constraining the cosmological parameters. Indeed, contrary to usual simplifications used in weak lensing, in this paper, the value of (Ω, Λ) will not be arbitrarily fixed and, instead of mixing all the distorded background galaxies in a single mean source plan, every information concerning the redshift of the sources will be taken in account.

Section 2 recalls the main weak lensing equation and introduces the lens factor, the cosmology dependent part of the ellipticity of distorded background galaxies. In order to cancel the dependency on the potential of the lensing cluster (through its convergence κ and shear γ) , triplets of sources neighbouring in the image plan are considered to build an operator G equal to zero for the actual values of the cosmological parameters (Ω_o, Λ_o) (see section 3). From its linear construction, the biases on G behave as noises decreasing as the inverse square root of the number of distorded galaxies. Hence the power of the method depends on the number of clusters considered. In section 3 simulations are performed with an acceptable redshift distribution which takes in account a presence of high redshift galaxies. Reachable constraints on (Ω, Λ) are given for 500 clusters. The results are generalized for 20 clusters and discussed in section 4.

2 The method

2.1 The weak lensing equation

Let us first recall the main weak lensing equation giving the image ellipticity of a distorded galaxy (the observable ϵ) as a function of the intrinsic source ellipticity ϵ_S, the cluster potential (through κ and γ) and the lens factor $\omega = \frac{Dls}{Dos}$:

$$\epsilon_i = \epsilon_{S,i} + \frac{\omega_i^o \gamma}{1 - \omega_i^o \kappa}, \tag{1}$$

where the i lower index refers to a source at redshift z_i and the ^{o} upper index to the actual values of the cosmological parameters : Ω_o,Λ_o. We have used complex notations for the ellipticities as in Seitz & Schneider [4]. The second term of the right part of equation 1 thus contains the cosmological information.

2.2 Construction of G_{ijk}

The easiest way to build an operator depending on (Ω, Λ) and equal to zero in (Ω_o, Λ_o) whatever κ and γ are is to consider a triplet of neighbouring galaxies at redshifts z_i, z_j and z_k. So we construct G_{ijk} , taking the easy form of the determinant of a 3-3 matrix built with the observed ellipticities ϵ_i,ϵ_j and ϵ_k. G_{ijk} is the sum of two terms : a main term G_{ijk}^{main} actually equalling zero in (Ω_o, Λ_o) independently of the cluster mass and a bias :

$$G_{ijk}(\Omega,\Lambda) = \begin{vmatrix} 1 & \omega_i & \omega_i \epsilon_j \epsilon_k^* \\ 1 & \omega_j & \omega_j \epsilon_k \epsilon_i^* \\ 1 & \omega_k & \omega_k \epsilon_i \epsilon_j^* \end{vmatrix} \equiv \begin{vmatrix} 1 & \omega_i & \omega_i/\omega_i^o \\ 1 & \omega_j & \omega_j/\omega_j^o \\ 1 & \omega_k & \omega_k/\omega_k^o \end{vmatrix} \omega_i^o \omega_j^o \omega_k^o \, \gamma^2 + Bias. \tag{2}$$

There are three sources of biases. The first one is due to the intrinsic source ellipticity ϵ_S. the second one comes from the error in redshift of the photometric determination leading to the shifts on ω. Finally, even if the three galaxies of each triplet are close together (with a mean density of 50 galaxies $/'^2$ neighbours can be taken closer to 10") they have not exactly the same shear, leading to a third source of bias due to the shifts on γ.

What is important to see is that the signs of these biases are randomly distributed when considering many different triplets of galaxies. Averaging G_{ijk} on triplets will then make the biases vanish as a noise in $1/\sqrt{N}$, where N is the total number of sources (and not the total number of triplets since many triplets are redundant).

2.3 Construction of G

The last remark will be helpfull provided that the main cosmological G_{ijk}^{main} does not also behave randomly with the triplets (ijk). Fortunately this is the case when choosing only ordered triplets: $z_i < z_j < z_k$. Therefore $G(\Omega, \Lambda)$ is simply built by averaging G_{ijk} on as many ordered triplets as possible. G is then also the sum of two terms: a cosmological main term G^{main} and a noise which variance σ behaves with the variance σ_{Bias} of the bias as $\sigma = \sigma_{Bias}/\sqrt{N}$. The method can be finally summed up as the zero search of G.

$$G(\Omega_o, \Lambda_o) \equiv 0. \tag{3}$$

Since the behaviour of the noise is nearly gaussian (as the sum of many nearly gaussian biases), we can directly derive from G an (Ω, Λ) probability distribution :

$$p_{(\Omega,\Lambda)}(\Omega, \Lambda) \equiv exp(-G^2(\Omega, \Lambda)/2\sigma^2). \tag{4}$$

This last equality has just to be normalized on the considered domain of (Ω, Λ), for example $\Omega + \Lambda = 1$.

3 Simulations and results

In the simulations, we assumed that the redshift of each galaxy was perfectly known and we took the following redshift distribution $n(z)$ taking in account both the usual peak of galaxies near $z = 1$ (described by the redhift distribution $p(z)$ from Brainerd *et al.*[6]) and a second peak near $z = 3$:

$$n(z) = \alpha_1 p(z) + \alpha_2 p(z-2) \; with \; p(z) = \frac{\beta z^2}{\Gamma(\frac{3}{\beta}) z_0^3} e^{-(\frac{z}{z_0})^\beta} \times \{^{1 \; if \; z>0}_{0 \; if \; z<0}. \quad (5)$$

With $z_0 = 1/3$ and $\beta = 1$, the $p(z)$ and $p(z-2)$ distributions give respectively an average redshift equal to 1 and 3. With $\alpha_1 = 0.7$ and $\alpha_2 = 0.3$, the proportions of high and low redshift galaxies found by Fort & Mellier [2] is respected.

We introduced realistic uncertainties on the photometric redhift of galaxies taken as a Gaussian with a redshift dispersion equal to 0.02 for redshifts inferior to 0.8 and equal to 0.1 for redshifts greater than 0.8.

The intrinsic ellipticity distribution is chosen as follows :

$$p_{\epsilon_S}(\epsilon_S) = \frac{1}{\pi \sigma_{\epsilon_S}^2 (1 - e^{-1/\sigma_{\epsilon_S}^2})} e^{-(\frac{\epsilon_S}{\sigma_{\epsilon_S}})^2}, \quad (6)$$

with the intrinsic ellipticity dispersion $\sigma_{\epsilon_S} = 0.02$.

The κ profile of clusters has been taken decreasing as the inverse of the radius to the center and a 0.2 ellipticity has been introduced. No core radius was taken in account since its influence in the weak lensing area would have been slight and we recall that the principle of the method is to cancel any dependency on the mass map of the cluster.

The size of the observation window has been taken similar to what will give the VLT instrument FORS : $6' \times 6'$. To this window, a circle of 90" radius representing the arclets and strong lensing regimes is cancelled.

So, with an average of about 50 galaxies $/'^2$, each observation of a cluster contains about 1000 background galaxies. Now, the question that the simulations have to solve is : what is the accuracy we can reach on the cosmological parameters for a given number of observed clusters ?

Figure (1) gives the contours $p_{\Omega,\Lambda}$ for simulations concerning 500 clusters in two cases : first case, $\Omega_o = 0.3$ and $\Lambda_o = 0.7$; second case, $\Omega_o = 0.3$ and $\Lambda_o = 0$.

The results of these simulations are very promising. They prove that with about 500 clusters $\Lambda^{+0.05}_{-0.07}$ (in the case $\Omega + \Lambda = 1$) and $\Omega^{+0.07}_{-0.07}$ (in the case $\Lambda = 0$) can be reached with a 70% confidence level.

4 Conclusion and prospects

One could sum up the advantages and limitations of the above method by saying that though it is dependent on the oncoming advances of photometric redshift determination (photometry should be soon improved by the use of higher wavelength filters as J and K and with the calibrations enabled thanks to spectroscopy), it is a no-model dependent and purely geometrical method. It applies directly to the observed data: ellipticities of distorded galaxies and photometric redshifts.

By the very construction of G, the method will be all the more efficient (need less clusters) as the redshift distribution of galaxies is wide spread (indeed, if $z_i \approx z_j \approx z_k$ then the main cosmological G^{main} is nearly 0 and does not bring any cosmological information). Fortunately it seems to be the case as indicated by the work of Fort & Mellier [2], who found a 30 % presence of high redshift galaxies in deep blue surveys.

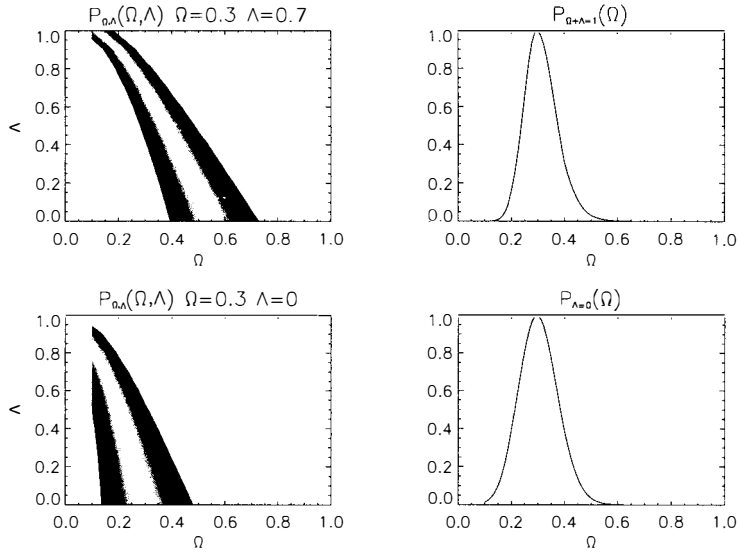

Figure 1: Simulation of the $p_{(\Omega,\Lambda)}$ distribution probability for 500 clusters data. The top panel considers the case $\Omega = 0.3$, $\Lambda = 0.7$ and the bottom one $\Omega = 0.3$, $\Lambda = 0$. On the left are given the $p_{(\Omega,\Lambda)}$ degeneracy contours in the (Ω, Λ) plan. On the right are given the variations of the (non normalized) probability distribution $p(\Omega)$ restricted to the domains $\Omega + \Lambda = 1$ (top) and $\Lambda = 0$ (bottom).

As the results of the simulations showed, 500 clusters, that is to say between 150 and 200 nights of observation with the VLT would lead to an accuracy on (Ω, Λ) (figure (1) shows the geometry of the degeneracy) of roughly 5%. Or, in a less ambitious but still very tempting perspective, with about 8 nights of observations we can reach $\Lambda^{+0.25}_{-0.35}$ in the case $\Omega + \Lambda = 1$ or $\Omega^{+0.35}_{-0.35}$ in the case $\Lambda = 0$. These constraints could definitely prove the existence of Λ.

Any way this method must not be seen individually. Its (Ω, Λ) degeneracy is perpendicular to the degeneracy of other methods like the (m, z) test on high redshift Supernovae. Therefore, with the joined constrains of many methods like these, Ω and Λ should be known with a good accuracy, nearly 10% in a short term.

References

1. Fort, B.,Mellier, Y. 1994, A&AR 5,239.
2. Fort, B., Mellier, Y., Dantel-Fort, M. 1996, astro-ph/9606039.
3. Brunner, R.J. et al. 1997, astro-ph/9703058.
4. Hogg, D.W. et al. 1998, astro-ph/9801133.
5. Seitz, C., Schneider, P., 1997,A&A, 318, 687.
6. Brainerd T.G., Blandford R.D., Smail I., 1996, ApJ, 466, 623.

ARCS STATISTICS AS A PROBE OF GALAXY EVOLUTION

J. BEZECOURT
Observatoire Midi-Pyrénées, 14 avenue E. Belin,
31400 Toulouse, France

Number counts and redshift distribution of gravitational arcs are computed in the field of massive clusters of galaxies to probe the universe at high redshift. Using an accurate modelling for the cluster mass distribution and a model for the spectrophotometric evolution of galaxies, the redshift distribution of gravitational arclets is computed in the field of cluster Abell 2218 and in the Hubble Deep Field where a cluster is artificially located. Counts are very well reproduced in the B band but an important population appears at high redshift which is not seen in deep spectroscopic surveys. Unfortunately, the very high sensitivity of the counts with respect to the model for galaxy evolution and to the mass distribution prevents from estimating the cosmological parameters with arcs statistics. Future works have to concentrate on high redshift clusters and take advantage of objects with smaller distortions.

1 Number counts and redshift distribution of gravitational arclets

A powerful way to investigate the population of high redshift galaxies is to use the magnification by the gravitational potentiel of massive clusters of galaxies. The spectrophotometric evolution of galaxies can then be probed by counts and redshift distribution of gravitational arcs.

The number counts of gravitational arclets in the field of a massive cluster of galaxies are a competition between, first, the magnification of the luminosity by the cluster potential that makes more objects visible and, second, the surface dilution that decreases the surface density of arclets by the same factor as for the magnification. If the surface density of galaxies up to magnitude m is $n(< m) = n_0 10^{\alpha m}$, the ratio of the density of arcs over the density of field galaxies is $\frac{n_{arc}(<m)}{n(<m)} = M^{2.5\alpha-1}$ where M is the magnification. For observations at faint level in the blue band, the counts remain roughly unchanged while from the R to K wavebands ($\alpha < 0.4$) a depletion takes place with respect to an empty field (Broadhurst 1995, Fort et al. 1996).

The number of arcs brighter than magnitude m with an axis ratio greater than q_{min} and a surface brigthness brighter than μ_0 within the field of a cluster of galaxies is:

$$N(m, q_{min}, \mu_0) = \sum_i \int_{z_l}^{z_{max}} \int_{q_{min}}^{\infty} S(q, z) \int_{L_{min}}^{L_{max}} \Phi_i(L, z)\, dL\, dq \frac{dV}{dz} dz$$

The sum is over the different morphological types i. z_l is the lens redshift and $z_{max}(\mu_0, i)$ is the redshift cutoff corresponding to the limit in central surface brightness μ_0. $S(q, z, H_0, \Omega)$ is the angular area in the source plane (at redshift z) that gives arcs with an axis ratio between q and $q + dq$. The luminosity L is given by the model of Bruzual and Charlot (1993, GISSEL96) using the results of Pozzetti et al. (1996).

It was required as a preliminary step that counts and redshift distribution in empty field and in various wavebands are correctly reproduced. We used the model for galaxy evolution of

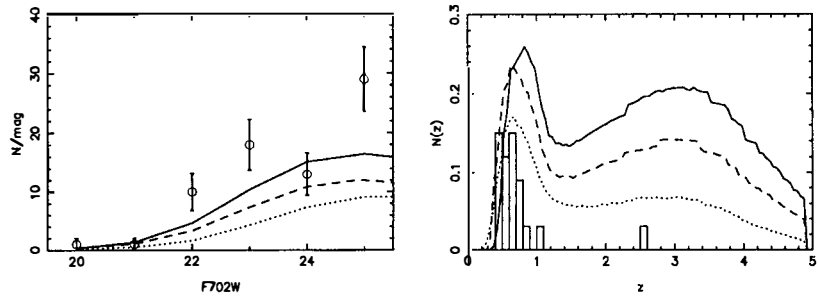

Figure 1: Left: Number counts of arclets in A2218 with the F702W filter, per bin of one magnitude ($a/b > 2$, $\mu^0_{F702W} \leq 25.5$). o: observed counts. Predicted counts are displayed for three mass distributions: SIS (dotted line), bimodal mass distribution of Kneib et al. (1995) (dashed line) and a mass distribution including substructures from Kneib et al. (1996) (solid line). Error bars correspond to statistical fluctuations. Right: Redshift distribution of arclets in A2218 per bin of 0.05 in z ($a/b > 2$, $R_{F702W} \leq 23.5$ and $\mu_R \leq 24$). Same notations as for the left figure. The histogram corresponds to the redshifts compiled by Ebbels et al. (1997), ordinate is in arbitrary units.

Bruzual and Charlot (1993) with the prescriptions of Pozzetti et al. (1996) (see Bézecourt et al. 1998 for details). In order to check the sensitivity to the cluster mass distribution, three different potentials are used for cluster A2218. The simpler one is a singular isothermal sphere (SIS) whose velocity dispersion is determined by the location of a giant arc at $z = 0.702$ ($\sigma = 1031\ km\ s^{-1}$). The second one is a bimodal mass distribution centered on the two main galaxies of the cluster (Kneib et al. 1995). The more complex potential used was obtained by Kneib et al. (1996) and includes galaxy scale components to account for the numerous substructures in the cluster. Unless specified otherwise, $H_0 = 50\,km\,s^{-1}\,Mpc^{-1}$, $q_0 = 0.5$ and $\Omega_\Lambda = 0$.

2 Results

2.1 Absolute number counts in cluster A2218

The detection of elongated objects in A2218 was performed in the frame of the WFPC2 HST image (6200 sec.) in filter F702W (Kneib et al. 1996).

The observed and predicted number counts of arclets are in very good agreement in the B band considering the mass distribution of Kneib et al. (1996). Counts in the R band are shown in Figure 1. The predicted total number of arcs ($R_{F702W} \leq 23.5$ and $a/b \geq 2$) with the best mass model is lower than the observed number by a factor of 1.8. The bimodal model of Kneib et al. (1995) and the SIS model underpredict the counts by factors of respectively 1.5 and 2 with respect to the model of Kneib et al. (1996) including galaxy scale potentials. This is a clear justification for the use of accurate mass distributions in statistics on gravitational arcs.

2.2 Redshift distribution

The redshift distribution of arclets selected in the F702W filter is presented in Figure 1 and can be partially compared to the results of a spectroscopic survey of arclets (Ebbels et al. 1997). However, this survey may be biased in the arclets selection criterion and in the ability to determine a redshift which mostly depends on the existence of emission lines in the optical part of the spectrum. This observed distribution peaks at a value of $z \simeq 0.6$, with only two objects at $z > 1$. Figure 1 shows the redshift distribution of arclets expected with the same selection conditions than those adopted by Ebbels et al. (1997). A peak also appears at a similar redshift ($z \simeq 0.8$, solid curve). The slight difference between the observed and the predicted peak is

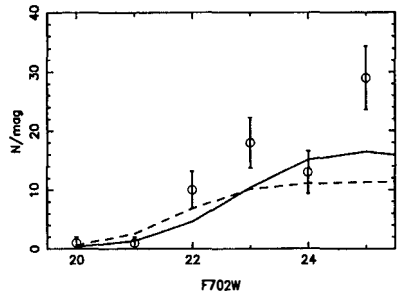

Figure 2: Same figure as Figure 1 for $q_0 = 0.5$ (solid line) and $q_0 = 0$ (dashed line) with the complex mass distribution of Kneib et al. (1996).

due to the hypothesis of circularity for the sources which prevents from obtaining arcs at low redshift just behind the cluster because of a less efficient lensing power.

However, another population of objects is expected at $z > 2$ which is not seen in the data. This high redshift tail is mainly produced by elliptical-type galaxies and shows the limit of the evolution model for young galaxies and early epochs.

3 Cosmological parameters

Figure 2 shows the predicted counts in A2218 for two different values of q_0, 0 and 0.5. The difference between the two curves is of the same order of magnitude as the uncertainty due to the mass distribution between mass modellings of Kneib et al. (1995) and (1996). This means that q_0 cannot be inferred from counts of gravitational arcs. A low q_0 doesn't help to reconcile with the data, hence one could argue that it implies a high value for Ω_Λ as it would increase the counts. However, this is unlikely as the counts of arclets in the B band are very well reproduced and a similar analysis performed in cluster A370 (Bézecourt et al. in preparation) doesn't require a high value of Ω_Λ. Moreover, uncertainties in galaxy evolution are too high to allow for a determination of Ω_0 and Ω_Λ with arcs counts.

4 The Hubble Deep Field

The results presented above can suffer from a privileged line of sight in the direction of A2218 and a representative view of the distant universe is then needed. This sample of distant galaxies is given by the images of the Hubble Deep Field (Williams et al. 1996). The model developped in the previous sections can be pushed to fainter limits by locating artificially the mass distribution of cluster A2218 (Kneib et al. 1996) in front of the HDF. Miralles and Pelló (1998) have determined photometric redshifts for a sample of 1400 galaxies in the HDF enabling to lens these objects by a cluster like A2218.

The predicted counts of arcs in the field of the HDF (F450W filter) with an axis ratio greater than 2 are in excellent agreement with the counts of simulated arcs (Figure 3). The redshift distribution resulting from the combination of the mass model with the evolution model for objects selected in the B band shows a deficit at $z < 0.5$ due to the circularity of sources. On the contrary, an excess of sources at high-z appears as in Figure 1. A different approach is then needed for galaxy evolution at early epochs, particularly in the hierarchical scenario.

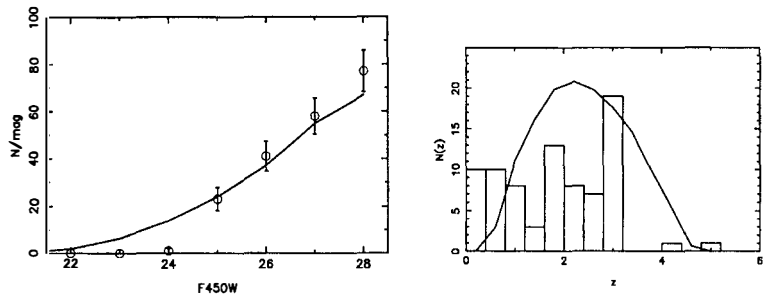

Figure 3: Left: Counts of arclets in the HDF lensed by A2218 artificially located in front of it (arclets with an axis ratio $a/b > 2$). α simulated "observed" counts. Solid line: predicted counts for the lens model by Kneib et al. (1996) and $q_0 = 0.5$. Right: Redshift distribution of arclets in the HDF per bin of 0.4 in z for $a/b > 2$ and $B_{F450W} < 27.5$ for the simulated "observed" arclets (histogram) and the predicted distribution (solid line).

5 Conclusions

It is now obvious that arcs statistics can only be performed with mass distributions including substructures, too simple potentials should be avoided. Number counts of arclets are in good agreement with observations in the B band and the redshift distribution of arclets at $z \leq 1.0$ is correctly predicted by the model. The important population of arclets expected at $z \geq 1.0$, which is not observed in spectroscopic surveys, is highly dependent on the modelling of high redshift ellipticals and the role of dust absorption in the rest frame UV.

Unfortunately, the geometry of the universe cannot be determined with arcs statistics because of too important uncertainties in clusters mass distributions and in the model for galaxy evolution. Geometrical effects have now to be investigated with clusters at redshift greater than 0.5 considering also the weak lensing regime. High-z lens efficiency relates more directly to cosmology and counts of all the background objects in a cluster field enable accurate measurement of the magnification bias that probes the high redshift population.

Acknowledgments

I wish to thank the group of cosmology of the Observatoire Midi–Pyrénées of Toulouse for very fruitful discussions on galaxy evolution and gravitational lensing. I'm also grateful to Yannick Mellier and to the European Union for financial support.

References

1. J. Bézecourt, R. Pelló, G. Soucail, *A&A* **330**, 399 (1998)
2. T.J. Broadhurst, 1995, astro-ph/9511150
3. G.A. Bruzual and S. Charlot, *ApJ* **405**, 538 (1993)
4. T.M.D. Ebbels, R.S. Ellis, J.–P. Kneib, J.F. Le Borgne, R. Pelló, I.R. Smail, B. Sanahuja, submitted to *MNRAS* (1997), astro-ph/9703169
5. B. Fort, Y. Mellier, M. Dantel–Fort, 1997, *A&A* **1997**, 321 (353)
6. J.–P. Kneib, Y. Mellier, R. Pelló, J. Miralda–Escudé, J.F. Le Borgne, H. Böhringer, J.–P. Picat, *A&A* **303**, 27 (1995)
7. J.–P. Kneib, R.S. Ellis, I. Smail, W.J. Couch, R.M. Sharples, *ApJ* **471**, 643 (1996)
8. J.M. Miralles and R. Pelló, submitted to *ApJ* (1998), astro-ph/9801062
9. L. Pozzetti, G.A. Bruzual, G. Zamorani, *MNRAS* **281**, 953 (1996)
10. R. Williams et al., *AJ* **112**, 1335 (1996)

Gravitational Lens Magnification: Analysis of A1689

S.Dye & A.N.Taylor
IfA, University of Edinburgh, Royal Observatory, Blackford Hill, Edinburgh, EH9 3HJ, U.K.

E.Van Kampen
TAC, Juliane Maries Vej 30, DK-2100 Copenhagen, Denmark.

T.J.Broadhurst & N.Benitez
Dept of Astronomy, Campbell Hall, University of California, Berkeley, USA.

In the first ever application of lens magnification bias to calculate the absolute projected mass of a lensing cluster, we find that the mass of Abell 1689 interior to $0.24h^{-1}$Mpc is $M_{2D}(< 0.24h^{-1}\mathrm{Mpc}) = (0.50 \pm 0.09) \times 10^{15} h^{-1} M_{\odot}$. We produce both radial mass profiles and two dimensional mass maps of A1689 using magnification bias and find them to be in good agreement with results from shear analysis [3]. The possibility of A1689 being composed of clumps of matter along the line of sight is suggested by comparing our derived lensing mass with those from X-ray temperature and virial velocity measurements.

1 Introduction

Galaxy cluster mass determinations from X-ray temperatures and virial velocities have long shown evidence of mass greatly in excess of visible amounts. This is also true of mass calculations using the more recent techniques of gravitational lensing although the need to assume equilibrium conditions within the cluster is alleviated.

Exploiting the distortions of light from background objects produced by the lensing effects of a foreground cluster enables unambiguous mass estimates to be achieved without having to make any assumptions about the cluster's dynamical state. Such exploitations generally fall into either the category of shear analysis or that of magnification bias. Shear analysis concerns itself with the mapping of intrinsic distortions produced in individual galaxy images across the field of view. Because essentially only differential mass estimates can be made, only a lower bound on a cluster's total mass can be obtained. Magnification bias methods on the other hand, look

for variations in the number density of background objects resulting from the amplification of image size and flux. If number counts are normalised either to the edge of the field of view or to some random offset field, then absolute mass measurements can be determined. Magnification bias provides an intuitively simple and easy to use method which we utilise in this work.

2 The Magnification Effect

Lens magnification has the dual effect of increasing background object fluxes and increasing the angular separation of these objects on the sky. In a flux limited sample, both effects compete; the increase in flux acting to increase object number density as fainter objects are brought within the sample flux limits and the increase in separation diluting number density. The resulting lensed number denstiy, $n^{'}(\boldsymbol{x})$, at any point $\boldsymbol{x}$ in the field of view can be given by [8]:

$$n^{'}(\boldsymbol{x}) = n_0 A^{\beta-1}(\boldsymbol{x})\,(1+\Theta(\boldsymbol{x})) \tag{1}$$

where n_0 is the expected mean number density, β is the logarithmic slope of the integrated luminosity function of the background objects, $n(L) \sim L^{-\beta}$, and $\Theta(\boldsymbol{x})$ is a perturbation which describes angular clustering. The index $\beta-1$ accounts for both the increase in object separation and flux. The lens amplification factor A is expressed as

$$A = \left|(1-\kappa)^2 - \gamma^2\right|^{-1} \tag{2}$$

where κ is the scaled surface mass density of the lens, the ultimately desired quantity, and γ is the amplitude of the shear field, discussed in the next subsection.

2.1 Estimators of κ

It follows from equation (2) that unless we have an understanding of the shear, it is not possible to determine κ. To circumvent this snag, we introduce the concept of the κ estimator[9] (Taylor et al 1998, T98 hereafter). T98 show that since a real cluster lies somewhere between the extremes of being an isothermal sphere and a sheet of material, one can bound the true value of κ by obtaining an estimated value for each.

The upper bound on κ, κ_+, comes from assuming that the cluster is a sheet of material so that $\gamma = 0$ and equation (2) gives $\kappa_+ = 1 - \mathcal{P}A^{-1/2}$, with $\mathcal{P}$ being the image parity such that $\mathcal{P} = -1$ in regions inside the caustic and $\mathcal{P} = +1$ outside. Similarly, the lower bound, κ_-, is reached by assuming an isothermal structure with $\gamma = \kappa$ so that (2) gives $\kappa_- = \frac{1}{2}(1 - \mathcal{P}A^{-1})$.

2.2 Maximum Likelihood Application

Measuring $n^{'}$ in a given binned area of the sky and using a value of n_0 taken from an offset field (or from object number counts at the edges of the field of view where the lens effect is weakest) would enable direct calculation of the amplification in that area using equation (1) if it weren't for the complication of clustering. In practice, it is not possible to determine $\Theta(\boldsymbol{x})$ since no distinction can be made between the intrinsic clustering of background objects and the lensed changes in number density. This degeneracy could be overcome with redshift information [2], however is dealt with in this work by treating the clustering as noise and applying maximum likelihood theory to calculate the lens amplification (T98). We also allow for shot noise contributions arising from the binning of the discrete distribution of background objects and adopt a lognormal-poisson model for the background probability distribution with a variance taken from the CFRS [4].

3 Data

The data comprises 10,000 seconds integration time in the V & I bands taken with ESO's 3.6m NTT and covers $\sim$ 30sq.arcmin of the cluster. Our offset field to which we normalise number counts and measure β from was observed with the Keck telescope [7] in VRI to R$\simeq$ 27.

4 Results

It is apparent from equation (1) that in order to maximise the lensing signal and thus minimise errors, it is necessary to select a population of background objects which has a value of β as different as possible from the lensing invariant $\beta = 1$. This is achieved by selecting background galaxies redward of the cluster sequence such that the same colour cuts with our offset field yield a value of $\beta = 0.22 \pm 0.05$ (in comparison, cuts selecting faint blue galaxies yielded $\beta \simeq 0.9$).

Approximately 3000 objects were detected in our lensing field with reliable V & I magnitudes and of these, $\sim$ 270 were selected redward of the cluster sequence, to form the background distribution. This background population was then binned into annuli about the cluster's centre (see fig 1a). Obscuration by the cluster was allowed for by masking out cluster galaxies (again chosen by colour) and adjusting the expected number count in each annulus accordingly. Figure 1b) shows that the radial variation in number counts looks similar to the isothermal fit apart from a large underdensity. This underdensity manifests itself in the radial κ profile in figure 2a) as a mass overdensity. We attribute this to lobe-like structure in the cluster's 2D mass distribution shown in figure 2b). This plot is generated in a similar manner to the radial κ plot except a 12 $\times$ 12 grid of bins are used instead of annuli. These structures agree well with mass maps of A1689 generated from shear analysis [3].

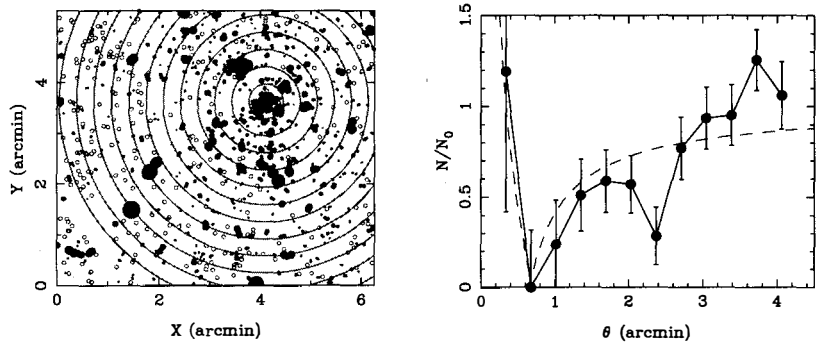

Figure 1: a) Annular bins around the cluster centre. Open dots are galaxies selected redward of the cluster sequence. Grey patches show areas of obscuration by the cluster which were interpolated over. b) Radial variation in ratio of measured number of objects to expected number of objects allowing for cluster obscuration. Error bars account only for shot noise.

To convert κ to real mass units [6], we take the redshift of A1689 derived elsewhere as $z_L = 0.18$ and the mean redshift of the selected background galaxy population from the CFRS to be $z_S = 0.8$. Integrating the κ profile to a radius of 2.4arcmin($\simeq 0.24h^{-1}$Mpc) gives a total projected mass contained within that radius of $M_{2D}(< 0.24h^{-1}\mathrm{Mpc}) = (0.50 \pm 0.09) \times 10^{15}h^{-1}\mathrm{M}_{\odot}$. This is slightly larger but still within the error bounds of Kaiser's result from shear analysis [3] of $M_{2D}(< 0.24h^{-1}\mathrm{Mpc}) = (0.43 \pm 0.05) \times 10^{15}h^{-1}\mathrm{M}_{\odot}$.

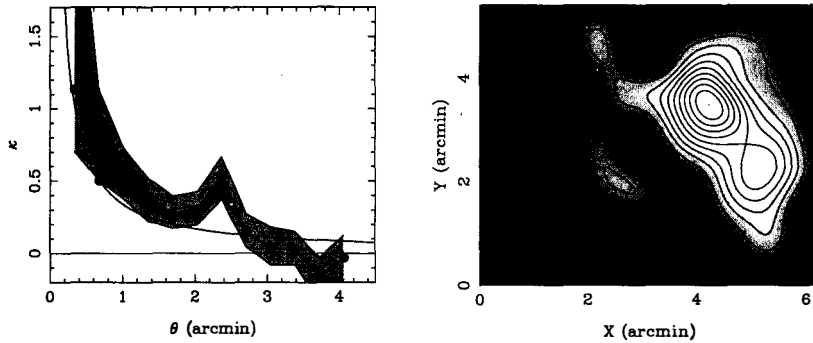

Figure 2: a) Surface mass density profile of A1689. The solid line is an isothermal fit. The dark shaded region is the area bounded by the κ_+ & κ_- estimators. The lighter shaded region is the uncertainty derived from maximum likelihood errors due to clustering and shot noise. b) 2d surface mass density distribution smoothed from 12 x 12 grid

5 Conclusion

Using magnification bias, we have determined the mass of the lensing cluster Abell 1689 contained within a radius of $0.24h^{-1}$Mpc to be $M_{2D}(< 0.24h^{-1}\text{Mpc}) = (0.50 \pm 0.09) \times 10^{15}h^{-1}M_{\odot}$. We have produced a 2D projected mass map of the cluster and find that the structures observed correlate well with those found from shear analysis [3].

Comparing our mass result with mass estimates of A1689 from virial velocity arguments and X-ray temperatures shows slight evidence that $M_{X-ray} < M_{lens} < M_{virial}$ providing further evidence that A1689 could be several structures along the line of sight. (for further discussion, see Miralde-Escudé & Babul [5]).

References

1. T.J.Broadhurst, A.N.Taylor, J.A.Peacock, *ApJ* **438**, 49 (1995)
2. S.Dye et al., *in preparation*
3. N.Kaiser,'*Gravitational Dynamics*', Proc. of the 36th Herstmonceux Conf., eds. O.Lahav, E.Terlevich, R.J.Terlevich. (1996)
4. O.Le Févre, D.Hudon, S.J.Lilly, D.Crampton, F.Hammer, L.Tresse, *ApJ* **461**, 534 (1996)
5. Miralde-Escudé & Babul, APJ **449**, 18 (1995)
6. P.Schneider, J.Ehlers, E.E.Falco, '*Gravitational Lenses*', Springer-Verlag
7. I.Smail, D.W.Hogg, L.Yan, J.G.Cohen, *ApJ Lett.* **449**, L105 (1995)
8. A.N.Taylor & S.Dye, preprint for submission to *MNRAS* (1998)
9. A.N.Taylor, S.Dye, E.Van Kampen, T.Broadhurst, N.Benitez, *astro-ph/9801158* (1998)

HIPPARCOS and DISTANCE AND AGE PRIMARY INDICATORS [a]

C. TURON
DASGAL, URA CNRS 335, Observatoire de Paris, 92195, Meudon Cedex, France

After a brief description of the Hipparcos mission and an overview of the astrometric and photometric results obtained from the mission, more details are given on the basic distance and luminosity information newly available. Applications of this fantastic amount of accurate data are presented: calibration of photometric and spectroscopic distances, of open cluster main sequence fitting, of period-luminosity relations for pulsating variables; age determination for open and globular clusters. Finally, it is shown how this new data help solving the previous discrepancy between the age of the Universe and the age of the oldest objects.

1 Introduction

The ESA Hipparcos satellite, included in the European Space Agency scientific programme in 1980, was launched by Ariane in August 1989. High quality scientific data were obtained during 37 months, from November 1989 to March 1993. Operations were terminated on 15 August 1993. Comprehensive description of the Hipparcos mission is given in Perryman et al. (1992).

The Hipparcos Catalogue (ESA 1997) includes 118218 preselected stellar entries brighter than V $\simeq$ 12.4, 117955 with associated astrometry, 118204 with associated photometry (Perryman et al. 1997a). Observations were made from 1989.85 to 1993.21, with a mean epoch close to J1991.25, adopted as the catalogue epoch. Standard errors are functions of magnitude and ecliptic latitude. Median standard errors for stars brighter than $Hp = 9$ mag are smaller than 1 mas for positions and parallaxes, of 1 mas/yr for proper motions. Systematic parallax errors are estimated to be smaller than 0.1 mas from various investigations (Arenou et al. 1997). The coincidence with the adopted reference system (ICRS) is estimated to be within $\pm$ 0.6 mas about all 3 axes, and the deviation from inertial in the range $\pm$ 0.25 mas/yr, also about all 3 axes (Kovalevsky et al. 1997).

[a] Based on observations made with the ESA Hipparcos satellite

2 Distances, absolute magnitudes, ages

The Hipparcos data provide a dramatic increase, qualitatively and quantitatively, of the basic distance information available for many applications. The number of stars for which a relative accuracy better than 1, 5, 10 and 20% is now available from Hipparcos data and from ground-based data are given in Table 1.

Table 1: Number of stars per range of relative accuracy of trigonometric parallaxes.

	Hipparcos	ground-based
$\sigma_\pi / \pi < 1\%$	442	a few tens
$\sigma_\pi / \pi < 5\%$	7388	100 ?
$\sigma_\pi / \pi < 10\%$	22396	1 000 ?
$\sigma_\pi / \pi < 20\%$	50643	

Moreover, the range of spectral types and luminosity classes for which precise parallaxes are available is considerably enlarged, especially towards the upper part of the main sequence and towards the giant branch, where the 'clump' is already clearly evident when considering stars with relative accuracy better than 5%. The lower part of the main sequence is populated down to absolute Hp magnitude 14.

The comparison with ground-based distance determinations shows that many distances were underestimated. For example, stars selected to be within 25 pc of the Sun (i.e. very close to the Sun when compared to the galactic radius) from the best ground-based trigonometric, spectroscopic and photometric parallaxes are compiled in the Catalogue of Nearby Stars (CNS3, Gliese & Jahreiß 1991). All stars of this catalogue bright enough to be observed by Hipparcos have been included in its observing programme. The distribution of Hipparcos distances for these 1681 stars is shown in Figure 1. Some 40 per cent of CNS3 stars appear to be further than 25 pc from Hipparcos observations (Perryman et al. 1995).

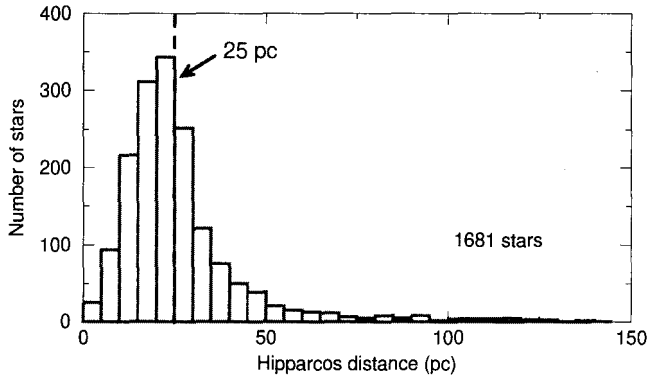

Figure 1: Hipparcos distances for stars selected to be within 25 pc of the Sun from the best ground-based trigonometric, spectroscopic and photometric parallaxes compiled in the Catalogue of Nearby Stars (CNS3).

A comparison with spectroscopic distances shows the same kind of systematic discrepancy: from 5610 stars classified as dwarf stars in the Michigan Spectral Survey (Houk et al. Vols. 1-3), and estimated to be at distances $\leq$ 80 pc, 2384 are shown by Hipparcos to be at distances $>$ 80 pc (Binney et al. 1997). The spectroscopic classifications have also been investigated by Gómez et al (1997), clearly showing a mixture of various groups, physically different, in one spectral type or luminosity class. For example, giant (class III) stars are spread among three different groups in the classical giant zone of the HR diagram, but a non-negligible number of stars are on the main sequence. These studies show how necessary is a revision of the calibration of spectroscopic parallaxes for bright objects used in further steps of distance scale determination.

A direct consequence of a better knowledge of absolute magnitudes is a more accurate positioning of the stars in the HR diagram. Age determination can be made from the comparison of a star position (or a sequence position for stars in an open or globular cluster) with theoretical isochrones derived from evolution models computed for the metal abundance of the considered object. For example, the age of the closest galactic open cluster, the Hyades, has been derived from the accurate Hipparcos distances of its member stars and an accurate positioning of these objects in the HR diagram: 625 $\pm$ 50 Myr (Lebreton et al. 1997, Perryman et al. 1998).

The second example deals with some of the oldest stars in our Galaxy: the subdwarf stars. The name of these stars comes from the fact that, in the HR diagram, they form a sequence which is below the main sequence, place of dwarf stars. Physically, they are distinguished by their low metallicity. Hipparcos distances brought the surprise that many of these stars have already left their low sequence and moved towards the upper-right part of the HR diagram, showing that they are evolved stars (Pont et al. 1997a and b, Cayrel et al. 1997). This fact allows a much better comparison of these stars with globular cluster stars which are of similar stellar population, and thereby, a much more accurate determination of the age of subdwarfs and of globular clusters (Reid 1997, Gratton et al. 1997, Pont et al. 1998). See section 5.2.

3 Open clusters

Open clusters are widely used for distance determination by main sequence fitting. Hipparcos offers for the first time the possibility of thoroughly studying the three-dimensional structure and the kinematics of the closest cluster, the Hyades, giving a mean distance modulus of 3.33 $\pm$0.01 mag for the stars observed by Hipparcos within 10 pc of the cluster center (Perryman et al. 1998), and to precisely place the main sequences of about 15 open clusters of various ages and chemical compositions in the HR diagram (Mermilliod et al. 1997, Robichon et al. 1997a and b, van Leeuwen & Hansen Ruiz 1997, Robichon et al. 1998). The surprise is that the positions of the different sequences cannot be explained by differences in metallicities, and that a scatter of Helium abundance of about 0.05 would be necessary to explain these discrepancies. A further use of the main-sequence fitting method requires the understanding of this problem.

4 Pulsating variables

Another kind of powerful distance indicators are pulsating variable stars. The main difficulty is to obtain a representative sampling of the stars considered, covering the whole period, colour, and metallicity ranges for each type of objects. Both the astrometric and photometric results obtained from the Hipparcos satellite will greatly improve our knowledge of the physics of these stars and the use which can be made of some of these in distance scale determinations (Turon & van Leeuwen 1995). No trigonometric parallaxes are available from ground-based observations for the three types of pulsating variables most commonly used for distance scale calibrations: Cepheids, RR Lyrae and Mirae. Hipparcos parallaxes of ten to twenty of each type of these stars are being used to re-discuss the zero-point of the period-luminosity relations: Feast &

Catchpole (1997), Feast & Whitelock (1997), Paturel et al. (1997), Feast (1998), Madore & Freedman (1998), Oudmaijer et al. (1998) and Luri et al. (1998) for Cepheids; Tsujimoto et al. (1997), McNamara (1997), Fernley et al. (1998) and Luri et al. (1998) for RR Lyrae; van Leeuwen et al. (1997), Whitelock et al. (1997) and Bergeat et al. (1998) for Mira and long period variables.

In addition, cluster membership is greatly improved using proper motions (Lyngå & Lindegren 1998), and a revision of the calibration of the main sequence position in the HR diagram versus abundances in Fe, He, etc. is under study (see paragraphs on open clusters and on subdwarf stars). This will have consequences on the calibration of the effect of colour and metallicity on the period-luminosity relations.

More photometric observations are strongly needed to better evaluate the intrinsic scatter in period-luminosity relations, the interstellar extinction, and the metallicities. However, only a project such as GAIA (Lindegren & Perryman 1996, Perryman et al. 1997b) would bring extremely accurate determinations of absolute magnitudes for extensive samples of pulsating variable stars and allow a comprehensive calibration of period-luminosity relations for all galactic variables of disk and halo stellar populations. Moreover, the trigonometric distances of the brightest Magellanic variables would be within reach, opening the first possibility to test the universality of these relations.

5 Results on LMC distance, Hubble constant, and globular cluster ages

5.1 LMC distance and Hubble constant

The results obtained for the distance of the Large Magellanic Cloud and the Hubble constant, H_0, from Hipparcos data and other ground-based observations are given in Table 2.

Table 2: Distance of the Large Magellanic Cloud and Hubble constant

Objects / reference	$(M\text{-}m)_0$ mag	H_0 km s^{-1} Mpc^{-1}
From Cepheids absolute magnitudes		
Feast & Catchpole 1997	18.70 ± 0.10	decreased by 10%
Paturel et al. 1997	18.72 ± 0.05	53 ± 6
Madore & Freedman 1998	18.44 ± 0.35 to 18.57 ± 0.11	–
Oudmaijer et al. 1998	18.56 ± 0.08	–
Luri et al. 1998	18.29 ± 0.17	79
From RR Lyrae absolute magnitudes		
McNamara 1997	18.57 ± 0.03	–
Fernley et al. 1998	18.26 ± 0.15	–
Luri et al. 1998	18.37 ± 0.23	79
From RR Lyrae absolute magnitudes, via subdwarfs and globular clusters		
Reid 1997	18.65	68 ± 9
Gratton et al. 1998	18.60 ± 0.07	≤ 64 or ≤ 83
From Mira or long-period variable absolute magnitudes		
van Leeuwen et al. 1997	18.54 ± 0.18	–
Whitelock et al. 1997	18.60 ± 0.18	–
Bergeat et al. 1998	18.50 ± 0.17	–

Most results are converging to a LMC distance modulus of 18.5-18.7, increasing the distance scale by nearly 10%, but some discrepancy remains between the distances obtained from RR Lyrae and from Cepheids. The Hubble constant decreases, in consequence, by the same percentage.

5.2 Globular cluster ages

Because of the detection system of Hipparcos, it was not possible to observe stars in globular clusters (the star density was too high). Moreover, the closest globular cluster is much too far for a trigonometric parallax observation at an accuracy of the milli-arcsecond. Such observations would be possible with GAIA, at the micro-arcsecond level.

On the other hand, Hipparcos brought accurate distance determinations of subdwarf stars, the only stars of the halo population in the solar vicinity. A few hundred of these stars have been observed by the satellite, giving significant samples within ranges of metal abundances. The calibration of subdwarf sequences for different [Fe/H] allows the determination of the distances and ages of globular clusters of similar metallicity (Pont et al. 1997b, Reid 1997, Cayrel et al. 1997, Gratton et al. 1997, Pont et al. 1998, Reid 1998, Chaboyer et al. 1998). The results for the age of the oldest globular clusters, obtained from Hipparcos data, many other ground-based observations, and theoretical models of stellar evolution are given in Table 3.

Table 3: Age determinations of the oldest globular clusters

Objects / reference	Age (Gyr)
Comparison with subdwarfs of similar metallicity	
Cayrel et al. 1997	$14 - 15$
Gratton et al. 1997	$11.8 + 2.1 - 2.5$
Reid 1997	$11 - 13$
Pont et al. 1997, 1998	14 ± 1
Via RR Lyrae absolute magnitudes	
Chaboyer et al. 1998	11.5 ± 1.3
Fernley et al. 1998	17.4 ± 3.0
Via Cepheids absolute magnitudes and LMC distance	
Feast & Whitelock 1997	11

There is some spread in the results, but most are converging towards 12-14 Gyr. These results, compared with the H_0 constant obtained from the distance of the Large Magellanic Cloud, go towards solving the previous discrepancy between the age of the Universe and the age of the oldest objects: they do not conflict anymore with standard inflationary models of the Universe.

6 Conclusion

A new and substantial contribution to the observational data necessary to derive distances and ages is provided by Hipparcos, with a qualitative and quantitative advance with respect to ground-based observations. However, many other ingredients are necessary to calibrate main sequence or isochrone fittings, period-luminosity relations, effects of chemical abundances on luminosity, etc.

The results presented here provide good examples of what is expected from Hipparcos data in conjunction with improved photometric and spectroscopic ground-based observations and improved evolutionary models. The next step forward would be a space mission such as GAIA, leading to direct distance determinations throughout our Galaxy, and even for the brightest objects in the Large Magellanic Cloud, of all distance indicators (open clusters, Cepheids, RR Lyrae, long-period variables, novae, etc.).

References

1. Arenou F., Mignard F., Palasi J., 1997, ESA SP-1200, Vol. 3, Ch. 20
2. Bergeat J., Knapik A., Rutily B., 1998, A&A, **332**, L53
3. Binney J.J., Dehnen W., Houk N. et al., 1997, in Hipparcos Venice '97, 473
4. Cayrel R., Lebreton Y., Perrin M.N., Turon C., 1997, Hipparcos Venice '97, 219
5. Chaboyer, B., Demarque, P., Kernan, P.J., Krauss, L.M., 1998, ApJ, **494**, 96
6. ESA, 1997, The Hipparcos and Tycho Catalogues, ESA SP-1200
7. Feast M.W., Catchpole R.M., 1997, MNRAS, **286**, L1
8. Feast M.W., 1998, MNRAS, **293**, L27
9. Feast M.W., Whitelock P.A., 1997, MNRAS, **291**, 683
10. Fernley, J., Barnes, T.G., Skillen, I. et al., 1998, A&A, **330**, 515
11. Gliese W., Jahreiß H., 1991, Astron. Rechen-Institut, Heidelberg
12. Gómez A.E., Luri X., Mennessier M.O. et al., 1997, in Hipparcos Venice '97, 207
13. Gratton R.G., Fusi Pecci F., Carretta E., et al., 1997, ApJ, **491**, 749
14. Hipparcos Venice '97 Symposium, M.A.C. Perryman & P.L. Bernacca (eds), ESA SP-402
15. Kovalevsky J., Lindegren L., Perryman M.A.C., et al, 1997, A&A, **323**, 620
16. Lebreton Y., Gómez A., Mermilliod J.C., Perryman M.A.C., 1997, in Hipparcos Venice '97, 231
17. van Leeuwen, F., Hansen Ruiz, C.S., 1997, Hipparcos Venice '97, 689
18. van Leeuwen F., Feast M.W., Whitelock P.A., Yudin B., 1997, MNRAS, **287**, 955
19. Lindegren L., Perryman M.A.C., 1996, A&A Suppl., **116**, 579
20. Lyngå G., Lindegren L., 1998, New Astronomy, **3**, 121
21. Luri X., Gmez A.E., Torra J., Figueras F., Mennessier M.O., 1998, A&A, in press
22. Madore B.F., Freedman`**W**.L., 1998, ApJ, **492**, 110
23. McNamara D.H., 1997, PASP, **109**, 1221
24. Mermilliod J.C., Turon C., Robichon N., Arenou F., Lebreton Y., 1997, in Hipparcos Venice '97, 643
25. Oudmaijer R.D., Groenewegen M.A.T., Schrijver H., 1998, MNRAS, **294**, L41
26. Paturel et al., 1997, in Hipparcos Venice '97, 629
27. Perryman M.A.C., Brown A.G.A., Lebreton Y., Gómez A., Turon C., Cayrel de Strobel G., Mermilliod J.C., Robichon N., Kovalevsky J., Crifo F., 1998, A&A, **331**, 81
28. Perryman M.A.C., Lindegren L., Kovalevsky J., et al. 1997a, A&A, **323**, L49
29. Perryman, M.A.C., Lindegren, L., Turon, C., 1997b, Hipparcos Venice '97, 743
30. Perryman M.A.C.., Lindegren L., Kovalevsky J., Turon C., et al. 1995, A&A, **304**, 69
31. Perryman M.A.C., Høg E., Kovalevsky J., Lindegren L., Turon C., Bernacca P.L., Crézé M., Donati F., Grenon M., Grewing M., van Leeuwen F., et al. 1992, A&A, **258**, 1
32. Pont F., Mayor M., Turon C., 1997a, in IAU Symp. 189, p 433
33. Pont F., Charbonnel C., Lebreton Y., et al., 1997b, in Hipparcos Venice '97, 699
34. Pont F., Mayor M., Turon C., VandenBerg D.A., 1998, A&A, **329**, 87
35. Reid I.N., 1997, AJ, **114**, 161
36. Reid I.N., 1998, AJ, **115**, 204
37. Robichon N., Arenou F., Turon C., Mermilliod J.C., Lebreton Y., 1997a, in Hipparcos Venice '97, 567
38. Robichon, N., Arenou, F., Turon, C., et al., 1997b, Highlights in Astronomy, **11**, in press
39. Robichon N., Arenou F., Turon C., Mermilliod J.C., 1998, in preparation
40. Tsujimoto T., Miyamoto M., Yoshii Y., 1998, ApJ, **492**, 79
41. Turon C., van Leeuwen F., 1995, in *Astrophysical Applications of Stellar Pulsation*, R.S. Stobie, P.A. Whitelock eds, p. 241
42. Whitelock P.A., van Leeuwen F., Feast M.W., 1997, in Hipparcos Venice '97, 213

Period-Luminosity relation for short period Cepheids towards the SMC

Florian Bauer
on behalf of the Eros2 collaboration
Collège de France, PCC, IN2P3 CNRS, 11 place Marcelin Berthelot, 75231 Paris Cedex, France

We present the Period–Luminosity relation from 290 Cepheids toward the LMC and 597 Cepheids towards the SMC respectively obtained from the monitoring of 1.134.000 and 504.000 stars over 150 nights using the two 4k × 8k CCD camera of the Eros2 microlensing project. A slope break of the Period–Luminosity relation has been observed for SMC fundamental mode Cepheids with periods smaller than 2 days. Different possible experimental biases, which could explain this effect have been investigated and could be discarded. This observed slope break could be due to evolutionary effects combined with convection effects.

1 Introduction

Cepheids are young, bright periodic variable stars, with typical masses of 2–10 $M_{\odot}$, that have evolved away from the main sequence. After having initiated the helium burning in the core, stars in the Cepheid mass range will follow an horizontal evolutionary track in the HR–diagram and cross a zone, called the instability strip, where their enveloppe will become vibrationally instable The period of pulsation is tightly correlated with the luminosity, and this Period–Luminosity relation (hereafter PL–relation) has been used for many decades to derive local and extragalactic distances. The microlensing searching projects towards the Magellanic Clouds have the ability of nightly photometric follow-up of millions of stars over long time-scales, and are therefore suitable to monitor variable stars in a systematic way. The Eros1 collaboration has already reported the discovery of 97 and 450 Cepheids towards the LMC and the SMC respectively (Beaulieu et al. 1995[5], Beaulieu et al. 1996[6]). Owing to their larger spatial coverage the MACHO collaboration has reported the discovery of 1466 single-mode and 73 double-mode Cepheids towards the LMC (Welch et al. 1996[12]). In order to understand the different systematics and the limitations of the use of the PL–relation as distance indicator, the Eros2 collaboration has made a dedicated campaign which will allow to undertake fine comparisons between Cepheids in both Magellanic Clouds.

2 The Period–Luminosity relations

Observations were obtained using the new Eros2 experimental setup, which consists of a 1 m Ritchey–Chretien telescope and two 4k × 8k CCD mosaic cameras allowing a simultaneous imaging in two focal planes with different color passbands (*blue* passband: 420–650 nm; *red* passband: 650–900 nm). Each CCD mosaic is made of eight 2k × 2k three edge buttable thick CCD's developped by Loral/U.Arizona. The available global field of view is 0.7° × 1.4°. The whole system has been mounted at the La Silla Observatory in Chile in June 1996 and details are described in Bauer et al. 1996[1] and Bauer 1997[2].
From October 1996 to February 1997, two fields ($2°^2$) were taken in the centre of both Magellanic Clouds at a rate of approximatively one measurement each night. A total of 130-150 images were obtained for each of the 4 fields. From the light curve of 1.134.000 LMC stars and 504.000 SMC stars, we were able to extract 5497 LMC and 1929 SMC variable stars, with intrinsic variations greater than 0.01 mag. Out of this two data sets we found 177 fundamental mode (1F) and 113 first overtone (1OT) Cepheids towards the LMC and 356 1F and 241 1OT Cepheids towards the SMC. The complete Cepheid search is described in details by Bauer 1997[2]. The Eros2 Cepheid catalog is under construction (Bauer et al. 1998[3]).

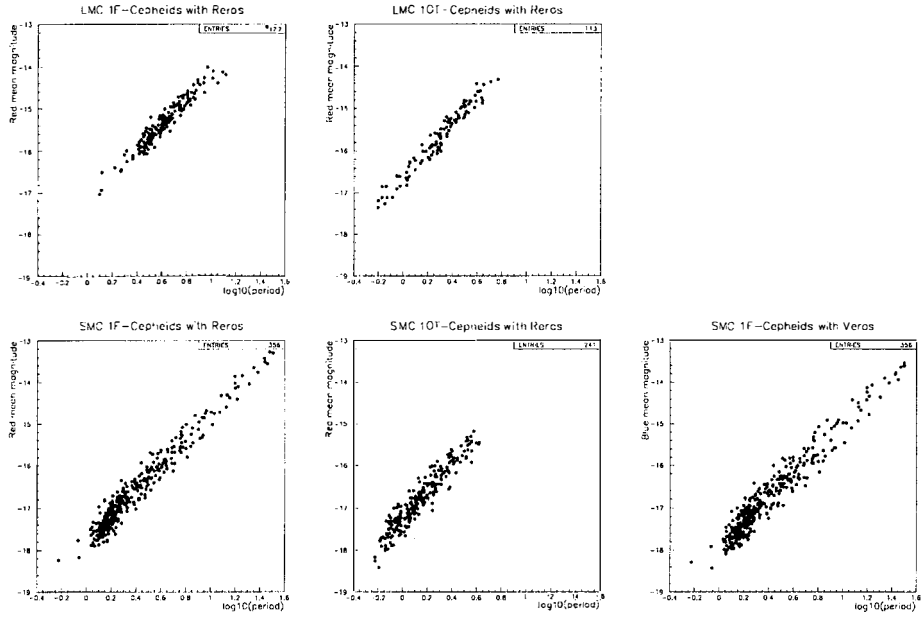

Figure 1: PL–relations for the fundamental mode Cepheids (left) and the first overtone Cepheids (center) towards the LMC (top) and the SMC (bottom) seen in the red Eros2 color passband R_{EROS}. The right figure represent the SMC 1F Cepheid PL–relation given in V_{EROS}

A first inspection of the PL–relations (figure 1) indicates a change in the slope for SMC 1F Cepheids with periods smaller than 2 days. This effect is visible in both colours. In order to quantify this effect we fitted the upper part of the PL–relation (Cepheids with periods P>2 day) and the lower part of the PL–relation (Cepheids with periods P<2 day). The deviation of the Cepheids with periods smaller than 2 days, compared with an extrapolation of the PL relation

SMC	blue			red			SMC	blue			red		
1F	all	P>2d	P<2d	all	P>2d	P<2d	1OT	all	P>1d	P<1d	all	P>1d	P<1d
β	2.86	2.76	3.35	3.00	2.92	3.46	β	2.98	2.99	3.88	3.12	3.14	3.79
σ_β	0.04	0.06	0.16	0.03	0.05	0.14	σ_β	0.08	0.11	0.59	0.07	0.09	0.53
N	356	165	191	356	165	191	N	241	171	70	241	171	70
LMC	blue			red			LMC	blue			red		
1F	all	P>2d	P<2d	all	P>2d	P<2d	1OT	all	P>1d	P<1d	all	P>1d	P<1d
β	2.72	2.69	2.47	2.88	2.88	2.03	β	3.10	3.12	3.36	3.14	3.19	3.16
σ_β	0.07	0.08	0.67	0.06	0.06	0.54	σ_β	0.08	0.10	0.70	0.07	0.09	0.75
N	177	170	7	177	170	7	N	113	100	13	113	100	13

Table 1: The slope β, the dispersion σ_β and the number of Cepheids N for different samples of cepheids.

fit for Cepheids with periods greater than 2 days, reaches 0.2-0.3 mag. In table 1 we compare the slopes resulting of the different fits. The slopes for Cepheids with periods smaller than 2 days are significantly higher than those for Cepheids with periods greater than 2 days (2.76 ± 0.06 to 3.35 ± 0.16 in the blue and from 2.92 ± 0.05 to 3.46 ± 0.14 in the red). Thus the fit of the entire SMC 1F PL-relation overestimates the slope and underestimates the distance to the SMC. On the other hand no significant deviation can be seen for 1F LMC Cepheids, 1OT LMC Cepheids and for 1OT SMC Cepheids.

3 Interpretation

In order to check the reality of this phenomena possible observational biases have been examined (for details see Bauer 1997[2]): We were able to show that our periodicity search is accurate to 10^{-3} days and that the non-linearity of the photometry does not exceed 0.03 mag for the faintest Cepheids (which is negligeable compared to the 0.2-0.3 mag deviation). Furthermore the Cepheids with periods smaller than 2 days are uniformly distributed on the SMC. Thus the slope break is not correlated with a CCD, a deep line of sight or a zone of the sky with an anomalous high extinction We searched for Cepheids in the SMC microlensing database of Eros2 which has been undertaken using 15 times longer exposures than the Cepheid follow-up. The slope break still remains visible. Finally the slope break is even visible in the Eros1 dataset (Beaulieu et al. 1996[6]); it was ignored because of its marginal statistical insignificance. It should be noted that the Eros1 dataset issues from different observations, photometry and the search software package, telescope and CCD array.
Compared to other catalogs (Caldwell and Coulson 1984[7], Mathewson et al. 1986[10], Laney and Stobie 1994[8]) the Eros1 and Eros2 SMC Cepheid datasets are the first catalogs which are sensitive to low-period SMC Cepheids using modern CCD technics. The only catalog with a sensitivity to SMC Cepheids with period smaller than 2.0 days was measured by Payne-Gaposchkin 1966[11] using photographic plates. Here no break of the slope is visible.

From Stefan-Boltzman law, one can show that the PL-relation is just a 2 dimensional projection of the Period-Luminosity-Colour plane (Madore and Freedman 1991[9]). The shape of the PL-relation is closely related to the shape of the instability strip in the Colour-Magnitude plane. Two plausible scenarios could explain the reported phenomena:
(1) As the horizontal evolution tracks become smaller with decreasing mass, it could be imaginable that at for a given mass, the length of the horizontal evolution tracks are too short to cross the entire instability strip. For Cepheids with periods smaller than 2.0 days, we would assist to a continuous depopulation of the instability strip (see figure 2, scenario 1).
(2) For small period Cepheids the blue edge of the instability strip becomes non-linear (see figure 2, scenario 2), due to convection effects in the stellar atmosphere.
As an issue of the reported observations, Baraffe et al. 1998[4] have computed evolutionary models, coupled to a linear non-adiabatic stability analysis, in order to get consistent Mass-Period-

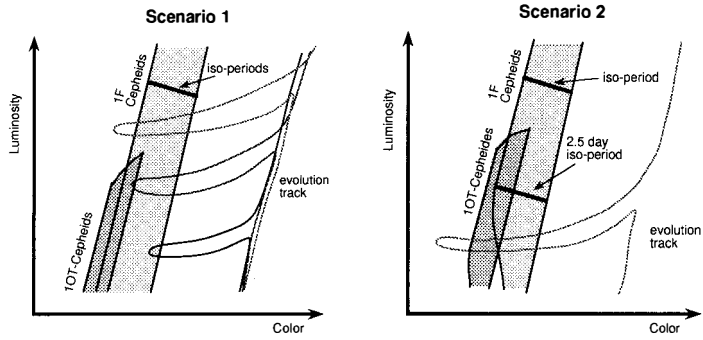

Figure 2: Two scenarios for a possible explanation of the reported phenomena.

Luminosity relations. They report a change in the slope consistent with the observations. This theoretical analysis corresponds to scenario 1.

On the other hand it is interesting to notice that only very few 1F Cepheids with period smaller than 2.0 days are observed towards the LMC. This is due to the the fact that the horizontal evolutionary tracks are very sensitive to metallicity. For a same mass the horizontal evolutionary track for a LMC star will be smaller than for a SMC star. So if the reported break in the slope would be only due to scenario 1, it should even be visible on the LMC at larger period.

4 Conclusion

We have presented the PL relation issued of a dedicated LMC/SMC Cepheid campaign. For the first time a break in the slope of the PL relation Cepheids with periods shorter than 2 days has been observed. For 1F SMC Cepheids with period smaller than 2.0 days the magnitude deviation compared to the entire PL relation reaches 0.2-0.3 mag. These observations can represent a useful constraint for pulsation theory. Higher statistics of short period Cepheid in other galaxies will be useful to understand, if this slope break depends on metallicity. It is interesting to note that the reported slope break should not affect the determination of H_0 by the HST Key Project, which uses only long period Cepheids, in order to reduce observation time and to avoid contamination by 1OT Cepheids.

References

1. Bauer F. et al., 1996, Eso Workshop, *Optical Detectors for Astronomy*
2. Bauer F., 1997, PhD. Thesis, Universitée Paris VII, or Saclay Report Dapnia SPP 97/10
3. Bauer F. et al., 1998, *in prep.*
4. Baraffe C., Alibert Y., Méra D., Chabrier G., Beaulieu J.P., 1998, *submitted to AA*
5. Beaulieu et al., 1995, *AA*, **303**, 137
6. Beaulieu J.P., Sasselov D., 1996, IAP Coll., *Astron. Returns of microlensing surveys*, 193
7. Caldwell J.A.R., Coulson I.M., 1984, *SAAOC*, **8**, 1
8. Laney C.D., Stobie R., 1994, *MNRAS*, **266**, 441
9. Madore B, Freedman W., 1991, *PASP*, **103**, 933
10. Mathewson D.S., Ford V.L., Visvanathan N., 1986, *ApJ*, **301**, 664
11. Payne–Gaposchkin C.H., Gaposchkin S. 1966, *Vistas Astron.*, **8**, 191
12. Welch, D.L. et al. 1996, IAP Coll., *Astron. Returns of microlensing surveys*, 205

INTERMEDIATE REDSHIFT SUPERNOVAE SEARCH WITH EROS

Delphine HARDIN
Service de Physique des Particules, DAPNIA, CEA-Saclay, France

After emphasizing the need for supernovae at intermediate redshifts for cosmology, I will quickly present the various searches for supernovae at intermediate distance underway in the world. I then detail our own project: the EROS supernovae search, now in full operation, will provide a sample of intermediate redshift supernovae at $z \sim 0.1$ with a well understood search efficiency.

1 Introduction

Supernovae are bright stellar objects resulting from the explosion of a star. They are classified according to their spectra: type II supernovae exhibit hydrogen lines in their spectra while type I supernovae do not. Type I are further subclassified : type Ia supernovae are characterized by the presence of a deep Si II absorption line near 615 nm, whereas type Ib and Ic, which lack this feature, are distinguished by the presence or absence of He I lines. Type Ia supernovae are thought to arise from thermonuclear explosion of C+O white dwarfs ("thermonuclear supernovae") and type II, Ib and Ic from the gravitational collapse of a massive star core ("gravitational collapse supernovae").

Type Ia supernovae can be observed up to a redshift of $z \sim 1$. The "intermediate" redshift distance range begins out in the Hubble Flow, at $z \sim 0.02$, and stretches into the linear part of the Hubble diagram, up to $z \sim 0.25$.

I quickly review in section 2 the use of low redshift type Ia supernovae for cosmology. I present in section 3 the few searches in the world tackling the intermediate redshift range. EROS search is detailed in section 4.

2 Cosmology with intermediate redshift supernovae

Supernovae are widely used in cosmology as distance indicators. At small redshifts, type IIp supernovae make good distance indicators via the expanding photosphere method (see Eastman

et al.[3]), and the relative uniformity of type Ia supernovae has led to their use as standard candle, up to a redshift of $z \sim 1$. In the following, I will concentrate on this last topic.

At small redshifts, the absolute magnitude M and the apparent magnitude of an object m are related to its recession velocity cz (in km/s) and the value of the Hubble constant H_0 (in $\mathrm{km\,s^{-1}\,Mpc^{-1}}$) through :

$$m = M - 5\log(H_0) + 5\log(cz) + 25 \tag{1}$$

which reflects the fact that the observed flux scales as the inverse of the squared distance.

Standard candles are a class of objects for which the absolute magnitude M is supposed to be constant. Traditionally, type Ia supernovae have been considered as perfect standard candles, when observed at their peak brightness. In building the Hubble diagram of nearby supernovae, i.e. plotting the apparent magnitude at peak as a function of the logarithm of the recession velocity, the linear relationship described in Eq.1 is observed (see figure 1-a, adapted from Perlmutter *et al.*[6]). The value of the intercept $\mathcal{M}$ at $\log(cz) = 1$ is related to both the

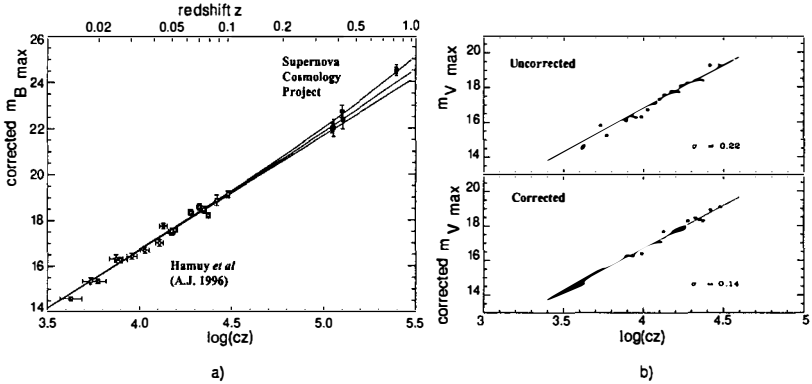

Figure 1: a) Hubble diagram constructed with nearby supernovae from Hamuy *et al.* and high redshift supernovae from the Cosmology Project. m_B max is the apparent corrected peak magnitude in the B band. The top, middle and bottom curve correspond to $(\Omega_M, \Omega_\Lambda) = (0,0), (1,0), (2,0)$. b) Hubble diagrams constructed from the Calan-Tololo nearby color-selected supernovae sample. m_V max is the apparent peak magnitude in the V band. On top panel, no correction has been applied whereas on bottom panel, the experimental peak luminosity-decline rate dependence has been used to assign each supernovae its true absolute magnitude.

value of H_0 and the absolute magnitude at maximum:

$$\mathcal{M} = M - 5\log H_0 \tag{2}$$

Thus, the Hubble diagram $m - \log(cz)$ alone cannot yield the value of H_0. A calibration of the absolute magnitude M at maximum for type Ia supernovae has to be obtained first by using a redshift independent distance indicator, like Cepheids for example. Then the Hubble diagram with intermediate redshift supernovae, together with this calibration, can be used to derive the value of H_0 (see M. Hamuy[5], A.G. Riess[8], A. Saha[9] and D. Branch[2] for a general review).

At greater distances, in the high redshift range ($z > 0.5$), the relationship $m - \log(cz)$ is no longer linear, and a correction has to be added to equation 1, depending on the redshift z, the density paramter Ω_M and the cosmological constant Ω_Λ (figure 1-a) :

$$m = M - 5\log(H_0) + 5\log\left(cz\,\mathbf{f}(z;\Omega_M,\Omega_\Lambda)\right) + 25 \tag{3}$$

The cosmological parameters Ω_M and Ω_Λ are measured independently of H_0 by estimating the deviation at $z > 0.5$ from the linear part at $z < 0.2$ [6]. Obtaining a homogeneous sample of type Ia supernovae at intermediate redshift would improve the constraint on the linear part of the Hubble diagram.

However, type Ia supernovae samples exhibit a scatter in peak brightness magnitude up to $\sigma \sim 0.4 - 0.5$ mag.[1]: type Ia supernovae can no longer be considered as perfect standard candles. Luckily, various ways to standardize them have been found, either by selecting a subsample of "normal supernovae", and assigning each of them the same peak magnitude, or by estimating for each supernova its "true" peak magnitude, using the observed correlations between the peak brightness and some distant independant observables. These methods succeed in reducing the scatter down to $\sigma \sim 0.2$ mag. In figure 1-b, adapted from Hamuy *et al.*[5], a Hubble diagram constructed with nearby color-selected type Ia supernovae before and after correction for the peak lumosity-decline rate dependence is presented. These standardisation techniques are applied to high redshift supernovae to determine their true magnitudes before they enter the Hubble diagram, but are based on intermediate redshift supernovae observations. Obtaining a larger sample of accurately measured type Ia supernovae is thus a crucial issue.

3 Intermediate redshift supernovae searches

They are about half a dozen ongoing search for supernovae at intermediate redshifts. Although some searches like the *Second Palomar Sky Survey* directed by Jean Mueller rely on visual scanning of photographic plates, most supernovae searches at intermediate redshifts are using CCD techniques. The *Calan-Tololo Supernovae Search Search* ended in 1993 and yielded around 30 accurately measured type Ia supernovae discovered with photographic plates (Hamuy *et al.* [4]). They are now engaged in a new search. The *Mont Stromlo Abell Cluster Supernovae Search* is running since 1996 and is monitoring 70 Abell clusters with the MACHO Group 1.3-m telescope, in the $0.02 < z < 0.08$ redshift range. They have discovered about 20 supernovae (Reiss *et al.* [7]), using CCD techniques. Very similar is the recent *University of Texas - Mac Donald Observatory Supernovae Search*: they are monitoring 70 Abell clusters up to a redshift of 0.15, using a 0.76-m telescope. I shall detail our own search in the next section.

4 EROS supernovae search first results

EROS-2 consists of three observing programs: EROS is at first a microlensing project, that began in 1990. EROS also performs a red and white dwarfs proper motion survey and an intermediate distance supernovae search. EROS-2 uses a completely refurbished and fully automated 1-m telescope, in operation at the European Southern Observatory at La Silla, Chile. A dichroic cube allows the simultaneous imaging in two wide pass-bands of a 1 square degree field, each color channel being covered by an 8-CCD camera.

EROS-2 supernovae search aims at discovering a homogeneous supernova sample in the redshift range $0.05 < z < 0.2$. Because we are using CCD techniques, the efficiency of the search can be derived, and we should finally obtain a sample at $z \sim 0.1$ for which the systematics will be known. Such a sample of supernovae in the linear part of the Hubble diagram can be used to study supernovae characteristics and measure relative type II/type I rates. Although supernovae detection is performed on the EROS telescope, photometric and spectroscopic follow-up must be done on other telescopes.

Our strategy is quite standard: we subtract two frames of the same field taken at least three weeks apart and search the subtracted frame for new stellar point sources. The technique is illustrated on figure 2. The fields are chosen away from the Galactic Plane and taken when the

moon is set with a 10 minutes exposure time. Each month, during a five-day run, about 10 square degrees (1 Gbytes of data) are monitored each night.

Our discovery rate of 1 supernova per 10 square degrees, or equivalently 2 hours of observing time, has been confirmed during this fall runs. Around 100 square degrees were monitored in October and November 1997 and yielded 9 supernovae with a redshift in the range $0.03 < z < 0.17$. A very peculiar event was observed, two type Ia supernovae exploding 50 days apart in the same galaxy.

The photometric follow-up was achieved on the EROS telescope, and on the Danish 1.5-m telescope at ESO. The spectroscopic follow-up was performed on the ARC telescope at Apache Point Observatory although we also benefited from courtesy time at ESO.

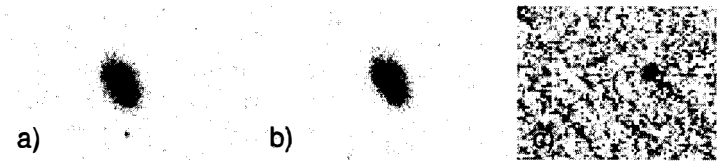

Figure 2: a) The host galaxy on the reference frame at a redshift z∼0.1. b) The galaxy and its supernova, which can barely be distinguished from the galaxy nucleus. c) The subtracted frame, obtained after pixel and flux alignment of a) and b) frames. The stars PSF are matched by convolving the best image. The supernova now stands alone.

The fisrt part of our project is achieved: EROS is now regularly discovering new supernovae. To fulfill the second part of our project, we are now working on obtaining and studying photometric and spectroscopic data on our supernovae sample.

5 Conclusion

Whereas the measurement of Ω_M and Ω_Λ is achieved with high redshift supernovae (The Cosmology Project[6] and the High-Z Team[10]), the various ways to correct their apparent magnitude before they enter the Hubble diagram are derived on nearby supernovae[5]. Obtaining a sample of intermediate redshift supernovae with a well understood search efficiency has thus become a crucial issue for the estimation of the cosmological parameters. EROS search for supernovae at intermediate distance is now in full operation, with a total of 11 discovered supernovae. Our discovery rate of 1 supernova per 2 hours of observing time makes it possible to schedule the discovery of small supernovae samples each month. We are now focusing on gathering photometric and spectroscopic data.

References

1. D. Branch & D. L. Miller, ApJ 405, L5 (1993)
2. D. Branch, astro-ph/98101065
3. R.G. Eastman, ApJ 466, 911-937 (1996)
4. M. Hamuy *et al.*, Astron. J. 112, 2391-2397 (1996)
5. M. Hamuy *et al.*, Astron. J. 112, 2398-2407 (1996)
6. S. Perlmutter *et al.*, astro-ph/9712212
7. D.J. Reiss *et al.*, Astron. J. 115, 26-36 (1998)
8. A.G. Riess *et al.*, ApJ 473, 88 (1996)
9. A. Saha *et al.*, ApJ 486, 1-20 (1997)
10. B.P. Schmidt *et al.*, IAU Circ. No. 6646

A REVIEW OF THE HIGH-REDSHIFT SUPERNOVA SEARCHES

A.G. KIM
PCC, Collège de France, 11, Place M. Berthelot,
75231 Paris, France

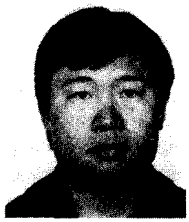

Observations show that Type Ia Supernovae (SNe Ia) form a homogeneous class of objects. They share similar spectroscopic evolution, light-curve shapes, and peak absolute magnitudes. The slight departures from homogeneity that are observed can be used to produce a "calibrated candle" with corrected magnitudes with even smaller dispersion. The existence of this intrinsically bright distance indicator has inspired two coordinated high-redshift supernova searches: the Supernova Cosmology Project and the High-z Supernova Search Team. To date $\sim$ 100 SNe Ia have been discovered by the two groups. The preliminary analysis of the first of these objects demonstrate how well SNe Ia can be used to measure the mass density of the universe Ω_M and the normalized cosmological constant $\Omega_\Lambda \equiv \Lambda/3H_0^2$.

1 Introduction

For the past several years, two independent groups have been discovering and following high-redshift supernovae ($z > 0.3$) using telescopes from all over the world and beyond. The lofty and imposing goal of these searches? To determine the ultimate fate of the universe! But before I tell you what the answer is (so far), I should explain what makes supernovae so special and give you an idea of what's been observed to date. Then comes the answer, along with a discussion of some of the systematic errors involved and how we can address them. I conclude by presenting the scientific course we plan to take in the near future.

2 Type Ia Supernovae as Distance Indicators

One of the big reasons that supernovae are exciting for cosmologists is because of the remarkable homogeneity of the type Ia's (SN Ia) [a]. This homogeneity is seen in their evolving spectra

[a]The supernova classification system is empirical and is based on the spectrum, SNe Ia exhibit no hydrogen (hence the "I") and have strong silicon P-Cygni features (hence the "a") during their photospheric phase.

(Filippenko[1]), their light-curve shapes (Leibundgut[2]), and their peak absolute magnitudes which have a dispersion of $\sigma \approx 0.3 - 0.5$ mag depending on the sample (Branch and Tammann[3]). SNe Ia are also whoppingly bright, at peak they can emit as much light as their host galaxy. This combination of brightness and homogeneity means that they can be used to measure distances out to very high redshifts.

The standard model for the SNe Ia progenitor system has a white dwarf in a binary system accreting matter from its companion until it reaches the Chandrasekhar mass ($\sim 1.4 M_{\odot}$) triggering a thermonuclear runaway which we observe as a supernova. This idea neatly explains the homogeneity and the lack of hydrogen in the spectra. Detailed theoretical work has provided strong support for this model (Nomoto *et al.*[4]) although there are a few outstanding questions that have to be resolved, for example the nature of the binary companion and the hydrodynamics of flame propagation.

Strong evidence for intrinsic *in*homogeneity first came with the light curves of the Calán-Tololo supernova search. It was shown that the light-curve shape was correlated with the supernova peak brightness in such a way that the slow decliners tend to be brighter than the rapid decliners (Hamuy *et al.*[5]; Riess, Press, and Kirshner[6]). The slow decliners were also bluer in the optical passbands (Riess, Press, and Kirshner[7]) and had a much stronger UV flux (Branch, Nugent, and Fisher[8]). The line ratios of particular spectral features at maximum light also vary with light-curve shape, an effect that has been modeled as being due to differences in the supernova's photospheric temperature (Nugent *et al.*[9]).

We can take advantage of this inhomogeneity by using relations between the absolute magnitude and these other independent observables to produce a "calibrated candle" with an even tighter absolute magnitude dispersion than before. Such corrections using light-curve shapes yield corrected magnitude dispersions of $\sigma \simeq 0.18$ mag.

Note that $\mathcal{M} \equiv M - 5 \log H_0 = m - 5 \log(cz)$ is the "absolute magnitude" accurately measured for supernovae in the Hubble flow. It is not sensitive to the uncertainty in the Hubble constant and so is used in lieu of the true absolute magnitude.

3 The Searches

There are currently two independent teams that are running coordinated search and follow-up observations of high-redshift supernovae. They are the Supernova Cosmology Project (SCP) (Perlmutter *et al.*[10]) which was launched in 1989, and the High-Z Supernova Search Team (HIZ) (Garnavich *et al.*[11]) which found their first supernova in 1995. Both teams use similar techniques (described in detail in Perlmutter *et al.*[12]) and resources as follows.

A special strategy is needed to find these rare and random events. Several days after new moon, a series of wide-field images are taken on a 4-m class telescope, with each field containing over a thousand galaxies that can potentially host a supernova. Several weeks later the same fields are re-observed and scanned for new point sources. After applying cuts to reject asteroids, AGN, quasars, cosmic rays, and other sources of background, we are left with supernova candidates. Having run the search right before new moon we have optimal observing conditions for pre-scheduled spectroscopy to identify the candidates, and photometry to build their multi-band light curves. The three week gap in the search is well matched for the ~ 20 day (rest frame) rise time for SNe Ia, meaning that most all the supernovae will be discovered before or at maximum light. With the allocated search time (typically a pair of two nights) both groups have been yielding ~ 12 supernovae per run.

Most of the current searching is performed on the 30'x30' field of the BTC at the CTIO Blanco Telescope. With its 10-m diameter collecting area, the Keck Telescope is the spectroscopic workhorse for both groups, allowing us to efficiently observe and confirm a large number of faint candidates. Photometric follow-up is performed at a host of 2 to 4-meter telescopes all

around the world.

In total, there have been $\sim$ 100 SNe Ia with spectral confirmation discovered at $z > 0.3$ by the two groups. Histograms describing their redshift distributions are given in Figure 1. The mean redshifts of the discovered supernovae have been steadily increasing with each successive search run, as we have specifically tailored the filters and exposure times to search at progressively larger distances.

Even though we have been chugging along doing practically the same thing for several years, there are a couple of new developments that I find exciting. We now have found 4 supernova with $z > 0.8$ and we expect that number to grow quickly. By pushing our detectors to the limit, we could search even deeper than we are now. (The furthest supernova to date with a confirmed SN spectrum is SN1998I at $z = 0.89$, discovered by the HIZ group.) Both groups have scheduled HST time for photometric follow-up, giving us precise photometry and host morphology identification. Furthermore, at higher redshifts a supernova's rest-frame optical light reaches us in the infra-red. The HST NICMOS camera (while it lasts) gives us a superior view in this wavelength regime than would be possible from the ground. The first results using the HST data have already been published (Perlmutter *et al.*[10]; Garnavich *et al.*[11]).

4 Measurement of Ω_M and Ω_Λ

By using SNe Ia as distance indicators, we can measure the cosmological parameters. The standard Friedmann-Lemaître cosmology gives a magnitude-redshift relation as a function of Ω_M and the normalized cosmological constant $\Omega_\Lambda \equiv \Lambda/3H_0^2$:

$$m_R(z) = \mathcal{M}_B + 5\log(\mathcal{D}_L(z;\Omega_M,\Omega_\Lambda)) + K_{BR}, \tag{1}$$

where K_{BR} is the K correction relating B magnitudes of nearby SNe with R magnitudes of distant objects (Kim, Goobar, and Perlmutter[13]) and the "absolute magnitude", $\mathcal{M}_B$, is determined using local supernovae in the Hubble flow. (Recall that it is $\mathcal{M}_B$ that depends on the light curve shape.) Here we use $\mathcal{D}_L$, the "Hubble-constant-free" part of the luminosity distance, d_L:

$$\mathcal{D}_L(z;\Omega_M,\Omega_\Lambda) \equiv d_L H_0 = \frac{c(1+z)}{\sqrt{|\kappa|}} \quad \mathcal{S}\left(\sqrt{|\kappa|}\int_0^z \left[(1+z')^2(1+\Omega_M z') - z'(2+z')\Omega_\Lambda\right]^{-\frac{1}{2}} dz'\right), \tag{2}$$

where for $\Omega_M + \Omega_\Lambda > 1$, $\mathcal{S}(x)$ is defined as $\sin(x)$ and $\kappa = 1 - \Omega_M - \Omega_\Lambda$; for $\Omega_M + \Omega_\Lambda < 1$, $\mathcal{S}(x) = \sinh(x)$ and κ as above; and for $\Omega_M + \Omega_\Lambda = 1$, $\mathcal{S}(x) = x$ and $\kappa = 1$, where c is the speed of light in units of km s^{-1}.

What these equations show is that the difference between the absolute and observed magnitudes of a supernova at a given redshift corresponds with a strip (a line if we don't include uncertainties) in the Ω_M – Ω_Λ plane. Furthermore, the shape and orientation of the band are different at different redshifts, meaning that supernova measurements from a wide range of redshifts have confidence regions whose intersection gives a closed area in the Ω_M – Ω_Λ plane (Goobar and Perlmutter[14]). This allows us to make a simultaneous measurement of Ω_M and Ω_Λ with the added bonus the answer does not depend on the Hubble constant.

Both groups have published results from the first handful of supernovae found (Perlmutter *et al.*[15]; Perlmutter *et al.*[16]; Perlmutter *et al.*[10]; Garnavich *et al.*[11]). I will present here the preliminary results from the analysis of the first $\sim$ 40 supernovae from SCP. Results from the HIZ collaboration are presented in Leibundgut's paper in these proceedings and a new paper based on their first $\sim$ 15 events is in the works.

Figure 2 shows the preliminary confidence regions in the Ω_M – Ω_Λ plane for the first $\sim$ 40 SCP supernovae. The length of the region shows that at the moment we cannot simultaneously

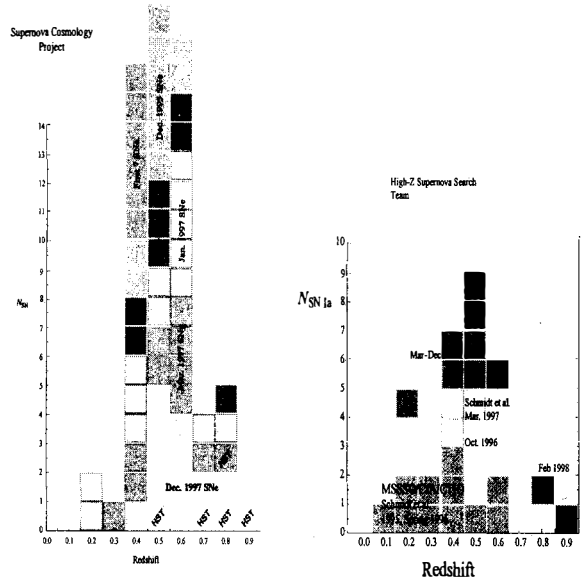

Figure 1: The redshift distributions of the SNe Ia found by the two searches. Note that four of the first seven SCP supernovae shown do not have spectroscopic confirmation.

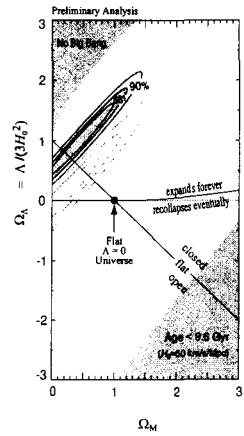

Figure 2: Preliminary confidence regions from the first $\sim$ 40 SCP supernovae. The confidence regions are strictly statistical, the lower contours show the results if there is a 0.2 magnitude systematic difference between local and distant supernovae.

constrain Ω_M and Ω_Λ down to an interesting level because we currently lack a large number of $z > 0.8$ supernovae. The skinniness of the region is due to the reduced statistical error from the large number of supernovae observed at $z \sim 0.5$. It allows us to make statistically significant measurements of the cosmological parameters if we assume a flat ($\Omega_M + \Omega_\Lambda = 1$) universe, $\Omega_M = 0.025 \pm 0.06 \pm 0.3$, or a $\Lambda = 0$ universe, $\Omega_M = -0.4 \pm 0.1 \pm 0.5$, where the first error is statistical and the second is an estimate of systematic error. Of profound interest is the fact that our supernovae strongly disfavor the flat $\Lambda = 0$ universe predicted by the simplest theories of inflation. Fortunately the HIZ team is getting similar results.

5 Systematics

Its clear that our results are now limited by systematic errors and that these errors need to be seriously addressed. The confidence regions shown in Figure 2 are calculated using only our statistical uncertainty. To illustrate the effect of systematic errors, we plot a second set of contours in Figure 2, which show how our confidence region would shift if high-redshift supernovae were systematically 0.2 mag fainter than the nearby calibrators, (while maintaining the same light-curve shapes). Systematic errors generally have the effect of shifting our contours in the $\Omega_M - \Omega_\Lambda$ plane, smearing the confidence of our measurement. Detailed descriptions of how we handle some of these systematics are given in Perlmutter *et al.*[16]

Malmquist bias is a fancy way of saying that in a magnitude limited sample, we are more likely to observe intrinsically brighter objects. For a given redshift, this produces a shift in the mean observed magnitude as compared to the intrinsic mean. Such an effect in our distant supernova would cause us to overestimate Ω_M so corrections for this effect would moves us even further from a $\Lambda = 0$ flat universe. To measure the influence of Malmquist bias, we have determined the detection efficiencies and thresholds for our search and performed a fit using only the subsample of supernovae found far from the detection limit; no statistically significant change in Ω_M–Ω_Λ is seen. More disturbing is the fact that the effect of Malmquist bias on the local calibrators is not easily calculable. Many of the nearby supernovae were found either randomly or on photographic plate searches. A correction for Malmquist bias in the nearby sample would move us closer to a $\Lambda = 0$ flat universe. What is now needed is a determination of the intrinsic population of SNe Ia from a large sample of local supernovae found in CCD searches with known detection efficiencies. The similar distributions currently seen in high-z and local light-curve shapes do indicate there is no large relative difference in the effect of Malmquist bias in the two samples.

There is no guarantee that local and distant supernovae are exactly the same. One may expect systematic differences in the progenitor system metallicity or in the white dwarf C/O ratio. Our most powerful test for evolution is with the comparison of distant and nearby supernova spectra, because in spectra we should see the effects of different initial progenitor compositions (Höflich, Wheeler, and Thielemann[17]). Fortunately no such spectral redshift evolution has been noted in the spectra observed to date, e.g. SN1997ap at $z = 0.83$ (Perlmutter *et al.*[10]). Important information could also come from supernovae at $0.1 < z < 0.3$ because it is feasible to obtain spectral time series which could show the first effects of redshift evolution.

In order to see the effect of extinction, we have compared the k-corrected color distributions of the local and distant supernovae. The negligible difference between the two indicates that the samples have similar $E(B-V)$ distributions. We also directly fit $E(B-V)$ for each supernova using the multi-band data and again find similar distributions for the two sets. Work is currently being performed to try to reduce the errors involved in individual supernova corrections. The fairly large uncertainty in $B-V$ for supernova at maximum as a function of light-curve shape translates into a large correlated uncertainty in magnitude absorption. In addition the extinction properties (R_B) at high-redshift are not well known.

There are population effects that can be seen in local supernovae. For example, supernovae in ellipticals on whole have skinnier light curves and are fainter than their spiral counterparts. The magnitude–light-curve shape relation in principle corrects such effects. However, considering all the possible population dependencies, we would like to select local and distant supernovae subsets that share as many population characteristics as possible. The steady stream of new nearby supernovae coming from a wide range of environments will allow us to do this.

We currently believe that we understand the effects of most of these systematics, at least to first order. We await new data from high-quality nearby supernovae searches to confirm our findings and to give us even stronger constraints on our errors. Specifically, the new data will supply us with the intrinsic supernova luminosity function and a large homogeneous set of light curves that start before maximum. The data will also provide us with large sample from which we can select subsamples with which to explore systematic errors.

6 Conclusion

We can confidently say that our data disfavors an $\Omega = 1$, $\Lambda = 0$ universe, considering the huge amount of systematic error required to make the two consistent. For the future, we need to pursue two opposite directions in order to get a more precise value of the cosmological parameters. By finding more supernovae at $z > 0.8$, we will attempt to reduce the length of the contour in Figure 2 to give a better simultaneous measurement of Ω_M and Ω_Λ. By finding supernovae at $z < 0.2$ we will learn more about their intrinsic properties and give a larger sample with which we can study and hopefully reduce systematic effects. SCP is now dedicating a large part of its efforts in nearby supernova searching, and in collaboration a group of French scientists is planning to use the CFHT specifically for $z > 0.8$ searches. (HIZ's most distant candidate was in fact found using the CFHT). Members of the HIZ team are already heavily involved in nearby searches and as a whole are pursuing higher redshifts. With all this focused activity, reduction of the systematic and statistical errors should not be far off in the future.

References

1. A. V. Filippenko. *ARAA*, 35:309, 1997.
2. B. Leibundgut. PhD thesis, University of Basel, 1988.
3. D. Branch and G. A. Tammann. *ARAA*, 30:359, 1992.
4. K. Nomoto, H. Yamaoka, T. Shigeyama, S. Kumagai, and T. Tsujimoto. In *Supernovae : Les Houches, session LIV)*, page 199. North-Holland:Amsterdam, 1994.
5. M. Hamuy, M. M. Phillips, N. B. Suntzeff, R. A. Schommer, J. Maza, and R. Aviles. *AJ*, 112:2391, 1996.
6. A. G. Riess, W. H. Press, and R. P. Kirshner. *ApJ*, 438:L17, 1995.
7. A. G. Riess, W. H. Press, and R. P. Kirshner. *ApJ*, 473:88, 1996.
8. D. Branch, P. Nugent, and A. Fisher. In *Thermonuclear Supernovae*, page 715. Dordrecht:Kluwer, 1997.
9. P. Nugent, M. Phillips, E. Baron, D. Branch, and P. Hauschildt. *ApJ*, 455:L147, 1995.
10. S. Perlmutter *et al. Nature*, 391:51, 1998.
11. P. M. Garnavich *et al. ApJ*, 493:L53, 1998.
12. S. Perlmutter *et al.* In *Thermonuclear Supernovae*, page 749. Dordrecht:Kluwer, 1997.
13. A. G. Kim, A. Goobar, and S. Perlmutter. *PASP*, 108:190, 1996.
14. A. Goobar and S. Perlmutter. *ApJ*, 450:14, 1995.
15. S. Perlmutter *et al. ApJ*, 440:L41, 1995.
16. S. Perlmutter *et al. ApJ*, 483:565, 1997.
17. P. Höflich, J. C. Wheeler, and F. K. Thielemann. *astro-ph/9709233*, 1997.

Cosmic Deceleration measured with Type Ia Supernovae[a]

B. Leibundgut and J. Spyromilio
European Southern Observatory, Karl-Schwarzschild-Strasse 2
D-85748 Garching, Germany

With the observations of distant type Ia supernovae cosmological parameters can be measured with an unprecedented accuracy. It is found that the distant supernovae appear dimmer than expected in an empty universe indicating contributions by the vacuum energy density. Systematic errors are the largest uncertainties at the moment. Evolution, extinction, weak lensing, and sample discrepancies are the most important ones. All these systematics can in principle be tested observationally. The current data sample also indicates an age of the universe which is consistent with the oldest stellar components of the Galaxy.

1 Introduction

Type Ia Supernovae (SNe Ia) have proven to be excellent distance indicators when treated suitably[1,2]. They have several virtues that come with standard candles, even though they are not pure standard candles themselves. Combined with the high luminosity of the objects, which makes them detectable out to redshifts near 1, they can be used to measure cosmological distances and provide a determination of the deceleration of the universe[3,4]. The light curve shape corrections, however, are purely empirical and have changed considerably since their first application. Attempts to explain the empirical correlation between the peak luminosity and the decline rate of SNe Ia after maximum are still controversial.

With samples of nearby ($z < 0.1$) and distant ($z > 0.3$) supernovae we can measure the curvature of the universe and any possible contributions of a vacuum energy density based on luminosity distances. The deceleration can be determined by comparing the distant supernovae with the local sample[4,5]. Two experiments are trying to make use of SNe Ia to achieve a

[a]We report results by the High-z Supernovae Search Team. Members of the team are P. Challis, A. Clocchiatti, A. Diercks, A. Filippenko, P. Garnavich, R. Gilliland, C. Hogan, S. Jha, R. Kirshner, M. Phillips, D. Reiss, A. Riess, B. Schmidt, R. Schommer, C. Smith, C. Stubbs, N. Suntzeff, J. Tonry, and P. Woudt.

determination of the deceleration[6,7,8,9,10,11]. We report here the recent results obtained by the High-z SN Search Team.

2 Type Ia supernovae as distance indicators

The light curves and spectral evolution show distinct variations among individual events. In particular the near-infrared light curves show a second maximum for many, but not all, SNe Ia[12]. The strength of the second maximum changes considerably and is also distinguishable in bolometric light curves[13].

A generally accepted theory of SN Ia explosions has not emerged yet. For more than a decade explosion models with a subsonic burning front have been favored[14,15], but the physics which sustains such a burning front without turning it into a detonation is not understood. New models which explode a white dwarf through He detonation at the surface[16,17], rather than the direct explosive carbon burning inside, cannot be distinguished by the current observations[18]. The exact trigger of the explosion and the reaction of the white dwarf is not constrained by observations and many models have been proposed. The radiation transport is largely unsolved. The supernova radiation is not thermalized in the ejecta and the observed pseudo-continuum is dominated by line radiation. A simple way to see this, is provided by the fact that the occurrence of maximum in the observed filter light curves does not indicate a cooling shell, but rather a very complex redistribution of the emission[13]. The bolometric light curves display the characteristic shoulder of the near-infrared light curves and the total energy changes from event to event.

Despite the lack of understanding of the explosion physics, observational trends have been found to account for the light curve and luminosity variations. The correlation between luminosity and light curve decline is well established[1,2]. The rest-frame colors are good indicators of reddening towards a supernova and extinction corrections can be applied. In this sense, SNe Ia appear to be an ordered set and can empirically be used as distance indicators.

3 Ω_M and Ω_Λ from SNe Ia

The determination of the cosmological energy density rests on the measurement of objects distant enough so that the curvature of the universe becomes significant. SNe Ia discovered at redshifts larger than 0.3 are very well suited for such an investigation.

Garnavich et al.[9] and Riess et al.[11] report the results from samples which include about 30 SNe Ia in the local sample and 10 objects at redshifts $z \geq 0.3$. With the exception of the most distant object, SN 1997ck at $z = 0.97$, all objects have been classified by a spectrum and detailed light curves in at least two filters are available, which allows us to apply the light curve corrections, either template fitting and the Δm_{15} analysis[1,19] or MLCS[2]. The color information is essential to obtain an estimate of the extinction towards the supernova. The local sample is used to determine the correlations between light curve shape and luminosity which are then applied to the distant supernovae.

Of fundamental importance are systematic effects which can alter the result. Several technical steps lead to the luminosity distances. Accurate photometry of faint sources on a spatially variable background, phase-dependent K-corrections, and light curve determinations have to be applied. All of these corrections have been tested independently in several applications[10,11].

Other uncertainties are introduced by the light curve shape correction, extinction, evolution between the distant and the nearby supernovae, sample selection, and (de-)magnification due to gravitational lensing. A careful analysis can test for all effects with the exception of gravitational lensing which is achromatic and static. The systematic influence of weak lensing, however, is expected to be very small[20].

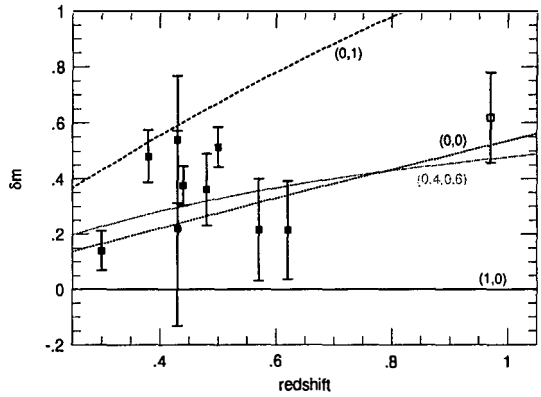

Figure 1: Magnitude difference from an Einstein-de Sitter Universe ($\Omega_M = 1, \Omega_\Lambda = 0$). The empty case ($\Omega_M = 0, \Omega_\Lambda = 0$) and a mixed model with ($\Omega_M = 0.4, \Omega_\Lambda = 0.6$) are also indicated. The observed δm for the supernovae are based on B and V light curves. SN 1997ck is shown as an open symbol.

A luminosity shift between SNe Ia in early and late type galaxies has been observed. This has been attributed to the different ages, masses, or metalicities of the progenitor population. The light curve corrections can successfully neutralize the offset and the luminosity difference between samples in elliptical and spiral galaxies can be reduced to 0.05 magnitudes[10]. This is an indication of what has to be expected for a comparison between the nearby and the distant sample. A critical parameter appears to be the C/O composition of the progenitor white dwarf[21]. Extinction can be detected through the color of the supernovae. Very few distant objects appear reddened[9,11]. There is a bias which favors discovery of unabsorbed objects due to the luminosity and also the selection of objects well separated from the host galaxy. The latter is not a true selection by the search, but rather is applied when decisions on the follow-up observations are taken. Thus, the absorption in the distant sample is likely to be less on average than in the nearby sample.

Of paramount importance is the concordance of the nearby and the distant supernova sample. Any systematic shift between the two would result in a distortion of the derived cosmological parameters. Contamination by objects which are not SNe Ia has to be avoided. The spectroscopy and the light curves provide ample information to make such a distinction, but there is at least one case where a luminous SN Ic could not be excluded[11]. No classification of SN 1997ck, with no observed supernova spectrum and only one filter light curve, is available. The light curve is, however, consistent with a SN Ia at the observed galaxy redshift[9,5]. An obvious systematic effect would be different average luminosities of the two samples. To first order, this can be tested by comparing the light curve shapes. For our sample of 10 distant and 27 nearby supernovae the average Δ of the MLCS method is -0.126 and -0.147 for the nearby and the distant sample, respectively. The systematic offset is thus 0.02 magnitudes, which is negligible. The weighted mean Δm_{15} for the local sample is 1.296, while the distant sample has 1.184 on average. This difference translates into a zero-point offset of 0.09 magnitudes using the second order treatment proposed by Phillips et al.[19] The local sample is on average less luminous than the distant one.

Figure 1 displays the magnitude difference of the observed supernovae from an Einstein-de Sitter Universe ($\Omega_M = 1, \Omega_\Lambda = 0$). Many objects lie above the line for an empty universe (0,0) and thus indicate a contribution of the vacuum energy to the energy density of the universe.

The 10 distant supernovae appear to be too dim even for an empty universe. The magnitude offset is 0.11 ± 0.03 magnitudes. However, the RMS of the distribution is 0.19 magnitudes. Excluding SN 1997ck does not change the values.

An analysis based on probability density functions finds that no solution for a positive matter density ($\Omega_M > 0$) exists, if $\Lambda = 0$ at a $> 2.5\sigma$ significance from both methods[11]. This confirms the preliminary result presented by Garnavich et al.[9] and is also in accordance with the one reported by Perlmutter et al.[7] Due to the rather limited range of redshifts an exact value for Ω_M and Ω_Λ cannot be derived yet without further constraints.

4 Conclusions

The analysis of our distant set with two slightly different methods resulted in a signature of a positive cosmological constant barring undetected systematic errors. A universe with negligible Λ is (statistically) excluded at the 2.5 σ level, as no solution with a positive matter density is found. The effect is so strong that the value of the deceleration parameter q_0 is negative[11] which indicates an accelerated expansion over the time span sampled by our observations (5 Gyr).

The dynamic age shows a dependency very similar to the uncertainty regions determined by the supernovae. It is thus possible to restrict the dynamic age of the universe quite accurately. Riess et al.[11] find values in the range of 13 to 15 Gyr which is consistent with most age determination of the oldest stellar components.

Essential issues remain the systematic uncertainties of the experiment. The magnitude offset from an empty universe model is very small ($\sim$0.1 mag) and even small systematic effect are important. Evolution, extinction and sample selection are the most important contributors. The only checks for evolution are extensive observations of distant objects to detect any differences with nearby supernovae. A spectroscopic sequence with good signal would allow us to investigate small differences in the ejecta. There are clear signatures in the R and I light curves of SNe Ia which can be observed for objects with $z < 0.4$.

References

1. Hamuy, M., et al. 1996a, AJ, 112, 2398
2. Riess, A. G., Press, W. M., & Kirshner, R. P. 1996, 473, 88
3. Carroll, S. M., Press, W. H., & Turner, E. L. 1992, ARA&A, 30, 499
4. Goobar, A., & Perlmutter, S. 1995, ApJ, 450, 14
5. Leibundgut, B. 1998, Supernovae and Cosmology, eds. L. Labhardt, B. Binggeli, & R. Buser, Basel: University of Basel, in press (astro-ph/980169)
6. Perlmutter, S., et al. 1997, ApJ, 483, 565
7. Perlmutter, S., et al. 1998, Nature, 391, 51
8. Leibundgut, B., et al. 1996, ApJ, 466, L21
9. Garnavich, P., et al. 1998, ApJ, 493, L53
10. Schmidt, B. P., et al. 1998, ApJ, in press
11. Riess, A. G., et al. 1998, AJ, submitted
12. Suntzeff, N. B. 1996, IAU Colloquium 145: Supernovae and Supernova Remnants, ed. R. McCray, (Cambridge: Cambridge University Press), 41
13. Contardo, G., Leibundgut, B., & Vacca, W. D. 1998, in preparation
14. Nomoto, K., Thielemann, F.-L., & Yokoi, K. 1984, ApJ, 286, 644
15. Woosley, S. E., & Weaver, T. A. 1986, ARA&A, 24, 205
16. Arnett, W. D., & Livne, E. 1994, ApJ, 427, 315
17. Woosley, S. E., & Weaver, T. A. 1994, ApJ, 423, 371
18. Branch, D., Livio, M., Yungelson, L. R., Boffi, F. R., & Baron, E. 1995, PASP, 107, 1019
19. Phillips, M. M., et al. 1998, in preparation
20. Wambsganss, J., Cen, R., Xu, G., & Ostriker, J. P. 1997, ApJ, 475, L81
21. Höflich, P., Wheeler, J. C., & Thielemann, F.-K. 1998, ApJ, 495, 617

SUMMARY AND CONCLUSIONS

TODAY'S COSMOLOGICAL CONSTANTS

R.G. CARLBERG
Carnegie Observatories, 813 Santa Barbara Street, Pasadena, CA 91101, USA
on leave from:
Department of Astronomy, University of Toronto, Toronto, M5S 3H8, Canada

Knowledge of the constants that describe the current cosmological world model, H_0, t_0, and the three Ωs is central to physical cosmology. Although there is a vast range of suggested tests and existing constraints much of the recent discussion of cosmological constants involves three time variable photospheres: Cepheids, SNIa, and the CMB last scattering surface. These concluding remarks for the Moriond XXXIII meeting are made at a time when many of the established methods have made careful, interesting, statements about the values of various cosmological constants based on data of small random errors. The flood of new data over the next few years will lead to a satisfying increase in the precision of both direct and model dependent estimates of the main cosmological parameters.

1 Introduction

Commenting on the progress being made in estimating the values of the cosmological parameters has perils not unlike those of critiquing a great artwork, perhaps an opera, while it is being staged for the first time. The problem is that there is no working consensus for the values of the cosmological constants. There are rather wide compromise ranges which accommodate most of the derived values. However the values of the cosmological constants at one end of a compromise range are completely incompatible with those at the other, both in physical meaning and in stated measurement error.

An aspect of cosmological parameter determination that is fascinating for any interested scientist is that it continues to reward an integrated view of the entire subject from trigonometric parallaxes to photometric response functions to radio interferometric mapping to X-ray plasma analysis to the outer limits of particle theory, to name but a few. Martin Rees has described Cosmology as the "Grandest of the Environmental Sciences" [17] which serves to remind us of the difficulty of relating the observations of the universe to the simple cosmological models of

interest. Although the FRW model and an interest in its parameters have been around for a long time, it was not until the 1980's when development of solid state detectors of very low noise and very high quantum efficiency allowed virtually every waveband used by astronomy to greatly increase both the quality and the abundance of data. The objects now examined range from nearby white dwarfs to galaxies at redshifts beyond 5, to precise measurements of the CMB radiation all over the sky.

The following discussion discusses the broad comprise ranges for the basic cosmological parameters. In most cases the data have small random errors. The problems for all methods come in calibration and model uncertainties. For instance Cepheids distances have random errors of about 1%, nevertheless the total error in the Hubble constant is generally quoted to be at least 10 times larger as a result of potential calibration and systematic errors. Even those apparently large error budgets are hard won from vast efforts to control, measure and remove systematic errors. The true error ranges of these are continuing to shrink significantly and steadily, such that sometime in the next decade our understanding will undergo a phase transition, hopefully a crystallization not a meltdown.

2 t_0

The age of the Universe is currently most accurately measured from the Globular Clusters in our own galaxy. This is an impressively mature subject which interprets very high precision photometry using immensely detailed physical models of relatively simple stars. There have been two slightly startling developments in the past few years. First, when allowance was made for helium diffusion [14] the ages of globular clusters came down about 10%. Second, the Hipparcos satellite provided new distances to local subdwarf stars which can be used to calibrate the distance to similar stars in globular clusters. The surprise was that the distances were somewhat larger than anticipated, meaning that the stars were brighter and hence younger. The quoted ages are 11.5 ± 1.5 Gyr [1] and a minimum of 13 Gyr [13]. The physical complexities of confidently predicting the model luminosities in the observed filter bands leads to some further uncertainty. Although the results are statistically compatible, within this range one can draw quite different cosmological conclusions. Since one generally adds 1 Gyr to the Globular cluster ages to derive a t_0 it appears that the traditional first year astronomy values of 12 to 15 Gyr remain acceptable values. There is great excitement that white dwarfs will soon provide an alternate dating method to some of the nearby globular clusters.

3 H_0

In principle, measuring H_0 is simple. In practice it is a dimensional constant which effectively requires carrying the standard meter from the earth to cosmological distances where the fractional perturbations to the Hubble flow are small. The classical methods are entirely geometric, relying on parallax and the $1/d^2$ law, but require building a "distance ladder". A variety of newer methods are single step, but, model dependent. For instance, combining cluster X-ray and Sunyaev-Zeldovich measurements, or, gravitational lenses with measurable time delays between images, gives a quantity that depends on the Hubble constant.

Classical estimation of H_0 has been advanced enormously with CCD photometry and telescopes with greatly improved angular resolution, allowing the brightness of point-like objects to be accurately measured at relatively large distances. Cosmology has always been a matter of dealing with state of the art detection of photons from distant, faint objects which are themselves the focus of research. It is not surprising that it has been slow progress since Hubble's original discovery (whose 1936 book gave a well considered Hubble constant of about 600 km s^{-1} Mpc^{-1}). The Hubble constant search has become a substantial industry with many approaches to the

problem. The HST Key Project [7] to measure Cepheid distances to a representative set of objects in the local supercluster is generally regarded as a piece of bedrock which is a standard rod against which other measurements approaches are calibrated or compared. Although the distances to the various galaxies that have been measured are fairly non-controversial, the implied Hubble constant remains quite controversial. It would be desirable if more SNIa would co-operate and explode in some of these galaxies with carefully measured disteances.

It is impressive that in about the last 10 years the scatter in the values of the Hubble constant have decreased by a factor of two or perhaps a little more[11]. Many would accept that the Hubble constant lies someplace in the range of 55 to 75 km s^{-1} Mpc^{-1}. No one is really comfortable with such a large range. The good news is that the Key Project has more results to announce, and the rate at which data are being collected in other approaches to this problem is increasing. The next 10 years will see total errors reduced another factor of two, which should lead to consensus of some sort.

Newer methods like the SZ/X-ray technique [2,15] or the gravitational lens time delay measurements [18] are promising one-step methods with simple physics, however in both cases the results at the moment have a fairly large scatter compared to classical estimators and there remain genuine complications in modelling the potentials involved in the cluster potentials and the the lensing potentials. On the other hand, the interest, effort and data quality of these new methods are ascending very rapidly.

4 The Three Ωs

The three controversial Ωs are the Ω_B, Ω_X, and Ω_Λ, the density parameters of the baryons, dark matter and the Λ term, respectively. The matter density, $\Omega_M = \Omega_B + \Omega_X$, is the total density of gravitating matter which has no significant pressure. The fourth Ω is that of radiation, which although by far the smallest at the current epoch, is known to fabulously high precision through the measurement of the spectrum of the CMB radiation.

Over the past 10 years there has been a great deal of new work on the baryonic Ω_B which probably hasn't changed the formal error range that much, but, many systematic errors have been reconsidered. The range of quoted values is about a factor of three from the bottom end of the "Helium" value to "low Deuterium" value, $\Omega_B = 0.007 - 0.024h^{-2}$ [19]. Helium is particularly difficult because one needs to derive the primordial abundance from systems that have been partially contaminated with stellar Helium. Deuterium is both very fragile in stars and difficult to observe. Galaxy clusters estimate the baryon fraction, the ratio of the gas plasma baryonic mass to total mass within some radius, $f_B \simeq 0.12 \pm 0.02 h_{50}^{-3/2}$ [21], which is consistent with the BBN Ω_B provided that Ω_M is less than approximately 0.4. This suggests, but does not yet prove, that clusters contain a representative gas-to-mass ratio.

An extremely significant, and confident result, is that although Ω_B is about an order of magnitude larger in gas than in stars, it is still about an order of magnitude less than the total gravitating mass. Hence, the unknown dark matter continues to be the dominant mass in the universe. Another puzzle is that the current location of most of the baryons is not known, with the IGM being the usual suspect, although MACHOs are a new possibility.

The total Ω_M has seen a lot of variation over the past 20 years, coming back to rest someplace near the views of the classic article of the mid-1970's [8], which argued for an $\Omega_M \simeq 0.1$. In spite of the apparent lack of change this subject has gone the full circle with tremendous profit to astrophysics. The circle began when Peebles derived the Cosmic Virial Theorem [16] which helped to provide the motivation for large redshift surveys. One of the first redshift surveys was the CfA, which indicated $\Omega \simeq 0.2$ [4], under the assumption that galaxies trace the mass. About the same time there were two theoretical developments which lead to hesitation in accepting this result. First, inflation [9] argues very persuasively that $\Omega_M = 1$. Second, the concept of formation

of objects at peaks of the density fluctuation field immediately demonstrated that galaxies could be clustered much more strongly than the underlying total mass[10], hence the derived Ω_M could be severe underestimates. Virtually all theorists concluded that in the absence of overwhelming evidence to the contrary, $\Omega_M = 1$. A little later there was the largely unanticipated discovery of large scale flows of galaxies[6] which appeared to be a very strong argument for $\Omega_M \simeq 1$.

In the past few years, the Ω_M tide has reversed to generally favouring lower Ω_M values again. That is, evidence for a low Ω_M that strikes many as overwhelming is gradually being accumulated. A prediction of high Ω_M is that clusters should have an increasing M/L with radius, as the Milky Way galaxy does beyond the disk. However, X-ray, redshift survey and weak lensing data all find that cluster galaxies are distributed like the dark matter to the virial radius. Furthermore, as newer catalogues of peculiar velocities and nearly-all sky surveys become available it appears that the flow fields are actually consistent with Ω_M as low as 0.2 or so[5,3]. Galaxies cannot be completely unbiased with respect to the total matter content of the universe, since various galaxy types and luminosities have different clustering properties. However, it is gradually coming clear that the bias cannot be very large. Much of the community would agree that Ω_M is someplace in the range $0.1 - 0.4$. Direct dynamical data favour $\Omega \simeq 0.2$, but CMB fitting suggests the higher values. Now that much of the community has adopted a low density universe as the most likely model, there is a growing tension between very low Ω_M, those less than 0.2, and moderate Ω_M, those greater than 0.3, which point to some unresolved systematic error in the various data involved.

The most uncertain, and puzzling, of the Ωs is Ω_Λ. Here the measurement situation is far from mature. An upper limit on Ω_Λ comes from the number of split images of distant sources produced by gravitational lensing from intervening galaxies. The very few splittings seen argues that Ω_Λ is less than about 0.7. This argument hasn't changed a lot since the 1980's[20] but it has become a lot more secure as worries about optical selection and evolution in the lensing galaxies have been addressed[12]. The preliminary evidence from the CMB fluctuation measurements (see various contributions to this meeting) is that if Ω_M is low there must be a nonzero Ω_Λ to produce a peak in the angular power spectrum at a sufficiently large angle.

A scientific banquet of ground based, balloon borne and satellite CMB experiments is beginning, such that this meeting stands at a moment when exponential growth of effort is happening in the kitchen, with the expectation that a feast of high quality results begin in about a year. Many of these experiments have made impressive claims for the precision of their measurements, which are certainly true if the instruments perform to specification and the universe and the foregrounds correspond to the various model assumptions.

A completely classical approach to Ω_Λ is the magnitude-redshift relation, which is underway with the SNIa measurements. These objects can be detected and reliably studied up to redshift of one, which provides considerable leverage on the $\Omega_M - \Omega_\Lambda$ pair. The obvious concern is that some unknown evolution or systematic measurement error could creep in. The two teams are well aware of these possibilities and appear to be recalibrating, worrying about the astrophysics and the astronomy as much as anyone else. As much as joint analyses have the power to produce better parameter estimates, one looks forward to independent methods giving completely independent results with small errors, that do agree.

It is impossible to avoid a philosophical note when contemplating the Ω values. That is surely the point. On the other hand, the universe can do what it wants and it is our job to measure and try to understand the results, which is a lesson from the history of particle physics. However, one cannot help but note the conundrums of a Λ dominated universe. If Ω_Λ was much larger than unity, the universe would have started to exponentiate before galaxies (and presumably most stars) ever formed. Similarly even if $\Omega_\Lambda + \Omega_M = 1$, then we are currently well into a round of inflation. We might ask about the prospects for our scientific descendents. Taking a rather modest extrapolation, by astrophysical standards, of 20 times the current age

of the universe, then at that future time there will have been about 20 e-folds of expansion, so the CMB temperature will be nearly zero, the local group will merge with a few satellites left orbiting, and, all other galaxies will have receded to unobservable redshifts. The result is that future astronomers are left in a universe that has one significant galaxy: the merger product of ours and M31. Most peculiar, but, evidently possible within this model framework.

5 Conclusion

The current situation is precisely why the measurement of the cosmological parameters is the primary activity of many astronomers and astrophysicists. The exciting likelihood is that most of the major cosmological constants will be known to a satisfying degree of on the time scale of a decade.

The Moriond meetings provide an ideal format for frank discussion of extremely controversial cosmological issues. I thank the organizers for the splendid job they did in managing to bring us all together and providing a never ending flow of food and stimulus for mind and body.

References

1. Chaboyer, B., Demarque, P., Kernan, P. J. & Krauss, L. M. 1998, ApJ, 494, 96
2. Cooray, A. R., Carlstrom, J. E., Joy, M., Grego, L., Holzapfel, W. L., & Patel, S. K. 1997 (astro-ph/9804149)
3. da Costa, L. N., Nusser, A., Freudling, W., Giovanelli, R., Haynes, M. P., Salzer, J. J. & Wegner, G. submitted to MNRAS (astro-ph/9707299)
4. Davis, M. & Peebles, P. J. E. 1983, ApJ, 267, 465
5. Davis, M., Nusser, A. & Willick, J. A. 1996, ApJ 473, 22
6. Dressler, A., Faber, S. M., Burstein, D., Davies, R. L., Lynden-Bell, D., Terlevich, R. J. & Wegner, G. 1997, ApJ, 313, 37
7. Freedman, W. L., Mould, J. R., Kennicutt, R. C., & Madore, B. F. 1998, to appear in IAU Symposium 183, *Cosmological Parameters and the Evolution of the Universe* (astro-ph/9801080)
8. Gott, J. R., Gunn, J. E., Schramm, D. N., & Tinsley, B. M. 1974, ApJ, 194, 543
9. Guth, A. 1981, Phys. Rev. D., 23, 34
10. Kaiser, N. 1984, ApJL 284, L9
11. Kennicutt, R. C., Freedman, W. L., Mould, J. R. AJ, 110, 1476
12. Kochanek, C. S. 1996, ApJ, 473, 595
13. Pont, F., Mayor, M., Turon, C. & VandenBerg, D. A. 1998, A&Ap, 329, 87
14. Proffitt, C. R. & Michaud, G. 1991, ApJ, 371, 584
15. Myers, S. T., Baker, J. E., Readhead, A. C. S., Leitch, E. M. & Herbig, T. 1997, ApJ, 485, 1
16. Peebles, P. J. E. 1976, ApJL, 205, L109
17. Rees, M. J. 1997 in *"Critical Dialogues in Cosmology"* ed. N. Turok, World Scientific: Singapore
18. Williams, L. L. R. & Schechter, P. L. 1997, in *"Jodrell Bank Golden Lenses Workshop"* astro-ph/9709059
19. Schramm, D. N. & Turner, M. S. 1997, submitted to Rev. Mod. Phys. (astro-ph/9706069)
20. Turner, E. L. 1990, ApJ, 365, 43
21. White, D. A., Jones, C. & Forman, W. 1997, MNRAS, 292, 419

THE GOLDEN AGE OF COSMOLOGY

EDWARD W. KOLB
Fermi National Accelerator Laboratory and The University of Chicago

Neutrinos may come in three flavors, but cosmologists come in two flavors: theorists and observers. The observers (our colleagues who toil on the night shift) have spoken. In response, I would like to make some concluding remarks from the perspective of a early-universe theorist.

1 "We Are Entering a Golden Age" (when in doubt, chant that mantra—repeat as often as necessary)

The present mass density of the universe, the division of the mass density into its various constituents, the spatial curvature of the universe, the expansion rate of the universe, the present age of the universe, its temperature, the pattern of its temperature fluctuations, the amount and nature of the dark matter, and the power spectrum of the matter fluctuations, are among the cosmological "parameters" reviewed at this meeting. As someone who only vaguely knows which end of the telescope to look through, I am overwhelmed by the imagination, ingenuity, and hard work employed our observer colleagues to measure these parameters.

With space telescopes, satellites, observatories in places as remote as Antarctica, a new generation of large optical telescopes, surveys dedicated to answering cosmological questions, amazing advances in instrumentation, and the incredible explosion of computational power and sophistication, we have at our disposal tools and techniques of unprecedented power and versatility. It seems that new results are reported at every meeting. Success breeds confidence, and many of the proposed experiments are among the most ambitious astronomical projects ever conceived.

There is another important dynamic contributing to the enthusiasm of the community of cosmologists. Cosmology (indeed all of astronomy and astrophysics) is more than respectable: it's fashionable! Not too long ago cosmology was considered to be little more than science fiction decorated with a few equations and indices. For many, many years it was thought that cosmology would never be capable of making hard predictions—so no one worked on it (which,

of course, assured that there were no hard predictions). Now everyone seems to be in on the cosmological bandwagon. Astronomers, particle physicists, nuclear physicists, and interlopers from many other fields all seem to be contributing to the development of modern cosmology.

The mantra most often invoked during the meeting when discussing the present situation in cosmology is that we are entering a "golden" era, in which all the elusive cosmological parameters will soon be determined to the accuracy that anyone would ever need.

It is really hard to argue with the "golden agers." By any measure, we live in an era when cosmology is growing by leaps and bounds. It may be that we are at a time when the fundamental parameters that determine space and time in the universe are settled for once and for all.

I have no intention to conclude such a wonderful meeting with remarks that might be construed as pessimistic. But it might be useful to refer people to the material written around the time of the dedication of the Mt. Palomar 200″ telescope. The promise then was that the telescope would produce definitive values for H_0, Ω_0, etc. Let's hope that there is a limit to the elusiveness of cosmological parameters, and this time we really will nail them.

2 Cosmological parameters are not just a bunch of numbers!

An important aspect of meetings such as Moriond is that it brings together both theorists and observers. That seems like a very obvious thing to do. After all, cosmology is a science, and since the 15th century the interplay of theory and experiment/observation is the way science proceeds. The theorist–experimentalist/observer interplay might be desirable, but they have not always had a lot of common ground in the field of cosmology. There is no clearer indication of the health and vigor of cosmology than the active and fruitful interplay between theorists and experimentalists/observers demonstrated here.

It is obvious that theorists have to understand the observational situation with regard to the cosmological parameters. It is also true that observers have to be aware of the cosmological context of the parameters they determine. The cosmological parameters are not just a bunch of numbers, but they have to fit together into a consistent cosmology. The baryon density from big-bang nucleosynthesis, the matter density from clusters, and the spatial curvature from the Doppler peak of the cosmic background radiation are different parts of a single basic parameter. The Hubble constant is related to the age of the universe, etc. It is important that people don't get locked into their own little piece of the universe, but they have to see how it fits into the big picture. I believe this meeting has been unusually successful in this regard.

3 Precision measurements without a "standard model"

One of the great successes in science in the last decade has been the precision tests of the standard model of particle physics. In some respects, we are now in a position to start precision tests of the standard model of cosmology. About the only thing holding us up, is that we don't have a standard model to test! The Friedmann–Lemaître–Robertson–Walker cosmology, augmented with inflation and dark matter, is a good place to start. But that model is not restrictive enough for precision tests.

About the closest thing we have to a standard model is CDM. The CDM model appeared in just about every presentation; usually with the remark that it doesn't agree with data. Many people seem to enjoy kicking CDM around. But if it is such a bad model, why is it still the benchmark for comparison of data and observation?

I think that the reason CDM is the model everyone loves to hate is that it comes damn close to working. In fact, the best proof that we are in the era of precision cosmology is that we can disprove CDM. While its failures are most often mentioned, CDM has some notable successes.

The most important question today in early-universe cosmology is whether CDM is on the right track, i.e., whether some variant of CDM will emerge as the standard model.

There are just a few basic ingredients needed to season the Friedmann–Lemaître–Robertson–Walker stock. As we learn here every evening, manipulation of just a few ingredients can produce a marvelous variety in the end product. Cosmologists have been as imaginative with the cosmological ingredients as a great French chef. There is now a tasty menu of CDM variants from which to sample. In the literature one can taste models from the unspeakably nasty open-CDM, to very bitter (but suddenly stylish) Λ-CDM, to the very elegant tilted-CDM, to "little-of-everything" crudités like HCDM, H^2CDM, νCDM, etc. Everyone agrees that bland, vanilla CDM is dead, but who need this flavor of the month cosmology?

Critics of modern cosmology point to the explosion of flavors and say that we really don't know what we are doing, and we just seem to be adding an endless progression of epicycles to save the phenomena. The situation seems too "untidy" to many.

4 In Defense of Epicycles

I believe the infusion of ideas from particle physics—inflation and particle dark matter, have revolutionized cosmology. Perhaps we are now in the end game of that revolution, but we have not witnessed the final product of the revolution. The reason cosmology seems so messy today is that the revolution is not complete. Because we don't have the final form, we are forced to add a seemingly large number of parameters (cold plus hot dark matter, tilt, Λ, etc.).

To the amateur philosopher of science (a group which encompasses most physicists, including this speaker) "epicycle" is a pejorative term. We all know the origin of epicycles: they were added to the geocentric model of the solar system to account for the retrograde motion of the planets. But as the observational database improved, just one epicycle per planet didn't suffice, and additional epicycles were added. Most recognize the profusion of epicycles in the Ptolemaic model of the solar system as indicative that the basic tenet of the model was wrong. But then the Copernican model emerged, doing away with the clumsy epicycles. Or so the legend goes.

Anyone who thinks that the Copernican model was simpler than the Ptolemaic model is invited to take a good look at Book III of *De Revolutionibus!* Examination of the Copernican model, as proposed by Copernicus, reveals epicycles; in fact, by some counts, more epicycles than in the Ptolemaic model.

The reason Copernicus had to have epicycles is that his model was not quite correct. Copernicus believed that the most important feature of astronomy is that all heavenly motions must be uniform circular motion. Copernicus had a revolutionary idea, that the solar system is centered on the Sun, but his insistence upon uniform velocities and circular motions was wrong.

The Copernican revolution was not completed until Kepler realized that the motions were not uniform or circular, and until Isaac Newton was able to show that Kepler's laws of planetary motion follow from fundamental laws of physics. Perhaps the present situation in cosmology is similar to the situation after Copernicus, but before Kepler and Newton. We have revolutionary ideas, inflation-produced curvature perturbations and dark matter (in its simplest realization CDM), but there is a missing piece, or a misapplication of one of the extant pieces.

Listening to the theoretical and observational presentations at this meeting I often thought of Copernicus, Tyco, Kepler, and Newton. It was the precision measurements of Tyco that led Kepler to formulate his empirical laws of motion, and it was developments in understanding of basic concepts of physics that allowed Newton to connect Kepler's laws to the fundamental laws of nature.

We are now developing precision measurements of cosmological parameters. Several people have tried to use precision measurements of the angular spectrum of microwave background fluctuations and the power spectrum of the matter distribution to construct an empirical model

for the emergence of structure in the universe. Others have tried to apply ideas from theoretical particle physics to connect inflation to grand unified theories, supersymmetry, supergravity, superstrings, branes, etc.

It could be that we are on the wrong track and we are just adding epicycles to a hopeless model. If that is true, then we are in an age of pyrite. But we just might be right. It may be that precision measurements will point to an empirical variant of the CDM idea, and that we will be able to connect inflation to fundamental physics. If that is the future, then we are truly lucky to be cosmologists in a golden age.

Acknowledgments

I would like to thank J. Trân Thanh Vân for enabling another in along line of incredibly productive meeting. I would like to acknowledge conversations with many people, in particular with Joel Primack, about the comparison of modern cosmology with cosmology at the time of Copernicus,. This work was supported by the Department of Energy and NASA under grant number NAGW-7092.

RÉSUMÉS DES CONTRIBUTIONS

1 L'UNIVERS PRIMORDIAL

William Kinney : L'observation du fond micro-ondes comme moyen de différenciation des modèles d'inflation
Les futures missions sur satellite MAP et Planck mesureront le spectre des fluctuations du CMB (Fond micro-ondes cosmologique) avec une précision jusqu'alors inégalée. Nous discutons de l'utilisation de ces données pour différencier les modèles de cosmologie inflationnaire.

David Langlois : Le dipôle du CMBR pourrait-il être cosmologique?
Le dipôle observé est généralement interprété comme un effet Doppler dû au mouvement de la Terre par rapport au référentiel du CMBR (rayonnement fossile cosmologique). On montrera qu'un dipôle significatif peut être obtenu à partir de perturbations *isocourbures* d'échelles ultra-grandes (supérieures à une centaine de fois le rayon de Hubble actuel), mais ceci uniquement dans un univers *plat* ou *quasi-plat*. Finalement, on montrera qu'un modèle simple d'inflation double peut produire le spectre de perturbations requis pour obtenir une contribution cosmologique significative au dipôle.

Jean-Philippe Uzan : Défauts topologiques dans des univers multi-connexes
Quand la topologie de l'univers n'est pas triviale, il existe une contrainte sur le réseau de défauts topologiques susceptibles d'apparaître lors d'une transition de phase de brisure spontanée de la symétrie dans l'Univers primordial. Je résumerai tout d'abord cette contrainte puis effectuerai une revue de ces implications cosmologiques. J'expliquerai ensuite comment la topologie peut être réduite à un ensemble de paramètres et donnerai les limites sur ces paramètres venant de l'observation d'un défaut topologique.

Alejandro Gangui : Conséquences cosmologiques et astrophysiques des cordes cosmiques supraconductrices et des vortons.
Nous présentons une revue complète des différents points d'intéret concernant les cordes cosmiques supraconductrices et les vortons. Nous dicuterons successivement des diverses possibilités de courants confinés dans les cordes en termes microscopiques, des développement récents de la description macroscopique des vortons pour terminer sur une étude des possibilités observationnelles astrophysiques qui signeraient les cordes de façon non ambigüe.

Juan Garcia-Bellido : Préchauffement de l'Univers dans l'inflation hybride
Un des problèmes fondamentaux de la cosmologie moderne est d'expliquer l'origine de toute la matière et du rayonnement présents dans l'univers. La transition de l'ère d'inflation à l'ère de rayonnement fut à l'origine appelée réchauffement ; nous comprenons aujourd'hui qu'elle peut, en fait, être décomposée en trois étapes: préchauffement, rétro-réaction et rediffusion, puis décohérence et thermalisation. Dans cette communication, j'expose en détail la phase du préchauffement, en insistant sur les différences dans les modèles d'inflation chaotique et hybride.

Richard Holman : R. Holman. Aspects de non-équilibre de la cosmologie inflationnaire.
La théorie du champ quantique de non équilibre est appliquée à la dynamique de l'inflation. Nous montrons comment, dans les nouveaux modèles inflationnaires, sont générées les grandes fluctuations du quantum non perturbatif. Nous discutons ensuite de la façon dont les petites perturbations métriques deviennent alors compatibles, au moins dans une large approximation N.

Antonio Riotto : Développements récents dans la baryogénèse électrofaible.
Nous discutons de quelques développements récents dans le calcul de l'asymétrie du baryon générée à l'échelle électrofaible. Nous insistons sur le fait que les asymétries locales de densité du nombre de particules impliquées dans la baryogénèse supersymétrique électrofaible doit être décrite par un jeu d'équations du Quantum Boltzmann.

Gabriele Veneziano : D'où venons-nous ? Que sommes-nous? Où allons-nous ?
Le but de cette présentation est double : présenter un panorama général de la cosmologie du pré-*big bang* et dresser un cadre pour les 4 présentations qui vont suivre.

Alessandra Buonanno : Traces magnétiques primordiales de la cosmologie des cordes dans le pré *big-bang*.
Nous étudions la formation de champs magnétiques galactiques dans un scénario cosmologiquedes cordes spécifique du pré *big-bang*, comprenant des modules dynamiques et des bosons de gauge abélienne Kaluza-Klein.

Ram Brustein : Fond cosmologique d'ondes gravitationnelles en cosmologie des cordes cosmiques.
Les modèles cosmologiques incluant les cordes cosmiques prédisent un fond cosmologique stochastique d'ondes gravitationnelles. Je décrirai les limites actuelles sur ce fond et les moyens de le détecter avec les détecteurs d'ondes gravitationnelles.

Mairi Sakellariadou : Germe des anisotropies à grande échelle du fond diffus cosmologique en théorie cosmologique des cordes cosmiques
Dans le cadre de la cosmologie inspirée par la théorie des cordes (cordes duales), nous examinons comment des perturbations ayant un germe électromagnétique ou axionique peuvent être à l'origine des fluctuations de densité demandées par la formation des grandes structures qui sont effectivement observées, et expliquer l'anisotropie du rayonnement de fond cosmique?

Burt Ovrut : Dualité de U et cosmologie de la théorie de M.
Une approche covariante de la dualité de U pour la théorie cosmologique de M est discutée et appliquée à des cosmologies dans la dimension D = 5.

Julien Lesgourgues : Quelques modèles cosmologiques avec un spectre non invariant d'échelle
Deux modèles d'inflation associés à des spectres primordiaux non invariants d'échelle sont confrontés aux contraintes observationnelles provenant de l'observation des structures aux grandes échelles et des anisotropies du fond diffus. On constate que ces modèles ne résolvent pas les problèmes du scénario cosmologique standard avec $\Omega = 1$. En revanche, en présence d'une constante cosmologique, le deuxième modèle donne de bons résultats, et pourrait expliquer l'observation récente d'un pic dans le spectre de puissance actuel.

Andrew Liddle : L'inflation et le fond diffus cosmologique
Je discute le lien entre l'inflation et les anisotropies du fond diffus cosmologique, pointant en particulier la précision que les prédictions de l'inflation nécessitent, et l'importance de l'inflation comme paradigme sous-jacent aux estimations des paramètres cosmologiques.

Sean Carroll : Survivance des champs magnétiques primordiaux
Les champs magnétiques observés dans les galaxies aujourd'hui pourraient trouver leur origine dans le jeune Univers. Un certain nombre de mécanismes existent qui rendent compte des larges amplitudes des champs initiaux, mais l'évolution postérieure de ces champs est d'une importance capitale. Cette communication est la présentation d'un travail en cours dans lequel nous étudions un scénario contraint par des effets pseudoscalaires à la transition de phase électrofaible et concernant un champ primordial. Nous suggérons qu'un tel scénario est intéressant, même s'il est encore incertain qu'un champ suffisamment important puisse survivre.

Yasunori Fujii : Non-zero et nouveau type de structure dissipative.
Pour comprendre les tous nouveaux résultats cosmologiques indiquant le non-zéro, nous présentons un modèle théorique qui semble suggérer, de façon inattendue, un nouveau type intéressant de structure dissipative.

Jérome Martin : Amplitude des perturbations cosmologiques plus grandes que l'horizon
Nous étudions l'influence du *reheating* sur les perturbations de densité et les ondes gravitationnelles plus grandes que l'horizon. Nous corrigeons de fausses affirmations faites à propos du raccordement des perturbations lors des transitions cosmologiques et à propos de leur quantification.

2 LE RAYONNEMENT DE FOND DIFFUS COSMOLOGIQUE

2.1 Anisotropies

2.1.1 Détermination des paramètres cosmologiques à partir du rayonnement de fond diffus cosmologique

Marc Kamionkowski : Détermination des paramètres cosmologiques avec les anisotropies de température et la polarisation du fond micro-onde cosmique.
Les expériences futures sur le ciel micro-ondes cosmique (CMB) nous fourniront de nouveaux tests précis sur les théories de formation de structure et sur les paramètres cosmologiques. De plus, les «objets observables inflationnaires» qui déterminent les formes et les amplitudes des spectres primordiaux des perturbations de densité et des vagues gravitationnelles longues produites par l'inflation, peuvent aussi être mesurés et fournir ainsi plusieurs nouveaux tests de l'inflation. Des travaux récents ont montré que la polarisation du CMB a fourni une mine d'informations uniques qui seront peut-être particulièrement importantes pour la détermination des objets observables inflationnaires.

Uros Seljak : Polarisationdu rayonnement diffus cosmologique- propriétés statistiques et physiques
Nous parlerons des propriétés physiques et statistiques de la polarisation du fond diffus cosmologique, à la fois dans l'espace réel et dans celui de Fourier.

James Bartlett : Contraintes des paramètres cosmologiques par les résultats des études sur le fond cosmique micro-ondes
Nous utilisons les données actuelles des études sur le fond micro-ondes pour contraindre les paramètres cosmologiques. Les résultats sont présentés comme des régions de confiance dans le plan Ω-H_0 pour des géométries à la fois ouvertes et plates et sont basés sur une minimisation χ^2 par rapport au spectre de puissance. L'espace paramétrique, couvrant Ω, H_0, n, $\Omega_\beta h^2$, est le plus grand espace jamais observé.

Mairi Sakellariadou : Prédictions théoriques et comparaison avec les observations des anisotropies du fond diffus cosmologique engendrées par des germes invariants d'échelle.
Nous calculons le spectre angulaire des anisotropies du rayonnement de fond cosmique engendrées par des germes invariants d'échelle , et vérifiant les contraintes de conservation de l'énergie-impulsion. Nous utilisons un test du χ^2 pour comparer les prédictions théoriques et les mesures récentes *flat-band*.

2.1.2 Contraintes topologiques données par le rayonnement de fond diffus cosmologique.

Tarun Souradeep : L'anisotropie du CMB comme moyen d'investigation de la topologie cosmique.
Les mesures d'anisotropie du CMB nous ont ouvert une fenêtre d'investigation de la topologie globale de l'univers sur des échelles de 1 ongueur comparables au radius de Hubble. Nous avons développé une nouvelle méthode pour calculer l'anisotropie du CMB dans des modèles avec une topologie non triviale. Nos résultats démontrent que des contraintes fortes apparaissent sur la densité.

2.1.3 Les défauts topologiques.

Ue-Li Pen : Défauts topologiques avec une invariance d'échelle interrompue
Les modèles de défauts ont récemment été déclarés non valables parce qu'ils prédisent un fond micro-ondes et des fluctuations de matière très nettement différents de ce que nous observons. Nous défendons ici l'argument que beaucoup de défauts sont automatiquement détruits au moment de la transmission radiation-matière, et de ce fait, on voit ressurgir les modèles de défauts. Si ce modèle est correct, les missions MAP et PLANCK mesureront non pas les oscillations attendues mais un grand arc.

Richard Battye : Les cordes cosmiques dans un univers avec une densité de matière non critique.
A la lumière des travaux récents qui suggèrent que la formation de la structure par des cordes cosmiques dans un univers de densité de matière critique demande de larges distortions, nous discutons de l'effet produit par la réduction de la densité de la matière. Nous trouvons que les univers avec Ω=0,7 - 0,8 conviennent à la forme de distribution des galaxies observées, avec toutefois une distortion d'environ 2. Ceci entraîne des implications intéressantes pour l'anisotropie et la polarisation du ciel micro-ondes.

2.2 Autres anisotropies

2.2.1 Anisotropies secondaires

Gianfranco De Zotti : Les sources de points extragalactiques et la mission Planck.
Nous étudions les estimations de fluctuations à petite échelle dues aux sources de points extragalactiques dans les bandes de fréquence de la mission Planck. Les sources familières de radio à spectre plat devraient montrer des caractéristiques spectrales qui apporteront des informations essentielles sur leurs propriétés physiques. Des informations essentielles seront fournies sur la nature des sources radio avec des spectres fortement inversés. Les scénarios d'évolution cosmologique des galaxies seront entièrement vérifiés.

Nabhila Aghanim : Anisotropies secondaires dues à des lentilles gravitationnelles en mouvement
Dans le cadre de la nouvelle génération d'instruments pour la cosmologie, l'étude des anisotropies secondaires revêt une importance considérable. Il est en effet crucial de prédire et quantifier l'effet des anisotropies secondaires sur le Fond Diffus Cosmologique Micro-onde (FDCM). Nous présentons ici, les principaux résultats de notre étude des anisotropies secondaires générées par le mouvement transverse, par rapport à la ligne de visée, de lentilles gravitationnelles.

Keith Grainge : Sources d'émission de spectre de l'avant-plan cosmique
Nous avons tenté d'utiliser les données les plus appropriées pour estimer au mieux la contribution des sources d'émission de spectres. Ce sont les sources qui présentent le plus grand défi pour la discrimination spectrale par rapport au CMB. Les résultats préliminaires indiquent de l'ordre de 5 sources d'émission à 30 GHz par degré carré au niveau mJy. Bien sûr, une sélection à de plus hautes fréquences améliorera nos connaissances futures. Ce travail sera repris en détail par Edge *et al.*.

Andrew Blain : Effet de lentille gravitationnelle sur les avant-plans submillimétrique et le rayonnement de fond diffus cosmologique
A l'aide de télescopes à haute sensibilité, il est facile de sélectionner des échantillons de galaxies lointaines dans les bandes de fréquences millimétriques (mm) ou sub-millimétriques (sub-mm). Des observations récentes de lentilles gravitationnelles ont permis, pour la première fois, de contraindre directement la densité de sources dans le sub-mm. Cet article souligne les caractéristiques fondamentales de l'effet de lentilles gravitationnelles dans la bande sub-mm et discute les opportunités qui seront bientôt offertes par ces projets en ce qui concerne la recherche de lentilles gravitationnelles.

Richard Saunders : Pourquoi la mesure de $H_\circ$ par l'examen combiné des mesures en X et de l'effet S-Z marche-t-elle?
Des hypothèses très simplificatrices sont faites pour estimer la valeur de $H_\circ$ à partir des observations en X et des mesures de l'effet S-Z en direction des amas. Il est montré que les incertitudes sur l'épaisseur dans la ligne de visée ne donneront qu'une erreur de quelques pourcents sur la mesure de $H_\circ$ basée sur une douzaine d'amas.

Siang Peng Oh, David N. Spergel and Gary Hinshaw : Détermination rapide du spectre de puissance pour les cartes du fond diffus cosmologique
Les études statistiques du fond diffus cosmologique (FDC) ont d'énormes potentiels pour la cosmologie. Le spectre de puissance angulaire des anisotropies du FDC est une statistique particuliérement importante. Le sattelite MAP produira des cartes de l'ordre d'un million de pixels de la temperature du FDC à plusieures fréquences ; ainsi, les algorythmes existants ne sont pas utilisables. Nous introduisons un algorithme qui demande $O(N^2)$ operations et $O(N^{3/2})$ unités de stockage, et qui determine le spectre de puissance avec une variance minimale. Nous presentons nos resultats en analysant une simulation contenant 2 millions de pixels. Notre algorythme est a peu prés un million de fois plus rapide que les méthodes existantes, et rend donc possible une analyse qui etait jusqu'àlors impraticable.

2.2.2 Avant-plans galactiques

Althea Wilkinson : Emission de synchrotron à partir du fond galactique.
L'émission de synchrotron galactique est un avant-plan potentiellement déroutant, à la fois en puissance et en polarisation, pour la radiation du Ciel micro-ondes. Il contient aussi beaucoup d'informations physiques propres. Cette étude passe en revue l'amplitude, le spectre de puissance angulaire et le spectre de fréquence de l'émission de synchrotons tels qu'ils sont décrits sur les cartes disponibles.

Philippe Amram, James Bartlett : Émission *free-free* galactique et la raie H_α Nous passons en revue, dans cet article, la compréhension que nous avons de l'émission *free-free* dans la Galaxie et de son importance potentielle pour la compréhension des mesures des fluctuations du fond diffus cosmologique.

Shiv K. Sethi : Émission de rayonnement polarisé par la poussière de la Galaxie et polarisation du fond diffus cosmologique.
Nous estimons l'émission polarisée de notre galaxie à haute latitude, principal contaminant des mesures

de polarisation du FCM par l'instrument HFI de la mission ESA Planck Surveyor. Nous comparons cette émission avec celle du FCM et concluons que pour des échelles $\simeq 1°$, le signal polarisé du FCM d'origine scalaire, ainsi que la corrélation de ce signal avec l'émission non polarisée de ce même fond sont nettement supérieurs au niveau de contamination de la poussière à 100GHz. Le signal polarisé d'origine tensorielle du FCM est quant à lui au mieux comparable au niveau de contamination.

Simon Prunet : Filtre de Wiener multi-fréquences sur les données du fond diffus cosmologique avec polarisation et estimation des paramètres cosmologiques.
Nous présentons une méthode de soustraction des contaminants pour une mesure polarisée du FCM. Nous en déduisons les erreurs résultantes sur les spectres de puissance de l'émission polarisée du FCM d'une part, et de la corrélation de ce signal avec la partie non-polarisée de l'émission d'autre part. Nous concentrons notre étude sur l'instrument HFI de la mission ESA PLANCK , et estimons les erreurs correspondantes sur la détermination des paramètres cosmologiques.

2.3 Expériences en cours

Suzanne Staggs : Mesure du fond diffus cosmologique à 3 cm
Aucune déviation relative à un corps noir n'a encore été détectée dans le spectre du Fond Diffus Cosmologique (FDC). L'université de Chicago et de Princeton ont récemment collaboré sur une mission ballon ayant pour objectif de mesurer la température du FDC à 3 cm. Cette longueur d'onde est plus grande que celles sondées par COBE FIRAS. Les résultats préliminaires ont étés publiés (Staggs *et al.* 1996); ce rapport résume l'état actuel de cette expérience.

Jose Maria Diego-Rodriguez : Analyse multifractale des résultats sur quatre ans de l'expérience COBE-DRM.
Dans cette étude, nous appliquons l'analyse multifractale aux données obtenues en 4 ans et nous obtenons le spectre des dimensions fractales. Nous vérifions la fiabilité de cette méthode avec cette sorte d'informations et 'intérêt d'une telle méthode lorsqu'on souhaite obtenir des paramètres cosmologiques tels que la valeur de normalisation quadrupole Qrms-PS et l'index spectral n. Nous recherchons le modèle probable le plus adapté à ce type de données et nous comparons ces résultats avec les résultats obtenus par d'autres méthodes.

Paolo De Bernardis : Mesure des anisotropies du fond diffus cosmologique en utilisant des ballons stratosphériques
Mesure d'anisotropies du fond diffus cosmologique (CMB) avec des ballons stratosphériques. Nous étudions les mesures de CMB effectuées par des télescopes portés par des ballons. Après une courte description de la méthodologie expérimentale, nous décrivons les problèmes particuliers de ces expériences, leurs principaux résultats ainsi que les perspectives futures.

2.4 Expériences au sol

Antony Lasenby : Revue des mesures du rayonnement de fond diffus cosmologique par des expériences au sol
Nous présentons dans cet article une brève revue des expériences terrestres pour l'observation du rayonnement fossile. Nous commençons par rappeler les principaux problèmes expérimentaux ainsi que les solutions adoptées. Nous résumons ensuite les expériences menées à Tenerife et en donnons les résultats les plus récents. Plusieures autres expériences (IAC-Bartol, Python, Saskatoon, MAT et OVRO) sont également présentées. Nous considérons ensuite les expériences à venir, en particulier les nouveaux interférometres comme le VSA, CBI et DASI. Pour finir, nous présentons un travail récent sur l'estimation

de paramètres cosmologiques grâce à l'analyse conjointe de données sur le rayonnement fossile et sur la structure de l'Univers à grande échelle.

Joanne Baker : Détection des anistropies du fond diffus cosmologique dans un 2e champ de l'expérience CAT
Le *Cambridge Cosmic Anisotropy Telescope* (CAT) a été utilisé pour regarder, aux fréquences proches de 15 GHz, une région du ciel de 2"x2". Après soustraction des sources d'avant-plans discrètes, des structures sont détectées à l'échelle du demi-degré. De nouvelles limites sur la valeur de H_o et Ω sont déterminées.

Michaël Jones : Le point sur le VSA.
Un télescope interférométrique est en cours de construction, le VSA, dont la fonction sera d'étudier le ciel cosmique micro-ondes à des échelles angulaires 0,2-4,5°. La conception mécanique et électronique du télescope a été optimisée afin d'obtenir une protection maximum des effets systématiques, tout en fournissant une sensibilité suffisante pour produire des images signal-bruit de grande précision.

2.5 Expériences sur satellite

Carlo Burigana : Effets du faisceau principal et des lobes secondaires sur les observations de la mission Planck
L'extrême sensibilité des observations de Planck requiert que tous les effets systématiques potentiels soient corrigés ou réduits sensiblement. Des effets systématiques peuvent être générés par un fonctionnement non-idéal des optiques, par des instabilités des récepteurs, des effets thermiques, un pointage imprécis. L'impact de chaque effet sur les mesures doit être estimé correctement, et devrait être réduit par un dessin attentif de l'instrument et une stratégie d'observation adéquate, plutôt que par des corrections a-posteriori de leurs effets combinés. Nous nous concentrons ici sur l'étude des effets introduits par les distortions du faisceau pour le dessin optique de Planck. Nous soulignons les conditions principales de l'ouverture du premier miroir pour obtenir l'objectif cosmologique principal: une résolution angulaire de 10′ dans la fenêtre astrophysique "propre" de 100 GHz.
Benjamin Wandelt : Analyse topologique des MAPS (Etude du fond anisotropique micro-ondes) à haute-résolution du CMB.
Nous décrivons le développement des outils numériques pour l'analyse topologique des cartes globales du ciel avec un résolution inférieure au degré. Le logiciel mis au point dans HEALFAST (VO.9) définit les relations pour la mosaïque HEALPIX de la sphère. Nous appliquons cette procédure dans une étude extrêmement rapide qui donne une échelle strictement linéaire dans le nombre de pixels N_p. Nous présentons également un algorithme assez puissant pour simuler les champs de vecteur gradiant et de tenseur de courbure en accord avec la carte de température, avec seulement un surcroit d'opérations de l'ordre de $N_p \log_2 N_p$.

Michaël Hobson : L'effet induit par des sources ponctuelles sur les observations spatiales du fond cosmologique
Nous étudions l'effet induit par la présence de sources ponctuelles extra-galactiques sur les futures observations spatiales du fond cosmologique. Dans l'objectif de séparer les contributions causées par différents types de sources, une méthode de maximun-entropie est appliquée à des simulations d'observations telles qu'il est prévu d'en obtenir avec le satellite Planck Surveyor. En plus de sources ponctuelles , les simulations prennent en compte le signal provenant du fond cosmologique, bien sûr, mais aussi les perturbations dues aux effets Sunyaev-Zel'dovich (thermique et cinétique) ainsi que l'émission galactique (poussière, free-free et synchroton). Nous montrons que les principales composantes introduites en amont de la simulation sont reconstruites avec un bon niveau de confiance. En particulier, la qualité de la reconstruction

du fond cosmologique n'est que très légèrement altérée par la présence de sources ponctuelles.

Etienne Pointecouteau : Détermination de la température du gaz intergalactique par les mesures SZ
L'interprétation des données SZ sur les amas de galaxies nécessite la connaissance de la température électronique du gaz intergalactique. Jusqu'à maintenant, cette température a été déduite des données X, avec une précision allant de 0,5 a 4 keV. Nous montrons que l'effet Sunyaev- Zel'dovich, mesuré aux longueurs d'ondes millimétriques et submillimétriques, peut permettre la détermination de la température du gaz, et ce indépendamment des données X. Notre méthode novatrice pourrait être le seul moyen d'estimer la température électronique du gaz intergalactique, dans le cas d'amas distants pouvant se trouver hors de portée des futures missions spatiales X.

Norman Jarosik : Map - *The Microwave Anisotropy Probe*
Le satellite MAP (Microwave Anisotropy Probe) est une mission MIDEX sponsoriséepar la NASA. MAP produira une carte complète du Fond Diffus Cosmologique dans une bande de séquence allant de 20 à 106 GHz. La résolution angulaire dans le canal à haute séquence sera de 0,21 degrés. L'instrument est différentiel par construction et minimise ainsi les effets systématiques. Les observations se dérouleront sur une période de 2 ans, à partir du point L2 du système terre-soleil. Le lancement de MAP est prévu pour l'automne 2000.

Jan Tauber : Rapport sur Planck.
Nous faisons le point sur les résultats de la mission Planck et décrivons ses prochaines étapes au sein du programme scientifique de l'Agence Spatiale Européenne ainsi que les principaux changements techniques et budgétaires intervenus depuis le choix de COBRAS/SAMBA (ancien nom de Planck) depuis 1996.

F. Villa : Etudes des charactéristiques optiques du télescope de la mission Planck
La nouvelle génération de missions satellitaires, comme Planck et MAP, requiert des larges télescopes couplés à des réseaux de détecteurs pour mesurer les anisotropies du fond micro-onde cosmique sur petites échelles angulaires.. La prédiction précise des performances optiques de ces télescopes joue un rôle crucial pour l'optimisation de la configuration optique et pour une correcte évaluation des effets systématiques associés. Un bref résumé des calculs optiques effectués pour le télescope Planck sont présentés ici. Les résultats obtenus sont ainsi utilisés pour évaluer les distorsions optiques et optimiser le positionnement des *feehorns* de l'instrument Planck/LFI (*Low Frequency Instrument*)

Jacques Delabrouille : Mesure des anisotropies du FRC par balayage circulaire
Nous présentons une méthode de production de cartes du fond de rayonnement cosmologique (FRC) à partir des données temporelles du satellite Planck Surveyor. Cette méthode utilise les propriétés spécifiques du balayage de PLANCK pour décomposer le problème de la production de cartes en deux parties qui peuvent être traitées indépendamment. Ceci simplifie de facon significative le problème de réduction des données. Nous présentons également succintement les avantages de cette méthode pour la compréhension, l'identification et la soustraction des effets parasites d'origine instrumentale.

Lucia Popa : Propriétés à grande échelle du fond diffus infra-rouge.
Nous avons analysé les cartes COBE/FIRAS pour rechercher un fond isotropique à longueur d'ondes millimétriques en exploitant les propriétés de corrélation des cartes sans nécessiter l'addition de données supplémentaires pour la soustraction propre de la Galaxie. Nous affirmons que la valeur *rms* de la brillance est égale à $(\nu I_\nu)_{rms} \simeq 4 \times (\lambda/400\mu\mathrm{m})^{-3.1}\mathrm{nWm^{-2}sr^{-1}}$ pour $\lambda \geq 400\mu$m. Les distributions "genus" des cartes de lumière diffuse sont en accord avec un champ gaussien casuel avec un angle de cohérence

$\sim$ 5°, 9°, en accord avec COBE-*DMR*. Conformément aux indications obtenues par les catalogues de galaxies, nous trouvons une fonction de corrélation plus raide sur échelles angulaires de quelques degrés à quelques dizaines de degrés que sur celle dérivée par catalogues de galaxies sur plus petites échelles angulaires. Ces évidences sont une forte indication que les résidus du fond obtenus dans le lointain infrarouge sont d'origine extragalactique.

3 NOUVELLES APPROCHES POUR MESURER LES PARAMÈTRES COSMOLOGIQUES FONDAMENTAUX

3.1 Amas et structures à grande échelle comme sonde cosmologique.

Alain Blanchard : Utilisation des amas de galaxies pour les contraintes cosmologiques.
Les propriétés des amas de galaxies fournissent quelques unes des contraintes les plus rigoureuses pour les modèles de formation des galaxies, essentiellement parce que les amas sont des objets rares, et que donc leurs propriétés sont sensibles aux fluctutations sous jacentes de densité. Je discute brièvement de l'utilisation des amas pour contraindre les paramètres cosmologiques et comment un modèle auto-consistant des amas de rayons X peut être construit. Les applications préliminaires de ce test sur des clusters à rayons X fournissent une évidence pour un univers de haute densité.

Ray Calberg : Les contraintes sur $\Omega_M - \Omega_\Lambda$ à partir des amas détectés par CNOC Le catalogue d'amas de galaxies avec une mesure du décalage vers le rouge obtenu par CNOC permet de mesurer Ω_M à partir de $\Omega_e(z) = M/Lxj/\rho_c$. Le résultat obtenu montre que Ω_M décroît si $\Omega_\Lambda > 0$ et que $\Omega_\Lambda < 1,5$.

Paolo Tozzi : Étude de Ω_o avec des amas de rayons X : une approche physique.
L'émission des rayons X à partir des amas de galaxies est un des champs d'observation les plus utilisés pour étudier la distribution de la matière noire et son paramètre de densité Ω_o. Le lien crucial permettant de déduire les statistiques des objets observables d'une théorie dynamique est constitué par les caractéristiques physiques des baryons diffus (ICP) responsables des émissions de rayons X. Nous proposons un modèle physique pour l'ICP qui conduit à une définition de la relation L-T. Puis nous développons une expérience cosmologique basée sur la physique, qui met en évidence trois univers de matière noire froide : un CDM critique avec des secousses, un CDM plat avec Ω_o=0,3 et un CDM ouvert avec Ω_o=0,5 qui sont observés sur la base de RDCS (Etude Rosat des amas profonds)

Hanadi Abdelsalam : Profil de masse d'amats à partir de lentilles fortes et faibles combinées
Nous présentons une nouvelle méthode non-paramétrique pour reconstruire la carte de masse en deux dimensions d'amats de galaxies à partir de leur effet de lentilles sur des galaxies en arrière plan. La méthode combine les contraintes de lentilles en régimes forts et faibles d'une manière linéaire et rompt la "dégénérescence masse-feuille" qui a longtemps empesté les techniques de lentilles faibles. La faisabilité de la méthode est démontrée par son application au spectaculaire amat lentille Abell 2218.

William Forman : De l'influence de structures à grande échelle sur les sous-structures et la distribution de températures des amas
Nous discutons des interactions entre la structure des amas et les structures à grande échelle, telles que les filaments, en nous appuyant sur l'exemple d' A85. Comme prédit par des simulations numériques, les structures à petite échelle dans les amas s'alignent sur des structures filamentaires beaucoup plus grandes dans lesquelles les amas sont englobés et dont ils sont issus. Nous décrivons aussi les profils de tempéra-

ture ASCA pour un échantillon donné d'amas de galaxies et montrons que tous les amas offrent un profil de température similaire. Nous comparons ces observations à des simulations numériques.

Christine Jones : Les amas de galaxies et la cosmologie
Nous résumons les résultats d'une étude ROSAT récente sur les amas lointains de galaxies. La grande résolution angulaire de cette étude permet de vérifier les rapports précédents sur l'évolution des clusters. Nous confirmons qu'il y a une évolution négative significative des amas de galaxies pour les amas très lumineux, i.e., à très grand décalage vers le rouge, il y a moins d'amas lumineux qu'à l'époque précédente. Nous comparons aussi les rayons du coeur de l'amas avec les mesures de l'étude Einstein sur des amas proches et ne trouvons pas d'évolution dans les rayons du coeur de l'amas. Enfin nous décrivons les capacités d'AXAF, en insistant sur sa très grande résolution angulaire.

Monique Arnaud : Cosmologie et amas de galaxies avec XMM. Dans cet article, nous présentons les détecteurs du satellite XMM (*X-ray Multi-mirror Mission*) ainsi que leurs performances. Leur sensibilité exceptionnelle, associée à une bonne capacité de spectroscopie, permattra la détection et l'observation d'amas à des distances cosmologiques (z 1).

Marguerite Pierre : Le *survey* XMM à $z \sim 1-2$
Dans le cadre du temps garanti XMM, nous avons défini un *survey* couvrant 25 degrés carrés avec une sensibilité de $\sim 10^{-14}$ erg/s/cm^2 sur le domaine d'énergie [0,1-10] keV. Ceci constituera une base de données unique pour étudier les grandes structures jusqu'à $z \sim 1-2$

Claude Canizares : Le sondage du milieu inter-galactique chaud avec le satellite AXAF
Les spectromètres d'AXAF auront une sensibilité et une résolution en énergie suffisantes pour détecter des raies d'absorption en X dans le spectre des quasars distants. cela pourrait permettre de sonder le cœur de la matière baryonique de l'Univers jusqu'à des décalages vers le rouge de 2-3.

George Djorgovski : Les quasars à très grand décalage vers le rouge comme sondes des structures primordiales à grande échelle et de la formation des galaxies
Plusieurs arguments laissent penser que les quasars à $z > 4$ pourraient être au cœur des futures galaxies elliptiques géantes. Ils pourraient donc être utilisés comme marqueurs des premiers sites de formation des galaxies.

Ruth Daly : Mesure des paramètres globaux cosmologiques par des sources classiques doubles de radio.
Quatorze galaxies classiques avec des redshifts entre 0 et 2 ont été utilisés pour déterminer les paramètres cosmologiques Ω_m, Ω_Λ et Ω_k, lorsque ces derniers sont les valeurs normalisées de la densité moyenne de masse, de la constante cosmologique, et de la courbure de l'espace à l'époque actuelle. Une valeur faible de Ω_m est obtenue, et Ω_m=1 est exclue à 97,5% de degré de confiance. Ainsi, il apparaît que soit constante cosmologique, soit une courbure de l'espace est nécessaire de façon significative à l'époque actuelle. Cela veut dire que l'univers est en cours d'évolution, ou vient d'évoluer, en transition entre l'état de domination de la matière et l'état où soit une constante cosmologique soit la courbure de l'espace détermine le taux d'expansion de l'univers.

3.2 Matière noire dans les halos galactiques.

Maurice Chapellier : Revue sur les expériences de détection de matière noire non-baryonique.
Nous présentons les techniques de base utilisées pour la détection cryogénique de matière noire non-baryonique ainsi que les premiers résultats obtenus par les expériences existantes.

Marc Moniez : Revue sur les expériences de détection de matière noire baryonique.
L'effet de microlentille gravitationnelle est probablement l'un des outils d'observation les plus prometteurs de la décade. Nous présentons ici les résultats obtenus par les différentes collaborations travaillant dans ce domaine qui vont de la recherche de matière noire galactique à la recherche de planètes extrasolaires.

Elena Pierpaoli : Etude de la formation des structures et de la matière noire chaude des gravitinos légers.
Les gravitinos légers ($m = 0, 1 - 1\,\mathrm{keV}$) sont en principe les particules supersymétriques les plus légères dans les modèles supersymétriques régis par la loi de Gauge. Nous étudions la possibilité qu'ils constituent la fraction dominante de la matière noire dans l'univers. Après avoir montré qu'il se comportent typiquement comme la matière noire (WDM) avec une échelle de répartition libre de l'ordre de l'échelle de la masse des galaxies, nous étudions la formation de structures cosmiques à l'intérieur de ce cadre. Nous considérons plusieurs variantes du scénario WDM et comparons avec les données récentes leurs prédictions sur la densité de nombre et l'abondance d'hydrogène neutre dans les objets à haut spectre tirant vers le rouge. Aucun de ces modèles ne satisfait aux deux contraintes en même temps : l'obligation d'assurer l'abondance adéquate d'amas empêche d'avoir assez de puissance sur une petite échelle pour former des objets à grand décalage vers le rouge.

3.3 Structures à grande échelle

Michal Chodorowski : Rapports densité/vitesse à large échelle.
Je décris les progrès récents réalisés dans les modèles théoriques des relations cosmologiques densité-vélocité dans le régime faiblement non linéaire. Les relations sont locales, basées sur la théorie rigoureuse des perturbations et incluent les effets d'atténuation de la densité et des champs de vitesse. Les rapports peuvent être utilisées pour les comparaisons densité-vitesse, avec une estimation satisfaisante de Ω et fournir une méthode pour résoudre Ω et le biais.

Stéphane Colombi : Quelle devrait être la géométrie d'un catalogue de galaxies?
J'étudie les effets de la géométrie du catalogue sur l'erreur cosmique reliée à la mesure du moment factoriel d'ordre 2, F_2, des comptages dans des cellules dans un relevé de décalages vers le rouge. A titre d'exemple, je détermine une stratégie d'échantillonnage préliminaire pour le futur relevé à grands décalages vers le rouge VIRMOS.

Max Tegmark : Complémentarité cosmique : observations combinées du CMB et des supernovæ
Nous calculons la précision avec laquelle Ω_m et Ω_Λ peuvent être mesurés en combinant les futures expériences SN Ia et CMB, tout en déduisant une expression pratique de la matrice d'information SN Ia Fisher. Les deux ensembles de données se révèlent hautement complémentaires : une analyse combinée réduit les barres d'erreurs de plus d'un ordre de grandeur par rapport à une analyse séparée de chaque ensemble de données.

3.4 Structures à grande échelle et effet de lentille gravitationnelle faible.

Francis Bernardeau : Les effets gravitationnels faibles pour sonder les paramètres cosmologiques
Les distorsions gravitationnelles sont en train de devenir un moyen précieux de sonder les concentrations de masses de l'Univers. On a pu montrer que les effets de lentilles faibles sont mesurables à toutes les échelles, des amas de galaxies aux grandes structures de l'Univers. Il faut en particulier noter que des cartes de masse projetée de taille significative vont être disponibles bientôt. Avec de telles cartes il sera

possible de contraindre des paramètres cosmologiques fondamentaux comme l'amplitude et la forme du spectre de puissance ou le paramètre de densité Ω, avec une précision remarquable.

Bhuvnesh Jain, Uros Seljak : Simulations numériques de l'effet de lentille gravitationnelle faible provoqué par les structures à grande échelle
Nous utilisons des simulations numériques pour étudier l'effet de lentille gravitationnelle faible provoqué par des structures à grande échelle. Nous montrons en particulier l'existence de différences majeures obtenues entre des modèles ayant des valeurs différentes de Ω_m.

Jose-Luis Sanz : Lentilles faibles gravitationnelles et corrélations des sources de l'avant-plan et du fond cosmologique. Nous étudions, dans le cadre de l'observation du ciel avec des lentilles faibles, la corrélation entre l'amplification ou la polarisation des sources d'avant-plan et du fond cosmologiques. En ce qui concerne la corrélation croisée de la magnification du fond et la distribution de matière de l'avant-plan, le maximum est à un décalage zéro et l'amplitude reste supérieure à quelques pourcentages pour les échelles inférieures à 1', tandis que la corrélation la polarisation du fond et la distribution de matière de l'avant-plan présente un maximum de l'ordre de 1% à un angle non nul dans la bande 0.4'-1'. Nous appliquons ces résultats pour estimer la fonction de corrélation quasar-galaxie w_{qg} due au weak lensing.

Hanadi Abdelsalam : Profil en masse des amas en utilisant les effets de lentille gravitationnelle fort et faible
Nous présentons une nouvelle méthode, sans paramètre libre, permettant de reconstruire les cartes de masse à 2 dimensions des ams de galaxies à partir de l'effet de lentille gravitationnelle qu'ils induisent sur la lumière émise par les galaxies d'arrière-plan.

3.5 Les paramètres cosmologiques et leur évolution.

Laurent Gautret : Distorsion faible autour des amas pour contraindre Ω et Λ.
Dans le régime de distorsion faible, un amas introduit une déformation elliptique sur les galaxies de fond. Cette distorsion dépend de la cosmologie (Ω, Λ) par l'intermédiaire du facteur géométrique $\omega = \frac{Dls}{Dos}$, bras de levier de la lentille par rapport à la source. Voulant utiliser au mieux les récents progrès dans la détermination des *redshifts* photométriques, la méthode de contrainte de (Ω, Λ) qui est présentée ici est basée sur la construction d'un opérateur purement géométrique. Les simulations conduisent à un résultat encourageant. Une contrainte très significative sur (Ω, Λ) peut être atteinte: $\Lambda^{+0.07}_{-0.07}$ dans le cas $\Omega + \Lambda = 1$ ou $\Omega^{+0.07}_{-0.07}$ dans le cas $\Lambda = 0$, à un niveau de confiance de 70%, à partir d'observation de environ 500 amas sur le VLT (environ 150 nuits). En conclusion, un objectif moins ambitieux mais tout aussi tentant, celui de savoir enfin si le contraste cosmologique est nul ou non, pourrait être atteint avec un programme d'observations bien plus restreint (environ 10 nuits)

Jocelyn Bezecourt : Statistiques des arcs gravitationnels comme sonde de l'évolution des galaxies.
Des comptages d'arcs gravitationnels ainsi que leur distribution en décalage spectral sont calculés dans le champ d'amas de galaxies massifs afin d'examiner l'univers lointain. En utilisant un modèle de masse pour l'amas et un modèle pour l'évolution spectrophotométrique des galaxies, la distribution en *redshift* d'arcs gravitationnels est calculée dans le champ de l'amas Abell 2218 et du HDF où un amas est artificiellement placé. La très grande sensibilité des comptages par rapport au modèle d'évolution et à la distribution de masse empêche une estimation des paramètres cosmologiques par les statistiques d'arcs. Les travaux futurs devront considérer pour cela des amas lentilles à grand z et des objets de distortion plus faible.

Simon Dye : Gravitational Lens Magnification - Analysis of A1689
Le travail décrit dans cet article donne la première application de l'effet du biais venant da la magnification optique. Nous l'avons appliqué pour trouver la masse de l'intérieur d'Abell 1689, et nous le trouvons être de $M_{2D}(< 0,24h^{-1}\,\mathrm{Mpc})$=(0,50±0,09)x$10^{15}h^{-1}M_{\odot}$. Nous donnons les profils de la masse radiale, ainsi que des cartographies en deux dimensions, en utilisant l'effet d'augmentation du nombre des galaxies. Les résultats sont bien d'accord avec l'analysis qui utilise l'effet de cisaillement. Nous avons comparé notre estimation pour la masse avec les mesures de la température x-ray, ainsi que des vitesses virielles, et cela nous indique qu'il y a une possibilité que A1689 soit composé des *clumps* de matière qui sont situés dans notre ligne de vue.

3.6 Distances cosmologiques et paramètres cosmologiques.

Catherine Turon : Hipparcos - la distance et lâge des indicateurs primaires de distance.
Après une brève description de la mission Hipparcos et des premiers résultats astrométriques et photométriques obtenus, nous présentons, avec plus de détails, le informations maintenant disponibles sur les échelles de distance de base.

Florian Bauer : La relation période-luminosité pour les Céphéides de courte période vers le Petit Nuage de Magellan
Nous présentons les relations Période-Luminosité pour 290 céphéides vers le Petit et 597 Céphéides vers le Grand Nuage de Magellan. obtenues par la collaboration Eros2. Pour les Céphéides du Petit Nuage de Magellan une brisure de pente de la relation Période-Luminosité a pu être observée. Différents biais observationnels, pouvant expliquer ce phénomène, ont été analysés et écartés. La brisure de pente observée pourrait être due à des effets d'évolution stellaire combinés avec des effets de convection.

Delphine Hardin : Etude des supernovæ à redshift intermédiaire.
Après avoir souligné l'intérêt cosmologique des supernovae à redshift intermédiaire, je présente rapidement les différentes recherches en cours sur les supernovae à distance intermédiaire. Je détaille ensuite notre propre projet : l'expérience EROS qui nous fournira un échantillon de supernovae à redshift intermédiaire à z 0.1 avec une meilleure efficacité de recherche.

Alex Kim : Revue des recherches de supernovæ de type Ia à grand redshift
Les observations nous montrent que les supernovæ de type Ia (SNe Ia) forment une classe d'objets homogènes. Elles ont en commun une évolution spectrale, la forme de leur courbe de lumière, et la magnitude absolue au maximum qui leur sont similaires. Les petites déviations qui sont observées peuvent être utilisées pour produire une "chandelle calibrée" dont la dispersion en magnitudes corrigées est même plus petite. L'existence de cet indicateur de distance intrinséquement brillant a inspiré deux recherches coordonnées de supernovae à grand z : le *Supernova Cosmology Project* et le *High-z Supernova Search Team.* Jusqu'à aujourd'hui $\sim$ 100 SNe Ia ont été découvertes par les deux équipes. L'analyse préliminaire des premiers de ces objets montre comment les SNe Ia peuvent être utilisées pour mesurer la densité de masse dans l'Univers Ω_M et la constante cosmologique normalisée $\Omega_\Lambda \equiv \Lambda/3H_0^2$.

Bruno Leibundgut : Décération cosmique mesurée en utilisant les supernovæ de type Ia.
Grâce à l'utilisation des supernovæ lointaines de type Ia, les paramètres cosmologiques peuvent être mesurés avec une précision sans égale.

LIST OF PARTICIPANTS

Hanadi ABDELSALAM
h.abdelsalam1@physics.oxford.ac.uk
Astrophysics laboratory
University of Oxford
Keble Road
OX1 3RH Oxford
UK

Andreas ALBRECHT
a.albrecht@ic.ac.uk
Theory Group - Blackett lab
Imperial College
Prince Consort Road
SW7 2BZ London
UK

Philippe AMRAM
amram@observatoire.cnrs-mrs.fr
Observatoire de Marseille
2 Place Le Verrier
13248 Marseille
France

Reza ANSARI
ansari@lal.in2p3.fr
LAL
Bât 200
Centre d'Orsay
91405 Orsay
France

Monique ARNAUD
arnaud@sapvxg.saclay.cea.fr
Service d'Astrophysique
CEA Saclay
Ormes des Merisiers
91191 Gif sur Yvette
France

Joanne BAKER
jcb@mrao.cam.ac.uk
Cavendish Laboratory
Madingley road
CB3 OHE Cambridge
UK

Jean BALLET
jballet@cea.fr
DSM/DAPNIA/SAP
CEA Saclay
BAT 709
91191 Gif sur Yvette
France

Rennan BARKANA
barkana@ias.edu
School of Natural Sciences
Institute for Advanced studies
NJ 08540 Princeton
USA

Rita Belen BARREIRO
barreiror@besaya.unican.es
Institute of Physics
Faculty of Sciences
Los Castros Avenue
S-39005 Santander
Spain

James BARTLETT
bartlett@astro.u-strasbg.fr
Observatoire Astronomique
11 rue de l'Université
67000 Strasbourg
France

Richard BATTYE
r.a.battye@damtp
DAMTP
University of Cambridge
Silver st
CB3 9EW Cambridge
UK

Florian BAUER
bauer@cdf.in2p3.fr
PCC - Collège de France
11 place Marcelin-Berthelot
75231 Paris
France

Francis BERNARDEAU
fbernard@spht.saclay.cea.fr
SPHT
CE de Saclay
91191 Gif sur Yvette
France

Jocelyn BEZECOURT
bezecour@astro.obs-mip.fr
Observatoire de Midi Pyrénées
10 avenue E. Belin
31400 Toulouse
France

Pierre BINETRUY
binetruy@qcd.th.u-psud.fr
LPTHE
Université Paris-Sud
Bat 210
91405 Orsay
France

Andrew BLAIN
awb@mrao.cam.ac.uk
Cavendish Laboratory
University of Cambridge
Madingley road
CB3 OHE Cambridge
UK

Alain BLANCHARD
blanchard@astro.u-strasbg.fr
Observatoire Astronomique
11 rue de l'Université
67000 Strasbourg
France

Katherine BLUNDELL
k.blundell1@physics.oxford.ac.uk
Astrophysics laboratory
University of Oxford
Keble Road
OX1 3RH Oxford
UK

Stefano BORGANI
borgani@pg.infn.it
INFN - Dept. of Physics
University of Perugia
Via A. Pascoli
I-06123 Perugia
Italy

François BOUCHET
bouchet@iap.fr
IAP
98bis boulevard Arago
75014 Paris
France

Jacques BOUCHEZ
bouchez@hep.saclay.cea.fr
DAPNIA-SPP
CEA Saclay
91191 Gif sur Yvette
France

Malcolm BREMER
bremer@iap.fr
IAP
98bis boulevard Arago
75014 Paris
France

Ram BRUSTEIN
ramyb@bgumail.bgu.ac.il
Department of Physics
Ben Gurion University
84105 Beer-Shiva
Israel

Ari BUCHALTER
ari@astro.columbia.edu
Department of Astronomy
Columbia university
550 West 120th Street
NY10027 New York
USA

Alessandra BUONANNO
buonanno@ihes.fr
IHES
Les Bois Maries
35 route de Chartres
91440 Bures-sur-Yvette
France

Carlo BURIGANA
burigana@tesre.bo.cnr.it
Institute TESRE
Via Gobetti 101
I-40129 Bologna
Italy

Claude CANIZARES
crc@space.mit.edu
Massachussets Institute
Center for space research
37241 - 70 Vassar Street
MA 02139 Cambridge
USA

Ray CARLBERG
carlberg@ociw.edu
Carnegie Observatories
813 Santa Barbara Street
CA 91101 Pasadena
USA

Sean CARROLL
carroll@itp.ucsb.edu
Theoretical Physics Institute
University of California
CA93106 Santa Barbara
USA

Francisco Javier CASTANDER

University of Chicago
5640 S Ellis Avenue
AAC
IL 60637 Chicago
USA

Marie-Noelle CELERIER
celerier@obspm.fr
Observatoire de Paris
5 place Jules Janssen
92195 Meudon
France

Maurice CHAPELLIER
chap@spec.saclay.cea.fr
SPEC - CE Saclay
91191 Gif sur Yvette
France

Michal CHODOROWSKI
michal@camk.edu.pl
Copernicus Astronomical Center
Ul. Bartycka 18
00-716 Warsaw
Poland

Sarah CHURCH
sec@astro.caltech.edu
Institute of Technology
MS 59-33
CA91125 Pasadena
USA

Sergio COLAFRANCESCO
cola@coma.mporzio.astro.it
Observatory of Roma
Via del Osservatorio
Monteporzio Catone
00040 Roma
Italy

Stéphane COLOMBI
colombi@iap.fr
IAP
98bis boulevard Arago
75014 Paris
France

Catherine CRESS
cress@astro.columbia.edu
Astronomy Department
Columbia university
550 West 120th Street
NY10027 New York
USA

Youri DABROWSKI
youri@mrao.cam.ac.uk
Cavendish Laboratory
Mullard Radio Astronomy
Observatory
Madingley road
CB3 OHE Cambridge

Ruth DALY
daly@pupgg.princeton.edu
Department of Physics
Princeton University
NJ 08544 Princeton
USA

Thibault DAMOUR
damour@ihes.fr
IHES
35 Route de Chartres
91440 Bures-sur-Yvette
France

Paolo DE BERNARDIS
paolo.de bernardis@roma1.infn.it
Univ. Roma 1 "La Sapienza"
Piazale Aldo Moro 2
I-00185 Roma
Italy

Gianfranco DE ZOTTI
dezotti@pdmida.pd.astro.it
Observatory of Padova
Vicolo dell'osservatorio 5
I-35122 Padova
Italy

Nathalie DELABROUILLE
nathalie@hep.saclay.cea.fr
CEA/DAPNIA/SPP
Bât 141
91440 Gif sur Yvette
France

Jacques DELABROUILLE
jacques.delabrouille@ias.fr
IAS
Université Paris XI
Bât 121
91405 Orsay Cedex
France

Jose Maria DIEGO
diegoj@besaya.unican.es
Instituto de Fisica de Cantabria
Faculdad de Ciencias
Avenida de los Castros
39005 Santander
Spain

George DJORGOVSKI
george@oracle.caltech.edu
CALTECH
MS105-24
CA91125 Pasadena
USA

Hervé DOLE
dole@ias.fr
IAS
Université Paris Sud
Bât 121
91405 Orsay
France

Marian DOUSPIS
douspis@wirtz.u-strasbg.fr
Observatoire de Strasbourg
11 rue de l'Université
67000 Strasbourg
France

Jacques DUMARCHEZ
jacques.dumarchez@cern.ch
LPNHE
University Paris VI and VII
Tour 33 - 4 place Jussieu
75252 Paris
France

Simon DYE
sd@roe.ac.uk
Institute for Astronomy
Royal Observatory of Edinburgh
Blackford Hill
EH93HJ Edinburgh
UK

William FORMAN
wrf@cfa.harvard.edu
Smithsonian Observatory
60 Garden Street
MA 02138 Cambridge
USA

Katherine FREESE
ktfreese@umich.edu
Physics Department
University of Michigan
MI 48109 Ann Arbor
USA

Yasunori FUJII
fujii@handy.n-fukushi.ac.jp
Nihon fukushi University
Higashi-Haemi-cho
475-0012 Handa
Japan

Alejandro GANGUI
gangui@obspm.fr
DARC
Observatory of Paris Meudon
92195 Meudon
France

Juan GARCIA-BELLIDO
bellido@mail.cern.ch
TH Division
CERN
CH 1211 Genève 23
Switzerland

Laurent GAUTRET
gautret@mesiom.obspm.fr
DEMIRM - Observatoire de Paris
61 avenue de l'Observatoire
75014 Paris
France

Yannick GIRAUD-HERAUD
ygh@cdf.in2p3.fr
PCC - Collège de France
11 place Marcelin-Berthelot
75231 Paris
France

Keith GRAINGE
kjbg1@mrao.cam.ac.uk
Cavendish Laboratory
Madingley road
CB3 OHE Cambridge
UK

Jean-Christophe HAMILTON
hamilton@cdf.in2p3.fr
PCC - Collège de France
11 place Marcelin-Berthelot
75231 Paris
France

Andrew J.S. HAMILTON
ajsh@dark.colorado.edu
JILA
Box 440
University of Colorado
CO 80309 Boulder
USA

Frode HANSEN
f.k.hansen@astro.uio.no
Theoretical Astrophysics Institute
PO box 1029
N-0315 Oslo
Norway

Delphine HARDIN
hardin@hep.saclay.cea.fr
CEA/DAPNIA/SPP
91191 Gif sur Yvette
France

Philip HELBIG
p.helbig@jb.man.ac.uk
Nuffield Laboratories
University of Manchester
Jodrell Bank
SK11 9DL Cheshire
UK

SuneHERMIT
sune@astro.ku.dk
Astronomical Observatory
Juliane Maries Vej 30
DK-2100 Kbh
Denmark

Michael HOBSON
mph@mrao.cam.ac.uk
Cavendish Laboratory
Madingley road
CB3 0HE Cambridge
UK

Richard HOLMAN
holman@cmuhep2. phys.cmu.edu
Carnegie Mellon University
5000 Forbes Avenue
PA 15213 Pittsburg
USA

Bhuvnesh JAIN
bjain@pha.jhu.edu
John Hopkins University
Department of Physics
520 Bloomberg Bdg
MD 21218 Baltimore
USA

Norman JAROSIK
jarosik@pupgg.princeton.edu
Department of Physics
25D Jadwin Hall
Princeton University
NJ 08544 Princeton
USA

Michael JONES
mike@mrao.cam.ac.uk
Cavendish Laboratory
University of Cambridge
Madingley road
CB3 OHA Cambridge
UK

Christine JONES
cjf@cfa.harvard.edu
Smithsonian Observatory
60 Garden Street
MA 02138 Cambridge
USA

Marc KAMIONKOWSKI
kamion@phys.columbia.edu
Columbia university
Department of Physics
538 West 120th Street
NY 10027 New York
USA

Alex KIM
kim@cdf.in2p3.fr
PCC - Collège de France
11 place Marcelin-Berthelot
75231 Paris
France

Rita KIM
kim@iap.fr
IAP
98bis boulevard Arago
75014 Paris
France

Morvan LE DOUR
ledour@astro.u-strasbg.fr
Observatoire Astronomique
11 rue de l'Université
67100 Strasbourg
France

Brian MASON
mason@cosmo.physics.upenn.edu
Dpt. of Physics and Astronomy
209 S - 33rd Street
PA19104-6396 Philadelphia
USA

William KINNEY
kinneyw@fnal.gov
FERMILAB
NASA
MS209
IL 60510-0500 Batavia
USA

Bruno LEIBUNDGUT
bleibundgut@eso.org
ESO
Karl Schwarzschild Strasse 2
D-85748 Garching
Germany

Pasquale MAZOTTA
mazzotta@roma2.infn.it
Department of Physics
University "Tor Vergata"
Via Ricerca Scientifica
00133 Roma
Italy

Chris KOCHANEK
ckochanek@cfa.harvard.edu
Harvard-Smithonian Center
Garden Street 60 - MS51
MA 02138 Cambridge
USA

Martin LEMOINE
lemoine@oddjob.uchicago.edu
DARC
CNRS - Observatoire de Paris
92195 Meudon
France

Yannick MELLIER
mellier@iap.fr
IAP
98bis boulevard Arago
74014 Paris
France

Edward KOLB
rocky@rigoletto.fnal.gov
FERMILAB
Astrophysics Department
MS209
IL 60510-0500 Batavia
USA

Julien LESGOURGUES
lesgourg@astro.phys.univ-tours.fr
Lab. de Physique théorique
Faculté des Sciences
Parc de Grandmont
37000 Tours
France

Ben METCALF
bmetcal@physics.berkeley.edu
Dpt. of Physics and Astronomy
University of California
752 Campbell Hall
CA 84720 Berkeley
USA

Andrew LANGE
ael@astro.caltech.edu
CALTECH
CA 91125 Pasadena
USA

Andrew LIDDLE
a.liddle@sussex.ac.uk
Astronomy centre
University of Sussex
BN2 2UX Brighton
UK

Marc MONIEZ
moniez@lal.in2p3.fr
LAL
Bat 200
Centre d'Orsay
91405 Orsay
France

David LANGLOIS
david.langlois@obspm.fr
CNRS - Observatoire de Paris
Département d'astrophysique
92195 Meudon
France

Christophe MAGNEVILLE
cmv@hep.saclay.cea.fr
CEA/DAPNIA/SPP
91191 Gif sur Yvette
France

Adi NUSSER
adi@mpa-garching.mpg.de
Max Planck Institute
Karl-Schwarzschild St 1
D-85740 Garching
Germany

Anthony LASENBY
a.n.lasenby@mrao.cam.ac.uk
Cavendish Laboratory
MRAO
Madingley road
CB3 OHE Cambridge
UK

Jerome MARTIN
martin@edelweiss-obspm.fr
DARC
Observatory of Paris Meudon
UPR 176 - CNRS
92195 Meudon
France

Burt OVRUT
ovrut@ovrut.hep.upenn.edu
David Rittenhouse laboratory
Department of Physics
University of Pennsylvania
PA 19104 Philadelphia
USA

Thierry LASSERRE
lasserre@hep.saclay.cea.fr
CEA/DAPNIA/SPP
Bat 141 - Pièce 150
91191 Gif sur Yvette
France

Enrique MARTINEZ-GONZALEZ
martinez@ifca.unican.es
Instituto de Fisica de Cantabria
Avenida de los Castros
S-39005 Santander
Spain

Reynald PAIN
rpain@lpnas1.in2p3.fr
LPNHE
Université Paris VII
Tour 33 - 4 place Jussieu
75252 Paris
France

Ue-Li PEN
upen@cfa.harvard.edu
Harvard-Smithonian Center
Garden Street 60 - MS51
MA 02138 Cambridge
USA

Elena PIERPAOLI
pierpa@sissa.it
SISSA-ISAS
V-Beirut 2-4
I-34013 Trieste
Italy

Marguerite PIERRE
mpierre@cea.fr
Service d'Astrophysique
CE Saclay
91191 Gif sur Yvette
France

Pedro PINA AVELINO
pedro@astro.up.pt
Centro de Astrofisica
University of Porto
Rua del Campo Alegre 823
4150 Porto
Portugal

Santina PIRAINO
piraino@ifcai.pa.cnr.it
IFCAI CNR
University of Palermo
Via Ugo La Malfa N.153
I-90146 Palermo
Italy

Etienne POINTECOUTEAU
pointeco@cesr.fr
CESR
9 avenue du Colonel Roche
31028 Toulouse
France

Lucia Aurelia POPA
popal@cmb.ifa.ro
Institute for space Science
R76900 Bucarest
Romania

Simon PRUNET
prunet@ias.fr
IAS
Bat 121
Campus d'Orsay
91405 Orsay
France

Andreu RAIG
araig@mizar.am.ub.es
Department of Astronomy
University of Barcelona
Congost 25, PPAL 2
E-08024 Barcelona
Spain

Alexandre REFREGIER
refreg@astro.princeton.edu
Dept. of Astrophysics
Princeton University
Peyton Hall
NJ 08544 Princeton
USA

Benoît REVENU
revenu@cdf.in2p3.fr
PCC - Collège de France
11 place Marcelin-Berthelot
75231 Paris
France

Alain RIAZUELO
riazuelo@mesioq.obspm.fr
Observatoire de Paris
Département d'astrophysique
5 place Jules Jansen
92190 Meudon
France

Antonio RIOTTO
riotto@thphys.ox.ac.uk
Theory Division
CERN
CH-1211 Genève 23
Switzerland

Giuseppe ROMEO
gomero@udel.edu
Sharp Lab - S. College
University of Delaware
21286 Towson
USA

Mairi SAKELLARIADOU
mairi@amorgos.unige.ch
Dpt. de Physique théorique
Université de Genève
24 quai Ernest Ansermet
CH-1211 Genève 4
Switzerland

Jose-Luis SANZ
sanzj@besaya.unican.es
IFCA
Faculty of Sciences
Avenue de Los Castros
39005 Santander
Spain

Richard SAUNDERS
rdes@mrao.cam.ac.uk
Cavendish Laboratory
Cambridge University
Madingley road
CB3 0HE Cambridge
UK

Mikhail SAZHIN
sazhin@sai.msu.su
Sternberb Astronomical Institute
Moscow State University
Universitetsky pr 13
119899 Moscow
Russia

Christoph SCHMID
chschmid@itp.phys.ethz.ch
Institute for Theoretical Physics
ETH Honggerberg
CH-8093 Zurich
Switzerland

David SCIALOM
scialom@mesioq.obspm.fr
CNRS - Observatoire de Paris
Département d'Astrophysique
92195 Meudon
France

Uros SELJAK
useljak@cfa.harvard.edu
Harvard-Smithonian Center
Garden Street 60 - MS51
MA 02138 Cambridge
USA

Shiv SETHI
sethi@iap.fr
IAP
98bis boulevard Arago
75014 Paris
France

Tarun SOURADEEP
tarun@cita.utoronto.ca
Theoretical Astrophysics Institute
University of Toronto
60 St George street
ON M5S 3H8 Toronto
Canada

Suzanne STAGGS
staggs@pupgg.princeton.edu
Department of Physics
Princeton University
Jadwin Hall - PO box 708
NJ 08544-0708 Princeton
USA

Alexei STAROBINSKY
alstar@landau.ac.ru
Landau Institute
Russian Academy of Sciences
Kosygina 2
117940 GSP-1 Moscow
Russia

Helen TADROS
helent@astr.cpes.susx.ac.uk
School of chemistry
University of Sussex
BN1 9QH Brighton
UK

Jan TAUBER
jtauber@astro.estec.esa.nl
ESA - ESTEC
Astrophysics division
PO box 299
2201AZ Noordwijk
Netherlands

Brian TAYLOR
btaylor@astro.estec.esa.nl
ESA - ESTEC
Astrophysics division
2201AZ Noordwijk
Netherlands

Andy TAYLOR
ant@roe.ae.uk
Institute for Astronomy
Royal Observatory of Edinburgh
Blackford Hill
EH9 3HJ Edinburgh
UK

MaxTEGMARK
max@ias.edu
Institute for Advanced studies
Olden Lane
NJ 08540 Princeton
USA

Paolo TOZZI
tozzi@roma2.infn.it
Department of Physics
University "Tor Vergata"
Via Ricerca Scientifica
00133 Roma
Italy

Jean TRAN THANH VAN
tran@qcd.th.u-psud.fr
LPTHE
Université de Paris sud
Bât. 211
91405 Orsay Cedex
France

Catherine TURON
catherine.turon@obspm.fr
Observatoire de Paris
DASGAL/URA 335
92195 Meudon CEDEX
France

Jean-Philippe UZAN
uzan@mesiop.obspm.fr
DARC
CNRS - Observatoire de Paris
92195 Paris
France

Gabriele VENEZIANO
venezia@nxth04.cern.ch
CERN/TH
1211 Geneva 23
Switzerland

Fabrizio VILLA
villa@tesre.bo.cnr.it
CNR-TESRE
Via P. Gobetti 101
I-40129 Bologna
Italy

Nicola VITTORIO
vittorio@roma2.infn.it
Department of Physics
University "Tor Vergata"
Via Ricerca Scientifica
00133 Roma
Italy

Benjamin Dan WANDELT
wandelt@tac.dk
Theoretical Astrophysics Centre
Juliane Maries Vej 31
DK 2100 Copenhagen
Denmark

Jochen WELLER
j.weller@ic.ac.uk
Theorical Physics Group
Imperial College
Prince Consort Road
SW7 2BZ London
UK

Peter WIDERIN
widerin@itp.phys.ethz.ch
ETH
Hoenggerberg
8093 Zurich
Switzerland

Althea WILKINSON
aw@jb.man.ac.uk
Nuffield Laboratories
Jodrell Bank
Maclesfield
SK11 9DL Cheshire
UK

Achevé d'imprimer sur les presses de l'Imprimerie BARNÉOUD
B.P. 44 - 53960 BONCHAMP-LÈS-LAVAL